RESEARCH PAPERS

TECHNICAL BRIEFS

The ASME Journal of Turbomachinery is abstracted and indexed in the following:

Aluminum Industry Abstracts, Aquatic Science and Fisheries Abstracts, Ceramics Abstracts, Chemical Abstracts, Civil Engineering Abstracts, Compendex (The electronic equivalent of Engineering Index), Corrosion Abstracts, Current Contents, Ei EncompassLit, Electronics & Communications Abstracts, Energy Information Abstracts, Engineered Materials Abstracts, Engineering Index, Environmental Science and Pollution Management, Excerpta Medica, Fluidex, Fuel and Energy Abstracts, INSPEC, Index to Scientific Reviews, Materials Science Citation Index, Mechanical & Transportation Engineering Abstracts, Mechanical Engineering Abstracts, METADEX (The electronic equivalent of Metals Abstracts and Alloys Index), Metals Abstracts, Oceanic Abstracts, Pollution Abstracts, Referativnyi Zhurnal, Shock & Vibration Digest, Steels Alert

Influence of Thermodynamic Models in Two-Dimensional Flow Simulations of Turboexpanders

John Harinck
e-mail: j.harinck@tudelft.nl

P. Colonna
e-mail: p.colonna@tudelft.nl

Energy Technology Section,
Process and Energy Department,
Delft University of Technology,
Leeghwaterstraat 44,
2628 CA Delft, The Netherlands

A. Guardone
Dipartimento di Ingegneria Aerospaziale,
Politecnico di Milano,
Via La Masa 34,
20159 Milano, Italy
e-mail: guardone@aero.polimi.it

S. Rebay
Dipartimento di Ingegneria Meccanica,
Università di Brescia,
Via Branze 38,
25123 Brescia, Italy
e-mail: rebay@ing.unibs.it

This paper presents a quantitative comparison of the effect of using thermodynamic models of various degrees of complexity if applied to fluid-dynamic simulations of turboexpanders operated at conditions affected by strong real-gas effects. The 2D flow field of a standard transonic turbine stator is simulated using the state-of-the-art inviscid ZFLOW computational fluid-dynamic solver coupled with a fluid property library containing the thermodynamic models. The considered thermodynamic models are, in order of increasing complexity, the polytropic ideal-gas (PIG) law, the Peng–Robinson–Stryjek–Vera (PRSV) cubic equation of state, and the highly accurate multiparameter equations of state (MPEoSs), which are adopted as benchmark reference. The fluids are steam, toluene, and R245fa. The two processes under scrutiny are a moderately nonideal subcritical expansion and a highly nonideal supercritical expansion characterized by the same pressure ratio. Using the PIG model for moderately nonideal subcritical expansions leads to large deviations with magnitudes of up to 18–25% in density, sound speed, velocity, and total pressure loss, and up to 4–10% in Mach number, pressure, temperature, and mass flow rate. The PIG model applied to highly nonideal supercritical expansions leads to a doubling of the deviations' magnitudes. The advantage of the PIG model is that its computational cost is roughly 1/11 (or 1/3 if saturation-checks in the MPEoS are omitted) of the cost of the MPEoSs. For the subcritical expansion, adopting the physically more correct cubic PRSV model leads to comparatively smaller deviations, namely, <2% (toluene and R245fa) and <4% (steam) in all flow parameters, except for the total pressure loss error, which is comparable to that of the PIG model. The PRSV model is reasonably accurate even for the highly nonideal supercritical expansion, for which the errors are at most 4%. The computational cost of the PRSV model is roughly nine times higher than the cost of the PIG model (or twice as high if saturation-checks in the PRSV are omitted). Contrary to low-complexity fluids like water, for complex fluids like toluene and R245fa the deviations in density, speed of sound, and velocity ensuing from the use of the PIG model vary strongly along the isentropic expansions. This invalidates the approach commonly used in practice of correcting the PIG model with a properly chosen constant compressibility factor. [DOI: 10.1115/1.3192146]

1 Introduction

Turboexpanders are widely used in industry to expand high-pressure gas producing useful mechanical work. They can be found in the power, oil, gas, process and refrigeration industries. Examples of power applications are organic Rankine cycle (ORC) turbogenerators [1–4], which are rapidly spreading as energy converters for biomass fuels and low-grade heat (from geothermal or industrial waste heat sources). ORCs feature the same working principle as conventional steam power plants, except for the working fluid, which is formed by organic molecules. The choice of the fluid allows for the optimal design of the cycle and turbine, depending on the temperature of the heat source and the design power output [2]. In the low power range, steam turbines cannot attain the same level of efficiency of ORC turbines with the same level of technology.

In the oil and gas industries, high-pressure turboexpanders are used in cryogenic natural gas processing to condense and remove heavy hydrocarbons from natural gas streams. Given a certain pressure reduction, an almost isentropic expansion in a turboexpander allows for a lower temperature of the expanded gases than an isenthalpic expansion by means of a throttling valve (in which the refrigerating effect is caused by the Joule–Thompson effect). In addition, a turboexpander recovers some of the energy released

during expansion and converts it into power that is often used for recompression of the methane. Turboexpanders are typically used in large-capacity liquefaction plants with high feed gas pressures, where efficiency, compact plant layout, varying feed products, and a large amount of ethane recovery are desired [5].

Often the design and performance assessment of (turbo)expanders is based on computational fluid-dynamic (CFD) simulations employing the ideal-gas law to describe the fluid's thermodynamic properties. This choice is based on the assumption that the deviation of the real thermodynamic behavior from ideal-gas behavior is small, which should result in equally small deviations in the predicted flow field and calculated performance parameters. (Turbo)expanders in the aforementioned applications are, however, often operated at reduced pressures and temperatures (made dimensionless with the critical values of the fluid) close to and above unity [5]. They therefore operate, at least partly, in the dense-gas thermodynamic region where the ideal-gas law is a poor approximation of the true thermodynamic behavior. Using the ideal-gas assumption can in this case lead to inaccurate predictions of the flow structure and performance parameters of the (turbo)expander.

In the case of ORCs, for example, accurate thermodynamic models are required for both a correct cycle analysis and turboexpander design. This is exemplified by a study of a recently developed ORC turbogenerator with toluene as working fluid [6,7], whose cycle and turbine were designed using the most accurate thermodynamic model for the working fluid available at that time [8]. The prototype, however, showed a considerable deviation

from the calculated power output in design conditions. After analysis [9] using a more recent and accurate thermodynamic model of toluene [10], it became apparent that this was attributable to the inaccuracy of the original thermodynamic model, which, for the considered expansion, overpredicts the specific enthalpy and underpredicts the density both by as much as 6%. This deviation has in turn a significant effect on the fluid-dynamic design of the turbine.

The motivation for this study is the current potential for improvement of dense-gas (turbo)expander performance through fluid-dynamic design that properly takes into account the nonideal thermodynamic behavior of the fluid. This requires a better understanding of how the fluid dynamics deviates from ideal-gas fluid-dynamic behavior and of the capabilities and limitations of the available thermodynamic models if applied to fluid-dynamic simulations. This paper addresses this issue by studying the influence of real-gas thermodynamic models on the flow field and performance parameters.

Previous studies reported in literature have addressed real-gas effects in transonic and supersonic flows in the classical gas dynamic region. These studies focus on one-dimensional steady flows in simple geometries, for example, the one-dimensional converging-diverging nozzle [11], which allows for the use of analytical solutions. Others also studied two-dimensional flows of simple geometries, e.g., using linearized theory [12] or finite-volume (FV) numerical schemes for simple nozzle flows [13] and around simple airfoil geometries in cryogenic wind tunnels [14,15].

Practical simulations of real-gas flow through more complex two- and three-dimensional geometries have been conducted in the field of turbomachinery. Here, the need for simulating fluid-dynamic processes in the dense-gas region has lead to the interfacing of existing finite-volume CFD solvers with more accurate thermodynamic property data. Four different approaches can be distinguished: the direct analytical calculation from the equation of state for both primitive quantities and derivatives [16–18], the analytical calculation for primitive quantities and numerical differencing for derivatives [19], the interpolation of thermodynamic property data (look-up) tables [6,20,21], and the use of relatively simple polynomial functions that are fitted to these tables prior to the simulation [22,23]. The analytical calculation from the equation of state allows for the highest accuracy; however, the evaluation of derivatives and properties that are represented by the independent variables in the EoS can be computationally costly, in particular, when they are evaluated iteratively from complex EoSs. The two latter approximate methods, on the other hand, are simpler to implement and allow for property evaluation at limited extra cost with respect to the ideal-gas model case. Their disadvantage is their inherently lower accuracy due to the introduction of fitting or interpolation errors (see Refs. [20,21] for more details).

Numerous EoSs exist, which account for non-ideal-gas behavior with various degrees of accuracy. They range from cubic EoSs such as the van der Waals model [24] applied to fluid-dynamic simulations of nozzles in Refs. [13,25] and Redlich–Kwong/Peng–Robinson-type EoSs [26,27] used for nozzle [11,28] and turbomachinery simulations [19] to state-of-the-art multiparameter EoSs (MPEoSs) [29,30]. The functional form of a MPEoS is often specific for a single fluid or type of fluid and often highly complex (e.g., the MPEoS for water contains 51 terms [31]). This allows for accurate predictions of thermodynamic properties (in most cases within experimental data uncertainty) over the entire thermodynamic region and for some MPEoSs even close to the critical point. The validation of flow solvers linked to accurate thermodynamic models for simulations in the non-ideal-gas region is unfortunately hindered by a lack of experimental fluid-dynamic data in this region.

In the aforementioned real-gas studies, relatively simple EoSs or gas tables were adopted to model fluid properties and their

results were not compared to highly accurate predictions of fluid properties, since the latter have only recently become available for the fluids under scrutiny [29]. A study of the influence of thermodynamic models employed on the flow field and performance parameters as detailed in this paper calls for the use of MPEoSs as a reference because of their highly accurate predictions and validity. In Ref. [32], it is shown that, from a computational point of view, evaluating the fluid properties including analytical derivatives is more convenient than the use of numerical differencing formulas. The inclusion of highly accurate thermodynamic fluid models such as MPEoSs into CFD codes was made possible only lately [16] and consequently the thorough analysis that these simulation tools allow is a recent achievement.

As an exemplary case of a dense-gas turboexpander, this study considers the flow field generated by the expansion through a standard two-dimensional axial turbine stator blade profile designed for the transonic flow regime. Expansions in the dense-gas region are simulated for subcritical and supercritical inflow conditions, representing cases of moderate to high thermodynamic nonideality. The influence of the thermodynamic model and the molecular complexity of the fluid is analyzed based on blade surface distributions and integral performance parameters. The conclusions that are drawn can be used as guidance in the preliminary design phase of dense-gas expanders.

The fluids chosen for the comparison vary in molecular complexity and weight. They are steam, toluene, and refrigerant R245fa (HFC245fa), all expanded from the same reduced pressure and temperature. These fluids are currently used in power applications. In particular, both toluene and R245fa are used in ORCs. They are taken as examples of fluids of high molecular complexity. The influence of real-gas thermodynamic models is studied by comparing thermodynamic models that differ in complexity and accuracy. In other words, they vary in their ability to take into account nonideal thermodynamic behavior. Three thermodynamic models are selected, which represent the three most widely used types of thermodynamic models. The thermodynamic models employed are the polytropic (i.e., with constant isochoric specific heat) ideal-gas law (PIG), the Peng–Robinson (Stryjek–Vera modified) cubic equation of state (PRSV) [26,27], and state-of-the-art reference MPEoSs [29,30].

The effect of the different fluid models on the fluid dynamics and performance parameters is evaluated by comparing distributions of the Mach number, pressure coefficient, flow velocity, temperature, density along the blade, outlet flow angles, mass flows, and shock losses.

In Sec. 2, the novel Euler solver and the three thermodynamic models are briefly described. Section 2.3 presents the validation of the numerical scheme and demonstrates that grid convergence is obtained for the grid used in the comparison as well as that the solver and the method for evaluating the thermodynamic properties are validated for the transonic fluid-dynamic problem under consideration. Section 3 proceeds with the study of the effect of the thermodynamic models on the fluid-dynamic behavior, starting from subcritical inflow conditions to more nonideal supercritical inflow conditions, followed by the conclusions.

2 The Euler Solver and the Thermodynamic Models

2.1 The Euler Solver. Numerical solutions of the two-dimensional inviscid Navier–Stokes (Euler) equations are computed with the ZFLOW program [16,33–35], linked to a fluid property library containing several thermodynamic models and a large set of fluid data [36]. The main features characterizing the ZFLOW CFD code are briefly summarized. The solver uses a hybrid finite element (FE)/FV approach in which the finite-volume metric quantities are formulated based on the Lagrangian linear shape functions typically used in finite element methods [37]. The spatial approximation of the inviscid Navier–Stokes equations is constructed with a high resolution finite-volume method suitable for general unstructured and hybrid grids. The high resolution upwind

discretization is constructed based on the Roe approximate Riemann solver [38], generalized to the case of fluids characterized by arbitrary equations of state according to the method of Vinokur and Montagné [39]. This class of discretization schemes is particularly well suited to the computation of high Mach number flows. The use of unstructured grids allows for the straightforward treatment of domains of arbitrarily complex geometry. Another important feature of ZFLOW is represented by the adopted implicit time integration scheme, which computes steady state solutions in a much more efficient way with respect to conventional explicit schemes. The gain in computational efficiency is crucial when complex EoSs are needed for an accurate flow simulation. The ZFLOW solver has been successfully validated for ideal-gas simulations (see, e.g., Refs. [16,33]) and validation on a nonideal process is planned. The extension of ZFLOW to the viscous Reynolds-averaged Navier–Stokes (RANS) equations will be documented soon.

2.2 The Thermodynamic Models. The CFD code ZFLOW is linked to a rich thermodynamic library for the calculation of properties of pure fluids and mixtures, which has been extended to include the particular (secondary) thermodynamic functions required by the implicit upwind flow solver [32]. The software library [36,40,41] contains, amongst others, a cubic EoS and various state-of-the-art multiparameter EoSs, e.g., Martin–Hou [42], Benedict–Webb–Rubin, Span–Wagner [43,44], and Starling [45] MPEoSs (TPSI, REFPROP [40]). The thermodynamic properties required by ZFLOW, including derivatives, are efficiently computed from their analytical expressions [16].

In this study, the thermodynamic behavior of the fluid is modeled with three types of EoSs that differ in complexity and accuracy: the PIG model, the PRSV cubic EoSs, and very accurate state-of-the-art MPEoSs.

2.2.1 Polytropic Ideal-Gas Law. The PIG law model is given by the pressure equation supplemented by the ideal-gas isobaric specific heat:

$$P = \frac{RT}{v}, \quad C_P^0 = \frac{\gamma R}{\gamma - 1} \tag{1}$$

where P is the pressure, T is the temperature, and v is the specific volume. R is the specific gas constant, which is defined as $R = \bar{R}/M$, where M is the molecular weight and $\bar{R} = 8.314$ J/mol K^{-1} is the universal gas constant. γ denotes the ratio of the isobaric to the isochoric specific heat, $\gamma \equiv C_P^0 / C_v^0$, where C_P^0 and C_v^0 are the ideal-gas isobaric and isochoric heat capacities, respectively. The ratio γ is constant under the polytropic assumption considered here and according to the energy equipartition theory bounded by $1 < \gamma \leq 5/3$.

2.2.2 Peng–Robinson–Stryjek–Vera EoS. Compared to the polytropic ideal-gas EoS (1), a cubic EoS allows for more accurate predictions in the dense-gas region and states close to the saturation line. Its accuracy is usually sufficient for the design and analysis of many technical applications. Moreover, its simple form requires limited input information, i.e., limited knowledge of the thermodynamic properties of the fluid, and can be easily extended to multicomponent fluids by means of theoretically correct mixing rules [27,32,46–48]. However, it is still inherently inaccurate near the critical point (i.e., $P/P_c \gtrsim 0.9$) and on the liquid side at high reduced temperatures.

The PRSV [27] cubic EoS is of the form

$$P = \frac{RT}{(v - b)} - \frac{a(T)}{v(v - b) + b(v - b)} \tag{2}$$

where a and b are the coefficients of the contributions of, respectively, the attractive and short-range repulsive intermolecular forces. In the Stryjek–Vera modification [27] of the Peng–Robinson EoS, the temperature-dependent term $a(T)$ is dependent

on a parameter denoted by k_1 [27] and the acentric factor ω. The new functional form has allowed the extension of the range of applicability of the EoS to the low reduced temperature region ($T/T_c \lesssim 0.7$) as well as to polar fluids. The main feature is that it allows for vapor-pressures estimates accurate within 2% of the experimental data. This reflects in an improved prediction performance of superheated vapor thermodynamic properties in the region adjacent to the saturation curve.

For the calculation of all caloric properties, the PRSV EoS (2) is supplemented by the ideal-gas contribution to the specific heat at constant pressure, which has been approximated here as a polynomial function of the temperature [49]:

$$C_P^0(T) = A + BT + CT^2 + DT^3 \tag{3}$$

2.2.3 Multiparameter EoS. The increased number of parameters in MPEoSs allows for accurate computations of all relevant thermodynamic properties, with the highest possible accuracy, which is required for the design and analysis of advanced technical applications as well as scientific purposes. After the initial development of MPEoSs for classes of fluids in the 1970s, the state of the art has become the MPEoSs formulated in terms of reduced Helmholtz energy, of which both the functional form and the parameters are optimized on experimental data, resulting in an EoS that is highly accurate. The functional form of these MPEoS can be substance specific or it can be tailored to a specific class of substances, such as the Starling EoS for light hydrocarbons [45]. For pure substances, Helmholtz-based MPEoSs can be classified into empirical reference EoSs and technical EoSs. The basic idea behind the concept of *reference EoS* is that a single equation should be able to describe all experimental thermodynamic property data available for a certain fluid within their experimental uncertainty. Reference EoSs therefore have a substance-specific functional form and are developed using thoroughly assessed experimental data for which only the most accurate and reliable data are chosen. In this way, the EoS itself can be used as a reference for all thermodynamic properties over the entire thermodynamic range, even in the close proximity of the critical point [30], like the Wagner–Pruss EoS for water [31], for which the uncertainties in the vapor phase are less than 0.1% and 0.2% for volumetric and caloric properties, respectively. For the calculation of all caloric properties, the MPEoSs used in this study are supplemented by the ideal-gas contribution to the specific heat at constant pressure that has been determined together with the MPEoSs [10,31].

2.3 ZFLOW Validation: Simulation of the Ideal-Gas Flow Around the VKI LS-89 Blade. In this section, the ZFLOW solver linked to the accurate thermodynamic model is validated for the transonic fluid-dynamic problem considered in this study, in which the expansion occurs at ideal-gas conditions. The validation of the flow solver coupled with the thermodynamic models for simulations in the real-gas region is unfortunately hindered by a lack of experimental fluid-dynamic data in this region. This is planned for the near future. Nonetheless, the validation of the solver linked to the accurate thermodynamic models for expansions at ideal-gas conditions, together with the validated high accuracy of all thermodynamic models even at strongly nonideal conditions (see Sec. 2.2.3), warrants the validity of the simulations of real-gas flows presented in this study.

The ZFLOW code is validated by comparing the results of simulations to the measurements of two well-known and reliable turbomachinery test cases [50] for dry air at ideal-gas conditions. In both test cases, the geometry is the VKI LS-89 blade, which is a standard high-pressure turbine nozzle guide vane, mounted in a linear cascade. The first test case (MUR43) is at subsonic flow conditions (Ma$_{is}$=0.84), while the second test case (MUR49) is at transonic flow conditions (Ma$_{is}$=1.02). The isentropic Mach number Ma$_{is}$ is the Mach number observed in case shock losses would be absent. The conditions are given in Table 1. The thermodynamic properties are calculated with a 19-parameter reference

Table 1 Test case conditions from Ref. [50]

|		MUR43	MUR49
Total inlet pressure	P_{01}, bar	1.435	1.608
Pressure ratio	P_{01}/P_2	1.587	1.938
Total inlet temperature	T_{01}, °C	146.85	146.85
Compressibility factor at inlet	Z_1	1	1
Static outlet pressure	P_2, bar	1.333	2
Isentropic Mach number at outlet	$Ma_{2,is}$	0.84	1.02

equation of state [51]. Even though such an equation of state is unnecessary given the ideal-gas conditions of the simulations, the results verify the correct implementation of such complex thermodynamic models in the software.

All flow solutions have converged up to at least a reduction of five orders of magnitude measured in the L^2-norm of the conserved variables. The Mach number distribution along the blade surface obtained from the inviscid computation is compared to the experimental data of the test cases.

The periodic grid is generated in a transformed domain, in which periodic boundaries are mapped into internal curves to simplify the task of obtaining periodic nodes [52]. In the transformed space, the grid is generated by the front-advancing/Delaunay method [53] and then transformed back into the physical space of XY-coordinates by introducing a suitable cut. This translates into
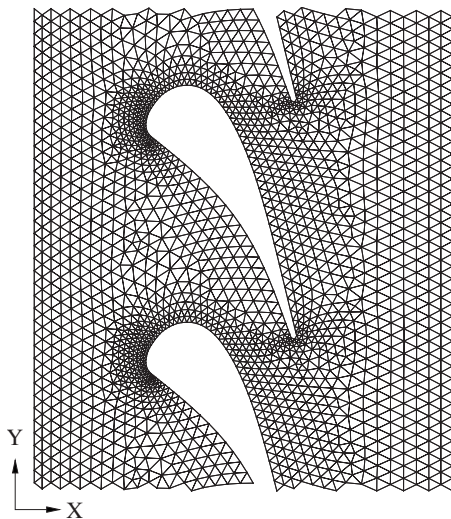
Fig. 1 Coarse grid (1302 nodes) of the VKI LS-89 blade. Periodicity allows the computations to be performed using only the top half of the grid shown here.
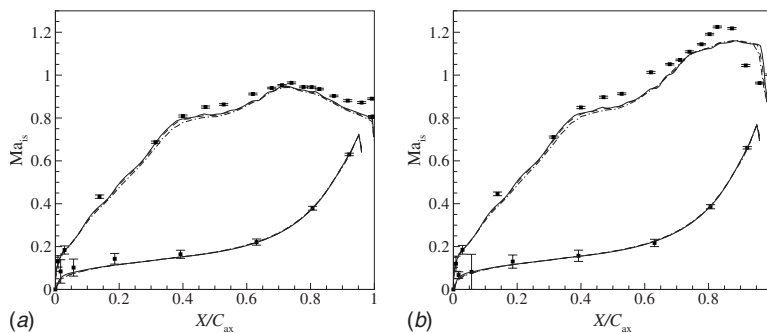
the sawlike edge of the periodic boundaries shown in Fig. 1. A sharp trailing edge is adopted to ensure correct trailing edge flow separation simulated with the inviscid solver.

In order to determine the error due to the discretization, a grid convergence study is performed by computing the solution on three increasingly finer grids using the accurate MPEoSs. The fine grid and the coarse grid are generated by, respectively, halving and doubling the number of grid elements with respect to the initial grid. The coarse grid consists of 1302 nodes and 2032 elements, the medium grid consists of 2383 nodes and 3958 elements, and the fine grid consists of 4153 nodes and 7184 elements. Figure 1 shows the coarse grid and the blade geometry. The lines in Figs. 2(a) and 2(b) show the Mach number distributions for the MUR43 and MUR49 test cases, respectively, solved on the coarse, medium, and fine grids. They are plotted as a function of the reduced coordinate X/C_{ax}, where X is the axial coordinate and C_{ax} is the axial blade chord. From this result, it appears that the computed solution on the fine grid is sufficiently grid independent. The fine grid is therefore used for all subsequent simulations. Grid convergence was similarly checked for the subsequent simulations with steam, toluene, and R245fa presented hereafter.

The ZFLOW code is validated for this transonic fluid-dynamic problem by comparing the numerical solution to the experimental data of the test case, given in Ref. [50]. The static pressure measurement data have an uncertainty of 0.5%, leading to uncertainties in the isentropic Mach number as indicated by the error bars in Fig. 2. In general, the numerical results show a good agreement with the experimental results for both test cases. A discrepancy is, however, observed for the suction side, where the numerical values fall outside of the experimental uncertainty range. In the MUR49 transonic test case (Fig. 2(b)), the location of the shock wave that terminates the supersonic region is predicted by ZFLOW to be at the end of the blade profile ($X/C_{ax}=0.95$), whereas the measurements indicate that the shock wave is further upstream ($X/C_{ax}=0.88$). This could be the result of the inability of the inviscid solver to simulate shock-boundary layer interaction. Still, the difference is small and the agreement is deemed satisfactory.

3 The Effect of the Thermodynamic Model on the Flow

The effect of the thermodynamic model on the flow field generated by an axial turboexpander is studied for three different fluids and two different process conditions. This is done using the geometry of the VKI LS-89 turbine stator and the pressure ratio of the MUR49 transonic expansion case used in the validation of Sec. 2.3. The pressure ratio is in the same range ($P_{01}/P_2<5$) as the majority of axial reaction turboexpanders [5]. For each fluid, the simulations employing the accurate predictions from the MPEoSs are used as a reference with which the simulations em-

Fig. 2 Mach number distribution for the MUR43 test case (a) and the MUR49 test case (b). Shown are the experimental measurements (■) from Ref. [50] and the numerical solution on the coarse grid (·····), the medium grid (— — —), and the fine grid (—).

Table 2   Fluid properties and EoS parameters

Fluid		Steam	Toluene	R245fa
Chemical formula		H_2O	C_7H_8	$CF_3CH_2CHF_2$
Molecular weight	M, g/mol	18	92.1	134.1
Fundamental derivative	Γ^V_{min}	0.524	0.004	0.119
Critical pressure	P_c, bar	220.6	41.3	36.4
Critical temperature	T_c, °C	374	318.6	154.1
PIG parameter in Eq. (1)	γ	1.2912	1.0447	1.0608
PRSV parameters in Eq. (2)	k_1	−0.0664	0.0385	0.0060
	ω	0.3438	0.2632	0.3724
MPEoS parameters		[31]	[10]	[10]
Isobaric specific heat coefficients in Eq. (3)	A	32.2	−24.35	226.85
	$B \cdot 10$	1.92	512.5	28.16
	$C \cdot 10^3$	10.6	−276.5	335.45
	$D \cdot 10^6$	−3.6	49.11	−144.21

ploying the other EoSs are compared. The three selected fluids are water, toluene, and R245fa (HFC245fa) because these molecules are representatives of a wide range of molecular complexities and also because they are used in practice as working fluids in Rankine power cycles and refrigeration cycles. The fluid-specific parameters in the three EoSs are given in Table 2.

The reference MPEoS used for steam is the IAPWS-95 formulation, which is in the form of a fundamental equation explicit in the Helmholtz free energy with 51 terms [31]. In the vapor region that is of interest in this study, the uncertainties are less than 0.1% and 0.2% for volumetric and caloric properties, respectively. The short (12-term) nonpolar Helmholtz equation of state is adopted for toluene [10]. This MPEoS was recently developed for technical applications by optimization to a specific class of nonpolar or slightly polar fluids [43]. The coefficients of these short forms for the equations of state were fitted to substance-specific data [10]. Although this new technical equation suffers from a slight loss in accuracy compared to a MPEoS whose functional form is optimized for a specific fluid, their shorter forms allow for faster computations. For the determination of thermodynamic properties of R245fa, the polar version of the 12-term MPEoS as described in Ref. [10] is used. The MPEoSs for toluene and R245fa in the vapor region that are of interests in this study have estimated uncertainties of less than 1% and 2% for volumetric properties and caloric properties, respectively.

The critical data, acentric factor, and values of the k_1 parameter in the PRSV EoS are taken from Ref. [27]. The relation for the ideal-gas contribution to the isobaric specific heat, C_P^0, used together with the PRSV EoS, is given in Eq. (3). The coefficients for steam and toluene, given in Table 2, are taken from Ref. [49]. For the refrigerant R245fa, they have been determined by fitting Eq. (3) to data obtained using the accurate MPEoS model. In the temperature range of interest, the average absolute deviations of the ideal-gas specific heat relation with respect to those used in the MPEoS models are 0.28%, 0.79%, and 0.08% for steam, toluene, and R245fa, respectively.

For the PIG model, the choice of the ideal-gas isobaric specific heat, C_P^0, in Eq. (1), determines the caloric behavior of the fluids and therefore affects their fluid-dynamic behavior if the PIG model is used to compute the thermodynamic properties [54,55]. A correct value for C_P^0 must be chosen in order to ensure a fair comparison with the simulations employing more complex thermodynamic models. In this work, C_P^0 is evaluated at the critical temperature, i.e., $C_P^0 = C_P^0(T_c)$, since both the subcritical and the supercritical expansion occur close to the critical temperature, as is evident from Table 3. It is common practice in turbomachinery design to use an averaged ideal-gas isobaric specific heat, e.g., obtained by integration between the temperatures representative of the expansion [55], i.e.,

$$\bar{C}_P^0 = \frac{1}{T_2 - T_{01}} \int_{T_{01}}^{T_2} C_P^0(T) dT \qquad (4)$$

For the fluids and temperatures considered here, the resulting value of $\bar{C}_P^0$ is very close to $C_P^0(T_c)$ adopted in this study. For water, the values are 2051 $J/mol\,K^{-1}$ and 2054 $J/mol\,K^{-1}$. Furthermore, a comparison showed that $C_P^0(T_c)$ leads to a slightly better agreement of the computational results obtained with the PIG model with those obtained with the accurate MPEoS. To ensure a comparison between the thermodynamic models that is as fair as possible, it was decided to evaluate C_P^0 at the critical temperature.

To investigate the influence of the EoSs on the flow parameters of real-gas expansions, two expansions in the dense-gas region are simulated, for which the inlet pressure and temperature are at higher reduced values in comparison with the validation case. The two expansions start from subcritical and supercritical inflow conditions, representing cases of moderate to high thermodynamic nonideality, respectively. Figure 3 compares the subcritical process in the temperature-entropy diagram for the three considered fluids. It should be noted that the blade shape is designed for ideal-gas flows and it is therefore not expected to perform the same as for ideal-gas conditions.

3.1   Subcritical Inflow Conditions. Subcritical inlet flow conditions are first considered. The process conditions used for all three fluids are given in reduced terms in Table 3. For each fluid, the resulting dimensional process conditions are given in Table 4. The compressibility factor, defined as $Z \equiv (Pv)/(RT)$, is identically equal to unity for an ideal gas; it is therefore often used to quantify the nonideality of a thermodynamic state. In this case, the compressibility factor is approximately 0.9 for both the inlet and outlet states and this indicates that they are both mildly nonideal.

Apart from assessing the magnitude of the difference in the flow parameters for the different EoSs, it is also shown how the former relate to the differences between the predictions of thermodynamic properties. The differences in the most relevant thermodynamic properties density and sound speed are determined

Table 3   Process conditions for the considered simulations in terms of reduced variables

		Subcritical	Supercritical
Reduced total inlet pressure	P_{01}/P_c	0.7	1.05
Reduced total inlet temperature	T_{01}/T_c	1.1	1.05
Pressure ratio	P_{01}/P_2	1.938	1.938
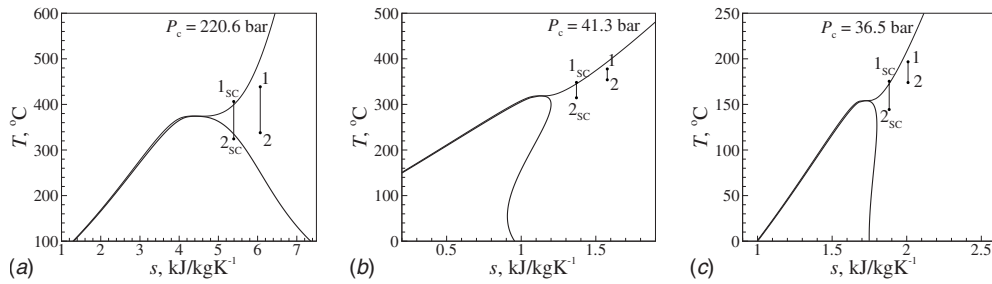
Fig. 3 Representation of the six expansion processes considered in this work in the temperature-specific entropy diagrams of (a) steam , (b) toluene, and (c) R245fa. The inlet conditions are the same in terms of reduced temperature and pressure. For each fluid, one expansion starts from a supercritical state (denoted by 1_{SC} on the diagram) and the other from a subcritical state (1).

and plotted in Fig. 4 as function of pressure (from outlet to inlet pressure) at the isentrope along which the subcritical expansion takes place. Here, the MPEoS is again used as a reference to estimate the deviation with respect to the PIG and PRSV models.

3.1.1 Steam. A computation on the fine grid using the accurate MPEoS is used to investigate the flow field of the expansion process at subcritical operation. The two-dimensional flow field is visualized in Figs. 5(a) and 5(b) by displaying, respectively, the variation in Mach numbers and pressure coefficients, as defined in Eq. (3), with streamlines throughout the blade passage. Figure 5(c) shows the Mach number flow field based on the PIG model. From the inflow boundary on the left hand side of the domain, the fluid accelerates through the passage formed by the stator blade cascade to supersonic velocities (Fig. 5(a)). At the blade's trailing edge, a shock wave can be observed, which terminates the supersonic region. The numerical solution shows an unphysical over-expansion region at the trailing edge, since the actual turbulent trailing edge wake cannot be described by the Euler equations.

The pressure coefficient, shown in Fig. 5(b), decreases as the flow expands and increases across the shock wave.

The Mach number distribution along the blade surface is given in Fig. 6(a). The line that indicates early expansion (with a maximum in the Mach number) pertains to the suction side of the blade, the line with retarded expansion to the pressure side. Close to the trailing edge, the distribution is locally obscured by non-physical overexpansion and dissipation at the trailing edge flow due to the assumption of inviscid flow and is therefore for the larger part not visualized in the figures. At the location X/C_{ax} =0.64 and 0.70, the Mach number distribution of the suction side does not vary smoothly, indicating irregular expansion. The Mach number distribution appears surprisingly similar for all EoS models. Figure 7(a) reveals that the difference in Mach number due to the use of the PIG model with respect to the reference model is approximately 2%, while it is approximately 3% if the PRSV model is employed (not taking into account the high error near the trailing edge, which is a result of nonphysical overexpansion).

Table 4   Parameters characterizing the expansion processes depicted in Fig. 1

		Subcritical			Supercritical		
		Steam	Toluene	R245fa	Steam	Toluene	R245fa
Total inlet pressure	P_{01}, bar	154.5	28.9	25.5	231.7	43.3	38.2
Total inlet temperature	T_{01}, °C	438.7	377.8	196.8	406.3	348.2	175.4
Compressibility factor at inlet	Z_1	0.81	0.79	0.81	0.58	0.57	0.60
Static outlet pressure	P_2, bar	79.7	14.9	13.2	119.5	22.4	19.8
Compressibility factor at outlet	Z_2	0.83	0.88	0.88	0.59	0.88	0.89
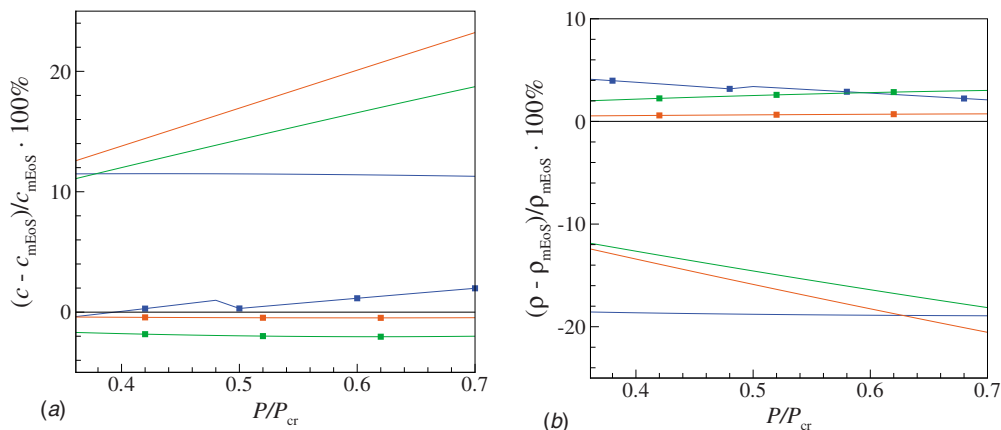
Fig. 4 Percentage difference of thermodynamic properties (a) sound speed and (b) density along the subcritical expansion isentrope computed based on the PRSV model (■) and the PIG model (no symbol) with respect to the values computed based on the MPEoS. Results are given for steam (blue line), toluene (red line), and R245fa (green line). (Color representation of this figure is available at ASME.org)
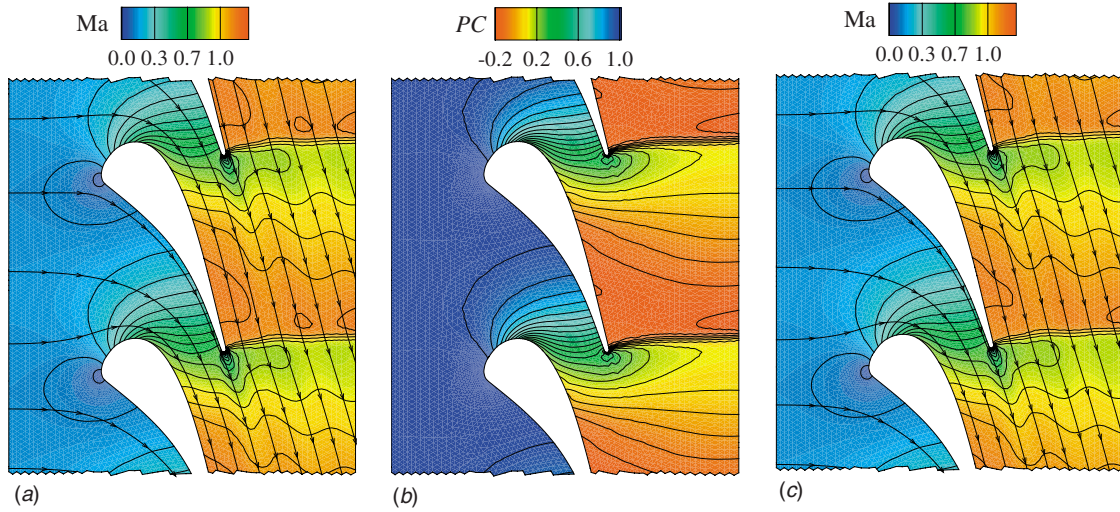
Fig. 5 Flow field distributions of steam: (*a*) **Mach number and** (*b*) **pressure coefficient distribution and streamlines based on the MPEoS;** (*c*) **Mach number distribution and streamlines based on the PIG model**

The distribution of the pressure coefficient defined as

$$PC = \frac{P - P_2}{P_{01} - P_2} \qquad (5)$$

where P_{01} is the total inlet pressure and P_2 is the static outflow pressure, is shown in Fig. 6(*b*). Its trend is opposite to that of the

Mach number. Note that the same pressure values are prescribed at the inflow and outflow boundaries for all EoSs. The PIG and PRSV models both compute the pressure along the blade profile with an accuracy of 1%, as shown in Fig. 7(*b*). The differences in the predictions of density, sound speed, and isochoric specific heat are shown in Fig. 2 as a function of the pressure. Consequently,
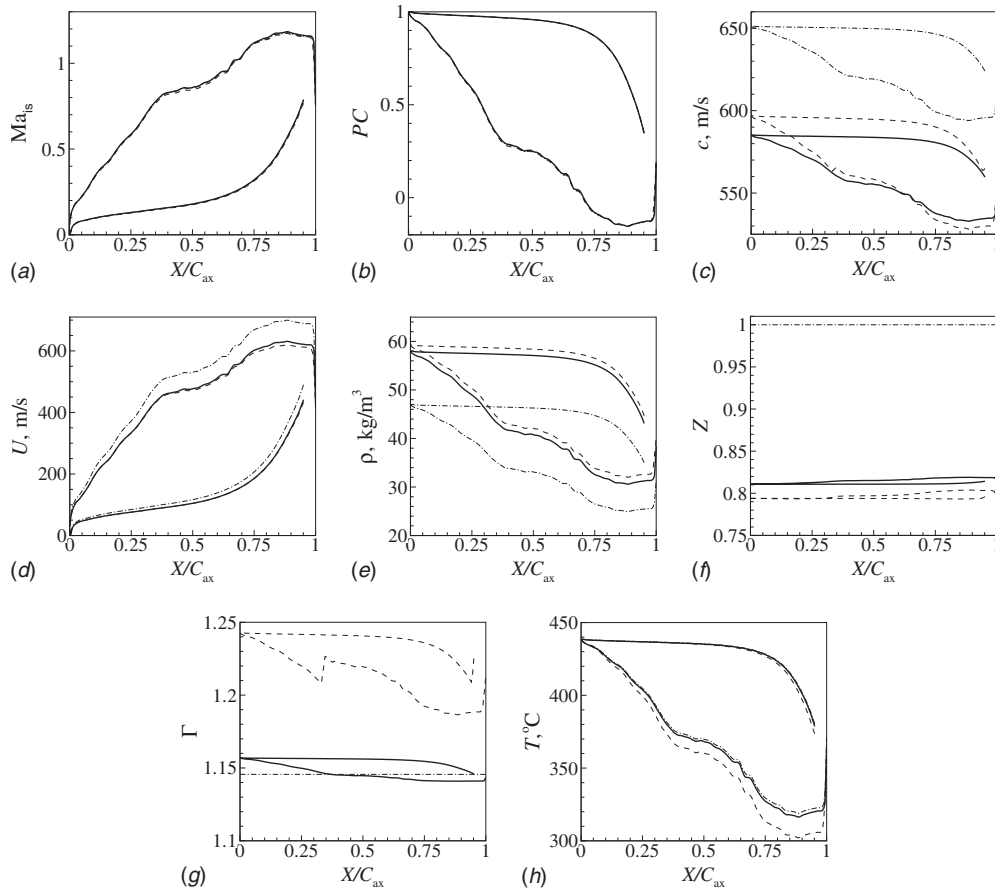
Fig. 6 Blade surface distributions for steam of (*a*) **the isentropic Mach number,** (*b*) **pressure coefficient,** (*c*) **sound speed,** (*d*) **velocity,** (*e*) **density,** (*f*) **compressibility factor,** (*g*) **fundamental gasdynamic derivative, and** (*h*) **temperature, computed based on the MPEoS (—), PRSV (- - -), and PIG (-·-·-·) model**
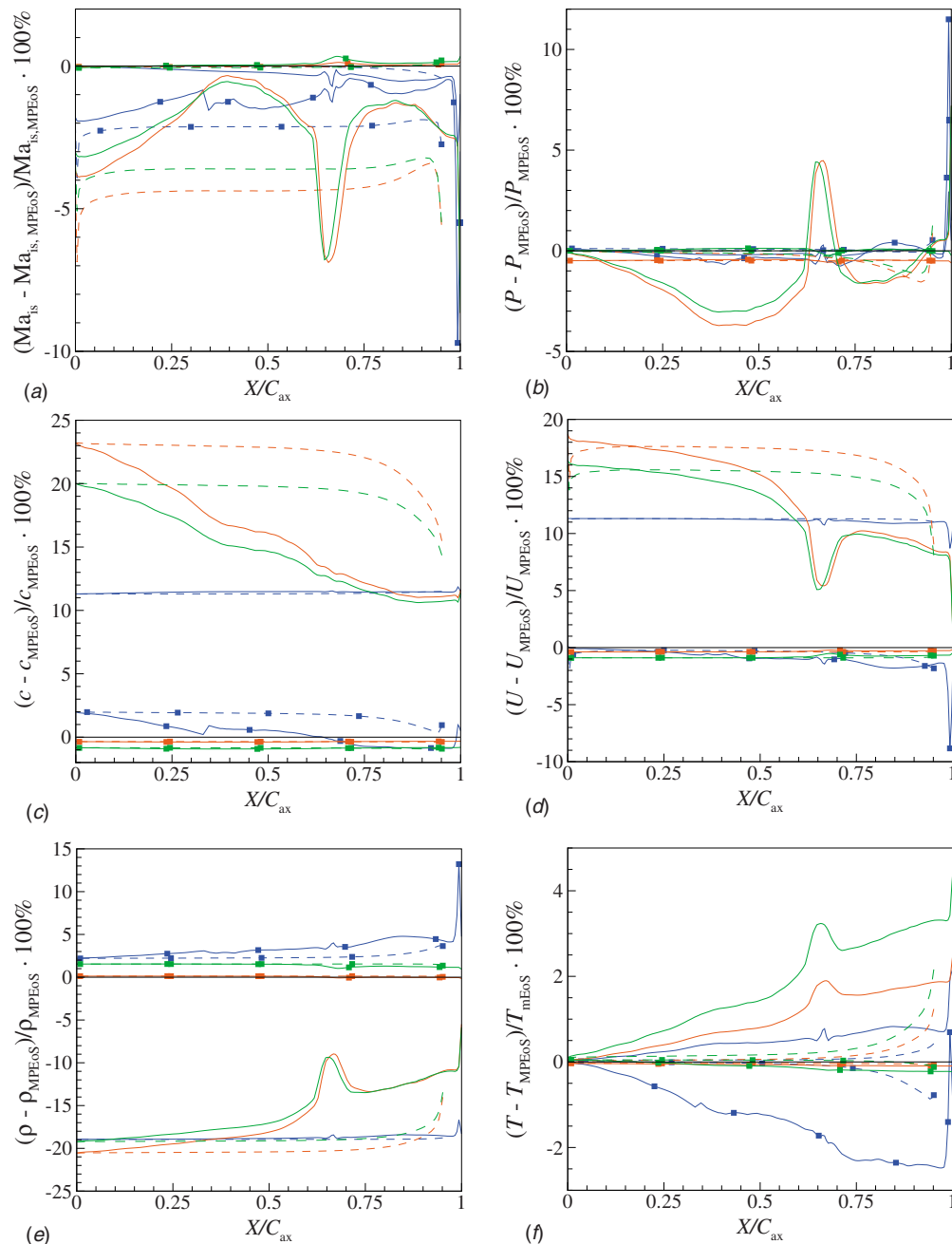
Fig. 7 Percentage difference of (a) the isentropic Mach number, (b) pressure, (c) sound speed, (d) velocity, (e) density, and (f) temperature, along the blade surface, computed based on the PRSV model (■) and the PIG model (no symbol) with respect to the values computed based on the MPEoS. Results are given for steam (blue line), toluene (red line), and R245fa (green line). The blade suction and pressure sides are distinguished by the continuous and dashed lines, respectively. (Color representation of this figure is available at ASME.org)

these differences are somewhat differently distributed in comparison with the distributions of the deviations along the blade surface.

The sound speed, denoted by c, is shown in Fig. 6(c). Simulations using the PIG model show a high sound speed of steam ($c = 651$ m/s), which decreases as the fluid expands. The PRSV and the MPEoS, on the other hand, predict a lower sound speed ($c = 584$ and 595 m/s, respectively) in the initial phase of the expansion, which is more realistic. The deviation in the sound speed predicted by the PIG model is approximately 11% and is constant along the blade surface, as shown in Fig. 7(c). The PRSV EoS has

a deviation in the sound speed below 3%. The same differences are obtained from a direct comparison of sound speeds between the EoSs at the same conditions, shown in Fig. 4(a).

The Mach number distribution is surprisingly similar between the thermodynamic models. The relative difference in Mach number between the PIG model and the MPEoS (Fig. 7(a)) is at most 2%, which is very small compared to the relative difference in sound speed of approximately 11%. This results from the fact that the higher sound speed is compensated by a velocity magnitude (Fig. 6(b)) that is similarly higher (11%), as shown by the comparison in Fig. 7(d). The figure shows the percentage difference of

Table 5 Percentage difference of the mass flow rate ($\Delta\dot{m}$), total pressure loss coefficient (ΔC_{PL}), and outflow angle ($\Delta\beta$) for the PIG and PRSV EoS models with respect to the values computed based on the MPEoS. The total pressure loss coefficient is defined as the mass-weighted average over the outflow boundary of $C_{PL}\equiv1-P_{02}/P_{01}$, where P_{01} is the total inlet pressure and P_{02} is the local total outflow pressure.

	$\Delta\dot{m}$ (%)		ΔC_{PL} (%)		$\Delta\beta$ (deg)	
	PIG	PRSV	PIG	PRSV	PIG	PRSV
Subcritical						
Steam	−9.8	2.1	−0.32	−4	0.06	0.12
Toluene	−6.2	−0.25	−14	11	0.78	−0.02
R245fa	−6.4	0.63	−26	−14	0.71	−0.04
Supercritical						
Toluene	−14	0.15	−30	0.38	2	0
R245fa	−14	1.7	−27	2.5	1.7	−0.22

velocity magnitude for the PIG model and PRSV with respect to the MPEoS.

Very large differences in densities between the EoS models can be observed in Fig. 6(*e*). At the leading edge, the difference based on the PIG model with respect to the MPEoS is as high as 19% (Fig. 7(*e*)). The large difference can be expected (see Fig. 4(*b*)), since pressure and temperature are the prescribed variables at inflow and outflow and density depends on the EoS model. The density error predicted by the PIG model is therefore equal to the deviation from ideal gas in terms of the compressibility factor (Fig. 6(*f*)). The maximum difference in density predicted by the PRSV EoS with respect to the MPEoS is 5% (not taking into account the high error at the trailing edge).

Table 5 lists the deviations in mass flow rate, total pressure loss coefficient, and outflow angle as a result of using the PIG and PRSV models as compared to the MPEoS. The mass flow rate through the stator is given by $\dot{m}=\rho UA$, where ρ, U, and A denote density, flow velocity, and cross-sectional area, respectively. For the simulation employing the PIG model, the 19% underprediction of density combined with the 11% overprediction of velocity magnitude results in a net underprediction of the mass flow rate of 9.8%. A previous study [11] based on a cubic EoS in which the expansion of methane in a nozzle was simulated from reduced reservoir conditions $P_{01}/P_c=5$ and $T_{01}/T_c=1.4$ for pressure ratios between $1<P_{01}/P_2<2.5$ showed a similar mass flow underprediction of the PIG model (14%) for the pressure ratio $P_{01}/P_2=1.9$ used in the present study.

If this turbine stator blade were designed by computing the thermodynamic properties using the PIG model, this large error in the predicted relation of mass flow with respect to pressure ratio would lead to a different pressure, mass flow characteristic, which would also affect the operation of the other components in the cycle, leading to suboptimal cycle performance. Note that the mass flow rate deviation obtained from the simulation using the PRSV model is 2.1%, which can often be considered acceptable for a technical application.

The same inflow temperature is prescribed for all EoSs (see Fig. 6(*h*)), but the relative difference in temperature (based on °C) becomes larger as the flow expands. As shown in Fig. 7(*f*), the deviation is small (1%) for the PIG model. For the PIG model, the constant value of the ideal-gas specific heat, C_P^0, is calculated using the MPEoS model. The fact that for the particular case of steam, a low-complexity fluid, the PIG model leads to low deviations in temperature along the expansion process is explained in Sec. 3.2. For the simulations employing the PRSV model, the temperature deviates by at most 2.5%. The higher deviation observed for the PRSV model may be explained by the fact that at reduced temperatures above approximately $T/T_c\gtrsim0.9$ and close to the saturation curve (Fig. 8(*a*)), physically based cubic EoSs such as the PRSV EoS are known to perform less well for polar molecules (such as steam) as compared to nonpolar molecules [27,56].

The shock wave located at the trailing edge (Fig. 3) leads to a loss of total pressure and thus reduces the overall efficiency of the expansion. The total pressure loss coefficient is defined as the mass-weighted average over the outflow boundary of $C_{PL}\equiv1-P_{02}/P_{01}$, where P_{01} is the total inlet pressure and P_{02} is the local total outflow pressure. Its value relative to the one based on the MPEoS is 0.3% lower for the simulations employing the PIG model and 4% lower for the simulations employing the PRSV EoS, as reported in Table 5. The small deviation for the PIG model is an exception as compared to the other fluids. This is explained from the fact that the total pressure loss is derived from

Fig. 8 Expansion isentropes as obtained using the MPEoS (—), PIG (- - -), and ZPIG (-·-·-) models in the pressure-specific volume diagrams (showing the saturation line) of steam (*a*), toluene (*b*), and R245a (*c*). In the ZPIG model, the compressibility factor *Z* is set to the value given in Table 4. The dotted intersection of MPEoS and ZPIG indicates the subcritical inlet state.
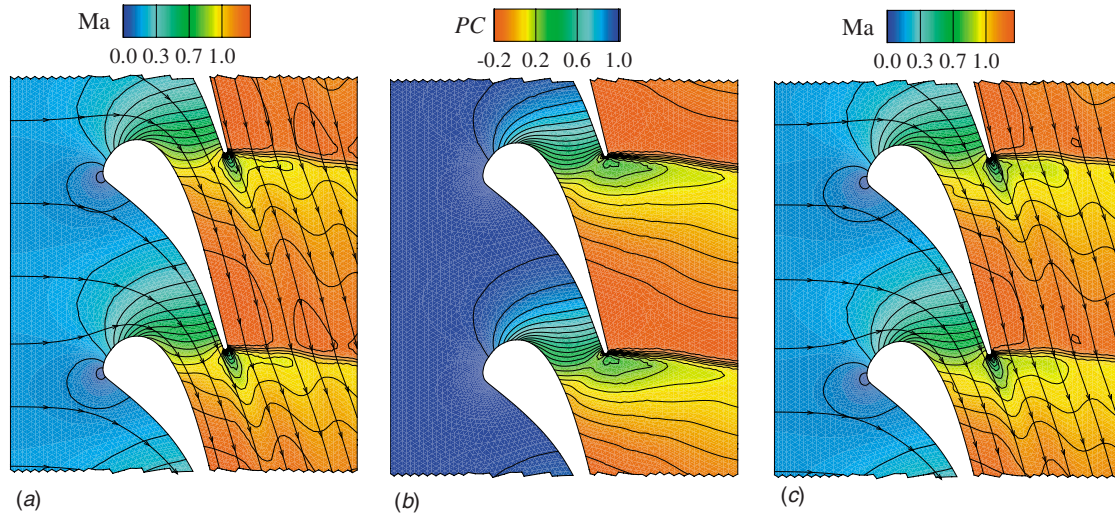
Fig. 9 Flow field distributions of toluene: (*a*) Mach number and (*b*) pressure coefficient distribution, and streamlines based on the MPEoS; (*c*) Mach number distribution and streamlines based on the PIG model
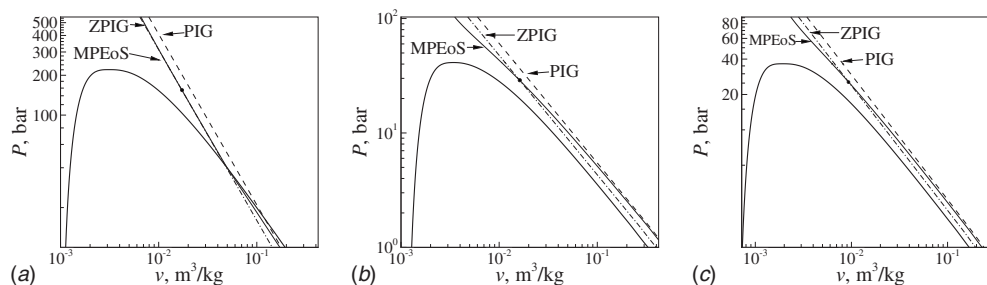
caloric properties. As mentioned before, the PIG model is well suitable for predicting caloric properties of simple fluids such as steam, thus leading to the observed small deviation in total pressure loss for this particular fluid.

The deviation in the outflow angle β is also listed in Table 5. It is an important flow parameter in the context of turbomachinery design as it affects the design of the downstream rotor blade. For both the PIG and PRSV models, the deviation in velocity magnitude from the values computed by the simulation employing the MPEoS (Fig. 7(*d*)) are approximately equal for the suction and pressure side of the blade. Consequently, the error in the outflow angle is small; less than two-tenths of a degree for both EoSs.

3.1.2 Toluene. Toluene (C_7H_8), also known as methylbenzene, is a heavier molecule than steam and its molecule is more complex than both steam and R245fa. Owing to these properties, toluene is used in so-called ORC turbogenerators [6,7].

The two-dimensional flow fields for subcritical expansion obtained using the MPEoS are plotted in Fig. 5. Since the expansion is equal to the one for steam in terms of reduced inflow conditions and pressure ratio, the flow structure is similar. However, the Mach number distribution and the increased angle of the shock wave show that the flow attains higher Mach numbers as compared to steam. The pressure coefficient is similarly different.

Figure 10 shows the surface distributions of the flow parameters for toluene. Even though toluene has different fluid characteristics, and consequently some flow parameters are different in absolute terms (velocity and density), their trend is similar to steam. Differences can be seen in the compressibility factor in Fig. 10(*f*), which increases more steeply compared to steam, resulting in a thermodynamical outlet state that is closer to dilute gas conditions, and in the sound speed in Fig. 10(*c*), which in this case increases as the fluid expands. This behavior will be discussed in detail below.

The local fluctuation observed at $X/C_{ax}=0.67$ of the suction side distribution calculated using the PIG model in the flow parameters Mach, pressure coefficient, velocity, density, and temperature is the result of the onset of a weak trailing edge shock impinging on the suction side blade surface of the next stator blade. As can be observed by comparing Figs. 9(*a*) and 9(*c*), the weak shock wave simulated using the PIG model is locally stronger than the one obtained by employing the reference model, leading to local recompression. This means that, based on the PIG model, the pressure gradient is locally adverse, thus possibly inducing boundary layer separation in the real viscous flow. It is interesting to note that since this nonmonotonicity is visible in the

absolute velocity magnitude (Fig. 10(*d*)), but not in the sound speed (Fig. 10(*c*)), this results in the most significant deviation in the Mach number (Figs. 7(*a*) and 9(*a*)).

In the case of toluene, the deviations between the simulations performed with the PIG model with respect to the ones employing the MPEoS are appreciably larger than in the case of steam. The relative differences in the Mach number (Fig. 7(*a*)) and pressure (Fig. 7(*b*)) vary widely and reach values of 7% and 5%, respectively. Unlike the constant deviations observed for steam, for toluene the sound speed and velocity magnitude errors induced by the PIG model clearly decrease as the fluid expands toward the ideal-gas region. At the inflow they are 23% and 18%, respectively (thus largely compensating each other to lead to the smaller aforementioned error in the Mach number), but both reduce to values of approximately 15% and 13%, respectively (maintaining the compensation). Also the error in density computed using the PIG model is nonuniform along the blade surface and has a maximum value of 21%. The temperature at the outlet is overpredicted by at most 2%. Except for the temperature, all deviations of flow parameters computed using the PIG model with respect to the reference model decrease, since the flow expands to more ideal-gas conditions (see Table 4).

As the fluid expands, the more physically correct PRSV and MPEoS models predict an increase in sound speed (Fig. 10(*c*)), rising from $c \approx 202$ to a value of $c \approx 218$ m/s. The PIG model, on the contrary, incorrectly predicts a decreasing sound speed, which, under ideal-gas theory, is always the case for an isentropic expansion. The correct increase in sound speed across an isentropic expansion as seen here can occur only for molecularly complex fluids within a certain thermodynamic region, which lies in the dense-gas region [57]. The fundamental derivative of gas dynamics, denoted by Γ, is defined as

$$\Gamma \equiv \frac{v^3}{2c^2}\left(\frac{\partial^2 P}{\partial v^2}\right)_s = 1 - \frac{v}{c}\left(\frac{\partial c}{\partial v}\right)_s \qquad (6)$$

Here, v is the specific volume and s is the specific entropy. The complexity of the fluid molecules causes the isentropic relation between sound speed and temperature to be inverted with respect to the ideal-gas behavior for a finite range of pressures and temperatures in the single-phase region where $\Gamma < 1$. In this region, the sound speed increases across an isentropic expansion and decreases across an isentropic compression. The complexity of a fluid can be quantified by Γ_{min}^V, the minimum value of the fundamental derivative along the saturation line, which is shown in Table 2. Note that Γ is the parameter that, if negative, indicates
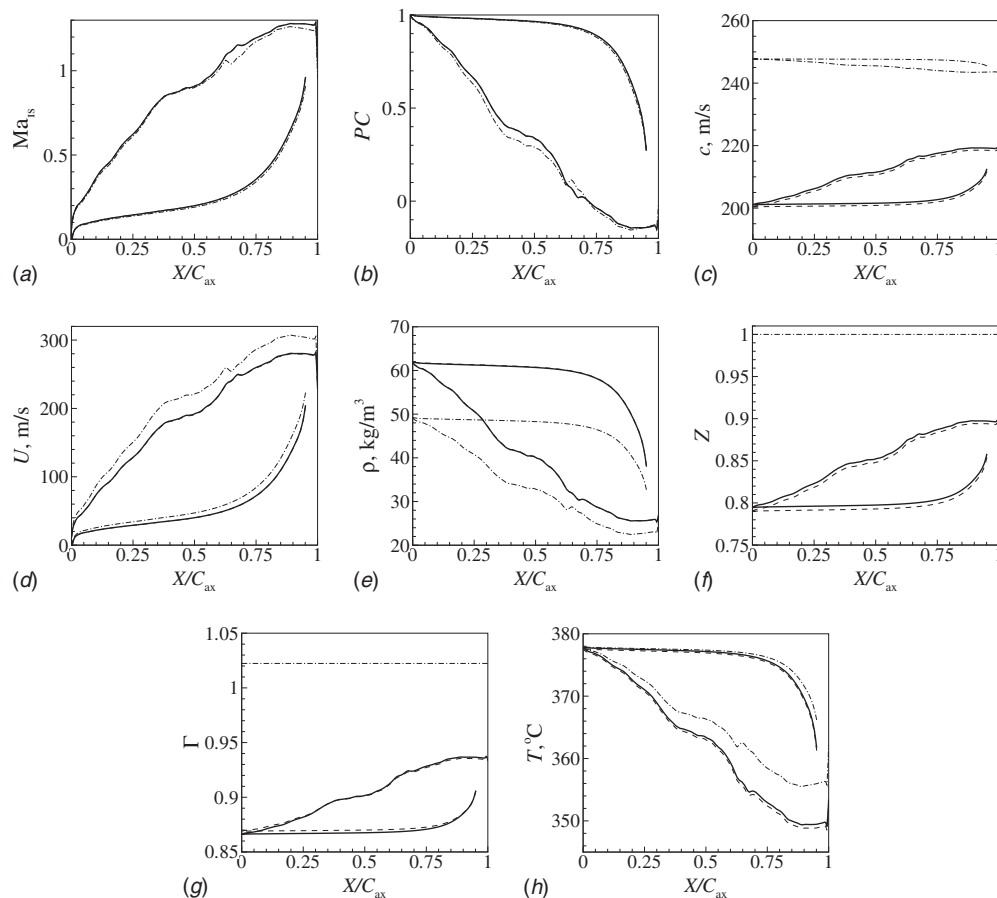
Fig. 10 Blade surface distributions for toluene of (a) the isentropic Mach number, (b) pressure coefficient, (c) sound speed, (d) velocity, (e) density, (f) compressibility factor, (g) fundamental gasdynamic derivative, and (h) temperature, computed based on the MPEoS (—), PRSV (- - -), and PIG (-·-·-) model

the possible occurrence of so-called nonclassical gas dynamic behavior [57–59]. Neither toluene nor R245fa are molecularly complex enough to display a region of negative gamma for dense vapor states. Among the fluids compared in this study, toluene has the lowest value of Γ_{min}^V indicating that it is the most complex molecule.

Figure 10(g) shows the distribution of the fundamental gas dynamic derivative for the subcritical expansion of toluene. The results for the MPEoS show that the entire expansion process occurs at $\Gamma < 1$, which is in accordance with the increase in sound speed observed in Fig. 10(c) for the PRSV and MPEoS models. Initially, its value is $\Gamma = 0.87$ (MPEoS and PRSV) and it increases to $\Gamma = 0.9 - 0.94$. The PIG model incorrectly predicts a value of $\Gamma = 1.022$, since for an ideal gas Eq. (6) reduces to a constant $\Gamma = (\gamma + 1)/2$.

The temperature (Fig. 10(h)) shows a comparatively small temperature drop, typical for the expansion of molecularly complex fluids.

Similar to steam, also in the case of toluene does the use of the PIG model shows large but compensating errors in sound speed and velocity, leading to a comparatively smaller deviation in Mach number.

The mass flow rate relative to the one based on the MPEoS is 6.2% lower for the PIG model and only 0.3% lower for the PRSV EoS. The total pressure loss coefficient, C_{PL}, is 14% lower in case the PIG model is used and 11% higher in case the PRSV model is used. This is a result of the overprediction of the velocity magnitude (Fig. 10(d)), leading to a lower total pressure loss coefficient.

Unlike for steam, the error in the velocity magnitude (Fig. 7(d)) is not equal for the suction and the pressure sides induced by the

PIG model. The difference causes an error in the outflow angle β of 0.8 deg, which is significant for the design of turbomachinery blades. The error in the outflow angle induced by the use of the PRSV EoS is negligible (−0.02%).

3.1.3 R245fa. The hydrofluorocarbon R245fa is a nonflammable and nontoxic refrigerant that is used to synthesize polyurethane foam because of its low thermal conductivity and zero ozone depleting potential. Compared to other refrigerants, it has a high critical temperature. Because of this, it has recently also been applied as a working fluid in ORCs for geothermal heat sources [4]. Its molecular weight is considerably higher than that of steam and toluene, as shown in Table 2, but its complexity, although lower, has the same order of magnitude of that of toluene.

The two-dimensional flow fields for the subcritical expansion obtained using the MPEoS are plotted in Fig. 10. The flow fields are nearly identical to those of toluene, even though R245fa is 45% heavier.

When comparing the real behavior of the fluids, i.e., based on the simulations using the MPEoS, it is noted that, due to its higher molecular weight, the expansion of R245fa shows even lower sound speeds (Fig. 12(c)) than those of toluene; nonetheless, they are compensated by similarly lower velocities, resulting in equal Mach number distributions (both fluids have a maximum Mach number of 1.28). The qualitative behavior of the flow parameters is similar to that of toluene. As expected, there is a considerable quantitative difference in density and temperature, which are, respectively, higher and lower due to the larger molecular weight of R245fa.

As expected, the distribution of the fundamental gas dynamic
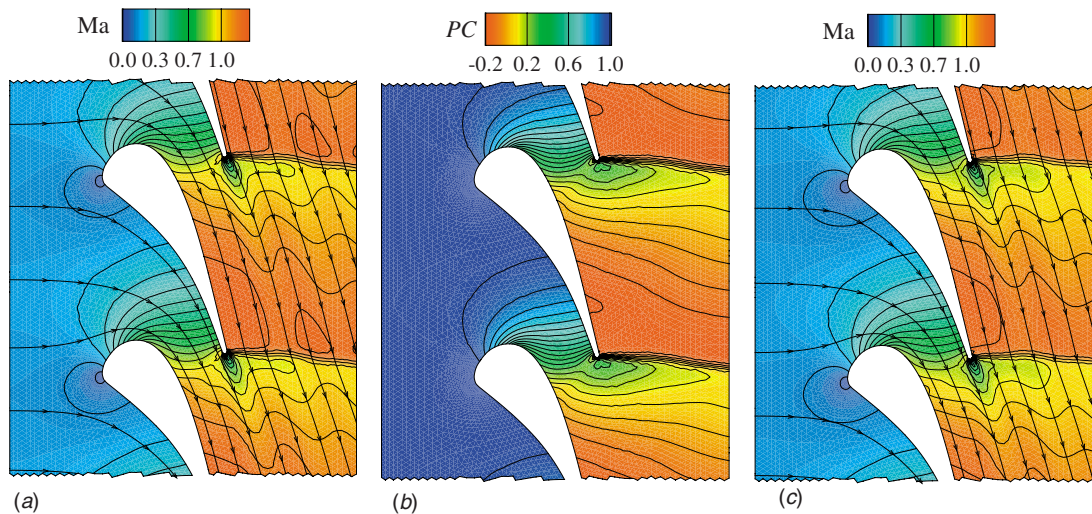
Fig. 11 Flow field distributions of R245fa: (*a*) Mach number and (*b*) pressure coefficient distribution and streamlines based on the MPEoS; (*c*) Mach number distribution and streamlines based on the PIG model

derivative Γ obtained using the MPEoS, depicted in Fig. 12(*g*), shows that the entire expansion process of this complex fluid occurs at $\Gamma < 1$, which is in accordance with the increase in sound speed observed in the simulations using the PRSV and MPEoS models (Fig. 12(*c*)). However, in the case of the expansion of R245fa, the value of Γ is higher than for toluene, resulting in a less pronounced increase in the speed of sound, as confirmed by Fig. 12(*c*). The values of the fundamental derivative of gas dynamics calculated with the PRSV model for R245fa are less accurate if compared to values for toluene calculated with the same equation of state. These differences in Γ are even more pronounced for steam (Fig. 6(*g*)). The origin of these differences is to be found in the different data on which the thermodynamic models are based, namely, (1) the difference among the adopted critical temperature and pressure, (2) a small difference in the experimental data used to fit the vapor pressure, and (3) the different functional form. A full account of this topic is given in Ref. [60].

In the comparison of EoSs of Fig. 7, it is observed that for R245fa the deviations resulting from the use of the PIG model in all flow parameters are similar to those of toluene; deviations in Mach, pressure, and temperature are approximately 5% and errors in sound speed, velocity magnitude, and density are approximately 20%. The only difference in comparison to toluene is that for all flow parameters except for temperature, the errors, although still large, have reduced slightly.

Compared to the PIG model, the use of the PRSV EoS leads to much smaller deviations in all flow parameters of the R245fa expansion; the maximum error is 1.5% in all parameters and only 0.2% in the temperature.

With respect to the errors in mass flow rate and outflow angle, similar values are obtained as for toluene. The deviations in the total pressure loss coefficient, however, have further increased to -26% (PIG) and -14% (PRSV).

3.2 Corrected Polytropic Ideal-Gas Model for Steam. As observed in Sec. 3.1.3, the deviations of the PIG model in density, speed of sound, and velocity are constant in the case of water, whereas for toluene and R245fa they vary along the blade surface. This peculiar behavior can be attributed to the fact that the PIG model is able to correctly approximate the qualitative behavior of isentropes of low-complexity fluids, like steam. In the pressure range of interest of steam (Fig. 8(*a*)), the PIG model only leads to an absolute deviation in volumetric and volume-dependent properties but is qualitatively correct. The constant absolute deviation for low-complexity fluids in this thermodynamic region warrants the use of a corrected PIG model (ZPIG),

$$P = Z\frac{RT}{v} \tag{7}$$

where Z is a constant compressibility factor that assumes, e.g., the value at the inlet determined based on the generalized PvT-properties of gases (see, e.g., Ref. [61]). This approach is commonly used in turbomachinery practice for the thermodynamic modeling of arbitrary fluids expanded at nonideal thermodynamic conditions. In the case of steam, it is shown to perfectly approximate the isentrope based on the MPEoS for a limited but large pressure range. The isentropes of complex fluids, like toluene (Fig. 8(*b*)) and R245fa (Fig. 8(*c*)), however, behave differently and they approximate isotherms [57], as shown in Fig. 8. For complex fluids, however, the PIG model no longer qualitatively represents the isentropes and therefore the ZPIG model can no longer be used, as evidenced by the fluid-dynamic results.

3.3 Supercritical Inflow Conditions. In this section, the same study is conducted for an expansion from supercritical conditions, in order to investigate the influence of increased thermodynamic nonideality on the deviations of flow parameters entailed by the PIG and PRSV models. The pressure ratio is chosen equal to the subcritical expansion. The process conditions are given in reduced values in Table 3. The expansions from supercritical conditions for the three fluids, given in the *T*-*s*-diagrams in Fig. 3, show that the expansion takes place closer to the critical points of the fluids. As a result, the compressibility factor at the inlet, given in Table 4, is lowered to $Z \approx 0.6$ for all fluids, indicating strong thermodynamic nonideality. As the fluid expands to lower pressures, the compressibility factor also increases. At the outlet, it is $Z \approx 0.9$, which is approximately equal to the one in the mildly nonideal subcritical expansion.

Since the expansion occurs closer the critical point, it also approaches the vapor saturation line of the fluids. This poses no problem in the case of toluene and R245fa, which are retrograde fluids, but in the case of steam, condensation occurs, as shown in the *T*-*s*-diagram in Fig. 3(*a*). Since the ZFLOW solver is not yet able to compute two-phase flows, the results for steam cannot be presented in this case.

For conciseness, only the distributions of the errors in the flow parameters for the PIG and PRSV models with respect to the MPEoS model are presented and they are given in Fig. 13. A comparison of the distributions of toluene and R245fa shows that the error distributions ensuing from the PIG model are qualitatively similar to the subcritical error distributions presented in Sec. 3.2 (see Fig. 7). On the other hand, the inflow state of this
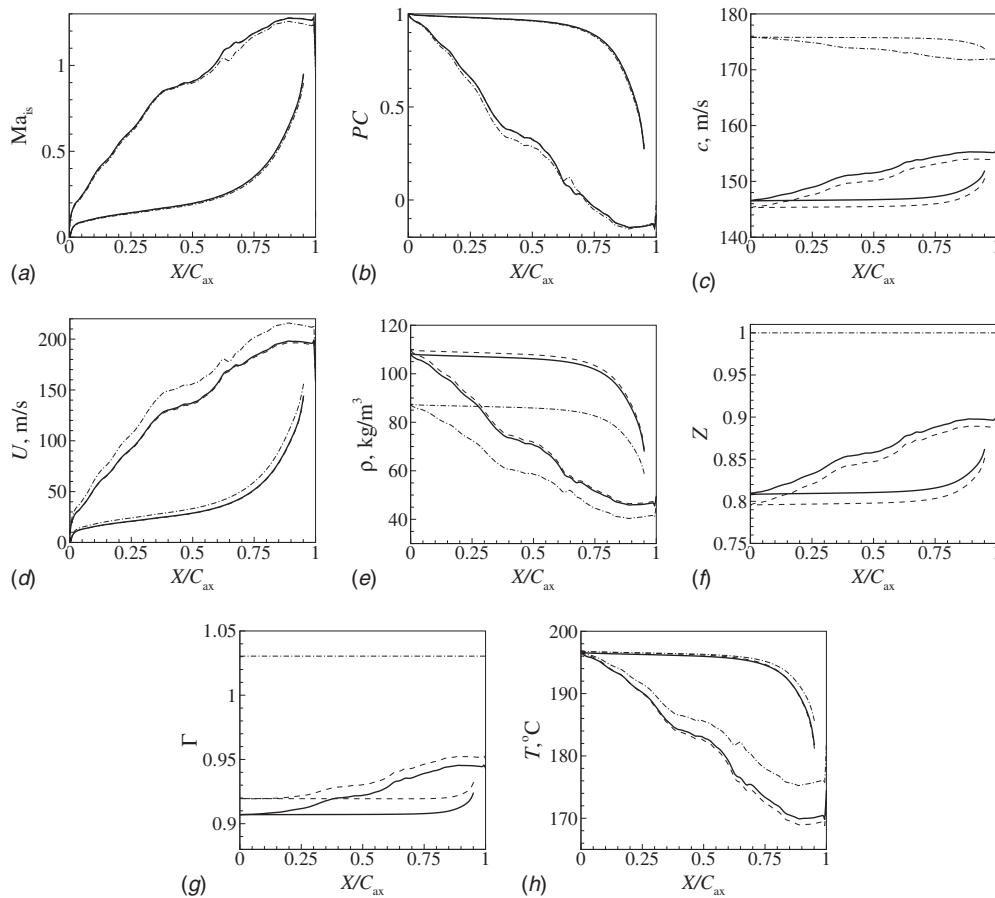
Fig. 12 Blade surface distributions for R245fa of (*a***) the isentropic Mach number, (***b***) pressure coefficient, (***c***) sound speed, (***d***) velocity, (***e***) density, (***f***) compressibility factor, (***g***) fundamental gasdynamic derivative, and (***h***) temperature, computed based on the MPEoS (——), PRSV (- - -), and PIG (-·-·-) model**

expansion is now closer to the critical temperature (Table 3) at which the ideal-gas ratio of specific heats γ is determined, which may locally mitigate the deviation.

As expected from the lower compressibility factor, all errors associated with the PIG model are quantitatively significantly higher for the supercritical expansion as visible in Fig. 8. The errors in the Mach number ensuing from the PIG model have approximately doubled to 8–10% for toluene and 7–10% for R245fa. The pressure errors have doubled to maxima of 9% for toluene and 7% for R245fa. The supercritical expansion takes place closer to the critical point, where the thermodynamic speed of sound has its minimum value. As a result, the error in the sound speed ensuing from the PIG model has more than doubled to maxima of 52% and 63% for R245fa and toluene, respectively. This increase is again balanced by similarly higher (both quantitatively and qualitatively) maximum velocity errors of 50% for toluene and 42% for R245fa, except for the location where the weak trailing edge shock wave impinges. As can be expected from the compressibility factor in Table 4, the maximum errors in density caused by the use of the PIG model have increased to 43 and 40% for toluene and R245fa, respectively. For the supercritical expansion, the PIG model overpredicts temperatures by as much as 7% and 13% for toluene and R245fa, respectively.

Even for the supercritical strongly nonideal expansion, using the PRSV leads to errors of at maximum 3% in all investigated flow parameters, except for the total pressure loss.

At the trailing edge $(X/C_{ax}=1)$, the deviation from ideal-gas behavior is low and approximately equal to the one for the subcritical expansion as indicated by the outlet compressibility factor Z_2 in Table 4. The throat is located at $X/C_{ax}\approx 0.66$ on the blade

suction side, where the thermodynamic nonideality is still high, thus leading to larger errors. The error in the mass flow rate induced by the PIG model is a result of the combined errors in density and velocity at the throat location. As can be seen from Table 5, it has decreased to approximately −14% for both toluene and R245fa. Compared to this, the errors ensuing from the PRSV model are much smaller and have remained small, 0.2% and 1.7% for toluene and R245fa, respectively.

The errors in C_{PL}, induced by the PIG model are −30% and −27% for toluene and R245fa, respectively. The errors have increased with respect to the subcritical expansion case as a result of the increased overprediction of the velocity magnitude as evident from Fig. 13(*d*). For the PRSV model, the errors in C_{PL} are much lower, viz., 0.4% for toluene and 2.5% for R245fa.

As a result of the increased nonideality of the supercritical expansion, an even larger overprediction of the velocity at the suction side is observed in the simulations using the PIG model. The overprediction at the pressure side has increased less. Consequently, the PIG model predicts increased turning of the flow for the supercritical expansion. The outflow angle errors caused by the use of the PIG model are 2% for toluene and 1.7% for R245fa. Again, in case the PRSV model is used, this error is low, negligible for toluene and −0.2% for R245fa.

4 Computational Cost

In many engineering applications, the computational cost of a CFD simulation is, like accuracy, an important aspect. This is particularly true for automated design optimization procedures, which commonly evaluate a large number of different designs and
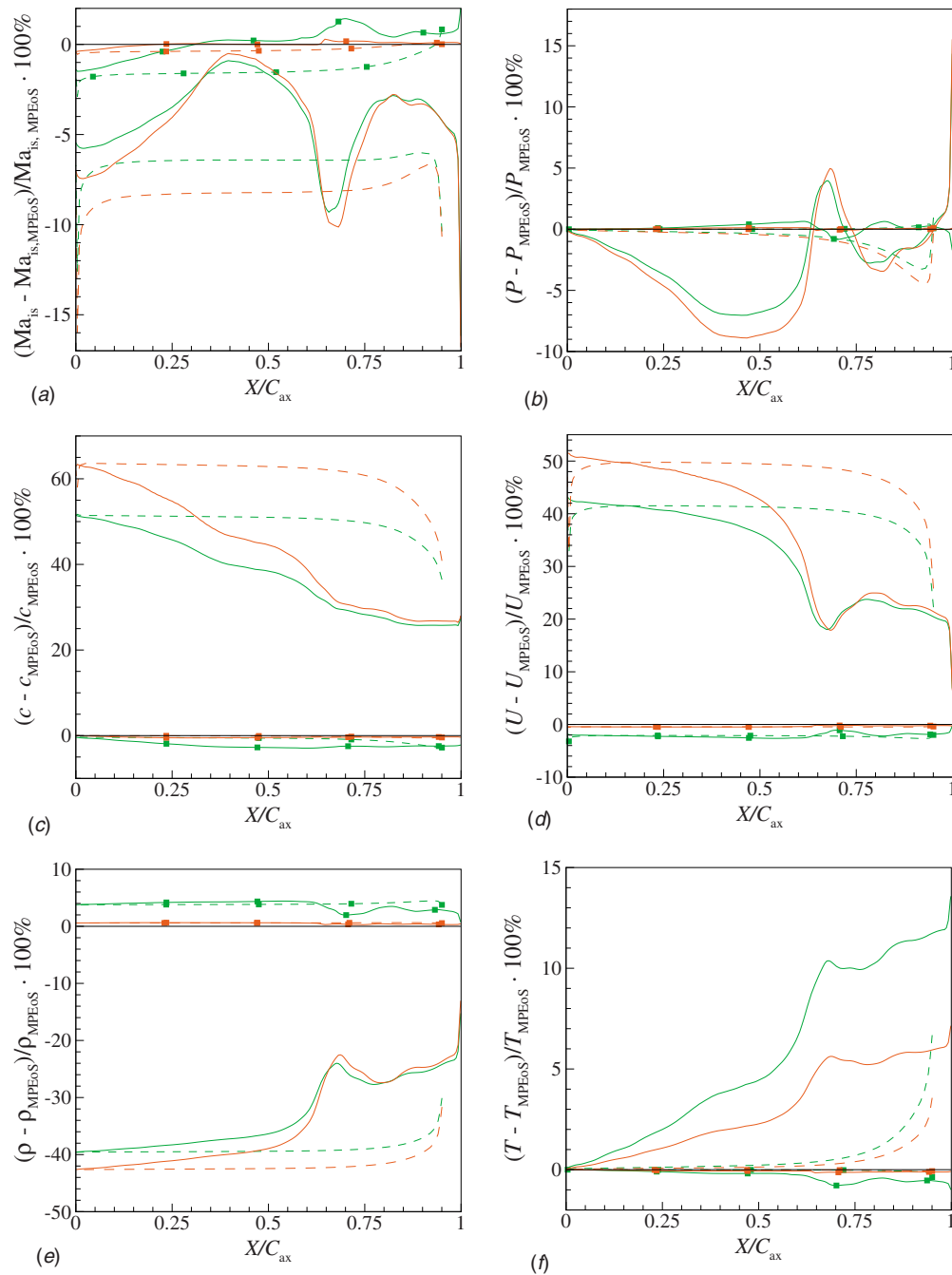
Fig. 13 Supercritical expansion: percentage difference of (a) the isentropic Mach number, (b) pressure, (c) sound speed, (d) velocity, (e) density, and (f) temperature, along the blade surface, computed based on the PRSV model (■) and the PIG model (no symbol) with respect to the values computed based on the MPEoS. Results are given for toluene (red line) and R245fa (green line). The blade suction and pressure sides are distinguished by the continuous and dashed lines, respectively. (Color representation of this figure is available at ASME.org)

usually require a CFD computation for each design. A valuable comparison of the thermodynamic models should therefore include a comparison of the computational cost. Table 6 shows the CPU time required for the convergence of the subcritical expansion case for steam discussed in Sec. 3.1.1. Computations using the PRSV and MPEoS model take approximately 9 and 11 times (respectively) as long as compared to the PIG model.

The large computational resources required for the PRSV and MPEoS models can be largely attributed to the saturation state calculations. For each thermodynamic property evaluation using the PRSV or MPEoS model, the fluid phase is first determined

from a saturation state calculation. Depending on whether the state is in the single-phase or in the vapor-liquid mixture region, the desired property is evaluated in a different way. The saturation state calculation is often an iterative procedure, making it very costly as compared to the subsequent evaluation of the properties. If it is known a priori that the simulated process occurs in the vapor region, as it is in this case, then saturation-checks are not needed and can be left out. In this way, the cost of the computations (Table 6) is reduced by a factor 4–5. With this reduction, the computations without saturation state calculations require only 2 (PRSV) and 3 (MPEoS) as much time as the computations that

Table 6 CPU time required for the convergence of the subcritical expansion case for steam (see Sec. 3.1.1) on the fine grid (4153 grid nodes) computed using an Intel Pentium 4 2.8 GHz processor. In all cases convergence (a reduction in the residuals by five orders of magnitude) was obtained after 436 iterations.

Thermodynamic model	Saturation (VLE) calculations	CPU time (s)	time/time$_{PIG}$	time/time$_{no\ VLE}$
PIG	No	141	-	-
PRSV	No	263	2x	-
PRSV	Yes	1332	9x	5x
MPEoS	No	416	3x	-
MPEoS	Yes	1549	11x	4x

employ the PIG model. Care must, however, be taken especially for processes that take place close to the saturation line, for which it is not know beforehand whether or not saturation occurs locally, e.g., due to overexpansion.

5 Conclusions

The state-of-the-art inviscid ZFLOW CFD solver coupled with a fluid property library containing several thermodynamic models, including highly accurate ones, is used to simulate the fluid dynamics of turboexpander processes in thermodynamic conditions affected by strong real-gas effects.

This paper presents a quantitative comparison of the effect of using thermodynamic models of various degrees of complexity with regard to the application to fluid-dynamic simulations of turboexpanders operated in this thermodynamic region. The considered thermodynamic models are, in order of increasing complexity, the PIG law, the PRSV cubic EoS, and multiparameter MPEoS. The investigated processes are moderately nonideal (compressibility factor of $0.8 < Z < 0.9$) subcritical expansions and highly nonideal (compressibility factor of $0.6 < Z < 0.9$) supercritical expansions. The chosen fluids are steam, toluene, and R245fa. The pressure ratio is the same for all cases and the two inlet conditions are specified in reduced terms (the reference values being the critical temperature and pressure of the considered fluids). A standard transonic turbine stator blade geometry is used as an example of a turboexpander. Distributions of fluid-dynamic parameters along the blade surface and performance parameters based on the two EoSs are compared to those obtained using highly accurate MPEoSs of the respective fluids.

Prior to the comparative simulations, the ZFLOW solver linked to the accurate thermodynamic model is successfully validated for the transonic fluid-dynamic problem under consideration. For the validation, however, the expansion occurs at ideal-gas conditions. Experimental data of fluid expansions at nonideal (e.g., supercritical) conditions is unfortunately not yet available, hindering the validation of the flow solver linked to the accurate thermodynamic model for these conditions. This is planned for the near future. Nonetheless, the validation of the solver and thermodynamic model at ideal-gas conditions and the guaranteed high accuracy of the thermodynamic model even at strongly nonideal conditions warrant the validity of the simulations of real-gas flows presented in this study. For the presented simulations, it is furthermore demonstrated that grid convergence is obtained.

The comparison of the fluid dynamics between the three thermodynamic models shows that, as expected, using the simplest model, the PIG model, for a moderately nonideal expansion (compressibility factor of $0.8 < Z < 0.9$) leads to large deviations. The deviations are nonuniformly distributed, except for steam. For the most complex fluid, toluene, the large errors (maximum of the blade distribution) are encountered in the density (-20%), sound speed (25%), and velocity (18%). However, other fluid-dynamic parameters such as the Mach number (7%), pressure (5%), and temperature (4%) also deviate considerably as a result of using the PIG model. The aforementioned deviations cause similar errors in the integral stator performance parameters. In spite of the fact that

the density and velocity errors are opposite in sign, using the PIG model still causes a high error in the mass flow rate, which is consistent for the three fluids and highest for steam (-10%). In the case of toluene and R245fa, the total pressure loss due to the trailing edge shock wave is largely underpredicted (-25%) and the error in the outflow angle is 0.8 deg. Not surprisingly, employing the PIG model for a highly nonideal (compressibility factor of $0.6 < Z < 0.9$) supercritical expansion leads to even higher errors in comparison with the subcritical expansion. The maximum errors encountered in the density (-43%), sound speed (73%), velocity (50%), Mach number (-10%), pressure (-9%), and temperature (12%) have all increased. The stronger deviations are therefore also observed in the predictions of overall performance parameters; the mass flow is underpredicted by 14%, the total pressure loss is underpredicted by 30%, and the outflow angle is off by 2%.

For the subcritical expansion, adopting the physically more correct cubic PRSV model instead leads to comparatively small errors of $<1.5\%$ (toluene and R245fa) and $<4\%$ (steam) in all flow parameters along the blade wall. Similarly, the mass flow rate of steam based on the PRSV EoS is off by at most 2.1% and the error in the outflow angle is negligibly small. The error in the total pressure loss coefficient, however, is as high and in some cases higher than the one observed for the PIG model. The PRSV model is reasonably accurate even for the highly nonideal supercritical expansion. The errors in the sound speed, velocity, and density are at most 4%, in the Mach number at most 2%, and only 1% for the temperature. Correspondingly, the integral performance parameter values are only slightly higher.

For the expansion of steam, which has a low molecular complexity, the deviations in the flow parameter are the smallest and uniformly distributed. In the case of low-complexity fluids like water, the deviations in density, speed of sound, and velocity ensuing from the use of the PIG model are constant along the isentropic expansion because the PIG model is able to correctly approximate the qualitative behavior of isentropes of low-complexity fluids in a limited region. The absolute deviation can in this case be reduced by employing the PIG model corrected by a constant compressibility factor. The high nonuniform deviation in the sound speed observed for R245fa and toluene is caused by the inability of the PIG model to describe the increasing sound speed upon isentropic expansion of complex fluids in the dense-gas region. However, for all three fluids, the sound speed and velocity are both overpredicted to more or less the same degree, leading to a smaller error in the Mach number.

For the more complex fluids R245fa and toluene, the deviations are larger and vary strongly along the isentropic expansion. It is found that using the PIG model leads to the largest deviations in the case of toluene, which is the more complex fluid. Deviations in almost all flow variables are largest for this fluid, the exception being the temperature.

It is important to note that the mentioned error values associated with the PIG model are, in fact, lower bounds for the considered expansion conditions because the accuracy of the PIG model is strongly dependent on the choice of the ratio of the

specific heats. For the expansions studied in this work, the specific heat evaluated at the critical temperature is used as it leads to minimal thermodynamic deviations in the results using the PIG model with respect to the accurate MPEoS, ensuring a fair comparison.

The mentioned error levels are significant and can have drastic consequences on the performance of any turboexpander. The mentioned overpredictions of the velocity magnitude and outflow angle, for instance, strongly affect the design of the downstream stator blade. The results of this study can in this respect be useful as guidelines for designers of (turbo)expanders operating in the non-ideal-gas region, as it provides an indication of the magnitude and variation in the flow variable errors as a result of using a low-complexity thermodynamic model for real-gas CFD simulations, e.g., in case a MPEoS for a certain fluid is not available or due to computational-time requirements. It is envisioned that in the future CFD methods will be thoroughly validated and will have become much more accurate and reliable allowing them to be used as a design tool coupled with automatic optimization. In that case, even small errors as a result of inaccurate thermodynamic modeling might play a role. Although the mentioned deviations are obtained using a practical geometry, the conclusions apply to inviscid expansions in nozzles in general.

In many engineering applications, the computational cost of a CFD simulation is, like accuracy, an important aspect. Computations using the PRSV and MPEoS model take approximately 9 and 11 times (respectively) as long as compared to the PIG model. The large computational resources required for the PRSV and MPEoS models can be largely attributed to saturation-check calculations. Computations without saturation state calculations require only 2 (PRSV) and 3 (MPEoS) as much time as the computations that employ the PIG model.

Acknowledgment

Nomenclature

A = coefficient in ideal-gas isobaric specific heat equation
a = coefficient of attractive forces
b = coefficient of repulsive forces
C = specific heat, blade chord, coefficient
c = speed of sound
k = parameter in Peng–Robinson equation of state
Ma = Mach number
M = molecular weight
$\dot{m}$ = mass flow rate
P = pressure, power
PC = pressure coefficient
R = specific gas constant
$\bar{R}$ = universal gas constant
s = entropy
T = temperature
U = velocity
v = specific volume
X = stator axial coordinate
Y = stator circumferential coordinate
Z = compressibility factor
$ZPIG$ = polytropic ideal-gas law, corrected by a constant compressibility factor, $P=Z\rho RT$

Greek Symbols

β = stator outflow angle
Δ = difference
Γ = fundamental derivative of gas dynamics

γ = ratio of specific heat capacities
ρ = density
ω = acentric factor

Subscripts

0 = total (or stagnation)
1 = stator inlet
2 = stator exit
ax = axial
c = critical point
is = isentropic
min = minimum
P = isobaric, pressure
PL = total pressure loss
x = stator axial coordinate

Superscripts

0 = ideal-gas contribution
V = saturated vapor

References

[1] Curran, H., 1981, "Use of Organic Working Fluids in Rankine Engines," J. Energy, **5**(4), pp. 218–223.

[2] Angelino, G., Gaia, M., and Macchi, E., 1984, "A Review of Italian Activity in the Field of Organic Rankine Cycles," *VDI Berichte—Proceedings of the International VDI Seminar*, VDI, Zurich, Vol. 539, pp. 465–482.

[3] Obernberger, I., Thonhofer, P., and Reisenhofer, E., 2002, "Description and Evaluation of the New 1000 kW ORC Process Integrated in the Biomass CHP Plant in Lienz, Austria," Euroheat and Power, **31**(10), pp. 18–25.

[4] Brasz, J. J., and Biederman, B. P., 2003, "Low Temperature Waste Heat Power Recovery Using Refrigeration Equipment," 21st International Congress of Refrigeration 2003, Washington, DC, Paper No. ICR0587.

[5] Bloch, H., and Soares, C., 2001, *Turboexpanders and Process Applications*, Gulf Professional, Houston, TX.

[6] Hoffren, J., Talonpoika, T., Larjola, J., and Siikonen, T., 2002, "Numerical Simulation of Real-Gas Flow in a Supersonic Turbine Nozzle Ring," ASME J. Eng. Gas Turbines Power, **124**(2), pp. 395–403.

[7] Van Buijtenen, J. P., Larjola, J., Turunen-Saaresti, T., Honkatukia, J., Esa, H., Backman, J., and Reunanen, A., 2003, "Design and Validation of a New High Expansion Ratio Radial Turbine for ORC Applications," *Proceedings of the Fifth European Conference on Turbomachinery*, pp. 1–14.

[8] Goodwin, R., 1989, "Toluene Thermophysical Properties From 178 to 800 K at Pressures to 1000 bar," J. Phys. Chem. Ref. Data, **18**(4), pp. 1565–1636.

[9] Harinck, J., Turunen-Saaresti, T., and Colonna, P., 2007, "Predictions of Performance and Flow Fields of a High-Expansion-Ratio Radial ORC Turbine," Department of Process and Energy, Delft University of Technology, Technical Report No. ET-2262.

[10] Lemmon, E., and Span, R., 2006, "Short Fundamental Equations of State for 20 Industrial Fluids," J. Chem. Eng. Data, **51**(3), pp. 785–850.

[11] Bober, W., and Chow, W. L., 1990, "Nonideal Isentropic Gas Flow Through Converging-Diverging Nozzles," ASME J. Fluids Eng., **112**, pp. 455–460.

[12] Anders, J. B., Anderson, W. K., and Murthy, A. V., 1999, "Transonic Similarity Theory Applied to a Supercritical Airfoil in Heavy Gases," J. Aircr., **36**(6), pp. 957–964.

[13] Drikakis, D., and Tsangaris, S., 1993, "Real Gas Effects for Compressible Nozzle Flows," ASME J. Fluids Eng., **115**, pp. 115–120.

[14] Wagner, B., and Schmidt, W., 1978, "Theoretical Investigation of Real Gas Effects in Cryogenic Wind Tunnels," AIAA J., **16**(6), pp. 580–586.

[15] Anderson, W. K., 1991, "Numerical Study of the Aerodynamic Effects of Using Sulfur Hexafluoride as a Test Gas in Wind Tunnels," NASA Technical Paper No. 3086.

[16] Colonna, P., and Rebay, S., 2004, "Numerical Simulation of Dense Gas Flows on Unstructured Grids With an Implicit High Resolution Upwind Euler Solver," Int. J. Numer. Methods Fluids, **46**, pp. 735–765.

[17] Cinnella, P., and Congedo, P., 2004, "A Numerical Solver for Dense Gas Flows," Fourth AIAA Fluid Dynamics Conference and Exhibit, AIAA Paper No. 2004-2137, pp. 1–12.

[18] Cinnella, P., and Congedo, P., 2007, "Inviscid and Viscous Aerodynamics of Dense Gases," J. Fluid Mech., **580**, pp. 179–217.

[19] Cravero, C., and Satta, A., 2000, "A CFD Model for Real Gas Flows," ASME Paper No. 2000-GT-518.

[20] Boncinelli, P., Rubechini, F., Arnone, A., Cecconi, M., and Cortese, C., 2004, "Real Gas Effects in Turbomachinery Flows—A Computational Fluid Dynamics Model for Fast Computations," ASME J. Turbomach., **126**, pp. 268–276.

[21] Cirri, M., Adami, P., and Martelli, F., 2005, "Development of a CFD Real Gas Flow Solver for Hybrid Grid," Int. J. Numer. Methods Fluids, **47**(8–9), pp. 931–938.

[22] Patek, J., 1996, "Functional Forms to Describe Thermodynamic Properties of Gases for Fast Calculations," ASME J. Eng. Gas Turbines Power, **118**, pp. 210–213.

[23] Turunen-Saaresti, T., Tang, J., and Larjola, J., 2006, "A Practical Real Gas Model in CFD," European Conference on Computational Fluid Dynamics

(ECCOMAS CFD 2006), P. Wesseling, E. Onate, and J. Périau, eds.

[24] Van der Waals, J., 1873, "On the Continuity of the Gas and Liquid State," Ph.D. thesis, University of Leiden, Leiden, The Netherlands.

[25] Aldo, A. C., and Argrow, B. M., 1995, "Dense Gas Flows in Minimum Length Nozzles," ASME J. Fluids Eng., **117**, pp. 270–276.

[26] Peng, D. Y., and Robinson, D. B., 1976, "A New Two-Constant Equation of State," Ind. Eng. Chem. Fundam., **15**, pp. 59–64.

[27] Stryjek, R., and Vera, J. H., 1986, "PRSV: An Improved Peng-Robinson Equation of State for Pure Compounds and Mixtures," Can. J. Chem. Eng., **64**, pp. 323–333.

[28] Kim, H., Lee, J., Park, K., Setoguchi, T., and Matsuo, S., 2007, "A Study of the Critical Nozzle for Flow Rate Measurement of High-Pressure Hydrogen Gas," J. Therm. Sci., **16**(1), pp. 28–32.

[29] Span, R., 2000, *Multiparameter Equations of State—An Accurate Source of Thermodynamic Property Data*, Springer-Verlag, Berlin.

[30] Span, R., Wagner, W., Lemmon, E. W., and Jacbosen, R. T., 2001, "Multiparameter Equations of State—Recent Trends and Future Challenges," Fluid Phase Equilib., **183–184**, pp. 1–20.

[31] Wagner, W., and Pruß, A., 2002, "The IAPWS Formulation 1995 for the Thermodynamic Properties of Ordinary Water Substance for General and Scientific Use," J. Phys. Chem. Ref. Data, **31**(2), pp. 387–535.

[32] Colonna, P., and Silva, P., 2003, "Dense Gas Thermodynamic Properties of Single and Multicomponent Fluids for Fluid Dynamics Simulations," ASME J. Fluids Eng., **125**, pp. 414–427.

[33] Colonna, P., Guardone, A., Harinck, J., and Rebay, S., 2006, "Numerical Investigation of Dense Gas Effects in Turbine Cascades," 15th U.S. National Congress on Theoretical and Applied Mechanics Conference, Boulder, CO.

[34] Colonna, P., Rebay, S., Harinck, J., and Guardone, A., 2006, "Real-Gas Effects in ORC Turbine Flow Simulations: Influence of Thermodynamic Models on Flow Fields and Performance Parameters," ECCOMAS CFD 2006 Conference, Egmond Aan Zee, North Holland.

[35] Colonna, P., Harinck, J., Rebay, S., and Guardone, A., 2008, "Real-Gas Effects in Organic Rankine Cycle Turbine Nozzles," J. Propul. Power, **24**(2), pp. 282–294.

[36] Colonna, P., and Van der Stelt, T., 2005, "FLUIDPROP: A Program for the Estimation of Thermophysical Properties of Fluids," Energy Technology Section, Delft University of Technology, The Netherlands, www.fluidprop.com

[37] Selmin, V., 1993, "The Node-Centered Finite Volume Approach: Bridge Between Finite Differences and Finite Elements," Comput. Methods Appl. Mech. Eng., **102**(1), pp. 107–138.

[38] Roe, P. L., 1981, "Approximate Riemann Solvers, Parameter Vectors, and Difference Schemes," J. Comput. Phys., **43**(2), pp. 357–372.

[39] Vinokur, M., and Montagné, J. L., 1990, "Generalized Flux-Vector Splitting and Roe Average for an Equilibrium Real Gas," J. Comput. Phys., **89**(2), pp. 276–300.

[40] Lemmon, E. W., McLinden, M. O., and Huber, M. L., 2002, REFPROP, Reference Fluid Properties Software, NIST.

[41] Reynolds, W. C., 1979, *Thermodynamic Properties in S.I.*, Stanford University, Stanford, CA.

[42] Martin, J. J., and Hou, Y. C., 1955, "Development of an Equation of State for Gases," AIChE J., **1**(2), pp. 142–151.

[43] Span, R., and Wagner, W., 2003, "Equations of State for Technical Applications. II. Results for Nonpolar Fluids," Int. J. Thermophys., **24**(1), pp. 41–109.

[44] Span, R., and Wagner, W., 2003, "Equations of State for Technical Applications. I. Simultaneously Optimized Functional Forms for Nonpolar and Polar Fluids," Int. J. Thermophys., **24**(1), pp. 1–39.

[45] Starling, K. E., 1973, *Equation of State and Computer Prediction—Fluid Thermodynamic Properties for Light Petroleum Substances*, Gulf, Huston, TX.

[46] Wong, D. S. H., and Sandler, S. I., 1992, "A Theoretically Correct Mixing Rule for Cubic Equations of State," AIChE J., **38**, pp. 671–680.

[47] Wong, D. S. H., Sandler, S. I., and Orbey, H., 1992, "Equation of State Mixing Rule for Nonideal Mixtures Using Available Activity Coefficient Model Parameters and That Allows Extrapolation Over Large Ranges of Temperature and Pressure," Ind. Eng. Chem. Res., **31**, pp. 2033–2039.

[48] Angelino, G., and Colonna, P., 1998, "Multicomponent Working Fluids for Organic Rankine Cycles (ORCs)," Energy, **23**(6), pp. 449–463.

[49] Poling, B. E., Prausnitz, J. M., and O'Connell, J. P., 2001, *The Properties of Gases and Liquids* (Chemical Engineering Series), 5th ed., McGraw-Hill, New York.

[50] Arts, T., Lambert de Rouvroit, M., and Rutherford, A. W., 1990, "Aero-Thermal Investigation of a Highly Loaded Transonic Linear Turbine Guide Vane Cascade," Von Karman Institute for Fluid Dynamics, Technical Note 174.

[51] Lemmon, E. W., Jacobsen, R. T., Penoncello, S. G., and Friend, D., 2000, "Thermodynamic Properties of Air and Mixtures of Nitrogen, Argon, and Oxygen From 60 to 2000 K at Pressures to 2000 MPa," J. Phys. Chem. Ref. Data, **29**(3), pp. 331–385.

[52] Guardone, A., and Rebay, S., 2006, "Unstructured Periodic Grid Generation," *Proceedings of the ECCOMAS CFD 2006 Conference*.

[53] Rebay, S., 1993, "Efficient Unstructured Mesh Generation by Means of Delaunay Triangulation and Bowyer–Watson Algorithm," J. Comput. Phys., **106**(1), pp. 125–138.

[54] Northall, J. D., 2006, "The Influence of Variable Gas Properties on Turbomachinery Computational Fluid Dynamics," ASME J. Turbomach., **128**, pp. 632–638.

[55] Rubechini, F., Marconcini, M., Arnone, A., Maritano, M., and Cecchi, S., 2006, "The Impact of Gas Modeling in the Numerical Analysis of a Multistage Gasturbine," ASME Paper No. GT 2006-90129.

[56] Abbott, M. M., 1973, "Cubic Equations of State," AIChE J., **19**, pp. 596–601.

[57] Colonna, P., and Guardone, A., 2006, "Molecular Interpretation of Nonclassical Gasdynamics of Dense Vapors Under the van der Waals Model," Phys. Fluids, **18**(5), p. 056101.

[58] Monaco, J. F., Cramer, M. S., and Watson, L. T., 1997, "Supersonic Flows of Dense Gases in Cascade Configurations," J. Fluid Mech., **330**, pp. 31–59.

[59] Brown, B. P., and Argrow, B. M., 2000, "Application of Bethe-Zel'dovich-Thompson Fluids in Organic Rankine Cycle Engines," J. Propul. Power, **16**(6), pp. 1118–1123.

[60] Colonna, P., Nannan, N., Guardone, A., and Stelt van der, T. P., 2009, "On the Computation of the Fundamental Derivative of Gas Dynamics Gamma, Using Equations of State," Fluid Phase Equilib., in press.

[61] Augnier, R., 2006, *Turbine Aerodynamics: Axial-Flow and Radial-Inflow Turbine Design and Analysis*, ASME, New York.

Turbine Efficiency Measurement System for the QinetiQ Turbine Test Facility

Paul F. Beard

Thomas Povey

Department of Engineering Science,
University of Oxford,
Parks Road,
Oxfordshire, OX1 3PJ, UK

Kamaljit S. Chana
QinetiQ Ltd.,
Cody Technology Park,
Ively Road,
Farnborough, GU14 0LX, UK

A turbine efficiency measurement system has been developed and installed on the turbine test facility (TTF) at QinetiQ Farnborough. The TTF is an engine-scale short-duration (0.5 s run time) rotating transonic facility, which can operate as either single stage (HP vane and rotor) or $1\frac{1}{2}$ stage (HP stage with IP or LP vane). The current MT1 HP stage is highly loaded and unshrouded and is therefore relevant to current design trends. Implementation of the efficiency measurement system forms part of the EU Turbine Aero-Thermal External Flows (TATEF II) program. The following aspects of the efficiency measurement system are discussed in this paper: mass-flow rate measurement, power measurement by direct torque measurement, turbine inlet and exit area traverse measurement systems, computation of efficiency by mass weighting, and uncertainty analysis of the experimentally determined turbine efficiency. The calibration of the mass-flow rate and torque measurement systems are also discussed. Emphasis was placed on the need for a low efficiency precision uncertainty, so that changes in efficiency associated with turbine inlet temperature distortion and swirl can be resolved with good accuracy. Measurements with inlet flow distortion form part of the TATEF II program and will be the subject of forthcoming publications. [DOI: 10.1115/1.3066271]

1 Introduction

The accurate measurement of efficiency is essential in the developmental testing of advanced gas-turbine designs. Recent improvements in materials and cooling configurations have allowed designers to increase the turbine inlet total temperature, directly contributing to an improvement in efficiency.

Industrial techniques for the evaluation of turbine efficiency are generally confined to continuous or steady state facilities in which thermal equilibrium is established. These facilities require substantial power (~ 3 MW) and hence are costly to operate. This limits their use to large industrial gas-turbine manufacturers. Over the past few decades, the development of transient testing facilities has enabled turbine testing to be performed at comparatively low cost. Transient testing matches all of the nondimensional parameters important to heat transfer and aerodynamics (Reynolds number, Mach number, pressure ratio, nondimensional speed, and gas-to-wall temperature ratio). Gas is typically vented through a test section for a short period under quasi-steady conditions. Transient facilities have been developed with test times between 20 ms and 1 s. Subtle changes in the operating point during the quasi-steady test period mean that all instrumentation must have suitable frequency response. Transient facilities can be classified into two groups: those that maintain constant rotational speed during the run with the aid of a braking system (such as the MIT Blowdown Facility [1] and the QinetiQ Turbine Test Facility (TTF) [2]), and those that are unbraked and allow the turbine to accelerate during the test (such as the Oxford Rotor Facility [3] and the VKI Compression Facility [4]). Transient techniques have several advantages over conventional steady state facilities, most notably the greatly reduced cost of testing and the suitability for heat transfer measurements (gas-to-wall temperature ratio can be matched).

As the heat load in the HP stage currently limits further increases in inlet total temperature, heat transfer measurements conducted in transient test facilities provide valuable data that will lead to improvements in cooling geometries. The aim of this work is to improve the capability of the QinetiQ Turbine Test Facility to allow measurements of turbine efficiency to be conducted. The work forms part of the larger TATEF II program, the aim of which is to investigate the effects of engine representative hot streaks and swirl on turbine efficiency and heat transfer. An emphasis has been placed on achieving precision and absolute measurement accuracies of ±0.25% and ±2.0%, respectively, for efficiency. Feasibility studies for the measurement of turbine efficiency in transient facilities were conducted by Guenette et al. [5] and Halderman et al. [6], both concluding that the measurements could be conducted with the required accuracy. The details of the measurement of turbine efficiency at the MIT Blowdown Facility [7,8], von Karman Institute [9,10], and Oxford University [11] have been previously published.

The efficiency of an adiabatic turbine is defined as the ratio of the actual power extracted by the rotor from the fluid to the ideal power obtained from an isentropic expansion between the same inlet and exit pressures. To determine the efficiency of a turbine in a transient facility, in which the gas-to-wall temperature ratio is matched to engine conditions, the heat transferred to the surrounding surfaces from the fluid must be accounted for. Extensive heat transfer measurements have previously been conducted for the MT1 turbine stage in the TTF using thin film gauge instrumentation; see, for example, Refs. [12–15]. The evaluation of ideal power requires the measurement of stage mass-flow rate, inlet enthalpy flux, and stage pressure ratio. The evaluation of the actual power requires the measurement of shaft torque, rotational speed, and acceleration.

The efficiency measurement system developed for the QinetiQ TTF is now described.

2 The QinetiQ Turbine Test Facility

A schematic of the TTF at QinetiQ, Farnborough is shown in Fig. 1. The turbine facility currently operates with the full-scale MT1 turbine stage. An aerodynamic braking system [16], or turbobrake, is mounted on the same shaft as the turbine. The parameters specifying the operating point of the turbine are summarized in Table 1.

Fig. 1 The QinetiQ turbine test facility

Fig. 2 Enthalpy-entropy chart showing a turbine expansion under adiabatic and nonadiabatic conditions
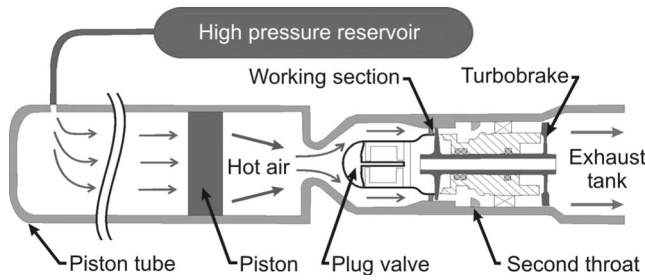
Before a run, the working section is evacuated, and the turbine disk and turbobrake assembly is spun to the design speed (9500 rpm) using an air motor. Air from a high pressure reservoir is injected into the pump tube, of volume 10 m³, behind a light free piston (see Fig. 1). The piston is forced to traverse the pump tube, thereby compressing and heating the air in front of it. The compression process is approximately isentropic. When the desired working section inlet total pressure and temperature (4.6 bars and 444 K) are achieved, the fast-acting plug valve (Fig. 1) is opened. The test gas flows out of the pump tube at approximately 17.4 kg s⁻¹ through the pump tube contraction into a large annulus ahead of the inlet contraction. The working section is shown in Fig. 3. Constant total pressure is achieved by matching the volumetric flow rate into and out of the pump tube. The stage pressure ratio is set by adjusting a choked throat downstream of the turbine. The run ends when the piston reaches the end of the pump tube. A run time with approximately 400 ms of steady flow is achieved. The free turbine power under these conditions is 1.8 MW.

3 Uncertainty Analysis

Any experimentally measured value has an inherent error associated with it, which leads to an uncertainty in the derived result. The total error of a measurement is commonly expressed as the combination of two components: a fixed bias error and a random precision error. The precision error defines the repeatability of a measurement. In this case it determines the smallest change in efficiency that can be resolved. The bias uncertainty is an offset and does not affect the repeatability of a measurement. Abernethy et al. [17] presented the methodology that is the basis of ASME Standards for uncertainty analysis. It is standard to quote the total uncertainty of a variable, x, to a 95% confidence level given by the root-sum-square (RSS) of the associated precision and bias errors:

$$S_x = \{(C_{x1}S_{x1})^2 + (C_{x2}S_{x2})^2 + \cdots + (C_{xn}S_{xn})^2\}^{1/2} \qquad (1)$$

The target uncertainty in the turbine efficiency measurement in the TTF is with precision and bias errors of $\pm 0.25\%$ and $\pm 2.0\%$, respectively. A detailed uncertainty analysis has been performed for each measurement, and the influence coefficients on the un-

Table 1 Turbine MT1 operating point

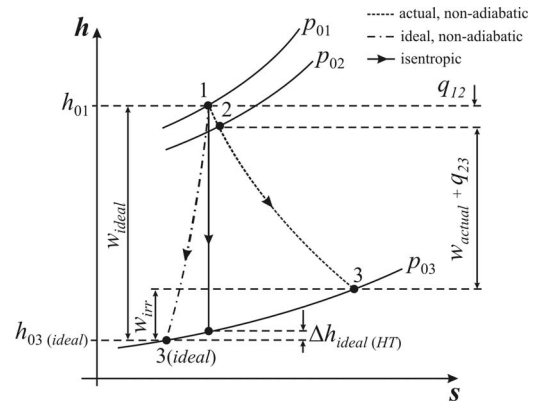| Parameter	Value
Reynolds number based on NGV axial chord	1.61×10^6
Mach number at NGV exit	0.879
Capacity, $\dot{m}\sqrt{T_{01}}/p_{01}$	7.97×10^{-4} kg K$^{1/2}$ Pa^{-1}
Corrected speed, $N/\sqrt{T_{01}}$	451.3 rpm K^{-1}
Inlet total temperature	444 K
Inlet total pressure	4.6×10^5 Pa
Pressure ratio, $\bar{p}_{01}/\bar{p}_{03}$	2.5
Gas-to-wall temperature ratio, T_{gas}/T_{wall}	1.52

certainty in the overall efficiency measurement have been calculated. The influence coefficient of a measured variable, x, on a derived parameter, η, is defined as follows:

$$C_x = \frac{d\eta}{dx} \cdot \frac{x}{\eta} \qquad (2)$$

An overview of the uncertainty analysis performed for the individual measurements detailed in this paper will be presented at the end of the relevant sections. The uncertainty analysis for the final efficiency measurement is presented at the end of this paper.

4 Efficiency Measurement Theory

The efficiency of a machine is a measure of its loss of performance. The loss of performance in turbomachinery components is indicated by the generation of entropy as a result of irreversible processes, for example: viscous losses in boundary layers, mixing of the flow and nonequilibrium processes resulting from the presence of shock waves. Entropy changes also result from heat transfer across surfaces, but this process is reversible, and thus, such entropy changes do not contribute towards a loss in performance.

Almost adiabatic conditions exist in steady state facilities as the temperature of the blade surfaces approaches that of the fluid; the only correction required is for small steady state conduction terms. Hence, the ratio of the actual work extracted from the turbine to the ideal work possible from an isentropic expansion across the same pressure ratio is approximately the same as the *adiabatic efficiency*:

$$\eta_{ad} = \frac{\dot{W}_{actual}}{\dot{W}_{is}} = \frac{\dot{W}_{is} - \dot{W}_{irr}}{\dot{W}_{is}} = \frac{\dot{H}_{01} - \dot{H}_{03}}{\dot{H}_{01} - \dot{H}_{03,is}} \qquad (3)$$

In facilities in which the gas-to-wall temperature ratio is matched to engine conditions (as is the case in the TTF) surface heat fluxes are significant, and processes can no longer be approximated as adiabatic. Heat is lost to the surrounding surfaces, which are relatively cooler. Thus, at the turbine stage exit, the entropy of the fluid is lower than for an equivalent adiabatic process ($ds = dQ/T$).

Casey and Fesich [19] comprehensively discuss the problem of defining efficiency in nonadiabatic flows. Although it has been common practice to define efficiency for nonadiabatic expansion processes in relation to an equivalent ideal isentropic process, the authors argue that it is more logical to define efficiency in terms of a process with the same heat transfer as the real process, but with no irreversibilities that would give rise to additional entropy changes. That is, the reference process in nonisentropic but nonetheless reversible. This appears to be a logical way of addressing the problem. The ideal reference process and actual nonadiabatic expansion process are shown on the h-s chart in Fig. 2 below. The

isentropic process is also indicated. Considering an energy balance:

$$\dot{W}_{\text{ideal}} = \dot{W}_{\text{actual}} + \dot{Q}_{12} + \dot{Q}_{23} + \dot{W}_{\text{irr}} \tag{4}$$

The MT1 stage heat transfer, $(\dot{Q}_{13}=\dot{Q}_{12}+\dot{Q}_{23})$, has been estimated from extensive measurements using thin film gauge instrumentation (previous studies). The power is approximately 100 kW ($\sim$5% of the ideal power). Referring to Fig. 2, the specific power from the ideal reference process, w_{ideal}, may be considered as the combination of the specific power from the isentropic process, w_{is}, and the change in exit enthalpy (from isentropic) as a result of the heat transfer during the expansion, $\Delta h_{\text{ideal},(HT)}$. Therefore:

$$\dot{W}_{\text{ideal}} = \dot{W}_{\text{is}} + \Delta \dot{H}_{\text{ideal},(HT)} \tag{5}$$

Using Eqs. (4) and (5), the efficiency of a turbine measured in a nonadiabatic environment is given by:

$$\eta = \frac{\dot{W}_{\text{ideal}} - \dot{W}_{\text{irr}}}{\dot{W}_{\text{ideal}}} = \frac{\dot{H}_{01} - \dot{H}_{03}}{\dot{H}_{01} - \dot{H}_{03,\text{ideal}}} = \frac{\dot{W}_{\text{actual}} + \dot{Q}_{13}}{\dot{W}_{\text{is}} + \Delta \dot{H}_{\text{ideal}(HT)}} \tag{6}$$

4.1 Ideal Power Measurement. The ideal reference turbine power is given by the combination of isentropic power and the correction term for the change in total exit enthalpy flux (from isentropic) as a result of the heat transfer during the expansion (Eq. (5)). The correction term (Guenette et al. [5]) is–strictly–the integral of dQ/T, but can be estimated by assuming that the heat fluxes in the stator and rotor are transferred at the mean total temperatures of the fluid in the respective passages. For the current situation the correction is estimated to be approximately $0.79\dot{Q}_{13}$. Therefore, the ideal expansion power is given by:

$$\dot{W}_{\text{ideal}} = \dot{W}_{\text{is}} + 0.79\dot{Q}_{13} \tag{7}$$

The isentropic turbine power is determined by considering an expansion between the stage inlet and exit total pressures at constant entropy and with no heat transfer. If the fluid is considered to be an ideal gas, enthalpy is purely a function of temperature. The total inlet enthalpy flux is given by the area integral of the product of local density, axial flow velocity, specific heat capacity, and total temperature. The ideal exit plane temperature is found by considering the isentropic expansion of the working fluid through the turbine stage over the inlet to exit total pressure ratio:

$$\dot{W}_{\text{is}} = \int_{A_1} \rho u_{\text{ax}} c_p T_{01} dA_1 - \int_{A_3} \rho u_{\text{ax}} c_p T_{01} \left(\frac{p_{03}}{p_{01}}\right)^{(\gamma-1)/\gamma} dA_3 \tag{8}$$

In the experimental evaluation of the integrals, the variables must be sampled at sufficiently high spatial resolution to achieve well within the target efficiency bias error of 2.0%. Cumpsty and Horlock [18] provided a clear discussion of how averaging should then be performed and offered suitable schemes applicable to situations involving ideal gases in turbomachines. In the present case a mass-averaging scheme is appropriate. Further details of the mass-averaging scheme and survey instrumentation are given at the end of this paper.

To accurately evaluate the isentropic power, the variation of specific heat capacity, c_p, and ratio of specific heats, γ, with temperature must be considered—the variations are approximately 1.2% and 0.47%, respectively, for an expansion between $\bar{p}_{01}$ and $\bar{p}_{03}$ for the given turbine. The expansion total-to-total pressure ratio is divided into N pressures, where $p_0|_{i=1}=\bar{p}_{01}$ and $p_0|_{i=N}=\bar{p}_{03}$, to create $(N-1)$ successive small expansions. The isentropic power extracted is given by the sum of the power extracted across each small expansion:

$$\dot{W}_{\text{is}} = \sum_{i=1}^{i=N-1} \dot{m}(c_p)_i T_{0,i} - \dot{m}(c_p)_{i+1} T_{0,i} \left(\frac{p_{0,i+1}}{p_{0,i}}\right)^{(\gamma-1)/\gamma} \tag{9}$$
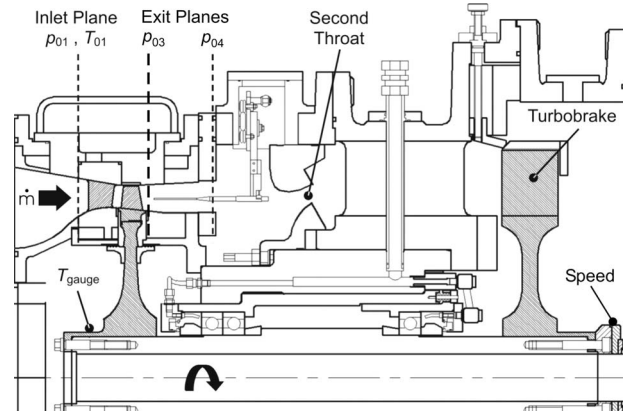

Fig. 3 TTF working section

Across each small expansion, the exit c_p and γ are found iteratively, and the power extracted determined using a mean value of γ across each small expansion. A difference of approximately 3% is predicted between the isentropic powers evaluated using the above scheme and those evaluated by assuming c_p, and γ are constant and equal to the values at the inlet to the turbine stage. To predict the precision uncertainty associated with the evaluation of adiabatic efficiency, the ideal power term is simplified to:

$$\dot{W}_{\text{ideal}} = \dot{m} c_{p_1} \bar{T}_{01} - \dot{m} c_{p_3} \bar{T}_{01} \left(\frac{\bar{p}_{03}}{\bar{p}_{01}}\right)^{(\gamma-1)/\gamma} + 0.79\dot{Q}_{13} \tag{10}$$

4.2 Actual Power Measurement. The actual power that would be developed in the turbine is given by the product of turbine torque and angular velocity. In the TTF the net torque on the shaft assembly (including the turbobrake) is the product of the moment of inertia and angular acceleration. This term appears only as a small correction as the turbobrake maintains constant speed to within 25 rpm in 9500 rpm. A small amount of work is done against drag from the friction in the bearings and windage on the rotor disk. The total torque developed in the rotor is found by considering the equilibrium of the rotating assembly:

$$T_{\text{rotor}} = I_{\text{ass}}\dot{\omega} + T_{\text{brake}} + T_{\text{wind}} + T_{\text{bearings}} \tag{11}$$

A strain gauge system mounted on the rotor disk, detailed in Sec. 5, was used to measure the rotor torque. By mounting the strain gauge bridge in the location shown in Fig. 3, the measured torque, T_{gauge}, is equal to the torque developed in the rotor without a correction due to the acceleration of the rotor disk (not the remaining entire rotating assembly) and a correction due to windage; thus:

$$T_{\text{gauge}} = T_{\text{rotor}} - T_{\text{windage}} - I_{\text{rotor}}\dot{\omega} \tag{12}$$

An advantage of this system is that direct evaluation of the bearing drag, which changes with axial load, is not required. In similar facilities, the measurement of bearing drag has been performed using *spin-down* tests (see, for example, Ref. [11]). The change in bearing torque with axial load is not evaluated using this procedure. During a test run, the windage drag is computed using a Rolls-Royce (UK) correlation and measurements of the front and rear rotor cavity pressures. As the cavity pressures increase, the windage term increases, reaching a maximum of 2.7% of the rotor torque. Therefore, the indicated power developed in the rotor is given by:

$$\dot{W}_{\text{actual}} = \dot{W}_{\text{rotor}} = (I_{\text{rotor}}\dot{\omega} + T_{\text{gauge}} + T_{\text{wind}})\omega \tag{13}$$

The moment of inertia used in Eqs. (12) and (13) is that between the strain gauge location and the rotor blades. The total moment of inertia disk was calculated by Hilditch et al. [2] at 1.415 kg m^2: a correction of -0.35% is required with the gauges

Table 2   Efficiency influence coefficients

Variable	Nominal value	Influence coefficient	$\|C_x\|$
ω	995 rad s^{-2}	$C_{T_{\text{gauge}}} = \dfrac{\dot{W}_{\text{actual}}}{\dot{W}_{\text{actual}} + \dot{Q}_{13}}$	~1
$\dot{\omega}$	~7 rad s^{-2}	$C_{T_{\text{gauge}}} = \dfrac{T_{\text{rotor}}\dot{\omega}\omega}{\dot{W}_{\text{actual}} + \dot{Q}_{13}}$	5.3×10^{-3}
T_{gauge}	~1759 N m	$C_{T_{\text{gauge}}} = \dfrac{T_{\text{gauge}}\omega}{\dot{W}_{\text{actual}} + \dot{Q}_{13}}$	~0.97
T_{wind}	~50 N m	$C_{T_{\text{gauge}}} = \dfrac{T_{\text{gauge}}\omega}{\dot{W}_{\text{actual}} + \dot{Q}_{13}}$	~0.03
$\dot{m}$	17.4 kg s^{-1}	$C_{\dot{m}} = \dfrac{\dot{W}_{\text{ideal}} - \dot{Q}_{13}}{\dot{W}_{\text{ideal}}}$	1
$\bar{T}_{01}$	444 K	$C_{\bar{T}_{01}} = \dfrac{\dot{W}_{\text{ideal}} - \dot{Q}_{13}}{\dot{W}_{\text{ideal}}}$	1
$\bar{P}_r = \dfrac{\bar{p}_{03}}{\bar{p}_{01}}$	0.4	$C_{\bar{P}_R} = \dfrac{\dot{m}c_p\bar{T}_{01}\left(\dfrac{\gamma-1}{\gamma}\right)\bar{P}_R{}^{(\gamma-1)/\gamma}}{\dot{W}_{\text{ideal}}}$	0.8
$\dot{Q}_{13}$	~100 kW	$C_{\dot{Q}_{13}} = \dfrac{\dot{Q}_{13}}{\dot{W}_{\text{actual}} + \dot{Q}_{13}} - \dfrac{0.79\dot{Q}_{13}}{\dot{W}_{\text{ideal}}}$	1.3×10^{-2}

Fig. 4   Strain gauge torque measurement system

5   Torque Measurement

Successful shaft power measurements have been performed in unbraked facilities by Atkins and Ainsworth [20] and Dénos et al. [9]. Both systems determine the turbine acceleration, and hence shaft power, from the accurate measurement of rotor speed using a high resolution optical encoder. The MIT facility [7] includes an eddy current braking system, from which the induced current is measured to determine the turbine torque.

Strain gauges are commonly used in industry and engineering situations to measure strain as they are so robust and simple and are well suited to the application in the TTF. Strain gauge measurement systems provide highly accurate measurements (typical accuracy of order 0.1%), and designs can compensate for temperature variations and axial, centrifugal, and bending forces.

5.1   Strain Gauge Theory. Wire resistance strain gauges exploit the fact that the resistance of a conducting wire changes with length, cross-sectional area, and metal density. The strain sensitivity of a strain gauge, known as gauge factor, is defined as:

$$k = \frac{dR/R}{\varepsilon} = 1 + 2\upsilon + \frac{d\rho/\rho}{\varepsilon} \qquad (15)$$

For most metals $\upsilon = 0.3$, and thus the gauge factor is typically between 2.0 and 2.2. As the change in strain gauge resistance is proportional to the applied strain, gauges are best located in a position of high local strain. Under torsion, the local shear strain is dependent on the applied torque, the radius from the moment axis, the polar second moment of area, and the shear modulus of the material:

$$\varepsilon = \frac{\tau}{2G} = \frac{1}{2G}\frac{Tr}{J} \qquad (16)$$

5.2   TTF Strain Gauge Torque System. The strain gauge torque measurement system deployed in the TTF is shown in Fig. 4. The two main design considerations were as follows: the positioning of the strain gauges on the rotor disk in an area of high local shear strain, and their mounting orientation and electrical connection to amplify the individual strain gauge signals and reject unwanted strain components. The torque is constant throughout the turbine disk, and therefore the smallest sections at large radius will experience the largest local shear strain. The gauges were positioned on the endcap of the turbine disk where the rotor disk connects to the shaft (see Figs. 3 and 4). Here the gauges are subject to relatively low centrifugal forces because of the low radius. Modeling the endcap section as a thin walled cylinder, the local strain is 79.5 μstrain in this section.

Sixteen strain gauges (eight half-bridges) were distributed around the endcap in the same axial plane at equally spaced locations. The gauges were connected in a standard Wheatstone bridge
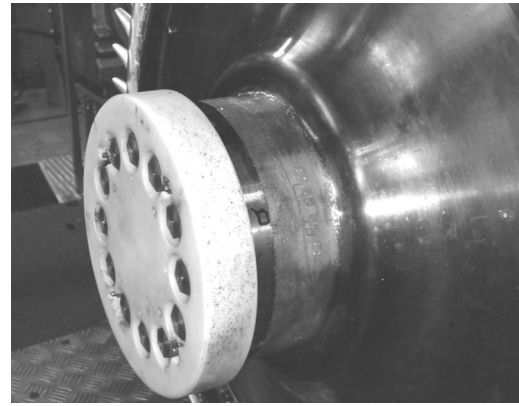
in the location shown. Turbine speed is measured using a 60 line optical encoder mounted on the shaft, which is sampled at 1 MHz.

4.3   Adiabatic Efficiency. The adiabatic efficiency of a turbine tested in the TTF at QinetiQ is found by substituting Eqs. (10) and (13) into Eq. (6) and is given by Eq. (14) below. Figure 3 shows the location of the inlet and exit planes and provides a summary of the measurements required for this measurement:

$$\eta = \frac{(I_{\text{rotor}}\dot{\omega} + T_{\text{gauge}} + T_{\text{wind}})\omega + \dot{Q}_{13}}{\dot{m}c_{p_1}\bar{T}_{01} - \dot{m}c_{p_3}\bar{T}_{01}\left(\dfrac{\bar{p}_{03}}{\bar{p}_{01}}\right)^{(\gamma-1)/\gamma} + 0.79\dot{Q}_{13}} \qquad (14)$$

4.4   Efficiency Measurement Uncertainty Analysis. The design point nominal values and influence coefficients for each of the measurements required to evaluate stage efficiency are summarized in Table 2. For presentation purposes, the expressions for influence coefficient are given in terms of the actual work extracted by the rotor, $\dot{W}_{\text{actual}}$, and the ideal work extracted by the rotor, $\dot{W}_{\text{ideal}}$, which are defined by Eqs. (13) and (10), respectively.

The uncertainty contributed by each variable on the overall efficiency measurement uncertainty may be estimated by the product of the associated influence coefficient and measurement uncertainty for each variable. Measurement uncertainties associated with each variable in Eq. (14) are the subject of the remainder of this paper. The influence coefficients associated with each variable are summarized in Table 2, and it is apparent that the coefficients with $\dot{m}$, T_{01}, $\bar{p}_{03}/\bar{p}_{01}$, ω, and T_{gauge} are over an order of magnitude larger than those for the remaining variables. Therefore, it is to these variables that particular attention is turned to ensure both accurate measurement and evaluation of the uncertainty. The rotor disk moment of inertia has no precision uncertainty associated with it as the change in mass/mass distribution (due to oil accrual, etc.) during the program is entirely negligible.
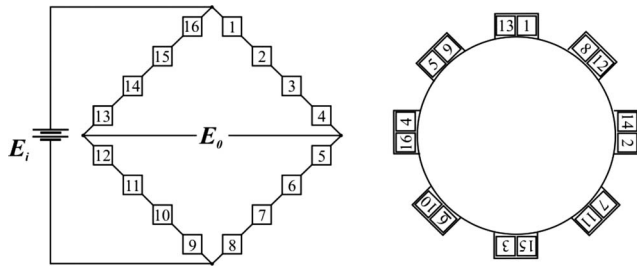
Fig. 5 Strain gauge Wheatstone bridge circuit

Fig. 6 Torque calibration facility

configuration (see Fig. 5). The output potential difference is found by considering all resistances in the bridge to be a result of active strain gauges:

$$E_0 = E_i\left[\frac{R_{9-12}}{R_{9-12} + R_{13-16}} - \frac{R_{5-8}}{R_{1-4} + R_{5-8}}\right] \quad (17)$$

The change in output voltage, or signal level, is found by evaluating the appropriate partial derivatives:

$$\delta E_0 = E_i\left[\frac{R_{5-8}dR_{1-4} - R_{1-4}dR_{5-8}}{(R_{1-4} + R_{5-8})^2} + \frac{R_{13-16}dR_{9-12} - R_{9-12}dR_{13-16}}{(R_{9-12} + R_{13-16})^2}\right] \quad (18)$$

The Wheatstone bridge is carefully balanced, so that each leg of the bridge has equal resistance, and gauges with almost identical gauge factors have been selected. By substituting Eq. (15) into Eq. (18), the strain gauge bridge sensitivity (millivolts of signal per volt of excitation) is found in terms of the local strains:

$$\frac{\delta E_0}{E_i} = \frac{k}{4}(\varepsilon_{1-4} - \varepsilon_{5-8} + \varepsilon_{9-12} - \varepsilon_{13-16}) \quad (19)$$

Careful positioning of the strain gauges within the Wheatstone bridge gives good signal amplification and elimination of unwanted strain components. A shaft in pure torsion experiences a strain distribution, which has maximum and minimum values along principal axes at ± 45 deg to the longitudinal axis of the shaft. The strain gauges are positioned along the principal axes to measure the principal strains. Each half-bridge contains both a strain gauge under tension and one under compression, these of equal but opposite magnitudes. Strain gauges 1–4 and 9–12 are mounted along the primary principal axis, and gauges 5–8 and 13–16 are mounted along the secondary axis. By considering Eq. (19), mounting the strain gauges in this arrangement results in a bridge sensitivity four times greater than a single strain gauge. It also eliminates the measurement of strains as a result of rotor temperature variations and axial, centrifugal, and moment forces.

The strain gauge bridge signal is processed by a rotating in-shaft electronics processing unit (EPU) mounted along the center axis of the shaft. The EPU excites the strain gauge bridge with a nominally smooth 6 V signal and contains a high-gain strain gauge amplifier, analog-to-digital converter, microprocessor, volatile memory, and RS232 driver. In normal operation (prior to a run in the TTF), the torque signal is sampled at 4.6 Hz, digitized into 8 bits at a resolution of 1:2000, and transmitted in real time through the slip ring. This enables monitoring of the turbine during the spin-up in vacuum. When triggered, a 2.2 s burst capture at 30 kHz is stored in the EPU memory. The data captured at the high sample rate are downloaded after the run is finished. This avoids the noise associated with real-time transmission through the slip ring.

5.3 Torque System Calibration. The torque calibration facility at Oxford University, shown in Fig. 6, is used to apply a known reference torque to the turbine disk in order to calibrate the strain gauge bridge sensitivity. A reference inline torque transducer (accuracy of $\pm 0.03\%$) and the rotor disk are mounted on the
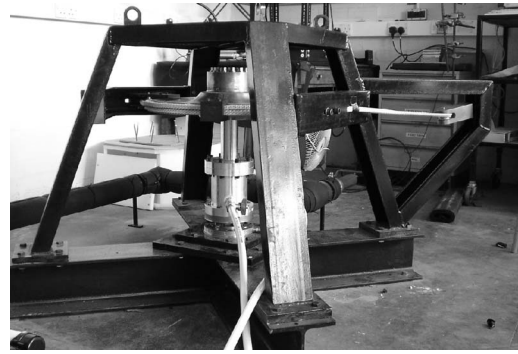
same vertical shaft, with a direct torque path between them. The reference transducer has been calibrated by the German Calibration Service (DKD), which is traceable to International Standards. Kevlar webbing is attached to the disk in two blade roots (180 deg apart), wrapped around the disk to protect the blade roots from damage, and fed through a pulley system used to apply a static torque of up to 2500 N m. This arrangement ensures that the reference torque is applied symmetrically to the rotor disk and that no cross-loads exist. The turbine disk and in-shaft electronics are housed in heater boxes, and their temperatures can be independently varied between ambient conditions and $80\,^\circ$C. Thus, the relatively small temperature dependence of the calibration can be accounted for.

5.4 Torque Measurement Uncertainty Analysis. A graph of strain gauge bridge output voltage against reference torque obtained from the calibration of the torque measurement system is presented in Fig. 7. A plot that shows the difference between the calibration data and the linear regression is also given. The standard deviation of residuals is ± 0.1690 μV per volt of excitation. The strain torque system has a full range value of 2500 N m, at which point the bridge signal is 0.1856 mV per volt of excitation. The standard deviation of the residuals is $\pm 0.091\%$ of the maximum bridge signal (2500 N m). Thus, the associated precision uncertainty is $\pm 0.182\%$ to 95% confidence.

Despite careful system design of the bridge system, both the strain gauge bridge zero signal and sensitivity (slope in Fig. 7) are weak functions of rotor disk temperature. Although the disk temperature distribution is inherently axisymmetric, allowing a single temperature correction to be computed, small run-to-run variations in this temperature cannot be eliminated. The bridge sensitivity was determined for a disk temperature range of $20-80\,^\circ$C: the nominal disk temperature was $20\,^\circ$C. An insulated box and surface heaters were used for this purpose, and long settling times were allowed so that isothermal conditions prevailed before a calibration was performed. A variation in strain gauge bridge sensitivity (slope of the calibration data in Fig. 7) of 0.28%/10 K change in disk temperature was observed. During testing, the disk temperature was monitored using four surface-mounted thermocouples evenly distributed around the disk mounting cap adjacent to the strain gauges. The rise in disk temperature during a typical test run was approximately 5 K, and the estimated error in applying the correction for the change in calibration slope was $\pm 0.07\%$. The change in output signal for zero torque (the zero offset) is a function of both the bridge temperature and the temperature of the electronics. Calibration experiments were performed in which the temperatures of the bridge and electronics were independently varied over the range of $20-80\,^\circ$C. These experiments indicated that the zero offset was only a weak function of both temperatures. During a test run, the thermal drift in zero offset is accounted for in post-processing by measuring the value prior to the onset of flow–at this point the torque rotor torque is zero. The total precision uncertainty in the measurement
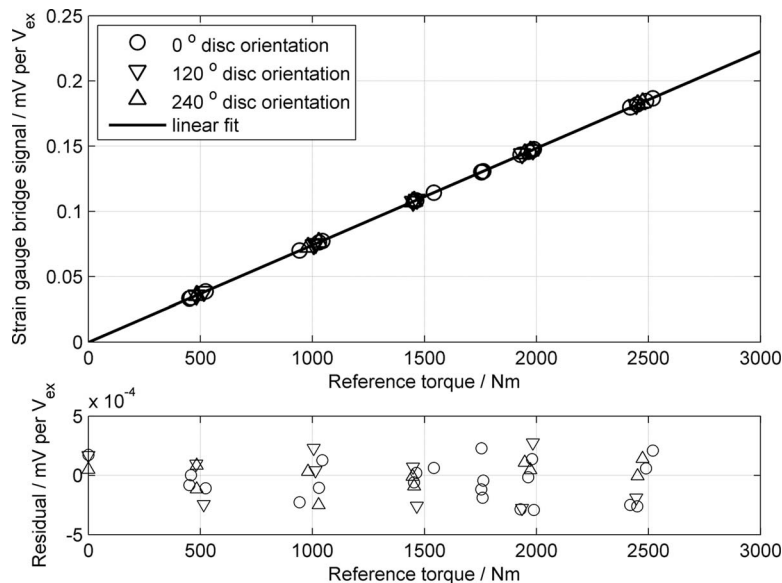
Fig. 7 TTF strain gauge torque system calibration data

of shaft torque, given by the root-sum-square of the uncertainty in the regression analysis ($\pm 0.182\%$) and the error in applying the correction for the change in calibration slope with temperature ($\pm 0.07\%$), is $\pm 0.195\%$.

The bias uncertainty associated with the torque measurement system arises primarily from the uncertainty associated with the inline reference transducer (nominal accuracy of $\pm 0.03\%$). The reference transducer is also a strain gauge based system, and hence the increase in uncertainty associated with the change in calibration slope with temperature ($\pm 0.03\%/10$ K), the zero drift with temperature ($\pm 0.033\%/10$ K), and the combined nonlinearity and hysteresis errors ($\pm 0.05\%$) must be accounted for. Also, although the calibration facility was designed to minimize parasitic loads (axial, lateral, and additional moment loads) on either the reference transducer or the turbine disk, small misalignments in the system are unavoidable. The worst-case estimates of the axial, lateral, and moment loads were 1.2 kN, 0.2 kN, and 0.2 kN m, respectively. This represents 38% of the cross-load limit of the reference transducer. The uncertainty of the reference torque transducer increases from $\pm 0.03\%$ with zero cross-load to $\pm 0.2\%$ with maximum cross-load. Therefore, with the calculated worst-case cross-load, the additional uncertainty was $\pm 0.095\%$. Assuming a maximum change in transducer temperature of 10 K, the root-sum-square of the (bias) uncertainties associated with the reference torque transducer was $\pm 0.117\%$.

5.5 Preliminary Torque Results. The torque measurement system in the TTF provides a continuous measurement of shaft torque. The spin-up data are recorded, and the net shaft torque for each run is simply calculated from the change in torque at the onset of flow. The temperatures of the rotor disk endcap (strain gauge location) and the in-shaft electronics are recorded during each TTF test run. The temperature of the endcap is measured with four surface thermocouples (bare wire 51 μm bead) mounted next to the strain gauge locations. The in-shaft electronics temperature is monitored with two surface-mounted thermocouples of similar sizes. All of the thermocouples are mounted in similar positions to those used in the calibration of the system.

During processing the net torque is filtered with a 200 Hz cutoff impulse digital filter to match the bandwidth of the other measurements. Figure 8 shows torque data taken for ten runs in the TTF at MT1 design conditions.

During a normal TTF run, the MT1 NGVs are approximately choked. Ignoring subtle changes in turbine pressure ratio and non-

dimensional speed ($N/\sqrt{T}$), the extracted power should simply vary with stage mass-flow rate, which is primarily a function of inlet total pressure under choked conditions. The shaft torque and inlet total pressure for a typical run are both plotted in Fig. 9. The left hand axis shows shaft torque, and the right hand axis shows inlet total pressure. The measured shaft torque accurately follows both a slight upward trend and the pressure fluctuations (as a result of the piston oscillation) in the trace of inlet total pressure without any phase delay.

6 Mass Flow Rate Measurement

A number of techniques have been used in transient facilities to measure the stage mass-flow rate. In the MIT Blowdown Facility [7], a calibrated critical flow venturi is employed downstream of the rotor. A correction is required to account for the change in stored mass between the turbine stage and the venturi. The Oxford Rotor Facility uses the contraction of the inlet duct and vane throat as a venturi [11], which was calibrated by blowdown experiments. The VKI Compression Tube Facility uses a "zero-dimensional model" to calibrate the turbine stage as a flowmeter at a given operating condition. Thereafter, the capacity of the turbine stage is regarded as fixed (at the given operating condition), and the mass-flow rate is computed as for a choked nozzle [21].
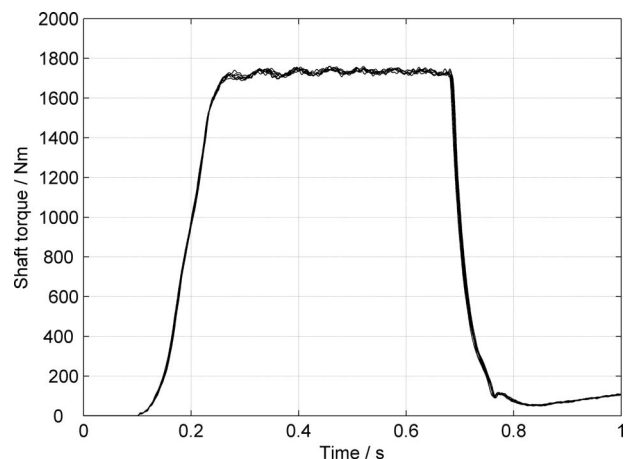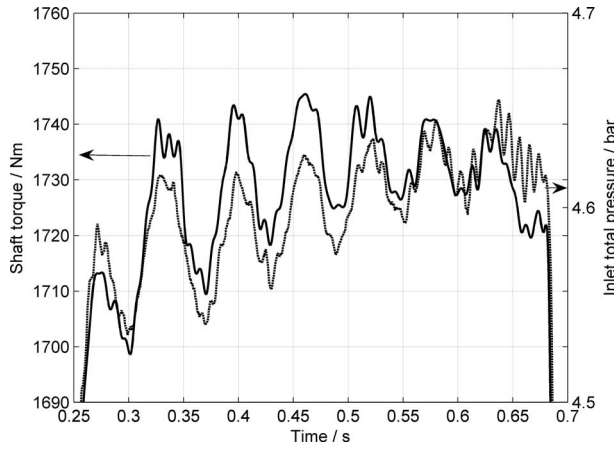

Fig. 8 MT1 shaft torque

Fig. 9 MT1 shaft torque with inlet total pressure

Fig. 11 CFD prediction of static pressure on the pump tube contraction wall

The use of the turbine nozzle as a venturi has much to recommended itself: the flow here is almost choked, and the nozzle effective area is therefore a weak function of the downstream conditions. However enhanced inlet temperature distortion [22] and inlet swirl, both of which can be simulated in the TTF, alter the effective area of the NGV throat. A calibrated nozzle downstream of the turbine was considered impractical on grounds of installation effects and the additional uncertainty that would arise as a result of residual temperature distortion and swirl.

The technique developed for the TTF uses the exit contraction of the pump tube, shown in Fig. 10, which acts as a subsonic converging-diverging. The mass-flow rate was evaluated by considering continuity of mass and allowing for compressibility effects. The mass-flow rate is given as follows:

$$\dot{m}_t = p_0 A_{\text{eff}} M \sqrt{\frac{\gamma}{RT_0}} \left(1 + \frac{\gamma-1}{2} M^2\right)^{-(\gamma+1)/2(\gamma-1)} \quad (20)$$

The total temperature of the flow at the throat is measured using four evenly distributed rakes of thermocouples downstream of the contraction, as shown in Fig. 10. Each rake contains five 25.4 μm bare thermocouples. The throat Mach number is found by measuring the total-to-static pressure ratio at the venturi throat. Although the Mach number distribution is nonuniform across the throat section, the distribution is well defined, and a single Mach number evaluated using the static pressure at the throat can be used to compute the mass-flow rate. To correct for the nonuniformity, the effective area term, A_{eff}, is evaluated in a calibration experiment:

$$M = \sqrt{\frac{2}{\gamma-1}\left\{\left(\frac{p_0}{p}\right)^{(\gamma-1)/\gamma} - 1\right\}} \quad (21)$$

The effective area term also allows for the displacement effect of viscous boundary layers to be accounted for. It can be assumed that A_{eff} is dependent on Reynolds number, Mach number, Prandtl number, and gas-to-wall temperature ratio.
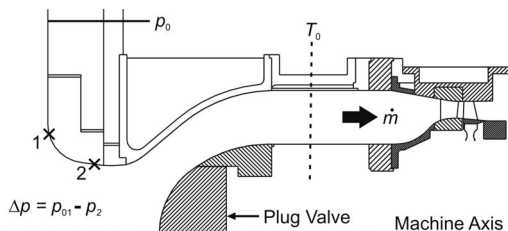

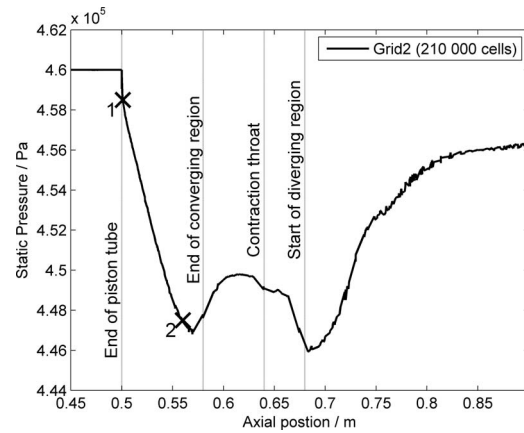Fig. 10 TTF pump tube contraction and mass-flow rate instrumentation

6.1 CFD Modeling. The optimum location of the pressure tappings used to compute mass-flow rate was determined using computational fluid dynamics (CFD). The flow in the pump tube contraction was modeled using the steady, three-dimensional, viscous CFD flow-solver FLUENT 6.1. The Spallart–Allmaras turbulence model was used. The gas was treated as ideal and incompressible ($M \sim 0.16$). The boundary conditions were set such that inlet total pressure (4.6 bars) and mass-flow rate (17.4 kg/s) were matched to nominal conditions. The results of the CFD model are shown in Fig. 11. The prediction shows a 0.1 bar drop in static pressure through the contraction. To achieve the required accuracy, the static pressure was measured using differential transducers referenced to the upstream total pressure. The CFD prediction was used to optimize the position of tappings, which correspond nominally to an upstream total pressure measurement and a throat static pressure measurement. An over-acceleration of the flow is predicted upstream of the throat, after which the pressure recovers to the throat value. As a result of the increasing pressure gradient just upstream of the throat location, placing the static tapping at the throat risks the measurement being placed in an area of localized flow separation. The throat static pressure tapping is located in the region of over-acceleration just before the pressure begins to recover (position 2 in Figs. 10 and 11). The upstream total pressure tapping is located just inside the contraction (position 1 in Figs. 10 and 11) to protect the transducer from over-pressure as the piston hits the end of the pump tube. The downstream tapping is also circumferentially offset 20 mm from the upstream tapping to ensure that the throat tapping is not affected by its presence. The stage mass-flow is calculated using four differential measurements of this type evenly distributed around the pump tube contraction.

6.2 Stage Mass Rate. The finite mass of the piston causes $\pm 1\%$ fluctuations in the total pressure at a frequency of approximately 16 Hz. These inlet pressure fluctuations cause the stored mass in the diffuser volume between the contraction throat and the NGV inlet to vary during a test run. To calculate the stage mass-flow rate, the variation in stored mass in this volume must be accounted for. Temperature and pressure are measured at various locations within the intermediate plenum so that this correction can be performed. The change in stored mass is given by the time derivative of the ideal gas law. Thus, the stage mass-flow rate is given by

$$\dot{m} = \dot{m}_t - \frac{V_{\text{diff}}}{R} \frac{d}{dt}\left(\frac{p_{\text{diff}}}{T_{\text{diff}}}\right) \quad (22)$$

6.3 Measurement of Mass-Flow Rate. A method used for flowmeter calibration in primary facilities is the blowdown experi-
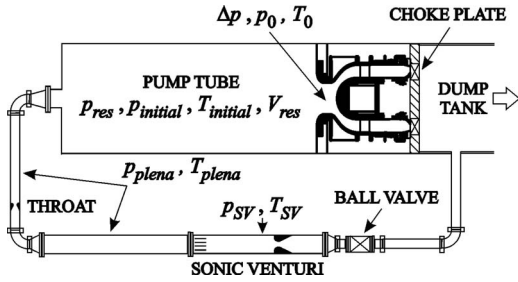
Fig. 12 Schematic of mass-flow rate blowdown calibration (not to scale)

Fig. 13 Π_1 as a function of time for 44 experiments and best fit line

ment, in which the change in stored mass in a plenum of known volume is determined under conditions of thermal equilibrium by the thermodynamic method of measuring pressure and temperature. In a somewhat analogous manner, a novel calibration experiment was performed in which the stored mass in the pump tube (which acts as the plenum) was determined as a function of the pressure in the tube and under conditions of thermal nonequilibrium [23]. This calibration was conducted using a sonic venturi nozzle with traceable calibration.

This permitted a second calibration of blowdown experiments to calibrate the subsonic contraction at the pump tube exit plane (see Fig. 10) over a wide range of Re and M. To achieve conditions in the calibration either side of the nominal run condition (in both Re and M), the nozzle guide vanes were replaced with a choke plate of adjustable area either side of the nominal area.

The circumlocutory calibration method described has two advantages. First, it negates the need of permanently introducing a calibrated flow meter in the main flow path. Second, it ensures that the flow through the pump tube contraction is representative of run conditions during the calibration experiment. The experimental layout is shown schematically in Fig. 12. The two calibration experiments are now described in turn.

6.4 Blowdown Calibration Experiment. In the first calibration experiment, the plug valve (between the pump tube and working section) was sealed, and the pump tube was vented though the calibrated sonic venturi nozzle. Experiments were conducted over a wide range of initial pressures and venting time constants. The time constant was varied by adjusting a throat near the exit of the plenum. For a blowdown process, which is isentropic—that is, no heat transfer from the walls—the mass-flow rate exiting a plenum is related to the pressure in the plenum by the following equation:

$$\dot{m}_{\text{isentropic}} = \frac{d}{dt}\left\{\frac{p_{\text{res}}V_{\text{res}}}{RT_{\text{initial}}}\left(\frac{p_{\text{initial}}}{p_{\text{res}}}\right)^{(\gamma-1)/\gamma}\right\} \quad (23)$$

The assumption is that the temperature in the vessel is related to the pressure as for an isentropic expansion of an ideal gas. Physically this is not so, and as the expansion progresses, a relatively warm layer of gas forms at the wall of the vessel as a result of heat transfer with the wall. It is possible to express this nonisentropic effect in the form of a correction factor [23]. It can be shown that the ratio of the measured mass-flow rate leaving the vessel to the mass-flow rate that one would infer from the pressure measurement alone (assuming an isentropic temperature trend) is given as follows:

$$\Pi_1 = \frac{\gamma RT_{\text{initial}}}{V_{\text{res}}}\frac{dm/dt}{dp/dt}\left(\frac{p_{\text{res}}}{p_{\text{initial}}}\right)^{(\gamma-1)/\gamma} \quad (24)$$

The nominal value of the parameter, Π_1, is unity, but the value increases with time, as heat transferred to the enclosed gas increases. A series of 44 experiments was conducted, and it was demonstrated that a very good collapse of Π_1 could be achieved against time. A graph of Π_1 against t is presented in Fig. 13. The
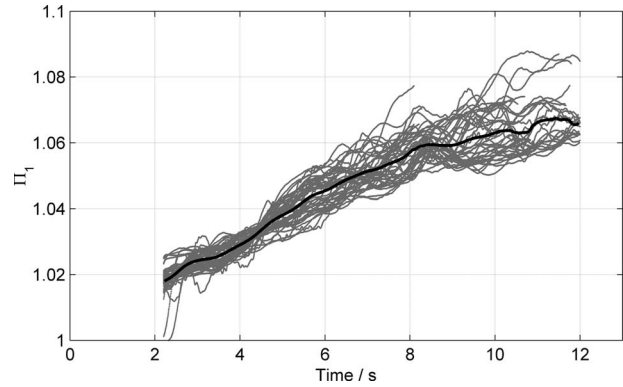
best fit line is also shown. It is seen that the magnitude of the correction factor Π_1 is significant, reaching approximately 1.06 at 10 s.

The bias error (defined as the mean difference between the inferred mass-flow rate—calculated using the nonisentropic correction factor—and measured mass-flow rate at a given time) and the standard deviation (the root mean square (rms) difference between the inferred and measured mass-flow rates at a given time) are presented as a percentage of $\dot{m}_0(t)$ in Fig. 14 and as a function of time over the same period as in Fig. 13. The mean standard deviation over this period is $\pm 0.47\%$. The mean absolute bias error is $+0.048\%$.

The standard deviation gives an indication of the precision uncertainty in mass-flow rate for a single blowdown experiment: to 95% confidence, the precision uncertainty is $\pm 0.94\%$. The bias uncertainty in $\dot{m}_0(t)$ is approximately $\pm 0.89\%$ to 95% confidence; this arises primarily from the uncertainty associated with the discharge coefficient of the secondary device (the venturi nozzle) used to perform the calibration. That accuracy comparable to conventional tertiary flowmeters can be achieved is a powerful demonstration of the utility of this technique.

6.5 Effective Area Calibration Blowdown. The second calibration experiment is now described. In this experiment the blowdown calibration—just described—was used to determine the mass-flow rate exiting the pump tube. The bias and precision uncertainties in the mass-flow rate so determined are approximately $\pm 0.89\%$ and $\pm 0.94\%$ to 95% confidence (RSS $\pm 1.29\%$). The flow direction was reversed by sealing the rear of the pump tube, as in normal TTF operation, and using the plug valve to control the discharge. By venting the pump tube in this manner, the subsonic contraction at the pump tube exit plane (see Fig. 12) was calibrated: that is, the effective area was found. To achieve con-
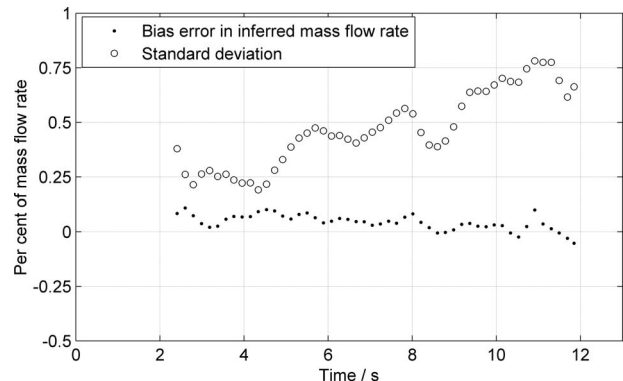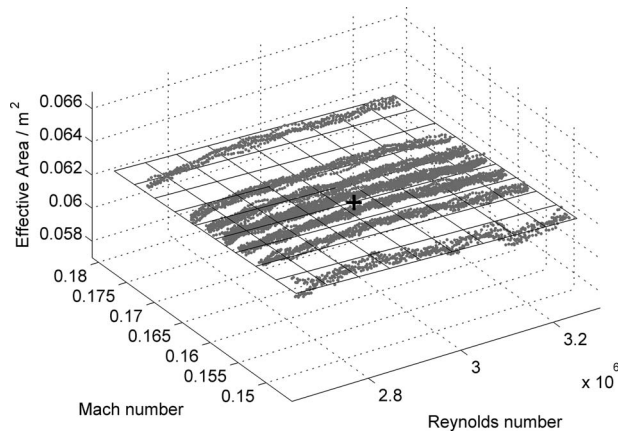

Fig. 14 Bias error and standard deviation as a function of time

Fig. 15 Pump tube contraction effective area versus Reynolds number and Mach number

Variable	Influence coefficient (C_*)	Sensitivity (S_*)	Uncertainty $U_* = |C_* S_*|$
p_0	$C_{p_0} = 1$	$S_{p_0} = 0.05$	0.05
A_{eff}	$C_{A_{\text{eff}}} = 1$	$S_{A_{\text{eff}}} = 0.012$	0.012
T_0	$C_{T_0} = -0.5$	$S_{T_0} = -0.11$	0.055
M	$C_M = 0.962$	$S_M = 0.057$	0.055
$\dot{m}_{\text{diff}}$	$C_{\dot{m}_{\text{diff}}} \sim 0.01$	$S_{\dot{m}_{\text{diff}}} \sim 10$	~ 0.1
Total uncertainty (RSS)			$\pm 0.137\%$

The precision uncertainty in mass-flow rate is estimated by considering the influence coefficients from Eqs. (20)–(22). The uncertainty in the effective area of the pump tube contraction is determined by the degree of accuracy with which it is possible to map onto the calibration surface by evaluating the Reynolds number and Mach number at this location. Table 3 provides a summary of the analysis, estimating a mass-flow rate precision uncertainty of $\pm 0.137\%$.

6.7 Preliminary Mass-Flow Rate Results. During normal operation of the TTF, the mass-flow rate through the pump tube contraction is found by considering Eq. (20). Results of mass-flow rate exiting the pump tube from ten runs at the MT1 operating point are shown in Fig. 16 below. A mean mass-flow rate of 17.35 kg s^{-1} is observed during the steady region of the run (0.3–0.65 s), which compares well with the QinetiQ numerical prediction of 17.4 kg s^{-1} at nominal conditions. The fluctuations in mass-flow rate are a result of the oscillations in upstream total pressure.

The MT1 stage mass-flow rate is evaluated by considering Eq. (22). Figure 17 plots the MT1 stage mass-flow rate for ten test

ditions in the calibration either side of the nominal run condition (in both Re and M), the nozzle guide vanes were replaced with a choke plate of adjustable area either side of the nominal area.

The effective area of the contraction was assumed to be a function of Reynolds number, Mach number, Prandtl number, and gas-to-wall temperature ratio. At the beginning of each blowdown experiment, the pump tube gas was approximately at room temperature; the temperature decreases during the blowdown. Hence, the gas-to-wall temperature ratio will not be matched to that of a normal test run. As the gas temperature is lower than in a normal test run, the Prandtl number will also be different. Therefore, the thermal boundary layer in the contraction will be different in the calibration experiment to a typical run. In fact the temperature profile in the thermal boundary layer will be reversed. The effect of changing the gas-to-wall temperature ratio was studied numerically using CFD. The predicted difference between the evaluated mass-flow rate at the nominal TTF condition ($T_{\text{gas}}/T_{\text{wall}} = 1.52$) and the blowdown condition ($T_{\text{gas}}/T_{\text{wall}} = 0.91$) was approximately 0.26%. The uncertainty associated with the application of this correction is a second order effect and is negligible.

The effective area of the pump tube contraction was evaluated over a $\pm 10\%$ range of both design point Reynolds number and Mach number. The contraction Mach number was set by varying the area of the choke plate. Reynolds number varies during a blowdown experiment, but the initial pump tube pressure sets the range of contraction Reynolds number during the calibration. The inferred mass-flow rate—evaluated using the nonisentropic correction factor—is used to determine the effective area of the contraction under calibration. The effective area is given as follows:

$$A_{\text{eff}} = \frac{A_t \dot{m}_{\text{actual}}}{\dot{m}_t} = \frac{\Pi_1 \left\{ \dfrac{dp}{dt} \dfrac{V_{\text{res}}}{\gamma R T_{\text{initial}}} \left(\dfrac{p_{\text{res}}}{p_{\text{initial}}} \right)^{(1-\gamma)/\gamma} \right\}}{p_0 M \sqrt{\dfrac{\gamma}{R T_0}} \left(1 + \dfrac{\gamma-1}{2} M^2 \right)^{-(\gamma+1)/2(\gamma-1)}}$$

(25)

6.6 Mass-Flow Rate Measurement Uncertainty. Figure 15 shows the calibration map of effective area versus Mach number and Reynolds number for the pump tube contraction. The effective area has a small dependency on both of these variables as expected.

The data are fitted using a principal component analysis (minimizing the least square error). The standard deviation in the plane fitting error is 0.23%. A bias error in mass-flow rate of approximately $\pm 1.37\%$ arises from the combination of the total uncertainty in the measurement of actual mass-flow rate exiting the pump tube and the plane fitting area for the pump tube contraction effective area.
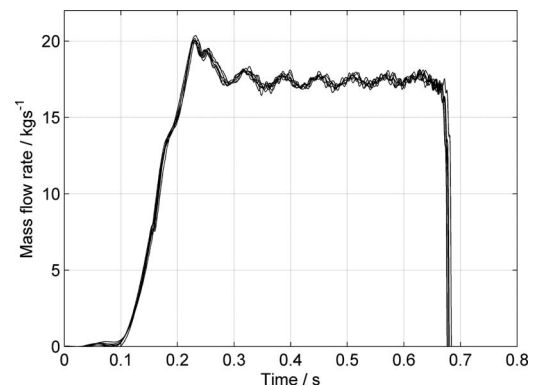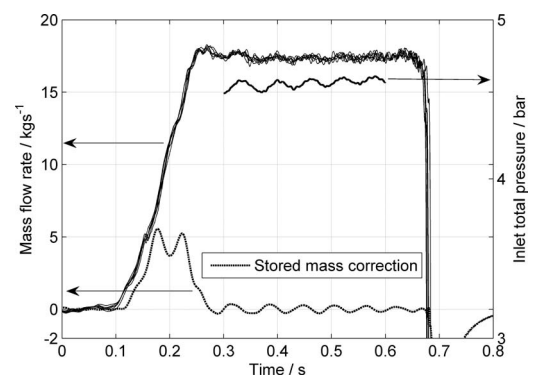

Fig. 16 Pump tube contraction mass-flow rate for ten runs

Fig. 17 MT1 stage mass-flow rate

runs at design conditions (left hand axis) with a typical trace of inlet total pressure (right hand axis). A typical mass-flow rate correction compensating for the change in stored mass in the diffusing plenum between the pump tube exit and the NGV throat is also plotted. The MT1 NGVs are approximately choked; hence the stage mass-flow rate should be primarily a function of the upstream stagnation conditions. As expected the stage mass-flow rate follows the trends observed in the inlet total pressure.

7 Mass-Weighted Area Surveys

High resolution area surveys of the inlet total pressure and temperature and exit total pressure are conducted in order to determine the ideal power by mass weighting the flow at the inlet and exit to the turbine. The positions of the inlet and exit planes are shown in Fig. 3. The inlet plane is 21 mm upstream of the NGV leading edge plane. The exit plane is 4.5 mid-height axial chords downstream of the rotor trailing edge. Over N discrete points, the mass average of a measurement, X, is given by:

$$\bar{X} = \frac{1}{\dot{m}} \sum_{n=1}^{N} \rho_n u_n A_n X_n \qquad (26)$$

The sum of the individual cell mass-flow rates is normalized by the stage mass-flow rate, which is measured in the manner described previously. This negates the bias error associated with the sum of the individual cell mass-flow rates. The following sections describe instrumentation for each of the mass-averaged area surveys.

7.1 Inlet Total Pressure. The inlet total pressure is surveyed over two NGV pitches at 19 circumferential positions. The profile of the inlet total pressure is acquired by traversing three radial fixed rakes each with nine Kiel head pitot tubes. A number of runs are required to obtain the complete profile, and the pressure profile is normalized using three fixed rakes (each of five Kiel head pitot tubes), which are distributed around the annulus at the same axial plane. The largest variation in total pressure and mass-flow rate is within the boundary layers. Previous boundary layer measurements have been performed with pneumatic and hot wire probes. The thickness of the boundary layers is approximately 0.5 mm (1% of the annulus height at the inlet plane).

The inlet static pressure profile is also required to perform mass weighting over the surveyed area, and CFD is used to determine the profile. The inlet plane hub and casing static pressures are measured at three locations around the annulus (differential to upstream total pressure). The CFD is referenced at hub and casing to these measurements to correct the small difference in the predicted profile at these points.

7.2 Exit Total Pressure. The exit plane area survey is performed over 2.2 NGV pitches with a circumferential pneumatically actuated traverse. As the axial flow velocity and density are required to mass-weight the flow, knowledge of the yaw angle and total temperature profiles are also required. Area surveys of yaw angle, total pressure, total temperature, and Mach number are performed using a three hole probe with two *nose-mounted* 25.4 μm aspirated thermocouples. The probe is traversed at 17 radial heights. The area-survey measurements are normalized with respect to the turbine stage inlet conditions.

Four fixed radial rakes each with four Kiel head pitot pressure tubes and a three hole probe at mid-height and four fixed radial rakes of five aspirated thermocouples were distributed around the annulus to monitor the turbine exit conditions. In addition, hub and casing static pressure measurements are made at four locations around the annulus.

7.3 Pressure Calibration. Pressure instrumentation used for this research needs both precision and absolute uncertainties much lower than the target values of the efficiency measurement and a response capable of resolving the frequency content of the flow.

High accuracy transducers with small fill volume were used. A static calibration was performed on every transducer with a digital pressure controller (accuracy ~0.009%). All transducers show repeatability in the region of 0.04%. The response of a pneumatic pressure measurement is mainly a function of transducer fill volume and the pneumatic line length and diameter (see, for example, Ref. [24]). Performing a fast Fourier transform on the inlet total pressure shows a frequency content of 0–100 Hz. The target bandwidth for all measurements is set at 200 Hz. Step response tests performed by bursting a pressurized balloon were conducted using the pneumatic lines used in the experiment. These tests demonstrated that the effective frequency cut-off was 400 Hz, two times greater than the highest frequency with which it was desired to measure the oscillations in total pressure.

7.4 Inlet Total Temperature. The area survey of the inlet total temperature is performed in the same manner as those of the inlet total pressure. Three radial rakes of thermocouples are traversed over two NGV pitches. Each rake contains nine 25.4 μm bare k-type thermocouples. Three fixed rakes of five similar thermocouples are distributed around the annulus for monitoring purposes. In a similar manner, the temperature profile measurements are made dimensionless with respect to the fixed measurements.

Thermocouple performance has been investigated in numerous studies (see, for example, Ref. [25]) and is dependent on bead diameter, flow velocity, and length-to-diameter (L/D) ratio. The thermocouple measurements need to have fast response and low conduction error. It can be shown that radiation errors are small in this type of testing. Increasing the L/D ratio of a thermocouple reduces the conduction error. However, the maximum L/D ratio is determined by the structural integrity of the thermocouple. To provide a balance between response and structural integrity, all of the inlet temperature measurements are made with 25.4 μm thermocouples with a L/D ratio of approximately 80. The thermocouple response time was modeled using an unsteady heat transfer model, in which the thermocouple bead was modeled as a sphere in a flow governed by forced convection. The Nusselt number was estimated using a correlation given by Incropera and DeWitt [26], recommended in this application by Whitaker [27]. At a flow velocity of 60 ms^{-1} (representative of the NGV inlet plane), the thermal time constant of the thermocouple bead (diameter of 25.4 μm) was estimated to be 1.1 ms. At $t=8\tau$ following a step change in temperature, the thermocouple reaches 99.97% of the step value. This corresponds to 8.8 ms or, very approximately, to 100 Hz.

The mean flow velocity at the turbine inlet plane is approximately 60 ms^{-1}. The dynamic temperature is therefore 1.79 K. The temperature recovery factor is approximately 0.75. If the correction term is ignored, the incurred error is approximately 0.10%.

8 Speed Measurement

Even though the turbine is braked, small changes in turbine speed must be taken into account. In the TTF, the turbobrake keeps the rotor within (typically) 25 rpm of the design speed during a test run. Assuming a choked turbine nozzle, the turbine power, and hence speed, may be considered to contain the same frequency content as the inlet total pressure. Therefore, in addition to changes in turbine speed resulting from the inexact matching of the turbine power and turbobrake power, fluctuations at approximately 3.5 Hz (run starting process), 16 Hz (piston oscillations), and 80 Hz (reflected pressure wave) are expected. Accurate speed measurement at these frequencies is important.

Turbine speed is measured in the TTF using a 60 line disk and optical encoder, which is sampled at 1 MHz. Traditionally a revolution average technique is used with such a system, typically averaging over one revolution to remove errors resulting from inaccurate positioning of the lines (also called disk characteristic) and the eccentricity of the rotation. The accuracy of this technique is determined by the uncertainty in detecting the timing of the two

Table 4 Speed uncertainty analysis

	Starting pulse	Piston oscillation	Reflected pressure wave
Frequency (Hz)	3.5	16	80
Magnitude	100%	±1%	±0.3%
Quantization error	±0.01%	±0.01%	±0.01%
Frequency response error	±0.03%	±0.34%	±4.39%
Finite sampling	±0.03%	±0.03%	±0.03%
Speed error	±0.04%	±0.003%	±0.013%

Table 6 Efficiency precision uncertainty

Variable	Influence coefficient (C_*)	Sensitivity (S_*)	Uncerainty $U_* = \lvert C_* S_* \rvert$
ω	1	0.042	0.042
$\dot{\omega}$	5.3×10^{-3}	6.60	0.035
ΔT_{gauge}	0.97	0.195	0.189
ΔT_{wind}	0.03	~ 1	0.03
$\dot{m}$	1	0.137	0.137
$\bar{T}_{01}$	1	0.113	0.113
$\bar{P}_r = \bar{p}_{03} / \bar{p}_{01}$	0.8	0.071	0.057
$\dot{Q}_{13} - \Delta \dot{H}_{03(HT)}$	1.3×10^{-2}	~ 5	0.065
Total uncertainty (RSS)			±0.280%

edge crossings over which the average is performed. This is a function of the sampling rate and rotational speed. The timing of each edge crossing is uncertain to ±1 sample, so at 9500 rpm (158.3 rev/s) and with a sample rate of 1 MHz the uncertainty is ±0.03% or ±3 rpm. The cutoff frequency is approximately 160 Hz, however, as the time interval over which the speed is computed is approximately 1/160 s.

However, the revolution average technique is extremely sensitive to noise. An alternative technique using a frequency domain based measurement is presented by Atkins and Ainsworth [20]. This method uses a short-time Fourier transform (STFT) to evaluate the frequency content of a windowed section of the encoder signal and hence to determine the rotational speed. As a result of its insensitivity to noise (and secondly its greater frequency response with a similar measurement time interval), this method is used to evaluate the rotational speed in the TTF. The length of the Gaussian window determines the frequency response of the technique, and the length of the fast Fourier transform determines the quantization error. A numerical model was used to determine the frequency response of the STFT method, and a window length of 2^{13} and FFT length of 2^{20} (quantization error ±0.01%) were selected. The uncertainty of the edge timings also impacts on this method, and as the selected window length corresponds to approximately one revolution, the uncertainty due to a finite sample rate is approximated at ±0.03% (as for the time domain analysis above). The uncertainty analysis of the speed measurement, including the frequency response model results are summarized in Table 4. The uncertainty in speed at each frequency is estimated as the RSS of each error term multiplied by the magnitude of the frequency fluctuation. The total uncertainty in the speed measurement is given by the RSS of the speed errors at each frequency and is equal to ±0.042%.

The acceleration is given by the time differential of the speed measurement. Differentiating amplifies any error in the speed measurement at a given frequency, f, by a factor of $2\pi f$. The uncertainty analysis of the acceleration measurement is summarized in Table 5 below.

9 Efficiency Measurement Uncertainty

The influence coefficients for each of the measurements required to evaluate efficiency have been previously summarized in

Table 5 Acceleration uncertainty analysis

Component	Frequency (Hz)	Speed error $(C_\omega S_\omega)$	Acceleration error $(2\pi f \cdot C_\omega \cdot S_\omega)$
Starting pulse	3.5	±0.04%	±0.88%
Piston oscillation	16	±0.003%	±0.30%
Reflected pressure wave	80	±0.013%	±6.53%
Total error (RSS)			6.60%

Table 2. Details of each of these measurements along with their predicted uncertainties have been presented. The uncertainty analysis for the overall efficiency measurement is summarized in Table 6.

During this work an emphasis has been placed on achieving a precision uncertainty of ±0.25%. The pretest uncertainty analysis predicts a precision uncertainty of ±0.280%. The uncertainty values are not affected by the run-to-run changes in tunnel conditions, as the turbine efficiency is evaluated as a function of non-dimensional mass-flow rate, specific speed, and stage pressure ratio at each sampling point during a test run. Measurements are taken in real time, which allows these parameters to be determined during the test run. This permits turbine efficiency to be accurately evaluated over a wide range of operating conditions. The uncertainty associated with these measurements is accounted for in the overall uncertainty of the evaluated turbine efficiency.

The bias uncertainty associated with the evaluation of turbine adiabatic efficiency is dominated by three terms. First, the total uncertainty (RSS of bias and precision errors) associated with the mass-flow rate calibration technique is ±1.29%. Second, the bias error associated with applying the Rolls-Royce windage correlation is conservatively estimated at ±30%. With an influence factor of 0.03, this impacts the efficiency bias error by ±0.9%. Finally, a significant bias uncertainty results from the error in measuring the nonuniformities in pressure and temperature at the inlet and exit planes. This is dependent on the gradient of the profiles and the measurement grid density at each plane. The bias uncertainty associated with this source of error was approximately ±0.8%. This was estimated using a numerical code, which sampled realistic area profiles at the actual measurement locations. All other bias errors were at least an order of magnitude lower. The root-sum-square of all bias errors was ±1.76%, within the target value of ±2.0%.

10 Conclusions

An efficiency measurement system has been implemented at the Turbine Test Facility at QinetiQ, Farnborough. This has been used to measure the efficiency of the engine-scale MT1 transonic HP turbine stage.

The efficiency measurement system uses a shaft-mounted strain gauge system to provide, to the author's knowledge, the first direct measurement of torque in such a facility. The torque system was calibrated in a specifically designed calibration facility using an inline reference torque transducer with an accuracy of ±0.117%. The temperature dependence of the system was also evaluated during calibration. The precision uncertainty associated with the measurement of shaft torque in the TTF was ±0.182%.

The turbine stage mass-flow rate was measured using the piston tube exit contraction as a subsonic venturi upstream of the turbine. The effective area of the piston tube contraction was evaluated

over a $\pm 10\%$ range in Re and M, using a novel technique that allowed for the effects of thermal nonequilibrium during a blowdown calibration using a stored mass technique. The measurement bias and precision uncertainties were $\pm 1.29\%$ and $\pm 0.137\%$, respectively. The flow structure and the inlet and exit of the turbine were accurately resolved by performing high resolution area surveys of the flow conditions at the stage inlet and exit.

A full uncertainty analysis has been conducted—and presented in this paper—which demonstrates that turbine efficiency can be evaluated in this transient facility to a precision error of 0.280% and an estimated bias error of $\pm 1.76\%$. Studies currently underway will use the efficiency measurement system to evaluate the impact of inlet temperature distortion and swirl on turbine performance.

Acknowledgment

Nomenclature

A = area, m^2
A_{eff} = effective area, m^2
c_p = specific heat capacity, $J\,kg^{-1}\,K^{-1}$
C = influence coefficient
E = potential difference, V
G = shear modulus, Pa
$\dot{H}$ = total enthalpy flux, $J\,s^{-1}$
HP = high pressure
I = moment of inertia, $kg\,m^2$
IP = intermediate pressure
J = polar second moment of area, m^4
k = gauge factor
LP = low pressure
$\dot{m}$ = mass-flow rate, $kg\,s^{-1}$
M = mach number
N = rotational speed, rpm
NGV = nozzle guide vane
p = pressure, Pa
P_r = stage total pressure ratio
$\dot{Q}$ = heat transfer rate, $J\,s^{-1}$
r = radius, m
R = resistance, Ω, specific gas constant, $J\,kg^{-1}\,K^{-1}$
S = precision uncertainty
t = time, s
T = torque, N m, temperature, K
u = velocity, $m\,s^{-1}$
V = volume, m^3
$\dot{W}$ = power, $J\,s^{-1}$
ε = strain
γ = ratio of specific heats
η = efficiency
Π_1 = blowdown nonisentropic correction factor (ratio of actual to inferred isentropic mass-flow rates)
ρ = density, $kg\,m^{-3}$
τ = shear stress, $N\,m^{-2}$
υ = Poisson's ratio
ω = angular velocity, $rad\,s^{-1}$
$\dot{\omega}$ = angular acceleration, $rad\,s^{-2}$

Subscripts

0 = total conditions, output
1 = NGV inlet conditions
2 = NGV exit/turbine inlet conditions
3 = rotor exit conditions
$^{-}$ = mass-averaged value
actual = actual value
ass = entire assembly value
ax = axial value
bearing = main shaft bearing term
brake = turbobrake value
corr = correction term
diff = diffuser value
gas = main flow value
gauge = strain gauge value
HT = heat transfer term
i = input
ideal = ideal value (reference process)
ind = nonadiabatic conditions
initial = initial value
irr = irreversible value
is = isentropic value
plena = individual plenum value
res = main reservoir value
rotor = turbine rotor value
SV = sonic venturi value
t = pump tube throat conditions
wall = wall surface value
wind = disk windage term

References

[1] Epstein, A. H., and Guenette, G. R., 1984, "The MIT Blowdown Facility," ASME Paper No. 84-GT-116.
[2] Hilditch, M. A., Fowler, A., Jones, T. V., Chana, K. S., Oldfield, M. L. G., Ainsworth, R. W., Hogg, S. I., Anderson, S. J., and Smith, G. C., 1994, "Installation of a Turbine Stage in the Pyestock Isentropic Light Piston Facility," ASME Paper No. 94-GT-277.
[3] Ainsworth, R. W., Schultz, D. L., Davies, M. R. D., Forth, C. J. P., Hilditch, M. A., Oldfield, M. L. G., and Sheard, A. G., 1988, "A Transient Flow Facility for the Study of the Thermofluid-Dynamics of a Full Stage Turbine Under Engine Representative Conditions," ASME Paper No. 88-GT-144.
[4] Sieverding, C. H., and Arts, T., 1992, "The VKI Compression Tube Annular Cascade Facility CT3," ASME Paper No. 92-GT-336.
[5] Guenette, G. R., Epstein, A. H., and Ito, E., 1989, "Turbine Aerodynamic Performance Measurements in Short Duration Facilities," AIAA Paper No. 89-2690.
[6] Halderman, C. W., Dunn, M. G., Lotsof, J., MacArthur, C. D., and Cohrs, B., 1991, "Uncertainty Analysis of Turbine Aerodynamic Performance Measurements in Short Duration Facilities," *AIAA/ASME/SAE/ASEE 27th Joint Propulsion Conference*.
[7] Keogh, R. C., Guenette, G. R., and Sommer, T. P., 2000, "Aerodynamic Performance Measurements of a Fully-Scaled Turbine in a Short Duration Facility," ASME Paper No. 2000-GT-486.
[8] Keogh, R. C., Guenette, G. R., Spadaccini, C. M., Sommer, T. P., and Florjanic, S., 2002, "Aerodynamic Performance Measurements of a Film-Cooled Turbine Stage—Experimental Results," ASME Paper No. 2002-GT-30344.
[9] Dénos, R., Paniagua, G., Yasa, T., and Fortugno, E., 2006, "Determination of the Efficiency of a Cooled HP Turbine in a Compression Tube Facility," ASME Paper No. GT2006-90460.
[10] Yasa, T., Paniagua, G., and Bussolin, A., 2007, "Performance Analysis of a Transonic High Pressure Turbine," *Proceedings of the Seventh European Conference on Turbomachinery*, Athens, Greece.
[11] Atkins, N. R., Miller, R. J., and Ainsworth, R. W., 2004, "The Development of Aerodynamic Performance Measurements in a Transient Test Facility," *Proceedings of the ASME TURBO EXPO 2004*, Vienna, Austria.
[12] Chana, K. S., and Jones, T. V. J., 2002, "An Investigation on Turbine Tip and Shroud Heat Transfer," ASME Paper No. GT2002-30554.
[13] Povey, T., Chana, K. S., and Jones, T. V. J., 2003, "Heat Transfer Measurements on an Intermediate Pressure Nozzle Guide Vane Tested in a Rotating Annular Turbine Facility—and the Modifying Effects of a Non-Uniform Inlet Temperature Profile," Proc. Inst. Mech. Eng., Part A, **217**, pp. 421–431.
[14] Chana, K. S., and Singh, U. K., 2004, "Turbine Heat Transfer and Aerodynamic Measurements and Predictions for a 1.5 Stage Configuration," ASME Paper No. GT2004-53951.
[15] Adami, P., Salvadori, S., and Chana, K. S., 2006, "Unsteady Heat Transfer Topics in Gas Turbine Stages Simulations," ASME Paper No. GT2006-90298.
[16] Goodisman, M. I., Oldfield, M. L. G., Kinsgcombe, R. C., Jones, T. V., Ainsworth, R. W., and Brookes, A. J., 1992, "An Axial Turbobrake," ASME J. Turbomach., **114**, pp. 419–425.
[17] Abernethy, R. B., Benedict, R. P., and Dowdell, R. B., 1985, "ASME Measurement Uncertainty," ASME Trans. J. Fluids Eng., **107**, pp. 161–164.

[18] Cumpsty, N. A., and Horlock, J. H., 2005, "Averaging Non-Uniform Flow for a Purpose," ASME Paper No. GT2005-68091.

[19] Casey, M. V., and Fesich, T. M., 2009, "On the Efficiency of Compressors With Diabatic Flows," ASME Paper No. GT2009-59015.

[20] Atkins, N. R., and Ainsworth, R. W., 2005, "The Measurement of Shaft Power in a Fully Scaled Transient Turbine Test Facility," ASME Paper No. GT2005-68998.

[21] Porreca, L., and Dénos, R., 2002, "Turbine Stage Mass Flow Evaluation in a Compression Tube Facility," The 16th Symposium on Measurement Techniques in Transonic and Supersonic Flow in Cascades and Turbomachines, Cambridge, UK.

[22] Chana, K. S., Hurrion, J. R., and Jones, T. V., 2003, "The Design, Implementation and Testing of a Non-Uniform Inlet Temperature Generator for the QinetiQ Transient Turbine Test Facility," *Proceedings of the ASME TURBO EXPO 2003*, Atlanta, GA, Jun. 16–19.

[23] Povey, T., and Beard, P. F., 2008, "A Novel Experimental Technique for Accurate Mass Flow Rate Measurement," Flow Meas. Instrum., **19**(5), pp. 251–259.

[24] Hougen, J. O., Martin, O. R., and Walsh, R. A., 1963, "Dynamics of Pneumatic Transmission Lines," Control Eng., **10**(9), pp. 114–117.

[25] Paniagua, G., Dénos, R., and Oropesa, M., 2002, "Thermocouple Probes for Accurate Temperature Measurements in Short Duration Facilities," *Proceedings of the ASME TURBO EXPO 2002*, Amsterdam, The Netherlands.

[26] Incropera, F. P., and DeWitt, D. P., 2002, *Fundamentals of Heat and Mass Transfer*, 5th ed., Wiley, New York.

[27] Whitaker, S., 1972, "Forced Convection Heat Transfer Correlations for Flow in Pipes, Past Flat Plates, Single Cylinders, Single Spheres, and for Flow in Packed Beds and Tube Bundles," AIChE J., **18**(2), pp. 361–371.

Experimental and Numerical Investigation of Impingement Cooling in a Combustor Liner Heat Shield

Sebastian Spring[1]
e-mail: sebastian.spring@itlr.uni-stuttgart.de

Diane Lauffer
e-mail: diane.lauffer@itlr.uni-stuttgart.de

Bernhard Weigand
e-mail: bernhard.weigand@itlr.uni- stuttgart.de

Institut für Thermodynamik der Luft-und
Raumfahrt (ITLR),
Universität Stuttgart,
Pfaffenwaldring 31,
70569 Stuttgart, Germany

Matthias Hase
Siemens Energy,
Mellinghofer Strasse 55,
45473 Mülheim, Germany
e-mail: matthias.hase@siemens.com

A combined experimental and numerical investigation of the heat transfer characteristics inside an impingement cooled combustor liner heat shield has been conducted. Due to the complexity and irregularity of heat shield configurations, standard correlations for regular impingement fields are insufficient and detailed investigations of local heat transfer enhancement are required. The experiments were carried out in a perspex model of the heat shield using a transient liquid crystal method. Scaling of the model allowed to achieve jet Reynolds numbers of up to $Re_j = 34,000$ without compressibility effects. The local air temperature was measured at several positions within the model to account for an exact evaluation of the heat transfer coefficient. Analysis focused on the local heat transfer distribution along the heat shield target plate, side rims, and central bolt recess. The results were compared with values predicted by a standard correlation for a regular impingement array. The comparison exhibited large differences. While local values were up to three times larger than the reference value, the average heat transfer coefficient was approximately 25% lower. This emphasized that standard correlations are not suitable for the design of complex impingement cooling pattern. For thermal optimization the detailed knowledge of the local variation of the heat transfer coefficient is essential. From the present configuration, some concepts for possible optimization were derived. Complementary numerical simulations were carried out using the commercial computational fluid dynamics (CFD) code ANSYS CFX. *The motivation was to evaluate whether CFD can be used as an engineering design tool in the optimization of the heat shield configuration. For this, a validation of the numerical results was required, which for the present configuration was achieved by determining the degree of accuracy to which the measured heat transfer rates could be computed. The predictions showed good agreement with the experimental results, both for the local Nusselt number distributions as well as for averaged values. Some overprediction occurred in the stagnation regions, however, the impact on overall heat transfer coefficients was low and average deviations between numerics and experiments were in the order of only 5–20%. The numerical investigation showed that contemporary CFD codes can be used as suitable means in the thermal design process.*
[DOI: 10.1115/1.3103924]

Keywords: gas turbine, heat shield, impingement cooling, TLC, CFD

1 Introduction

Modern gas turbines are under continuous development. Requirements are being imposed by demands for increased power output and efficiency as well as for reduced emissions. High thermal efficiency can be realized by increasing turbine inlet temperatures and compressor pressure ratios. As a result of this, many gas turbine components are operated at temperatures substantially above actual material limits. In order to assure durability and long operating intervals, effective cooling concepts are required for these highly loaded components. Despite the drawback of a generally higher associated pressure drop, impinging jets, due to their ability to achieve high heat and mass transfer rates, are finding increased use in gas turbine cooling applications such as the cooling of rotor disks, turbine vanes and blades, or combustion chamber walls [1–4].

In particular, for combustion chamber liners, different cooling

concepts have been considered in the past. In recent years, the design emphasis has changed from formerly used film cooling to convective cooling concepts. This applies, in particular, to regions where mixing of the cooling flow with the hot gas stream cannot be accepted due to emission restrictions. One design approach is the use of impingement cooled heat shields that are placed on the outside combustor walls for heat protection. Compressor air is routed into these shields and then impinges through several holes onto a target plate, i.e., the wall that is to be cooled. The flow is usually discharged through gaps along the heat shield side rims.

Impingement cooling configurations have been investigated in numerous studies in the past. Interesting reviews are, for example, provided by Martin [5], Han and Goldstein [6], and Jambunathan et al. [7]. However, jet impingement for cooling applications of combustion chambers differs from the cooling concepts of other components in terms of the dimensionless quantities involved. For example, the jet Reynolds number Re_j under consideration for an impingement cooled combustion chamber can reach values of $Re_j > 20,000$. The avoidance of flow Mach numbers to reach into the compressible regime ($Ma > 0.3$) typically results in very large geometries required for experimental investigations of these high

---

Reynolds numbers. Consequently, the Reynolds number range of interest for combustion chamber cooling has been covered by only few experimental studies.

For example, arrays of impinging jets, with both inline and staggered arrays, were investigated in a number of studies by Metzger et al. [8] and Florschuetz and co-workers [9–12]. They evaluated the influence of initial and developing crossflows on heat transfer rates and found a decrease in the latter ones when the crossflow had become too strong. They further developed correlations for impingement arrays that are still being used in design processes today. An extension to this correlation was presented by Bailey and Bunker [13] based on their extensive study on the effects of jet array geometry. Another detailed investigation on the impact of crossflow was performed by Obot and Trabold [14]. They compared average heat transfer rates of an impingement array for three different crossflow schemes and confirmed that heat transfer is decreasing with increasing flow restriction, which is stronger crossflow. They also showed that for a constant mass flow rate heat transfer coefficients decrease with an increasing number of jets and with an increasing jet-to-target plate spacing. Further investigations focusing on the effects of crossflow were performed by Huang et al. [15], Cheong et al. [16], and Uysal et al. [17]. Configurations designed to reduce the effects of crossflow were experimentally investigated by Esposito et al. [18]. For impingement configurations relevant for gas turbine applications, they studied the effects of two designs at very high jet Reynolds numbers. Further studies on impingement arrays at very high jet Reynolds numbers were carried out by Van Treuen et al. [19], Son et al. [4], Chambers et al. [20], and Gritsch et al. [21], for example.

From a numerical point of view, the prediction of jet impingement heat transfer is not trivial. The presence of a stagnation point along with the development of a wall boundary layer and strong streamline curvature contribute to a high level of complexity. Some investigations have focused on numerical modeling of jet impingement and the evaluation of different turbulence models, such as the studies of Behnia et al. [22], Zuckerman and Lior [23] or Coussirat et al. [24]. While CFD heat transfer predictions for single jet configurations with and without crossflow yield results of high accuracy, the numerical simulation of complete fields or arrays of impinging jets can be problematic due to stability and convergence issues. This is particularly true when large numbers of jets and high jet Reynolds numbers are considered [25,26].

For the particular case of jet impingement in a combustor liner heat shield, to our knowledge only few studies are available. Preliminary numerical investigations were carried out by Luff and McGuirk [27,28] who investigated an impingement cooled heat shield around a combustor fuel nozzle. They developed and tested a computational model suitable for the prediction of the combined fluid flow and heat transfer inside the heat shield. However, no reference data that could have been used for validation of the computed results was presented. Riahi and Borns [29] calculated temperature and stress distributions in a heat shield configuration. They also investigated the effects of newly introduced U-shaped ribs along the impingement target plate.

Out of this motivation, the focus of the present study was set on the detailed investigation of the heat transfer characteristics inside an impingement cooled combustor liner heat shield. Measuring methods used on operating gas turbines such as irreversible temperature indicating paints can suffer from poor resolution and thus are not suitable as design tools for cooling optimization [30]. Due to the complexity and the irregularity of heat shield configurations, standard correlations for regular impingement fields are insufficient, and the investigation of local heat transfer enhancement is required. In order to achieve flow conditions similar to engine conditions, a scaled perspex model was generated. For an exact evaluation of the heat transfer coefficient, local air temperatures were measured at several positions within the model. Special attention was addressed to the realistic modeling of outflow conditions, which was realized by an accurate reproduction of outflow gaps on all four rims. These outflow gaps were suspected to have an impact on the development of crossflow schemes within the heat shield and thus influence the heat transfer pattern. The primary objective of this investigation was the determination of local heat transfer coefficients, primarily along the target plate of the heat shield but also on all side rims and the central bolt recess. The results are required as a basis for future optimization of the heat shield cooling design for which improvements can be derived from the present configuration. To our knowledge, for heat shield configurations this is the first detailed investigation of its kind. The experimental part was complemented by a numerical investigation. Due to the complex structure of the heat shield and the correspondingly high costs of the experimental investigation, our motivation was to evaluate whether CFD can be used as an engineering design tool in the optimization of the heat shield configuration. This required, as a first step, the validation of the numerical results. Thus, the secondary objective of this investigation was to determine the degree of accuracy to which a commercial CFD code is capable of predicting the measured heat transfer rates. No problem-specific modifications or adoptions were made to the code so that the results computed represent the current state of the art in predictive accuracy. In order to ensure that the capabilities of the CFD code were exploited to the maximum extent, the three-dimensional mesh featured a full reproduction of the experimental facility without simplifications, and effort was spent on the compliance of quality parameters affecting the numerical solution.

Details on the experimental setup along with information on the measurement technique and measurement uncertainties are provided in Sec. 2. The numerical setup is introduced in Sec. 3. There, information on the flow solver, the computational domain, and the numerical grid are summarized. Furthermore, the convergence behavior and a comparison of steady and unsteady computational approaches are discussed, and the results of a grid independency study are presented. Section 4 shows the results obtained from both measurements and CFD predictions. After addressing temperature variations at jet exits over time and the impact of jet Reynolds numbers, the resulting local Nusselt number distributions on the target plate are presented. The results from experiments and numerics are compared with each other. This section concludes with a comparison of area averaged heat transfer coefficients. The main conclusions of this investigation are summarized in Sec. 5. Preliminary experimental results of the current configuration can be found in the work of Lauffer et al. [31].

2 Experimental Setup

In this section, an overview on the experimental facility is presented. The measurement technique is introduced and the data processing of the thermochromic liquid crystal (TLC) images is described. An estimate on the measurement uncertainty is given.

2.1 Test Section. A sketch of the experimental setup is shown in Fig. 1. The mainstream flow in the test channel was generated by a vacuum pump system. The desired flow rate was regulated by adjusting the volume flow measured by a vortex meter. The air entered the channel at atmospheric conditions via a filter and a heater. The heater consisted of several meshes made out of stainless steel and was able to heat the air within less than 0.3 s from ambient temperature up to $100°C$. The air then entered a plenum followed by the impingement plate and the actual heat shield model. The walls of the measuring section were made out of perspex material because of its low thermal conductivity and because it allowed good optical access, which, in turn, was necessary for the heat transfer measurements.

Figure 2 shows a sketch of the impingement pattern along with a cut through the impingement section along the symmetry line. While the upper part of Fig. 2 shows all investigated walls and the coordinate system used for the data evaluation, the lower part
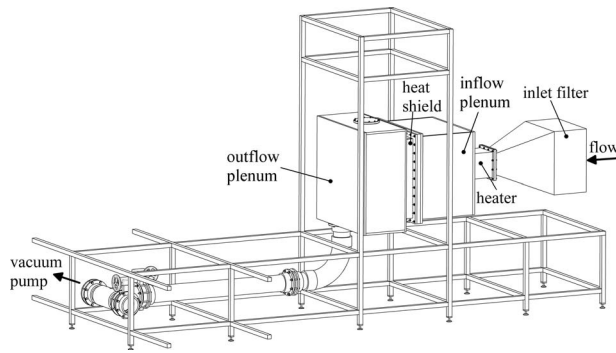
Fig. 1   Experimental setup

Fig. 3   Detailed view on the positioning of TC 3

illustrates details of the impingement zones and the outlet gaps. The heat shield model was symmetrical, therefore results are only shown for half of the model.

There was a total of 45 impingement holes with different diameters in order to satisfy local cooling needs. Therefore, the ratio of the jet-to-plate distance ($z/D=3-5$) and the ratio of the jet-to-jet distance (B/D and W/D) were both irregular. In addition, the impingement holes, which are situated close to the right exit rim of the heat shield, were inclined; all other jets were impinging perpendicular to the target plate.

The main discharge gap was located between the right rim and the target plate, which corresponds to the right hand side of Fig. 2. There were additional outlet gaps along the three remaining side rims. However, at these locations the gaps were situated along the upper parts of the rims whereas the main outlet path was led along the lower part of the rim (refer to lower part of Fig. 2). Dimensions of the outflow gaps were defined according to an expected condition after thermal deformation of the heat shield at machine operation.

The positions of the thermocouples (TC 1–8) used for the data evaluation are also shown in Fig. 2. The thermocouples were placed directly at the jet exits. Grooves were milled into the lower wall of the impingement plate, which is the part with the impingement holes, and the thermocouples along with their wires were glued into these grooves. A detailed view on the positioning of TC 3 is provided in Fig. 3.

Jet Reynolds numbers in the experiments were varied between 17,000 and 34,000 (based on the average jet exit diameter) in order to realize engine representative flow conditions.

2.2   Measurement Technique. For the measurement of the heat transfer, a transient method using TLCs was used [32]. The liquid crystals, which have the property of changing their color as a function of temperature, were applied directly onto all investi-
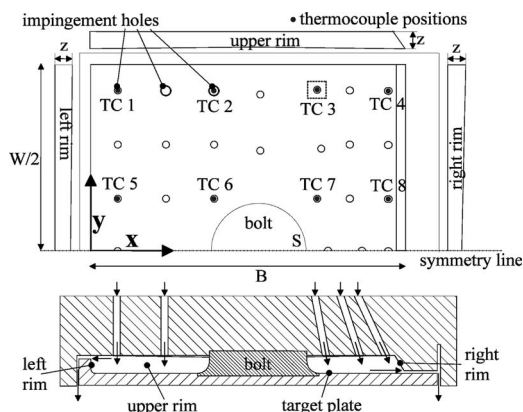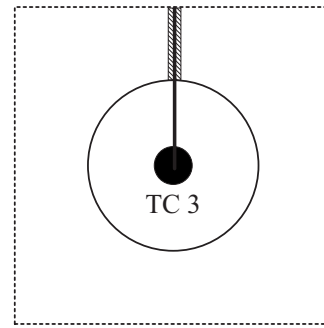

Fig. 2   Impingement configuration

gated walls. A coating of black paint covered the liquid crystals in order to provide a uniform background and to enhance contrast. Narrow bandwidth liquid crystals (with a temperature range of $38-39\,°C$) were used in the present study. All walls were observed from the outside with CCD video cameras.

The transient method uses the temperature response of the wall to a sudden change in the fluid temperature. It needs a defined starting condition, where the flow is already set and the test model has the initial temperature T_0. At time $t=0$ the fluid temperature is suddenly raised to the higher bulk temperature T_B. Due to this temperature change the walls are heated. Once the walls reach a specific temperature, the liquid crystals change their color. This color change is recorded by the video cameras and digital recorders. For short measurement times the assumption of a semi-infinite wall can be made. Therefore, the one-dimensional heat conduction equation needs to be solved to get a relation between the temperature on the wall surface T_W and the heat transfer coefficient h.

$$\Theta = \frac{T_W - T_0}{T_B - T_0} = 1 - \exp\left(h^2 \frac{t}{k\rho c}\right)\mathrm{erfc}\left(h\sqrt{\frac{t}{k\rho c}}\right) \qquad (1)$$

where k, ρ, and c are the material properties (thermal conductivity, density, and specific heat) of the perspex wall. Equation (1) can be solved numerically in order to obtain the heat transfer coefficient for a measured wall temperature T_W and the time t by which this temperature is reached (indicated by the color change in the liquid crystals). The raw data from the experiments was then evaluated by an in-house data processing software [33]. Equation (1) is only valid for an ideal temperature step within the flow. But in reality, the thermocouple records a time-dependent temperature evolution in the channel. To overcome this problem the temperature data are divided into a series of N small discrete intervals. Within these intervals the temperature evolution can be considered to be a temperature step. Thus Eq. (1) can be extended for a temperature evolution according to the Duhamel principle [34].

$$T_W - T_0 = \sum_{i=1}^{N} \Theta(t-t_i)(T_{B,i} - T_{B,i-1}) \qquad (2)$$

where $T_{B,i}$ is the jet exit bulk temperature at one specific time t_i.

The given jet Reynolds numbers Re_j represent an average value for all impinging jets. They have been calculated from the known mass flow rates, fluid properties, and an average jet exit diameter for the whole field. Thus the different geometrical dimensions of the jet exits were not considered in the jet Reynolds number.

In all subsequent results the Nusselt number has been referred to an average reference Nusselt number Nu_{ref} according to [5]

$$\mathrm{Nu}_{ref} = \mathrm{Pr}^{0.42}\sqrt{A_r}\frac{1 - 2.2\sqrt{A_r}}{1 + 0.2(z/D - 6)\sqrt{A_r}}\mathrm{Re}_j^{2/3} \qquad (3)$$

which basically relates $\mathrm{Nu}_{ref} \sim \mathrm{Re}_j^{2/3}$ with correction terms representing the geometry. The correlation was derived from experiments for a regular impingement field with square arrays of round

Table 1 Measurement uncertainties

Quantity	T (K)	t (s)	k (W/m K)	c (J/kg K)	ρ (kg/m³)
Uncertainty	0.2	0.2	0.01	20	10

nozzles, constant jet-to-target-plate distance, and a relative impingement area A_r. It is valid for a range of $2000 \leq \mathrm{Re}_j \leq 100{,}000$, $0.004 \leq A_r \leq 0.04$, and $2 \leq z/D \leq 12$.

2.3 Measurement Uncertainties. The accuracy of the measured heat transfer coefficients depended mainly on the accuracy of the thermocouples used, the calibration of the liquid crystals, and the material properties of the perspex wall. Furthermore, the resulting error can be influenced substantially by choosing the heater power and thus influencing the temperature ratio $\Theta = (T_W - T_0)/(T_B - T_0)$. If the flow temperature is very high, the color change in the liquid crystals occurs very fast and therefore the uncertainty of the video resolution and of the sampling rate of the temperature measurement outweigh. On the other hand, if the flow temperature is too close to the ambient temperature, the uncertainty of the temperature measurement is higher, and in addition, because of the longer total measurement time, three-dimensional heat conduction effects within the wall are increasing. It is therefore important to find an optimum temperature ratio. More information on this subject can be found in Ref. [35]. For the current experiments the temperature ratio was chosen at $0.4 < \Theta < 0.6$. Based on an error analysis according to Kline and McClintock [36], this resulted in a measurement uncertainty for the heat transfer coefficient below 8% for all experiments carried out in this study. It should be noted in this context that due to a very fast response of the TLCs in the stagnation regions on target plate, the measurement uncertainty was higher. However, those zones were very limited in their spatial extent so that the impact on the overall heat transfer coefficients was small.

The measurement uncertainties for the different measured quantities are listed in Table 1.

3 Numerical Setup

This section describes the setup of the numerical investigation. Details on the flow solver, on the computational domain with its boundary conditions, and on the mesh used for spatial discretization are given. Numerical stability and discretization errors are assessed in detail as they have a large impact on the overall results and thus on the decision as to whether CFD are a suitable design tool for further optimization studies on this configuration.

3.1 Flow Solver. For the numerical investigation of the heat shield configuration, the commercial CFD software package ANSYS CFX version 11 was used. Spatial discretization was based on the second-order accurate upwind scheme.

Due to its superior performance in previously investigated jet impingement configurations, the shear stress transport (SST) turbulence model was selected for all simulations [37,25,26].

For the description of the near-wall region, a low-Reynolds number approach was used, which allows the resolving of details in the viscous sublayer by applying very fine mesh length scales near the walls. This approach requires the dimensionless wall distance of the first node in the flow to be $y^+ < 2$, where

$$y^+ = \frac{u_\tau \Delta y}{\nu} \qquad (4)$$

with u_τ representing the shear velocity, Δy is the absolute distance from the wall, and ν is the kinematic viscosity of the fluid. In regions where the mesh resolution criteria of the low-Reynolds number method are not fulfilled, wall-functions are used for the description of the viscous sublayer.

3.2 Computational Domain and Boundary Conditions. The computational domain was generated from a computer aided design (CAD) model of the actual experimental facility in order to allow a reproduction of the measurements as realistic as possible. Symmetry of the geometry allowed accounting for only half of the original setup. The domain boundaries were defined with respect to the following objectives. On the one hand, a reduction in the overall dimensions in order to benefit the achievable mesh resolution on the available computing resources. On the other hand, a verification that the flow in the regions of interest was not affected by the choice of domain boundaries and boundary conditions. In order to achieve a partially developed velocity profile at the nozzle exit, the axial length of all jets was modeled. A large upstream plenum chamber ensured a realistic mass flow distribution over the different jets. As in the experimental investigation special attention was addressed to a realistic modeling of the outflow conditions; the gaps restricting the outflow to all sides were also included in the CFD analysis. However, the outflow plenum chamber was not modeled as it was assumed that the major impact on the flow field stemmed from the geometrical shapes of the outflow areas themselves rather than from the downstream plenum. This assumption was strongly supported by measurements and by other experimental investigations, where it has been shown that for long impingement holes ($L/D > 10$) as the ones used in the present study, the effect of the plenum is negligible.

Boundary conditions were applied to the computational model from the data recorded during the experiments. All walls were treated as adiabatic no-slip walls except for the target plate, the bolt, and the side rims where a constant heat flux was prescribed. At the outlet gaps, pressure type boundary conditions with static pressure values from the experiments were defined. At the plenum inlet, a mass flow rate was specified in the first step. From the result of this simulation, an average jet Reynolds number based on the average jet velocity at the nozzle exits was calculated. The mass flow at the inlet was then modified in order to achieve similarity of the Reynolds numbers between experiment and simulation. With one iteration of this procedure, average jet Reynolds numbers in the numerical study matched the experimental reference data at 1% accuracy.

From the CFD results, Nusselt numbers were obtained from the known wall heat flux, the local wall temperature, and the jet total temperature as a fixed reference temperature.

3.3 Numerical Grid. The mesh for the CFD analysis was generated with ANSYS ICEMCFD, version 11. Spatial discretization of the computational domain was realized by a block-structured grid with hexahedral elements. In the process of mesh generation, no simplifications were applied to the original model. Thus, the complexity of the present model resulted in a mesh with 1816 blocks and a total number of 4,441,428 cells.

In order to ensure cell orthogonality, O-grid type blocks were used for all jets and for the resolution of the bolt and the fillet regions. Due to the limited available computer resources, the requirements of the SST turbulence model regarding the near-wall resolution ($y^+ < 2$) could be fulfilled for the impingement target plate only where the average value was $\overline{y^+} = 0.58$. We considered this to be valid as local heat transfer rates were evaluated only in this area. At all other walls, where no detailed heat transfer evaluation was made, y^+ values were approximately 10 times higher.

Figure 4 shows a three-dimensional view of the mesh.

3.4 Numerical Accuracy: Quantification of Stability and Discretization Errors. For the evaluation of numerical stability, heat transfer coefficients in the stagnation regions and jet velocities at all nozzle exits were monitored during each simulation. When fluctuations in the latter ones were in the order of 1–2%, the simulation was considered stable. Iterative convergence was considered sufficient, when the normalized root mean square (rms) residuals had decreased by at least four orders of magnitude, which typically required between 400 and 500 iterations. A further
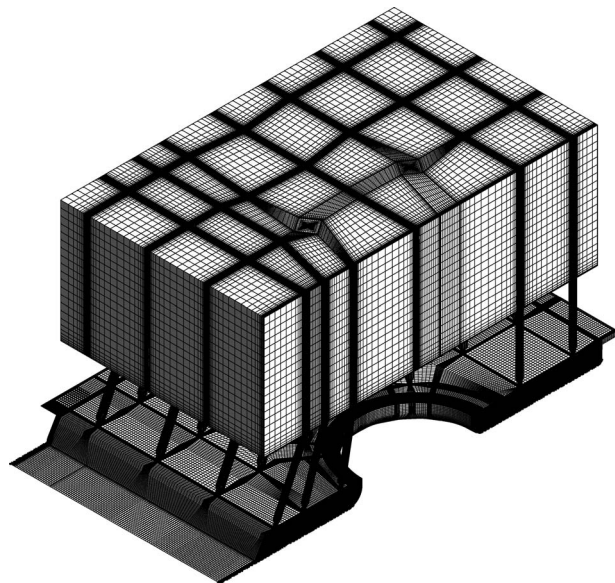
Fig. 4   Numerical grid used in the CFD analysis

Table 2   Grid parameters used in the mesh refinement analysis

Grid	N	Max y^+	$\overline{Nu}/Nu_{ref}$
Coarse (C)	910,354	3.06	0.8632
Intermediate (B)	2,040,624	2.39	0.8673
Fine (A)	4,441,428	1.90	0.8828

target plate were considered. An overview on the grid cell numbers N of the different grids along with the corresponding maximum values of y^+ of the first node on the target plate and the area averaged Nusselt numbers is provided in Table 2.

For the area averaged Nusselt numbers, this resulted in a GCI of 0.73% on the fine grid, which suggested that the solution was mesh independent.

In order to quantify the local variation of the discretization error, the GCI method was applied to the Nusselt number distributions from the three different grids along a line on the target plate (line 1 in Fig. 5). The calculated GCI for the solution on the fine grid is shown in Fig. 6. In general, the values of the GCI are rather low suggesting again that the solution is depending on the mesh to a very small extent only. From this and from the very low average discretization error, we concluded that the mesh was a good compromise between numerical accuracy and computational effort.
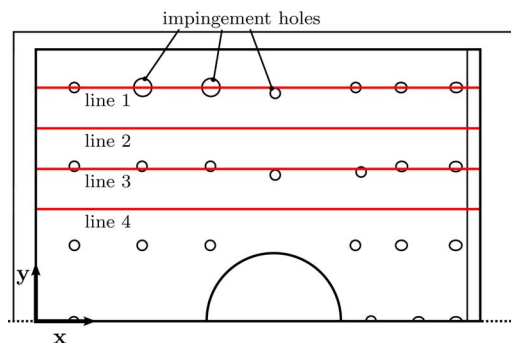
requirement for convergence was that the global imbalance for each solved equation was below 1%. For all cases of the present investigation, no stability or convergence problems were encountered. All simulations were of steady state.

In order to quantify the impact of eventual transient effects, a transient simulation was carried out. Here, the rms residuals of all equations decreased by five orders of magnitude. However, with five iterations per time step the computational effort of the transient study increased by a factor of 20 compared with the steady-state case. The two different approaches yielded only minor differences in the local distributions of the heat transfer rates. For the target plate, the difference in area averaged Nusselt number was approximately 3%. From this we concluded that for the present configuration transient effects were not dominating and therefore a steady simulation was sufficient. This was underlined further by the enormous increase in computational effort for the transient approach.

In order to assess the numerical accuracy of the computed results, an a priori mesh sensitivity analysis was performed before comparing the numerical results to the experimental data. The error that can be quantified by mesh refinement is the so-called discretization error. For the quantification of the latter one, we chose an established method recommended by the Fluids Engineering Division of ASME [38]. The method is based, in principle, on the generalized Richardson extrapolation theory [39]. Based on this, Roache [40,41] developed a more generalized formulation applicable to a wider range of practical CFD cases. The suggested grid convergence index (GCI) method can be considered a procedure for uniform reporting on grid refinement studies with the objective to derive a discretization error band for the investigated variable rather than a mathematically exact estimate on the actual discretization error. The GCI by its definition does not account for general modeling errors, such as the choice of boundary conditions or turbulence model; only the error due to an insufficient spatial resolution can be quantified by this method.

In the present investigation, the GCI method complied with the following requirements. The grid refinement was done systematically, which means that the grids were refined uniformly in every direction of space and only geometrically similar cells were used. Distances between all walls and their first nodes off the wall were also scaled to account for changes in y^+. As the error was expected to increase with the jet Reynolds number, the case with the highest value of Re_j was selected ($Re_j=34,000$). For an evaluation of the average discretization error, area averaged Nusselt numbers on the

Fig. 5   Positions of lines used in the evaluation of local Nusselt numbers

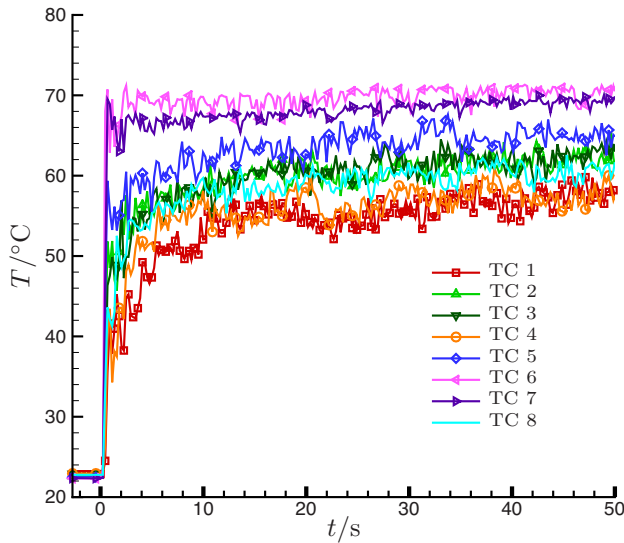**Fig. 6   Local distribution of the discretization error (GCI) along line 1 for $Re_j=34,000$**

Journal of Turbomachinery   JANUARY 2010, Vol. 132 / **011003-5**

Downloaded 28 May 2010 to 128.113.26.88. Redistribution subject to ASME license or copyright; see http://www.asme.org/terms/Terms_Use.cfm

Fig. 7   Measured temperature evolution of thermocouples

Fig. 8   Impact of the jet Reynolds number on heat transfer

4   Results and Discussion

This section presents the results from both the experimental part and the numerical part. Before full local heat transfer coefficient distributions are presented, the temperature distribution within the heat shield and the influence of the jet Reynolds number is discussed. Heat transfer results from experiments and CFD are always shown together facilitating a direct comparison and thus the assessment of the adequacy of present numerical methods in terms of predictive accuracy and suitability as an engineering design tool.

4.1   Temperature Distribution Within the Heat Shield Model. In large and complex geometries, there is a large variation in the local temperature distribution. In the present experimental configuration, the channel widened up considerably after the heater and the overall mass flow was relatively small. This caused a noticeable temperature gradient from the center of the impingement plate toward the side walls. Typical temperature evolutions during an experiment are shown in Fig. 7 (for the positions of the thermocouples refer to Fig. 2). At $t=0$ the heater was switched on. It can be seen that throughout the experiment temperatures in the center of the heat shield (thermocouples 6 and 7) were about $10-20°C$ higher than in the corners of the model (thermocouples 1 and 4). Temperatures near the side rims (thermocouples 2, 3, 5, and 8) ranged in between. In addition, the temperature evolution of the thermocouples in the center of the heat shield was much closer to a temperature step, whereas in the outer regions the flow heated up more slowly. It also becomes clear from Fig. 7 that there were variations in the evolution of the temperature, which presumably occurred because of the abrupt widening of the plenum downstream of the heater provoking a system of vortices within the flow.

Due to these local differences in the temperature distribution, it was essential to know the exact distribution of the local reference temperature for an accurate evaluation of the heat transfer coefficient. For this reason the thermocouples had been placed directly in the jet outlet in every other impingement row. The temporal evolution of all thermocouples was then interpolated both spatially and temporally by the evaluation software, so that one obtained a time-dependent temperature distribution for every local position.

4.2   Impact of the Jet Reynolds Number. The impact of the jet Reynolds number on the overall heat transfer rates is quantified in this section. Figure 8 shows area averaged Nusselt numbers
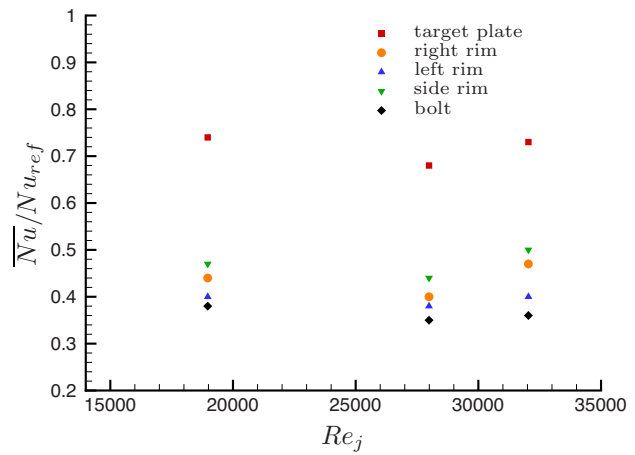
from the experiments for the different sections of the heat shield as a function of the average jet Reynolds numbers through the impingement holes Re_j.

Only minor variations in the overall Nusselt numbers could be observed when the jet Reynolds number was varied. This confirmed that the selected proportionality of $Nu \sim Re_j^{2/3}$ (see Eq. (3)), although derived for a regular impingement field, was valid also for the present cases. In Secs. 4.3–4.5 we will therefore be showing results for one jet Reynolds number only.

4.3   Nusselt Number Contours on the Target Plate. Figure 9 shows the local Nusselt number distributions on the target plate for a jet Reynolds number of $Re_j=34,000$. In the upper part, Nusselt numbers obtained from the measurements are presented
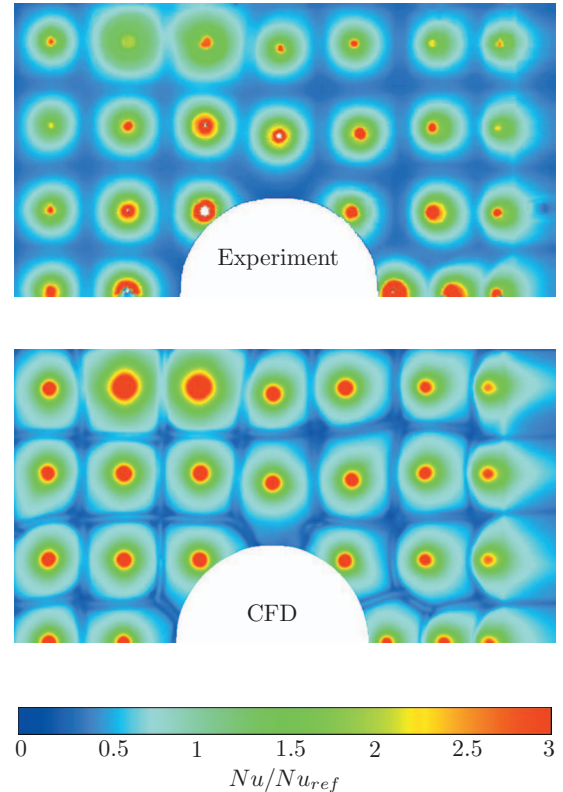

Fig. 9   Local Nusselt number distributions on the target plate for $Re_j=34,000$ obtained from measurements (top) and CFD (bottom)

while the lower part of Fig. 9 shows the results predicted by the CFD simulations. The Nusselt number is again referred to the average reference Nusselt number as defined in Eq. (3). It should be noted in this context that due to the very fast responses of the TLCs in some stagnation regions, the uncertainty of the measured heat transfer coefficients was high. Therefore some of those areas are blanked in Fig. 9, e.g., near the location of TC 6.

The overall impression of the Nusselt number distribution suggested that the mass flow through the impingement holes was not homogeneously distributed. In the central region of the heat shield, stagnation point heat transfer rates were higher than in the vicinity of the side rims. We suspected that this was related to the geometrical shape of the air supply and an insufficient axial length of the upstream plenum.

The positions of the impingement jets are clearly visible in the heat transfer pattern on the target plate. In the stagnation points, i.e., in the geometrical centers of the jets, heat transfer rates were very high but then decreased quickly in radial direction outwards. The heat transfer contours from the two jets with enlarged exit diameters differed in terms of the area affected by impingement. For those jets, the Reynolds numbers were approximately 40% higher compared with the smaller jets. In combination with the enlarged diameter, this resulted in a larger spreading of the jets and thus the altered Nusselt number contours.

The inclination of the two rows of jets near the right exit rim (right hand side of Fig. 9) only had a minor effect on the Nusselt number distribution. The pattern on the target plate was slightly altered with a shift in the stagnation point to the left and a variation in its originally circular shape. However, as these two rows of jets were situated next to the main discharge gap, this trend might also have been an effect of the secondary flow developing toward this outflow. As the effects on heat transfer contours resulting from jet inclination and jet-crossflow interaction are very similar, the combined effects here could not be separated. However, the analysis of the local Nusselt number distribution, in general, allowed the conclusion that the crossflow, which developed within the heat shield, was fairly low for the present design. For example, the three secondary outflow gaps seemed to have no impact on the heat transfer at all. Stronger crossflow within the heat shield would have resulted in altered heat transfer contours on the target plate to a significantly larger extent with a corresponding decrease in heat transfer rates. Small amounts of crossflow, as in the present case, are known to beneficially influence heat transfer coefficients [42].

From a design point of view, the current configuration delivered a well satisfying cooling performance. In particular, the fact that only a moderate crossflow developed within the heat shield was a positive outcome of this investigation. The small amount of the remaining crossflow that we suspected to eventually influence the jets located next to the main outlet could be reduced further by allowing more mass flow to exit through the secondary outlets. Another optimization objective could be a more homogeneous distribution of the heat transfer coefficient on the target plate. This would possibly reduce thermal stresses within the heat shield and thus benefit both lifetime expectation and the thermal deformation at machine conditions. One optimization strategy for this could be the enlargement of the exit jet diameters. As could be seen from Fig. 9, the two larger jets contributed to a larger area being affected by impingement and thus to a beneficial smoothing of temperature gradients on the target plate. Another possibility could be an increase in the total number of jets at a correspondingly denser arrangement.

Comparing the measured Nusselt number distribution with the results obtained from the predictions, the overall agreement was quite good. The contours of the heat transfer coefficients were reproduced correctly and the absolute values also agreed very well. The spreading of the jets, which can be derived from the Nusselt number contours and which is known to be problematic for two-equation turbulence models [43], was also predicted fairly
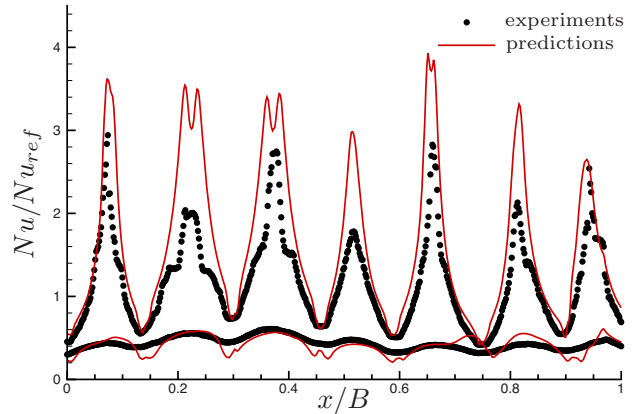

Fig. 10 Local Nusselt number distributions along lines 1 and 2 for $Re_j = 34,000$

accurate. Some deviations from the experimental reference data could be observed in the upper section of the target plate. Here, it seemed in the CFD results as if the massflow rate through the jets was higher than in the experiments and also more homogeneously distributed in general. However, this might have been due to the experimental setup as mentioned above. From the comparison of the two-dimensional Nusselt number distributions, we concluded that for this type of cooling configuration the present CFD codes can be a suitable means in the design process. Based on this evaluation, future optimization of the impingement pattern could be done numerically at reliable predictive accuracy. The accuracy regarding local values will be addressed in the following.

4.4 Local Nusselt Number Distributions on the Target Plate. For a quantitative comparison, this section presents local Nusselt number distributions along the target plate. The positions of the lines along which heat transfer coefficients were evaluated are shown in Fig. 5. Lines 1 and 3 were positioned to run through as many jet exits as possible while lines 2 and 4 were located between the rows of impinging jets.

Figures 10 and 11 show the local Nusselt numbers along lines 1–4 for the highest jet Reynolds number investigated ($Re_j = 34,000$). The results for the lower jet Reynolds numbers were almost identical, which proved the scaling of $Nu \sim Re^{2/3}$ to be valid. For the remaining areas of the target plate, heat transfer characteristics were very similar to those of lines 1–4 and therefore detailed distributions are not presented.

Local Nusselt number distributions showed significantly increased heat transfer coefficients when considering the evaluation
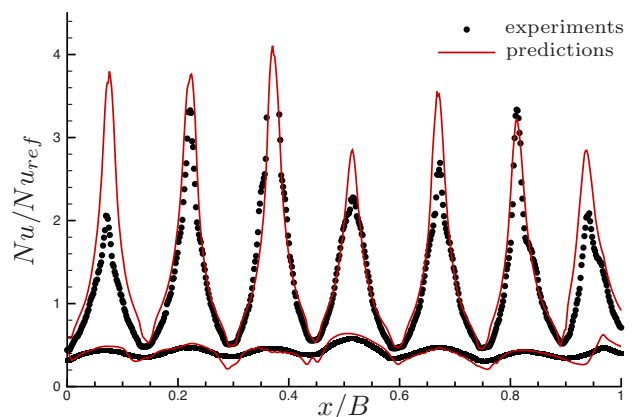

Fig. 11 Local Nusselt number distributions along lines 3 and 4 for $Re_j = 34,000$

Table 3 Comparison of area averaged Nusselt numbers

	Target plate	Left rim	Upper rim	Right rim	Bolt
Experiments [$\overline{Nu}/Nu_{ref}$]	0.73	0.40	0.50	0.47	0.36
CFD [$\overline{Nu}/Nu_{ref}$]	0.88	0.43	0.46	0.44	0.41

lines running through the stagnation points (lines 1 and 3). Compared with the correlation value from the regular impingement field Nu_{ref}, values of up to almost four times larger were observed. Average heat transfer enhancement for lines 1 and 3 measured approximately 40% compared with the reference value. For the lines running in between the rows of impinging jets, evaluation lines 2 and 4, heat transfer rates were significantly lower with average values of only $0.4 Nu_{ref}$. Those large variations of the heat transfer coefficient within the heat shield underlined the necessity of our investigation. The values provided by the correlation (Eq. (3)) were clearly insufficient for a thermal design. For high values of x/B, i.e., for the very right jet, some impact of the vicinity of the outflow gap was visible resulting in a slight shift in the Nusselt number distribution toward the right. This applied to all evaluation lines.

The overall agreement between the experimental data and the CFD predictions was good. The key parameters for jet impingement heat transfer such as stagnation point values, jet spreading behavior, and local minima were mostly reproduced correctly. The largest deviations between experiments and numerics were found for line 1, in particular, in and around the stagnation points. Thus, the average relative discrepancy of 40% was quite large for this line. However, those peak values in the stagnation regions only had a minor impact on the overall heat transfer coefficients. Furthermore, as outlined in Sec. 4.3, the massflow distribution in the experiments was most likely more inhomogeneous than in the CFD predictions contributing to larger deviations as well.

4.5 Averaged Nusselt Numbers. A comparison of global heat transfer coefficients on all investigated surfaces of the heat shield configuration is presented in this section. Table 3 shows area averaged Nusselt numbers for the different heat shield sections. All results are again shown for the maximum jet Reynolds number $Re_j = 34,000$ as results for the other jet Reynolds number were of the same order.

On the impingement target plate, the average heat transfer coefficient reached approximately 75% of the reference value obtained from the correlation for the regular impingement field Nu_{ref}. This again substantiated the motivation of our investigation. Due to the complexity of the heat shield, its heat transfer characteristics cannot be reflected accurately by a standard correlation. Predictions by the correlation were aggravated further by the irregularity of this configuration caused by, e.g., irregular jet-to-jet and jet-to-plate spacings, different nozzle diameters, nonuniform outflow conditions, and jet inclinations. Those irregularities were clearly reflected in the contour plots of local heat transfer coefficients (refer to Fig. 9).

On all side rims, average heat transfer rates were significantly lower than on the target plate. This was due to the impinging jets having lost most of their momentum before reaching the heat shield side walls.

The agreement between experimental and numerical values was again very good. While for the side rims the numerically predicted values were almost within the range of the measurement uncertainty, some deviation was found on the target plate. This was most likely due to the overprediction of heat transfer coefficients in the stagnation regions that was already observed in the local Nusselt number distributions (refer to Figs. 10 and 11). However, this overprediction is a common and well-known problem in predicting jet impingement with two-equation turbulence models [23–25]. Consequently, the numerical results could be optimized

further in terms of predictive accuracy by the use of more complex turbulence models that do not suffer from the aforementioned phenomenon or other advanced forms of numerical simulation (LES, DNS). However, this would increase the computational costs substantially. In terms of research activity, the adoption of a CFD code to a specific problem could also benefit overall performance. In our opinion, the numerical results presented here represent the current state of the art for engineering applications using commercial CFD software. However, this implies a compromise between accuracy and costs.

5 Conclusions

The present work investigated heat transfer characteristics in a combustor liner heat shield model with high Reynolds number jet impingement. Nusselt number distributions were measured on the impingement target plate and different side rims using a transient liquid crystal technique.

It was shown that for large and complex models it is essential to determine the local temperature distribution for an exact evaluation of the heat transfer coefficient. This was realized by interpolating the measured jet exit temperature both spatially and temporally.

Nusselt number distributions were shown for the target plate, which provided detailed information on the local variation of heat transfer enhancement. All results were compared with a reference value as expected by an existing correlation for a regular impingement field. Large deviations to the values predicted by the correlation were found. While local values were up to three times larger than this reference value, the average heat transfer coefficient of the present configuration was approximately 25% lower. This was mainly due to the irregular jet-to-jet spacing and the different outflow conditions. The experimental investigation emphasized that standard correlations are not suitable for the design of complex impingement cooling pattern. For the thermal optimization of an existing design, the detailed knowledge of the local variation of the heat transfer coefficient is essential. From the present configuration, some concepts for possible optimization were derived.

In addition to the experimental measurements, a numerical investigation was performed. Computations were carried out with a state of the art commercial CFD code with a two-equation turbulence model that, to our knowledge, is well suitable for the prediction of impingement configurations. The mesh was generated as a realistic three-dimensional model of the experimental setup without any simplifications. In order to achieve high numerical accuracy, a mesh sensitivity analysis was conducted, which resulted in an estimated grid convergence index of only 0.7% regarding area averaged heat transfer rates. Transient effects were investigated with an unsteady simulation but found to be of minor importance. Local and area averaged heat transfer coefficients were in very good agreement with the experimental reference data. Some overprediction occurred in the stagnation regions, however, the impact on overall heat transfer coefficients was low and average deviations between numerics and experiments were in the order of only 5–20%. Our investigation showed that contemporary CFD codes can be used as a suitable means in the thermal design process. However, an a priori evaluation of the computed results is necessary as predictive accuracy is limited to some extent. In the present investigation this was particularly true for the predicted local heat transfer coefficients.

Acknowledgment

Nomenclature

A = area, m^2
B = heat shield length, m
c = specific heat, J/kg K
D = impingement jet diameter, m
h = heat transfer coefficient, W/m^2 K
k = thermal conductivity, W/m K
L = length of impingement holes, m
N = number of cells
Nu = Nusselt number = $h \cdot D / k$
Pr = Prandtl number
T = temperature, K
t = time, s
Re = Reynolds number = $u \cdot D / \nu$
u = velocity, m/s
W = heat shield width, m
x = coordinate, m
y = coordinate, m
y^+ = nondimensional wall distance
z = heat shield height, m

Greek Symbols

ν = kinematic viscosity, m^2/s
ρ = density, kg/m^3
τ = shear stress, N/m^2
Θ = temperature ratio

Subscripts

0 = initial condition
B = bulk
i = index
j = jet
r = relative
ref = reference
W = wall

References

[1] Buchlin, J.-M., 2000, "Convective Heat Transfer in Impinging Gas-Jet Systems," Lecture Series 2000–03, von Karman Institute for Fluid Dynamics, pp. 1–33.

[2] Han, B., and Goldstein, R., 2000, "Aero-Thermal Performance of Internal Cooling Systems in Turbomachines," Lecture Series 2000–03, von Karman Institute for Fluid Dynamics, pp. 34–57.

[3] Chambers, A., Gillespie, D., Ireland, P., and Mitchell, M., 2006, "Enhancement of Impingement Cooling in a High Cross Flow Channel Using Shaped Impingement Cooling Holes," ASME Paper No. GT2006-91229.

[4] Son, C., Gillespie, D., Ireland, P., and Dailey, G., 2001, "Heat Transfer and Flow Characteristics of an Engine Representative Impingement Cooling System," ASME J. Turbomach., **123**, pp. 154–160.

[5] Martin, H., 1977, "Heat and Mass Transfer Between Impinging Gas Jets and Solid Surfaces," Adv. Heat Transfer, **13**, pp. 1–60.

[6] Han, B., and Goldstein, R., 2001, "Jet-Impingement Heat Transfer in Gas Turbine Systems," Ann. N. Y. Acad. Sci., **934**(1), pp. 147–161.

[7] Jambunathan, K., Lai, E., Moss, M., and Button, B., 1992, "A Review of Heat Transfer Data for Single Circular Jet Impingement," Int. J. Heat Fluid Flow, **13**, pp. 106–115.

[8] Metzger, D. E., Florschuetz, L. W., Takeuchi, D. I., Behee, R. D., and Berry, R. A., 1979, "Heat Transfer Characteristics for Inline and Staggered Arrays of Circular Jets With Crossflow of Spent Air," ASME J. Heat Transfer, **101**, pp. 526–531.

[9] Florschuetz, L. W., Berry, R. A., and Metzger, D. E., 1980, "Periodic Streamwise Variations of Heat Transfer Coefficients for Inline and Staggered Arrays of Circular Jets With Crossflow of Spent Air," ASME J. Heat Transfer, **102**, pp. 132–137.

[10] Florschuetz, L. W., Metzger, D. E., and Su, C. C., 1984, "Heat Transfer Characteristics for Jet Array Impingement With Initial Crossflow," ASME J. Heat Transfer, **106**, pp. 34–41.

[11] Florschuetz, L. W., and Su, C. C., 1987, "Effects of Crossflow Temperature on Heat Transfer Within an Array of Impinging Jets," ASME J. Heat Transfer, **109**, pp. 74–82.

[12] Florschuetz, L. W., Truman, C., and Metzger, D. E., 1981, "Streamwise Flow and Heat Transfer Distributions for Jet Array Impingement With Crossflow," ASME J. Heat Transfer, **103**, pp. 337–342.

[13] Bailey, J., and Bunker, R., 2002, "Local Heat Transfer and Flow Distributions for Impinging Jet Arrays of Dense and Sparse Extent," *Proceedings of the ASME Turbo Expo 2002*, Amsterdam, Netherlands.

[14] Obot, N. T., and Trabold, T. A., 1987, "Impingement Heat Transfer Within Arrays of Circular Jets: Part 1—Effects of Minimum, Intermediate, and Complete Crossflow for Small and Large Spacings," ASME J. Heat Transfer, **109**, pp. 872–879.

[15] Huang, Y., Ekkad, S. V., and Han, J.-C., 1998, "Detailed Heat Transfer Distributions Under an Array of Orthogonal Impinging Jets," J. Thermophys. Heat Transfer, **12**(1), pp. 73–79.

[16] Cheong, B. C. Y., Ireland, P. T., Ling, J. P. C. W., and Ashforth-Frost, S., 2005, "Flow and Heat Transfer Characteristics of an Impinging Jet in Crossflow at Low Nozzle-to-Plate Spacings," ASME Paper No. GT2005-68636.

[17] Uysal, U., Li, P. W., Chyu, M. K., and Cunha, F. J., 2006, "Heat Transfer on Internal Surfaces of a Duct Subjected to Impingement of a Jet Array With Varying Jet Hole-Size and Spacing," ASME J. Turbomach., **128**, pp. 158–165.

[18] Esposito, E., Ekkad, S., Kim, Y., and Dutta, S., 2007, "Comparing Extended Port and Corrugated Wall Jet Impingement Geometry for Combustor Liner Backside Cooling," ASME Paper No. GT2007-27390.

[19] Van Treuen, K., Wang, Z., Ireland, P., Jones, T., and Kohler, S., 1996, "Comparison and Prediction of Local and Average Heat Transfer Coefficients Under an Array of Inline and Staggered Impinging Jets," ASME Paper No. 96-GT-163.

[20] Chambers, A., Gillespie, D., Ireland, P., and Dailey, G., 2005, "The Effect of Initial Cross Flow on the Cooling Performance of a Narrow Impingement Channel," ASME J. Heat Transfer, **127**, pp. 358–365.

[21] Gritsch, M., Schönwälder, D., and Estaun-Echavarren, C., 2006, "Thermal Performance of Enhanced Combustor Liner Impingement Cooling Schemes," *Proceedings of the 11th International Symposium on Transport Phenomena and Dynamics of Rotating Machinery*, Honolulu, HI, Paper No. ISROMAC11-2006-20.

[22] Behnia, M., Parneix, S., and Durbin, P., 1997, "Accurate Modeling of Impinging Jet Heat Transfer," *Center for Turbulence Research, Annual Research Briefs*, NASA Ames/Stanford University, Stanford, CA, pp. 149–164.

[23] Zuckerman, N., and Lior, N., 2005, "Impingement Heat Transfer: Correlations and Numerical Modeling," ASME J. Heat Transfer, **127**, pp. 544–552.

[24] Coussirat, M., Van Beeck, J., Mestres, M., Egusguiza, M., Buchlin, J.-M., and Escaler, X., 2005, "Computational Fluid Dynamics Modeling of Impinging Gas-Jet Systems: I. Assessment of Eddy Viscosity Models," ASME J. Fluids Eng., **127**, pp. 691–703.

[25] Spring, S., Weigand, B., Krebs, W., and Hase, M., 2006, "CFD Heat Transfer Predictions of a Single Circular Jet Impinging With Crossflow," AIAA Paper No. 2006-3589.

[26] Spring, S., Weigand, B., Krebs, W., and Hase, M., 2008, "CFD Heat Transfer Predictions for a Gas Turbine Combustor Impingement Cooling Configuration," *Proceedings of the 12th International Symposium on Transport Phenomena and Dynamics of Rotating Machinery*, Honolulu, HI, ISROMAC12-2008-20222.

[27] Luff, J. K., and McGuirk, J. J., 2001, "Numerical Prediction of Combustor Heatshield Flow and Heat Transfer With Sub-Grid-Scale Modelling of Pedestals," ASME Paper No. 2001-GT-0144.

[28] Luff, J. K., and McGuirk, J., 2001, "Conjugate Heat Transfer Predictions of a Combustor Heatshield Containing Pedestals," *RTO AVT Symposium Proceedings of RTO AVT Symposium 2001*, Loen, Norway, May 7–11, Paper No. RTO-MP 069(1).

[29] Riahi, A., and Borns, F. G., 2004, "Gas Turbine Combustor Heat Shield Impingement Cooling Baffle," ASME Paper No. GT2004-53160.

[30] Lempereur, C., Andral, R., and Prudhomme, J. Y., 2008, "Surface Temperature Measurement on Engine Components by Means of Irreversible Thermal Coatings," Meas. Sci. Technol., **19**, p. 105501.

[31] Lauffer, D., Weigand, B., von Wolfersdorf, J., Dahlke, S., and Liebe, R., 2007, "Heat Transfer Enhancement by Impingement Cooling in a Combustor Liner Heat Shield," ASME Paper No. GT2007-27908.

[32] Ireland, P. T., and Jones, T. V., 2000, "Liquid Crystal Measurements of Heat Transfer and Surface Shear Stress," Meas. Sci. Technol., **11**(7), pp. 969–986.

[33] Poser, J., von Wolfersdorf, R., and Lutum, E., 2007, "Advanced Evaluation Of Transient Heat Transfer Experiments Using Thermochromic Liquid Crystals," Proc. Inst. Mech. Eng., Part A, **221**(6), pp. 793–801.

[34] Kays, W. M., Crawford, M. E., and Weigand, B., 2004, *Convective Heat and Mass Transfer*, McGraw-Hill, New York.

[35] Poser, R., von Wolfersdorf, J., Lutum, E., and Semmler, K., 2008, "Performing Heat Transfer Experiments in Blade Cooling Circuits Using a Transient Technique With Thermochromic Liquid Crystals," ASME Paper No. GT2008-50364.

[36] Kline, S. J. and McClintock, F. A., 1953, "Describing Uncertainties in Single-Sample Experiments," Mech. Eng. (Am. Soc. Mech. Eng.), **75**, pp. 3–8.

[37] Menter, F., 1994, "Two-Equation Eddy-Viscosity Turbulence Models for Engineering Applications," AIAA J., **32**(8), pp. 1598–1605.

[38] I. B. Celik, U. Ghia, P. J. Roache, C. J. Freitas, H. Coleman, and P. E. Raad, 2008, "Procedure for Estimation and Reporting of Uncertainty Due to Discretization in CFD Applications," ASME J. Fluids Eng., **130**, p. 078001.

[39] Richardson, L., and Gaunt, A., 1927, "The Deferred Approach to the Limit. Part I. Single Lattice. Part II. Interpenetrating Lattices," Philos. Trans. R. Soc.

London, Ser. A, **226**, pp. 299–361.

[40] Roache, P. J., 1994, "A Method for Uniform Reporting of Grid Refinement Studies," ASME J. Fluids Eng., **116**, pp. 405–413.

[41] Roache, P. J., 2003, "Conservatism of the Grid Convergence Index in Finite Volume Computations on Steady-State Fluid Flow and Heat Transfer," ASME J. Fluids Eng., **125**, pp. 731–735.

[42] Goldstein, R. J., and Behbahani, A. I., 1982, "Impingement of a Circular Jet With and Without Cross Flow," Int. J. Heat Mass Transfer, **25**(9), pp. 1377–1382.

[43] Pope, S. B., 1978, "An Explanation of the Turbulent Round-Jet/Plane-Jet Anomaly," AIAA J., **16**(3), pp. 279–281.

Transition Mechanisms in Separation Bubbles Under Low- and Elevated-Freestream Turbulence

Brian R. McAuliffe[1]
e-mail: brian.mcauliffe@nrc-cnrc.gc.ca

Metin I. Yaras
e-mail: metin_yaras@carleton.ca

Department of Mechanical and Aerospace
Engineering,
Carleton University,
1125 Colonel By Drive,
Ottawa, Ontaria K1S 5B6, Canada

Through numerical simulations, this paper examines the nature of instability mechanisms leading to transition in separation bubbles. The results of two direct numerical simulations are presented in which separation of a laminar boundary layer occurs over a flat surface in the presence of an adverse pressure gradient. The primary difference in the flow conditions between the two simulations is the level of freestream turbulence with intensities of 0.1% and 1.45% at separation. In the first part of the paper, transition under a low-disturbance environment is examined, and the development of the Kelvin–Helmholtz instability in the separated shear layer is compared to the well-established instability characteristics of free shear layers. The study examines the role of the velocity-profile shape on the instability characteristics and the nature of the large-scale vortical structures shed downstream of the bubble. The second part of the paper examines transition in a high-disturbance environment, where the above-mentioned mechanism is bypassed as a result of elevated-freestream turbulence. Filtering of the freestream turbulence into the laminar boundary layer results in streamwise streaks, which provide conditions under which turbulent spots are produced in the separated shear layer, grow, and then merge to form a turbulent boundary layer. The results allow identification of the structure of the instability mechanism and the characteristic structure of the resultant turbulent spots. Recovery of the reattached turbulent boundary layer is then examined for both cases. The large-scale flow structures associated with transition are noted to remain coherent far downstream of reattachment, delaying recovery of the turbulent boundary layer to an equilibrium state. [DOI: 10.1115/1.2812949]

1 Introduction

Separation bubbles are a common occurrence over airfoils at low Reynolds numbers, particularly over airfoils that develop high levels of lift such as those found in turbomachinery blade rows. The presence of separation can adversely affect the performance of such airfoils, for which reattachment due to laminar-to-turbulent transition plays an important role.

Transition in a separation bubble is affected by many environmental factors [1], such as Reynolds number, pressure gradient, freestream turbulence, surface roughness, noise, vibrations, and periodic wake passing. Elevated levels of disturbances generally promote transition and lead to shorter bubbles. Reliable transition models are important for the design of high-performance airfoils, and although most models used for turbomachinery flows are semiempirical in nature, their development requires a thorough understanding of the underlying physics of the transition process [2].

In the absence of any significant level of environmental disturbances, transition of a separated shear layer occurs through the Kelvin–Helmholtz instability mode whereby receptivity of the layer to small disturbances results in grouping of spanwise vorticity at selective streamwise wavelengths [3,4]. This is analogous to Tollmien–Schlichting instability growth in attached boundary lay-

ers under such conditions. The growth of this separated-shear-layer instability leads to roll-up of the vorticity contained in the layer into discrete spanwise vortex structures, which subsequently breakdown to small-scale turbulence, thereby initiating reattachment to the surface. This process closely resembles that which occurs in planar free-shear layers [5]. Under conditions with elevated levels of environmental disturbances, such as freestream turbulence, surface roughness, or periodically passing turbulent wakes, turbulent spots form in the separated shear layer consistent with what occurs in attached boundary-layer transition [6–8]. The spots then grow and merge to form a turbulent shear layer during reattachment to the surface.

Experimental studies have provided a wealth of knowledge regarding the parameters that affect transition in separation bubbles, as well as providing some indications of the associated physical mechanisms. However, their limitation in terms of simultaneous availability of temporal and spatial variations of flow parameters with adequate resolution has prevented the development of a complete picture of the transition process. The experimental studies on this topic are too numerous to cite; however, several have been found to be particularly useful to the present authors [6–16]. Given that the transition process is ultimately nonlinear, the limitation imposed upon the numerous linear theories that have been utilized in the study of instability mechanisms leading to transition is obvious. In recent years, advancements in computing power have led to increasing use of large-eddy simulation (LES) and direct numerical simulation (DNS) to study the physics associated with instability and transition in separated shear layers [4,17–25].

The present study was undertaken to comparatively examine the physical mechanisms associated with transition in separation bubbles under low and elevated levels of freestream turbulence.

Results from two DNSs are presented, one with an undisturbed freestream and one with elevated-freestream turbulence, to examine the spatial and temporal nature of the transition process in separation bubbles. To place the present effort in context, discussions of the transition mechanisms are aided by comparisons with transitional planar free-shear layers and attached boundary layers, and important references are discussed and cited in the appropriate sections.

2 Numerical Method and Simulation Conditions

DNS has been used for the present study of transition in separation bubbles. Details of the simulations were previously documented [4,26], and the following provides a summary of the computational details.

The simulations were performed using the ANSYS-CFX commercial CFD software package, which provides solution of the continuity and Navier–Stokes equations using a finite volume approach. The time-varying and incompressible form of the equations solved in the simulations are given, in compact Cartesian notation, by

$$\frac{\partial}{\partial x_j}(\rho U_j) = 0$$

$$\frac{\partial}{\partial t}(\rho U_i) + \frac{\partial}{\partial x_j}(\rho U_j U_i) = -\frac{\partial p}{\partial x_i} + \frac{\partial}{\partial x_j}\left[\mu\left(\frac{\partial U_i}{\partial x_j} + \frac{\partial U_j}{\partial x_i}\right)\right]$$

Central differencing was used for discretization of the spatial derivatives, and time discretization was realized through second-order Euler backward differencing. Solutions of the continuity and momentum equations at each time step were converged through an algebraic multigrid scheme within eight iterations such that the maximum residuals at the end of each time step were lower than 6×10^{-5}, except very near the inlet boundaries where the maximum residuals were on the order of 10^{-4}. rms residual levels were on the order of 10^{-6} after each time step. A general description of the algebraic multigrid method implemented in ANSYS-CFX is given by Raw [27], and the method makes use of the additive correction technique of Hutchinson and Raithby [28]. The method uses a W cycle with a coarsening rate of approximately 10, requiring five grid levels for the low-freestream-turbulence simulation (with 1.1×10^6 grid elements) and six grid levels for the elevated-freestream-turbulence simulation (with 4.2×10^6 grid elements). The spatial and temporal resolutions were chosen such that the turbulence scales in the turbulent boundary layer downstream of the separation bubble are resolved down to about 35 times the Kolmogorov scale. Through comparison with experimental data, previous studies of this research group [4,24] have shown this resolution to be adequate for capturing the turbulence associated with transition and reattachment of separated shear layers. The selected spatial and temporal resolutions are also consistent with recent DNSs involving separation bubbles, performed by other research groups [17,29,30].

The computational domain used for the elevated-freestream-turbulence case is shown in Fig. 1, and was selected to capture the complete boundary-layer development along a flat plate with a prescribed streamwise pressure distribution, under elevated-freestream-turbulence conditions. The domain used for the low-freestream-turbulence case is the same shape as the BUBBLE subdomain shown in Fig. 1; however the spanwise width is 0.060 m as opposed to 0.072 m. The configuration is based on an experimental setup used by this research group in a series of experiments on separated- and attached-flow transition. For details of the experimental setup, the reader is referred to the work of Roberts and Yaras [6]. The inlet boundary condition consists of a 4×4 array of uniform-velocity square jets of 13 mm width and 18 mm spacing, which simulates the flow through a turbulence-generating grid that was used in the wind-tunnel experiments. The "flat plate" begins 325 mm downstream of the domain inlet, pro-
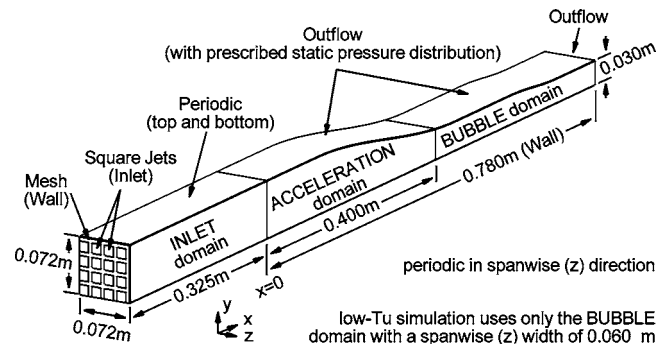

Fig. 1 Schematic of computational domain

viding a region of turbulence decay and resulting in a freestream turbulence intensity of 5.1% with an integral length scale of 7 mm at the plate leading edge. Periodic boundaries surround this initial turbulence decay region, which is labeled as the INLET subdomain in Fig. 1. The ACCELERATION and BUBBLE subdomains are bound by periodic boundaries in the spanwise direction, by a solid, no-slip wall on their lower side and an outflow boundary along their upper side. The upper outflow boundary upon which the streamwise pressure distribution is imposed was shaped such that fluid does not enter the domain through this boundary, and was placed well within the freestream region. This shaping was accomplished by first estimating the geometry of a converging-diverging wall-bounded flow path based on the desired freestream velocity distribution, using a one-dimensional flow assumption. The surface shape selected for the upper domain boundary provides a greater contraction than that estimated through the said one-dimensional calculation, ensuring that streamlines do not enter the computational domain through the upper surface. On the downstream end, the computational domain is terminated by an outflow boundary with a prescribed area-averaged static pressure. As this outflow boundary condition does not allow for convection of turbulence eddies through the boundary without distortion, the boundary was placed a conservative distance downstream of the flow region of interest. For the low-freestream-turbulence case, experimental data were used to provide inflow conditions at a location corresponding to $x=0.4$ m.

Averaging for the low-freestream-turbulence case was accomplished through spanwise and time averaging of data from five evenly spaced $x-y$ planes over 2048 time steps. For the elevated-freestream-turbulence case, spanwise and time averaging was accomplished over the entire BUBBLE domain over 3200 time steps. Over these periods, running averages of the auto- and cross correlation of velocity fluctuations within the transition regions show variation by no more than a few percent, providing confidence that the dominant physical aspects of the transition processes were captured.

Table 1 provides information on the two cases, including flow conditions and numerical details for each simulation. Figure 2 shows the boundary-layer-edge velocity distributions for both cases near and downstream of the suction peak, and provides the time-averaged locations of separation and reattachment for the observed separation bubbles. Both of the separation bubbles observed in the simulations can be classified as "short bubbles" in that, in the experiments upon which the simulations are based, they do not significantly alter the streamwise pressure distribution from that observed at higher Reynolds numbers in the absence of separation.

For the elevated-freestream-turbulence case, the streamwise rate of decay of freestream turbulence downstream of the simulated turbulence grid at the inflow boundary is consistent with grid-generated turbulence in wind tunnels [31], and a slight anisotropy of the turbulence is observed. Above the plate leading edge ($x=0$ m, $y=0.015$ m) where the turbulence intensity is 5.1%, the

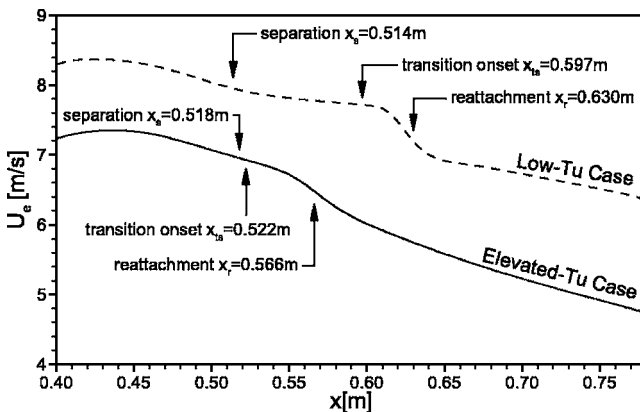**Table 1 Flow conditions and numerical details of simulations**

	Low Tu	Elevated Tu
Flow Reynolds number, Re_{sp}	440,000	390,000
Turbulence intensity, Tu_s	0.1%	1.45%
Turbulence integral length scale, Λ_s	0.020 m	0.011 m
Separation Reynolds number, $\mathrm{Re}_{\theta s}$	267	335
Number of time steps, N_{ts}	2048	3200
Time step, Δt	0.00020 s	0.00015 s
Streamwise node spacing, Δx^{+a}	24	19
Spanwise node spacing, Δz^{+a}	24	19
First node off the wall, y_1^{+a}	0.6	0.5
Number of mesh elements	1.1×10^6	4.2×10^6

[a]Based on wall friction in the turbulent boundary layer downstream of reattachment.

streamwise fluctuation levels are 10% higher than those in the other two coordinate directions, which is consistent with what has been observed downstream of turbulence-generating grids of similar configuration [31]. The strong streamwise acceleration imposed over the forward part of the flat plate causes a reduction in this streamwise turbulence intensity providing a streamwise turbulence level over the separation bubble that is 10% lower than those associated with the wall-normal and spanwise components of velocity. As a result of the accelerating flow over the forward part of the surface, the turbulence intensity at the time-averaged streamwise location of separation is 1.45%. Most studies presented in the literature, for which turbulence-generating grids were used, quote the level of turbulence intensity at the inlet of the test configuration. However, continual decay of the grid-generated turbulence combined with the streamwise acceleration typically observed in similar turbomachinery flows would tend to decrease the turbulence intensity upstream of separation to levels more comparable to those observed in the present case. Similar levels of decay were observed in some of the experimental test cases used in the development of the transition model of Roberts and Yaras [2].

3 Results and Discussion

Separated shear layers and the process of laminar-to-turbulent transition occurring therein share characteristics with both boundary-layer and free-shear-layer flows. In the following discussions, extensive reference to published literature is given in an effort to provide a context for the interpretation of the present simulation results. This includes a comparative analysis of separated and free-shear layers in the first part of this section, with regard to transition in a low-disturbance environment. The second

Fig. 3 Vorticity roll-up of the separated shear layer caused by the Kelvin–Helmholtz instability (trajectories of two roll-up vortices shown by white lines)

Fig. 2 Boundary-layer-edge velocity distributions for both simulations in the region 0.40 m < x < 0.78 m, and time-averaged locations of separation, transition onset, and reattachment

part describes transition of a separated shear layer under elevated-freestream turbulence and provides comparisons with transition phenomena observed in attached boundary layers.

3.1 Transition in Low-Disturbance Environments. In planar free-shear layers, the process of laminar-to-turbulent transition is typically initiated through receptivity of the inflectional velocity profile to environmental disturbances. In the absence of a bounding wall, the shear layer is unstable via the inviscid Kelvin–Helmholtz mode. Growth of the most-amplified instability frequency results in the roll-up and formation of vortices with a direction that is consistent with the vorticity of the shear layer. The dominant instability frequency has been shown to scale with the shear-layer momentum thickness through a Strouhal number, $\mathrm{Sr}_\theta = f\theta/\Delta U$, where ΔU is the velocity difference across the shear layer. Ho and Huerre [32] have identified the frequency of maximum amplification in an unforced planar free-shear layer to correspond to $\mathrm{Sr}_\theta = 0.016$.

The initial development of a separated shear layer in a low-disturbance environment exhibits the same characteristics as a planar shear layer. Downstream of separation, an instability develops that causes the vorticity in the shear layer to roll-up into distinct spanwise vortical structures. Based on the present simulation, an example of the transient vorticity roll-up that occurs in a separated shear layer is shown in Fig. 3. Approximately two periods of the dominant instability frequency are shown in this figure, and the trajectories of two distinct vortices are identified. As the vortices saturate and shed downstream of the separated shear layer, smaller
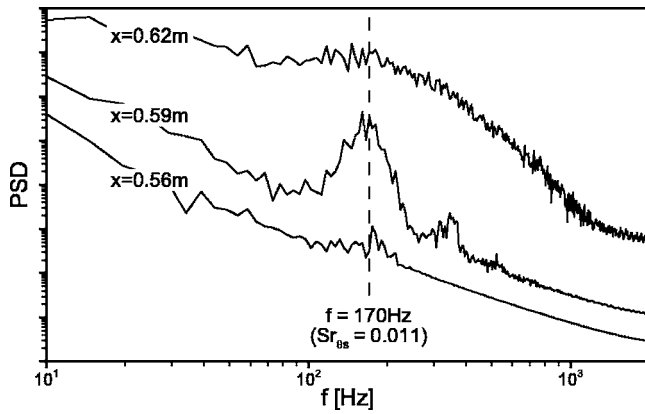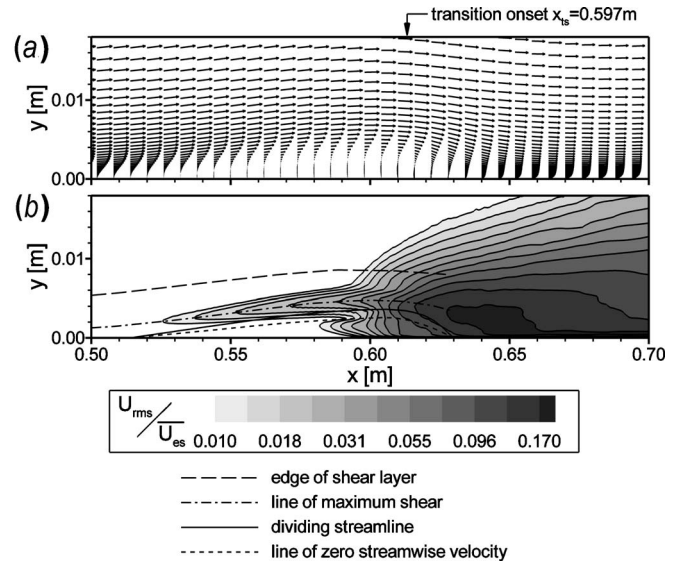
Fig. 4 Power spectra of velocity in the separation bubble under low-freestream turbulence (at $y=0.004$ m)

Fig. 5 Characteristics of the separation bubble under low-Tu freestream conditions (wall-normal coordinate stretched for better visualization); (*a*) time-averaged velocity vector profiles with every sixth profile shown; (*b*) rms-velocity contours

vortical scales are observed indicating that transition to small-scale turbulence has been initiated. The frequency content at various streamwise locations along the separation bubble is provided in Fig. 4, which shows maximum amplification of the instability at a frequency of 170 Hz, and a much broader frequency content in the downstream region of the bubble. For separated shear layers, the frequency associated with maximum amplification of the instability is generally in close agreement to that of planar free-shear layers and is conventionally presented as a Strouhal number based on conditions at separation ($Sr_{\theta s}=f\theta_s/U_{es}$). Table 2 presents the dominant instability Strouhal number observed in the present simulation together with those noted in several other experimental and computational studies of separated shear layers. The tabulated values are consistent with the most rapidly amplified instability frequency obtained through a stability analysis as presented by Dovgal et al. [3] for analytical velocity profiles similar to those prevailing in separation bubbles. The variation observed in Table 2 is attributed to differences in the level of reverse flow and shape of the base-flow velocity profiles.

Through analysis based on linear stability theory, Rist and Maucher [35] examined the effect of profile shape on the stability of velocity profiles with reverse flow near the surface, and found two regions in which the associated instabilities show differing characteristics. The outer "separated" part of the shear layer is unstable via an inviscid type instability, with minimal Reynolds number influence, while in the reverse-flow region near the wall, a viscous Reynolds-number-dependent instability is present. The dominance of one mode over the other was found to depend on the distance of the zero-velocity point from the surface and on the level of reverse flow prevailing near the wall. Increased distance from the surface promotes the outer-layer inviscid mode, as well as promoting an increase in the associated frequency and growth rates of this instability. Conversely, an increase in the level of reverse flow promotes the inner viscous instability, with an associated decrease in frequency and increase in growth rate. Comparing the velocity profiles of the present simulation (Fig. 5(*a*)) and

Table 2 Instability Strouhal numbers identified in several experimental and numerical studies involving shear layers with inflectional velocity profiles

Investigators	$Sr_{\theta s}=f\theta_s/U_{es}$
Present study	0.011
McAuliffe and Yaras [5,16]	0.008–0.016
Pauley et al. [33,34]	0.005–0.008
Yang and Voke [19]	0.005–0.011
Talan and Hourmouziadis [11]	0.010–0.014
Ho and Huerre [32] (free-shear layer, Sr_θ)	0.016

those of the studies outlined in Table 2 with those examined by Rist and Maucher, with respect to distance of the shear layer from the wall and level of reverse flow, would indicate a predominance toward the outer-layer inviscid instability. In examining the fluctuation levels observed in our present simulation (Fig. 5(*b*)), those associated with the inviscid instability in the separated shear layer appear to dominate, with coexistence of near-wall viscous instability as suggested by the near-wall fluctuation peak observed downstream of $x=0.58$ m. In experimental results presented by Lang et al. [36] for a separation bubble in which the most unstable inviscid frequency was forced by a vibrating wire upstream of separation, similar fluctuation peaks were found in the inner and outer regions of the separated shear layer with fluctuation profiles that were in very good agreement with linear stability analysis of the base-flow profile. These results provide evidence that although the dominant instability in separation bubbles leading to transition in a low-disturbance environment is of the inviscid Kelvin–Helmholtz type, the influence of viscous instability near the wall should not be dismissed, particularly in very thin separated shear layers or in those with significant levels of reverse flow.

Increased levels of reverse flow in a separated shear layer can lead to an absolute instability for which associated fluctuations can propagate upstream and become self-sustaining. A criterion often used to assess whether an absolute instability is present in a separation bubble is the level of reverse flow in the near-wall region. Alam and Sandham [17] identified a threshold of approximately 15–20% of the local freestream velocity, above which absolute instability prevails. However, most studies including our own indicate that laminar separation bubbles that occur over the surfaces of airfoils have reverse-flow levels much lower than this threshold, and the associated instability is therefore convective in nature. In our present simulation, for which the velocity profiles are presented in Fig. 5(*a*), the reverse-flow velocity in the separation bubble remained less than 10% of the local freestream velocity.

In planar free-shear layers, the spanwise vortices produced by the Kelvin–Helmholtz instability are unstable to subharmonic disturbances [37]. This instability leads to the vortex pairing phenomenon as observed in numerous experimental and numerical studies [32,38,39]. Specifically, this instability causes these primary vortices to be alternately shifted in the transverse direction. The vortices shifted to the higher-velocity side are then convected

at a rate higher than that those on the lower-velocity side, causing a rotation of two sequential vortices about each other. This rotation is then further amplified due to mutual induction of the two vorticity fields until the vortices merge. The mutually induced velocities generate strains, which deform the vorticity distribution; hence the vortices do not retain their original shape but become elongated in the flow direction during their rotation [40]. The resultant stronger new vortices have approximately double the spacing of the primary vortices, hence the identification of this process as a subharmonic of the primary instability. As was pointed out by Ho and Huang [41], the change of the local length scale of the shear layer as a result of the vortex merging makes the original subharmonic become neutrally stable, and the new subharmonic becomes the wave of most rapid amplification. This pairing of vortices is suggested as the dominant mechanism associated with growth of planar free-shear layers [32]. The same vortex-pairing phenomenon has been observed in separation bubbles [16,20,23,42]. However, the presence of pairing has only been observed at lower Reynolds numbers ($Re_{\theta s}$ of about 100) and was not observed in our current simulation in which $Re_{\theta s}$ had a value of 267.

A spanwise nonuniformity of planar free-shear layers is often observed, which has been tied to the development of streamwise counter-rotating vortex pairs [32,38]. It is surmised that this three dimensionality is associated with a secondary instability superimposed on the primary two-dimensional instability [43], similar to that which occurs in boundary-layer transition when streamwise stretching of Tollmien–Schlichting waves begins [44]. The generation of small-scale turbulence in a planar free-shear layer has been associated with the interaction of these streamwise vortices with the spanwise vortices originating from the primary instability. The data of Huang and Ho [38] revealed that small-scale fluctuations more frequently occur near the core of the streamwise vortices as they interact with a merging spanwise vortex pair. Malkiel and Mayle [42] suggest transition in a separation bubble to occur through this interaction of streamwise and spanwise vorticity. However, this interaction has not yet been identified in either spatially resolved measurements or in numerical simulations involving separation bubbles, including the present simulation. Numerical studies performed by Spalart and Strelets [18], Wissink and Rodi [21], Roberts and Yaras [24], and our present simulation indicate that in a separation bubble exposed to a low-disturbance environment, breakdown to turbulence occurs very quickly over a short streamwise distance. It should be noted that vortex pairing is not observed in any of these cases. In the present simulation, breakdown occurs in a time-periodic manner within the braid (high-shear) region between spanwise vortices. Figure 6(a) shows small distortions of the vorticity field in the roll-up region. These distortions are associated with small-scale turbulence activity between the spanwise vortices which, as they convect with these large-scale vortices, provide complete breakdown to small-scale turbulence over approximately one wavelength of the primary instability. Figure 6(a) also shows the redistribution of the vorticity to progressively smaller scales downstream of reattachment. This breakdown is also seen as an increase and redistribution of the frequency content over a much wider range, as observed in the PSD near reattachment ($x=0.62$ m) in Fig. 4. Despite this breakdown to small-scale turbulence, coherence of the spanwise vortical structures is still observed downstream of transition, but their structure becomes distorted and stretched. These vortex structures are identified in Fig. 6(b) by the low-pressure isocontours (dark contour surfaces). In the transition and reattachment region, stretching and reorientation of the vorticity contained in the vortical spanwise structures result in hairpinlike structures. These structures are reminiscent of those observed in turbulent boundary layers [45], and are also similar to those observed by Abdalla and Yang [23] as a result of vortex pairing. The reorientation of vorticity in the streamwise direction provides enhanced momentum exchange in the wall-normal direction, and is likely a key mecha-
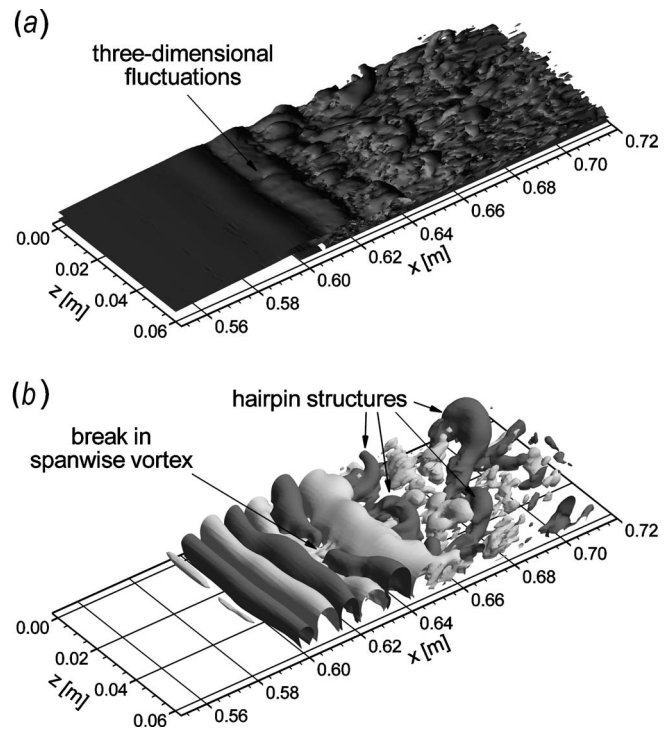
Fig. 6 Transitional structures in the separation bubble under low-Tu freestream conditions; (a) vorticity isosurface Ω =1500 s^{-1}, (b) pressure isosurfaces $p'=$ Pa (dark), $p'=1$ Pa (light)

nism associated with the reattachment process. Similar structures have been observed in the reattachment region of turbulent separation bubbles as well [46].

The transition process described above is altered significantly in the presence of elevated environmental disturbances. The next section describes the mechanisms associated with transition in a separation bubble under such conditions.

### 3.2 Transition in Elevated-Disturbance Environments.
Laminar-to-turbulent transition of a shear layer is promoted by the presence of elevated freestream disturbances. Under such conditions, disturbances that penetrate the shear layer undergo an algebraic growth followed by viscous decay, unless they manage to grow to sufficiently large amplitudes to yield a turbulent spot. This path to transition is also referred to as transient growth or nonmodal growth, with the latter referring to the fact that this mode is not predicted as one of the eigenmodes of the solution of linearized theories based on the Orr–Sommerfeld and Squire equations. There is no definitive threshold for when this bypass mechanism begins to dominate but it is strongly influenced by the magnitude of the disturbance as well as the receptivity of the shear layer to this disturbance. Once turbulent spots are produced, they grow and merge to form a fully turbulent shear layer in a manner originally proposed by Emmons [47]. Bypass transition has been observed experimentally in separation bubbles by many researchers (e.g., [6,12]), and several studies have examined the growth of turbulent spots induced by a traveling wave packet [9,10]. In these "forced spot" cases, selectively amplified frequencies emerge from the wave packet, forming a convecting wave pattern within which breakdown to turbulence occurs. However, descriptions regarding local flow development that leads to the creation of turbulent spots under elevated-freestream turbulence conditions are scarce. Analysis of the second test case of the present effort provides further information in this regard.

Under elevated-freestream-turbulence conditions, streamwise streaks appear in the laminar boundary layer upstream of separa-
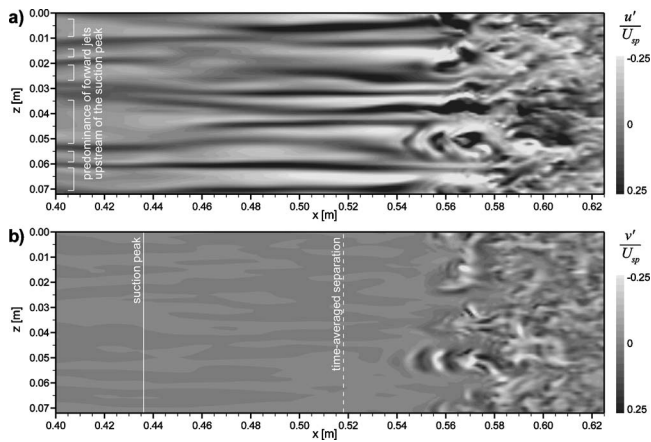
Fig. 7 Streamwise streaks in the shear layer observed in a plane where $\bar{U} \approx 1/2\overline{U_e}$; (a) streamwise fluctuations; (b) wall-normal fluctuations

tion and provide the conditions necessary for turbulent-spot production. These streaks result in a large variation in the instantaneous streamwise separation location with time and along the span. In Fig. 7, which shows velocity fluctuations in an $x–z$ plane where $\bar{U} \approx 1/2\overline{U_e}$, the strong spanwise variation and larger amplitude of the u' component compared to the v' component prior to transition is a clear indication that the streaks are comprised predominantly of fluctuations in the streamwise direction. The streaks originate near the leading edge of the flat plate, as this is a receptivity site where the mean flow changes rapidly [48]. The mechanism through which these streaks are produced in a laminar boundary layer is described by Jacobs and Durbin [49] and the references therein, and has been referred to as "shear sheltering." In this process, the time-mean shear in a laminar boundary layer acts to filter perturbations from the freestream turbulence. Viscous stresses are able to withstand much of the perturbation spectra associated with the freestream turbulence; however low-frequency components can penetrate and are then amplified by the mean shear. This results in the energy spectrum shifting to lower frequencies. Figure 8 provides the frequency content of velocity fluctuations at various streamwise locations through the separation bubble region and shows the elevated levels of low-frequency fluctuations near separation ($x=0.52$ m), which are of similar magnitude to those downstream of the bubble where transition is near completion ($x=0.58$ m). The elevated fluctuation spectra in the $10–20$ Hz range is also observed in the laminar boundary-layer well upstream of separation and is also apparent in experimental measurements by the present research group corresponding to similar flow conditions. This low-frequency range is much
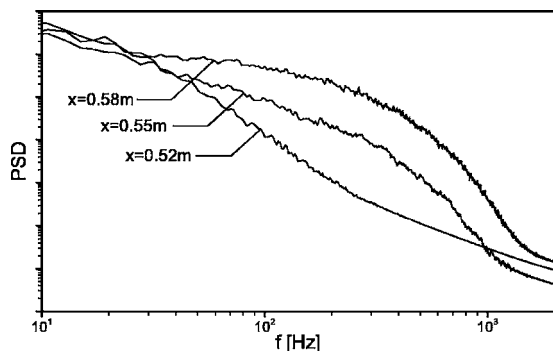
lower than the most energetic range associated with the freestream turbulent eddies and is also much lower than the frequency at which Tollmien–Schlichting waves would amplify. It is therefore assumed that these amplified low frequencies are a result of the "shear sheltering" effect, which generates the streamwise streaks in the boundary layer. This is contrary to what is observed under the condition with low levels of freestream turbulence, as seen in Fig. 4, where much lower amplitudes of this low-frequency range are observed in the laminar separated shear-layer compared with those downstream of transition.

Although the laminar streaks have a long streamwise wavelength, they have a much shorter spanwise extent (see Fig. 7), which is on the order of the boundary-layer thickness. This is consistent with the simulation results of Jacobs and Durbin [49] and experiments referenced therein. The streaks result in both forward and backward jets, relative to the mean flow profile. In Fig. 7, a predominance toward low-amplitude forward jets is noted upstream of the suction peak; however there is no bias toward either direction within the separated shear layer. This is likely a result of the adverse pressure gradient, which promotes reverse flow. In this region, the laminar streamwise fluctuation levels associated with the streaks are very high, and can exceed 25% of the local edge velocity. Asai et al. [50] provide evidence that this level of streamwise fluctuation is enough to bring a streak in a laminar boundary layer into a sinuous unstable mode, hence initiate a secondary instability in the form of spanwise waviness of the low-speed streaks. The present simulation data provide no indication that a sinuous wavering of the streaks is a precursor to turbulent-spot production, nor the varicose wavering pattern, which requires higher fluctuations levels. According to a recent experimental study by Konishi and Asai [51], the rate of growth of the varicose instability is weaker than the sinuous instability, and the growth rate of the latter at the fundamental mode is completely suppressed when the lateral spacing of the low-velocity streaks is less than about 2.5 times their width. In the present simulation, the spacing and width of the low-velocity streaks are of similar magnitude, and thus the absence of sinuous or varicose instability is consistent with the observations of Konishi and Asai in attached boundary layers.

Jacobs and Durbin [49] associate the generation of a turbulent spot with strong backward jets being lifted from near the surface toward the freestream. The present simulation results provide evidence that the generation of turbulent spots evolves more generally as a result of the strong shear associated with the streamwise streaks. The evolution of a turbulent spot is shown in Fig. 9 in a series of vector and vorticity plots in the x-y plane along the spot centerline. The wall-normal coordinate has been stretched to allow better visualization of the spot breakdown, and every fourth velocity vector profile is included in the figure as well. The platform structure of this particular spot is apparent in the x-z plots in Fig. 7 centered at about $x=0.56$ m and $z=0.05$ m. The uppermost plot in Fig. 9 presents the time-averaged flow field in which a discontinuity in the trajectory of maximum vorticity is observed as the shear layer transitions from a laminar separated shear layer to a turbulent reattached boundary layer. This discontinuity is caused in part by a redistribution of the spanwise vorticity to smaller scales as transition and reattachment progresses. At $t'=0$ s, a separated laminar shear layer is present with vorticity confined to a much thinner layer than in the time-averaged case. The smaller scales observed downstream of $x=0.57$ m are associated with the turbulence in the reattached shear layer (time-averaged reattachment is at $x_r=0.566$ m). As the flow field evolves in time, a wave pattern becomes apparent resulting in roll-up of the vorticity contained in the shear layer. As this secondary instability grows, fluid is entrained toward the surface, resulting in a patch of reattached flow, which convects downstream. The roll-up occurs in a three-dimensional manner and a series of vortex loops defines the topology of the newly formed turbulent spot. At $t'=0.006$ s, smaller scales are present in the shear layer indicative of the young tur-
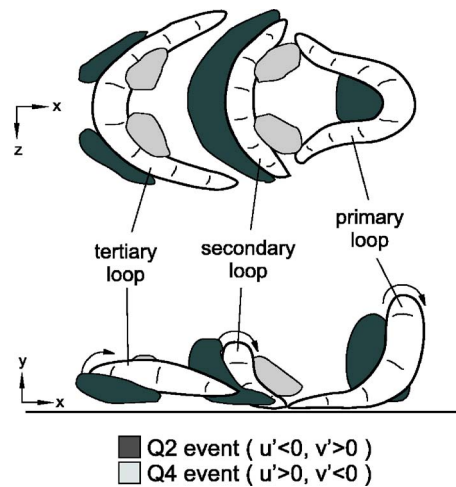

Fig. 8 Power spectra of velocity through the bubble region under elevated-freestream turbulence (at $y=0.00125$ m)
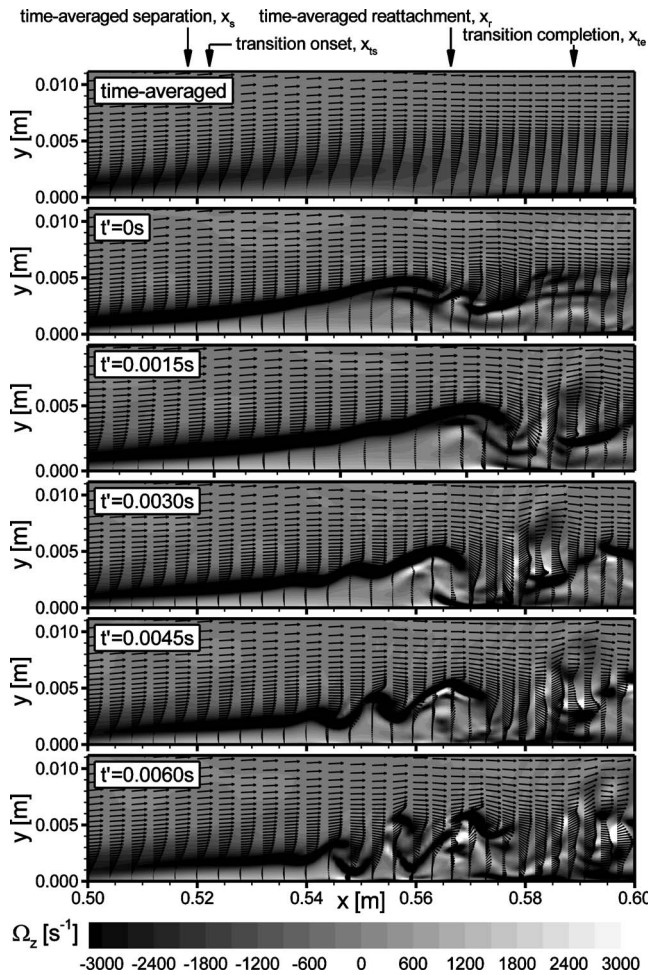
Fig. 9 Evolution of a turbulent spot through time sequence of *x-y* planes along the centerline of the spot (**averaged vectors and spanwise vorticity in uppermost plot**)

Fig. 10   Topology of a turbulent spot in a separated shear layer

bulence within the spot.

The instability that develops along the centerline of the spot is reminiscent of Kelvin–Helmholtz vorticity roll-up, as observed in Fig. 3 under low-freestream turbulence, and is, in fact, such an inviscid instability despite the locally three-dimensional nature of the shear layer. The Strouhal number associated with this instability, based on local conditions ($Sr_\theta = f\theta/\Delta U$), varies between 0.014 and 0.017, which is in good agreement with that for the Kelvin–Helmholtz instability in plane shear layers (see Table 2). Watmuff [9] also observed similar agreement with the Kelvin–Helmholtz instability for the wave frequency from which vortex loops roll-up in his wave-packet-induced turbulent-spot study. This would suggest that turbulent-spot production in a separated shear layer is the result of a local inviscid instability of the shear generated by the streamwise streaks convecting through the shear layer. A similar roll-up has been observed by Jacobs and Durbin [49] and Wu et al. [52] during the initial stages of turbulent-spot formation in simulations of freestream-turbulence-induced bypass transition and wake-induced bypass transition of a zero-pressure-gradient boundary layer, respectively.

Once a turbulent spot is initiated through the formation of vortex loops, the spot grows in the streamwise and spanwise directions as it convects downstream, in a manner consistent with models proposed for turbulent spots under strong adverse pressure gradients [26]. A schematic illustrating the topology of a newly formed turbulent spot is shown in Fig. 10 and is based on examining multiple spots in the present simulation. While the most

frequently observed configuration consists of three vortex loops as is shown in Fig. 10, there are also occurrences with only two distinct loops, and others with a weak fourth loop appearing on the upstream side of the spot. Regions within the spot that provide the greatest contribution to turbulent shear stresses ($-\overline{u'v'}$) are identified by the shaded regions. Q2 events ($u'<0, v'>0$), also referred to as "ejection" processes, appear to dominate the process of wall-normal momentum exchange over the Q4 events ($u'>0, v'<0$), which are commonly referred to as "sweep" processes [45]. As the spot convects, the spot-leading-edge (primary) vortex loop is lifted away from the surface as it interacts with the near-wall fluid ahead of the spot. This is reminiscent of the hairpin vortex structures observed in near-wall regions of turbulent boundary layers [45]. The primary loop also extends the furthest into the freestream, where it convects at a high rate due to the higher freestream velocity, thus contributing to the streamwise growth of the spot. The downstream orientation of the legs of the secondary and tertiary loops is a result of the blockage created by the column of low-momentum near-wall fluid ejected away from the wall by the induced effect of the primary vortex loop.

3.3   Turbulent Boundary-Layer Recovery. The two transition mechanisms identified in the two simulations of the present effort yield some differences in the characteristics of the shear-layer development and the turbulent boundary layer downstream of the separation bubble. Figure 11 presents a comparison of the streamwise intermittency distributions, the boundary-layer growth characteristics, and the velocity-fluctuation correlation distributions over the aft region of the flat plate for the two cases examined. Under conditions of low-freestream turbulence, the bubble is long and breakdown to turbulence occurs over a very short distance, with transition being complete very near the time-mean reattachment point. Conversely, the bypass mechanism associated with elevated-freestream turbulence results in a shorter and thinner bubble with breakdown occurring over a much larger streamwise distance, and with transition being completed approximately 50% of the bubble length downstream of reattachment. This provides a more gradual change in the shear layer growth characteristics through the bubble region.

The contour plots of fluctuation correlations in Fig. 11 also show differing characteristics between the two cases. Under low-freestream-turbulence conditions, fluctuation growth is initiated in the separated shear layer with peaks of $\overline{u'u'}$, $\overline{w'w'}$, and $\overline{u'v'}$ apparent in the outer separated shear layer and in the inner reverse-flow region of the bubble, consistent with the dual-mode instability discussed earlier in this paper. The streamwise fluctuations apparent prior to transition onset are due to growth of the
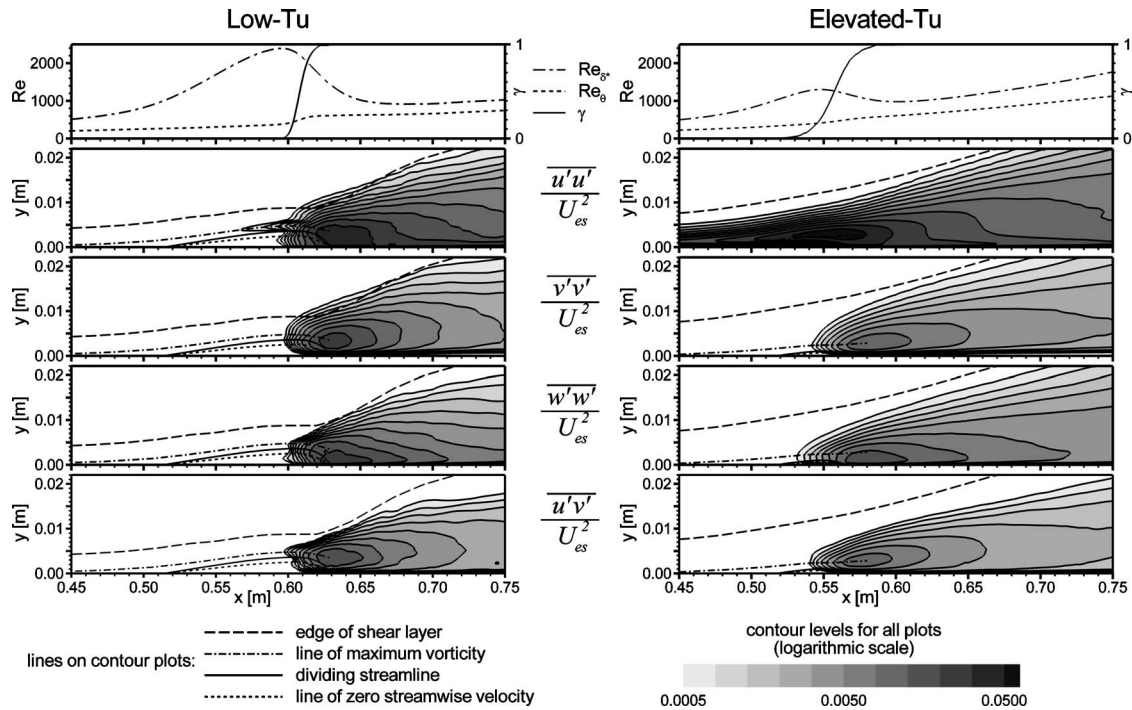
Fig. 11 Comparison of streamwise intermittency distribution, boundary layer growth characteristics, and velocity-fluctuation correlations for the two cases examined

spanwise-oriented vortices resulting from the Kelvin–Helmholtz instability. Peak levels of $\overline{v'v'}$ and $\overline{w'w'}$ are of similar magnitude to that of $\overline{u'u'}$, indicating strong three dimensionality of the resulting breakdown process. Contrary to this, under elevated-freestream turbulence the peak values of $\overline{v'v'}$ and $\overline{w'w'}$ are much lower than that for $\overline{u'u'}$. The high levels of $\overline{u'u'}$ in this case are associated with the streamwise streaks generated in the upstream laminar boundary layer that provide the conditions under which turbulent spots are generated in the shear layer. A more gradual streamwise growth and decay of fluctuations is observed under this elevated-freestream-turbulence condition.

In order to compare the turbulent boundary layer for the two cases, an effective bubble length has been selected such that the trailing end of this length corresponds to the location of minimum displacement thickness downstream of the bubble. This effective bubble length is representative of the region over which the bubble affects the freestream flow and its use in normalizing the streamwise coordinate provides a reasonable match in the streamwise rate of growth of the turbulent boundary layer. Figure 12 shows the boundary-layer velocity profile and the distribution of turbulent kinetic energy production for both cases, at various locations downstream of the time-mean point of reattachment. The distributions are plotted in wall coordinates, with the inner layer $(u^+=y^+)$ and logarithmic law-of-the-wall $(u^+=1/0.41 \log(y^+)+5.0)$ profiles plotted for reference.

For the low-Tu case, only profiles up to 50% of the effective bubble length downstream of the bubble are shown due restrictions in the length of the computational domain. At both 25% and 50% of the effective bubble length downstream, the velocity profiles show close agreement with the velocity levels of the logarithmic law of the wall. The majority of turbulence kinetic energy is produced very near the wall, around $y^+\approx10$ (see lower plot in Fig. 12). This is in close agreement with the location of maximum production in an equilibrium turbulent boundary layer $(y^+=12)$ [45]. The large-scale vortical structures shed from the separation bubble are also a source of turbulence kinetic energy, as indicated by the humps observed in the region $50<y^+<300$. Alam and Sandham [17] observed that these humps are similar to those oc-

curring in the upper half of a plane mixing layer. The humps disappear with increasing downstream distance again indicating recovery toward a conventional turbulent boundary layer. It should also be noted that the turbulence kinetic energy production is highest in the reattachment region, and decreases with downstream distance.

Under elevated-Tu conditions, recovery to a turbulent boundary layer occurs in a similar manner to that under low-Tu conditions. The velocity profiles in Fig. 12 are all below that for the logarithmic law of the wall, but a slow relaxation toward this equilibrium state is observed. The peak in turbulence kinetic energy production also occurs near $y^+\approx10$. In this case, however, higher production levels are observed in the outer region $(50<y^+<300)$ than those observed in the low-Tu case. This is likely due to the longer transition length, resulting in transition completion being much closer to the streamwise location of minimum displacement thickness.

An assessment of the full recovery length is not possible due to
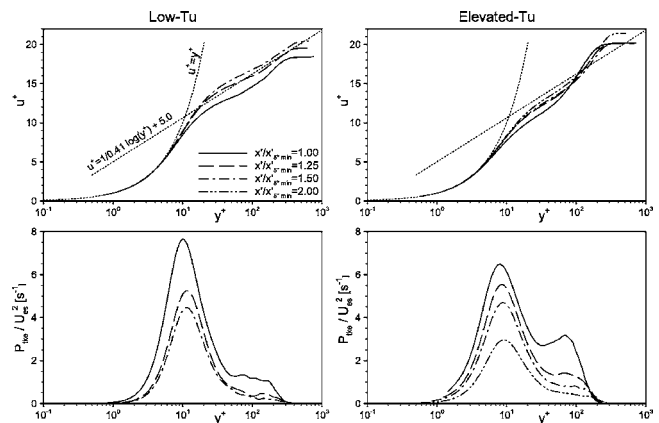
Fig. 12 Turbulent boundary-layer properties downstream of the separation bubble

limits in the length of the computational domain. However, the results presented herein are consistent with those observed by others in separation bubbles. For example, Alam and Sandham [17] found that reestablishment of the log law required seven bubble lengths downstream of time-mean reattachment. This can be attributed to a slow decay of turbulence kinetic energy in the outer part of the layer, resulting from the larger-scale structures produced during transition of the separated shear layer, be it the large hairpin vortices observed under low-Tu conditions or the vortex loops within a turbulent spot under elevated-Tu conditions.

4 Conclusions

Mechanisms associated with laminar-to-turbulent transition in separation bubbles have been examined in the context of DNSs performed under conditions with low and elevated freestream turbulence.

Under low-freestream-turbulence conditions, transition is initiated through receptivity of the laminar separated shear layer to small disturbances through the Kelvin–Helmholtz mechanism. Two regions of instability growth are observed, one in the outer separated shear layer and one in the reverse-flow region near the surface, and are consistent with the results of linear stability theory presented in the open literature. The outer inviscid mode is observed to be dominant for velocity profiles typical of those observed in laminar separation bubbles on airfoil surfaces. The frequency of this instability is found to be consistent with the dominant instability frequency of planar free-shear layers.

Amplification of the Kelvin–Helmholtz instability leads to small-scale fluctuations that develop within the braid region between spanwise vortices. These fluctuations then lead to stretching and reorientation of the spanwise structures into hairpin vortices, which are shed downstream.

Under elevated-freestream turbulence conditions, the receptivity mechanism leading to shear-layer roll-up is bypassed as a result of streamwise streaks convecting through the shear layer. These streaks originate near the leading edge and are a result of shear filtering, which allows only low-frequency perturbations from the freestream turbulence to enter the laminar boundary layer. The streaks are elongated in the streamwise direction, and have a spanwise length comparable to the boundary-layer thickness upstream of separation. Sinuous or varicose instability of these streaks is not directly observed as a precursor to the formation of turbulent spots. However, the strong shear associated with these streaks appears to provide the conditions under which turbulent spots form through a localized secondary instability, the frequency of which closely matches that of the inviscid Kelvin–Helmholtz mechanism. The spots consist of a series of vortex loops, which grow laterally through stretching of the upstream loops around the central core of the spot.

The vortex structures resulting from transition in the separated shear layer remain coherent downstream of reattachment and provide a source for turbulence kinetic energy production in the outer part of the boundary layer. Slow recovery toward an equilibrium turbulent-boundary-layer state is observed and is consistent with observations of long recovery lengths identified in the open literature.

Acknowledgment

Nomenclature

f = frequency
L_p = flat plate length
N_{ts} = number of time steps used for averaging
p = pressure
P_{tke} = turbulence kinetic energy production $= -\overline{u'v'}\,1/2(\partial u/\partial y + \partial v/\partial x)$
Re_{sp} = flow Reynolds number $= U_{sp}L_p/\nu$
$\mathrm{Re}_{\delta*}$ = displacement-thickness Reynolds number $= U_e \delta^*/\nu$
Re_{θ} = momentum-thickness Reynolds number $= U_e \theta/\nu$
Sr_{θ} = instability Strouhal number of free-shear layer $= f\theta/\Delta U$
$\mathrm{Sr}_{\theta s}$ = instability Strouhal number at separation $= f\theta_s/U_{es}$
t' = time referenced to arbitrary start time
Δt = simulation time step
Tu = turbulence intensity
U = velocity magnitude
U_i = velocity in Cartesian direction i
ΔU = velocity difference across shear layer
u = x-velocity component
v = y-velocity component
w = z-velocity component
x = streamwise coordinate
x_i = spatial coordinate in Cartesian direction i
x' = separation-referenced streamwise coordinate $= x - x_s$
y = wall-normal coordinate
z = spanwise coordinate
γ = intermittency
δ^* = displacement thickness
Λ = integral length scale of freestream turbulence
μ = dynamic viscosity
ν = kinematic viscosity
ρ = density
Ω = vorticity magnitude
Ω_z = spanwise vorticity $= \partial v/\partial x - \partial u/\partial y$
θ = momentum thickness

Subscripts

e = boundary-layer edge
r = reattachment
rms = root-mean-square quantity
s = separation
sp = suction peak
ts = start of transition
te = end of transition
min = minimum

Superscripts

$+$ = wall-scale coordinate
$'$ = fluctuation quantity

References

[1] Mayle, R. E., 1991, "The Role of Laminar-Turbulent Transition in Gas Turbine Engine," ASME J. Turbomach., **113**, pp. 509–537.
[2] Roberts, S. K., and Yaras, M. I., 2005, "Modeling Transition in Separated and Attached Boundary Layers," ASME J. Turbomach., **127**, pp. 402–411.
[3] Dovgal, A. V., Kozlov, V. V., and Michalke, A., 1994, "Laminar Boundary Layer Separation: Instability and Associated Phenomena," Prog. Aerosp. Sci., **30**, pp. 61–94.
[4] McAuliffe, B. R., and Yaras, M. I., 2008, "Numerical Study of Instability Mechanisms Leading to Transition in Separation Bubbles," ASME J. Turbomach., **130**(2), p. 021006.
[5] McAuliffe, B. R., 2007, "Transition in Separation Bubbles: Physical Mechanisms and Passive Control Techniques," Ph.D. thesis, Carleton University.
[6] Roberts, S. K., and Yaras, M. I., 2005, "Boundary-Layer Transition Affected by Surface Roughness and Free-Stream Turbulence," ASME J. Fluids Eng., **127**, pp. 449–457.
[7] Roberts, S. K., and Yaras, M. I., 2006, "Effects of Surface Roughness Geom-

etry on Separation-Bubble Transition," ASME J. Turbomach., **128**, pp. 349–356.

[8] Gostelow, J. P., and Thomas, R. L., 2006, "Interactions Between Propagating Wakes and Flow Instabilities in the Presence of a Laminar Separation Bubble," ASME Paper No. GT2006-91193.

[9] Watmuff, J. H., 1999, "Evolution of a Wave Packet Into Vortex Loops in a Laminar Separation Bubble," J. Fluid Mech., **397**, pp. 119–169.

[10] D'Ovidio, A., Harkins, J. A., and Gostelow, J. P., 2001, "Turbulent Spots in Strong Adverse Pressure Gradients Part 1—Spot Behavior," ASME Paper No. 2001-GT-0194.

[11] Talan, M., and Hourmouziadis, J., 2002, "Characteristic Regimes of Transitional Separation Bubbles in Unsteady Flow," Flow, Turbul. Combust., **69**, pp. 207–227.

[12] Volino, R. J., 2002, "Separated Flow Transition Under Simulated Low-Pressure Turbine Air-Foil Conditions: Part 1—Mean Flow and Turbulence Statistics," ASME J. Turbomach., **124**, pp. 645–655.

[13] Volino, R. J., 2002, "Separated Flow Transition Under Simulated Low-Pressure Turbine Airfoil Conditions: Part 2—Turbulence Spectra," ASME J. Turbomach., **124**, pp. 656–664.

[14] Roberts, S. K., and Yaras, M. I., 2003, "Effects of Periodic Unsteadiness, Free-Stream Turbulence and Flow Reynolds Number on Separation-Bubble Transition," ASME Paper No. GT2003-38626.

[15] Stieger, R. D., and Hodson, H. P., 2004, "The Transition Mechanism of Highly Loaded Low-Pressure Turbine Blades," ASME J. Turbomach., **126**, pp. 536–543.

[16] McAuliffe, B. R., and Yaras, M. I., 2005, "Separation-Bubble-Transition Measurements on a Low-Re Airfoil Using Particle Image Velocimetry," ASME Paper No. GT2005-68663.

[17] Alam, M., and Sandham, N. D., 2000, "Direct Numerical Simulation of Short Laminar Separation Bubbles With Turbulent Reattachment," J. Fluid Mech., **403**, pp. 223–250.

[18] Spalart, P. R., and Strelets, M. K., 2000, "Mechanisms of Transition and Heat Transfer in a Separation Bubble," J. Fluid Mech., **403**, pp. 329–349.

[19] Yang, Z., and Voke, P. R., 2001, "Large-Eddy Simulation of Boundary-Layer Separation and Transition at a Change of Surface Curvature," J. Fluid Mech., **439**, pp. 305–333.

[20] Wissink, J. G., and Rodi, W., 2002, "DNS of Transition In a Laminar Separation Bubble," *Advances in Turbulence IX; Proceedings of the Ninth European Turbulence Conference*, Southampton, UK, I. P. Castro and P. E. Hancock, eds.

[21] Wissink, J. G., and Rodi, W., 2003, "DNS of a Laminar Separation Bubble in the Presence of Oscillating External Flow," Flow, Turbul. Combust., **71**, pp. 311–331.

[22] Wissink, J., Michelassi, V., and Rodi, W., 2004, "Heat Transfer in a Laminar Separation Bubble Affected by Oscillating External Flow," Int. J. Heat Fluid Flow, **25**, pp. 729–740.

[23] Abdalla, I. E., and Yang, Z., 2004, "Numerical Study of the Instability Mechanism in Transitional Separating-Reattaching Flow," Int. J. Heat Fluid Flow, **25**, pp. 593–605.

[24] Roberts, S. K., and Yaras, M. I., 2006, "Large-Eddy Simulation of Transition in a Separation Bubble," ASME J. Fluids Eng., **128**, pp. 232–238.

[25] Wissink, J., 2006, "Separating, Transitional Flow Affected by Various Inflow Oscillation Regimes," Appl. Math. Model., **30**, pp. 1134–1142.

[26] McAuliffe, B. R., and Yaras, M. I., 2008, "Numerical Study of Turbulent-Spot Development in a Separated Shear Layer," ASME J. Turbomach., **130**(4), p. 041018.

[27] Raw, M., 1996, "Robustness of Coupled Algebraic Multigrid for the Navier-Stokes Equations," AIAA Paper No. 96-0297.

[28] Hutchinson, B. R., and Raithby, G. D., 1986, "A Multigrid Method Based on the Additive Correction Strategy," Numer. Heat Transfer, **9**, pp. 511–537.

[29] Na, Y., and Moin, P., 1998, "Direct Numerical Simulation of a Separated Turbulent Boundary Layer," J. Fluid Mech., **374**, pp. 379–405.

[30] Kalitzin, G., 2003, "DNS of Fully Turbulent Flow in a LPT Passage," Int. J. Heat Fluid Flow, **24**, pp. 636–644.

[31] Roach, P. E., 1987, "The Generation of Nearly Isotropic Turbulence by Means of Grids," Int. J. Heat Fluid Flow, **8**, pp. 82–92.

[32] Ho, C., and Huerre, P., 1984, "Perturbed Free Shear Layers," Annu. Rev. Fluid Mech., **16**, pp. 365–424.

[33] Ripley, M. D., and Pauley, L. L., 1993, "The Unsteady Structure of Two-Dimensional Steady Laminar Separation," Phys. Fluids A, **5**, pp. 3099–3106.

[34] Muti Lin, J. C., and Pauley, L. L., 1996, "Low-Reynolds-Number Separation on an Airfoil," AIAA J., **34**, pp. 1570–1577.

[35] Rist, U., and Maucher, U., 2002, "Investigations of Time-Growing Instabilities in Laminar Separation Bubbles," Eur. J. Mech. B/Fluids, **21**, pp. 495–509.

[36] Lang, M., Rist, U., and Wagner, S., 2004, "Investigations on Controlled Transition Development in a Laminar Separation Bubble by Means of LDA and PIV," Exp. Fluids, **36**, pp. 43–52.

[37] Kelly, R. E., 1967, "On the Stability of an Inviscid Shear Layer Which is Periodic in Space and Time," J. Fluid Mech., **27**, pp. 657–689.

[38] Huang, L. S., and Ho, C. M., 1990, "Small-Scale Transition in a Plane Mixing Layer," J. Fluid Mech., **210**, pp. 475–500.

[39] Estevadeordal, J., and Kleis, S. J., 1999, "High-Resolution Measurements of Two-Dimensional Instabilities and Turbulence Transition in Plane Mixing Layers," Exp. Fluids, **27**, pp. 378–390.

[40] Winant, C. D., and Browand, F. K., 1974, "Vortex Pairing: The Mechanism of Turbulent Mixing-Layer Growth at Moderate Reynolds Number," J. Fluid Mech., **63**, pp. 237–255.

[41] Ho, C., and Huang, L. S., 1982, "Subharmonics and Vortex Merging in Mixing Layers," J. Fluid Mech., **119**, pp. 443–473.

[42] Malkiel, E., and Mayle, R. E., 1996, "Transition in a Separation Bubble," ASME J. Turbomach., **118**, pp. 752–759.

[43] Pierrehumbert, R. T., and Widnall, S. E., 1982, "The Two-and Three-Dimensional Instabilities of a Spatially Periodic Shear Layer," J. Fluid Mech., **114**, pp. 59–82.

[44] Schlichting, H., and Gersten, K., 2000, *Boundary Layer Theory*, 8th ed., Springer-Verlag, Berlin.

[45] Panton, R. L., 2001, "Overview of the Self-Sustaining Mechanisms of Wall Turbulence," Prog. Aerosp. Sci., **37**, pp. 341–383.

[46] Kiya, M., and Sasaki, K., 1985, "Structure of Large-Scale Vortices and Unsteady Reverse Flow in the Reattaching Zone of a Turbulent Separation Bubble," J. Fluid Mech., **154**, pp. 463–491.

[47] Emmons, H. W., 1951, "The Laminar-Turbulent Transition in a Boundary Layer—Part 1," J. Aeronaut. Sci., **18**, pp. 490–498.

[48] Saric, W. S., Reed, H. L., and Kerschen, E. J., 2002, "Boundary-Layer Receptivity to Freestream Disturbances," Annu. Rev. Fluid Mech., **34**, pp. 291–319.

[49] Jacobs, R. G., and Durbin, P. A., 2001, "Simulations of Bypass Transition," J. Fluid Mech., **428**, pp. 185–212.

[50] Asai, M., Minagawa, M., and Nishioka, M., 2002, "The Instability and Breakdown of a Near-Wall Low-Speed Streak," J. Fluid Mech., **455**, pp. 289–314.

[51] Konishi, Y., and Asai, M., 2004, "Experimental Investigation of the Instability of Spanwise-Periodic Low-Speed Streaks," Fluid Dyn. Res., **34**, p. 299–315.

[52] Wu, X., Jacobs, R. G., Hunt, J. C. R., and Durbin, P. A., 1999, "Simulation of Boundary Layer Transition Induced by Periodically Passing Wakes," J. Fluid Mech., **398**, pp. 109–153.

Tip Clearance Effects on Inlet Hot Streak Migration Characteristics in High Pressure Stage of a Vaneless Counter-Rotating Turbine

Zhao Qingjun
e-mail: zhaoqingjun@mail.etp.ac.cn

Du Jianyi

Wang Huishe

Zhao Xiaolu

Xu Jianzhong

Institute of Engineering Thermophysics,
Chinese Academy of Sciences,
P.O. Box 2706,
Beijing 100190, China

In this paper, three-dimensional multiblade row unsteady Navier–Stokes simulations at a hot streak temperature ratio of 2.0 have been performed to reveal the effects of rotor tip clearance on the inlet hot streak migration characteristics in high pressure stage of a vaneless counter-rotating turbine. The numerical results indicate that the migration characteristics of the hot streak in the high pressure turbine rotor are dominated by the combined effects of secondary flow, buoyancy, and leakage flow in the rotor tip clearance. The leakage flow trends to drive the hotter fluid toward the blade tip on the pressure surface and to the hub on the suction surface. Under the effect of the leakage flow, even partial hotter fluid near the pressure surface is also driven to the rotor suction surface through the tip clearance. Compared with the case without rotor tip clearance, the heat load of the high pressure turbine rotor is intensified due to the effects of the leakage flow. And the results indicate that the leakage flow effects trend to increase the low pressure turbine rotor inlet temperature at the tip region. The air flow with higher temperature at the tip region of the low pressure turbine rotor inlet will affect the flow and heat transfer characteristics in the downstream low pressure turbine. [DOI: 10.1115/1.3103925]

1 Introduction

A vaneless counter-rotating turbine (VCRT) is composed of a highly loaded single-stage high pressure turbine (HPT) and a single-stage vaneless counter-rotating low pressure turbine/rotor (LPT/LPR). Due to the parts' elimination and size reduction, the VCRT can offer some significant benefits compared with conventional two-stage turbine, even 1+1 counter-rotating turbine, such as the elevated thrust-to-weight ratio of aero-engine, the improved performance of aircraft, the reduced cooling flow, and so on [1–4]. From the 1950s, counter-rotating turbines have been carefully investigated [5,6,3,4]. GE has also been developing counter-rotating turbine systems (CRTSs) since the 1980s. And the CRTS will apply to GEnx engines in the future. It indicates that the CRTS will also be selected in airline engines for the aim of economy.

Experimental data taken from gas turbine combustors indicate that the flow exiting the combustor can contain both circumferential and radial temperature gradients. The phenomenon is known as hot streaks. The hot streaks arise from the combination of the combustor core flow with the combustor bypass and combustor surface cooling flows. In turbine, the hot streaks convect through the vanes and interact with the rotor blades. They can cause local hot spots on the blade surfaces, leading to heat fatigue of blade and reducing blade life.

An earlier research on streamline pattern showed theoretically that inflow temperature gradients will not alter the streamline pattern in vanes as long as the inflow total pressure is uniform [7]. However, the following research on the secondary flow of rotating system, which was performed by Lakshminarayana and Horlock [8], indicated that inflow temperature nonuniformities can lead to secondary flow in the rotating blade rows. Butler et al. [9] carried out an experimental investigation on hot streak migration using the large-scale rotating rig (LSRR), which is often used in hot streak investigations. They also found that the temperature gradients have not altered the flow within the turbine stator but to have significant impact on the flowfield of rotor blade rows when the total pressure in the distortion is uniform. Their conclusion had been verified by some other experimental and numerical investigations [10–12]. The results, which were obtained by Butler et al. [9], Sharma et al. [13], and Roback and Dring [10] by experimental and numerical investigations, showed that hot streaks cause hotter gas to accumulate on the rotor blade pressure surfaces and colder gas to accumulate on the rotor blade suction surfaces. However, the numerical investigation results of Gundy-Burlet and Dorney [14] indicated that the migration patterns of hot streaks are directly related to the position of the hot streak in relation to the first-stage stator. When the hot streak impinges the leading edge (LE) of the first-stage stator, the hot gases are convected with the stator wake and migrate to the suction surface (SS) of the first-stage rotor. On the contrary, the hot gases migrate to the pressure surface (PS) of the first-stage rotor when the hot streak is located in the midpitch of the first-stage stator vanes. The different characteristic of hot streak migration in rotor blade rows should be investigated in detail. In addition to secondary flow and circumferentially relative location effect, Shang and Epstein [15] showed that hot streak migration is also affected by buoyancy, which tends to drive the hot streak toward the hub.

The experimental facilities most often used in hot streak investigations include the LSRR [9,10], NASA warm core turbine test rig (WCTTR) [16], and MIT blowdown turbine test rig (BTTR) [17]. The LSRR experiments were performed at low speed, but blade surface temperature (CO_2 concentrations) was measured. In the WCTTR experiments, blade surface temperature was not measured, but it is a high speed rig. Compared with LSRR and WCTTR, BTTR experiments not only were performed at high

speed, but also blade surface temperature can been measured. Shang et al. [18] performed hot streak experiments using BTTR in MIT in order to examine the effects of hot streak migration on blade surface temperature at high speed.

Dorney and Sondak [19] performed three-dimensional unsteady Navier–Stokes simulations to study the effects of tip clearance on hot streak migration in a high-subsonic single-stage turbine. The simulations indicate that the tip clearance increases the radial spreading of the hot fluid, and increases the integrated rotor surface temperature compared with the case without tip clearance. Castillon et al. [20] carried out an unsteady 3D numerical analysis on a hot streak transport through an axial high pressure turbine stage. The predicted results show that the hot gas driven on the pressure surface of the rotor can convect into the tip-gap and migrate into the suction surface.

In this paper, the effects of tip clearance on the inlet hot streak migration characteristics in the high pressure stage of the VCRT will be explored by means of 3D unsteady numerical simulations.

2 Numerical Algorithm

NUMECA software systems are employed to study this problem. The numerical method is described in detail in the user manual [21]. Here only a brief description about the main features is reported.

The governing equations in NUMECA are the time dependent, three-dimensional Reynolds-averaged Navier–Stokes equations. The solver of NUMECA is FINE/TURBO and it is based on a cell centered finite volume approach, associated with a central space discretization scheme together with an explicit four-stage Runge–Kutta time integration method.

Residual smoothing, local time-stepping, and multigridding are employed to speed up convergence to the steady state solution. The dual time-stepping method [22] and domain scaling method [23] are used to perform time accurate calculations.

Various turbulence models have been included in the solver for the closure of governing equations. The widely used approach based on one transport equation [24] has been selected in this paper. The Spalart–Allmaras model has become quite popular in the past years because of its robustness and its ability to treat complex flows. The main advantage of the Spalart–Allmaras model when compared with the one of Baldwin and Lomax is that the turbulent eddy viscosity field is always continuous. Its advantage over the k-ε model is mainly its robustness and the lower additional CPU and memory usage.

The time step limitations arising from the turbulent source terms are accounted for in the model so that computations can be performed with the maximum allowable Courant–Friedrichs–Lewy (CFL) number without penalizing numerical efficiency.

3 Boundary Conditions

In these simulations with inlet hot streaks, the theory of characteristics is used to determine the boundary conditions at the inlet and exit of computational domain. The total temperature is specified as a function of the spatial coordinates at the inlet. The total pressure and the circumferential and radial flow angles are given as many constants at the inlet. Due to selecting the Spalart–Allmaras turbulence model, the kinematic turbulent viscosity should be specified in the inlet boundary conditions. In this paper, it is 0.0001 m^2/s. At the inlet, the specify turbulence intensity of 3% is selected.

In these simulations, the flow variables in the hot streak must be modified. In the hot streak, the inlet flow variables used to define the specified boundary conditions can be written as

$$u_{hs} = u_\infty \sqrt{T_{hs}/T_\infty}, \quad v_{hs} = v_\infty \sqrt{T_{hs}/T_\infty}$$

$$w_{hs} = w_\infty \sqrt{T_{hs}/T_\infty}, \quad P_{hs} = P_\infty$$

Table 1 The flow conditions in the VCRT

Inlet total temperature (K)	500
Inlet total pressure (kPa)	300
Mass flow (kg/s)	17.7
Rotational speed of HPT rotor (rpm)	6970
Rotational speed of LPR (rpm)	−6970
Expansion ratio of HPT	2.93
Expansion ratio of LPT	2.07
SWR	1.77

$$a_{hs} = a_\infty \sqrt{T_{hs}/T_\infty}, \quad \rho_{hs} = \rho_\infty/(T_{hs}/T_\infty) \qquad (1)$$

where T_{hs} is the static temperature within the hot streak and T_∞ is the static temperature of the unaffected inlet flow. The static pressure and total pressure within the hot streak are assumed to be equal to that of the unaffected inlet flow.

At the exit, the circumferential and radial velocity components, entropy, and the downstream running Riemann invariant are extrapolated from the interior of the computational domain. The static pressure, P_6, is specified at the hub of the exit and the static pressure values at all other radial locations are obtained by integrating the equation for radial equilibrium. Periodicity is enforced along the outer boundaries of H–O–H grids in the circumferential direction.

No-slip boundary conditions should be enforced at solid wall surfaces for viscous simulations. In this paper, absolute no-slip boundary conditions are enforced at the hub and tip end walls of the HPT stator regions, along the surface of the HPT vane, and along the casing walls of the HPT rotor and LPR regions. Relative no-slip boundary conditions are imposed at the hub end walls of the HPT rotor and LPR regions, and the surfaces of the HPT rotor and LPR blades. It is assumed that the normal derivative of pressure is zero at the solid wall surfaces, and that the walls are adiabatic.

4 Vaneless Counter-Rotating Turbine

The VCRT studied in this paper is composed of a highly loaded single-stage HPT coupled with a vaneless counter-rotating LPT/LPR. It has high expansion ratio and operates in transonic regimes. The VCRT has some unique characteristics, which are different from the conventional two-stage turbine, even 1+1 counter-rotating turbine. These characteristics include the following.

- The HPT rotor and LPT/LPR are counter-rotating.
- The LPT is vaneless.
- There are high relative Mach number (~1.5) and relative flow angle (~70 deg) at the outlet of the HPT.

The design conditions of the VCRT are shown in Table 1.

The airfoil counts in the steady and unsteady models are reduced from the actual count 36/36/36 for the HPT stator, HPT rotor, and LPR, respectively, to 1/1/1 for computational efficiency. In this paper, the main interest is to analyze the effects of rotor tip leakage on the hot streak migration in the HPT. The effects of the rotor count ratios have not been investigated in this paper. In the future work, the investigation on the effects of airfoil count ratios will be performed. Although the 1/1/1 airfoil count ratio is not realistic, the fundamental flow characteristics can be still obtained by investigating the model VCRT. The tip clearance size studied in this paper is 2.0 mm (2.594% HPT rotor height) (see Fig. 1). The typical y^+ values of less than 15 are used at the boundaries. All of these result in computational fluid dynamics (CFD) models with about 0.42×10^6 (without tip clearance—Case 1) and 0.57×10^6 (with tip clearance—Case 2) grid points employing a sheared "H–O–H" mesh generated by NUMECA AUTOGRID (see Fig. 2). It will take about 1 week to compute an unsteady case using a 3.0 GHz one-Intel-CPU computer. According to the past experiences, which were obtained in the steady three-dimensional vis-
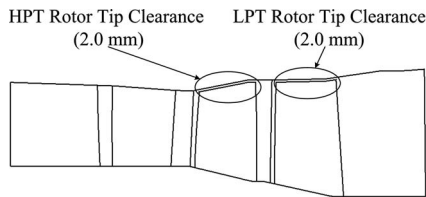
Fig. 1   Meridional section of the VCRT with rotor tip clearance

cous analyses about the VCRT [4], the grid size selected in this paper is adequate to the investigation.

5   Validating of Numerical Code

In order to validate the predicted accuracy of the numerical code, a three-dimensional multistage unsteady Navier–Stokes simulation with inlet radial hot streak has been performed in a test turbine. Then the time-averaged numerical data are compared with the available experimental data. The test turbine is a 0.767 scale rig modeling the first stage of a two-stage core turbine designed for a modern high bypass ratio engine. The vane has a constant section, and was designed for a constant exit flow angle of 75 deg from axial. The rotor inlet was designed to accept the vane exit flow with either zero or slight negative incidence. The rotor outlet is a free-vortex design. Both vane and blade axial chords are constant radially. The experimental turbine has 26 vane airfoils and 48 rotor airfoils. It was tested in the NASA Lewis Research Center's WCTTR [16]. The test conditions for the turbine are shown in Table 2.

The inlet radial temperature profile in the experiment was produced using the combustor exit radial temperature simulator (CERTS) inlet, which injected cool air through circumferential slots in the hub and tip end walls upstream of the vane. Figure 3
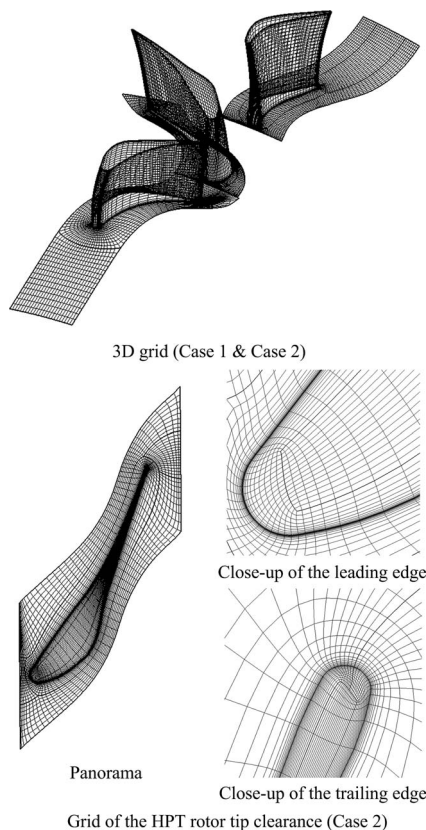
shows the inlet radial temperature distribution. The ratio of the maximum total temperature to the average total temperature is approximately 1.05, and the ratio of maximum to minimum total temperature is approximately 1.20 at the turbine inlet.

In order to reduce the cost of the calculation, the number of vanes in the first row is decreased to 24 and the size of the vane is increased by a factor of 26/24 to maintain the same blockage. So, a one-vane/two-rotor airfoil count ratio is used in the unsteady numerical simulation. And two geometry configurations with 1.2% tip clearance and without tip clearance for the rotor are selected in the numerical simulations.

Figures 4–6 show the comparisons between the predicted and experimental time-averaged critical velocity ratio distributions at the hub, midspan, and tip of the vane, individually. The predicted data are close to the experimental data, except for the suction surface near the trailing edge (TE) region at the hub of the vane, near the 40% axial chord region at the midspan and the tip of the vane.

Figure 7 illustrates the predicted and experimental total pressure distributions at the outlet of the turbine. There is a good agreement between the predicted and experimental results. Compared with the experimental results, the predicted accuracy of the case with 1.2% rotor tip clearance is higher than the case without

3D grid (Case 1 & Case 2)

Close-up of the leading edge

Panorama

Close-up of the trailing edge

Grid of the HPT rotor tip clearance (Case 2)

Fig. 2   H–O–H grid topologies of the VCRT
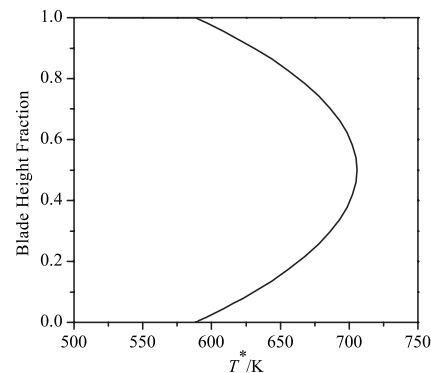
Fig. 3   Turbine inlet radial temperature profile
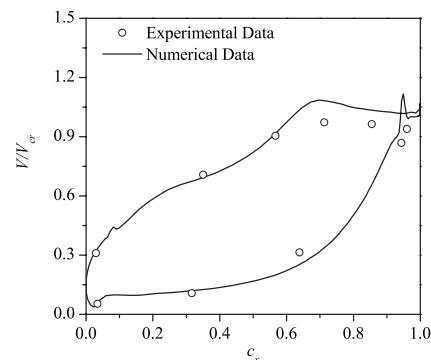
Fig. 4   Critical velocity ratio at the hub of the vane
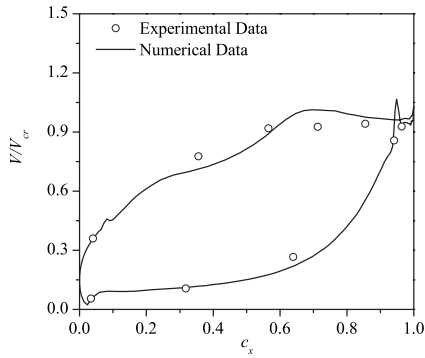
Fig. 5   Critical velocity ratio at the midspan of the vane

Fig. 8   Total temperature distribution at the outlet of the turbine

rotor tip clearance at the tip region of the turbine outlet. The reason is that the geometry configuration of the case with 1.2% rotor tip clearance is the same as that of the experiment. The tip clearance effects are considered in the case with 1.2% rotor tip clearance.

Figure 8 shows the predicted and experimental total temperature distributions at the outlet of the turbine. The predicted values show close agreement with the experimental values from hub to 70% span. Although the discrepancies between the numerical data and the experimental data are apparent from 70% span to tip, the trends predicted that total temperature distributions are similar to the experimental trends. And due to considering the tip clearance effects, the results in the case with 1.2% rotor tip clearance are more close to the experimental results than that of the case without tip clearance.

The above-mentioned results indicate that the flow characteris-

tics in the high-subsonic turbine can be qualitatively predicted by means of the numerical code. The numerical code is acceptable in this investigation.
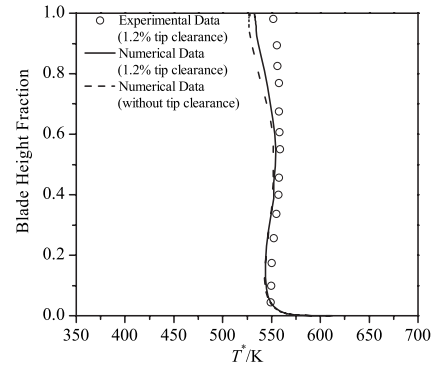
6   Inlet Hot Streak Profile

In this paper, a hot streak temperature ratio of 2.0 is selected. The hot streak is circular in shape with a diameter equal to 25% of the HPT stator span. The hot streak center is located at 50% of the span and the leading edge of the HPT stator. The hot streak profile is shown in Fig. 9.

7   Numerical Results

Figure 10 shows the instantaneous Mach number contours on the midspan section of the HPT rotor for the case with 1.2% rotor tip clearance. There are two high strength shock waves originated from the trailing edge of the HPT rotor, which are called inner-extending shock wave (IESW) and outer-extending shock wave (OESW), respectively. And a series of compression waves emanates from the rotor suction surface at about 64–82% axial chord region. The interaction between these compression waves and the IESW can be observed in the HPT rotor. Figure 10 shows that the wave system is very complex in the HPT rotor. The peak Mach number is approximately 2.0 in the HPT rotor. Such high Mach number is unusual in transonic turbine rotor. The complicated wave system and high outlet Mach number result in some unique aerodynamics characteristics in the HPT rotor compared with conventional two-stage turbine. And these waves can also affect the migration of the hot streak fluid in the HPT rotor. So, the investigation on the hot streak migration in the HPT rotor is very significant.

Figure 11 shows the static temperature distribution on the midspan section of the HPT at one instant in time. The migrating paths of the hot streaks in the HPT are exhibited by means of the temperature contour. The secondary flow induced temperature redistribution does not occur in the HPT stator as the hot streak directly impinges on the LE of the HPT stator. However, second-

Fig. 6   Critical velocity ratio at the tip of the vane

Fig. 7   Total pressure distribution at the outlet of the turbine
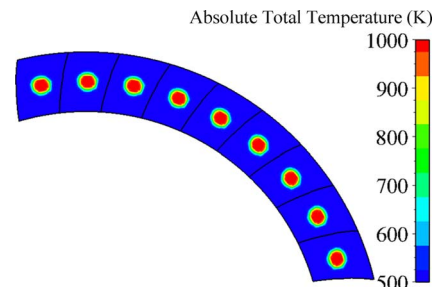
Fig. 9   Inlet hot streak profile (cases 1 and 2)
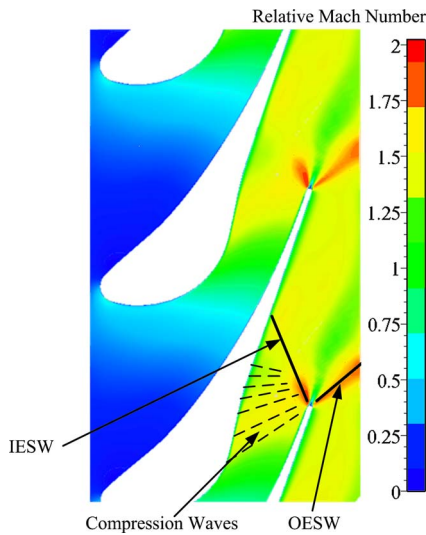
Fig. 10 Instantaneous Mach number contours on the midspan section of the HPT rotor

Fig. 12 HPT rotor blade tip leakage flow

ary flow and buoyancy cause the temperature redistribution in the HPT rotor when the hot streak mixes with the HPT vane wake and flows into the HPT rotor. Most of the hotter fluid convects toward the PS of the HPT rotor, while most of the colder fluid migrates to the SS of the HPT rotor. And a few of hotter fluid also rounds the LE of the HPT rotor and migrates to the SS of the rotor. The heat load of the HPT rotor is increased due to the introduction of the hot streak.

Figure 12 describes the leakage flow in the HPT rotor blade tip clearance. The fluid near the pressure surface tip region can be driven to the rotor suction surface by the leakage flow. So, as the inlet hot streaks are introduced, some hotter fluid migrated to the HPT rotor pressure surface tip region will convect into the rotor suction side. The migration induced by the leakage flow directly results in intensified heat load on the rotor suction surface. Figure 13 more clearly illustrates the above-mentioned phenomenon. When hotter fluid migrates to the pressure surface, the combined effects of secondary flow and buoyancy will drive the hotter fluid toward the hub and the tip. Those hotter fluids migrated to the tip region at the pressure side will enter the tip-gap and emerge over the suction side. The temperature distribution on the HPT rotor is significantly affected due to the existence of the leakage flow.

Figure 14 shows the time-averaged static temperature contour on the HPT rotor for case 1 (without tip clearance). The nonuniform temperature distribution on the HPT rotor indicates that most of the hotter fluid will migrate toward the pressure surface of the HPT rotor when it convects into the passage of the HPT rotor. And only a small quantity of hotter fluid will round the LE of the HPT rotor and migrate to the suction surface of the HPT rotor. The hot fluid, which migrates to the pressure surface, will migrate toward the hub and the tip along the flow direction. On the other hand, the hot fluid, which migrates to the suction surface, will migrate toward the midspan along the flow direction. The migration characteristics of the hot streak in the HPT rotor are dominated by the combined effects of secondary flow and buoyancy. The secondary flow drives the hotter fluid toward the hub and tip on the PS and toward the midspan on the SS (see Fig. 15). The buoyancy induces the hotter fluid near the rotor blade surface to migrate toward the hub [12]. The above-mentioned migration of the hot fluid results in a higher heat load on the HPT rotor.

The effect of buoyancy on the migration of the hot streaks can be explained by using the simple radial equilibrium theory. The radial equilibrium means the pressure forces balance the centrifu-

Fig. 11 Instantaneous static temperature contour on the midspan section of the HPT—case 1
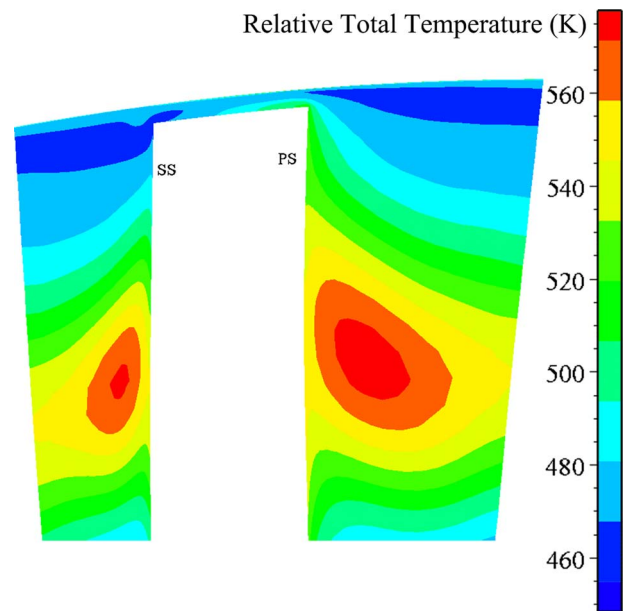
Fig. 13 Instantaneous temperature contour on a cross section (S3 section) of the HPT rotor passage—case 2
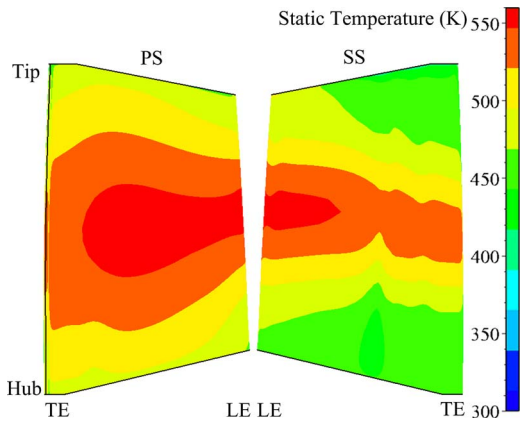
Fig. 14 Time-averaged static temperature contour on the HPT rotor (case 1)
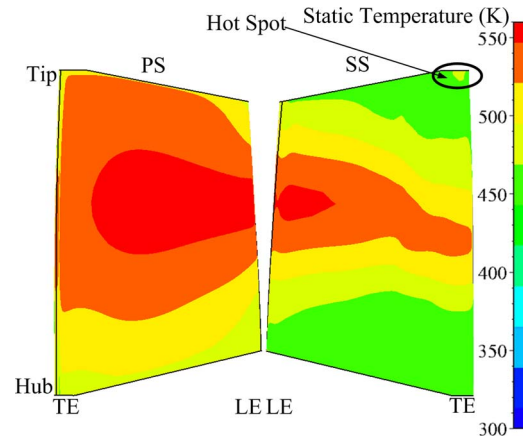
Fig. 16 Time-averaged static temperature contour on the HPT rotor (case 2)

gal forces along the radial direction. According to the simple radial equilibrium theory, the following equation (see Ref. [12]) can be deduced:

$$\frac{d^2 s_r}{dx^2} = \frac{1}{r}\left(\frac{T_{\mathrm{hs}}}{T_{\mathrm{cold}}} - 1\right)\frac{1}{\phi^2} \qquad (2)$$

Formula (2) offers an evaluation criterion on the buoyancy effect from physical mechanism. Near the region of the HPT rotor blade surface, the buoyancy effect is proportional to the static temperature ratio of the hot fluid to the cold fluid, and depends on the square of flow coefficient with inverse proportion.

Figure 16 shows the time-averaged static temperature contour on the HPT rotor for case 2 (with tip clearance). The nonuniform temperature distribution on the HPT rotor shows that the leakage flow also plays an important role in the hot streak migration besides the combined effects of secondary flow and buoyancy. The leakage flow drives the hotter fluid toward the tip on the PS and toward the hub on the SS. Under the effect of the leakage flow, even partial hotter fluid near the pressure surface tip region is driven to the rotor suction surface through the tip clearance. The tip leakage swirl induces a hot tip region on the suction surface (see Fig. 16 ellipse mark region). Compared with case 1 (without rotor tip clearance), the heat load of the HPT rotor is intensified due to the effects of the leakage flow. Considering the existence of

rotor tip clearance, the migration characteristics of the hot streak in the HPT rotor are dominated by the combined effects of secondary flow, buoyancy, and leakage flow.

Figure 17 indicates the time-averaged relative total temperature distributions in the HPT rotor passages for cases 1 and 2. In these two cases, the secondary flow drives the hotter fluid toward the PS along the flow direction. At the meantime, the buoyancy drives the hotter fluid toward the hub along the flow direction. When the hotter fluid migrates to the PS, the secondary flow will drive it toward the hub and tip along the flow direction, and the buoyancy will continue to drive it toward the hub along the flow direction. The combined effects of secondary flow and buoyancy directly control the migrating directions of the hotter fluid. Under the influences of the secondary flow and the buoyancy, the hotter fluid nearby the PS has a tendency toward the hub along the flow direction. The result has also been shown in Figs. 14 and 16. And
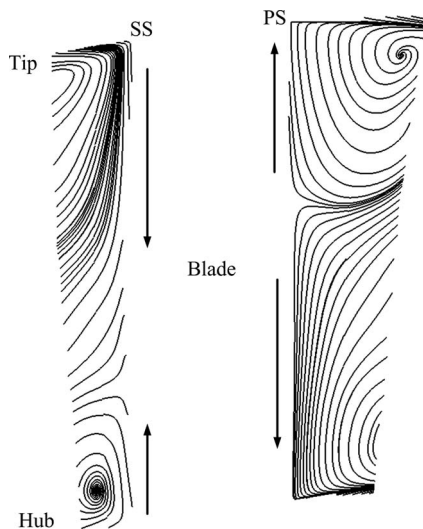
Fig. 15 Secondary flow streamline distributions on a S3 section of the HPT rotor passage
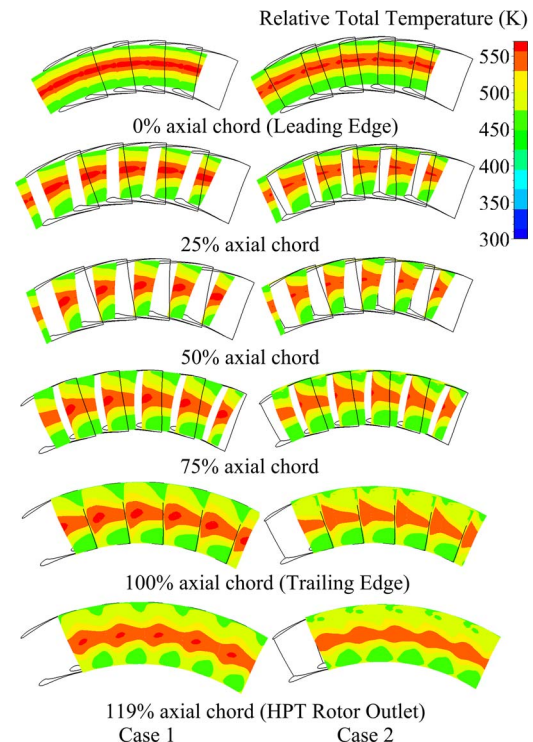
Fig. 17 Time-averaged relative total temperature contours on some S3 sections of the HPT rotor passage
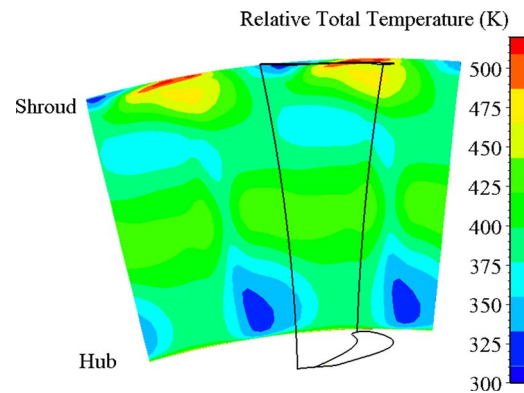
Relative Total Temperature (K)
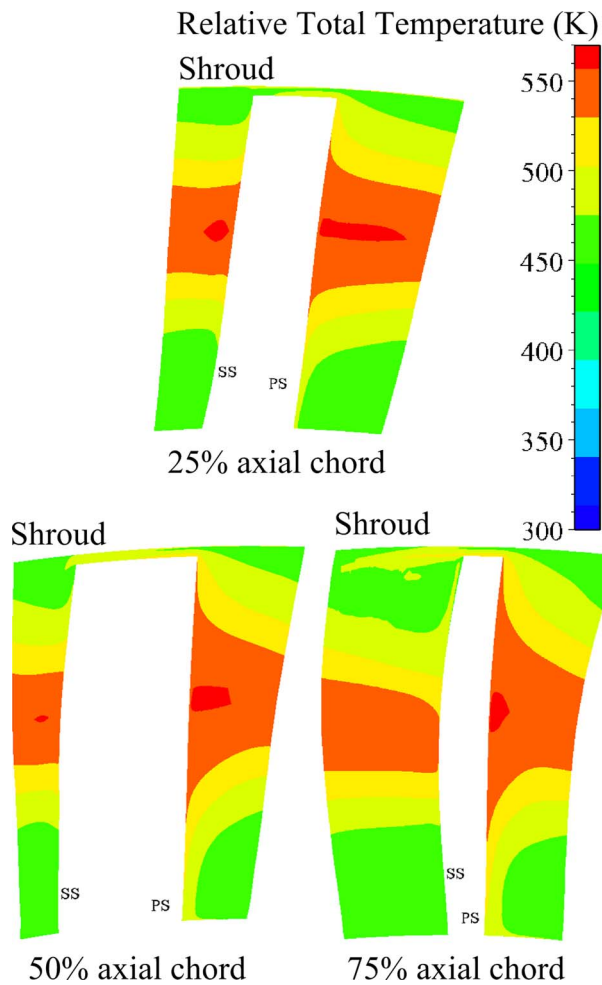
Fig. 18 Time-averaged relative total temperature contours on three S3 sections of the HPT rotor passage—case 2

Fig. 19 Instantaneous temperature contour at the LPR inlet—case 1

Fig. 20 Instantaneous temperature contour at the LPR inlet—case 2

the secondary flow also drives the colder fluid toward the SS along the flow direction accompanying the hot fluid movements. As the colder fluid migrates to the SS, the secondary flow drives the colder fluid toward the midspan along the flow direction. The hotter fluid, which rounds the leading edge of the HPT rotor and migrates to the suction surface, also moves toward the midspan along the flow direction under the effect of the secondary flow. The buoyancy still drives the hotter fluid on the suction surface toward the hub along the flow direction. As a result, the hotter fluid on the suction surface also has a trend toward the hub along the flow direction under the combined effects of secondary flow and buoyancy. This phenomenon may be also seen in Figs. 14 and 16. Comparing the results between cases 1 and 2 in Fig. 17, it is well known that the radial migration of the hotter fluid is also dominated by the leakage flow in the rotor tip clearance. The leakage flow trends to drive the hotter fluid toward the blade tip on the pressure surface and to the hub on the suction surface. Figure 18 more clearly shows the leakage flow effects. The effects of the leakage flow directly result in a different temperature distribution in HPT rotor between cases 1 and 2.

Figures 19 and 20 show the instantaneous temperature distribution at the LPR inlet for cases 1 and 2, respectively. Comparing the results in Figs. 19 and 20, it is well known that the leakage flow effects trend to increase the LPR inlet temperature at the tip region. The air flow with higher temperature at the tip region of the LPR inlet will affect the flow and heat transfer characteristics in the downstream LPT.

8 Conclusions

This paper aims to study the effects of the rotor tip clearance on the inlet hot streak migration characteristics in HPT of a VCRT. The major conclusions can be summarized as follows.

(1) The hot streak mixes with the vane wake and convects into the HPT rotor. Most of the hotter fluid migrates to the pressure surface of the HPT rotor. Only a few of the hotter fluids round the leading edge of the HPT rotor and migrate to the suction surface.

(2) The migration characteristics of the hot streak in the HPT rotor are dominated by the combined effects of secondary flow, buoyancy, and leakage flow in the rotor tip clearance.

(3) The leakage flow drives the hotter fluid toward the blade tip on the pressure surface and to the hub on the suction surface.

(4) The leakage flow trends to increase the heat load of the HPT rotor blade.

(5) The existence of the leakage flow will affect the flow and heat transfer characteristics in the downstream LPT.

Nomenclature

a = velocity of sound
c = nondimensional chord
P = static pressure
r = radius
s = displacement
SWR = ratio of specific work of the high pressure turbine to that of the low pressure turbine

T = static temperature
u, v, w = x, y, z components of velocity
V = absolute velocity
X = axial displacement
ρ = density
ϕ = flow coefficient

Superscripts

$*$ = total quantity

Subscripts

6 = LPT rotor exit quantity
cr = critical value
hs = hot streak quantity
r = radial direction
x = axial direction
∞ = freestream quantity

References

[1] Keith, B. D., Basu, D. K., and Stevens, C., 2000, "Aerodynamic Test Results of Controlled Pressure Ratio Engine (COPE) Dual Spool Air Turbine Rotating Rig," ASME Paper No. 2000-GT-0632.

[2] Haldeman, C. W., Dunn, M. G., Abhari, R. S., Johnson, P. D., and Montesdeoca, X. A., 2000, "Experimental and Computational Investigation of the Time-Averaged and Time-Resolved Pressure Loading on a Vaneless Counter-Rotating Turbine," ASME Paper No. 2000-GT-0445.

[3] Zhao, Q. J., Wang, H. S., Zhao, X. L., and Xu, J. Z., 2006, "Numerical Analysis of 3-D Unsteady Flow in a Vaneless Counter-Rotating Turbine," J. Eng. Thermophys., **27**(1), pp. 35–38.

[4] Zhao, Q. J., Wang, H. S., Zhao, X. L., and Xu, J. Z., 2006, "Three-Dimensional Numerical Investigation of Vaneless Counter-Rotating Turbine," J. Propul. Tech., **27**(2), pp. 114–118, 123.

[5] Wintucky, W. T., and Stewart, W. L., 1958, "Analysis of Two-Stage Counter-Rotating Turbine Efficiencies in Terms of Work and Speed Requirements," NACA, Report No. RM E57L05.

[6] Louis, J. F., 1985, "Axial Flow Contra-Rotating Turbines," ASME Paper No. 85-GT-218.

[7] Munk, M., and Prim, R. C., 1947, "On the Multiplicity of Steady Gas Flows Having the Same Streamline Pattern," Proc. Natl. Acad. Sci. U.S.A., **33**, pp. 137–141.

[8] Lakshminarayana, B., and Horlock, J. H., 1973, "Generalized Expressions for Secondary Vorticity Using Intrinsic Coordinates," J. Fluid Mech., **59**, pp. 97–115.

[9] Butler, T. L., Sharma, O. P., Joslyn, H. D., and Dring, R. P., 1989, "Redistribution of an Inlet Temperature Distortion in an Axial Flow Turbine Stage," J. Propul. Power, **5**(1), pp. 64–71.

[10] Roback, R. J., and Dring, R. P., 1993, "Hot Streaks and Phantom Cooling in a Turbine Rotor Passage: Part 1—Separate Effects," ASME J. Turbomach., **115**(4), pp. 657–666.

[11] Prasad, D., and Hendricks, G. J., 2000, "A Numerical Study of Secondary Flow in Axial Turbines With Application to Radial Transport of Hot Streaks," ASME J. Turbomach., **122**(4), pp. 667–673.

[12] Zhao, Q. J., Wang, H. S., Tang, F., Zhao, X. L., and Xu, J. Z., 2008, "Investigation of Influencing Factors of Hot Streaks Migration in High Pressure Stage of a Vaneless Counter-Rotating Turbine," Sci. China, Ser. E: Technol. Sci., **51**(2), pp. 127–144.

[13] Sharma, O. P., Pickett, G. F., and Ni, R. H., 1992, "Assessment of Unsteady Flows in Turbines," ASME J. Turbomach., **114**(1), pp. 79–90.

[14] Gundy-Burlet, K. L., and Dorney, D. J., 1996, "Three-Dimensional Simulations of Hot Streak Clocking in a 1–1/2 Stage Turbine," AIAA Paper No. 96-2791.

[15] Shang, T., and Epstein, A. H., 1997, "Analysis of Hot Streak Effects on Turbine Rotor Heat Load," ASME J. Turbomach., **119**(3), pp. 544–553.

[16] Stabe, R. G., Whitney, W. J., and Moffitt, T. P., 1984, "Performance of a High-Work Low-Aspect Ratio Turbine Tested With a Realistic Inlet Radial Temperature Profile," AIAA Paper No. 84-1161.

[17] Guenette, G. R., 1985, "A Fully Scaled Short Duration Turbine Experiment," ScD thesis, MIT, Cambridge, MA.

[18] Shang, T., Guenette, G. R., Epstein, A. H., and Saxer, A. P., 1995, "The Influence of Inlet Temperature Distortion on Rotor Heat Transfer in a Transonic Turbine," AIAA Paper No. 95-3042.

[19] Dorney, D. J., and Sondak, D. L., 2000, "Effects of Tip Clearance on Hot Streak Migration in a High-Subsonic Single-Stage Turbine," ASME J. Turbomach., **122**(4), pp. 613–620.

[20] Castillon, L., Laroche, E., and Sgarzi, O., 2003, "Unsteady Three-Dimensional Navier-Stokes Analysis of a Hot Streak Transport Through an Axial High Pressure Turbine Stage," ISABE Paper No. 2003-1063.

[21] 2005, Fine Turbo User Manual 6-2-9, NUMECA International.

[22] Arnone, A., and Pacciani, R., 1996, "Rotor-Stator Interaction Analysis Using the Navier-Stokes Equations and a Multigrid Method," ASME J. Turbomach., **118**(3), pp. 679–689.

[23] Rai, M. M., 1989, "Three-Dimensional Navier-Stokes Simulations of Turbine Rotor-Stator Interaction. Part I—Methodology," J. Propul. Power, **5**(3), pp. 305–311.

[24] Spalart, P., and Allmaras, S., 1994, "A One-Equation Turbulence Model for Aerodynamic Flows," Rech. Aerosp., **1**, pp. 5–21.

Aerodynamic Asymmetry Analysis of Unsteady Flows in Turbomachinery

Kivanc Ekici[1]
e-mail: ekici@utk.edu

Robert E. Kielb
e-mail: rkielb@duke.edu

Kenneth C. Hall
e-mail: kenneth.c.hall@duke.edu

Department of Mechanical Engineering and
Materials Science,
Duke University,
Durham, NC 27708-0300

A nonlinear harmonic balance technique for the analysis of aerodynamic asymmetry of unsteady flows in turbomachinery is presented. The present method uses a mixed time-domain/frequency-domain approach that allows one to compute the unsteady aerodynamic response of turbomachinery blades to self-excited vibrations. Traditionally, researchers have investigated the unsteady response of a blade row with the assumption that all the blades in the row are identical. With this assumption the entire wheel can be modeled using complex periodic boundary conditions and a computational grid spanning a single blade passage. In this study, the steady/unsteady aerodynamic asymmetry is modeled using multiple passages. Specifically, the method has been applied to aerodynamically asymmetric flutter problems for a rotor with a symmetry group of 2. The effect of geometric asymmetries on the unsteady aerodynamic response of a blade row is illustrated. For the cases investigated in this paper, the change in the diagonal terms (blade on itself) dominated the change in stability. Very little mode coupling effect caused by the off-diagonal terms was found. [DOI: 10.1115/1.3103922]

1 Introduction

Traditionally, researchers have used frequency-domain and time-domain methods to investigate the unsteady aerodynamics in turbomachinery. The frequency-domain methods, namely, time-linearized [1–3] and harmonic balance [4–6] methods, assume that the unsteady disturbances are temporally and spatially periodic, a condition satisfied to a good approximation for many unsteady flows of interest. The time-linearized techniques further assume that the disturbances are small compared with the mean flow, and the governing equations can be linearized about a nonlinear mean operating condition. The main drawback for time-linearized techniques is their inability to model dynamically nonlinear effects. On the other hand, the harmonic balance approach does not make any small-disturbance assumption and can model dynamically nonlinear problems very efficiently. The main advantage of the frequency-domain methods is that the computational domain for the entire blade row can be reduced to a single blade passage using complex periodic boundary conditions. The time-accurate, time-domain methods [7–9] do not rely on any assumptions regarding the size of the unsteady disturbance or the temporal and spatial periodicity. Therefore, this approach is relatively simple to implement. The main drawback of these solvers is the very large computational time required, on the order of one to two orders of magnitude more than the frequency-domain methods.

The airfoils in bladed disk assemblies and blisks are coupled both structurally and aerodynamically. It is well known that both coupling mechanisms can play a significant role in determining the stability and maximum airfoil resonant response. Also, it has been known that frequency mistuning always has a stabilizing effect that is caused by a strong mode coupling. In the majority of research presented in the literature, both frequency-domain and time-domain unsteady flow analyses have assumed that all the blades in a row are identical. Therefore, the computed unsteady response is identical except for an interblade phase angle shift. However, in reality, the blades may have manufacturing variations such as mis-staggering that may result in aerodynamic asymmetry (also known as aerodynamic mistuning). If the aerodynamic asymmetry in a blade row is large enough, it may play a significant role in the stability of the turbomachinery blades. In the past 50 years or so, turbomachinery mistuning research efforts have for the most part concentrated on blade-to-blade frequency variations with models only accounting for the structural coupling [10–17].

In contrast to frequency mistuning, the subject of aerodynamic asymmetries has received very limited attention in the literature. Although the previous work on aerodynamic asymmetries presented some important results, there is still need for further investigation of this problem. Fleeter and Hoyniak [18] studied the effect of variation on circumferential blade spacing. Alternating blade spacing was found to stabilize a system that was unstable with equal spacing. However, their analysis was limited to simple flat plate blade geometries. Sladojević et al. [19,20] studied the effect of alternating stagger angle on stability for a more realistic fan profile. Small deviations in stagger angle (0.5 deg) did not significantly affect the stability. However, larger variations (2.0 deg) were found to be significantly destabilizing. Note that the analysis of Sladojević et al. [19,20] investigated the effect of increasing the alternate stagger angle. However, the aerodynamic response of the blades can be fundamentally different if the stagger angle of the alternating blades is decreased. In addition, because of the fact that Sladojević et al. used a time-accurate solver, they had to model the entire wheel in their computations, which made the analysis very expensive. Kielb et al. [21] used an approach where they perturbed the aerodynamic force matrix obtained from a symmetric computational fluid dynamics (CFD) analysis. Specifically, they investigated three different aerodynamic asymmetries: single blade perturbation, symmetry group perturbation, and random perturbation. They concluded that single blade perturbation and symmetry group of 2 perturbations had a flutter suppressing effect, whereas random perturbations of all blades had a destabilizing effect. The main drawback with the work of Kielb et al. [21] was that their method was based on a probabilistic approach.

In this paper, the effect of aerodynamic asymmetries caused by alternate blade-to-blade spacing and alternate staggering (in either direction) on the stability of a rotor is investigated. The unsteady

---

[1]Corresponding author. Present address: Department of Mechanical, Aerospace, and Biomedical Engineering, University of Tennessee, 315 Perkins Hall, Knoxville, TN 37996-2030.

aerodynamics is modeled using the state-of-the-art mixed time-domain/frequency-domain harmonic balance approach. The use of harmonic balance method allows us to model the blade row using a computational grid spanning a single sector (symmetry group). This reduces the computational and memory requirements dramatically compared with similar time-accurate analyses [20].

2 Governing Equations

To motivate the present multistage harmonic balance analysis, we describe how the method may be applied to the solution of the three-dimensional Euler equations. Note, however, that although we analyze only inviscid flows in this paper, the method is equally applicable to the Navier–Stokes equations.

Consider the three-dimensional Euler equations, written in the blade row frame of reference, which may be stationary or rotating at a speed Ω about the x axis. The Euler equations in Cartesian coordinates are given by

$$\frac{d}{dt} \int \int \int_{\mathcal{V}} U d\mathcal{V} + \int \int_{\mathcal{A}} [F, G, H] \cdot n d\mathcal{A} = \int \int \int_{\mathcal{V}} S d\mathcal{V} \quad (1)$$

The vector of conservation variables, U, the flux vectors, F, G, and H, and the source vector, S, are given by

$$U = \begin{bmatrix} \rho \\ \rho u \\ \rho v \\ \rho w \\ \rho E \end{bmatrix}, \quad F = \begin{bmatrix} \rho u - \rho \dot{f} \\ \rho u^2 + p - \rho u \dot{f} \\ \rho u v - \rho v \dot{f} \\ \rho u w - \rho w \dot{f} \\ \rho u I - \rho E \dot{f} \end{bmatrix}, \quad G = \begin{bmatrix} \rho v - \rho \dot{g} \\ \rho u v - \rho u \dot{g} \\ \rho v^2 + p - \rho v \dot{g} \\ \rho v w - \rho w \dot{g} \\ \rho v I - \rho E \dot{g} \end{bmatrix}$$

$$H = \begin{bmatrix} \rho w - \rho \dot{h} \\ \rho u w - \rho u \dot{h} \\ \rho v w - \rho v \dot{h} \\ \rho w^2 + p - \rho w \dot{h} \\ \rho w I - \rho E \dot{h} \end{bmatrix}, \quad S = \begin{bmatrix} 0 \\ 0 \\ \rho(\Omega^2 y + 2\Omega w) \\ \rho(\Omega^2 z - 2\Omega v) \\ 0 \end{bmatrix}$$

where $\dot{f}$, $\dot{g}$, and $\dot{h}$ are the x, y, and z components of the velocity of the unsteady grid motion, respectively. For an ideal gas with a constant specific heat ratio, the pressure p is related to the conservation variables through

$$p = (\gamma - 1)\rho \left[E - \tfrac{1}{2}(u^2 + v^2 + w^2) + \tfrac{1}{2}(\Omega r)^2 \right]$$

In addition, the rothalpy I is defined as

$$I = \frac{\rho E + p}{\rho} = \frac{\gamma}{\gamma - 1} \frac{p}{\rho} + \frac{1}{2}(u^2 + v^2 + w^2) - \frac{1}{2}(\Omega r)^2$$

where r is the distance from the x axis ($r = \sqrt{y^2 + z^2}$). The Euler equations are nonlinear in the conservation variables, and so the equations will admit nonlinear solutions.

3 Harmonic Balance Method

For many flows of interest in turbomachinery aerodynamics, the flow (when viewed in the relative frame of reference) is periodic in time, with period $T = 2\pi/\omega$. Because the flow is temporally periodic, the flow variables may be represented as a Fourier series in time with spatially varying coefficients. For example, the conservation variables may be expressed as

$$U(x, y, z, t) = A_0(x, y, z) + \sum_{n=1}^{\infty} [A_n(x, y, z)\cos(\omega n t)$$
$$+ B_n(x, y, z)\sin(\omega n t)] \quad (2)$$

where ω is the fundamental frequency, and A_0, A_n, and B_n are the

Fourier coefficients of the flow variables. In principle, the summations in these series are taken over all integer values of n. In practice, however, the series may be truncated to a finite number of terms, N. Therefore, the flow variables can be computed and stored at $2N+1$ equally spaced points over one temporal period. Assembled together into the vectors U^* and $\tilde{U}$, the subtime level solutions and the Fourier coefficients can be written as

$$U^* \begin{Bmatrix} U_1 \\ U_2 \\ \vdots \\ U_{2N+1} \end{Bmatrix} = , \quad \tilde{U} = \begin{Bmatrix} A_0 \\ A_1 \\ \vdots \\ A_N \\ B_1 \\ \vdots \\ B_N \end{Bmatrix} \quad (3)$$

The Fourier coefficients can be determined from the subtime level solutions by a discrete Fourier transform. Conversely, the conservation variables at the subtime levels can be determined from the Fourier coefficients by the inverse discrete Fourier transform. Following Eq. (2) these relations can be written in matrix form as

$$U^* = \mathbf{F}^{-1} \tilde{U} \quad (4)$$

$$\tilde{U} = \mathbf{F} U^* \quad (5)$$

Note that $\mathbf{F}$ and $\mathbf{F}^{-1}$ are square matrices as the number of time sublevels is equal to the number of Fourier coefficients.

Next, we write the Euler equations at all subtime levels simultaneously so that

$$\frac{\partial U^*}{\partial t} + \frac{\partial F^*}{\partial x} + \frac{\partial G^*}{\partial y} + \frac{\partial H^*}{\partial z} = S^* \quad (6)$$

where, for example, F^* is the vector of x-fluxes evaluated at U^*. Hence, Eq. (6) has $5 \times (2N+1)$ equations. Note that the $2N+1$ sets of conservation equations (Eq. (6)) are coupled only through the time derivative term, which is approximated by the pseudospectral operator, $\mathbf{D}$. To motivate the development of $\mathbf{D}$, we note that

$$\frac{\partial}{\partial t} U^* = \sum_{n=1}^{N} [-\omega n \cdot A_n \sin(\omega n t) + \omega n \cdot B_n \cos(\omega n t)] \quad (7)$$

or in matrix form

$$\frac{\partial U^*}{\partial t} = \frac{\partial \mathbf{F}^{-1}}{\partial t} \tilde{U} \quad (8)$$

Making use of Eq. (5) gives the desired pseudospectral operator

$$\frac{\partial U^*}{\partial t} = \frac{\partial \mathbf{F}^{-1}}{\partial t} \mathbf{F} U^* = \mathbf{D} U^* \quad (9)$$

Finally, substitution of Eq. (9) into Eq. (6) gives the desired harmonic balance equations, i.e.,

$$\mathbf{D} U^* + \frac{\partial F^*}{\partial x} + \frac{\partial G^*}{\partial y} + \frac{\partial H^*}{\partial z} = S^* \quad (10)$$

The advantage of Eq. (10) over the classical form of the harmonic balance equations is that the fluxes in Eq. (10) are much easier to compute (order N operations). The fluxes are simply computed at each of the $2N+1$ time levels in the usual way.

To solve the harmonic balance equations, we introduce a "pseudotime" term so that the equations may be marched rapidly to a steady-state condition using a conventional computational fluid dynamics scheme. Thus, Eq. (10) becomes
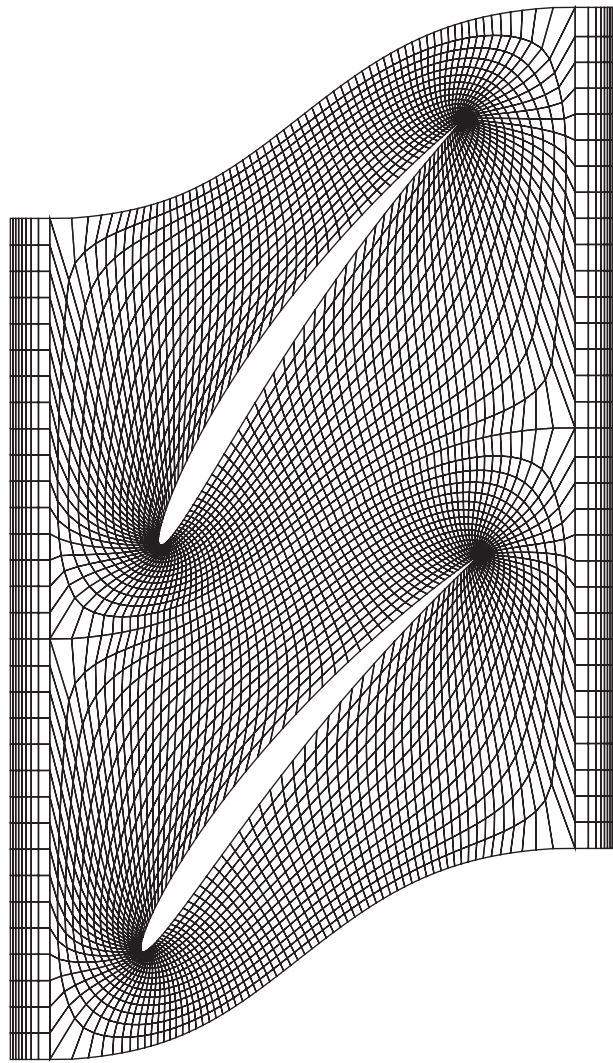
Fig. 1 Representative computational grid for a compressor with a symmetry group of 2

$$\frac{\partial U^*}{\partial \tau} + \mathbf{D}U^* + \frac{\partial F^*}{\partial x} + \frac{\partial G^*}{\partial y} + \frac{\partial H^*}{\partial z} = S^* \tag{11}$$

where τ is a fictitious or pseudotime, used only to march Eq. (11) to steady state, driving the pseudotime term to zero. Note that pseudotime harmonic balance equations are similar in form to the original time-domain form of the Euler equations, Eq. (1). Thus, existing well-developed *steady* CFD techniques may be used to efficiently solve the nonlinear harmonic balance equations with comparable number of iterations required.

Equation (11) is discretized on a computational grid spanning a single sector that has K blade passages for problems that satisfy complex periodic boundary conditions for a symmetry group of K. Similarly, for aerodynamically symmetric problems, the harmonic balance equations are discretized on a computational grid spanning only a single blade passage. A typical grid for a symmetry group of 2 is shown in Fig. 1. We use Ni's [22] two-step Lax–Wendroff scheme to discretize the harmonic balance equations. The Lax–Wendroff scheme is a node-centered conservative finite volume scheme. A combination of second and fourth difference smoothing is used to capture shocks. Also, because only "steady-state" solutions are desired, we use local time stepping and multiple-grid acceleration techniques to speed up convergence. The harmonic balance method as described here has some similarities to the classical "dual time step" method. Our approach,

however, has a number of important advantages. First, in the dual time step method, the solution is marched from one time level to the next time accurately, using pseudotime to drive the residual of the time-accurate equations to zero. The process is repeated over many time steps for several periods until a periodic solution has been reached. In our approach, we store the solution at just a few points over a single period, and the solutions at all these temporal points are advanced simultaneously using pseudotime marching until the solution converges. Second, because we solve for the solution over one complete period, a spectral operator may be used to compute the physical time derivative $\partial/\partial t$. The spectral time derivative is much more accurate than finite difference operators, which are used in the dual time step approach. Therefore, many fewer physical time levels are required using the present method. Finally, previous work by the authors indicates that the resulting scheme may be much less dissipative than conventional time-domain techniques.

4 Boundary Conditions

The boundary conditions consist of surface, far-field, and periodic boundary conditions and are applied once at every iteration in the flow solver. The solid surface boundary conditions require that there be no flow through the surface. Therefore, for an inviscid flow the normal velocity of the fluid on the surface must be equal to the normal velocity of the moving surface.

At the far-field of the computational domain, that is, at the inlet and the exit, we use quasi-three-dimensional nonreflecting boundary conditions [23] to eliminate the spurious reflections of the outgoing pressure, entropy, and vortical waves.

As mentioned previously, for problems with a symmetry group of K, the computational domain can be reduced to a single sector (with K blades) by making use of complex periodicity conditions along the periodic boundaries. To apply these conditions, the solution U^* is transformed along the periodic boundaries using Eq. (5) to find the vector of Fourier coefficients $\widetilde{U}$ (which contains the cosine and sine coefficients A_n and B_n). Inspection of Eq. (2) reveals that the appropriate boundary condition is given by

$$A_n(x,r,\theta + \theta_G) = A_n(x,r,\theta) \cdot \cos(\sigma n) - B_n(x,r,\theta) \cdot \sin(\sigma n) \tag{12}$$

$$B_n(x,r,\theta + \theta_G) = A_n(x,r,\theta) \cdot \sin(\sigma n) + B_n(x,r,\theta) \cdot \cos(\sigma n) \tag{13}$$

where θ_G is the tangential gap for the sector, and σ is the intersector phase angle. Note that we have momentarily switched to cylindrical coordinates for simplicity.

5 Aeroelastic Equations

By using the *single family of modes* approach the modal equations of motion for a mistuned bladed disk [24,25] can be written in traveling wave coordinates as

$$[(\Lambda_s + \Delta \mathbf{K}) - \omega^2(\mathbf{I} + \Delta \mathbf{M})]Y = F_B + F_W \tag{14}$$

where Λ_s is a diagonal matrix containing the squares of the tuned system mode frequencies due to structural coupling, $\Delta \mathbf{K}$ and $\Delta \mathbf{M}$ are the perturbations in modal stiffness and mass matrices due to frequency mistuning, and F_B and F_W are the modal force vectors due to blade motion and external excitations. Note that the aeroelastic equation (Eq. (14)) is an $N_B \times N_B$ reduced order model (ROM), where N_B is the total number of blades in the row. When the blades are aerodynamically symmetric (represented by subscript s) the aerodynamic forces due to blade motion can be expressed as

$$F_{Bs} = \mathbf{A}_s Y \tag{15}$$

where $\mathbf{A}_s$ matrix is a diagonal matrix containing the traveling wave unsteady aerodynamic coefficients that are determined from

the unsteady harmonic balance CFD analysis used in this study ($K=1$). For each traveling wave the physical forces on the blades are identical except for a constant interblade phase angle shift. When the blades are aerodynamically asymmetric, the forces due to blade motion can be expressed as

$$F_B = A_a Y \qquad (16)$$

where the $\mathbf{A}_a$ matrix is generally full.

In this study, we ignore the effects of any external excitations and focus only on the flutter problem. In addition, we assume that the mass ratio is high so that the aeroelastic eigenfrequencies are not significantly different from the structural eigenfrequencies. For the results presented herein the same mode shape and frequency were used for the entire range of interblade phase angles. Thus, the results are valid for a case where the blade mode shape is independent of the nodal diameter and where the unsteady aerodynamic forces do not change significantly over the frequency range of the system modes. With these assumptions, the modal equations of motion (Eq. (14)) can be rewritten as

$$[\mathbf{\Lambda}_s + \mathbf{A}_m - \mathbf{A}_a - \omega^2 \mathbf{I}]Y = 0 \qquad (17)$$

where $\mathbf{A}_m$ is the frequency mistuning matrix. Equation (17) is an eigenvalue problem whose eigenvalues are the frequencies and eigenvectors are the traveling wave displacements.

6 Aerodynamic Asymmetry

The physical system displacements, X, and the traveling wave displacements, Y, are related to each other with a pair of discrete Fourier and discrete inverse Fourier transformation matrices [26], i.e.,

$$X = \mathbf{E} Y \qquad (18)$$

$$Y = \mathbf{E}^{-1} X \qquad (19)$$

The physical aerodynamic forces, $\mathbf{A}_x$, also known as influence coefficients then become

$$\mathbf{A}_x = \mathbf{E} \mathbf{A}_a \mathbf{E}^{-1} \qquad (20)$$

$$\mathbf{A}_a = \mathbf{E}^{-1} \mathbf{A}_x \mathbf{E} \qquad (21)$$

When the blades are aerodynamically symmetric the physical aerodynamic matrix, $\mathbf{A}_x$, is circulant. The diagonal terms of the matrix are the force on a blade due to its own motion. The off-diagonal terms are the forces on a blade due to the motion of the neighboring blades. When the blades are aerodynamically asymmetric the circulant nature of this matrix is destroyed.

In this paper, the aerodynamic asymmetry caused by arranging the blades in a symmetry group of 2 ($K=2$) is investigated, although the method described herein is already applicable to any number of blades in a symmetry group. As mentioned previously, the aeroelastic matrix equation (Eq. (17)) is an $N_B \times N_B$ reduced order model. When a symmetry group of 2 is considered, the problem decouples into $N_B/2$ 2×2 systems. The current method uses a two-passage model as shown in Fig. 1 with one even (e) and one odd (o) blades. For a symmetry group of 2 Eq. (16) can be written in terms of two traveling waves as

$$\begin{bmatrix} a^{i,i} & a^{i,i+N_B/2} \\ a^{i+N_B/2,i} & a^{i+N_B/2,i+N_B/2} \end{bmatrix} \begin{Bmatrix} y^i \\ y^{i+N_B/2} \end{Bmatrix} = \begin{Bmatrix} F_B^i \\ F_B^{i+N_B/2} \end{Bmatrix} \qquad (22)$$

where i is the blade index. In addition, the aerodynamic forces can be written in terms of the physical aerodynamic forces as

$$\begin{Bmatrix} F_B^i \\ F_B^{i+N_B/2} \end{Bmatrix} = \mathbf{E}^{-1} \begin{Bmatrix} F_x^e \\ F_x^o \end{Bmatrix} = 0.5 \begin{bmatrix} 1 & e^{-j\beta_i} \\ 1 & -e^{-j\beta_i} \end{bmatrix} \begin{Bmatrix} F_x^e \\ F_x^o \end{Bmatrix} \qquad (23)$$

Substituting Eq. (23) into Eq. (22) results in

$$\begin{bmatrix} a^{i,i} & a^{i,i+N_B/2} \\ a^{i+N_B/2,i} & a^{i+N_B/2,i+N_B/2} \end{bmatrix} \begin{Bmatrix} y^i \\ y^{i+N_B/2} \end{Bmatrix} = 0.5 \begin{Bmatrix} F_x^e + F_x^o e^{-j\beta_i} \\ F_x^e - F_x^o e^{-j\beta_i} \end{Bmatrix} \qquad (24)$$

For each intersector phase angle, the coefficients in the previous equation need to be determined to solve the aeroelastic modal equation. For this, one must pick two sets of modal amplitudes and compute the physical forces on the blade. The choice of the traveling wave displacements is not unique. As an example, one may pick $y^i = 0.5$ and $y^{i+N_B/2} = 0.5$ as the first set of modal amplitudes. This translates to moving only the even blades (in their prescribed natural frequency and mode shape) and keeping the odd blades stationary in the physical space. As the second set, $y^i = 0.5$ and $y^{i+N_B/2} = -0.5$ values can be picked, which translates to moving only the odd blades and keeping the even blades stationary. These result in the following equations:

$$\begin{bmatrix} a^{i,i} & a^{i,i+N_B/2} \\ a^{i+N_B/2,i} & a^{i+N_B/2,i+N_B/2} \end{bmatrix} \begin{Bmatrix} 0.5 \\ 0.5 \end{Bmatrix} = 0.5 \begin{Bmatrix} F_x^{e,e} + F_x^{o,e} e^{-j\beta_i} \\ F_x^{e,e} - F_x^{o,e} e^{-j\beta_i} \end{Bmatrix} \qquad (25)$$

$$\begin{bmatrix} a^{i,i} & a^{i,i+N_B/2} \\ a^{i+N_B/2,i} & a^{i+N_B/2,i+N_B/2} \end{bmatrix} \begin{Bmatrix} 0.5 \\ -0.5 \end{Bmatrix} = 0.5 \begin{Bmatrix} F_x^{e,o} + F_x^{o,o} e^{-j\beta_i} \\ F_x^{e,o} - F_x^{o,o} e^{-j\beta_i} \end{Bmatrix} \qquad (26)$$

where $F_x^{e,o}$ is the physical force on the even blades when the odd blades are moving only, and similarly $F_x^{o,e}$ is the physical force on the odd blades when the even blades are moving only. After some algebra, the coefficients of the tridiagonal $\mathbf{A}_a$ matrix can be computed giving

$$a^{i,i} = 0.5[F_x^{e,e} + F_x^{e,o} + e^{-j\beta_i}(F_x^{o,e} + F_x^{o,o})]$$

$$a^{i,i+N_B/2} = 0.5[F_x^{e,e} - F_x^{e,o} + e^{-j\beta_i}(F_x^{o,e} - F_x^{o,o})]$$

$$a^{i+N_B/2,i} = 0.5[F_x^{e,e} + F_x^{e,o} - e^{-j\beta_i}(F_x^{o,e} + F_x^{o,o})]$$

$$a^{i+N_B/2,i+N_B/2} = 0.5[F_x^{e,e} - F_x^{e,o} - e^{-j\beta_i}(F_x^{o,e} - F_x^{o,o})] \qquad (27)$$

After the coefficients of the modal force matrix are computed, the eigenvalue problem given by Eq. (17) must be solved to analyze the flutter characteristics for the aerodynamically asymmetric cascade.

7 Numerical Results

Throughout this paper, we consider the middle blade row of a multistage inviscid subsonic linear cascade (configuration D [27]). The harmonic unsteady motion of the blades is assumed to be very small so that the unsteady aerodynamic response is linear. Therefore, in our harmonic balance analysis we only retain the mean and the first harmonics of the flow variables ($N=1$). That means we only need a total of three subtime level solutions in our analysis.

The blades of this geometry are made up of NACA four-digit (4.5)506 airfoils. The airfoils are staggered with 49.5 deg angle and the gap-to-chord ratio is 0.8. The total number of blades in the blade row is 40. The inlet relative Mach number and the flow angle are 0.7 and 60 deg, respectively. The nondimensional inlet total pressure and exit static pressure are 2.022 and 1.797. The lengths are nondimensionalized by the aerodynamic chord of the rotor blades, velocities by the relative inflow velocity, and the pressures by the inlet dynamic pressure. For the unsteady flow problem, we assume that the rotor blades pitch around the midchord with a frequency of 400 Hz, which corresponds to a reduced frequency $\omega_0 c/U$ of 0.3.

8 Symmetric Cascade

In this section, an aerodynamically symmetric cascade is investigated, and the current harmonic balance CFD flow solver is validated. In addition, the accuracy of the proposed method to com-
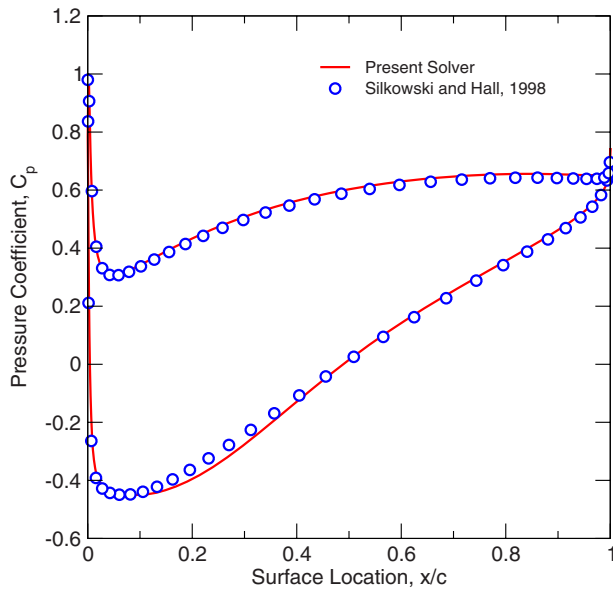
Fig. 2   Steady pressure distribution on the blade surface

pute the coefficients of the $\mathbf{A}_a$ matrix (Eq. (27)) is verified. First, the results obtained from the current harmonic balance CFD analysis are compared with those obtained using the potential flow solver of Silkowski and Hall [27].

Figure 2 shows the steady pressure distributions on the blade surface obtained using two different flows solvers. As can be seen, the agreement between the two solvers is very good. For the unsteady problem, the flow in a single blade passage for an interblade phase angle of 36 deg is computed first. Later, the same problem is solved on two passages for an intersector phase angle of 72 deg. Those results are compared with those obtained from the potential flow solver of Silkowski and Hall. Shown in Figs. 3 and 4 are the real and imaginary parts of the first harmonic of unsteady pressure. Here, the unsteady pressure is nondimensionalized by $\rho U \dot{\alpha}_0 c$, where ρ and U are the density and relative velocity at the inlet, $\dot{\alpha}_0$ is the pitching velocity, and c is the chord
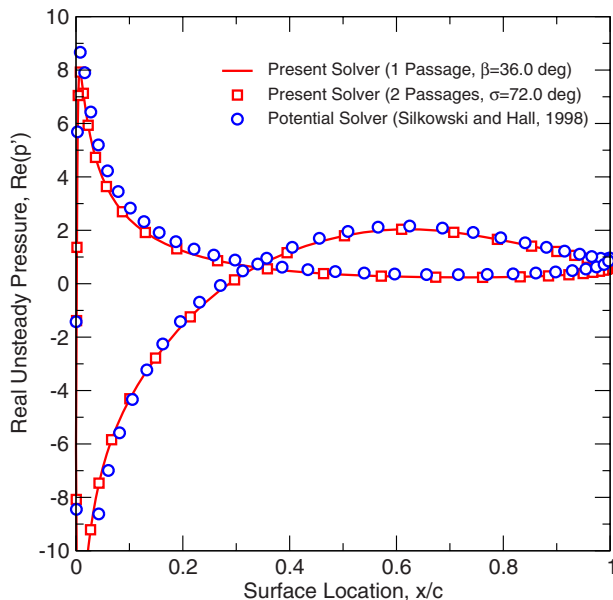
Fig. 3   Real part of computed unsteady surface pressure. The rotor blades vibrate in pitch with a reduced frequency of 0.3 and an interblade phase angle of 36 deg.
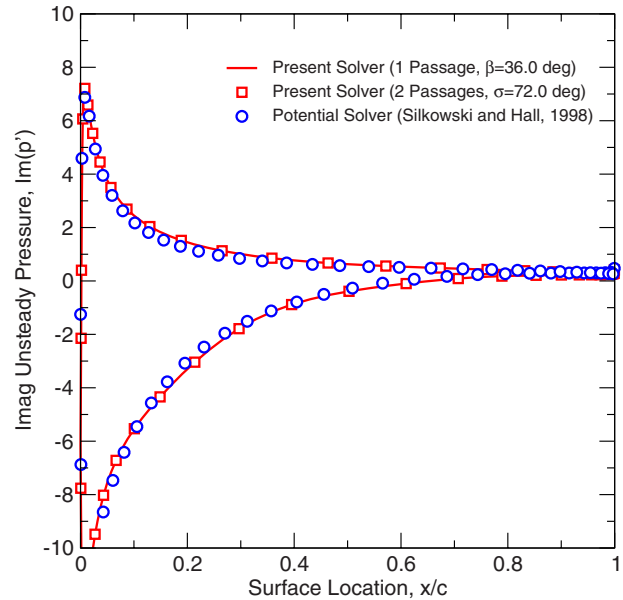
Fig. 4   Imaginary part of computed unsteady surface pressure. The rotor blades vibrate in pitch with a reduced frequency of 0.3 and an interblade phase angle of 36 deg.

of the blade. As in the case of the steady flow computations, our agreement to the code of Silkowski and Hall is very good. Also shown in the same figures is the unsteady pressure computation for two passages and an intersector phase angle of 72 deg. For an aerodynamically symmetric case, the unsteady response on the reference blade should be equal for one ($\beta=36$ deg) and two-passage solutions ($\sigma=72$ deg). As can be seen, these two cases give identical results, which validate the accuracy of our multipassage harmonic balance solver.

Next, the accuracy of the present technique used for computing the aerodynamic coefficients for a symmetry group of 2 is investigated. For this case, two different multipassage solutions are performed for an intersector phase angle of 72 deg. In the first run, only the even blades are vibrated and the odd blades are kept stationary and the physical generalized forces $F_x^{e,e}$ and $F_x^{o,e}$ are computed. In the second run, only the odd blades are vibrated and the even blades are kept stationary and the physical generalized forces $F_x^{e,o}$ and $F_x^{o,o}$ are computed. These values are given in Table 1.

Once the physical forces for an intersector phase angle of 72 deg are known, the traveling wave coefficients $a^{4,4}$, $a^{4,24}$, $a^{24,4}$, and $a^{24,24}$ can be computed using Eq. (27). For an aerodynamically symmetric case, the off-diagonal terms in the aerodynamic matrix must be 0.0. As can be seen from Table 2, the computed off-diagonal terms $a^{4,24}$ and $a^{24,4}$ are indeed 0.0. In addition, the two diagonal terms $a^{4,4}$ and $a^{24,24}$ are equal to the physical forces obtained from the single passage computations for $\beta=36$ deg and $\beta=-144$ deg, as expected.

Finally, the unsteady responses for all interblade phase angles are computed by running the CFD code for all intersector phase

Table 1   The physical aerodynamic forces for the two-passage tuned case ($\sigma=72$ deg)

Aerodynamic force	Real part	Imaginary part
$F_x^{e,e}$	0.211774	−0.135282
$F_x^{e,o}$	−0.136358	−0.061102
$F_x^{o,e}$	−0.146232	0.030717
$F_x^{o,o}$	0.091807	−0.233916

Table 2 Aerodynamic coefficients for the two-passage tuned case ($\sigma=72$ deg)

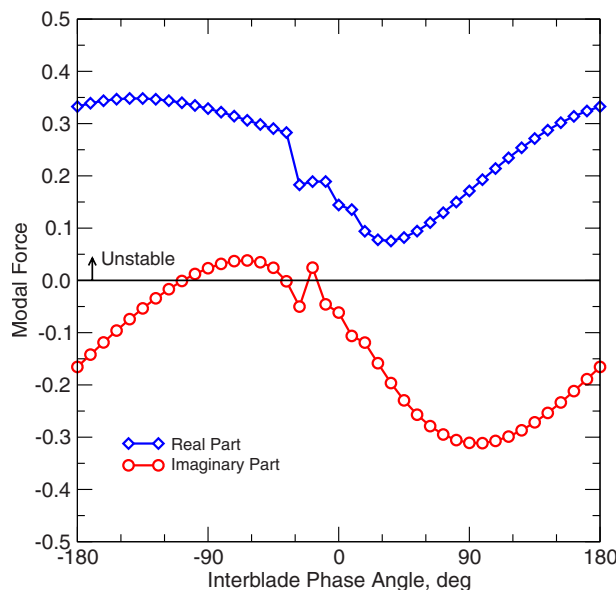| Coefficient	Real part	Imaginary part
$a^{4,4}$	0.075411	-0.196383
$a^{4,24}$	0.000000	0.000000
$a^{24,4}$	0.000000	0.000000
$a^{24,24}$	0.348128	-0.074178

angles twice. Shown in Fig. 5 are the real and imaginary parts of the modal force. For a frequency tuned and aerodynamically symmetric rotor the stability is determined by the imaginary part of the modal force. Thus, for this case, the rotor is unstable for the interblade phase angle range of -99 to -45 deg. In addition, Fig. 5 shows -63 deg interblade phase angle to be the most unstable.

9 Alternate Blade-to-Blade Spacing

Having validated our baseline CFD solver as well as our method for computing the diagonal and off-diagonal terms in the $\mathbf{A}_a$ aerodynamic force matrix, we now move our attention to the aerodynamic asymmetry analysis method described in this paper.

Here, the effect of alternate blade-to-blade spacing is investigated. As mentioned before the nominal blade-to-blade gap is 0.8 for the cascade analyzed here. For the first case, the blade-to-blade gap is changed to 0.9–0.7 in the two-passage model. The unsteady flow for all the possible intersector phase angles are then computed, and the diagonal and the off-diagonal terms in the $\mathbf{A}_a$ matrix are calculated. Figures 6 and 7 show the computed diagonal and off-diagonal terms of the aerodynamic matrix. As can be seen, changing the blade-to-blade spacing to 0.9–0.7 has virtually no effect on the diagonal terms. However, the off-diagonal terms are relatively large ($\pm 15\%$ of diagonal terms), so they may have an effect on the aeroelastic stability of the mistuned system.

For the second case, the unsteady response for 1.0–0.6 spacing is investigated, and the diagonal and the off-diagonal terms are calculated. As shown in Fig. 8, the diagonal terms are somewhat different than the symmetric cascade. However, the overall effect in the unstable region ($-99 \le \beta \le -45$) is very small. Compared with the 0.9–0.7 case, the off-diagonal terms are now even larger ($\pm 40\%$ of diagonal terms) (see Fig. 9).

Fig. 6 Diagonal terms of the aerodynamic matrix for 0.9–0.7 blade-to-blade spacing

Having computed all the terms of the aerodynamic matrix $\mathbf{A}_a$, one can now solve the flutter problem given by Eq. (17) for alternate blade-to-blade spacing and determine the eigenvalues of the system. For the results presented in this section, it is assumed that there is no frequency mistuning ($\mathbf{A}_m=0$) and no structural damping. Figure 10 compares the eigenvalues of the alternate spacing cases considered in this paper with the symmetric case. In all cases, the least stable eigenvector corresponds to seven nodal diameter backward traveling wave. The least stable eigenvalue for the symmetric case has a damping value of -0.32%. Note that in this work, the damping is defined as the critical damping ratio. As can be seen, overall the alternate spacing for both 1.0–0.6 and 0.9–0.7 cases improves the stability of the system. Similar findings were reported in a study by Fleeter and Hoyniak [18] for alternate spacing of flat plates. Most of the aeroelastic eigenvalues have increased damping. The stabilizing effect is apparent in the

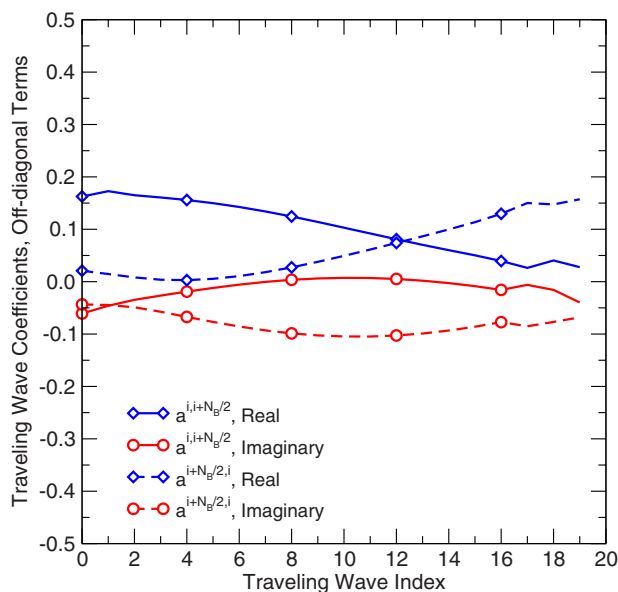**Fig. 5 Modal force for the aerodynamically symmetric cascade**
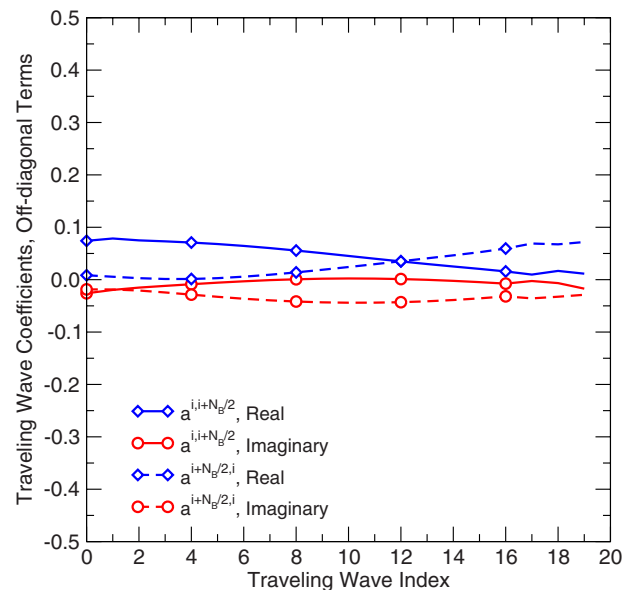
Fig. 7 Off-diagonal terms of the aerodynamic matrix for 0.9–0.7 blade-to-blade spacing

Fig. 8 Diagonal terms of the aerodynamic matrix for 1.0–0.6 blade-to-blade spacing

Fig. 10 Comparison of eigenvalues for symmetric and alternate blade-to-blade spacing cases
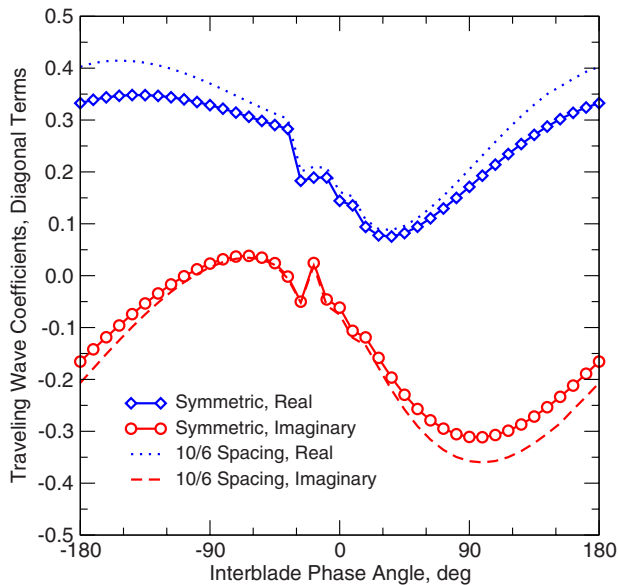
least damped region. However, the effect is negative for a small number of points in the stable region. As an example, for the 3 nodal diameter eigenvalue, the damping is slightly lower for the alternate blade-to-blade configurations compared with the symmetric case. Another thing to note is that the improvement in stability for the 1.0–0.6 case is more pronounced than the 0.9–0.7 case in the minimally damped region. However, both configurations are still unstable.

It is also of interest to examine the eigenvectors. For the least stable 1.0–0.6 eigenvalue shown in Fig. 10 the intersector phase angle is −36 deg. In terms of traveling waves the mode is dominated by a −18 deg interblade phase angle mode and is coupled with a 162 deg interblade phase angle mode with an amplitude that is 13% of the dominant mode. In terms of physical blade

displacements the even blades have 80.7% of the amplitude that of the odd blades. Within each sector the even blades lag the odd blades by a phase of 26.4 deg.

10 Alternate Blade Stagger

In an earlier work Sladojević et al. [20] analyzed the mis-staggering effect for a transonic viscous configuration. The conclusion of their work was that small deviations in stagger angle (0.5 deg) did not significantly affect the stability. However, larger variations (2.0 deg) were found to be significantly destabilizing. In this section, a similar study is performed, and the effect of alternating the blade stagger in a symmetry group of 2 is investigated. However, the flow regime and the solver used in this work are fundamentally different (subsonic inviscid flow).

The nominal blades in the rotor blade row have a stagger angle of 49.5 deg. First, the stagger angle of the odd blades is changed from their nominal values. As the final numerical study, the stagger angle of both the odd and even blades is alternated but in opposite directions. Note that the profiles of the blades are unchanged.

As in the previous test cases, a total of 40 different multipassage unsteady runs (20 for only the odd blades moving and 20 for only the even blades moving) is computed for each alternate stagger angle considered here. First, the stagger angle of the even blades is kept unchanged (49.5 deg) while the odd blades are rotated −2 deg (47.5 deg stagger angle). Shown in Fig. 11 are the real and imaginary parts of the off-diagonal traveling wave coefficients for the 0/−2 configuration. One can see that the off-diagonal terms are quite small compared with the previous alternate spacing cases. Although not shown here, there is almost no change in the diagonal terms.

Second, the stagger angles of the odd blades are changed +2 deg (51.5 deg stagger angle) and the multipassage CFD code is run for every possible intersector phase angle. The diagonal terms for this case are plotted in Fig. 12 showing some destabilizing effect in the minimally damped region. The off-diagonal terms are not presented since they show similar behavior with the 0/−2 case.
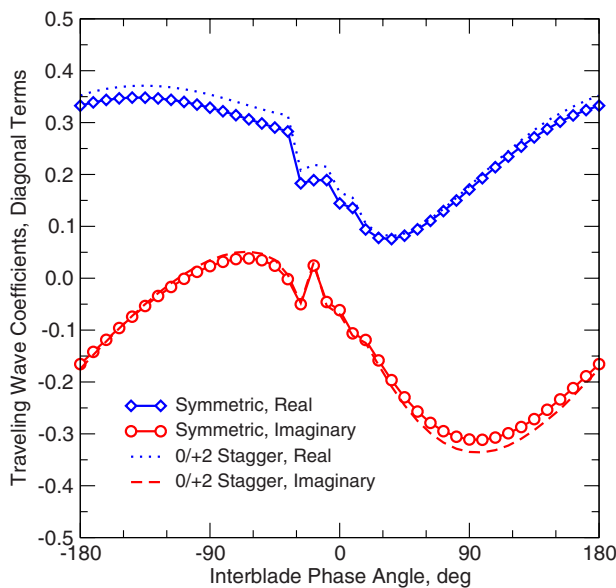
After each term in the $\mathbf{A}_a$ matrix is computed for 0/−2 and 0/+2 cases the eigenvalues of the aeroelastic problem must be analyzed using Eq. (17). Figure 13 compares the eigenvalues of the alternate stagger angles with the symmetric case. In all cases, the least stable eigenvector corresponds to seven nodal diameter
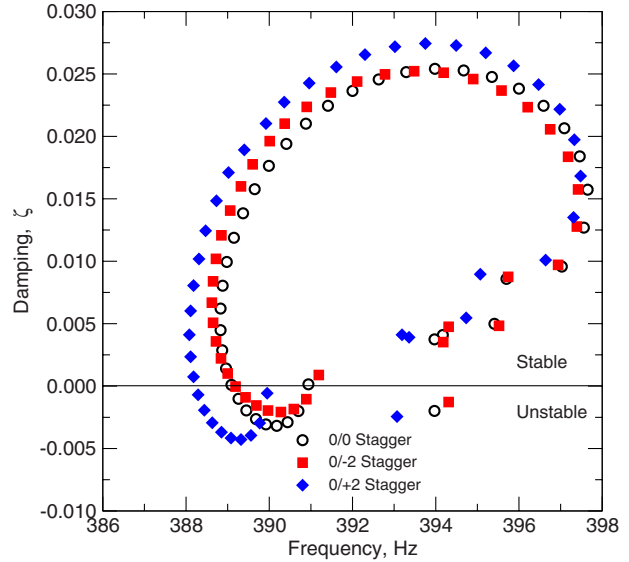

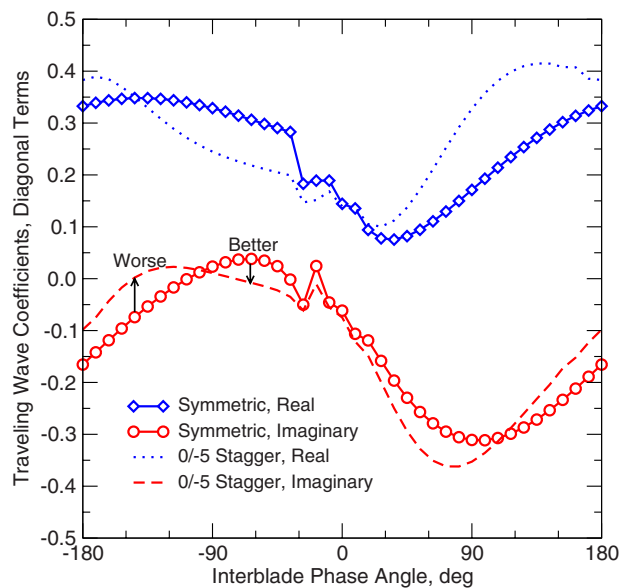**Fig. 9 Off-diagonal terms of the aerodynamic matrix for 1.0–0.6 blade-to-blade spacing**

Fig. 11 Off-diagonal terms of the aerodynamic matrix for 0/−2 stagger angle case

Fig. 13 Comparison of eigenvalues for symmetric and alternate stagger cases
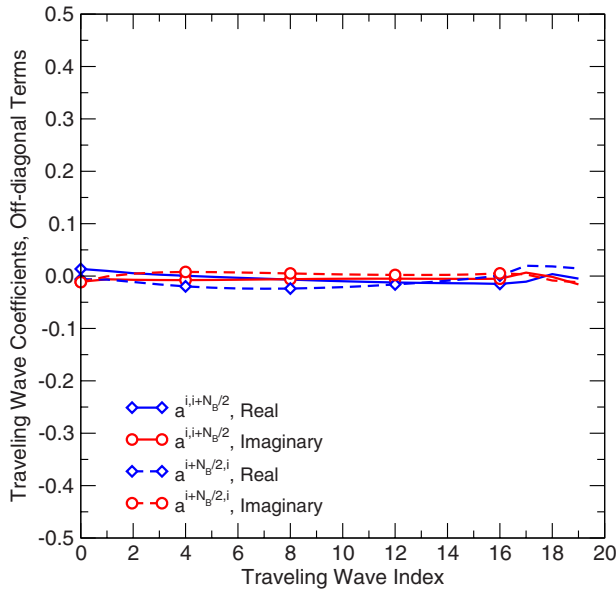
backward traveling wave. As mentioned before, the least stable eigenvalue has a damping of −0.32% for the symmetric system. It can be seen that the alternate stagger angle of 0/−2 improves the aerodynamic stability of the system increasing the least stable damping to −0.20%, whereas 0/+2 stagger angle decreases the least stable damping to −0.43%. Because the asymmetry of the stagger angles is relatively large (±2 deg), the change in the stability of the system may be attributed to the change in the mean background (steady) flow.

Next we consider the cases where the stagger angles of the odd blades are changed by ±5 deg. Figures 14 and 15 show the diagonal traveling wave coefficients for 0/−5 and 0/+5 configurations, respectively. In both cases, it can be seen that the change in the stagger angle changes the unsteady response substantially resulting in changes in the diagonal traveling wave coefficients. For the 0/−5 case, the values of the traveling wave coefficients de-

crease in the −99 ≤ β ≤ −45 deg range and increase in the −144 ≤ β ≤ −99 range. On the other hand, 0/+5 case seems to have a larger destabilizing effect for all of the negative interblade phase angles.

Shown in Figs. 16 and 17 are the off-diagonal traveling wave coefficients for 0/−5 and 0/+5 configurations. One can see that the off-diagonal terms are relatively large and might play an important role in the stability for both cases. Since there is also interest in the variation in the aerodynamic matrix in physical space (influence coefficients), examples from the 0/+5 case are now discussed. For the diagonal terms (blade on itself) the amplitudes of the even and odd blades are 4.0% higher and 3.6% lower, respectively, than those of the symmetric case. The variations in the first off-diagonal terms (the effect of the neighboring blades) are very large. For the +1 blades the even blades have nearly twice the amplitude of the symmetric case. For the −1 blades the amplitudes are less than half that of the symmetric case.

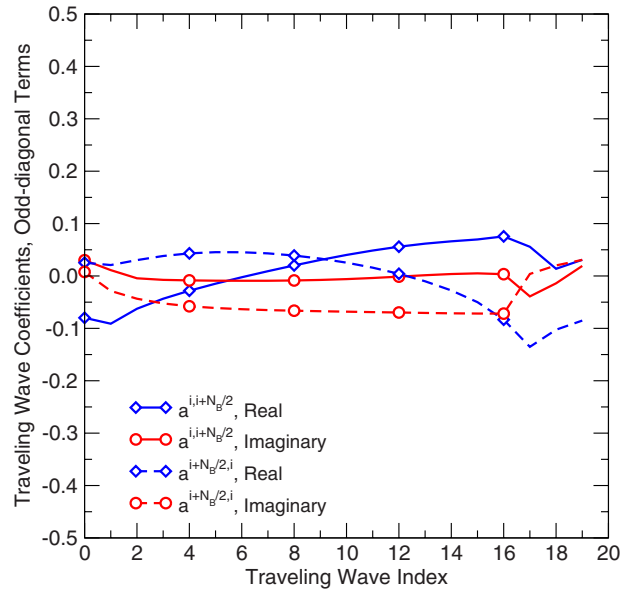Fig. 12 Diagonal terms of the aerodynamic matrix for 0/+2 stagger angle case

Fig. 14 Diagonal terms of the aerodynamic matrix for 0/−5 stagger angle case

Fig. 15 Diagonal terms of the aerodynamic matrix for 0/+5 stagger angle case
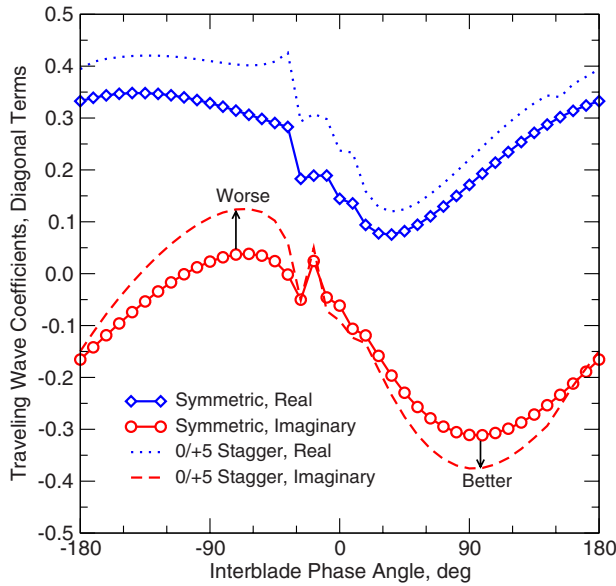
Fig. 17 Off-diagonal terms of the aerodynamic matrix for 0/ +5 stagger angle case

The eigenvalues are compared with the symmetric case in Fig. 18. The aerodynamic asymmetry results in an increase in the damping for the least stable eigenvalue from −0.32% to −0.14% for the 0/−5 case. However, the number of unstable eigenvalues increases from 8 to 11. In the case of 0/+5 alternate stagger, it is seen that overall the eigenvalues are more unstable with the least stable eigenvalue having a −1.1% damping. In addition, the number of unstable eigenvalues increases to 13. There are two possible causes for this significant decrease in stability for the 0/+5 case: (1) an increase in the positive values of the imaginary part of the diagonal terms and (2) a mode coupling effect caused by the off-diagonal terms. It was found for this case that the decrease in stability is greatly dominated by the diagonal terms. Therefore, the effect is that the asymmetric aerodynamics decreases the stability of the critical intersector traveling wave mode. It is not a mode coupling flutter behavior.

For the results presented in this section, the stagger angles of the odd blades were changed keeping the even blade stagger angle in their nominal value. It was observed that an increase in the stagger angle decreased the stability whereas a decrease in the stagger angle increased the stability. As mentioned before, this may be due to the change in the steady flow characteristics. Figure 19 shows the effect of alternate stagger angle variation on the steady flow of the even blades. As can be seen, an increase in the stagger angle of the odd blades increases the loading on the even blades. On the other hand, a decrease in the stagger angle decreases the loading. Therefore, the change in the stability of the system can directly be related to the change in the mean background (steady) flow.

As the last test case in this paper, the stagger angles of the odd and even blades are changed by +2.5 deg and −2.5 deg, respectively. The reason for this choice of alternate stagger is to keep the blade-to-blade stagger difference at 5.0 deg while accounting for a

Fig. 16 Off-diagonal terms of the aerodynamic matrix for 0/−5 stagger angle case
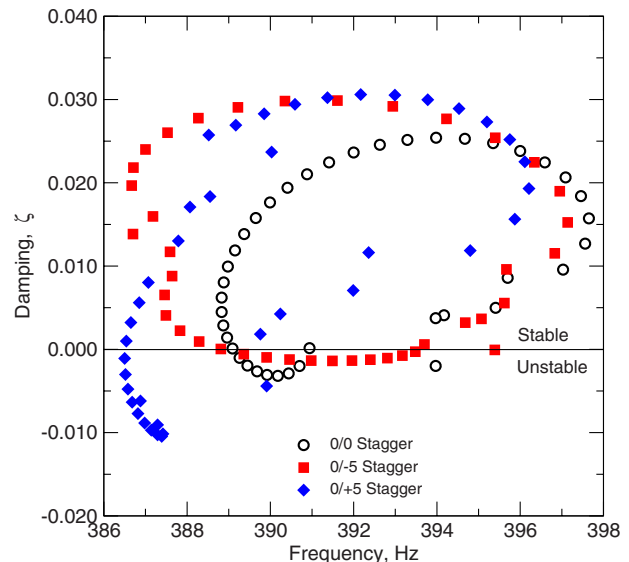
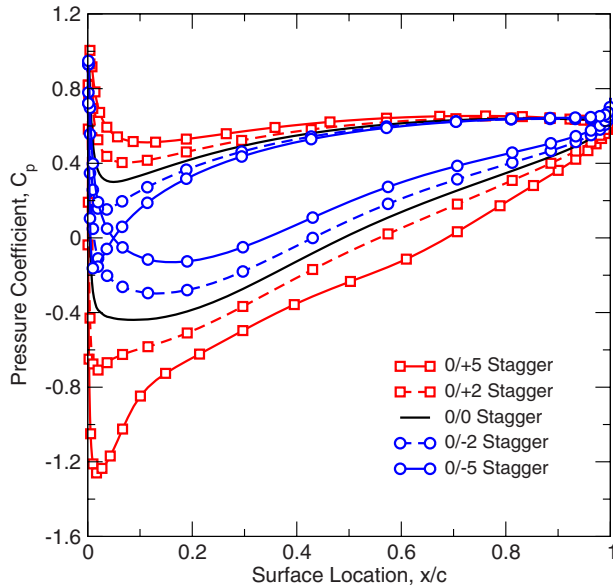**Fig. 18 Comparison of eigenvalues for symmetric and alternate stagger cases**

Fig. 19 Effect of stagger angle variation on the steady flow

change in stagger in either direction. Shown in Fig. 20 are the eigenvalues of the previous two cases as well as the +2.5/−2.5 case. As can be seen, the damping of the least stable eigenvalue increases to −0.20% compared with −0.32% for the symmetric case. Overall the +2.5/−2.5 case is more stable than the 0/+5 case and less stable than the 0/−5 case. However, the total number of unstable eigenmodes for +2.5/−2.5 is fewer than both.

11 Conclusions

In this paper, the effect of aerodynamic asymmetries caused by alternate blade-to-blade spacing and alternate staggering on the stability of a linear cascade is investigated. The method can be used for configurations that have any number of blades within the symmetry group. The method, which is particularly well suited for the computation of aerodynamic forces that produce flutter, can model flow nonlinearities and is very efficient. For the cases considered in this paper, results show that alternate blade-to-blade
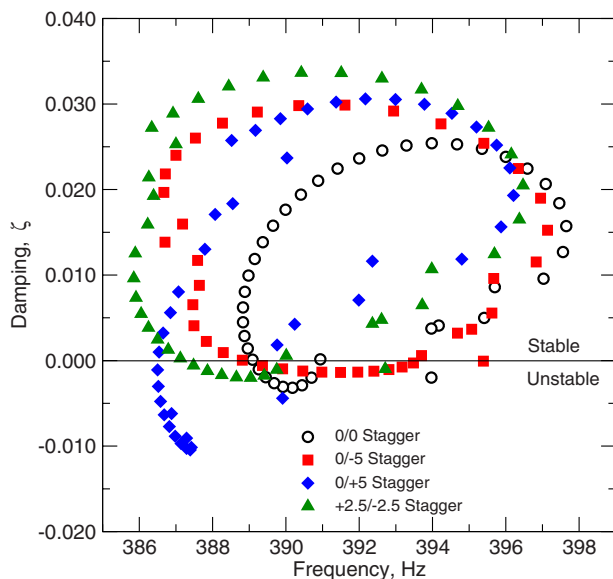
spacing improves the stability of the blades. Alternate staggering, on the other hand, may have stabilizing or destabilizing effect depending on the direction of mis-staggering. The change in the stability due to aerodynamic asymmetries can be attributed to a change in the steady aerodynamics, a change in the diagonal terms (blade on itself), and a mode coupling effect caused by the off-diagonal terms in the aerodynamic matrix. For the cases considered the change in the diagonal terms dominated the change in stability. Very little mode coupling effect was found. This behavior is fundamentally different than that of frequency mistuning. Finally, note that the method was only presented for an inviscid linear cascade, and additional investigation needs to be carried out for full three-dimensional transonic viscous flows, which is the subject of ongoing research.

Acknowledgment

Nomenclature

$a^{s,k}$ = force on blade s due to the motion of blade k
$\mathcal{A}$ = control surface
A_n, B_n = nth temporal Fourier coefficients
$\mathbf{A}_a$ = aerodynamic force matrix in traveling wave space
$\mathbf{A}_x$ = aerodynamic force matrix in physical space
$\mathbf{A}_m$ = frequency mistuning matrix
c = chord length
$\mathbf{D}$ = pseudospectral operator
E = total energy
$\mathbf{E}, \mathbf{E}^{-1}$ = discrete Fourier and inverse Fourier transformation matrices
$\dot{f}, \dot{g}, \dot{h}$ = control surface velocity
F_B = modal force vector due to blade motion
F_W = modal force vector due to external excitations
F, G, H = flux vectors
$\mathbf{F}, \mathbf{F}^{-1}$ = discrete Fourier and inverse Fourier transformation matrices
I = rothalpy
$\mathbf{I}$ = tuned mass matrix
j = $\sqrt{-1}$
K = number of blades in the sector
N_B = total number of blades in the blade row
p = pressure
r = distance from the axis of rotation
S = source vector
t = time
U = relative inflow velocity
U^* = vector of conservation variables in all subtime levels
$\tilde{U}$ = vector of Fourier coefficients
u, v, w = Cartesian velocities
$\mathcal{V}$ = control volume
x, y, z = Cartesian coordinates
x, θ, r = relative cylindrical coordinates
X, Y = physical and traveling wave blade displacements
$\dot{\alpha}_0$ = velocity of pitching motion
β = interblade phase angle
γ = specific heat ratio
$\Delta \mathbf{K}$ = stiffness matrix perturbation
$\Delta \mathbf{M}$ = mass matrix perturbation
θ_G = sector gap
ζ = critical damping ratio
Λ_s = tuned stiffness matrix

Fig. 20 Comparison of eigenvalues for symmetric and alternate stagger cases

ρ = density
σ = intersector phase angle
τ = pseudotime
ω = excitation frequency
Ω = wheel speed

References

[1] Hall, K. C., and Crawley, E. F., 1989, "Calculation of Unsteady Flows in Turbomachinery Using the Linearized Euler Equations," AIAA J., **27**(6), pp. 777–787.

[2] Clark, W. S., and Hall, K. C., 2000, "A Time-Linearized Navier-Stokes Analysis of Stall Flutter," ASME J. Turbomach., **122**, pp. 467–476.

[3] Hall, K. C., and Ekici, K., 2005, "Multistage Coupling for Unsteady Flows in Turbomachinery," AIAA J., **43**(3), pp. 624–632.

[4] He, L., and Ning, W., 1998, "Efficient Approach for Analysis of Unsteady Viscous Flows in Turbomachines," AIAA J., **36**(11), pp. 2005–2012.

[5] Hall, K. C., Thomas, J. P., and Clark, W. S., 2002, "Computation of Unsteady Nonlinear Flows in Cascades Using a Harmonic Balance Technique," AIAA J., **40**(5), pp. 879–886.

[6] Ekici, K., and Hall, K. C., 2007, "Nonlinear Analysis of Unsteady Flows in Multistage Turbomachines Using Harmonic Balance," AIAA J., **45**(5), pp. 1047–1057.

[7] Gerolymos, G. A., 1993, "Advances in the Numerical Integration of the Three-Dimensional Euler Equations in Vibrating Cascades," ASME J. Turbomach., **115**(4), pp. 781–790.

[8] He, L., and Denton, J. D., 1994, "Three-Dimensional Time-Marching Inviscid and Viscous Solutions for Unsteady Flows Around Vibrating Blades," ASME J. Turbomach., **116**(3), pp. 469–476.

[9] Davis, R. L., Shang, T., Buteau, J., and Ni, R. H., 1996, "Prediction of 3-D Unsteady Flow in Multi-Stage Turbomachinery Using an Implicit Dual Time-Step Approach," AIAA Paper No. 96–2565.

[10] Ewins, D. J., 1969, "The Effects of Detuning Upon the Forced Vibrations of Bladed Disks," J. Sound Vib., **9**(1), pp. 65–79.

[11] Kaza, K., and Kielb, R. E., 1982, "Flutter and Response of a Mistuned Cascade in Incompressible Flow," AIAA J., **20**(8), pp. 1120–1127.

[12] Dugundji, J., and Bundas, D. J., 1983, "Flutter and Forced Response of Mistuned Rotors Using Standing Wave Analysis," AIAA Paper No. 83–0845.

[13] Bendiksen, O. O., 1984, "Flutter of Mistuned Turbomachinery Rotors," ASME Paper No. 83-GT-153.

[14] Griffin, J. H., and Hoosac, T. M., 1984, "Model Development and Statistical Investigation of Turbine Blade Mistuning," ASME J. Vib., Acoust., Stress, Reliab. Des., **106**, pp. 204–210.

[15] Crawley, E. F., and Hall, K. C., 1985, "Optimization and Mechanisms in Mistuning in Cascades," ASME J. Eng. Gas Turbines Power, **108**, pp. 418–426.

[16] Srinivasan, A. V., and Tavares, G. G., 1994, "Direct Use of Unsteady Aerodynamic Pressures in the Flutter Analysis of Mistuned Blades," ASME Paper No. 94-GT-347.

[17] Lin, C. C., and Mignolet, M. P., 1997, "An Adaptive Perturbation Scheme for the Analysis of Mistuned Bladed Disks," ASME J. Eng. Gas Turbines Power, **119**, pp. 153–160.

[18] Fletter, S., and Hoyniak, D., 1989, "Aeroelastic Detuning for Stability Enhancement of Unstalled Supersonic Flutter," Int. J. Turbo Jet Engines, **6**, pp. 17–26.

[19] Sladojević, I., 2006, "Forced Response Analysis of Aeroelastically Coupled Mistuned Bladed Disks," Ph.D. thesis, Imperial College, London, England.

[20] Sladojević, I., Sayma, A. I., and Imregun, M., 2007, "Influence of Stagger Angle Variation on Aerodynamic Damping and Frequency Shifts," ASME Paper No. GT2007-28166.

[21] Kielb, R. E., Hall, K. C., and Miyakozawa, T., 2007, "The Effect of Unsteady Aerodynamic Asymmetric Perturbations on Flutter," ASME Paper No. GT-2007-27503.

[22] Ni, R. H., 1982, "A Multiple-Grid Scheme for Solving the Euler Equations," AIAA J., **20**(11), pp. 1565–1571.

[23] Saxer, A. P., and Giles, M. B., 1993, "Quasi-Three-Dimensional Nonreflecting Boundary Conditions for Euler Equations Calculations," J. Propul. Power, **9**(2), pp. 263–271.

[24] Feiner, D. M., and Griffin, J. H., 2004, "Mistuning Identification of Bladed Disks Using a Fundamental Mistuning Model–Part I: Theory," ASME J. Turbomach., **126**, pp. 150–158.

[25] Kielb, R. E., Feiner, D. M., Griffin, J. H., and Miyakozawa, T., 2004, "Flutter of Mistuned Bladed Disks and Blisks With Aerodynamic and FMM Structural Coupling," ASME Paper No. GT-2004-54315.

[26] Whitehead, D. S., 1966, "Effect of Mistuning on the Vibration of Turbomachine Blades Induced by Wakes," J. Mech. Eng. Sci., **8**, pp. 15–21.

[27] Silkowski, P. D., and Hall, K. C., 1998, "A Coupled Mode Analysis of Unsteady Multistage Flows in Turbomachinery," ASME J. Turbomach., **120**(3), pp. 410–421.

Separated Flow Measurements on a Highly Loaded Low-Pressure Turbine Airfoil

Ralph J. Volino

Department of Mechanical Engineering,
United States Naval Academy,
Annapolis, MD 21402
e-mail: volino@usna.edu

Boundary layer separation, transition, and reattachment have been studied on a new, very high lift, low-pressure turbine airfoil. Experiments were done under low freestream turbulence conditions on a linear cascade in a low speed wind tunnel. Pressure surveys on the airfoil surface and downstream total pressure loss surveys were documented. Velocity profiles were acquired in the suction side boundary layer at several streamwise locations using hot-wire anemometry. Cases were considered at Reynolds numbers (based on the suction surface length and the nominal exit velocity from the cascade) ranging from 25,000 to 330,000. In all cases, the boundary layer separated, but at high Reynolds number the separation bubble remained very thin and quickly reattached after transition to turbulence. In the low Reynolds number cases, the boundary layer separated and did not reattach, even when transition occurred. This behavior contrasts with previous research on other airfoils, in which transition, if it occurred, always induced reattachment, regardless of Reynolds number. [DOI: 10.1115/1.3104608]

1 Introduction

Boundary layer separation can lead to partial loss of lift and higher aerodynamic losses on low-pressure turbine (LPT) airfoils (e.g., Refs. [1–3]). As designers impose higher loading to improve efficiency and lower cost, the associated strong adverse pressure gradients on the suction side of the airfoil can exacerbate separation problems. The problem is particularly relevant in aircraft engines due to the lower density and therefore lower Reynolds numbers at altitude. A component efficiency drop of 2% may occur between takeoff and cruise in large commercial transport engines, and the difference could be as large as 7% in smaller engines operating at higher altitudes [4,5]. Prediction and control of suction side separation, without sacrifice of the benefits of higher loading, are therefore crucial for improved engine design.

Separation and separated flow transition, which can lead to boundary layer reattachment, have received considerable attention. Studies have included flows over flat plates subject to pressure gradients similar to those on the suction side of LPT airfoils, and flows over airfoils either in single passage facilities or multiblade cascades. Some have considered steady inflow conditions, while others have included the effect of unsteady wakes. Recent examples include Refs. [6–12]. Volino [13] provided a review of some earlier studies. In general, previous work shows that the strong acceleration on the leading section of the airfoil keeps the boundary layer thin and laminar, even in the presence of elevated freestream turbulence. When separation does occur, it is usually just downstream of the suction peak. If transition then occurs in the shear layer over the separation bubble, it is typically rapid and causes the boundary layer to reattach [13,14]. Transition is dependent on Reynolds number, freestream turbulence level, and the surface roughness conditions upstream of the separation point. Several correlations for separated flow transition have been developed based on experimental data, including those of Mayle [2], Hatman and Wang [15], Davis et al. [16], Yaras [17], Volino and Bohl [18], and Praisner and Clark [19].

The advances in separation understanding and prediction have

led to attempts at separation control. Zhang et al. [20], Bohl and Volino [21], Volino [22], and others provided examples using passive devices such as boundary layer trips. Others have used active devices such as vortex generator jets (e.g., Refs. [4,23]) or plasma devices (e.g., Ref. [24]).

Another way to improve performance is to design airfoils with pressure gradients more resistant to separation, as described by Praisner and Clark [19]. Forward loading, for example, makes airfoils more separation resistant by extending the adverse pressure gradient on the aft portion of the suction side over a longer distance. This reduces the local pressure gradient at all locations, making separation less likely. If separation does occur, forward loading provides a longer distance along the airfoil surface for reattachment. Forward loading has some disadvantages, however. As noted by Zhang et al. [20], the longer region of turbulent flow on a forward loaded airfoil can lead to increased profile losses. Forward loading also creates longer regions of strong pressure gradient on the endwalls, which can produce stronger secondary flows and losses. If flow control were incorporated in the design of an advanced airfoil, as discussed by Bons et al. [25], it might be possible to produce an aft loaded airfoil that was resistant to separation and had low profile and secondary loss characteristics over a range of Reynolds numbers.

The objective of the present study is to document the flow over a very highly loaded LPT airfoil. The airfoil chosen was designed at the Air Force Research Laboratory (AFRL), and is designated the L1A. It is available on a limited basis to U.S. researchers from Ref. [26]. Dimensions of the L1A as used in the present experiments are given in Table 1. Based on the design calculations of Clark [26], the L1A has 10% higher loading than the "ultrahigh lift" airfoils described by Zhang and Hodson [27], and 17% higher loading than the Pack B airfoil considered in several studies such as Refs. [13,14,4]. The design calculations indicate that the Zweifel coefficient increases from about 1.15 on the Pack B to about 1.35 on the L1A. If the definition for the Zweifel coefficient is taken as

$$Zw = 2 \cos^2 \alpha_2 (L_\phi/C_x)(\tan \alpha_1 + \tan \alpha_2) \qquad (1)$$

as given by Lakshminarayana [28], $Zw = 1.08$ for the Pack B (in agreement with the value given by McAuliffe and Sjolander [29]) and $Zw = 1.23$ for the L1A. The L1A has the same inlet and exit flow angles and loading as the L1M airfoil used by Bons et al. [25]. The L1M is a midchord loaded design and is resistant to

| Axial chord, C_x (mm)	True chord (mm)	Pitch, L_ϕ (mm)	Span (mm)	Suction side, L_s (mm)	Inlet flow angle (deg)	Exit flow angle (deg)
134	146	136	724	203	35	60

separation even at very low Reynolds numbers. While the L1M and L1A were designed with the same methodology, the L1A is aft loaded, and is therefore expected to be more prone to separation. It is expected to be a good test airfoil for future flow control work, in which separation may be suppressed while maintaining the benefits of both very high loading and aft loading. Figure 1 shows the inviscid flow pressure profiles for the L1A, L1M, and Pack B airfoils. The inviscid code used for the computations was adapted from Ref. [30]. Figure 1(a) shows the pressure coefficient Cp as a function of dimensionless axial position, x/C_x. These coordinates are useful for comparing the lift generated by the airfoils. Figure 1(b) shows Cp as a function of the streamwise distance along the airfoil surface, s/L_s, where L_s is the wetted surface length along the suction side. These coordinates are most useful for explaining the boundary layer development and are used to present the results below. The higher lift of the L1A and L1M compared with the Pack B is clear in Fig. 1. Also clear is the

stronger adverse pressure gradient of the L1A on the downstream region of the suction side. The pressure gradient is shown again in Fig. 2 as the product of the local acceleration parameter K and the Reynolds number. The Reynolds number, Re, is based on L_s and the nominal exit velocity from the cascade U_e (computed using the inlet velocity and the design inlet and exit flow angles). The parameter K is inversely proportional to Re, so K Re is independent of Reynolds number. The negative K values downstream of $s/L_s = 0.7$ are about twice as strong for the L1A than for the other two airfoils. This suggests more of a tendency for boundary layer separation and possibly less of a tendency for the flow to reattach.

2 Experimental Facility and Measurements

Experiments were conducted in a closed loop wind tunnel with a linear cascade in one corner of the loop. An axial fan sends air through turning vanes in the first corner of the tunnel and then through a heat exchanger. Following the heat exchanger is the second turn and a 6.25:1 area ratio contraction. Following the contraction is a 0.46 m square by 1.1 m long test section, which was not used in the present study. Following this test section is a 2.4 m long diffuser, which expands the flow area to 0.75 × 0.75 m². A fine screen with 0.12 mm mesh thickness, 0.42 mm mesh spacing and 49% blockage is located in the exit plane of the diffuser. The screen breaks up the boundary layers, which form on the diffuser walls and provides a uniform flow into the cascade test section. A seven blade cascade is located in the wind tunnel's third turn, as shown in Fig. 3. A generic airfoil shape is shown in the figure. The flow continues from the cascade into the tunnel's fourth turn, then through a second diffuser before returning to the fan.

The freestream turbulence entering the cascade was measured with a cross-wire probe positioned just upstream of the center blade. The streamwise velocity component had a turbulence intensity, TI, of 0.8%, while the component intensity in the direction across the cascade was 0.5%. The spanwise component intensity was assumed to also be 0.5% based on the symmetry of the wind tunnel. The combined freestream turbulence intensity based on all
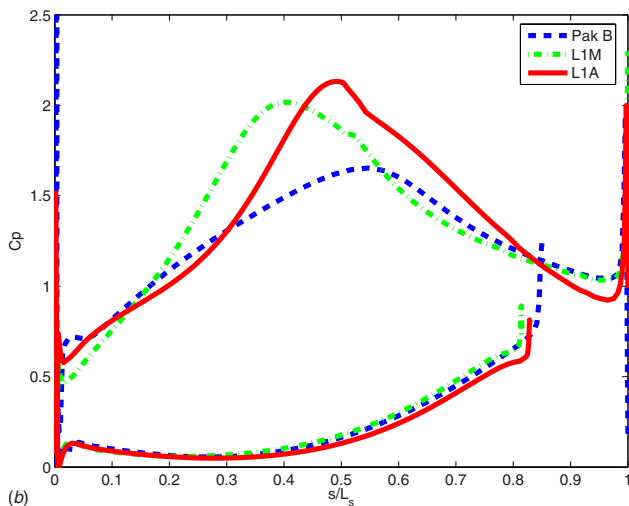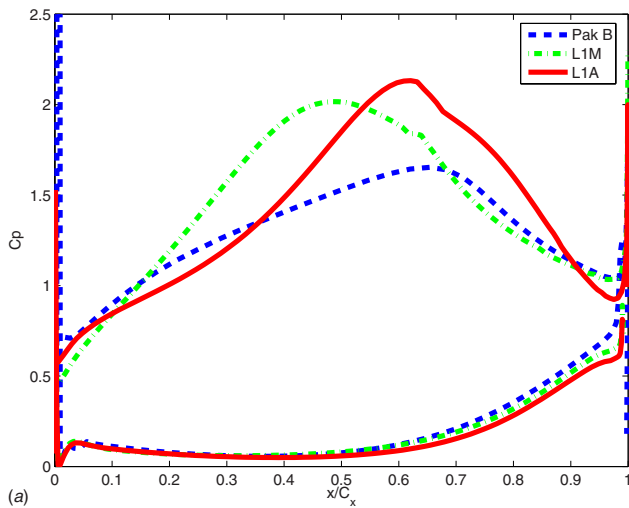
Fig. 1 Comparison of inviscid pressure profiles for the Pack B, L1M, and L1A airfoils: (*a*) *Cp* **versus axial position;** (*b*) *Cp* **versus streamwise location**
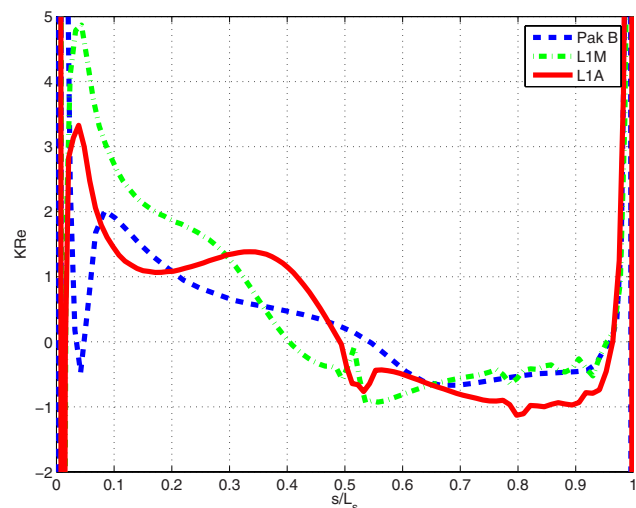
Fig. 2 Acceleration, *K* **Re, versus streamwise location for Pack B, L1M, and L1A airfoils based on inviscid solution**
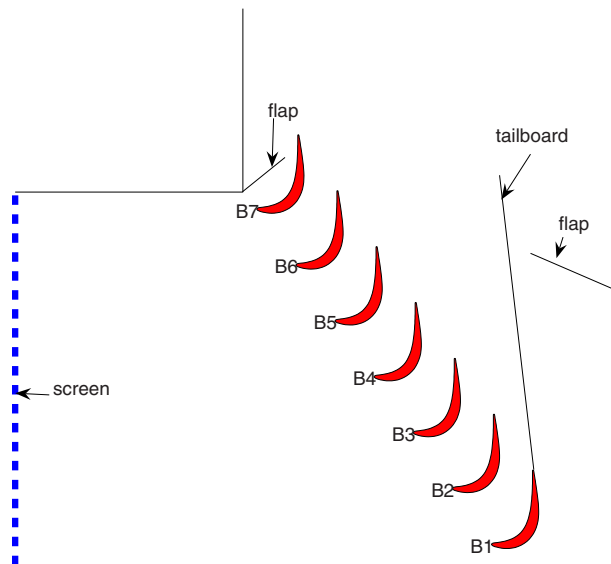
Fig. 3 Schematic of linear cascade

three components was 0.6%. Spectral measurements showed that 80% of the energy in the streamwise fluctuations was due to the unsteadiness at dimensionless frequencies $fL_s/U_e < 2$, where f is the frequency in hertz. Approximately 70% of the energy in the cross stream components was also below this frequency. If the turbulence is high pass filtered to remove this unsteadiness, the streamwise and cross stream component intensities are 0.36% and 0.27%, respectively, for an overall freestream turbulence intensity of 0.3%. The integral length scale of the freestream turbulence is 6.3 cm in the streamwise direction and 6.7 cm in the other directions. While such low freestream turbulence and large length scales are not representative of engine conditions, they are still of interest. In zero or favorable pressure gradient boundary layers, high TI can cause bypass transition, but under adverse pressure gradients, natural transition appears to play a role at all TI levels. Hughes and Walker [31], for example, observed evidence of Tollmien–Schlichting (TS) waves in cases with TI as high as 8%. Volino [14] also saw evidence of TS waves in both high and low TI cases. Low TI cases provide a somewhat simpler environment for explaining the already complex phenomenon of separated flow transition. The present low TI cases will also serve as comparison cases for future work with elevated TI. Higher TI and length scales closer to the boundary layer thickness are expected to hasten the transition process.

The blades in the cascade were machined from high density foam, which has a consistency much like hard wood. The center blade, designated B4 in Fig. 3, contains pressure taps near the spanwise centerline. A tailboard, shown in Fig. 3, was needed to produce the correct exit flow angle from the cascade. Its position was set to produce periodicity at high Reynolds numbers. A tailboard on the opposite side of the cascade and inlet guide vanes were found to be unnecessary. To produce the correct approach flow to the end blades (B1 and B7), the amount of flow escaping around the two ends of the cascade was controlled with the flaps shown in Fig. 3. The flap positions were set using a wool tuft upstream of each blade to check that the incoming flow approached the stagnation points with the correct angle. The inlet

flow angle at the center of the cascade was also checked with a three-hole pressure probe and found to be within 2 deg of the design angle. At high Reynolds numbers, the approach velocity to the middle four passages was measured to be uniform to within 6%, and the difference between any two adjacent passages was within 3%. At low Reynolds numbers, slightly more variation was observed, but the approach velocity to the middle two passages still agreed to within 5%. Good periodicity at high Reynolds numbers was also observed in the exit flow from the cascade, as evidenced by suction side velocity profiles acquired near the trailing edge of blades B2–B6 and by total pressure loss surveys, which are shown below. At low Reynolds numbers, when significant separation bubbles were present, the periodicity was not as good due to the suppression of the separation bubble thickness on the blades closest to the tailboard. This is an unavoidable result when using a finite linear cascade to study separated flow. It is considered acceptable for the present facility, since its intended purpose is for the study of flow control, which if successful should suppress separation on all blades, thereby restoring periodicity even at low Reynolds numbers.

2.1 Measurements. Pressure surveys were made using a pressure transducer (0–870 Pa range Validyne transducer). Stagnation pressure was measured with a pitot tube upstream of the cascade. Static pressure taps were located in the center blade as noted above. The uncertainty in the suction side pressure coefficients was 0.07. Most of this uncertainty was due to the bias error. Stochastic error was minimized by averaging pressure transducer readings over a 10 s period.

A four component traverse with three linear stages and one rotating stage was located in the wind tunnel downstream of the cascade. The traverse produced an acceptably low blockage when it was located at least two axial chord lengths downstream of the cascade. Variations in the wind tunnel velocity were less than 2% as the traverse was moved to various positions. The traverse was used to hold and move probes for velocity and downstream pressure measurements.

Total pressure losses were documented using a Kiel probe traversed across three blade spacings, $0.63C_x$ downstream of the cascade. To compute the mass flow averaged pressure loss, a velocity profile was also acquired along the same line as the total pressure surveys using a single-sensor hot-film probe.

Velocity profiles on the suction surface were measured at the six streamwise stations listed in Table 2. All stations are downstream of the inviscid pressure minimum at $s/L_s = 0.49$. Profiles were measured near the spanwise centerline of the airfoil. Profiles were acquired with a hot-wire anemometer (AA Lab Systems model AN-1003) and a single-sensor hot-film probe (TSI model 1201-20). The sensor diameter is 51 μm, and the active length is 1.02 mm. At each measurement location, data were acquired for 26 s at a 20 kHz sampling rate (2^{19} samples). All raw data were saved. The high sampling rate provides an essentially continuous signal, and the long sampling time results in low uncertainty in both statistical and spectral quantities. Data were acquired at 40 wall normal locations in each profile, extending from the wall to the freestream, with most points concentrated in the near-wall region. The probe was positioned as close to tangent to the airfoil surface as possible at each station, such that the probe body extended downstream of the sensor and the direction of the traverse was within 5 deg of normal to the surface. In most cases the closest point to the wall in each profile was within about 0.2 mm of the wall, which compares to boundary layer thicknesses rang-

Table 2 Velocity profile measurement stations

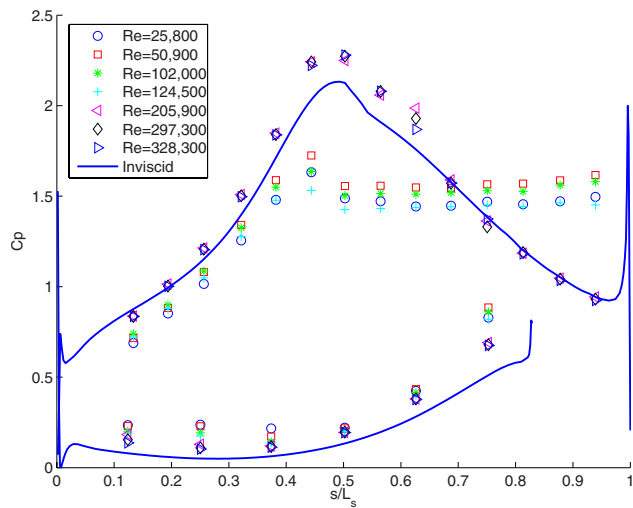| Station	1	2	3	4	5	6
s/L_s	0.53	0.59	0.69	0.78	0.88	0.97
x/C_x	0.65	0.72	0.80	0.86	0.92	0.97

Fig. 4 *Cp* profiles

Fig. 5 Lift based on integrated *Cp* profile

ing from 1.1 mm to over 40 mm.

Flow direction in a separation bubble cannot be determined with a single-sensor hot-wire, but velocity magnitude can be measured and was found to be near zero within the bubbles of the present cases when the flow was laminar. In cases where the flow became turbulent but remained separated, fluctuating velocities caused false high mean velocity readings in the separation bubble. With the exception of these turbulent separated cases, the uncertainty in the mean velocity is 3–5% except in the very near-wall region, where near-wall corrections [32] were applied to the mean velocity. Uncertainties in the momentum and displacement thicknesses computed from the mean profiles are 10%. The uncertainty in the shape factor, H, is 8%. Local skin friction coefficients were computed from the near-wall mean velocity profiles using the technique of Volino and Simon [33]. This technique accounts for streamwise pressure gradient effects on the mean profile. The uncertainty in C_f is 8%. The uncertainty in the fluctuating streamwise velocity is below 10%.

Pressure surveys and velocity profiles were acquired at nominal Re=25,000, 50,000, 100,000, 200,000, 300,000, and 330,000. An additional pressure survey was acquired at Re=125,000. The Reynolds number, as defined above, is based on the suction surface length and the nominal cascade exit velocity. The corresponding Reynolds numbers based on the cascade inlet velocity and the axial chord length ranged from 10,000 to 133,000.

3 Results

3.1 Pressure Profiles. Pressure profiles for all cases are shown in Fig. 4. The inviscid profile for the L1A airfoil is shown for comparison. At the three highest Re, with the exception of a slightly higher suction side peak, the data generally agree with the inviscid profile. This indicates that the boundary layer is attached over most of the airfoil in these cases. Some deviation between the three highest Re cases is visible at s/L_s=0.6 with the *Cp* value rising slightly at the lower Re. This may indicate a small separation bubble at this location. At the three lowest Reynolds numbers, the suction peak is suppressed and the *Cp* values have a constant value on the downstream part of the suction side. This plateau indicates that the boundary layer has separated. The *Cp* values never return to the inviscid line, indicating that the boundary layer never reattaches (i.e., the separation bubble bursts). At Reynolds numbers of 100,000 and below, the separation bubble always appeared to burst. At Re above 150,000 the boundary layer was attached over most of the airfoil. Between Re=100,000 and 150,000 the behavior was less predictable, with some dependence on whether the desired wind tunnel velocity was approached from
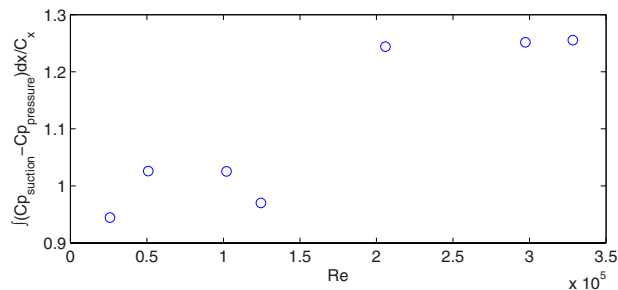
above or below. The Re=124,500 case in Fig. 4 shows the suppressed suction peak and burst bubble of the lower Re cases, but in some trials (not shown) the *Cp* values dropped somewhat from their plateau near the trailing edge.

The pressure side *Cp* values also show some change with Reynolds number. Near the leading edge, *Cp* is higher for the lower Re cases, suggesting more of a leading edge separation bubble. Near the trailing edge the *Cp* values are again higher at the lower Re. This is believed to result when the suction side separation bubble forces fluid toward the pressure side, thereby increasing the pressure side velocity.

The lift on the airfoil can be determined by integrating the difference between the suction and pressure side *Cp* values along the axial direction. The result is shown as a function of Reynolds number in Fig. 5. The lift is about 20% lower for the separated flow cases.

The results in Fig. 4 contrast with the results for the Pack B airfoil presented by Volino [13], Bons et al. [4], Simon et al. [34], and others. With low freestream turbulence, at Re≤50,000 the boundary layer on the Pack B airfoil separated and did not reattach, much like the L1A behavior of the present study. At Re ≥300,000, the boundary layer remained attached over most of the surface, again similar to the L1A behavior shown above. At intermediate Reynolds numbers, however, the Pack B results showed separation with reattachment after a large separation bubble. At Re=100,000, for example, the boundary layer on the Pack B airfoil separated just after the suction peak and did not reattach until near the trailing edge. As Reynolds number increased, the reattachment location gradually moved upstream. The L1A does not show this large separation bubble behavior, instead appearing to switch more abruptly between a nearly fully attached boundary layer and a burst bubble. This will be explored in more detail with the velocity profiles below.

3.2 Total Pressure Losses. The loss coefficient, ψ, is shown for all cases in Fig. 6. The coordinate ϕ indicates the distance in the direction perpendicular to the axial chord. The normalizing quantity L_ϕ is the blade spacing. The origin, $\phi=0$, corresponds to the location directly downstream of the trailing edge of the center blade in the direction of the exit design flow angle. At the two highest Reynolds numbers, the losses are low, and the locations of the loss peaks are in the expected positions downstream of the airfoils. This indicates that the actual flow angle is about equal to the design angle. The peaks downstream of blades B3–B5 are similar to each other, indicating periodicity in the cascade. The loss coefficient is near zero between the peaks. At Re=205,900, the loss coefficients are slightly larger than at the higher Re. Although the difference is within the uncertainty, the trend is consistent with the appearance of a small separation bubble at this Reynolds number, seen in Fig. 4 at s/L_s=0.6. At the lower Reynolds numbers, the burst separation bubble results in much higher losses, and forces the peaks about $0.35L_\phi$ toward the pressure side of each passage. This shift corresponds to a 14 deg change in the exit flow angle. The reduction in flow turning is consistent with
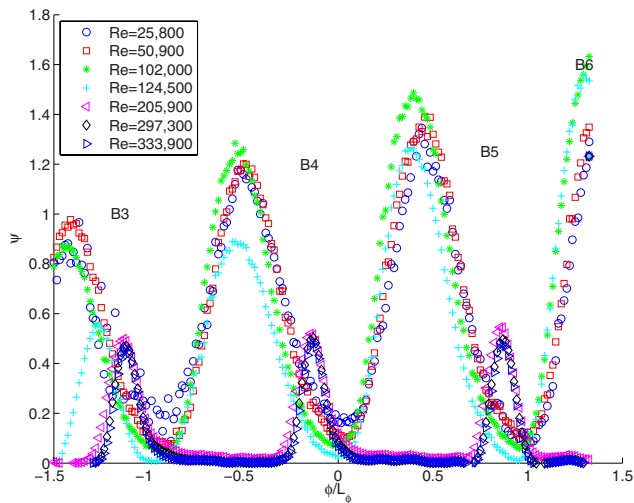
Fig. 6 Total pressure loss coefficient at $0.63C_x$ downstream of cascade

Fig. 8 rms fluctuating streamwise velocity at $0.63C_x$ downstream of cascade

the lower lift shown in Fig. 5. The peaks become noticeably smaller moving from B6 to B3, indicating the effect of the tailboard in reducing the separation bubble thickness.

The integrated loss around the center blade is computed as

$$\psi_{int} = \int_{-L_\phi/2}^{L_\phi/2} \psi U d\phi / \int_{-L_\phi/2}^{L_\phi/2} U d\phi \qquad (2)$$

and is shown in Fig. 7 as a function of Reynolds number. Losses increase with decreasing Re. Between Re=300,000 and 200,000, ψ_{int} increases by 37%, due to the thicker boundary layer at lower Reynolds numbers. The most dramatic increase, however, occurs between the attached and separated flow cases. The integrated loss increases by a factor of 7 between the highest and lowest Reynolds numbers.

The turbulence associated with the airfoil wakes is shown in Fig. 8. The rms fluctuating streamwise velocity at $0.63C_x$ downstream of the trailing edge is normalized on the nominal exit velocity for each case. At the higher Reynolds numbers, the boundary layer turbulence has decayed to about 4% of U_e. A double peak is apparent, with the slightly higher peak resulting from the suction side boundary layer and the smaller peak from the pressure side. Between blades the turbulence intensity is at the background level of the wind tunnel. At the lower Reynolds numbers, the turbulence level is much higher and in agreement with the loss coefficients, the peaks are shifted toward the pressure side of the passages.

3.3 Velocity Profiles. Velocity profiles for the six suction surface measurement stations are shown in Fig. 9 for the nominal Re=25,000 case. The top row in the figure shows the distance
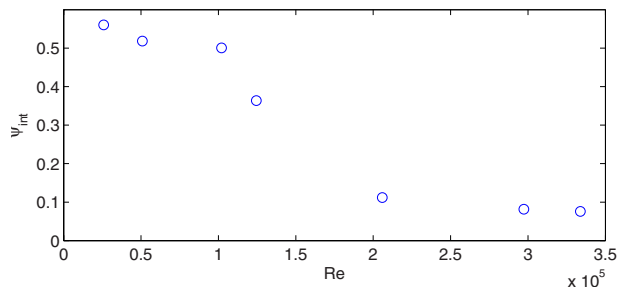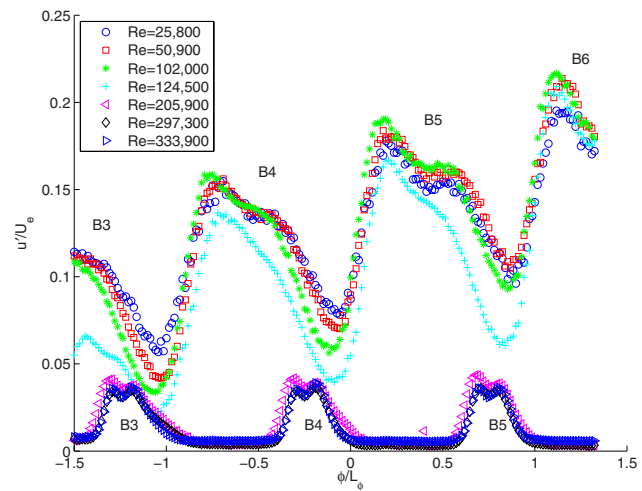
from the wall normalized on the suction surface length plotted against the local mean velocity normalized on the nominal exit velocity, U_e. The boundary layer has just separated at the first measurement station and the separation bubble grows larger at the downstream stations. The boundary layer does not reattach. The second row in Fig. 9 shows the rms streamwise fluctuating velocity, u', normalized with U_e. There is a very large peak located in the shear layer over the separation bubble, which reaches a dimensionless magnitude of about 0.2. The third row in Fig. 9 shows the intermittency, γ. The intermittency is the fraction of time the flow is turbulent. It was determined at each measurement location based on the instantaneous streamwise velocity signal, using the technique described in Ref. [35]. Turbulent flow is defined here to include a range of large and small scale eddies. A boundary layer or shear layer may have significant u' fluctuations but still be considered nonturbulent if these fluctuations are induced by an external source such as freestream turbulence or are associated with instability in a narrow frequency band. Transition to turbulence is characterized by the appearance of broadband fluctuations. In the intermittency processing routine, the velocity signal is high pass filtered, and the appearance of high frequency fluctuations is used to distinguish between turbulent and nonturbulent flows. The results in Fig. 9 indicate that the shear layer remains nonturbulent until the last measurement station, where a small peak indicates the possible beginning of transition.

Figure 10 presents another view of the transition process using the turbulence spectra. The spectra are computed from the fluctuating velocity signal acquired at the location of peak u' at each
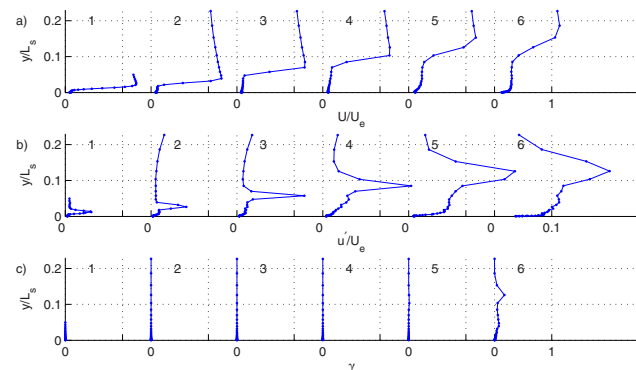

Fig. 7 Integrated total pressure loss coefficient for center blade as function of Re

Fig. 9 Profiles for Re=25,000 case: (*a*) mean velocity, (*b*) u'/U_e, and (*c*) intermittency
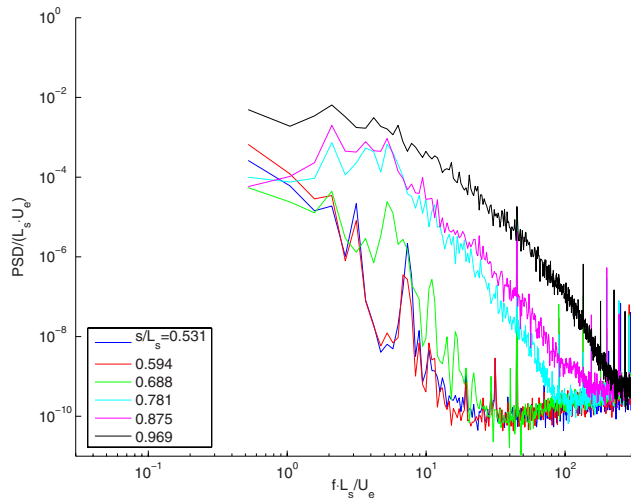
Journal of Turbomachinery

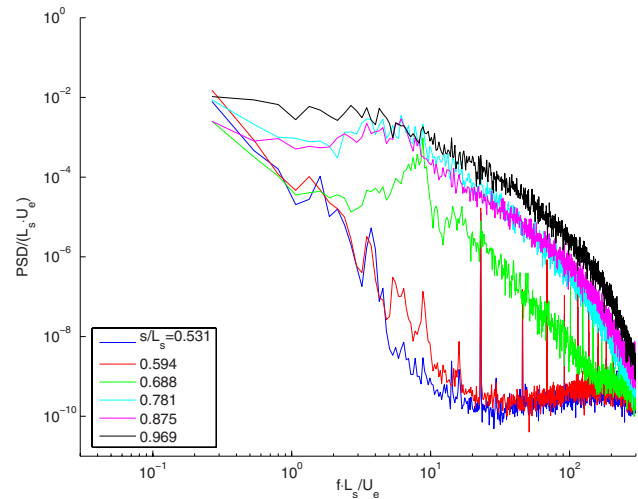Fig. 10 Turbulence spectra for Re=25,000 case

Fig. 12 Turbulence spectra for Re=50,000 case

measurement station shown in Fig. 9. Frequencies are resolved from 4.88 Hz to 10 kHz in 4.88 Hz increments using 4096 point fast Fourier transforms to compute the spectra. The frequencies and power spectral density (PSD) are normalized using L_s and U_e. There is a clear broadband rise in the spectra between the third and fourth measurement stations, and the magnitude continues to rise downstream. The rise indicates that transition may be beginning by the fourth station. The rise in the spectra is not as abrupt as at higher Reynolds numbers (shown below), however, which may indicate that transition is only in its earliest stages. This may explain the intermittency values near zero in Fig. 9.

The velocity profiles for the Re=50,000 case are shown in Fig. 11. The mean and fluctuating velocity show essentially the same behavior observed in the Re=25,000 case of Fig. 9. The boundary layer does not reattach, in agreement with the pressure profile of Fig. 4. The intermittency values rise slightly above zero at the third station and indicate that transition is clearly underway by the fourth station. The corresponding turbulence spectra of Fig. 12 agree, showing a clear rise in the power spectrum between the second and third stations and a further rise to a more turbulent state by the fourth station.

The initiation of transition without boundary layer reattachment shown in Figs. 11 and 12 is markedly different than the behavior observed in previous studies with other LPT airfoils. Volino [13] noted that on the Pack B airfoil, when transition began in the separated shear layer, the associated mixing almost immediately induced boundary layer reattachment. This behavior was utilized by Volino [22] and by Zhang et al. [20], who used small passive

devices on their airfoils to control separation. These devices were too small to trip the boundary layer to turbulent but introduced small disturbances, which accelerated the transition process in the shear layer, thereby moving reattachment upstream. Both Volino [22] and Zhang and Hodson [27] found that these small devices resulted in lower losses than large devices, which immediately tripped the boundary layer to turbulent. The present results suggest that such devices may not work with the L1A airfoil because transition is not sufficient to force reattachment. The strong negative acceleration parameter, shown in Fig. 2, particularly at low Re is apparently strong enough to prevent reattachment of the turbulent shear layer. A comparison of the present results to those of Volino [13] shows that the stronger pressure gradient results in a separation bubble on the L1A that is about four times thicker than that on the Pack B airfoil in terms of y/L_s at a given Reynolds number. When transition occurs, the turbulence in the shear layer is apparently too far from the airfoil to induce enough near-wall mixing to force reattachment. This suggests that transition, whether naturally occurring or induced through flow control, must occur far enough upstream to cause reattachment before the separation bubble becomes too thick.

Figure 13 shows the velocity profiles for the Re=100,000 case. Similar to the previous cases, the separation bubble grows in the streamwise direction, the boundary layer does not reattach, and there is a very high peak in the fluctuating velocity in the shear layer over the separation bubble. The intermittency rises slightly above zero at the second station and indicates fully turbulent flow by the third station, where $\gamma=1$ in the shear layer. As in the
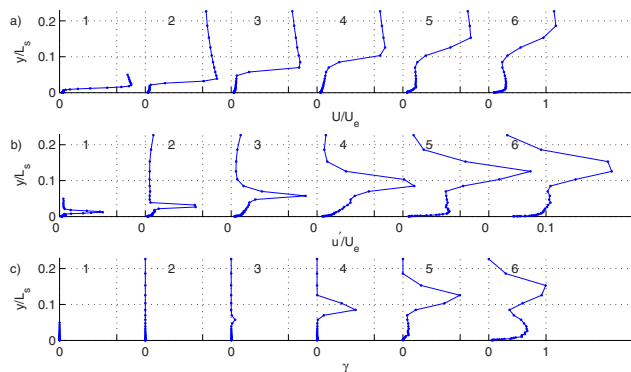

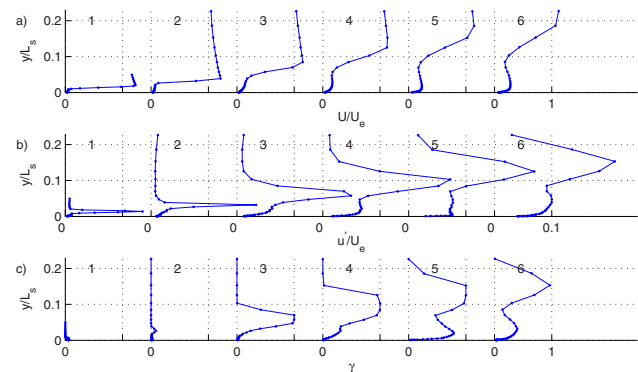Fig. 11 Profiles for Re=50,000 case: (*a*) mean velocity, (*b*) u'/U_e, and (*c*) intermittency

Fig. 13 Profiles for Re=100,000 case: (*a*) mean velocity, (*b*) u'/U_e, and (*c*) intermittency

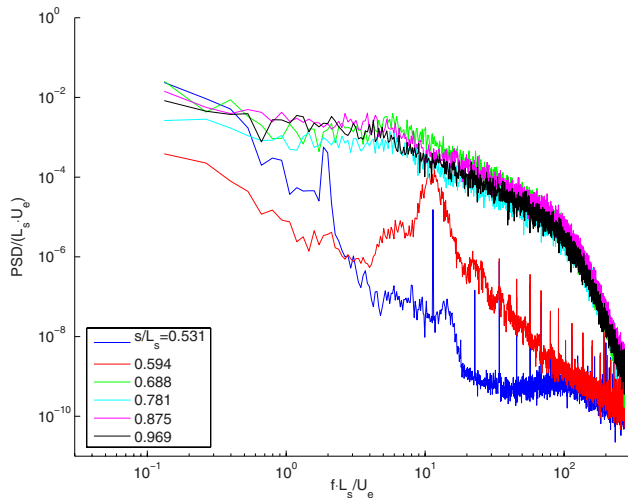Fig. 14 Turbulence spectra for Re=100,000 case

Fig. 16 Turbulence spectra for Re=200,000 case

previous case, the transition is not sufficient to induce boundary layer reattachment. Figure 14 shows the spectra for the Re =100,000 case. There is a clear narrowband rise in the spectrum between the first and second stations, centered about a dimensionless frequency of 12. A further broadband rise occurs by the third station, indicating a turbulent shear layer, in agreement with the intermittency profiles of Fig. 13. The peak at the second station in Fig. 14 indicates a shear layer instability, which likely initiates transition. Similar peaks are visible in the other Reynolds number cases, and will be discussed further below.

Velocity profiles for the Re=200,000 case are shown in Fig. 15. The boundary layer was laminar and on the verge of separation at the first two measurement stations. The small peak in intermittency at the first measurement station is believed to be erroneous, based on the spectra and the zero intermittency measurement at the second station. The skin friction, as determined from the nearwall velocity profile, was near zero at the first two stations, but any separation bubble was very thin. Between the second and third stations, the boundary layer underwent transition. The boundary layer was clearly attached and fully turbulent at the third station and remained attached at all downstream stations, in agreement with the pressure profiles of Fig. 4. The spectra for this case are shown in Fig. 16. The clear jump from laminar to turbulent flow is clear between the second and third stations.

The velocity profiles and spectra for the Re=300,000 case are shown in Figs. 17 and 18. The results are very similar to those of the Re=200,000 case, with transition occurring between the second and third stations, and the boundary layer remaining attached
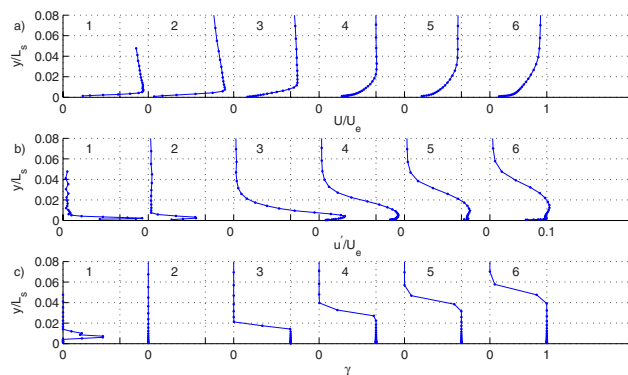
and turbulent downstream.

The shape factor, H, and skin friction coefficient C_f are good indicators of the state of the boundary layer with respect to separation and transition. The shape factor is shown for the high Re cases in Fig. 19. It is between 2.5 and 3.5 at the first two measurement stations, where the boundary layer is laminar and on the verge of separation. It then drops rapidly with the onset of transi-
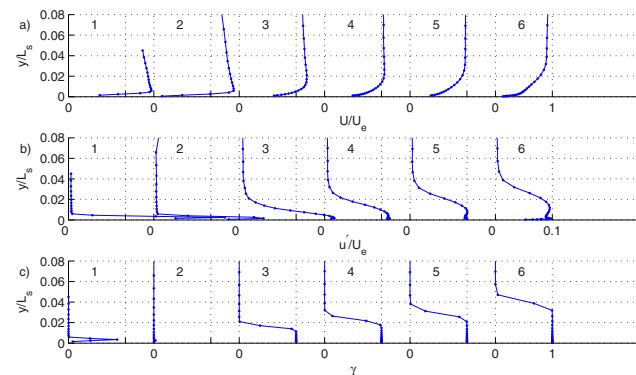

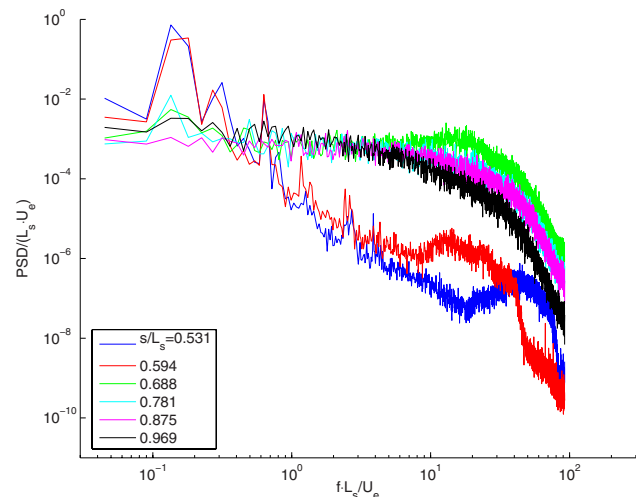Fig. 17 Profiles for Re=300,000 case: (a) mean velocity, (b) u'/U_e, and (c) intermittency
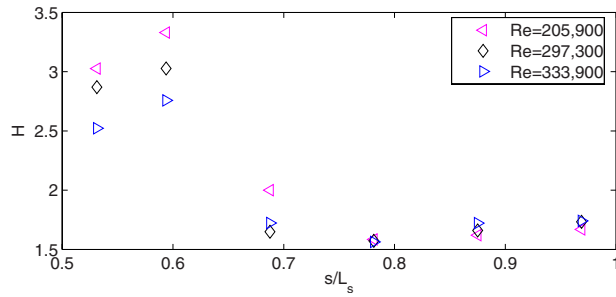

Fig. 18 Turbulence spectra for Re=300,000 case

Fig. 15 Profiles for Re=200,000 case: (a) mean velocity, (b) u'/U_e, and (c) intermittency

Journal of Turbomachinery

Fig. 19 Shape factor for high Re cases

Fig. 21 Frequencies of spectral peaks along with predicted most unstable TS frequencies at separation location

tion, reaching a minimum of about 1.57 at the fourth measurement station. While this value clearly indicates that the boundary layer is attached and turbulent, it is still above the zero pressure gradient turbulent value of about 1.4. At the downstream stations, H begins to rise, and it exceeds 1.7 by the last station. The skin friction coefficient is shown as a function of momentum thickness Reynolds number in Fig. 20. It rises from near zero after transition and decreases in the streamwise direction. Also shown is a standard flat-plate correlation for turbulent boundary layers from Schlichting [36] and the Ludwieg–Tillmann correlation. The present C_f values are as much as 40% lower than the flat-plate correlation and agree well with the Ludwieg–Tillmann correlation. The rising H and low C_f values are indicative of the strong adverse pressure gradient. The corresponding values on the Pack B airfoil [13] were closer to typical zero pressure gradient values, which is consistent with the weaker pressure gradient on the Pack B and the stronger tendency for reattachment at low Re on the Pack B.

3.4 Instability Prediction. The spectral peak noted above at the second station in Fig. 14 suggests an instability in the shear layer that likely initiates transition. Although less distinct, similar peaks are visible just before or just after transition inception at all Reynolds numbers. Volino [14] observed similar peaks in the boundary layer on the Pack B airfoil and associated them with TS waves, using an analysis from Ref. [37]. The TS waves are believed to form in the attached boundary layer between the beginning of the adverse pressure gradient region and the separation location. The TS waves then continued to grow in the separated shear layer until they became large enough to induce transition, as discussed in Ref. [18]. Walker [37] gave the most unstable frequency for TS waves as

$$2\pi\nu f/U_\infty^2 = 3.2\,\mathrm{Re}_{\delta^*}^{-3/2} \tag{3}$$

Hughes and Walker [31] noted that the frequency predicted by Eq. (3) is a function of streamwise position, since the freestream velocity, U_∞, varies in nonzero pressure gradient cases, and the displacement thickness, δ^*, changes as the boundary layer grows. Hence, a single frequency cannot be expected for all TS waves in a boundary layer. For the present study, U_∞ and Re_{δ^*} were taken at
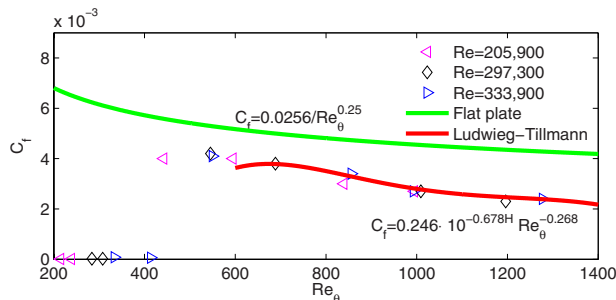

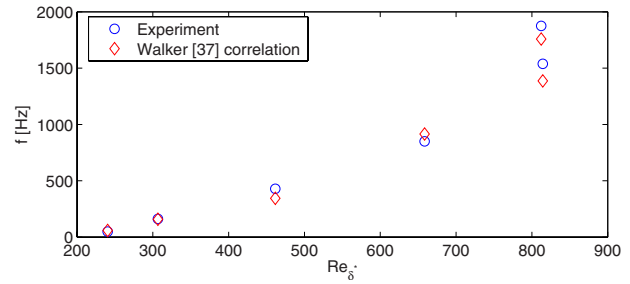**Fig. 20 Skin friction coefficient for high Re cases**

the separation location. The Re_{δ^*} value was estimated with the boundary layer code TEXSTAN [38]. The code was used to compute the laminar suction side boundary layer from the leading edge to the separation point using the pressure gradient from Fig. 4 as input for each case. The code stops when the flow separates, and the separation points computed were in good agreement with the pressure and velocity profiles presented above. Figure 21 shows the peak frequencies extracted from Figs. 10, 12, 14, 16, and 18 along with frequencies predicted by Eq. (3). The good agreement between the experimental and predicted values indicates that TS waves may play a role in the transition. It is also possible that other instability mechanisms are present. Stieger and Hodson [39], and Roberts and Yaras [40], for example, observed Kelvin–Helmholtz rollup of the shear layer.

3.5 Transition Correlations. Several correlations for predicting the starting location for separated flow transition are available in the literature, and some of these are tested below against the present data.

Mayle [2] presented the following correlations for short and long separation bubbles.

$$\mathrm{Re}_{st} = 300\,\mathrm{Re}_{\theta s}^{0.7}\quad\text{short bubble} \tag{4}$$

$$\mathrm{Re}_{st} = 1000\,\mathrm{Re}_{\theta s}^{0.7}\quad\text{long bubble} \tag{5}$$

where Re_{st} is the Reynolds number based on the freestream velocity at separation and the distance from separation to transition start.

The correlation of Davis et al. [16] is

$$\mathrm{Re}_{st} = 25000\,\log_{10}[\coth(0.1732\mathrm{TI})] \tag{6}$$

For the present experiments, TI could reasonably be set between 0.3% and 0.8%, as discussed above. Varying TI within this range does not significantly affect the correlation predictions. For Eq. (6) and all the correlations below, TI was set to 0.5%.

Hatman and Wang [15] identified several transition modes and present correlations for each of them. Their laminar separation mode transition correlation can be cast in terms of Re_{st} as

$$\mathrm{Re}_{st} = 0.0816\,\mathrm{Re}_s + 26805 \tag{7}$$

Yaras [17] proposed

$$\mathrm{Re}_{st} = 0.04\,\mathrm{Re}_s + 6.3\times10^4[1 - \tanh^3(TF')] \tag{8}$$

where $TF' = \max(TF, 1\%)$, and $TF = \mathrm{TI}(s_s/\lambda)^{0.2}$, where s_s is the distance from the leading edge to the separation point and λ is the integral length scale of the freestream turbulence.

Roberts and Yaras [40] presented

$$\mathrm{Re}_{st} = (785 - 30TF)\mathrm{Re}_{\theta s}^{0.7} \tag{9}$$

Praisner and Clark [19] presented the correlation

$$\mathrm{Re}_{st} = 173.0\,\mathrm{Re}_s\,\mathrm{Re}_{\theta s}^{-1.227} \tag{10}$$

The above correlations are based on the conditions at the separation location and in some cases the freestream turbulence inten-

Table 3 Conditions at suction peak and separation location based on laminar boundary layer calculation

Re	s_p/L_s	s_s/L_s	$\mathrm{Re}_{\theta p}$	$\mathrm{Re}_{\theta s}$
25,800	0.438	0.496	48	61
50,900	0.438	0.494	68	85
102,000	0.438	0.496	96	122
205,900	0.493	0.538	151	182
297,300	0.493	0.538	182	220
333,900	0.493	0.537	193	231

sity. Volino and Bohl [18] reasoned that instabilities begin to grow when the boundary layer becomes unstable at the start of the adverse pressure gradient region, and presented the following correlation:

$$\mathrm{Re}_{pt} = 8.80[6.37 - \log_{10}(\mathrm{TI}^2)]\mathrm{Re}_{\theta p}^{4/3} \qquad (11)$$

where Re_{pt} is based on the freestream velocity at the suction peak and the distance from the suction peak to the transition start.

The location of the suction peak for each case was taken from the experimental data of Fig. 4. The separation location and the momentum thickness Reynolds numbers at separation, $\mathrm{Re}_{\theta s}$, and at the suction peak, $\mathrm{Re}_{\theta p}$, were taken from the TEXSTAN calculations described above. Equations (4)–(11) were then used to compute s_t, which is defined as the distance from the leading edge to the start of transition. The Reynolds numbers used with the correlations are listed in Table 3. The s_t results are shown as a function of Re in Fig. 22. The experimental transition locations, as determined from Figs. 9–18, are also shown. The uncertainties in the experimental locations, which result from the finite spacing between the measurement stations, are indicated by the error bars in Fig. 22. Values of $s_t/L_s > 1$ in the figure indicate that transition is predicted downstream of the trailing edge of the airfoil.

The Mayle [2] short bubble correlation, which is only intended for separation bubbles that reattach, predicts transition somewhat too far upstream at all Reynolds numbers. For the Re $\geq$ 200,000 cases, all of the other correlations agree with the experimental results. For the lower Re cases, the Roberts and Yaras [40] and Volino and Bohl [18] correlations continue to agree with the experiment, while the other correlations predict transition too far downstream.
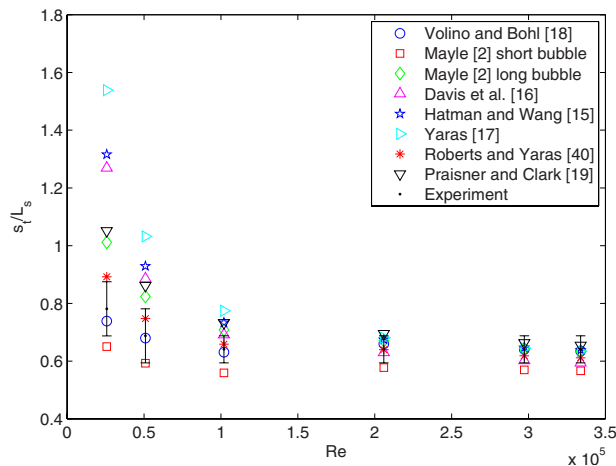
Fig. 22 Predicted and experimental transition start location: error bars indicate uncertainty due to finite spacing of measurement stations

4 Conclusions

The flow over the very high lift L1A airfoil was studied experimentally using a linear cascade. Reynolds numbers based on the suction surface length and nominal exit velocity ranging from 25,000 to 330,000 were considered. In all cases the laminar suction surface boundary layer separated, but at Reynolds numbers greater than 150,000, the separation bubble was very thin and short, and the boundary layer was attached over most of the surface. At lower Reynolds numbers, the boundary layer separated and never reattached. Separation without reattachment caused the lift on the airfoil to decrease by 20% and the total pressure losses increased by a factor of 7 above the highest Reynolds number case. Transition to turbulence occurred in all cases in the shear layer after separation, and appeared to be caused by the growth of Tollmien–Schlichting waves, which originated in the boundary layer upstream of separation. The transition location was well predicted by the correlations of Roberts and Yaras [40] and Volino and Bohl [18]. Transition caused immediate reattachment in the high Reynolds number cases, but the turbulent shear layer remained separated in the low Re cases. This behavior contrasts with previous studies on other LPT airfoils. In those studies, transition immediately triggered reattachment, even at low Reynolds numbers. On the present airfoil, the strong adverse pressure gradient prevents reattachment at low Re, even after transition occurs.

Nomenclature

C_f = skin friction coefficient
Cp = $2(P_T-P)/\rho U_e^2$, pressure coefficient
C_x = axial chord length
f = frequency
H = δ^*/θ, shape factor
K = $(\nu/U_\infty^2)(dU_\infty/ds)$, acceleration parameter
L_s = suction surface length
L_ϕ = blade spacing (pitch)
P = pressure
P_S = upstream static pressure
P_T = upstream stagnation pressure
P_{Te} = downstream stagnation pressure
Re = $U_e L_s/\nu$, exit Reynolds number
Re_{δ^*} = displacement thickness Reynolds number
Re_θ = momentum thickness Reynolds number
s = streamwise coordinate, distance from leading edge
TI = freestream turbulence intensity
U = mean streamwise velocity
U_∞ = local freestream velocity
U_e = nominal exit freestream velocity, based on inviscid solution
u' = time averaged rms streamwise fluctuating velocity
x = axial distance from leading edge
y = distance from wall
Zw = Zweifel coefficient
α_1 = inlet flow angle
α_2 = exit flow angle
δ^* = displacement thickness
ϕ = coordinate along blade spacing, normal to axial chord

γ = intermittency, fraction of time flow is turbulent
ν = kinematic viscosity
ρ = density
θ = momentum thickness
ψ = $(P_T - P_{Te})/(P_T - P_S)$, total pressure loss coefficient
ψ_{int} = total pressure loss integrated over blade spacing

Subscripts

p = pressure minimum (suction peak) location
pt = distance from suction peak to transition start
s = separation location
st = distance from separation location to transition start
∞ = freestream

References

[1] Hourmouziadis, J., 1989, "Aerodynamic Design of Low Pressure Turbines," *AGARD Lecture Series*, Vol. 167, Advisory Group for Aeronautical Research and Development, Paris.

[2] Mayle, R. E., 1991, "The Role of Laminar-Turbulent Transition in Gas Turbine Engines," ASME J. Turbomach., **113**, pp. 509–537.

[3] Sharma, O.P., Ni, R.H., and Tanrikut, S., 1994, "Unsteady Flow in Turbines," *AGARD Lecture Series*, Vol. 195, Advisory Group for Aeronautical Research and Development, Paris, Paper No. 5.

[4] Bons, J. P., Sondergaard, R., and Rivir, R. B., 2001, "Turbine Separation Control Using Pulsed Vortex Generator Jets," ASME J. Turbomach., **123**, pp. 198–206.

[5] Volino, R. J., and Hultgren, L. S., 2001, "Measurements in Separated and Transitional Boundary Layers Under Low-Pressure Turbine Airfoil Conditions," ASME J. Turbomach., **123**, pp. 189–197.

[6] McAuliffe, B.R., and Yaras, M.I., 2007, "Transition Mechanisms in Separation Bubbles Under Low and Elevated Freestream Turbulence," ASME Paper GT2007-27605.

[7] Mahallati, A., McAuliffe, B.R., Sjolander, S.A., and Praisner, T.J., 2007, "Aerodynamics of a Low-Pressure Turbine Airfoil at Low-Reynolds Numbers—Part 1: Steady Flow Measurements," ASME Paper GT2007-27347.

[8] Mahallati, A., and Sjolander, S.A., 2007, "Aerodynamics of a Low-Pressure Turbine Airfoil at Low Reynolds Numbers—Part 2: Blade-Wake Interaction," ASME Paper GT2007-27348.

[9] Zhang, X.F., and Howard Hodson, H., 2007, "Effects of Reynolds Number and Freestream Turbulence Intensity on the Unsteady Boundary Layer Development on an Ultra-High-Lift LPT Airfoil," ASME Paper GT2007-27274.

[10] Uzol, O., Zhang, X.F., Cranstone, A., and Hodson, H., 2007, "Investigation of Unsteady Wake-Separated Boundary Layer Interaction Using Particle-Image-Velocimetry," ASME Paper GT2007-28099.

[11] Opoka, M. M., and Hodson, H. P., 2008, "Transition on the T106 LP Turbine Blade in the Presence of Moving Upstream Wakes and Downstream Potential Fields," ASME J. Turbomach., **130**, p. 041017.

[12] Zoric, T., Popovic, I., Sjolander, S.A., Praisner, T., and Grover, E., 2007, "Comparative Investigation of Three Highly Loaded LP Turbine Airfoils—Part I: Measured Profile and Secondary Losses at Design Incidence," ASME Paper GT2007–27537.

[13] Volino, R. J., 2002, "Separated Flow Transition Under Simulated Low-Pressure Turbine Airfoil Conditions—Part 1: Mean Flow and Turbulence Statistics," ASME J. Turbomach., **124**, pp. 645–655.

[14] Volino, R. J., 2002, "Separated Flow Transition Under Simulated Low-Pressure Turbine Airfoil Conditions—Part 2: Turbulence Spectra," ASME J. Turbomach., **124**, pp. 656–664.

[15] Hatman, A., and Wang, T., 1999, "A Prediction Model for Separated Flow Transition," ASME J. Turbomach., **121**, pp. 594–602.

[16] Davis, R. L., Carter, J. E., and Reshotko, E., 1985, "Analysis of Transitional Separation Bubbles on Infinite Swept Wings," AIAA Paper No. 85-1685.

[17] Yaras, M. I., 2002, "Measurements of the Effects of Freestream Turbulence on Separation-Bubble Transition," ASME Paper GT-2002-30232.

[18] Volino, R.J., and Bohl, D.G., 2004, "Separated Flow Transition Mechanisms and Prediction With High and Low Freestream Turbulence Under Low Pressure Turbine Conditions," ASME Paper GT2004-53360.

[19] Praisner, T. J., and Clark, J. P., 2007, "Predicting Transition in Turbomachinery—Part 1: A Review and New Model Development," ASME J. Turbomach., **129**, pp. 1–13.

[20] Zhang, X. F., Vera, M., Hodson, H., and Harvey, N., 2006, "Separation and Transition Control on an Aft-Loaded Ultra-High-Lift LP Turbine Blade at Low Reynolds Numbers: Low-Speed Investigation," ASME J. Turbomach., **128**, pp. 517–527.

[21] Bohl, D. G., and Volino, R. J., 2006, "Experiments With Three-Dimensional Passive Flow Control Devices on Low-Pressure Turbine Airfoils," ASME J. Turbomach., **128**, pp. 251–260.

[22] Volino, R. J., 2003, "Passive Flow Control on Low-Pressure Turbine Airfoils," ASME J. Turbomach., **125**, pp. 754–764.

[23] Volino, R. J., 2003, "Separation Control on Low-Pressure Turbine Airfoils Using Synthetic Vortex Generator Jets," ASME J. Turbomach., **125**, pp. 765–777.

[24] Huang, J., Corke, T., and Thomas, F., 2003, "Plasma Actuators for Separation Control on Low Pressure Turbine Blades," AIAA Paper No. 2003-1027.

[25] Bons, J.P., Hansen, L.C., Clark, J.P., Koch, P.J., and Sondergaard, R., 2005, "Designing Low-Pressure Turbine Blades With Integrated Flow Control," ASME Paper GT2005-68962.

[26] Clark, J. P., 2007, private communication.

[27] Zhang, X. F., and Hodson, H., 2005, "Combined Effects of Surface Trips and Unsteady Wakes on the Boundary Layer Development of an Ultra-High-Lift LP Turbine Blade," ASME J. Turbomach., **127**, pp. 479–488.

[28] Lakshminarayana, B., 1996, *Fluid Dynamics and Heat Transfer of Turbomachinery*, Wiley, New York.

[29] McAuliffe, B. R., and Sjolander, S. A., 2004, "Active Flow Control Using Steady Blowing for a Low-Pressure Turbine Cascade," ASME J. Turbomach., **126**, pp. 560–569.

[30] Lewis, R. I., 1991, *Vortex Element Methods for Fluid Dynamic Analysis of Engineering Systems*, Cambridge University Press, Cambridge.

[31] Hughes, J. D., and Walker, G. J., 2001, "Natural Transition Phenomena on an Axial Compressor Blade," ASME J. Turbomach., **123**, pp. 392–401.

[32] Wills, J. A. B., 1962, "The Correction of Hot-Wire Readings for Proximity to a Solid Boundary," J. Fluid Mech., **12**, pp. 388–396.

[33] Volino, R. J., and Simon, T. W., 1997, "Velocity and Temperature Profiles in Turbulent Boundary Layers Experiencing Streamwise Pressure Gradients," ASME J. Heat Transfer, **119**, pp. 433–439.

[34] Simon, T. W., Qiu, S., and Yuan, K., 2000, "Measurements in a Transitional Boundary Layer Under Low-Pressure Turbine Conditions," NASA Report No. CR-2000-209957.

[35] Volino, R. J., Schultz, M. P., and Pratt, C. M., 2003, "Conditional Sampling in a Transitional Boundary Layer Under High Free-Stream Turbulence Conditions," ASME J. Fluids Eng., **125**, pp. 28–37.

[36] Schlichting, H., 1979, *Boundary Layer Theory*, 7th ed., McGraw-Hill, New York.

[37] Walker, G. J., 1989, "Transitional Flow on Axial Turbomachine Blading," AIAA J., **27**, pp. 595–602.

[38] Crawford, M.E., and Kays, W.M., 1976, "STAN5—A Program for Numerical Computation of Two-Dimensional Internal and External Boundary Layer Flows," NASA Report No. CR-2742.

[39] Stieger, R. D., and Hodson, H. P., 2004, "The Transition Mechanism of Highly Loaded Low-Pressure Turbine Blades," ASME J. Turbomach., **126**, pp. 536–543.

[40] Roberts, S. K., and Yaras, M. I., 2006, "Effects of Surface-Roughness Geometry on Separation-Bubble Transition," ASME J. Turbomach., **128**, pp. 349–356.

Analytical and Numerical Simulations of the Two-Phase Flow Heat Transfer in the Vent and Scavenge Pipes of the CLEAN Engine Demonstrator

Michael Flouros
MTU Aero Engines,
Dachauer Strasse 665,
80995 Munich, Germany

Advanced aircraft engine development dictates high standards of reliability for the lubrication systems, not only in terms of the proper lubrication of the bearings and the gears, but also in terms of the removal of the large amounts of the generated heat. Heat is introduced both internally through the rotating hardware and externally through radiation, conduction, and convection. In case where the bearing chamber is in close proximity to the engine's hot section, the external heat flux may be significant. This is, for example, the case when oil pipes pass through the turbine struts and vanes on their way to the bearing chamber. There, the thermal impact is extremely high, not only because of the hot turbine gases flowing around the vanes, but also because of the hot cooling air, which is ingested into the vanes. The impact of this excessive heat on the oil may lead to severe engine safety and reliability problems, which can range from oil coking with blockage of the oil tubes to oil fires with loss of part integrity, damage, or even failure of the engine. It is therefore of great importance that the oil system designer is capable of predicting the system's functionality. As part of the European Research program efficient and environmentally friendly aero-engine, the project component validator for environmentally friendly aero-engine (Wilfert, et al., 2005, "CLEAN–Validation of a GTF High Speed Turbine and Integration of Heat Exchanger Technology in an Environmental Friendly Engine Concept," International Symposium on Air Breathing Engines, Paper No. ISABE-2005-1156; Gerlach et al., 2005, "CLEAN–Bench Adaptation and Test for a Complex Demo Engine Concept at ILA Stuttgart," International Symposium on Air Breathing Engines, Paper No. ISABE-2005-1134) was initiated with the goal to develop future engine technologies. Within the scope of this program, MTU Aero Engines has designed the lubrication system and has initiated an investigation of the heat transfer in the scavenge and vent tubes passing through the high thermally loaded turbine center frame (TCF). The objective was to evaluate analytical and numerical models for the heat transfer into the air and oil mixtures and benchmark them. Three analytical models were investigated. A model that was based on the assumption that the flow of air and oil is a homogeneous mixture, which was applied on the scavenge flow. The other two models assumed annular two-phase flows and were applied on the vent flows. Additionally, the two-phase flow in the scavenge and vent pipes was simulated numerically using the ANSYS CFX package. The evaluation of the models was accomplished with test data from the heavily instrumented test engine with special emphasis on the TCF. Both the analytical and the numerical models have demonstrated strengths and weaknesses. The homogeneous flow model correlation and the most recent correlation by Busam for vent flows have demonstrated very good agreement between test and computed results. On the other hand the numerical analysis produced remarkable results, however, at the expense of significant modeling and computing efforts. This particular work is unique compared with published investigations since it was conducted in a real engine environment and not in a simulating rig. Nevertheless, research in two-phase flow heat transfer will continue in order to mitigate any deficiencies and to further improve the correlations and the CFD tools. [DOI: 10.1115/1.3068331]

1 Introduction

Excessive thermal impact on the lubrication system hardware is one of the reasons for severe engine problems such as self-ignition, coking, and premature aging of the oil and also bearing malfunctions. This would disable the proper performance of the system and of the engine in general and could lead to damage with possible in-flight shutdowns and consequently unplanned and expensive shop maintenance. Bearing chambers and oil tubes, which are located in the aft section of the engine, adjacent to the high or the low pressure turbine sections are most frequently affected.

Oil tubes usually pass through struts on their way to the bearing chamber. Scavenge pipes are always connected to the bottom of the chamber whereas vent pipes are in most applications con-
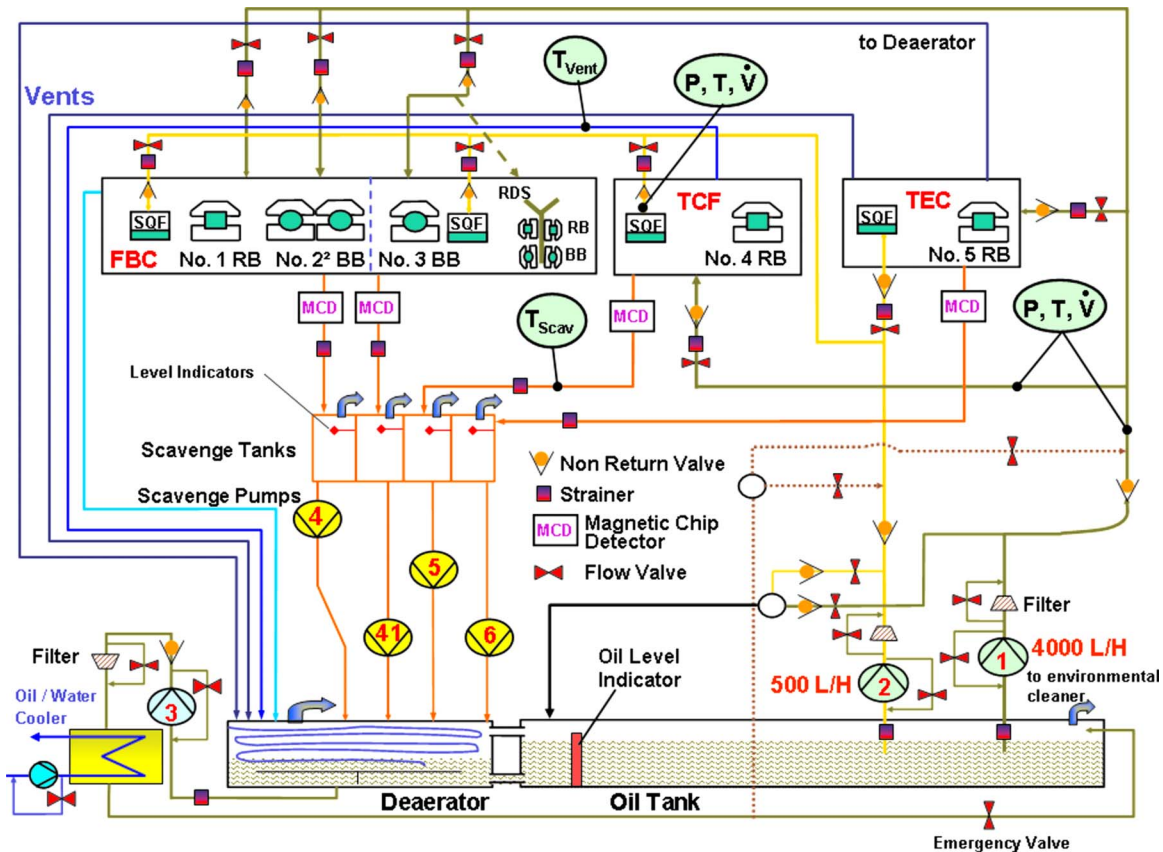
Fig. 1 Diagram showing the CLEAN engine lubrication system

nected to its upper half. The risk of an oil self-ignition in the scavenge or the vent pipes is significant since they transport not only the lubrication oil but also the air, which is used for sealing the bearing chambers. Particularly in the vent pipes the likelihood of oil self-ignition is much higher because of the elevated air-to-oil ratio as compared with the scavenge pipes. On the other hand however, the flow velocity in a scavenge pipe is dictated by the scavenge pump capacity, which leads to much lower air/oil mixture velocities compared with a vent pipe. The likelihood for fire stabilization is there higher. Where possible, vent and scavenge tubes usually are thermally protected by insulation or heat shields. Unfortunately, this may not be always possible because of space and aerodynamic restrictions in the strut design.

The self-ignition of lubrication oil is a very complex process for which there is a wealth of information in the technical literature particularly recommending a review on Refs. [1–3]. Oil self-ignition was recently investigated within the scope of the European Research program ATOS [4]. Research in ATOS had shown that the combination of bearing chamber pressure, droplet size of the oil spray, and aging of the oil considerably influence the self-ignition temperature threshold [3]. Whereas for Mobil Jet II oil (MIL-PRF-23699 standard) the self-ignition temperature at ambient pressure and stoichiometric conditions is about 640 K (367°C) this decreases to below 538 K (265°C) when the pressure is raised and a fine oil spray is present. Mobil Jet II was the oil brand that was used in the component validator for environmentally friendly aero-engine (CLEAN) engine. The gravimetric air-to-oil ratio is defined by Eq. (1) and the stoichiometric value is 0.91. In order to avoid stoichiometric mixtures in bearing chambers and also in order to achieve better engine performance, manufacturers may use seals designed to considerably restrict the amount of the sealing air. Such seals, for example, are carbon or brush seals, which when compared with the most common labyrinth seals allow (provided they do not deteriorate significantly)

less air to flow into the bearing chamber. Nevertheless, it cannot be completely assured that locally in a bearing chamber or in an oil pipe a critical stoichiometric air-to-oil ratio is present.

In order to provide a means of assessing oil fire risk in the vent and the scavenge pipes a heat transfer model was created. This model took into account the heat transfer mechanisms, which affect the fluid temperature in the tubes. These are the thermal radiation from the surroundings, the convective heat transfer from the air, which may flow around the tube, the conduction in the pipe, and of course the internal heat transfer by the air/oil mixture. Three heat transfer (Nusselt-number) correlations for air and oil mixtures were coded: a correlation that was developed by Groothuis and Hendal [5] and was refined by Kudirka et al. [6]. This was used during the CLEAN engine development. The second most recent correlation was developed by Busam [7] in the course of his Ph.D. research. These two correlations have been developed for vertical tubes and upward flow (vent flow). The third correlation has been developed by the author who assumed a homogeneous air and oil mixture flowing with mean physical properties. This has been evaluated for scavenge flows. A description of all three correlations is given in the following pages. Test results from the CLEAN engine have been compared with the analytical results derived herein.

2 Engine Description/Instrumentation

In order to obtain high quality measurements a vast instrumentation scheme was provided to the lubrication system and to the turbine center frame (TCF) as depicted in Figs. 1 and 2. In Fig. 1 the lubrication system is displayed. The system had a main feed pump (1), which supplied oil to the bearings. A second feed pump (2) supplied oil to the squeeze film dampers. The oil flow to the bearings and to the squeeze film dampers was controlled via bypass and control valves.
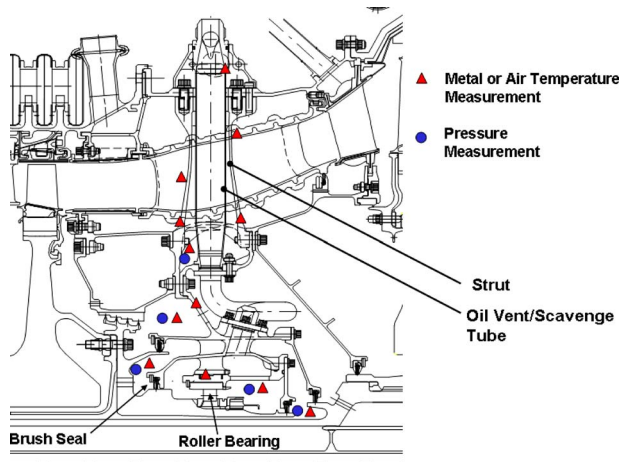
Fig. 2 A schematic of the turbine center frame with instrumentation setup

Fig. 3 A schematic of the secondary air system (SAS) in the TCF. The arrows depict the TCF air flow.

The main oil supply characteristic to the bearing chambers was a linear function of the main shaft speed. The oil was scavenged by four scavenge pumps (4), (41), (5), and (6). A recovery pump (3) pumped the scavenged oil from the deaerator tank (air/oil separator) through the water/oil cooler back into the main oil tank. This pump also served as an emergency pump in the event of a failure of a feed pump. Upstream of the bearing chambers the mass flow rate of the oil supplied to the bearings and to the squeeze film dampers, the oil pressures, and the temperatures were recorded. Downstream of the bearing chambers the vent and scavenge temperatures were recorded. Figure 2 depicts the instrumentation in the TCF with the bearing chamber and the vent or scavenge tubes depending on the angular location. Inside the TCF a vast number of thermocouples at multiple axial and angular locations were used to record metal and air temperatures. Additionally, pressure taps were installed to record the pressure of the air at the locations where the air temperature was measured. Inside the bearing chamber the air/oil mixture temperature and pressure were measured. The bearing outer race temperature was recorded in order to monitor the condition of the roller bearing. This bearing was a main shaft bearing and was designed to run up to maximum speed of 18,700 rpm. The scatter for the oil flow measurement was ±5 l/h and ±1.5% for the air flow. The scatter for the thermocouple temperature measurements in the TCF was ±1.5 K, whereas the scatter for the lube oil temperatures was ±5 K. The accuracy of the pressure measurement was ±0.15%.

In the TCF the air/oil mixture was removed by a scavenge pipe at the bottom and a vent pipe at the top of the bearing chamber. The two pipes were geometrically identical. Their streamline length from inlet A to outlet B (Fig. 3) was about 0.5 m.

The part of the tubes going through the struts had a noncircular cross section of 262 mm^2 whereas for the circular part the cross section was 235 mm^2. The length of the noncircular part was about 0.25 m. The bearing chamber was sealed by metallic brush seals. Figure 3 also shows how the secondary air was delivered. All air flows, pressures, and temperatures were controlled and measured during engine operation. This enabled accurate determination of the external heat transfer coefficients. The highest air/oil temperature was expected in the vent tube at the strut outlet (location T_S) as shown in Fig. 3.

The hot air supply temperature to the LPT (orange color line) was originally designed to rise up to 673 K (400°C) at maximum main shaft speed (100%NH). This requirement was a source of significant concern during engine development, since this might have considerably increased the risk of oil fire in the vent pipe during engine operation. Eventually the maximum engine speed was set at 94%NH. 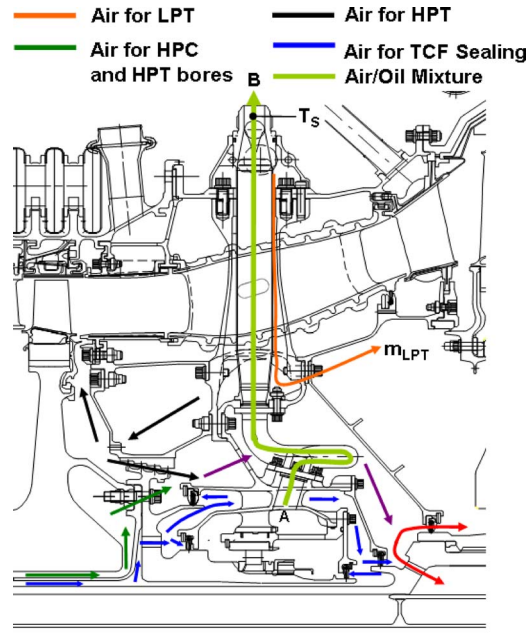Consequently no data measurements exist for the 100%NH speed. Nevertheless a prediction was performed for this speed based on the engine's performance prediction data.

3 Heat Transfer Correlations in Scavenge Pipes Assuming Homogeneous Two-Phase Flow Mixture

The major differences between scavenge and vent pipes are not only the location in the bearing chamber but also the fact that the scavenge pipe is connected to a scavenge pump. The scavenge pump capacity has an impact on the air-to-oil ratio in the tube. Generally the gravimetric air-to-oil ratio X in a scavenge tube is much lower than the ratio in the vent tube (Table 1). The scavenge pump was sized here to transport 2520 l/h of air and oil and was running constantly at this rate. The air and oil supply varied as functions of the NH speed.

The idea behind this model was that air and oil are homogeneously mixed at a low air-to-oil ratio and the resulting fluid has mixed properties. It was conceived based on flow regime findings in both scavenge and vent pipes. These findings were recognized within the scope of the European Research program ATOS [4]. In ATOS two sets of "flowcharts" created by Hewitt and Roberts [8] and Oshinowo and Charles [9], both of which were applicable on vertical two-phase flows in pipes, were successfully used to identify the flow regime present.

The work by Hewitt and Roberts [8] matched two-phase flow in vent pipes whereas the work by Oshinowo and Charles [9] matched scavenge flows. The latter were categorized in the "bubbly film flow" regime. With this in mind, the mixture was assumed to be "homogeneous" and therefore represented as resulting to one single phase with mixed physical properties. The model for scavenge flows described herein has delivered reliable results in other engine programs. The following mixing equations are recommended in Refs. [10] and [11].

For air-to-oil ratio,

$$X = m_{air}/(m_{air} + m_{oil}) \tag{1}$$

For average volume fraction,

$$\alpha = \rho_{oil}X/[\rho_{oil}X + \rho_{air}(1-X)] \tag{2}$$

For mixture density,

$$\rho_m = \rho_{air}\alpha + \rho_{oil}(1-\alpha) \tag{3}$$

Table 1 The selected operating points of the CLEAN engine used in the analysis

	NH (%)	NL (%)	X_{vent} (%)	X_{scav} (%)	P_{chamber} (bar)	$T_{\text{air/oil}}$ (°C)
1	86	91.7	51.5	1.5	1.30	90
2	83	66.7	47	1.9	1.31	84
3	93.7	95.5	64.2	1.3	1.28	102
4	90	87.6	57.3	1.4	1.31	96
5	70.7	25.7	66.1	1.6	1.18	69
6	86.3	96.7	49.6	1.7	1.40	90
7	86.3	72.7	60.9	1.4	1.30	88
8	75.3	41.9	73.9	1.3	1.22	64
9	79.4	53.2	54.2	1.6	1.24	66
10	85.7	98.2	58.2	1.4	1.29	88
11	85.7	30.3	49	1.6	1.35	89
12	92.6	88.6	44	1.6	1.41	97
13	79.4	41.9	52.5	1.7	1.25	68
14	82.8	55.3	49.8	1.6	1.30	85
15	93.2	84.3	53	1.3	1.26	101
16[*]	99	84.3	48.8	1.3	1.48	108

[*]Point 16 (at 100%NH) have been selected from the performance table.

For specific heat capacity of the mixture,

$$c_{\text{pm}} = c_{\text{poil}}(1 - X) + c_{\text{pair}}X \qquad (4)$$

For Reynolds-number of the mixture,

$$\text{Re}_m = (m_{\text{air}} + m_{\text{oil}})D/(\eta_m A) \qquad (5)$$

Collier and Thome [12] recommended for the homogeneous model the following approximation for the mixture dynamic viscosity:

$$1/\eta_m = X/\eta_{\text{air}} + (1 - X)/\eta_{\text{oil}} \qquad (6)$$

and for the thermal conductivity of the mixture Tye [13] recommended

$$\lambda_m = \lambda_{\text{oil}}^{(1-\alpha)}\lambda_{\text{air}}^{\alpha} \qquad (7)$$

and for mixture Prandtl-number,

$$\text{Pr}_m = \eta_m c_{\text{pm}}/\lambda_m \qquad (8)$$

The following Nusselt-number correlations are recommended by Ref. [14]: Laminar flow $\text{Re}_m < 2300$,

$$\text{Nu}_{\text{laminar}} = [(83.326 + (B - 0.6)^3 + C^3)^{1/3}](\text{Pr}_m/\text{Pr}_{mW})^{0.11}$$

with

$$B = 1.953(\text{Re}_m\ \text{Pr}_m\ D/L)^{1/3}$$

and

$$C = 0.924\ \text{Pr}_m^{1/3}(\text{Re}_m\ D/L)^{1/2} \qquad (9)$$

Pr_{mW} is the Prandtl-number of the mixture in the vicinity of the tube's wall.

For flow in the transition regime, $2300 < \text{Re}_m < 10,000$,

$$\text{Nu}_{\text{transition}} = [(1 - \gamma)E + \gamma F](\text{Pr}_m/\text{Pr}_{mW})^{0.11}$$

with

$$\gamma = 1.299 \times 10^{-4}(\text{Re}_m - 2300), \quad E = [83.326 + (G - 0.6)^3 + H^3]^{1/3}$$

$$G = 1.953(2300\ \text{Pr}_m\ D/L)^{1/3}, \quad H = 0.924\ \text{Pr}_m^{1/3}(2300D/L)^{1/2}$$

and

$$F = 38.5\ \text{Pr}_m/[(1 + 0.788(\text{Pr}_m^{2/3} - 1)\ ][1 + (D/L)^{2/3}] \qquad (10)$$

For turbulent flow $\text{Re}_m > 10,000$,

$$\text{Nu}_{\text{turbulent}} = \{[(\xi_m/8)\text{Re}_m\ \text{Pr}_m]/(1 + 12.7(\xi_m/8)^{1/2}(\text{Pr}_m^{2/3} - 1))\}$$
$$\times (1 + (D/L)^{2/3})(\text{Pr}_m/\text{Pr}_{mW})^{0.11}$$

with

$$\xi_m = [\ 1.8 \log_{10}(\text{Re}_m) - 1.5)]^{-2} \qquad (11)$$

4 Correlations for Heat Transfer in Vent Pipes Assuming Annular Two-Phase Flow

For the heat transfer analysis in vertical pipes with upward flow two correlations have been considered. The most recent one is from Busam [7] as a result of his Ph.D. research. It was based on rig test results for air and oil flows in a vent pipe. Busam [7] used a bearing chamber facility, which was developed at the University of Karlsruhe (Germany) and was used in several European Research activities with references in numerous technical publications 15–18. This bearing chamber rig had a roller bearing and Mobil Jet II oil was the lubricant. Busam's correlation [7] has not yet been published in the international literature and it appears for the first time with his kind permission

$$\text{Nu} = 0.077(\text{Re}_{\text{air}}^{0.52})(\text{Re}_{\text{oil}}^{0.14}) \qquad (12)$$

This correlation is valid for Reynolds-numbers, which range between 24,400 and 125,100 for the air and between 30 and 400 for the oil. The accuracy of the heat transfer coefficient is given by Busam [7] as ±15%. Busam [7] demonstrated in his work that the flow pattern in the vent is annular.

The second correlation was from Kudirka et al. [6]. This was based on experimental results with air/water and air/gas-oil mixtures and upward flows. They developed the following Nusselt-number correlation based on froth or bubbly slug flow with transition into annular flow

$$\text{Nu} = 125(U_G/U_L)^{0.125}(\eta_{\text{air}}/\eta_{\text{oil}})^{0.6}\ \text{Re}_{\text{oil}}^{0.25}\ \text{Pr}_{\text{oil}}^{1/3}(\eta_{\text{oil}}/\eta_{\text{oilW}})^{0.14} \qquad (13)$$

U_G and U_L are the superficial velocities for air and oil, respectively, and η_{oilW} is the dynamic viscosity of the oil in the vicinity of the tube's wall. This correlation was created for flows up to a combined Reynolds-number ($\text{Re}_{\text{oil}} + \text{Re}_{\text{air}}$) of about 70,000. The accuracy was given within the ±15% range. Kudirka et al. [6] mentioned in their work that maximum heat transfer is achieved when the flow is annular. This correlation yields higher heat transfer coefficients than the Busam correlation [7]. It was used during the early stages of the CLEAN engine development for prediction of the oil and air temperatures in the vent tubes.

5 Means of Analysis

A calculation code was created for performing the analysis. This code incorporated the above mentioned Nusselt-number cor-
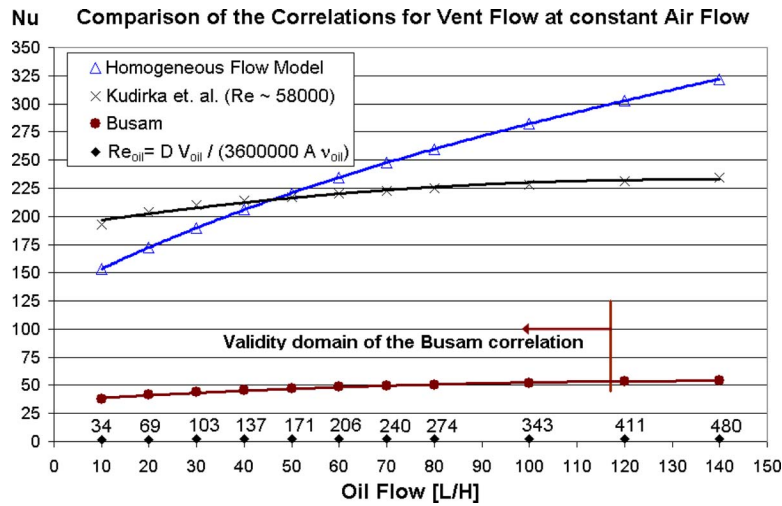
Downloaded 28 May 2010 to 128.113.26.88. Redistribution subject to ASME license or copyright; see http://www.asme.org/terms/Terms_Use.cfm

Fig. 4 Nusselt-number variation as a function of the oil flow at constant air flow (0.02 kg/s)

relations for the two-phase flow heat transfer and also the heat transfer by radiation from the surroundings, convective heat transfer from the hot LPT air, and also conduction through the walls of the pipes. The energy balance equation was

$$Q_{rad} + Q_{conv} = Q_{cond} = Q_{conv\_2ph} \quad (14)$$

Q_{rad} is the radiation heat from the surroundings, Q_{conv} is the convective heat from the air flow around the tube, Q_{cond} is the conduction heat through the pipe walls, and Q_{conv_2ph} is the two-phase flow heat, which is absorbed by the air/oil mixture.

The sealing air mass flow was calculated using brush seal models [19]. The oil distribution in the vent and scavenge pipes was calculated using LUSYS, an MTU internal code, which can calculate flow distribution and pressure drop in secondary air systems by evaluating the hydraulic resistances of the participating components [20]. It is also capable of calculating two-phase flow air and oil pressure drops in pipe work systems using modified Lockhart–Martinelli equations [21]. For the CFD analysis the latest ANSYS CFX code version 11 was used.

6 Results

6.1 Correlation Analysis. A comparison of Nusselt-numbers, obtained using all three correlations (Eqs. (9)–(13)), was performed in order to check for continuity and also to compare the results. A vent flow was assumed and the computations were performed by varying the air flow at constant oil flow and vice versa. The boundary conditions such as oil pipe dimensions, pressure, and temperature for the fluids were the same in all cases. The results of the analysis are depicted in Figs. 4 and 5.

Neither of the correlations showed any discontinuity even though in some cases the results were produced by violating the validity limits of the correlations. The comparison between the Kudirka et al. [6] with the Busam correlation [7] shows similar behavior in terms of rate of change with the Reynolds-number. This behavior seems typical for an annular flow. The Busam correlation [7] simply yields about four times lower Nusselt-numbers and consequently lower heat transfer coefficients. On the contrary, the rate of change in the Nusselt with the Reynolds-number in the
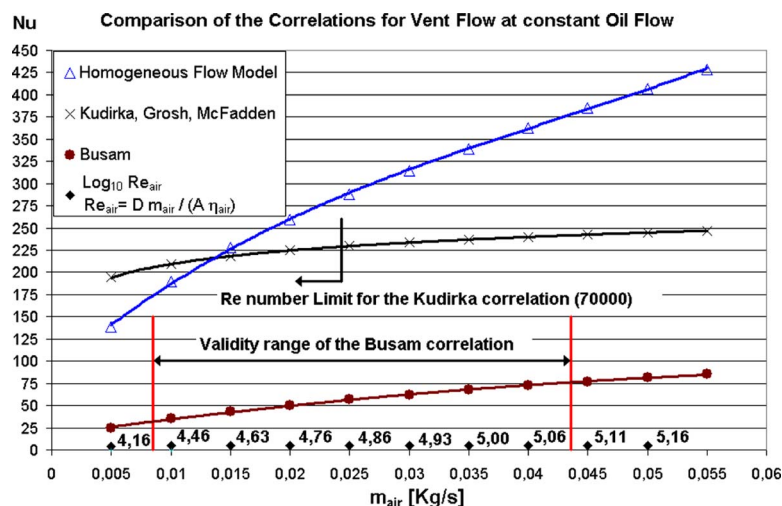
Fig. 5 Nusselt-number variation as a function of the air flow at constant oil flow (80 l/h)

Table 2 The LPT air flow information. Point 16 has been selected from the performance table.

Point	NH (%)	NL (%)	m_{LPT} (kg/s)	P_{air} (bar)	T_{air} (°C)
1	86	91.7	0.0474	1.51	193
2	83	66.7	0.04384	1.28	167
3	93.7	95.5	0.0703	2.41	282
4	90	87,6	0.0724	2.40	266
5	70.7	25,7	0.0272	1.10	106
6	86.3	96,7	0.0513	1.71	223
7	86.3	72.7	0.0478	1.47	195
8	75.3	41.9	0.0328	1.10	116
9	79.4	53.2	0.0386	1.08	145
10	85.7	98.2	0.0485	1.62	216
11	85.7	30.3	0.0502	1.51	193
12	92.6	88.6	0.0534	1.82	285
13	79.4	41.9	0.0387	1.19	150
14	82.8	55.3	0.0437	1.32	168
15	93.2	84.3	0.0732	2.46	296
16	99	84.3	0.08	2.40	400

homogeneous flow correlation shows a completely different behavior. This behavior is typical for the different origin and the different philosophy of this correlation. Therefore, it cannot be recommended for heat transfer calculations when annular flows are involved.

Sixteen operating points representing different cycle conditions of the engine had been selected and evaluated. These are presented in Tables 1 and 2. Operating Point 16 was scaled based on the engine's performance data. No measured data exist for this point.

Figure 6 depicts the results for the vent flow. The measured air/oil temperatures were compared with the computed temperatures using the referenced correlations. These mostly overpredicted the measurements taken. Nevertheless, the Busam correlation [7] has produced the more accurate results.

On average over the 15 performance points this correlation overpredicts the measurements by about 3 K whereas the correlation of Kudirka et al. [6] overpredicts them by about 6 K. Additionally the Busam correlation [7] has computed pipe wall temperatures, which were closer to the measured ones. Table 3 makes a comparison of the external and the internal wall temperatures derived by the two correlations for seven operating points.

The next important question that is raised herein is about the flow regime in the vent pipe. The investigation of flow regimes in oil pipes was recently carried out in the ATOS program [4] and the

method was applied here as well. For the vent pipe flow the Hewitt and Roberts [8] charts were used whereas for the scavenge flow the charts by Oshinowo and Charles [9]. The results for the vent flow are shown in Fig. 7.

All of the 16 operating points are in the "annular flow" domain. For the flow in the scavenge pipe all 16 points are in the domain, which is for a "falling bubbly film" (Fig. 8). The comparison between the measured and the computed fluid temperatures in the scavenge pipe is displayed in Fig. 9. Figure 10 shows how the vent and scavenge flow regimes may look.

The average accuracy of the computed results for the scavenge flow is less than 2 K. The homogeneous mixture correlation seems to adequately meet the requirements toward predicting temperatures in the scavenge pipes.

Of course, the model was based on the assumption that a homogeneous mixture with mean properties is present. This assumption is supported by the fact that the flow regime in the scavenge pipe is a bubbly film. Encouraged by these results, the application of the two-phase flow code was extended on an operating point, which could have been envisioned as the worst case scenario. This operating point was selected from the engine's performance table. It is listed in Tables 1 and 2 as Point 16.

The analysis was performed assuming maximum shaft speed of about 100% combined with maximum LPT air feed temperature
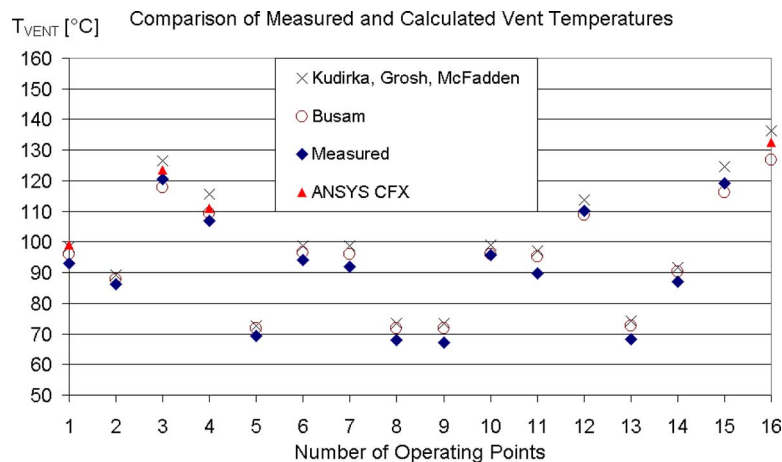

Fig. 6 Measured and calculated air/oil temperatures in the TCF vent pipe. Busam's correlation [7] yields best accuracy to the measurements. The CFD results are in between the results from the correlations.

Table 3 Comparison of the pipe wall temperatures in the vent and scavenge pipes passing through the strut. The numbers in parentheses are for the measured temperatures (vent pipe only).

Point	$T_{\text{pipe wall}}$ according to Busam[a] (°C)	$T_{\text{pipe wall}}$ according to Kudirka et al.[b] (°C)	$T_{\text{pipe wall}}$ according to the homogeneous flow model (°C)
1	136/134 (150)	116/113	145/143
3	216/212 (232)	160/153	244/241
5	83/82 (81)	78/77	88/87
10	141/139 (150)	119/116	151/149
12	183/179 (205)	144/139	193/190
13	102/101 (119)	90/88	116/115
15	208/204 (229)	160/153	211/206
16	263/256	187/175	305/300

[a]Reference [7].
[b]Reference [6].
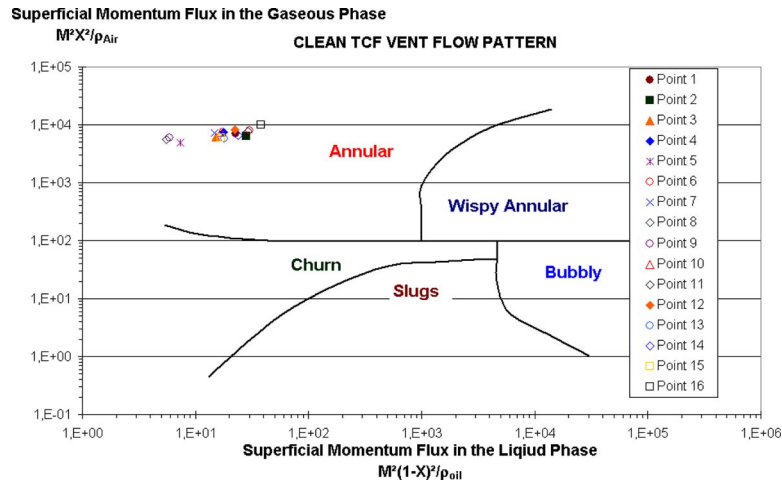
Fig. 7 The vent flow regime according to Hewitt and Roberts [8] is for annular flow. Operating Points 1–16 are given in Tables 1 and 2.
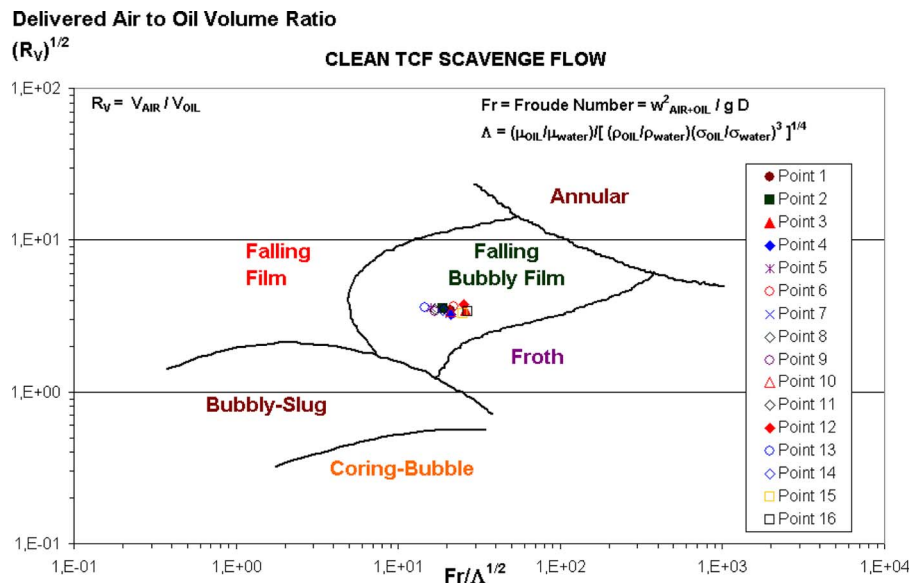
Fig. 8 The scavenge flow regime according to Oshinowo and Charles [9] is a bubbly film
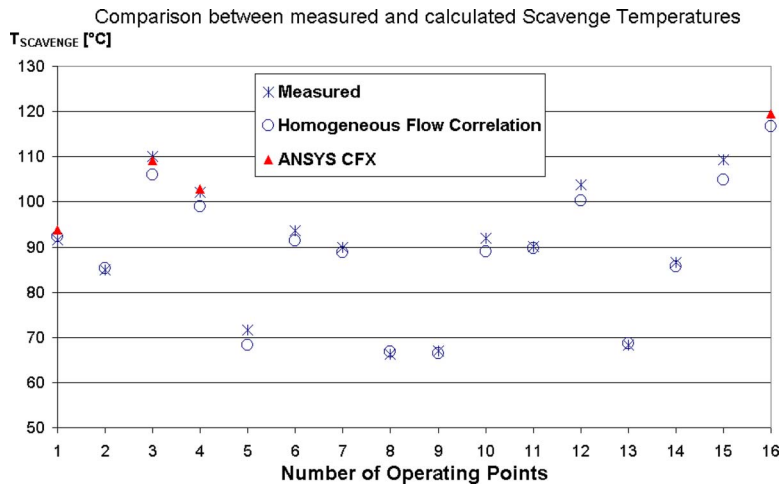
Fig. 9   Very good accuracy between measured and calculated air/oil temperatures in the scavenge pipe

of 673 K (400°C). Since no measured data exist for this case all boundary conditions were derived from the engine's performance table.

Using the flow maps (Figs. 7 and 8), the vent and scavenge flow regimes were predicted in Point 16 as annular and falling bubbly film, respectively. The calculated vent temperatures are depicted in Fig. 6. The temperature difference between the result from the correlation of Kudirka et al. [6] and the result from the Busam correlation [7] is about 10 K, which is the largest deviation of results from these two correlations so far. The calculated scavenge temperature with the homogeneous flow model is depicted in Fig. 9 (highest value in this survey).

In Table 3 the calculated metal temperatures for Point 16 are listed. Based on the results, the internal wall metal temperatures for both the vent and the scavenge pipes are much above the coking temperature, which is approximately 503 K (230°C). This is a risk that the designer should consider in the early stages of the engine development. Mitigation of these risks in a later stage and particularly after the engine is certified can be associated with a high technical effort and a considerable financial burden.

6.2   CFD Modeling and Analysis. The CFD analysis was per-

formed with the commercial code ANSYS CFX version 11. The code is capable of handling two-phase flow problems (bubble flows). An application to annular flows combined with an international publication is not known to the author. For this reason, special emphasis was given to the annular flow simulation.

The geometry of the model was imported into CFX from a CAD model. The mesh was built by 1.7×10^6 hexahedral elements. For the two-phase flow domain, a number of about 300,000 elements were used. The two-phase flow simulation was based on an Eulerian/Eulerian approach. At pipe inlet, the average static pressure (Table 1) was used as a boundary condition. Additionally the volumetric air-to-oil ratio was given. The liquid phase was represented as a continuous phase whereas the gas as the dispersed phase.

At the wall a nonslip boundary condition was used for the liquid phase and a free slip boundary condition was selected for the gas phase. At the outlet the total mass flow rate was given. The flow was simulated as turbulent using the shear stress transport (SST) model. The drag force between the bubbles was considered according to Ishii and Zuber [22] and the particle (bubble) induced turbulence was modeled according to Sato and Sekoguchi
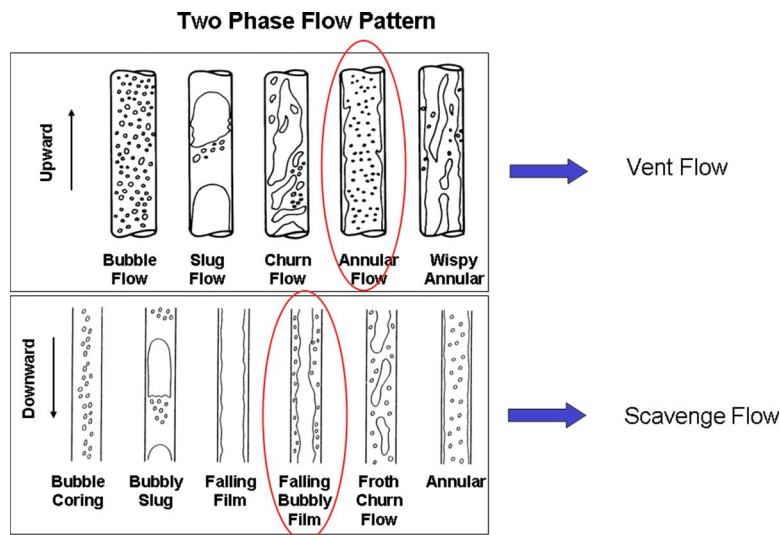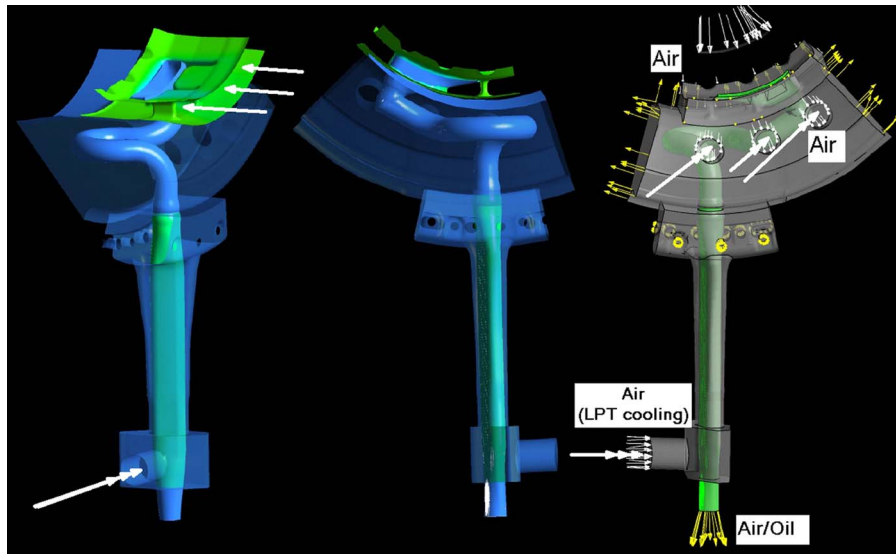

Fig. 10   Vent and scavenge flow regimes (highlighted) as by Hewitt and Roberts [8] (vent) and Oshinowo and Charles [9] (scavenge)

Fig. 11 The CAD model of the scavenge pipe shown in different viewing perspectives. The airstreams around the pipe are indicated.

[23]. The gravitation vector was acting in the flow direction in the case of the scavenge flow and against the flow direction in the case of the vent flow. The computation was performed on a Linux cluster with the use of 12 processors. The computation time was over 2000 CPU hours for a vent flow and about 400 CPU hours for a scavenge flow. Due to the high computational effort only four engine performance points could be computed. These were Points 1, 3, 4, and 16 (Tables 1 and 2).

The CFD analysis focused on the following investigations:

(1) oil and air flow regimes
(2) mixture temperatures at the pipe outlet
(3) pipe wall temperature distributions
(4) worst case scenario (Point 16)

In Fig. 3 the air supply system was depicted. Figure 11 shows the modeling domain with the scavenge pipe and also its surroundings. The inflows (white arrows) and the outflows (yellow arrows) of the different fluid streams in the domain are shown.

For conducting the CFD simulation, the volumetric and not the gravimetric oil-to-air ratio was used. This is defined as $X_v = V_{oil}/(V_{air}+V_{oil})$ where V_{oil} and V_{air} are the volumetric flow rates for oil and air, respectively. In the case of the gravimetric air-to-oil ratio, according to Eq. (1), the stoichiometric value is 0.91.

Using the volumetric ratio X_v, Eq. (1) can be written as

$$X = \rho_{air}/[\rho_{air} + \rho_{oil}X_v/(1 - X_v)] \tag{15}$$

The results of the numerical analysis for the *scavenge flow* are as follows.

(1) Figure 12 shows for Point 3 the oil volume fraction in the vicinity of the inner wall of the tube. A high oil volume fraction indicates high oil concentration with the air entrainment increasing when the colors change from red to navy blue. Based on experience from former research and technology programs the oil moves in circular scavenge pipes outwards toward the long arc of the bend. Perspectives (*a*) and (*b*) show that the oil indeed flows radially outwards along the long arcs (red areas). On the contrary no experimental experience is available on the flow transitioning from the circular into the noncircular region.

Perspectives (*c*) and (*d*) show that the oil covers one side of the noncircular tube more than the opposite side. The air

concentration increases from the inner wall to the centerline of the tube. This is shown in Fig. 13. Air with an oil volume fraction of approximately 1% (i.e., about 99% air) flows through the core of the tube. For the five marked positions in the selected noncircular cross section the oil volume fractions were calculated. Oil is mostly present on the pipe walls but moving toward the centerline of the tube the oil quantity decreases. The values for the oil fraction become nowhere in the tube 100% (pure oil) or 0% (pure air). Therefore it can be assumed that air is always entrained into the oil, which would result into a flow of a bubbly film.

The CFD simulation was repeated for other operating points as well. Since comparable results were achieved, this increased confidence about the quality of the numerical analysis.

Based on these results further research with special emphasis on the understanding of the flow regime in noncircular tubes will be initiated.

(2) Figure 9 shows that for Points 1, 3, 4, and 16 the CFD calculated fluid temperatures at the tube outlet are in very good agreement with the measured temperatures. Even though only these few performance points were numerically evaluated the accuracy of the results gives confidence about the CFD modeling and the simulation strategy, which was followed. Nevertheless further evaluation will follow.

(3) Contrary to averaged pipe wall temperatures produced by the correlations the CFD modeling calculates a temperature distribution on the entire pipe walls. This enables the localization of possible hot spots. The most critical area for the CLEAN oil system designer was the area of the oil pipe surrounded by the hot strut with hot LPT air flowing in between. Results for this case (Performance Point 3) will be discussed here.

As a consequence of the nonuniform oil flow distribution in the tube (Fig. 12), the temperature distribution on the pipe's wall is also nonuniform. Perspective (*d*) in Fig. 12 shows that the oil fraction there is lower than on the opposite side (perspective (*c*)). In Fig. 14 the left-hand side corresponds to perspective (*d*), whereas the right-hand side corresponds to perspective (*c*).

The temperature level on the side of the pipe visible in
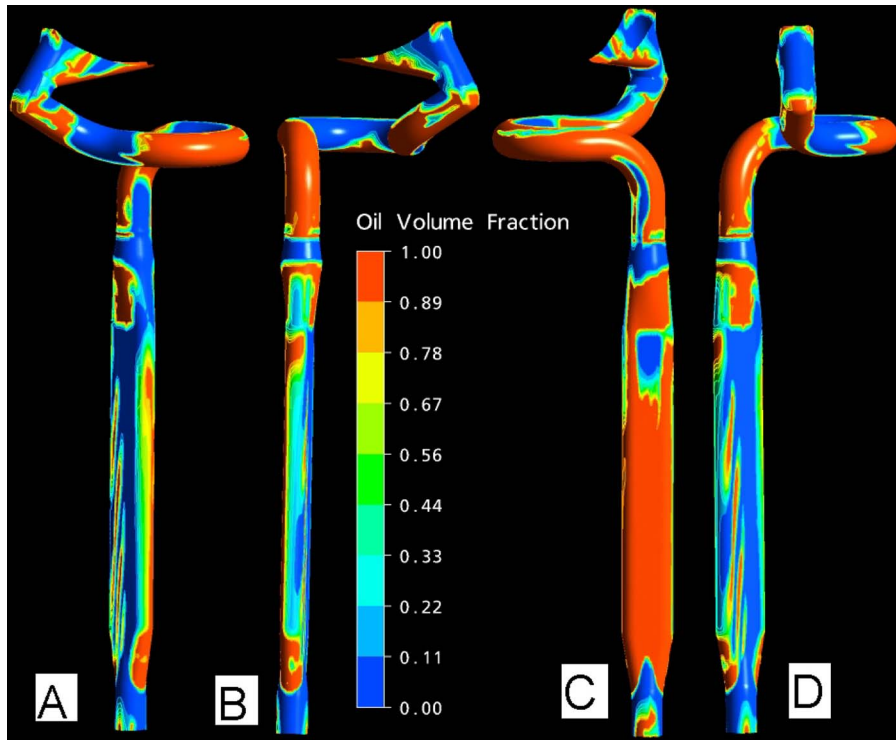
Fig. 12 The oil concentration (volume fraction) in the scavenge pipe from four viewing perspectives. Perspectives (a) and (b) show the oil accumulation along the longest arc in the bends. Perspectives (c) and (d) show the front and rear sides of the noncircular part of the pipe.

perspective (c) is lower than on side (d). Generally, the external metal temperature of the part of the tube, which passes through the hot strut, ranges between 420 K and 490 K.

A hot spot of about 490 K (217°C) has been identified on the pipe. The temperature there is below the ignition temperature of the oil but very close to the oil coking temperature.
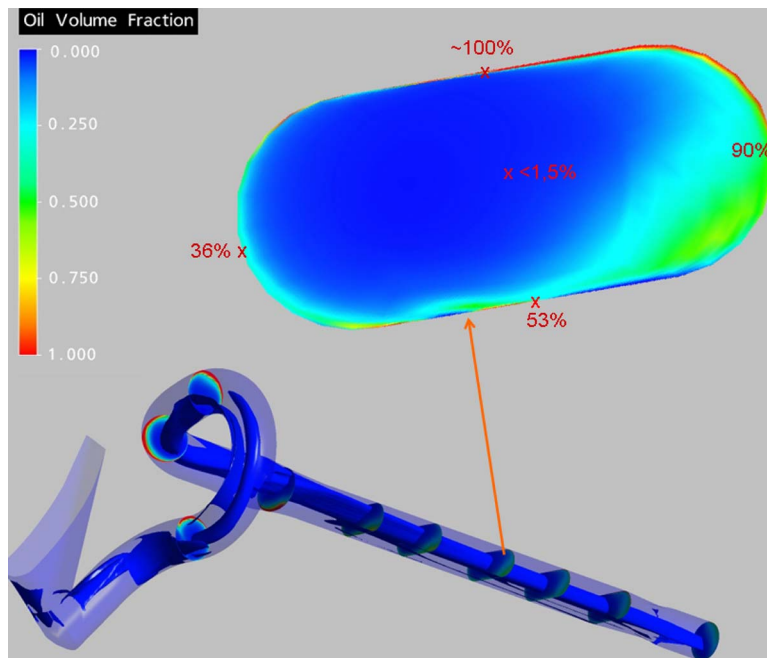
Fig. 13 A domain of almost pure air (~99%) occupies the center of the tube. The oil covers most of the tube's inner walls particularly the arcs in the bends.
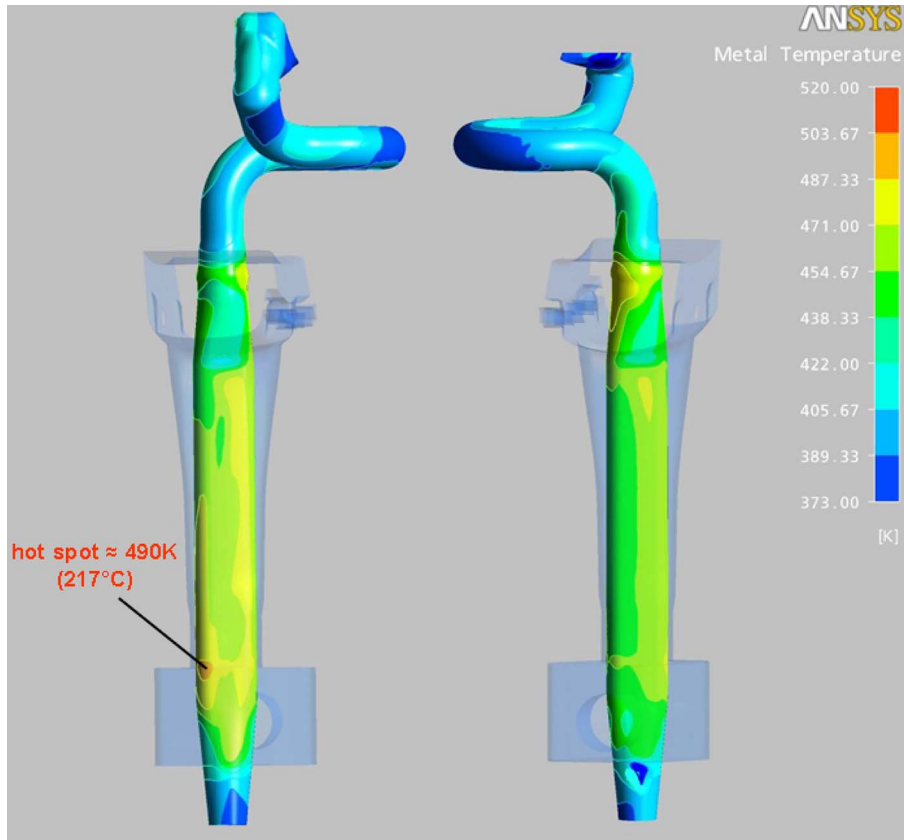
Fig. 14   The metal temperature distribution on the oil scavenge pipe for Performance Point No. 3

(4) The worst case scenario (Point 16) was investigated for the scavenge pipe. This scenario assumed that the temperature of the air around the pipe would rise up to 400°C (673 K). The interesting question in this case will be whether the pipe walls will be at a temperature that means a potential danger for the oil (coking or ignition). Figure 15 shows the oil and the temperature distributions on the tube's walls, respectively (oil distribution: perspectives (*a*) and (*c*); tem-
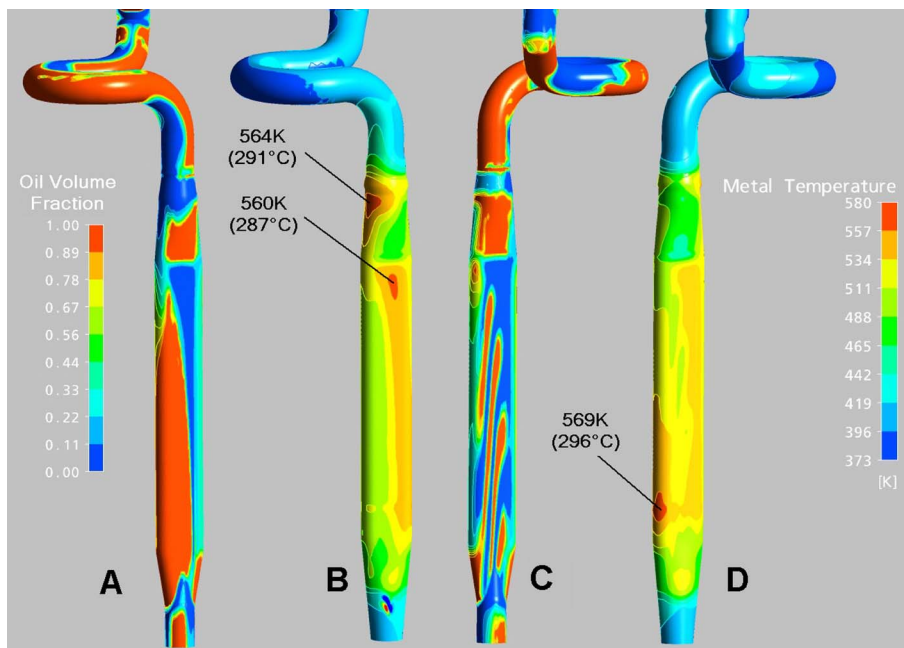
Fig. 15   The oil and temperature distributions on the scavenge pipe's walls at an air temperature around the tube of 400°C (Operation Point No. 16)
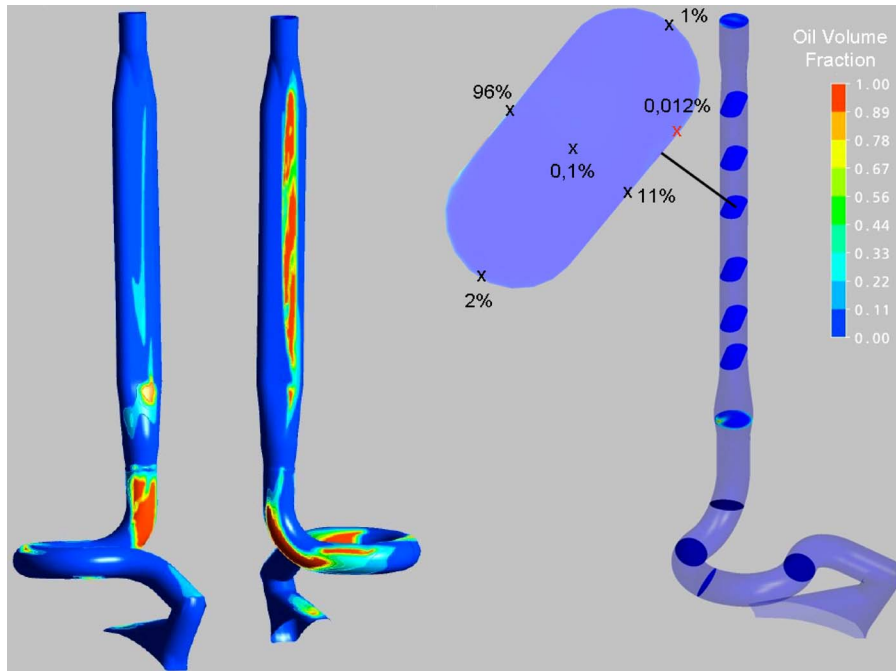
Fig. 16 The oil flow distribution in the vent pipe. In the arc areas the oil moves radially outwards. The core of the tube is almost free of oil.

perature distribution: perspectives (*b*) and (*d*)).

It is noted here that the temperature scale is different compared with the prior figure. Almost the complete surface of the tube part, surrounded by the strut, reaches temperatures above the oil coking temperature. The average external wall temperature in this area is 516 K (243°C). In this figure the colors from yellow to red are for temperatures above 500 K with the maximum temperature being at 569 K (296°C). The inner wall temperature is about 4 K lower. This temperature could cause ignition if locally a stoichiometric air-to-oil ratio was present. Fortunately, this is not the case here. Despite that, this should be forecasted and avoided during the early stages of the engine development.

The fluid temperature at the tube outlet is about 119°C (392 K). A comparison with the value from the homogeneous flow correlation is given in Fig. 9. The difference is about 3 K with ANSYS yielding a slight higher value.

The results of the *vent flow analysis* are as follows.

(1) Figure 16 shows for the Operation Point 3 the oil distribution in the vicinity of the inner wall of the tube. As already observed in the case of the scavenge pipe the oil moves radially outwards when it flows through the bends. Also, the oil is spread more on one side in the noncircular tube section than on the opposite side. The same figure shows the oil distribution in different cross sections. The core of the tube is almost completely oil less. There, the oil volume fraction is less than 0.1%. This implies that only very small droplets of oil are present there and are being swept by the air flow. Oil is only present in the vicinity of the tube's wall. This is the characteristic of the annular flow.

Since in the tube's core mostly air is present, Eq. (15) was used to calculate the air-to-oil ratio *X*. This yields 56.6%, a number well below 91% (the ignition threshold) and provides enough safety margin toward ignition. But, in the same figure, the red marked point indicates a very low volumetric oil concentration in the range of 0.012%. This yields a gravimetric air-to-oil ratio of 92%, which can be

regarded as critical. Nevertheless in this particular case the ignition potential is generally discarded since the wall temperature does not exceed 225°C (Fig. 17).

(2) The CFD analysis was performed for Points 1, 3, 4, and 16
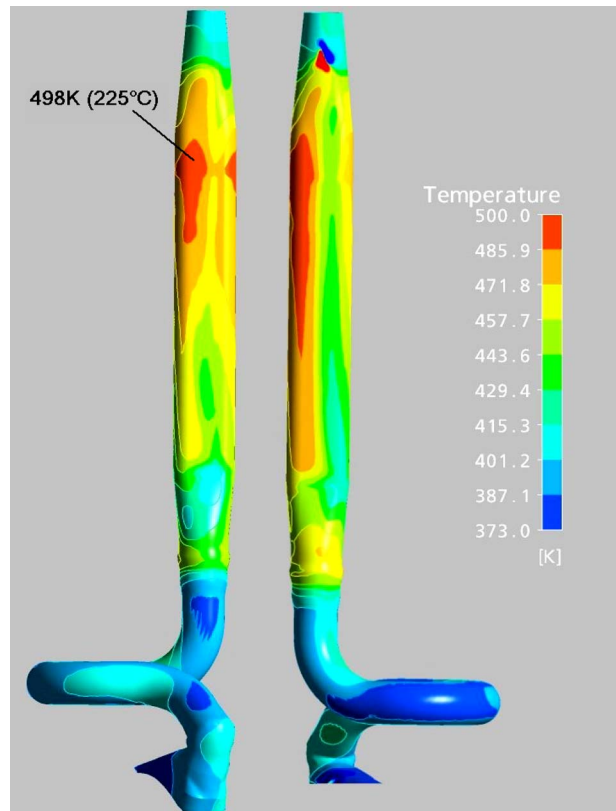
Fig. 17 The temperature distribution on the vent pipe's walls. The hot areas reach temperatures up to 225°C.
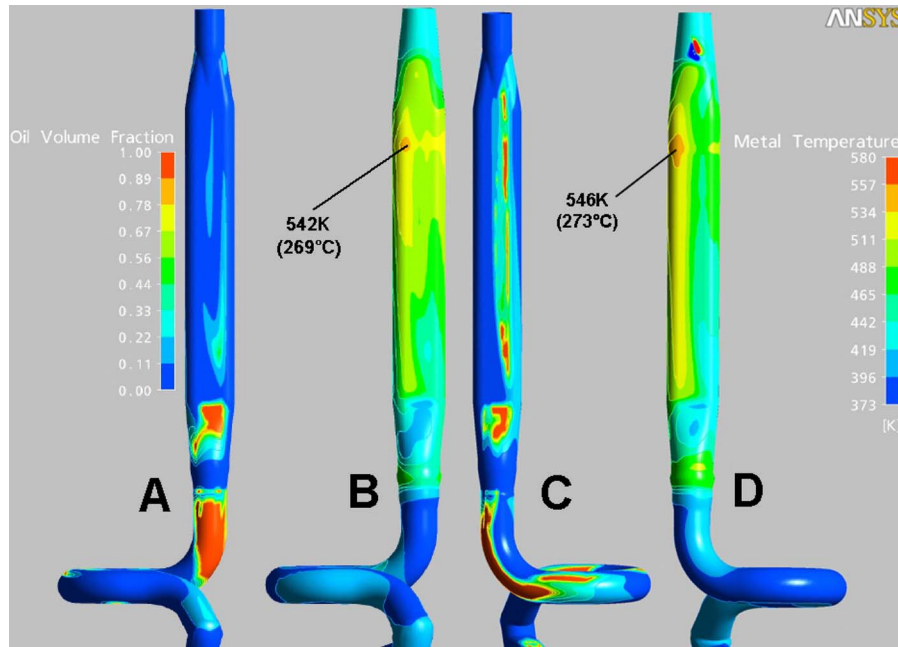
Fig. 18 The oil (*a*) and (*c*) and temperature (*b*) and (*d*) distributions on the vent pipe's walls when the air temperature around the tube is 400 °C (Point 16)

(Fig. 6). The calculated values overpredict the measurements by about 4 K. This provides a sufficient accurate simulation for engineering purposes. Still, further operating points will be simulated next so that more confidence about the quality of the CFD results can be gained.

(3) Figure 17 depicts the temperature distribution on the external pipe walls. In the noncircular part of the tube, which is surrounded by the hot strut, the hot areas (colored red) reach temperatures as high as 498 K. The internal wall temperature there is 496 K. The measured temperature on the vent pipe was 505 K (232 °C), a temperature which is very close to the calculated temperature. The hot areas on the vent pipe are a potential risk for the oil since the temperatures there are very close to the coking temperature of the oil. The range of the calculated external metal temperature on the part of the tube, which passes through the hot strut, is between 408 K and 498 K. In most cases the wall temperature levels in the vent pipe are lower than those on the scavenge pipe since the fluid velocity is much higher. But it was shown before that in the vent pipe locally the gravimetric air-to-oil ratio can be critical. This makes vent pipes potentially running into a higher risk for coking and oil ignition than the scavenge pipes.

(4) The worst case scenario (air at 400 °C around the pipe, Point 16) was investigated here as well. Figure 18 shows the oil and the temperature distribution on the tube's walls. Large sections of the tube's surface, which is surrounded by the strut, are at temperatures above 500 K (yellow and brown areas).

The average metal temperature of this tube section is 478 K (205 °C). The hot spots on the tube are at temperatures of 542 K and 546 K. These could cause ignition, but this scenario is remote since these spots are small and the fluid velocity is high (∼130 m/s) thus stabilization is not possible. The fluid temperature at the tube outlet is about 133 °C (406 K). A comparison with the value from the correlations is given in Fig. 6. The CFD calculated value is between the values from the correlations.

7 Conclusions

As part of the European Research program CLEAN an evaluation was performed of the two-phase flow heat transfer in scavenge and vent pipes passing through the turbine center frame of a real aero-engine. This was accomplished by using heat transfer models from different sources, which can reflect the flow conditions in these pipes. Additionally, the ANSYS CFX code was used in order to perform a CFD analysis. For the first time a vent flow simulation was performed using this tool. The following conclusions can be extracted.

(1) The homogeneous two-phase mixture correlation showed a very good agreement with the engine test results for the scavenge flow. Thus, this correlation can be used in the design of scavenge systems as long as the flow pattern is a bubbly film (Figs. 8 and 10). Other usage restrictions (i.e., specific Reynolds-number limits) have not currently been identified. However, further research is required to prove that this is the case. The CFD analysis of the scavenge flow has also led to accurate results. The fluid temperatures at the pipe outlet were calculated very close to the measured temperatures. The flow distribution in the bends is in agreement with the up to date experimental experience. The flow transition into the noncircular part of the tube is "observed" numerically for the first time. Further experimental investigation will be necessary in the future in order to establish more detailed information.

Depending on the operating condition, hot spots may arise. In the case of pipe transition from circular into noncircular cross section, a nonuniform distribution of the oil on the tube walls takes place. This increases the likelihood for hot spots. Due to the generally low air-to-oil ratio in the scavenge tube the probability of ignition is remote. Nevertheless the recommendation given would be to avoid abrupt bends and transitions since these design forms lead to zones of very low oil concentration with a potential high ignition risk.

Coking cannot be discounted during operation particu-

larly when permanently large areas of the oil tubes are subjected to temperatures over 500 K.

The designer should also focus on properly sizing the oil tubes in order to achieve uniform and thick oil films, which would hinder hot spots. Of course this has to be balanced against the pressure drop in the system.

Major obstacle for using the CFD analysis in complex geometries like in this case is the gigantic simulation and computation effort involved. Despite that, computation of worst case scenarios should be anticipated in order to identify critical hot spots, which may be the source for coking or oil fire.

(2) For the vent flow the correlation by Busam [7] has demonstrated best accuracy to the measured temperatures. Thus, it can be recommended as a reliable tool for calculating these temperatures in a modern turbine engine. Restrictions in using this correlation are given through the Reynolds-numbers for the air and the oil flow. The correlation has not been published in the technical literature so far. The CFD analysis was carried out for the vent flow for only two operating points and the quality of the results gives confidence about the quality of the simulation. The same recommendations given for the scavenge pipe are also valid for the vent pipe as well. Moreover since the vent pipes run hotter than the scavenge pipes and are much more vulnerable to coking or oil ignition, hot shields, insulations, thicker pipe walls, or coatings could inhibit high heat fluxes into the air and oil mixture. The engine designers should always be looking into these issues in the early stages of the engine development process.

8 Outlook

This survey has been a first step toward validation from rig based correlations to a real aero-engine environment. More testing and particularly engine testing will be needed in the future in order to demonstrate whether the derived correlations can be universally used, and reveal any deficiencies, limitations, and restrictions. It would be necessary, for example, to validate the correlations in bearing chambers, which are sealed by labyrinth or carbon seals. Particularly labyrinth seals are the most unrestrictive to the sealing air and may cause the creation of flammable mixtures in the bearing chamber.

In ATOS the use of screens around the bearings leads to reduction in the dwell time of the air/oil mixture in the bearing chamber [24]. Even though this was very effective in terms of reducing the parasitic losses in bearing chambers, it has also led to a considerable reduction in the oil amount leaving through the vent and created flammable mixtures. In a situation like that the designer has to decide between benefits and possible risks.

It is imperative that the conducted research will have to be extended so that the predictions of air and oil temperatures in the scavenge and vent tubes can cover a wide range of applications, hence meeting the future design requirements.

The CFD survey has been very successful with exceptionally accurate results; however, it requires extreme effort and is time consuming, which was the reason that only few points could be evaluated so far. A future follow-up is planned where more operating points will be surveyed.

Acknowledgment

Nomenclature

A = cross section of the tube (m^2)
BB = ball bearing
CAD = computer aided design
CFD = computational fluid dynamics
c_p = specific heat capacity (kJ/kg K)
D = hydraulic diameter (mm)
FBC = front bearing chamber
Fr = Froude number=$W^2_{air+oil}/gD$
g = acceleration of gravity=9.81 (m/s^2)
HPC = high pressure compressor
HPT = high pressure turbine
ID = internal diameter (mm)
L = length of the tube (m)
LPT = low pressure turbine
M = mass flux=m/A (kg/m^2 s)
MCD = magnetic chip detector
m = mass flow rate (kg/s)
NH = high pressure compressor shaft speed (%)
NL = low pressure compressor shaft speed (%)
Nu = Nusselt-number
P = pressure (absolute) (kPa)
Pr = Prandtl-number=$c_p\eta/\lambda$
Q = heat (W)
RB = roller bearing
RDS = radial drive shaft
R_v = V_{air}/V_{oil}=delivered air-to-oil volume ratio
Re = Reynolds-number=UD/ν
SQF = squeeze film damper
T = temperature (°C)
U = velocity (m/s)
V = volume flow (m^3/s)
W = superficial velocity of the fluid (m/s)
X = $m_{air}/(m_{air}+m_{oil})$=air-to-oil ratio (gravimetric)
X_v = $V_{oil}/(V_{air}+V_{oil})$=oil-to-air ratio (volumetric)
α = $\rho_{oil}X/[\rho_{oil}X+\rho_{air}(1-X)]$=average volume fraction
α_H = heat transfer coefficient (W/m^2 K)
η = dynamic viscosity (kg/ms)
λ = thermal conductivity (W/mK)
Λ = $(\mu_{oil}/\mu_{water})/[(\rho_{oil}/\rho_{water})(\sigma_{oil}/\sigma_{water})^3]^{1/4}$
ν = kinematic viscosity (m^2/s)
ρ = density (kg/m^3)
σ = surface tension (N/m)

Subscripts

m = mixture
mW = mixture in the vicinity of the tube's wall

References

[1] Kuchta, J. M., and Cato, R. J., 1968, "Ignition and Flammability Properties of Lubricants," Air Transportation Meeting, Society of Automotive Engineers, New York, Paper No. 680323.
[2] Nigmatulin, B. I., Vasiliev, N. I., and Guguchkin V. V., 1993, "Interaction Between Liquid Droplets and Heated Surface," Waerme- Stoffuebertrag., 28, pp. 313–319.
[3] Willenborg, K., Busam, S., Rosskamp, H., and Wittig, S., 2002, "Experimental Studies of the Boundary Conditions Leading to Oil Fires in Bearing Chambers and in the Secondary Air System of Aero Engines," ASME Paper No. 2002-GT-30241.
[4] Klingsporn, M., 2004, "Advanced Transmission and Oil System Concepts for Modern Aero-Engines," ASME Paper No. GT2004–53578.
[5] Groothuis, H., and Hendal, W. P., 1959, "Heat Transfer in Two-Phase Flow," Chem. Eng. Sci., 11, pp. 212–220.
[6] Kudirka, A. A., Grosh, R. J., and McFadden P. W., 1965, "Heat Transfer in Two-Phase Flow of Gas-Liquid Mixtures," Ind. Eng. Chem. Fundam., 4(3), pp. 339–344.
[7] Busam, S., 2004, "Druckverlust und Wärmeuebergang im Entlueftungssystem von Triebwerkslagerkammern (Pressure Drop and Heat Transfer in the Vent System in an Aero Engine's Bearing Chamber)," Ph.D. thesis, Logos, Berlin.
[8] Hewitt, G. F., and Roberts, D. N., 1969, "Studies of Two-Phase Flow Patterns

by Simultaneous X-Ray and Flash Photography," United Kingdom Atomic Energy Authority Research Group Memorandum, AERE–M 2159.

[9] Oshinowo, T., and Charles, M. E., 1974, "Vertical Two-Phase Flow, Part I. Flow Pattern Correlations," Can. J. Chem. Eng., **52**, pp. 25–35.

[10] Levy, S., 1999, *Two Phase Flow in Complex Systems*, Wiley, Canada, pp. 90–107.

[11] Storek, H., Brauer, H., and Forschungsheft, V. D. I., 1980, *Reibungsdruckverlust der Adiabaten Gas/Fluessig-Keitstroemung in Horizontalen und Vertikalen Rohren*, Vol. 599, VDI, pp. 8–9.

[12] Collier, J. G., and Thome, J. R., 2001, *Convective Boiling and Condensation*, 3rd ed., Oxford University Press, Oxford, p. 44.

[13] Tye, R. P., 1969, *Thermal Conductivity*, Vol. 1, Academic, New York, p. 319.

[14] 1997, *VDI-Waermeatlas*, 8th ed.

[15] Wittig, S., Glahn, A., and Himmelsbach, J., 1994, "Influence of High Rotational Speeds on Heat Transfer and Oil Film Thickness in Aero Engine Bearing Chambers," ASME J. Eng. Gas Turbines Power, **116**, pp. 395–401.

[16] Glahn, A., Busam, S., and Wittig, S., 1997, "Local and Mean Heat Transfer Coefficients Along the Internal Housing Walls of Aero Engine Bearing Chambers," ASME Paper No. 97-GT-261.

[17] Busam, S., Glahn, A., and Wittig, S., 2000, "Internal Bearing Chamber Wall Heat Transfer as a Function of Operating Conditions and Chamber Geometry," ASME J. Eng. Gas Turbines Power, **122**, pp. 314–320.

[18] Gorse, P., Willenborg, K., Busam, S., Ebner, J., Dullenkopf, K., and Wittig, S., 2003, "3D-LDA Measurements in an Aero Engine Bearing Chamber," ASME Paper No. GT2003–38376.

[19] Gail, A., and Beichl, S., 2000, "MTU Brush Seal-Main Features of an Alternative Design," AIAA Paper No. AIAA-2000–3375.

[20] Kutz, K. J., and Speer, T. M., 1992, "Simulation of the Secondary Air System of Aero Engines," ASME Paper No. 92-GT-68.

[21] Lockhart, R. W., and Martinelli, R. C., 1949, "Proposed Correlation for Isothermal Two-Phase, Two-Component Flow in Pipes," Chem. Eng. Prog., **45**, pp. 39–48.

[22] Ishii, M., and Zuber, N., 1979, "Drag Coefficient and Relative Velocity in Bubbly, Droplet or Particulate Flows," AIChE J., **25**(5), pp. 843–855.

[23] Sato, Y., and Sekoguchi, K., 1975, "Liquid Velocity Distribution in Two-Phase Bubble Flow," Int. J. Multiphase Flow, **2**, pp. 79–95.

[24] Flouros, M., 2006, "Reduction of Power Losses in Bearing Chambers Using Porous Screens Surrounding a Ball Bearing," ASME J. Eng. Gas Turbines Power, **128**, pp. 178–182.

Aerothermal Investigation of a Rib-Roughened Trailing Edge Channel With Crossing-Jets— Part I: Flow Field Analysis

Alessandro Armellini[1]
e-mail: alessandro.armellini@uniud.it

Filippo Coletti[2]
e-mail: coletti@vki.ac.be

Tony Arts
e-mail: arts@vki.ac.be

Department of Turbomachinery and Propulsion,
von Karman Institute,
Rhode Saint Genese, 1640, Belgium

Christophe Scholtes
Department of Methods,
Aerothermal Unit,
Snecma,
Groupe Safran,
Reau, 77550, France
e-mail: christophe.scholtes@snecma.fr

The present contribution addresses the aerothermal, experimental, and computational studies of a trapezoidal cross-sectional model simulating a trailing edge cooling cavity with one rib-roughened wall. The flow is fed through tilted slots on one side wall and exits through straight slots on the opposite side wall. The flow field aerodynamics is investigated in Part I of the paper. The reference Reynolds number is defined at the entrance of the test section and set at 67,500 for all the experiments. A qualitative flow model is deduced from surface-streamline flow visualizations. Two-dimensional particle image velocimetry measurements are performed in several planes around midspan of the channel and recombined to visualize and quantify three-dimensional flow features. The crossing-jets issued from the tilted slots are characterized and the jet-rib interaction is analyzed. Attention is drawn to the motion of the flow deflected by the rib-roughened wall and impinging on the opposite smooth wall. The experimental results are compared with the numerical predictions obtained from the finite volume Reynolds-averaged Navier–Stokes solver, CEDRE. [DOI: 10.1115/1.3103929]

1 Introduction

State-of-the-art gas turbine engines are designed to operate at turbine inlet temperatures over 1850 K. Since modern alloys can withstand temperatures of up to about 1350 K, efficient cooling must be applied to the turbine components exposed to the combustion gases. Many cooling schemes are employed in the high pressure stages of the turbine; in general the blade is cooled by a combination of external film cooling, which limits the heat flux from the hot stream, and of internal convection and impingement cooling, which extract the heat from the blade material. In the internal cooling method, air drawn from the compressor is fed through serpentine passages within the airfoil and removes heat by convection. The coolant is then ejected at the blade tip, through trailing edge cooling slots or through film cooling holes on the airfoil surface. The cooling channel walls are most often roughened with turbulators such as ribs, pins, and dimples. These devices enhance the cooling effectiveness by augmenting convective heat transfer and turbulence transport coefficients, besides increasing the surface area for convective heat transfer.

The best schemes provide high cooling effectiveness with minimal coolant mass flow rates and pressure drop penalties. Reviews of mechanisms and performance of heat transfer augmentation techniques were presented by Ligrani et al. [1] and Han et al. [2].

The literature about rib-roughened channels is particularly extensive. Chandra et al. [3] and Han and co-workers [4,5] concluded that geometrical parameters such as passage aspect ratio, blockage ratio, rib angle of attack, reciprocal ribs positioning, rib pitch to height ratio, and rib shape have pronounced effects on

both local and overall heat transfer coefficients. Taslim and Wadsworth [6] stressed the contribution of the on-rib heat transfer coefficient to the total heat transfer.

In standard rib-roughened channels the coolant usually flows along the main channel axis. However, internal forced convection cooling shows its maximum effectiveness when coupled with impingement cooling. The coolant bleeds through parallel cavities via rows of holes through the divider wall; jet arrays are produced and a large heat transfer enhancement is achieved in the impingement regions. Applications of this method to smooth cavities were demonstrated by Florschuetz et al. [7], Bunker and Metzger [8], Cho and Goldstein [9], Huang et al. [10], Pamula et al. [11], and Uysal et al. [12]. The dominant parameters in the system appear to be the jet to cross flow mass flow and momentum ratios, the jet Reynolds number, the pitch to hole diameter ratio, and the jet orientation. Haiping et al. [13], Akella and Han [14], Taslim et al. [15], and Rhee et al. [16] investigated the heat transfer impact of jets impinging on ribbed walls. Besides considerations valid for nonribbed geometries, these authors underlined the influence of parameters such as the relative position of the turbulators to the holes, the rib height to hole diameter ratio, and the heat transfer area increase.

Most of the studies available in literature deal with square or rectangular channels. In reality, the cross section of an internal cooling channel varies depending on its location; the cavity near the leading edge mostly exhibits a triangular cross section, while channels near the trailing edge might also be triangular or trapezoidal. The trailing edge should be as thin as possible for aerodynamical reasons. This is conflicting with the need of integrating internal cooling passages in this area of the blade. Cunha et al. [17] presented analytical models for representative trailing edge configurations and compared performances. Among others, Taslim et al. [18] and Kiml et al. [19] also investigated rib-roughened trailing edge cooling cavities. However, to the present authors' best knowledge, the only case resembling the geometry investigated in the present paper was presented by Taslim et al. [20].

None of the abovementioned studies presents a direct combination of flow measurements and heat transfer distributions in the same channel configuration. This is quite unfortunate, as any in-

---

Fig. 1 Test section

Fig. 2 Sketch of the setup
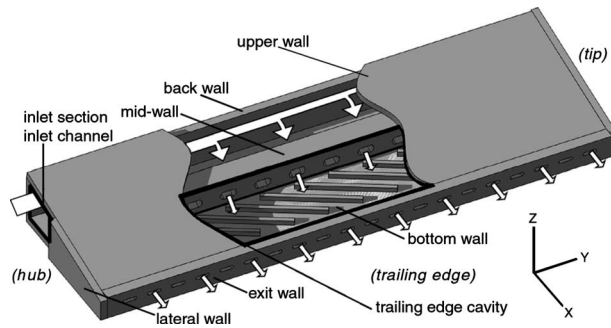
sight on the origin and impact of the fluid motion in the cooling cavities is greatly helpful to the designer. Furthermore, wide and trustworthy experimental databases are necessary to assess the reliability of computational fluid dynamics (CFD) codes in these complicated flow patterns. The strong three-dimensional nature of the flow in ribbed channels and its influence on the heat transfer was highlighted by Çakan [21], Rau et al. [22], and Casarsa and Arts [23] in a single-pass channel, and by Chanteloup et al. [24] in a two-pass channel. Roclawski et al. [25] used highly resolved flow measurements in a ribbed cavity to construct a synthetic velocity model.

The reported investigation addresses experimental and computational studies of a trapezoidal model simulating a ribbed trailing edge cooling cavity, also equipped with slots. High resolution aerodynamic and heat transfer measurements are presented, as well as numerical predictions obtained by means of a Reynolds-averaged Navier–Stokes solver (CEDRE). This work focuses on the effect of the jets impinging on the rib-roughened wall, illustrating the impact of the main flow structures on the heat transfer performance. Part I of the paper describes the test section, the aerodynamic measurements, and the proposed flow model, and compares them with the simulations. Part II of the paper presents the heat transfer coefficient distributions, stressing the link between flow field and thermal patterns, and compares the experimental results with the CFD predictions.

2 Experimental Apparatus and Procedures

2.1 Test Section. The measurement campaign is conducted on a large scale Plexiglas model. It reproduces a trailing edge cooling channel of a turbine blade (Fig. 1).

The model consists of two adjacent trapezoidal cavities separated by a midwall: the first one, the inlet channel, simulates the passage before the trailing edge and has a hydraulic diameter $D_{h,\text{inlet}}=81.4$ mm; and the second one is the trailing edge cavity under investigation. The two cavities are connected by means of a number of racetrack shaped slots with a hydraulic diameter $D_{h,\text{mid}}=21.9$ mm; these midwall slots have axes sloped down with an angle close to 30 deg with respect to the horizontal direction, in such a way that the issued crossing-jets impinge on the bottom wall of the trailing edge cavity. The midwall slots present an aspect ratio AR_{mid} of about 0.5 and their length is about twice their hydraulic diameter.

In the rib-roughened configuration the bottom wall of the trailing edge cavity is equipped with squared cross-sectional ribs. These obstacles are inclined at 30 deg with respect to the main axis of the channel (y-direction), their pitch is 7.5 rib heights and they present a mean blockage ratio of 0.3.

The flow exits the channel through a number of horizontal racetrack shaped slots with a hydraulic diameter $D_{h,\text{exit}}=11.7$ mm, their aspect ratio AR_{exit} is almost 0.2 and their length is about twice their hydraulic diameter.

The experimental setup is sketched in Fig. 2. The air flow is regulated by an upstream centrifugal blower discharging in a set-
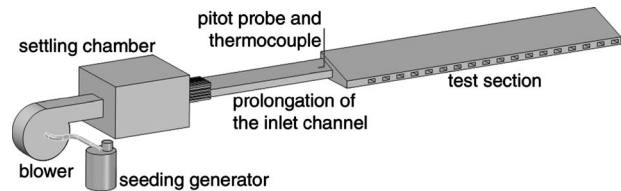
tling chamber. The latter is connected to the test section via prolongation of the inlet channel, as long as the test section itself.

2.2 Operating Conditions. The operating conditions are monitored in the inlet section (Fig. 1) by static pressure taps, a traversing Pitot probe, and one in-flow calibrated K-type thermocouple. All experiments are conducted at a fixed Reynolds number equal to 67,500. This reference Reynolds number is defined in the inlet section and is based on the hydraulic diameter $D_{h,\text{inlet}}$, the bulk flow velocity $U_{b,\text{inlet}}$, and the local fluid properties.

In order to check pressure drop and mass flow distributions across the various slots, static pressure taps are installed in each midwall and exit slots. The pressure penalty induced by the ribs results in a 4% increase in the friction factor with respect to the no-rib configuration. Considering this particular geometry and the present Reynolds number, the friction factor seems to be the most appropriate to characterize the channel performance rather than conventional geometrical parameters such as the blockage ratio. The outlet conditions are quantified by means of a Pitot probe and an in-flow calibrated K-type thermocouple traversing downstream the exit slots.

Reynolds number uncertainty is about 2% with a confidence level of 20:1 and is determined following the approach described by Kline and McClintock [26]. Using the same method, uncertainties of 0.2 K (20:1) are associated with the thermocouple temperature measurements.

As represented in Fig. 1, air enters the trailing edge cavity by slots on the midwall and exits through slots on the opposite wall; the periodical arrangement of slots and ribs gives rise to a periodical flow. This allows concentrating the experimental effort and measurements in the central area of the test section. Flow periodicity is preliminarily checked with various static and total pressure measurements. Apart from side effects due to the proximity to the lateral walls, maximum variations of 6% in inlet channel static pressure, 4% in crossing-jets static pressure, and 6% in exit jet velocity are identified along the channel. Particle image velocimetry (PIV) measurements confirm good flow field periodicity, with variations remaining within the uncertainty associated with the measurement technique. The investigated area can be considered as representative of most of the test section.

2.3 Surface-Streamline Flow Visualizations. In order to gain some insight into the flow field structure, surface-streamline flow visualizations are conducted along the bottom and upper walls of the channel, both for nonribbed and rib-roughened configurations. Two visualization techniques are used: ink dot surface flow visualization and wool tufts surface flow visualization. In the first technique the analogy between the ink streak length and the wall shear stress is exploited; in the second one the direction of the fluttering tufts gives indications about the flow direction. These flow visualizations also help in the choice of the PIV measurement planes.

2.4 Particle Image Velocimetry. The main aerodynamic investigation is performed by means of two-dimensional particle image velocimetry (2D-PIV). The light source is a pulsed Nd-Yag laser (250 mJ/pulse). The images are acquired by a digital camera with a spatial resolution of 1280×868 pixels; couples of images are recorded at a frequency of about 2 Hz with a minimum sepa-
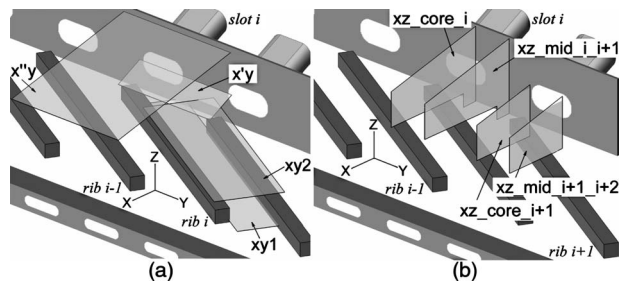
Fig. 3 Overall view of the PIV planes

ration time of 2 μs. The seeding particles (vaporized oil) are produced by a seeding generator directly connected to the intake of the blower and present a diameter of about $1-2$ μm.

The investigated flow field is highly three-dimensional; therefore, high cross-plane velocities can affect the accuracy of the PIV data. Bias due to parallax error is reduced by using long focal length lenses (105 mm). A low amount of nonvalid vectors in the cross-correlation is maintained by choosing small separation time, high image resolution, and correct laser sheet thickness. The PIV data reduction tool is Wi.D.I.M. (Window Displacement Iterative Multigrid). It was developed at the von Karman Institute by Scarano and Riethmuller [27,28]. The resolution of the processed data is about 3 vectors/mm.

The accuracy of the PIV data can be affected by two different kinds of error sources. The first one concerns biases due to incorrect estimation of the magnification factor, stability and accuracy of the trigger signals, velocity lag of tracer particles, optical distortion of the lens system, and cross-plane velocity component. It can be effectively controlled by an accurate choice of the measurement parameters and produces a minimum effect on the mean flow fields. The second type of error sources is associated with the evaluation process of the instantaneous images. These errors are random in nature [29,30] and can be filtered in the averaging process. Therefore, the uncertainty on the mean flow field is purely based on the finite sampling. In the present contribution, the time-averaged quantities are computed on the basis of 1000 samples; the sampling frequency is sufficiently low to consider each realization statistically independent from the others. From the theory of signal analysis, see Ref. [31], the uncertainties in the mean velocities and root mean square (rms) quantities are estimated to be 2% and 5%, respectively, both within a confidence level of 20:1.

PIV is performed in the central area of the test section along eight measurement planes. The position and nomenclature of these planes are provided in Fig. 3: $x'y$ and $x''y$ are two inclined planes, respectively, parallel to the midwall slot axis and parallel and close to the upper wall; $xy1$ and $xy2$ are two horizontal planes placed at, respectively, 0.2 and 1.5 rib heights from the bottom wall. The vertical planes xz are perpendicular to both bottom wall and midwall and are positioned at $\frac{3}{4}$ of the midwall slot width (xz_core_i at slot i, and xz_core_i+1 at slot $i+1$) or in between two successive slots ($xz\_mid\_i\_i+1$ and $xz\_mid\_i+1\_i+2$). The camera optical axis is placed perpendicular to the laser sheet, with optical access from the upper wall or the lateral wall. All the subsequent velocity fields are nondimensionalized by the bulk flow velocity $U_{b,\text{inlet}}$.

3 Flow Field Investigation

3.1 Configuration Without Ribs. The aerothermal investigation of the smooth channel establishes a baseline, which helps determining the impact of the turbulators in the ribbed configuration, i.e., the object of the study. A qualitative model of the flow field is sufficient for the purposes of the present work and is obtained via surface-streamline flow visualizations. The results of the experiments are summarized in Fig. 4 and highlighted the following three main features.

- Tilted crossing-jets issued from the midwall slots impinge on the bottom wall close to the midwall (Fig. 4(a)).
- After the impingement point, adjacent jets interact with each other (Fig. 4(a)), producing an upward jet rebound impacting the upper wall, where the scrubbing action is still remarkable.
- On the exit wall (Fig. 4(b)) quick evaporation and high smearing of ink dots in between the exit slots, as well as the direction of the fluttering tufts, suggest the existence of remarkable impingements on this part of the trailing edge.

This model is consistent with the heat transfer distributions on the upper and bottom walls presented in Part II of the paper [32].

3.2 Configuration With Ribs. The rib-roughened configuration is characterized by means of preliminarily surface flow visualizations along the bottom and upper walls, and PIV measurements in the planes described in Fig. 3. These measurements provide a detailed description of the main flow structures and an aerodynamic characterization to be linked to the thermal analysis described in Part II of the paper [32]. In the following, the experimental results will be commented drawing a detailed description of different flow features such as crossing-jet, inter-rib flow path, jet-rib interaction, and flow close to the upper wall; afterward an overall summary of the mean flow model will be presented.

3.2.1 The Crossing-Jet. The crossing-jet is characterized by

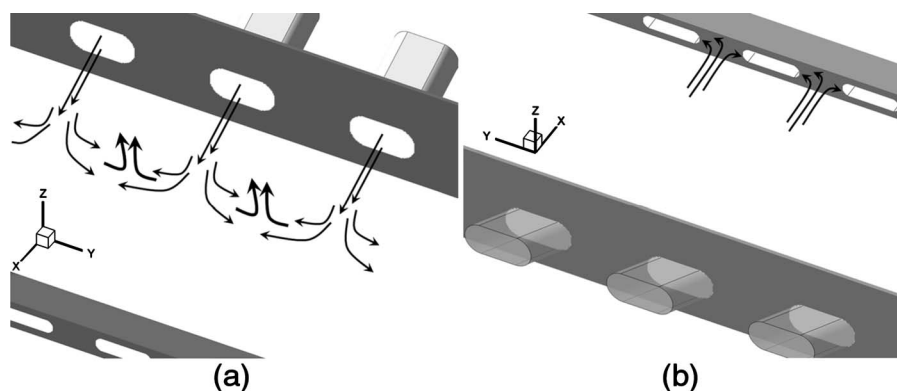
(a)   **(b)**

Fig. 4 Configuration without ribs—Mean flow model obtained by means of surface streamlines flow visualizations: (a) crossing-jets interaction, and (b) impingements at the exit wall
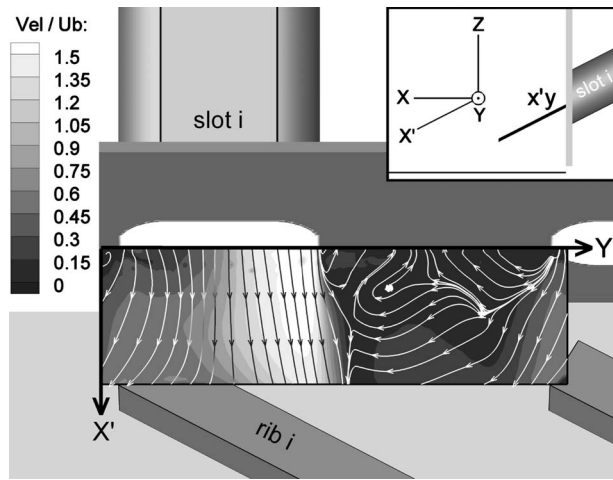
Fig. 5 Modulus of time-averaged in-plane velocity and streamlines path in plane $x'y$

means of PIV in planes $x'y$ and xz_core_i. Contour plots of time-averaged in-plane velocity and streamlines are presented in Figs. 5 and 6. Figure 5 shows the results on plane $x'y$. Both velocity levels and streamlines path highlight an important unbalancing of the crossing-jet; since only a part of the y-momentum initially present in the inlet channel is dissipated through the midwall slot, the jet is mainly present on the right side of the slot span. In order to characterize this feature in detail, data from plane $x'y$ are extracted along a line at 1 rib height from the midwall (Fig. 7). The streamwise velocity peak of the core is found at $Y/s=0.92$ and is 1.5 times higher than the value that it would achieve in the case of a uniform velocity distribution. Both $\sqrt{\overline{u'^2}}$ (fluctuation in x' direction) and $\sqrt{\overline{v^2}}$ are, respectively, 40% and 30% higher on the right side of the jet than on its left side. Based on the peaks of $\sqrt{\overline{u'^2}}$ and $\sqrt{\overline{v^2}}$ the spanwise dimension of the jet is quantified as 45% of the slot span. At both boundaries $\sqrt{\overline{u'^2}}$ is about 30% higher than $\sqrt{\overline{v^2}}$; at $Y/s=0.75$ (position of the vertical plane xz_core_i) the velocity fluctuations have similar intensity in all directions.

Figure 6 shows a three-dimensional view of the PIV results in both planes $x'y$ and xz_core_i. The flow issued by the midwall hole is tilted down with an angle close to the inclination of the slot; the velocity magnitude is evenly distributed in the
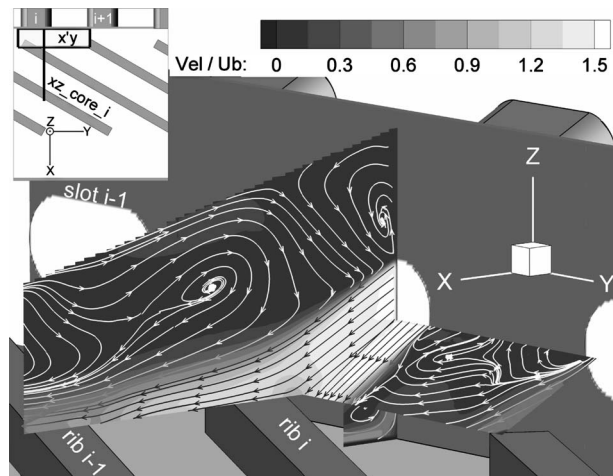
Fig. 6 Modulus of time-averaged in-plane velocity and streamlines path in planes $x'y$ and xz_core_i
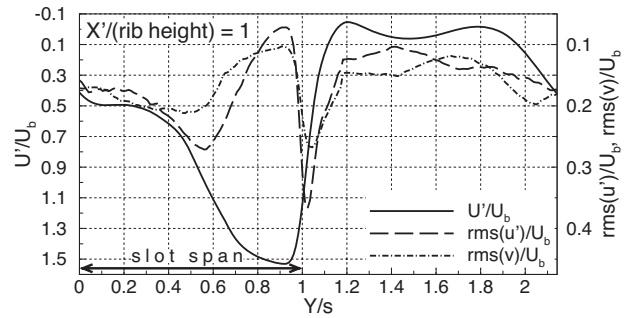
Fig. 7 Time-averaged streamwise velocity and rms of the velocity fluctuations in the crossing-jet

z-direction. The streamlines path highlights that almost half of the jet produced by slot i impinges on rib i and enters the inter-rib area comprised in between rib i and rib $i+1$. The other half partly impinges on rib $i-1$, partly overtakes it, and flows in the x-direction (likely impinging on rib $i-2$). Above the jet the flow is organized in a complex recirculation zone characterized by low in-plane velocity and organized in two different vortical structures. In between these two structures, and at the end of the measurement plane toward the exit wall, two separation points characterized by the downward motion are evident on the upper wall. The description of the flow close to the upper wall is helped by the measurements performed in plane $x''y$, described later.
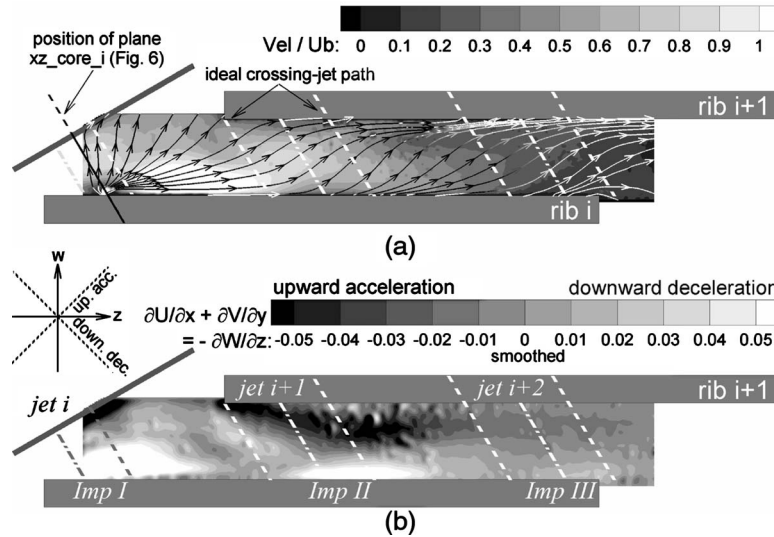
Velocity modulus and streamlines path measured in plane $x'y$ in between two midwall slots (Figs. 5 and 6) suggest that the flow in this area is mainly aligned in z-direction.

3.2.2 The Inter-Rib Area. If the crossing-jet claimed a lot of attention because this is the way the air enters the trailing edge cavity, the inter-rib area, i.e., the part of the test section comprised between two successive ribs, requires a detailed analysis too. This area is, in fact, the most active for the heat transfer performance as evidenced by the thermal analysis presented in Part II of the present contribution [32].

Preliminary surface flow visualizations performed for the rib-roughened configuration suggest the existence of remarkable jet-rib interactions. It has been observed that the tilted crossing-jet produces a strong impingement partially on the first part of the corresponding rib i and partially on the bottom wall. In between the ribs, after the impingement, wool tufts and ink dots show that the jet rebounds toward the adjacent obstacle and then lifts off as an upward structure. This upward deflection is strong enough to produce an impingement on the upper wall.

A refinement of this characterization is performed by means of PIV measurements in a horizontal plane ($xy1$, see Fig. 3(a)) 0.2 rib heights above the bottom wall, between ribs i and $i+1$.

Streamlines path and in-plane time-averaged velocity modulus presented in Fig. 8(a) confirm the presence of a strong impingement on the first part of rib i (Imp I in Fig. 8(b)). As suggested by the measurements performed in plane xz_core_i (Fig. 6), this first impingement is produced by the interaction of jet i with the corresponding rib i. After this source point, PIV data in plane $xy1$ (Fig. 8(a)) show that a part of the flow moves back toward the midwall, the remaining part is guided by the ribs and flows toward the trailing edge. The presence of a second impingement (Imp II in Fig. 8(b)), i.e., the impingement produced by jet $i+1$ on rib i, deviates the inter-rib flow toward rib $i+1$. The modulus of the velocity decreases steeply suggesting a significant out-of-plane motion revealed also by the flow visualizations. The end of the inter-rib domain close to rib $i+1$ is characterized by low momentum flow and low velocity fluctuations (data not reported in the present paper). At the extremity of rib i a perturbation of the streamlines path suggests the existence of a third impingement area (Imp III in Fig. 8(b)) by far weaker than the ones already

Fig. 8 Plane *xy*1: (a) modulus of time-averaged in-plane velocity, streamlines and ideal jet path (dashed lines); (b) cross-plane acceleration near the bottom wall

reported. As suggested by the measurements in plane xz_core_i (Fig. 6) and exploiting the periodicity of crossing-jets and ribs, this impingement appears to be produced by part of jet $i+2$ on rib i.

In order to quantify the cross-plane acceleration, the continuity equation for incompressible flow can be written as

$$\frac{\partial U}{\partial x} + \frac{\partial V}{\partial y} = -\frac{\partial W}{\partial z} \qquad (1)$$

where the left hand side can be calculated from the PIV results. Further simplification can be made taking into account the fact that the measurement plane is very close to the bottom wall; either an acceleration of the flow toward the wall ($-\partial W/\partial z < 0$ and $W < 0$) or a deceleration from the wall toward the measurement plane ($-\partial W/\partial z > 0$ and $W > 0$) can be discarded. Therefore, a positive value of $-\partial W/\partial z$ represents a downward deceleration, while a negative value represents an upward acceleration. The result is presented in Fig. 8(*b*); along rib i three zones of downward deceleration (Imp I, Imp II, and Imp III) correspond to the three impingement areas previously identified from the observation of the mean flow path. The strength decreases from the first to the last area. In the center of the inter-rib domain a wide area of upward acceleration confirms the upward motion discussed above.

The characterization of the flow just above the ribs is obtained by the measurements performed in a horizontal plane (xy2, see Fig. 3(*a*)) 1.5 rib heights above the bottom wall. Contour plots of time-averaged in-plane velocity and streamlines path over planes xy2 and $x'y$ are presented in Fig. 9. In order to help the comprehension of the fluid structures, the periodicity of the flow is exploited duplicating periodically the PIV data of plane $x'y$. These results show that the rib guidance effect is by far less important above the turbulators; this volume is mainly dominated by the effect of the crossing-jets and the upward structures generated in between the ribs. In plane xy2 the streamlines are aligned toward the trailing edge and velocity fluctuations with rms higher than $0.2U_b$ are observed in the jet core up to the center of the ribbed part of the cavity (data not shown in figure); in this region $\sqrt{\overline{u^2}}$ presents values even 60% higher with respect to $\sqrt{\overline{v^2}}$ and $\sqrt{\overline{w^2}}$.

3.2.3 Upward Jet Deflections. The experimental results previously described suggest the existence of upward jet deflections originating from the jet-rib interaction. A detailed description of these flow structures is obtained by means of PIV measurements

conducted in the vertical plane in between two midwall slots ($xz\_mid\_i\_i+1$). In Fig. 10 contour levels of time-averaged in-plane velocity modulus and streamline path in planes $xz\_mid\_i\_i+1$ and a small portion of xy1 are presented. The streamlines path shows that after the first impingement on rib i (Imp I, Fig. 8(*b*)), a part of jet i bounces back toward the midwall and rolls up. A part recirculates in the corner with the bottom wall, the remaining part ends up in an upward structure that impinges on the upper wall. As previously supposed by the results in $x'y$ (Figs. 5 and 6), the main velocity component in between two midwall slots is aligned with the z-direction; as the flow reaches the upper wall, it slightly spreads and looses part of its energy.

Further from the midwall, at the end of plane $xz\_mid\_i\_i+1$ (Fig. 10), remarkable values of in-plane velocity and almost vertical path of the streamlines confirm the presence of a second upward structure. In agreement with the analysis of the results in plane xy1 (Fig. 8(*b*)), the flow lifts off from the center of the inter-rib domain. The structure is sufficiently strong to reach the upper wall and to sustain a recirculation area bounded by the ribs, the upper wall and the flow close to the midwall. The strength of
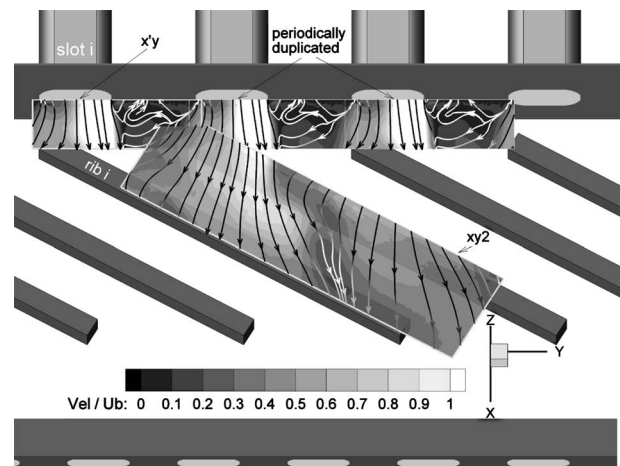
Fig. 9 Modulus of time-averaged in-plane velocity and streamlines path in planes *xy*2 and *x'y* (periodically duplicated)
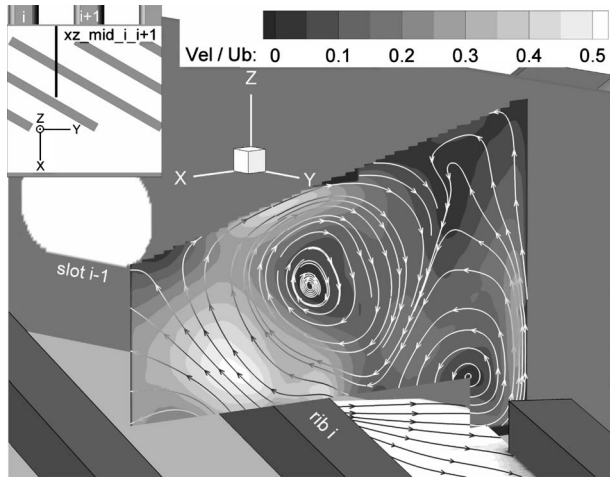
Fig. 10 Modulus of time-averaged in-plane velocity and streamline paths in planes *xz*_mid_*i*_*i*+1 and *xy*1
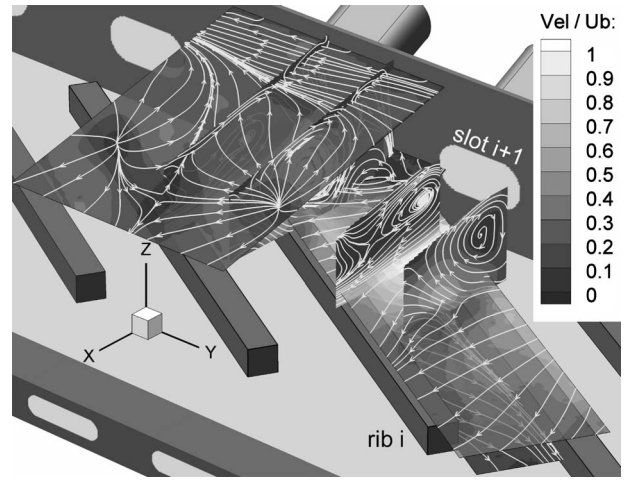

Fig. 12 Modulus of time-averaged in-plane velocity and streamlines in all PIV measurement planes

this upward flow motion is also confirmed by relevant values of in-plane velocity fluctuations (data not reported in the figure).

3.2.4 The Flow Close to the Upper Wall. The impact of the upward flow motions previously described can be appreciated by the study of the flow close to the upper wall. Figure 11 reports PIV results in *x″y*, an inclined plane parallel and close to the upper wall (see Fig. 3(*a*)). The figure shows contour levels of time-
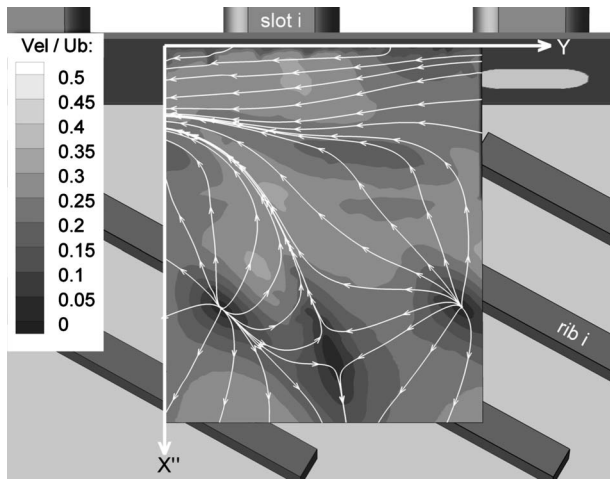
Fig. 11 Modulus of time-averaged in-plane velocity and streamlines path in *x″y*

averaged in-plane velocity modulus and streamlines path.

In agreement with preliminary flow visualizations, periodical impingement regions around the center of the upper wall are clearly put in evidence. From there, the flow spreads in all directions and then leaves the surface along two different separation lines. The first one describes an arc just above the core of the jet and divides the flows of similar periodical upward structures. The second one is parallel to the midwall and divides the flow that comes from the upward structures at the center of the cavity from the fluid that goes up close to the midwall in between two successive jets. The traces of both separation lines can be noticed also from the plot presented in Fig. 6. The main direction of the recirculating flow bounded by the midwall and the second separation line is toward the hub. This is mainly due to the driving effect of the turbulators: on the bottom wall, the ribs guide the flow toward one of the closed end-wall of the channel (i.e., the tip of the blade), but to satisfy the mass conservation part of the flow must have a negative component in *y*-direction in a region of low momentum, i.e., above the row of jets.

3.3 Final Mean Flow Model. Figure 12 provides an overall view of the PIV results. A model for the mean flow in the rib-roughened trailing cavity is deduced from the ensemble of these data and is presented in Fig. 13.

The flow inside the cavity is driven by inclined crossing-jets originating from the midwall. Only part of the momentum in the *y*-direction present in the inlet channel is dissipated through the midwall slots. This leads to a remarkable unbalancing within the jets: the core extends over less than half of the slot span.

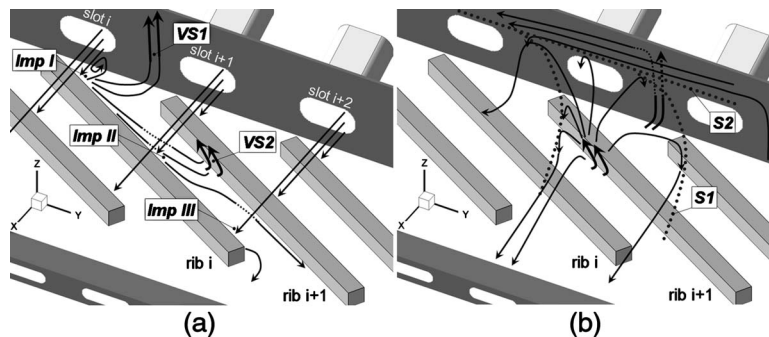The crossing-jets effectively penetrates inside the cavity up to

Fig. 13 Summary of the mean flow path model: (*a*) inter-rib region and vertical structures; (*b*) near the upper wall

the end of the ribbed part; each jet produces different impingements on the three turbulators that are in front of the slot. Looking at rib i, three impingement areas can be defined: Imp I, Imp II, and Imp III, respectively, produced by jets i, $i+1$, and $i+2$ (Fig. 13(a)). About half of jet i produces the first impingement, a part of the impinging jet bounces toward the midwall and rolls up under the jet itself or lifts off generating an upward structure (VS1) that reaches the upper wall. The remaining part of the fluid is guided by the ribs and flows under the jet produced by slot $i+1$. The presence of the second impingement area (Imp II) deviates the inter-rib flow toward rib $i+1$. The blockage effect produced by this turbulator forces the flow to separate from the bottom wall and to produce a second upward deflection (VS2) that goes up to the upper wall. The effect of the third impingement area (Imp III) is by far less evident; it mainly deviates the flow toward the exit slots but does not produce any vertical flow deflection. In proximity of the end of rib $i+1$ the flow is characterized by low momentum and low turbulence levels.

The vertical structure VS1 impinges on the upper wall in between two slots (Fig. 13(b)). Close to the corner between the upper wall and the midwall, the flow is organized in a recirculation structure whose main flow direction is toward the blade hub.

The upward structure VS2 produces another periodical impingement in between two slots approximately at the center of the upper wall. From this point the flow spreads in all directions. A part directly goes toward the trailing edge, the remainder separates from the upper wall along two different separation lines. The first one (S1) describes an arc above the jet core and divides the flow coming from similar vertical structures VS2, the second one (S2) is parallel to the midwall and separates the flow coming from VS1 and VS2. The area above the jet core is interested by a recirculating flow.

The nonribbed area close to the trailing edge is characterized by flow mainly aligned in the x-direction; the part of the fluid that is in front of the exit slots enters uniformly into the cavities, the remainder strongly impinges on the walls separating the exit slots and afterward exits through the trailing edge holes.

4 Numerical Predictions

4.1 The Numerical Model. The numerical simulation is performed by means of the code CEDRE (developed by ONERA). This code is a 3D solver of the Reynolds-averaged Navier–Stokes (RANS) equations based on a finite volume formulation. CEDRE is a multiphysics platform, which uses multidomain techniques on generally unstructured meshes; the finite volume cells are general polyedra based on any kind of polygonal contour, planar, or skewed [33].

The solution is computed in a 3D domain representing the complete test section including the prolongation of the inlet channel. The computation simulates the experimental conditions applied for the heat transfer measurements object of the second part of the present paper [32]. Mass flow and total temperature are imposed as boundary conditions at the end of the prolongation of the inlet channel. They are extrapolated from the pressure and temperature measurements performed in the inlet section (Fig. 1). The static pressure is imposed downstream of the exit slots. Air (considered as ideal gas) is used as working fluid.

Turbulence closure is provided by the $\kappa-l$ (turbulent kinetic energy and length scale) turbulence model developed by Smith [34]. The turbulent length scale l is defined as

$$l = C_\epsilon \frac{\kappa^{3/2}}{\epsilon} \qquad (2)$$

where ϵ is the rate of dissipation of κ, and C_ϵ is a constant of the model. With respect to other two-equation turbulence models, this closure scheme has the advantage of using a variable (the turbulent length scale) which is directly proportional to the wall distance. The interpolation is easier as is based on a field of linear
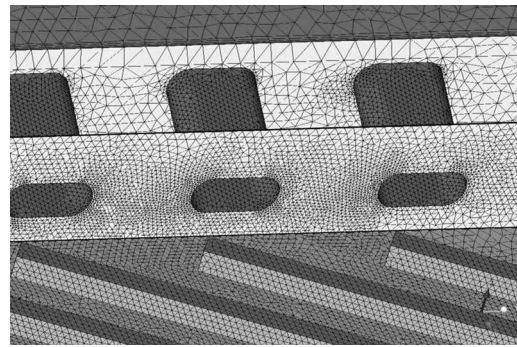

Fig. 14   CFD: computational mesh

variables, so the model results robust and does not need an extreme grid refinement at the wall.

A high Reynolds number formulation is used; near wall regions are treated by wall functions. Two types of grids were tested: an Octree mesh (overall number of elements about 2.7×10^6) and a Delaunay mesh (about 2.8×10^6). The second one gave better results owing to the higher control of elements size and was chosen for the presented computation. It consists of four layers of prismatic elements in the vicinity of the walls and tetrahedra elsewhere. The wall y^+ of the grid ranges from 3 to 10. A view of the computational mesh is provided in Fig. 14.

4.2   Comparison With the PIV Data. In view of a detailed comparison between heat transfer predictions and thermal characterization performed in the second part of the present contribution [32], this section is aimed at providing an analysis of the calculated flow field on the basis of the experimental investigation described above. A few topological discrepancies between computed and measured flow fields are found. The analysis of the CFD data therefore focuses more on the qualitative differences between predicted and measured flow structures. In the following, CFD results are presented extracting data on 2D slices placed in the same position of the PIV measurement planes defined in Fig. 3.

The predicted flow inside the test section is mainly characterized by the presence of a single impingement area on each inter-rib domain and a tip-to-hub flow organized in a single wide helicoidal structure situated above the ribs, close to the midwall.

Concerning the description of the crossing-jet, the velocity levels and distribution along the y-direction are similar to the experimental observations: the strong unbalancing toward the positive y-direction is correctly predicted.

In comparison with Fig. 6, Fig. 15 shows instead some differences in the vertical path of the jet. The core spreads much more quickly and no streamlines enter inside the second inter-rib volume in front of the slot. Moreover above the jet the recirculating flow is much more organized and no separation from the upper wall is predicted. This behavior is the direct consequence of the existence of a continuous helicoidal structure that flows toward the hub above the jets.

Topological discrepancies are found also in the plane placed in between two successive midwall slots. In comparison with Fig. 10, Fig. 16 shows that both the upward structures described by PIV are not predicted. The helicoidal structure deviates the flow that goes up close to the midwall and no streamline that comes out from the inter-rib region reaches the upper wall.

Finally, the different structure of the upward deflections is recognizable also in the predictions in plane $x''y$. In comparison with Fig. 11, Fig. 17 shows the absence of defined impingement points and the different way in which the flow separates from the surface is evident.
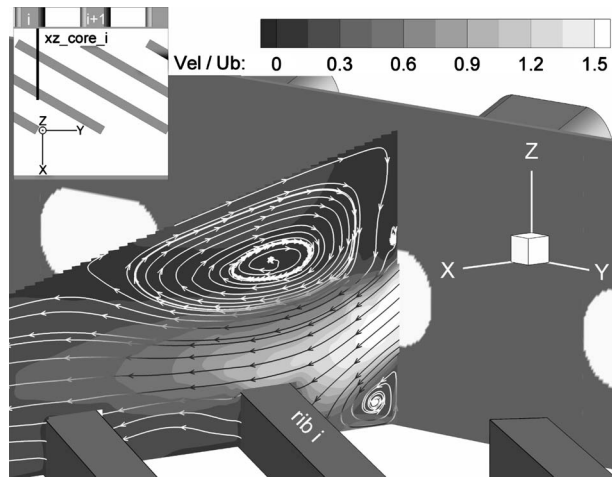
Fig. 15   CFD: modulus of mean in-plane velocity and streamlines path in plane *xz_core_i*

5   Conclusions

The present study addresses a detailed aerodynamic characterization of a trapezoidal cross-sectional model simulating a trailing edge cooling cavity with one rib-roughened wall and slots along
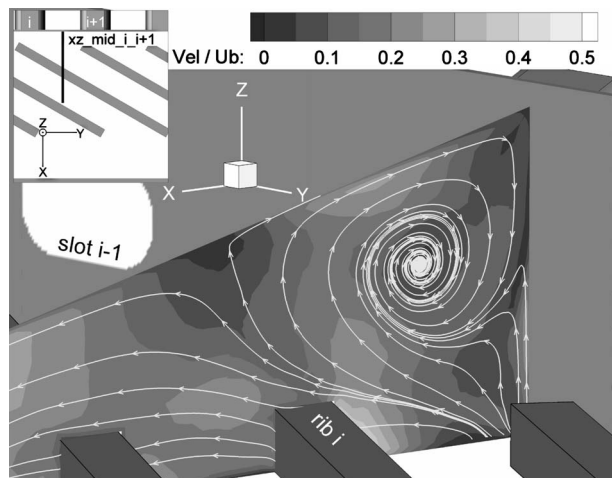

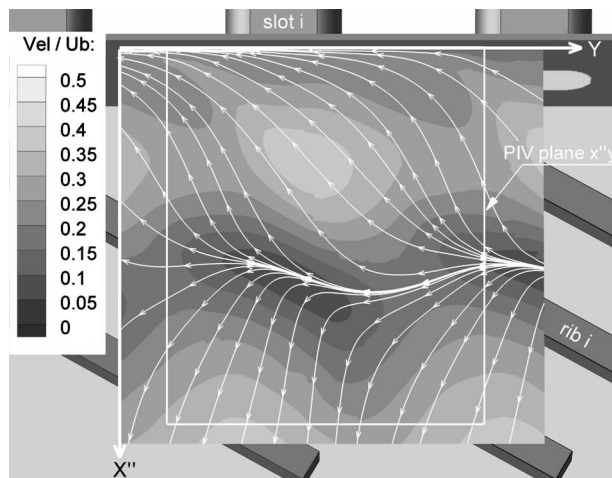**Fig. 16   CFD: modulus of mean in-plane velocity and streamlines path in plane *xz_mid_i_i+1***

Fig. 17   CFD: modulus of mean in-plane velocity and streamlines path in plane *x"y*

two opposite walls. The insertion of the turbulators produces an increase in the friction factor of about 4%; the periodicity of the design is reflected also in a periodic evolution of the flow inside the cavity. The characterization of the central part of the cavity can therefore be considered as representative of the flow evolution in the complete model.

Surface-streamline flow visualizations conducted in the model without ribs point out the following main features.

- The crossing-jet issued from the tilted slot produces a localized impingement on the bottom wall in the vicinity of the midwall.
- After the impingement, the jet interacts with the adjacent ones and is deflected toward the upper wall where it produces a remarkable scrubbing action.
- Strong impingement areas are detected at the trailing edge in between each couple of exit slots.

A three-dimensional reconstruction of detailed 2D-PIV measurements shows that the insertion of the ribs produces a complex interaction with the crossing-jets. The flow field can be summarized with the following features.

- The crossing-jet is characterized by a strong unbalancing toward the tip (already noticed in the nonribbed configuration).
- Each jet impinges on the three ribs that are in front of the slot, with the first impingement by far stronger than the others.
- On the bottom wall, the end of the inter-rib domain is characterized by an area of very low momentum flow.
- The jet-rib interaction produces two upward jet deflections for each inter-rib domain; these structures originate from the bottom wall and carry fluid to the upper wall where a periodic system of separation lines and impingements is observed.
- The main direction of the recirculating structures present near the upper wall is toward the hub.

The experimental results are compared with the numerical predictions obtained by a code solving the RANS equations (CEDRE) coupled with a two-equation $\kappa - l$ turbulence model. From the aerodynamic point of view, the predicted flow inside the test section is mainly characterized by the presence of a single impingement area on each inter-rib domain and a tip-to-hub flow organized in a single wide helicoidal structure above the ribs, near the midwall.

Nomenclature

$$AR = \text{aspect ratio, height/width}$$
$$C_\epsilon = \text{constant of the turbulence model}$$
$$D_h = \text{hydraulic diameter (m)}$$
$$l = \text{turbulent length scale (m)}$$
$$Re = \text{Reynolds number, } U_{b,\text{inlet}} D_{h,\text{inlet}} / \nu_{\text{air}}$$
$$s = \text{midwall slot span (m)}$$
$$U, V, W = \text{mean velocity components in } x, y, \text{ and } z \text{ (m/s)}$$
$$\sqrt{\overline{u^2}}, \sqrt{\overline{u'^2}}, \sqrt{\overline{v^2}}, \sqrt{\overline{w^2}} = \text{root mean squares of the velocity fluctuations in } x, x', y, \text{ and } z \text{ (m/s)}$$
$$x = \text{axis parallel to the exit slots axes}$$
$$x' = \text{axis parallel to the midwall slots axes}$$
$$x'' = \text{axis parallel to the upper wall}$$
$$y = \text{axis parallel to the main channel axis}$$
$$z = \text{axis perpendicular to the channel bottom wall}$$

Greek

$$\epsilon = \text{rate of dissipation of turbulent kinetic energy (m}^2/\text{s}^3)$$

κ = turbulent kinetic energy (m^2/s^2)
ν = kinematic viscosity (m^2/s)

Subscripts

B = bulk flow
exit = exit wall slot
inlet = inlet section
mid = midwall slot

References

[1] Ligrani, P. M., Oliveira, M. M., and Blaskovich, T., 2003, "Comparison of Heat Transfer Augmentation Techniques," AIAA J., **41**(3), pp. 337–362.

[2] Han, J. C., Dutta, S., and Ekkad, S., 2000, *Gas Turbine Heat Transfer and Cooling Technology*, Taylor & Francis, New York.

[3] Chandra, P. R., Han, J. C., and Lau, S. C., 1988, "Effect of Rib Angle on Local Heat/Mass Transfer Distribution in a Two-Pass Rib-Roughened Channel," ASME J. Turbomach., **110**(2), pp. 233–241.

[4] Han, J. C., 1988, "Heat Transfer and Friction Characteristics in Rectangular Channels With Ribs Turbulators," ASME J. Heat Transfer, **110**(2), pp. 321–328.

[5] Han, J. C., Zhang, Y. M., and Lee, C. P., 1992, "Influence of Surface Heat Flux Ratio on Heat Transfer Augmentation in Square Channels With Parallel, Crossed, and V-Shaped Angled Ribs," ASME J. Turbomach., **114**(4), pp. 872–880.

[6] Taslim, M. E., and Wadsworth, C. M., 1997, "An Experimental Investigation of the Rib Surface-Averaged Heat Transfer Coefficient in a Rib-Roughened Square Passage," ASME J. Turbomach., **119**(2), pp. 381–389.

[7] Florschuetz, L. W., Berry, R. A., and Metzger, D. E., 1980, "Periodic Streamwise Variations of Heat Transfer Coefficients for Inline and Staggered Arrays of Circular Jets With Crossflow of Spent Air," ASME J. Heat Transfer, **102**(1), pp. 132–137.

[8] Bunker, R. S., and Metzger, D. E., 1990, "Local Heat Transfer in Internally Cooled Turbine Airfoil Leading Edge Regions: Part I—Impingement Cooling Without Film Coolant Extraction," ASME J. Turbomach., **112**(3), pp. 451–458.

[9] Cho, H. H., and Goldstein, R. J., 1995, "Heat/Mass Transfer and Film Cooling Effectiveness With Injection Through Discrete Holes: Part I—Within Holes and on the Back Surface," ASME J. Turbomach., **117**(3), pp. 440–450.

[10] Huang, Y., Ekkad, S. V., and Han, J. C., 1998, "Detailed Heat Transfer Distributions Under an Array of Orthogonal Impinging Jets," J. Thermophys. Heat Transfer, **12**(1), pp. 73–79.

[11] Pamula, G., Ekkad, S. V., and Acharya, S., 2001, "Influence of Crossflow-Induced Swirl and Impingement on Heat Transfer in a Two-Pass Channel Connected by Two Rows of Holes," ASME J. Turbomach., **123**(2), pp. 281–287.

[12] Uysal, U., Li, P. W., Chyu, M. K., and Cunha, F. J., 2006, "Heat Transfer on Internal Surfaces of a Duct Subjected to Impingement of a Jet Array With Varying Jet Hole-Size and Spacing," ASME J. Turbomach., **128**(1), pp. 158–165.

[13] Haiping, C., Jingyu, Z., and Taiping, H., 1998, "Experimental Investigation on Impingement Heat Transfer From Rib-Roughened Surface Within Arrays of Circular Jet," ASME Paper No. 98-GT-208.

[14] Akella, K., and Han, J. C., 1999, "Impingement Cooling in Rotating Two-Pass Rectangular Channels With Ribbed Walls," J. Thermophys. Heat Transfer, **13**(3), pp. 364–371.

[15] Taslim, M. E., Bakhtari, K., and Liu, H., 2003, "Experimental and Numerical Investigation of Impingement on a Rib-Roughened Leading Edge Wall," ASME J. Turbomach., **125**(4), pp. 682–691.

[16] Rhee, D. H., Nam, Y. W., and Cho, H. H., 2004, "Local Heat/Mass Transfer With Various Rib Arrangements in Impingement/Effusion Cooling With Crossflow," ASME J. Turbomach., **126**(4), pp. 615–626.

[17] Cunha, F. J., Dahmer, M. T., and Chyu, M. K., 2006, "Analysis of Airfoil Trailing Edge Heat Transfer and its Significance in Thermal-Mechanical Design and Durability," ASME J. Turbomach., **128**(4), pp. 738–746.

[18] Taslim, M. E., Li, T., and Spring, S. D., 1995, "Experimental Study of the Effects of Bleed Holes on Heat Transfer and Pressure Drop in Trapezoidal Passages With Tapered Turbulators," ASME J. Turbomach., **117**(2), pp. 281–289.

[19] Kiml, R., Mochizuki, S., and Murat, A., 2001, "Effects of Rib Arrangements on Heat Transfer and Flow Behaviour in a Rectangular Rib-Roughened Passage: Application to Cooling of Gas Turbine Blade Trailing Edge," ASME J. Turbomach., **123**(4), pp. 675–681.

[20] Taslim, M. E., Li, T., and Spring, D., 1998, "Measurements of Heat Transfer Coefficients in Rib-Roughened Trailing-Edge Cavities With Crossover Jets," ASME Paper No. 98-GT-435.

[21] Çakan, M., 2000, "Aero-Thermal Investigation of Fixed Rib-Roughened Internal Cooling Passages," Ph.D. thesis, Universitè Catholique de Louvain/von Karman Institute for Fluid Dynamics, Belgium.

[22] Rau, G., Çakan, M., Moeller, D., and Arts, T., 1998, "The Effect of Periodic Ribs on the Local Aerodynamic and Heat Transfer Performance of a Straight Cooling Channel," ASME J. Turbomach., **120**(2), pp. 368–375.

[23] Casarsa, L., and Arts, T., 2005, "Experimental Investigation of the Aerothermal Performance of a High Blockage Rib-Roughened Cooling Channel," ASME J. Turbomach., **127**(3), pp. 580–588.

[24] Chanteloup, D., Juaned, Y., and Bölcs, A., 2002, "Combined 3-D Flow and Heat Transfer Measurements in a 2-Pass Internal Coolant Passage of Gas Turbine Airfoils," ASME J. Turbomach., **120**(2), pp. 368–375.

[25] Roclawski, H., Jacob, J. D., Yang, T. L., and McDonough, J. M., 2001, "Experimental and Computational Investigation of Gas Turbine Blade Cooling Passages," 31st AIAA Fluid Dynamics Conference, Anaheim, CA.

[26] Kline, S. J., and McClintok, F. A., 1953, "Describing Uncertainties in Single Sample Experiments," Mech. Eng. (Am. Soc. Mech. Eng.), **75**(1), pp. 3–8.

[27] Scarano, F., and Riethmuller, M. L., 1999, "Iterative Multigrid Approach in PIV Image Processing With Discrete Window Offset," Exp. Fluids, **26**, pp. 513–523.

[28] Scarano, F., 2000, "Particle Image Velocimetry Development and Application," Ph.D. thesis, Università Federico II di Napoli/von Karman Institute for Fluid Dynamics, Italy/Belgium.

[29] Keane, R. D., and Adrian, R. J., 1990, "Optimization of Particle Image Velocimeters. I. Double Pulsed Systems," Meas. Sci. Technol., **1**(11), pp. 1202–1215.

[30] Willert, C. E., 1996, "The Fully Digital Evaluation of Photographic PIV Recordings," Appl. Sci. Res., **56**(2-3), pp. 79–102.

[31] Bendat, J. S., and Piersol, A. G., 1986, *Random Data: Analysis and Measurement Procedures*, Wiley, New York.

[32] Coletti, F., Armellini, A., Arts, T., and Scholtes, C., 2008, "Aerothermal Investigation of a Rib-Roughened Trailing Edge Channel With Crossing-Jets—Part II: Heat Transfer Analysis," ASME Paper No. 08-GT-50695.

[33] Chevalier, P., Courbet, B., Dutoya, D., Klotz, P., Ruiz, E., Troyes, J., and Villedieu, P., 2005, "CEDRE: Development and Validation of a Multiphysics Computational Software," 1st European Conference for Aerospace Science (EUCASS), Moscow, Russia.

[34] Smith, B. R., 1994, "A Near Wall Model for the $\kappa - l$ Two Equation Turbulence Model," AIAA Paper No. 94-2386.

Experimental and Computational Fluid Dynamics Based Determination of Flutter Limits in Supersonic Space Turbines

Pieter Groth

Hans Mårtensson

Department of Aerothermodynamics,
Volvo Aero Corporation,
SE-461 81 Trollhättan, Sweden

Niklas Edin
Department of Turbines and Rotors,
Volvo Aero Corporation,
SE-461 81 Trollhättan, Sweden

Turbines operating at high pressure in high velocity flow are susceptible to flutter. As reduced frequencies become sufficiently low, negative aerodynamic damping will be found in some modes. Ensuring that the total system damping is positive over the entire turbine operating envelope for all modes is of utmost importance in any design since flutter in a turbine often causes blade failures. This is in contrast to the normal engineering approach, which is to require a positive aerodynamic damping. A unique test campaign with a 1.5 stage supersonic space turbine has been performed. The turbine was operated at simulated running conditions over a large operating envelope in order to map out flutter limits. During the test, flutter was intentionally triggered at seven different operating conditions. Unique data have been obtained during the test that supports validation of design tools and enables better understanding of flutter in this type of turbine. Based on the data the flutter boundary for the turbine could be established. Using computational fluid dynamics (CFD) tools flutter was predicted at all operating points where the flutter limit was crossed. Both in predictions and as evidenced in test the two nodal diameter backward traveling mode was the most unstable. In addition to this predicted values of aerodynamic damping at flutter agreed well with damping estimated from measured amplitude growth. [DOI: 10.1115/1.3072491]

1 Introduction

A turbopump in a rocket engine consists of a pump driven by a turbine. It delivers fuel or oxidizer to the thrust chamber where the propellants are brought to react and increase in temperature. Since the combustion process takes place under constant pressure, the chamber pressure is the net result of the turbopump system. Turbomachinery for liquid rocket propulsion share many of the design features and challenges found in gas turbines. The emphasis is on delivering very high power in a small machine, even to a greater extent than in jet engines.

The turbines used in gas generator cycle rocket engines are fed by bleeding off a percentage of the combustibles. A gas generator burns the combustibles to temperatures typically below 1000 K allowing for blades without cooling. If the combustibles are hydrogen and oxygen this is done using a hydrogen rich mixture. In our context it is worth noting that the sonic speed is very high in this mixture due to the presence of hydrogen. The entry pressure is equal to the chamber pressure, 90–120 bars, and an exit pressure that can be as low as atmospheric.

Volvo Aero Corporation (VAC) develops and manufactures the turbines for the liquid hydrogen and liquid oxygen pumps, which are components of the gas generator cycle engine of the European space launcher. They are velocity-compounded impulse turbines with relative Mach numbers up to 2. A rotor assembly consists of approximately a hundred blades to a disk.

The design trend is toward designing the rotors as blisks, i.e., the blades and disk are an integral part machined out from a forging. In a traditional bladed disk there is considerable damping in interfaces on shrouds and in blade fir tree attachments to the disk. In an integral design these are nonexistent. Hence, only a very low viscous material damping remains. Introduction of a

blisk design, therefore, may give rise to aeroelastic problems due to its much lower structural damping than a bladed disk. For a blisk without a damping device the aerodynamic damping becomes the dominating term of the total damping. In a computational study [1] it is suggested that this class of turbines is aeroelastically unstable for low nodal diameter system modes in the absence of material damping. It makes the turbine type particularly sensitive to flutter.

A well validated computational tool is a prerequisite when designing rotor blisks for this application. The in-house tools [2,3] used in design of the rocket turbines have been extensively validated against standard test cases [4] and some specific cascade test cases such as those in Ref. [5] and proprietary supersonic linear cascade tests. None of these cases is fully representative for the state in these supersonic turbines. Thus, a full scale aeromechanical test at simulated running conditions in air, with a 1.5 stage supersonic turbine, was performed in the turbine test rig at VAC. The objective of the test was to obtain test data for validation of design methods.

2 Experiment

The turbines of interest to us in this work are components of an engine working according to the gas generator cycle. The turbines are powered by a mixture of hydrogen and some steam. The ideal gas law is a good approximation for the state of this gas in the pressure and temperature range of interest. In the specific application the turbine inlet total pressure is typically 90–120 bars. The inlet total temperature is 900 K and the total-to-total pressure ratio is typically 15–20.

In the turbopump environment extensive testing is cumbersome and expensive. Using a turbine rig normally used for performance testing on site at VAC allows for a safe and controlled environment where the hardware can be pushed to its limits. Air is used as a working fluid, which means that no hot and explosive gases need to be handled. The maximum inlet total pressure in the test rig is 8 bars. The maximum inlet total temperature is 650 K and

total-to-total pressure ratios up to 20 are possible to reach. With these differences scaling laws are applied in order to restore both aerodynamic and aeroelastic properties to similarity by designing in suitable structural properties.

2.1 Scaling of Test. The straightforward rewriting of the Navier–Stokes equations and the equation of state in nondimensional form in conjunction with dimensional analysis leads to following similarity rule for the unsteady aerodynamics: For geometrical similar turbines, the unsteady flow fields will be *similar* if the pressure ratio, π, nondimensional speed, N_k, and reduced frequencies, k, are similar.

The reduced frequency ascertains similarity in unsteady aerodynamic response to a moving blade. For a similar relation between the structural dynamics and the aerodynamic response either the mass ratio between fluid and structure or a characteristic damping has to be similar. For aeroelastic similarity we require in addition that the characteristic nondimensional damping is made similar ζ^*.

This parameter may be viewed as an energy ratio. It is preferred over the mass ratio since it has a direct translation into the aerodynamic damping.

The first two parameters, which are purely aerodynamic, are easily obtained in the rig that has been used primarily for performance testing earlier. The nondimensional speed, N_k, and pressure ratio are defined as

$$N_k = \frac{\Omega \cdot r_m}{\sqrt{\gamma \cdot R \cdot T_{00}}} \tag{1}$$

$$\pi = \frac{P_{00}}{P_3} \tag{2}$$

Similarity in these parameters essentially gives a lowered shaft speed for testing in air following the sonic speed ratio. The disk centrifugal and thermal stresses are both much less severe on the rig and hence there are no new mechanical issues introduced going in this direction. Rather this gives margin in the operation of the turbine rotor.

The most difficult parameter to get equal in test rig and engine rig is the reduced frequency. In general it is almost impossible, since the parameter depends on structural eigenfrequencies and the flow velocity, according to

$$k = \frac{c\omega}{2v_{in}} \tag{3}$$

where c is the blade chord, ω is the structural eigenfrequency, and v_{in} is the flow velocity entering the rotor. As mentioned, the working fluids at engine conditions and in test rig are different. The gas constants for these gases differ by a factor of 8 and the ratio of specific heats differs by 2%. For all practical purposes the ratio of specific heats in engine and in air test rig may be considered to be equal. If the inlet total temperature in test is set to 400 K, the speed of sound in engine conditions and test rig conditions will differ by a factor of 4. The same is true for flow velocity since the Mach numbers will be similar if nondimensional speed and pressure ratio are equal in engine and test rigs. Based on practical and economical concerns the test object was chosen to have the same geometric dimension as the original turbine. This means that the eigenfrequencies of the test turbine rotor should be a quarter of the eigenfrequencies of true turbine rotor. To achieve this for all eigenfrequencies is impossible, since it necessitates the need for material properties, which do not exist in any known material today. For some modal frequencies, however, it may be possible depending on the characteristics of the mode. The modes of interest to us in the present work are low nodal diameter system modes. For these modes the blades oscillate as rigid bodies, close to point masses on the rim of an ideal disk. With most of the bending energy in the disk, the modal frequencies may be lowered by making the disk thinner. Note that a rotor modified in this way
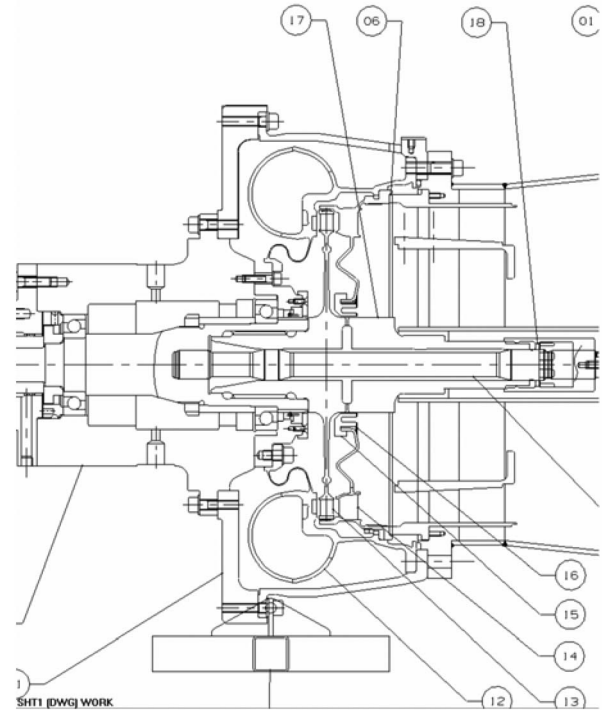

Fig. 1 Drawing of test turbine

from an aerodynamic point of view still will be geometrically similar to the original turbine rotor.

Based on above observations the disk part of the rotor blisk was milled down to minimum thickness allowed by the disk burst criterion when running the turbine in the air test cell.

The reduced frequency for two nodal diameter (ND) system mode of the modified rotor at design point in air test rig is 0.041. This is very close to the reduced frequency for the same mode of the original rotor at design point in engine, which is 0.038. Hence, very good similarity has been achieved for the two ND mode between air rig testing and engine running conditions.

The fourth scaling parameter, which is the characteristic damping ζ^*, is defined as

$$\zeta^* = \frac{N \cdot P_{00} \cdot L}{2\pi M \omega^2} \tag{4}$$

It can be controlled by selecting the inlet manifold pressure carefully. For the turbine type studied here where the reduced frequencies are very far below stability limit, this scaling parameter can be considered more important in practice.

2.2 Test Setup. The test turbine is based on a two-stage turbine, which is qualified for production. Two modifications were introduced in the test turbine. First, the second rotor was removed. Thus, the test turbine was a 1.5 stage turbine. The second modification was aimed at making the first stage rotor susceptible to low ND system mode flutter. The first stage rotor of the production turbine, which is a bladed disk, was replaced with a rotor blisk. Moreover, to lower the frequency and to achieve similarity in reduced frequency for at least one mode the disk part of the blisk was made as thin as the disk burst criterion permitted (cf. Sec. 2.1). Figure 1 shows the test hardware. The inlet manifold with the first stator is labeled 12. The rotor and second stator are labeled 13 and 14, respectively.

The blisk was instrumented with 14 strain gauges. Eight gauges were mounted at different angular positions on the disk rim to be able to assess the nodal diameter pattern of the eventual vibration. Two gauges were mounted on the blades and four on the shroud.

Fig. 2 Instrumented blisk

Figure 2 shows the instrumented blisk. Two tape recorders were used to record strain gauge signals with a bandwidth of 40 kHz. The turbine was also instrumented with probes for measuring total temperature and total pressures at the inlet and at the outlet, a Venturi probe for massflow measurement, pressure gauges between blade rows, and accelerometers on bearing housings.

A water brake was used to load the turbine.

3 Computational Method

For comparison and for validation flutter prediction analyses have been performed for the most interesting operating conditions of the test campaign. The in-house CFD solver VOLSOL has been used in all these analyses. It is a general structured multiblock finite volume solver for viscid and inviscid flows. For spatial discretization a third-order accurate upwind scheme due to Eriksson [6] is used. It is described in the open literature by Larsson [7]. The governing equations are integrated in time using a three-stage Runge–Kutta method. At inlets and exits one-dimensional nonreflecting boundary conditions [8] are used. The code allows for both nonlinear [3] and linear harmonic flutter analyses [2].

For the case of interest the hub-tip ratio is high and the relative flow is supersonic. Moreover, there is no radial variation of hub and shroud walls through the rotor. The design also has the same profile across the span. Experience has shown that the flow is dominated by the behavior of the shock systems, which is well captured in the 2D analyses. This is not to say that the flow is strictly 2D, but is taken as an indication that we can attempt to

work with relatively simple CFD analyses. There is a considerable interest from a design point of view to avoid very heavy analysis methods since many analyses are needed considering operating points, geometries, and modes. In order to yield a basic understanding of dominant features, it will be attempted to use relatively lightweight analyses in order to interpret the test evidences. Hence, to analyze the unsteady flow in this paper two-dimensional linear time-harmonic Euler computations were performed. Linear harmonic Euler methods have been developed and used for various types of flows by Refs. [2,9–11]. The method computes harmonic perturbations, due to some prescribed structural vibration, about a nonuniform mean flow. The prescribed vibration is commonly the structural eigenmodes.

In order to assess flutter and predict aerodynamic damping the aerodynamic work is computed from the linear Euler result. By definition the aerodynamic work per cycle is

$$W = -\int_{t=0}^{T} \oint_{S} p\mathbf{v} \cdot d\mathbf{S} dt \tag{5}$$

The aerodynamic damping is computed as a critical damping ratio from the aerodynamic work per cycle as

$$\zeta_{aero} = -\frac{W}{4\pi U} \tag{6}$$

where U is the total vibration energy in the mode. It is computed as

$$U = \tfrac{1}{2}M\omega^2 A^2 \tag{7}$$

where M is the modal mass, ω is the modal frequency, and A is the modal amplitude. When the aerodynamic damping is negative the aerodynamic forces act to increase the amplitude of the vibration during each cycle.

4 Results

Prior to the test uncoupled linear flutter analyses were performed. They indicated that flutter would occur during the test. A red line level was set to 150 μstrain on the strain gauges located at the rotor shroud.

4.1 Test Results. Eight test sequences were performed during the test campaign. These were run at the operating conditions defined by nondimensional speed, N_k, and total-to-static pressure ratio, π_{ts}, shown in Fig. 3. The horizontal axis and the vertical axis represent the total-to-static pressure ratio and the nondimensional speed, respectively.

The pressure ratio has been normalized by pressure ratio at reference operating condition. The operating points during differ-
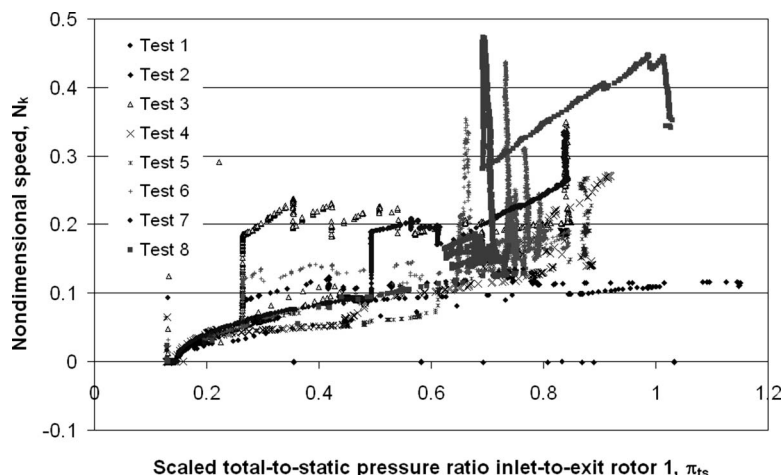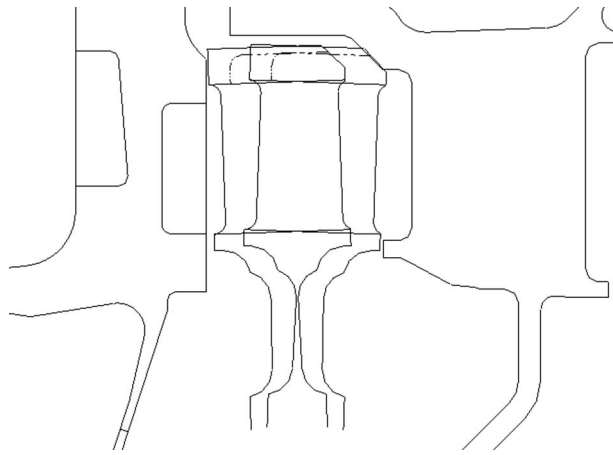

Fig. 3 Operating conditions in test

Fig. 4 Maximum displacement of rotor

Fig. 6 Waterfall diagram at the time of flutter in test 8

ent test sequences are shown as different symbols. The elapsed time between consecutive symbols in each test sequence is 0.5 s. Hence, the distance between consecutive symbols is a measure of the rate of change in operating conditions during the test sequence. The inlet total pressure varied between 150 kPa and 700 kPa and inlet total temperature was 400 K.

Unstable rotor vibrations occurred during seven test sequences. These vibrations were identified as flutter.

During testing the air supply was shut down immediately as soon as the red line level was exceeded. Despite rapid shutdown of air contact between rotor and stator shrouds could not be avoided in all test sequences. Figure 4 illustrates maximum displacement of the rotor when in contact with the stators.

Figure 5 shows the tested operation conditions π_{ts} and N_k and where flutter occurred. The flutter events are marked with gray diamonds.

Based on these flutter events a flutter boundary was constructed. It is depicted in Fig. 4 with a dashed line. The motivation for its shape is as follows. In test sequence numbers 1, 3, 5, 7, and 8 the changes in nondimensional speed and pressure ratio are slow as the flutter boundary is approached. Hence, the flutter events in these test sequences are on the flutter boundary or very close to it. It is difficult to see but the path of test sequence 5 follows the flutter boundary for a while. When the path change direction and conditions just beyond the depicted boundary are reached flutter occurs. In test sequences 2 and 4 the changes in pressure ratio and nondimensional speed are rapid, which the long distance between

consecutive sampling points indicates. Thus, it is highly plausible that the onset of flutter in these tests occurred at conditions that are different from the conditions where flutter finally was observed.

An unexpected flutter event occurred during test 8. In this test the speed was slowly decreased from a scaled pressure ratio of 1 and a nondimensional speed of 0.45. At a nondimensional speed of 0.36 the rotor went into flutter. The waterfall diagram, Fig. 6, shows the response of one strain gauge when this occurred. The horizontal axis represents the frequency of the vibration. The axis perpendicular to the frequency and in the horizontal plane represents the rotational speed (rpm). The vertical axis is the strain (μstrain). In the figure one can see that when the rotor speed is reduced a sudden high response occurs at 11,000 rpm. The frequency at the onset of flutter is 600 Hz. The air supply was shut down when the red line level was exceeded. Next the rotational speed rapidly decreased. The figure clearly shows how the flutter frequency decreases with decreasing rotor speed.

Figures 7–9 show measured strain gauge responses versus time at different flutter events. The figures show that that the amplitudes are growing exponentially in time at all events. By comparing Figs. 7–9 one can see that the amplitude growth in Fig. 9 is the most rapid. Hence, it is a more dramatic flutter event than the other two events. After the initial exponential growth the amplitude is saturated, which is a tell tale sign that some nonlinear mechanism has come into play. While this potentially could excite other modes the vibration is still dominated by the second nodal
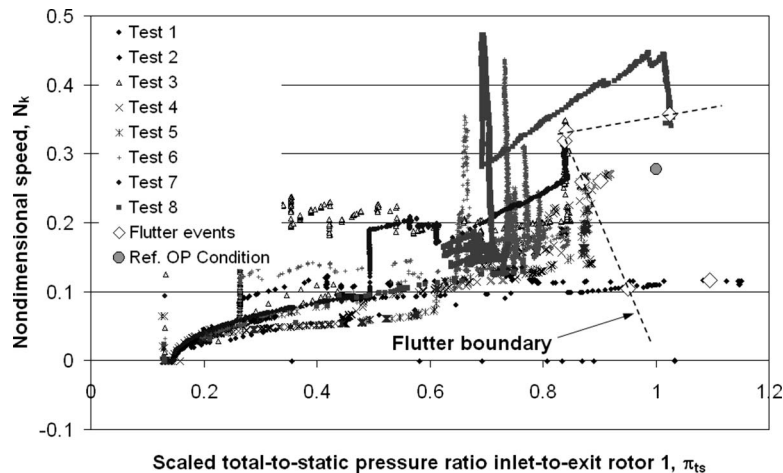

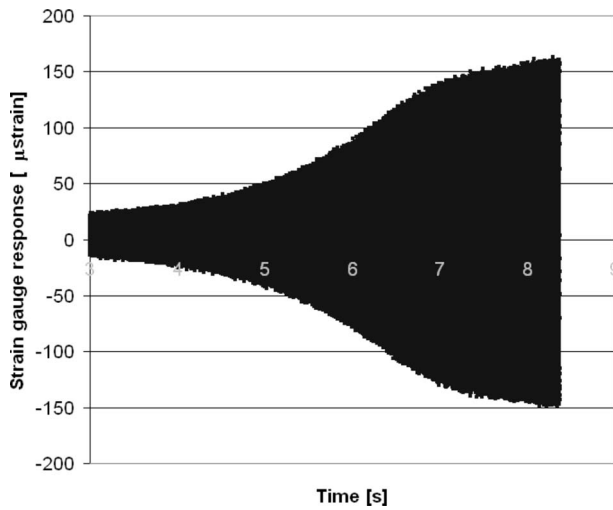**Fig. 5 Flutter events and flutter boundary**

Fig. 7 Strain gauge response of the 2ND mode versus time when flutter occurred during test 3
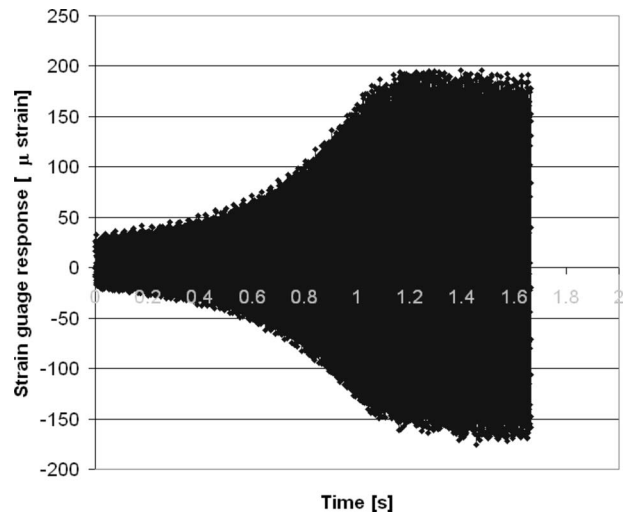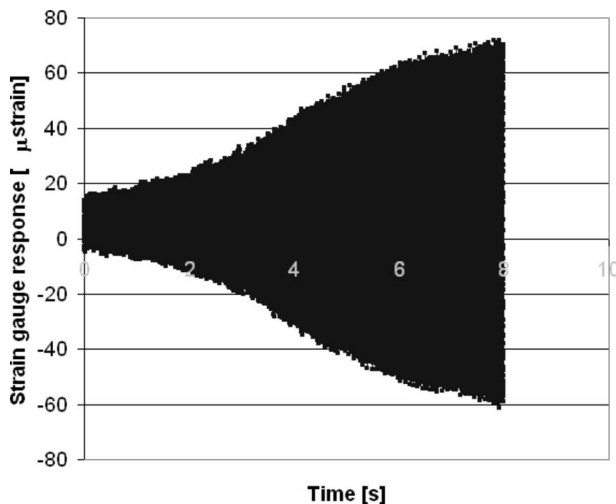

Fig. 9 Strain gauge response of the 2ND mode versus time when flutter occurred during test 8

diameter mode. During test sequence 8, Fig. 9, the strain has reached a constant value after 1 s, which is due to the limitation of amplitude by contact between rotor and stator shrouds.

When flutter is initiated and as long as nonlinear effects are negligible the amplitude of the response will grow exponentially in time, i.e., as a viscous damped system with negative damping. Hence, the total damping when flutter is initiated can be estimated by fitting e^x curves to the envelope of maxima of Figs. 7–9. Figure 10 shows the maxima of Fig. 9 and the curve fitted them in a linear-logarithmic diagram. Toward the right end of the curve one can see that the slope is decreased, which is due to nonlinear effects. In a viscous damped system the amplitude will grow as

$$A = Ce^{-\zeta_{tot}\omega t} \quad (8)$$

Comparison of Eq. (8) to the expression

$$A = 16.76e^{2.21t} \quad (9)$$

of the curve fitted to the measured data in Fig. 8 yields

$$\zeta_{tot} = -\frac{2.21}{\omega} = -\frac{2.21}{2\pi \cdot 600} = -0.06\% \quad (10)$$

The total damping in all other tests has been estimated in the way described above. A summary and comparison of estimated total damping from tests with predictions are presented in Sec. 4.3.

4.2 Computed Results. Flutter prediction analyses have been performed for all tests in order to validate an in-house developed code. For these analyses a 2D linear Euler method has been used [2]. The computational mesh used is shown in Fig. 11. It has 4 blocks and 8266 nodes.

Two examples of mean flow fields are shown in Fig. 12. The figure shows the contours of the relative Mach number before flutter, Fig. 12(a), and at the onset of flutter, Fig. 12(b), in test
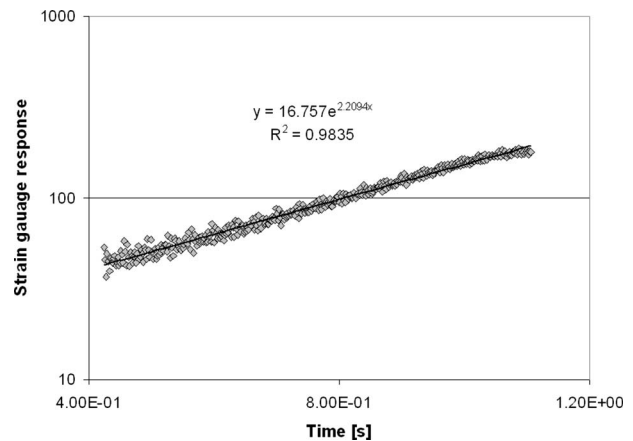
Fig. 10 Maxima of strain gauge response of Fig. 9 versus time

Fig. 8 Strain gauge response of the 2ND mode versus time when flutter occurred during test 5

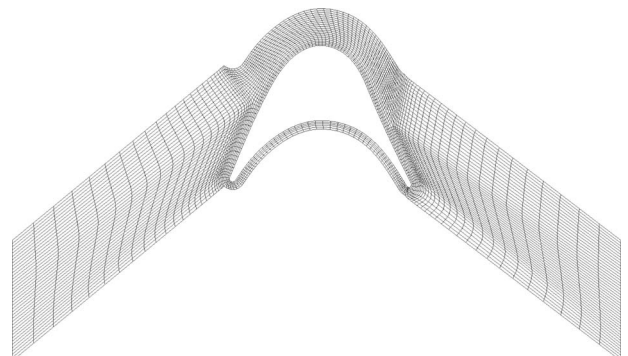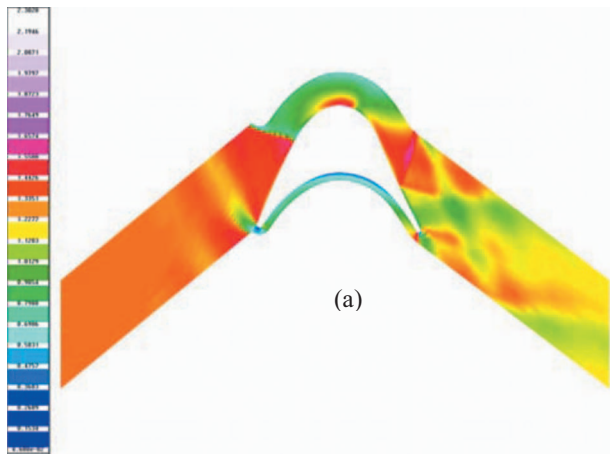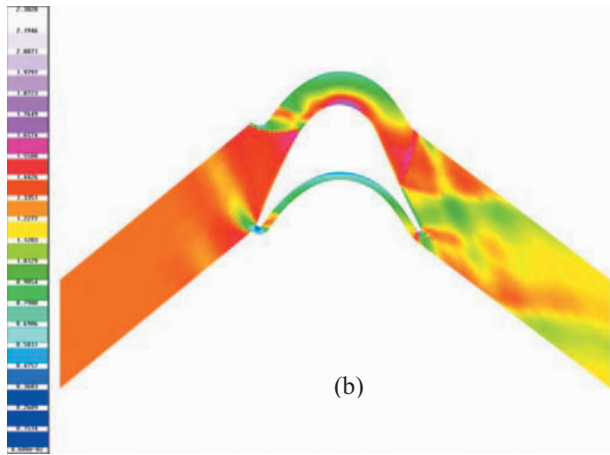

Fig. 11 Computational mesh

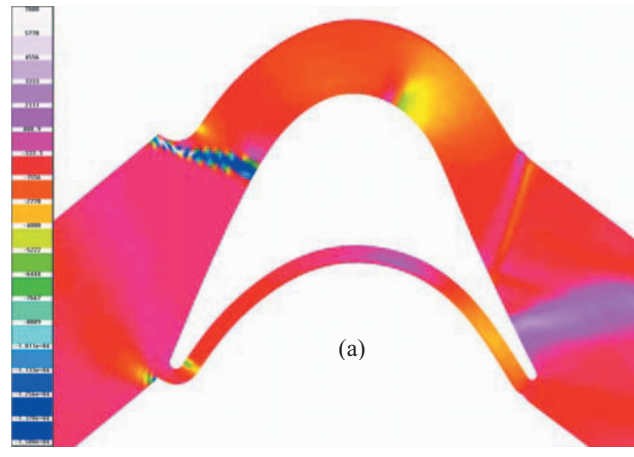Fig. 12   Contours of relative Mach number in test 8 in (*a*) prior to flutter in (*b*) at onset of flutter (white Mach=2.3, dark blue Mach=0.04)

Fig. 13   Contours of the imaginary part of unsteady pressure in test 8 in (*a*) prior to flutter in (*b*) at onset of flutter

sequence 8. Recall that during this test the speed was slowly decreased from a scaled pressure ratio of 1 and a nondimensional speed of 0.45, cf. Fig. 5. At a nondimensional speed of 0.36 the rotor went into flutter. Figure 12(*a*) shows the mean flow field just before the flutter boundary was reached. As one can see there is an oblique bow shock ahead of the leading edge. Behind the shock the flow becomes subsonic. On the pressure side it stays subsonic to the trailing edge. On the suction side the flow accelerates and becomes supersonic before the peak.

Soon after the peak the flow is reduced to subsonic speed by a normal shock. A short distance downstream this shock the flow again reaches supersonic speed. In the exit region a series of shocks brings it down to subsonic speed for the remaining part of the suction side.

Figure 12(*b*) shows the mean flow field at inception of flutter in test 8. Ahead of the leading edge there is a curved bow shock. Behind this the flow accelerates and becomes supersonic. It stays supersonic along the suction side through the blade passage until the exit region where a series of shocks makes it subsonic for the remaining part of the suction side. A normal shock near the leading edge makes the flow subsonic on the pressure side. It remains subsonic until the vicinity of the trailing edge where it locally is accelerated to supersonic speed.

The connection between the operating points and the occurrence of flutter is central to interpreting the test results. CFD analyses can help in this matter. Looking first at the flow pattern in test sequence 8 it can easily be seen that for N_k above the flutter boundary, the flow exhibits passage shock and an almost normal entry shock. As N_k is reduced the flow becomes started with su-

personic suction side and an almost matched entry shock. Comparing the unsteady pressure fields from the linear Euler analysis it is immediately clear that the change in shock system has a dramatic effect on the unsteady aerodynamics. For calculating the aerodynamic damping the imaginary part of the solution is the important element. Here the response in the passage is much larger for the started flow than for the unstarted flow. Figure 13 shows the imaginary part of the unsteady pressure field from test sequence 8 prior to flutter and when flutter started. In the unstarted case the pressure is nearly in phase with the motion, whereas in the case of started flow it exhibits large imaginary response in the passage. It is reasonable to believe that the lower response in the case with a near normal entry shock comes from the fact that the pressure rise is insensitive to geometric changes in the gas path, simply put it cannot get much worse. In contrast as expansion/compression waves are well matched forming a shock-free started flow the sensitivity to changes is greater.
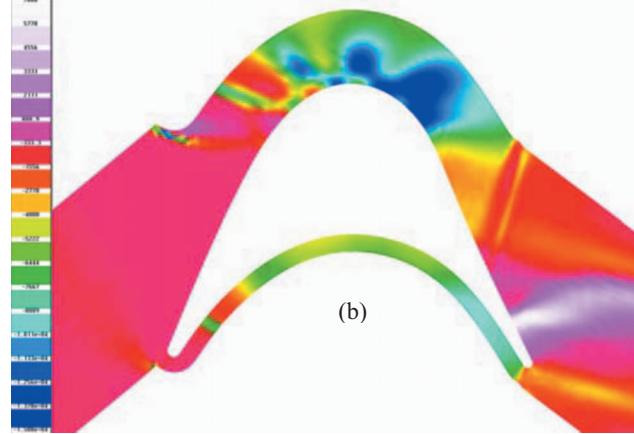
When the rotor blades vibrate in a mean flow like Fig. 12(*a*) pressure disturbances will emanate from the peak of the suction side and propagate both upstream and downstream. The predicted critical damping for the flow condition in Fig. 12(*a*) was positive.

When the rotor vibrates in the mean flow field of Fig. 12(*b*) pressure perturbations will emanate from the moving passage shock and propagate downstream. With the flow conditions in Fig. 12(*b*) the code predicted negative critical damping.

The computed mean flow fields at all of the observed flutter events have the same characteristics as the flow field shown in Fig. 12(*b*), supersonic flow along the suction side, a normal in-passage shock, and subsonic pressure side. The driving mechanism for the type of flutter, which occurred in all seven test se-
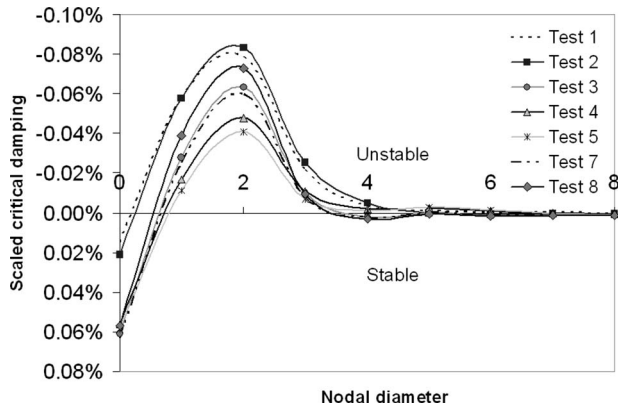
Fig. 14 Scaled critical damping versus nodal diameters for backward traveling disk modes

quences, is motion of the in-passage normal shock.

Figure 14 shows the scaled critical damping for backward traveling disk modes of zero to eight nodal diameters obtained using the linear Euler method. The frequency of the first family of modes increases with nodal diameter, which is the reason for the higher modes approaching zero damping, most easily seen by inspecting Eqs. (6) and (7). The critical damping has been scaled with relative inlet total pressure according to

$$\zeta_s = \zeta \cdot \frac{P_{ref}}{P_{0rel}} \quad (11)$$

where P_{ref} has been set to the relative inlet total pressure of test 1. It can be seen that the most unstable mode in all tests is the two nodal diameter modes. The 2ND mode is easily picked out from checking the frequency, which is well separated from 1ND and 3ND. Judging forward or backward is done by checking the phase difference of the strain gauges against the modal analysis. Also, note that if the curve for test 8 is excluded the remaining curves form three groups. A comparison of the mean flow fields will show that the flow within each group is similar. Hence, for similar flows, the magnitude of the aerodynamic damping scales linearly with the inlet total pressure.

4.3 Comparison Between Tests and Computations. A summary of the predicted aerodynamic damping and the estimated total damping at the flutter events in all tests is presented in Table 1. The second column of the table presents the predicted aerodynamic damping, ζ_{aero}, obtained with 2D linear Euler method. The third column of the table is the total damping estimated from tests, ζ_{tot}. It shows that we have been able to predict flutter in all cases where flutter occurred in the tests, i.e., the sign is negative everywhere. Comparing ζ_{aero} and ζ_{tot} we can see that the ordering of test cases in level of severity, based on the value ζ_{aero} or ζ_{tot}, produces the same results. The total damping is the sum of the

Table 1 Summary of predicted measured damping

Test No.	Predicted aerodynamic damping, ζ_{aero} (%)	Measured total damping, ζ_{tot} (%)
1	−0.08	−0.04
2	−0.04	−0.02
3	−0.02	−0.01
4	−0.02	−0.01
5	−0.01	−0.01
7	−0.06	−0.03
8	−0.08	−0.06

aerodynamic and the structural damping. Since the flutter mode is the same in all tests and the frequency is of the same order, the difference $\zeta_{tot} - \zeta_{aero}$ would ideally be constant.

From Table 1 we get that the difference $\zeta_{tot} - \zeta_{aero}$ is in the range 0.0–0.04%, which is in the interval we would expect to find the structural damping. In fact, a frequency response analysis has shown that the material damping of the blisk is 0.005%. Hence, we can conclude that the agreement between the test results and the predictions is quantitatively good.

5 Concluding Remarks

An aeromechanical test of a 1.5 stage supersonic turbine at simulated operating conditions in air has successfully been performed. During the test, free flutter was triggered at seven different operating conditions. Thus, some unique product relevant flutter data have been obtained. Based on these data the flutter boundary for the turbine was established. Using both testing and CFD has allowed a better understanding of the physics and flow mechanisms leading to flutter in this class of turbines.

The test data have also been used for validation of computational methods. Using a two-dimensional time-harmonic linear Euler method we have been able to predict flutter in all cases where we obtained flutter in the tests. The predicted values of aerodynamic damping at flutter agreed well with damping estimated from measured amplitude growth data. Although 2D CFD appears to capture the principal effects it can be foreseen that further understanding and important details will result from extending the CFD analyses to 3D.

Nomenclature

A = vibration amplitude
c = chord
k = reduced frequency
L = blade span
M = modal mass
N_k = nondimensional speed
n = number of blades of the blade row
P_{00} = manifold inlet total pressure
P_3 = exit static pressure
P_{0rel} = relative inlet total pressure
P_{ref} = reference pressure
R = gas constant
r_m = mean radius
T_{00} = manifold inlet total temperature
U = vibration energy
v_{in} = relative inlet velocity
W = aerodynamic work per cycle
ζ = critical damping ratio
ζ_s = scaled critical damping
ζ^* = characteristic damping
γ = ratio of specific heats
π_{ts} = total-to-static pressure ratio
Ω = rotational speed
ω = circular frequency

References

[1] Mårtensson, H., 2006, "Flutter Free Design of Aerodynamically Unstable Supersonic Turbines," 42nd AIAA/ASME/SAE/ASEE Joint Propulsion Conference & Exhibit, Sacramento, CA, July 9–12.

[2] Lindström, D., and Mårtensson, H., 2001, "A Method for Flutter Calculations Based on the Linearized Compressible Euler Equations," *Proceedings of IFASD Conference*, Vol. II.

[3] Groth, P., Mårtensson, H., and Eriksson, L.-E., 1996, "Validation of a 4D Finite Volume Method for Blade Flutter," ASME Paper No. 96-GT-429.

[4] Bölcs, A., and Fransson, T. H., 1986, "Aeroelasticity in Turbomachines Comparison of Theoretical and Experimental Cascade Results," Communication du Laboratoire de termique appliqueé et de turbomachines, No. 13, EPFL, Lausanne, Switzerland.

[5] Vogt, D., 2005, "Experimental Investigation of Three-Dimensional Mechanisms in Low-Pressure Turbine Flutter," Ph.D. thesis, Department of Heat and Power Technology, Royal Institute of Technology, Stockholm, Sweden.

[6] Eriksson, L.-E., 1990, "A Third Order Accurate Upwind-Biased Finite Volume Scheme for Unsteady Compressible Flow," Volvo Aero Corporation, VFA Report No. 9370-154.

[7] Larsson, J., 1998, "Numerical Simulation of Turbulent Flows for Turbine Blade Heat Transfer Applications," Ph.D. thesis, Department of Thermo and Fluid Dynamics, Chalmers University of Technology, Göteborg, Sweden.

[8] Giles, M., 1988, "Non-Reflecting Boundary Conditions for the Euler Equations," MIT Computational Fluid Dynamics Laboratory, Technical Report No. TR-88-1.

[9] Hall, K., and Crawley, E. F., 1989, "Calculation of the Unsteady Flow in Turbomachinery Using the Linearized Euler Equations," AIAA J., **27**(6), pp. 777–787.

[10] Holmes, D. G., and Chuang, H. A., 1991, "2D Linearized Harmonic Euler Flow Analysis for Flutter and Forced Response," *Unsteady Aerodynamics, Aeroacoustics and Aeroelasticity of Turbomachines and Propellers*, Springer, New York, pp. 213–230.

[11] Hall, K., and Clark, W. S., 1993, "Linearized Euler Prediction of Unsteady Aerodynamic Loads in Cascades," AIAA J., **31**(3), pp. 540–550.

Optimization of Nonaxisymmetric Endwalls in Compressor S-Shaped Ducts

Edward M. J. Naylor

Cecilia Ortiz Dueñas

Robert J. Miller

Howard P. Hodson

Whittle Laboratory,
University of Cambridge,
Cambridge,
Cambridgeshire CB3 0DY, UK

This paper presents a new design methodology for strutted S-shaped compressor ducts that allows for more aggressive designs while maintaining current levels of duct loss. A baseline duct geometry was selected, which had a radius change to length ratio that is 34% larger than current engine design limits. A large-scale low-speed model of the baseline duct was experimentally tested. The flow in the corner between the hub and the strut was found to separate due to the high local diffusion causing an increase in duct loss. Area ruling was applied to the baseline duct and was predicted to reduce the size and extent of the strut-hub corner separation, but the duct design was compromised. The duct loss coefficient at midpitch was predicted to increase compared with that of the baseline design. Nonaxisymmetric endwall profiling was then used on the duct wall, locally to the strut, to remove the strut-hub corner separation and thus reduce net duct loss, without compromising the duct design away from the strut. The endwall geometry was produced by numerical optimization. It was shown that the net duct loss was insensitive to casing profiling but highly sensitive to hub profiling. The optimal hub geometry was experimentally tested and shown to completely remove endwall strut-hub corner separation. The profiling was found to reduce the net duct loss by 16%. The paper shows that the key benefit to endwall profiling is that it can be used to safely increase the size of the design space in which aeroengine duct designers can operate.
[DOI: 10.1115/1.3103927]

1 Introduction

In aeroengines, an S-shaped annular duct is used to connect the high pressure (HP) compressor spool to the upstream spool. The duct is required because the spools are designed with different mean radii. The inlet to the duct is at the larger radius. Because the inlet and exit directions of the duct are approximately axial, there are two bends in the duct. The curvature in the S-shaped duct generates static pressure gradients normal to the streamlines. In the first bend, this results in a rise in the casing pressure and a fall in the hub pressure and, in the second bend, the opposite occurs. This results in the flow close to the hub wall being subjected to a small acceleration, followed by a large deceleration and then finally a small acceleration (Fig. 1). The flow close to the casing wall is subjected to the opposite trends, with a small initial deceleration followed by a large acceleration and then a small deceleration.

In addition to the pressure gradients caused by the curvature, the flow in the duct is subjected to streamwise pressure gradients generated by changes in area from inlet to exit. Typically, compressor ducts have a small overall area reduction, which helps to reduce the severity of adverse pressure gradients by accelerating the flow. In practice the magnitude of area change is set by the particular engine architecture.

In many aeroengines large nonlifting struts intersect the S-shaped duct. These serve two purposes. First, they are a structural element. Second they allow services, such as oil, cooling air, and the radial drive shaft, to traverse the duct. These constraints mean that the struts have a minimum cross-sectional area. Limitations on strut length, set by both upstream potential forcing lim-

its and by the duct length, result in the strut having a relatively high thickness-to-chord ratio, which is typically between 0.2 and 0.3 in modern engines.

The presence of the strut causes additional pressure gradients to be imposed on the duct wall local to the strut. At the front of the strut the flow stagnates. The flow is then accelerated to a velocity greater than that which occurs without the strut being present. Finally the flow is decelerated along the rear portion of the strut (Fig. 1). Close to the casing wall, the deceleration caused by the rear part of the strut usually occurs in the region of the S-shaped duct where curvature has resulted in a large acceleration. This means that the deceleration is unlikely to cause boundary layer separation on the casing. Close to the hub wall, the opposite occurs and the deceleration at the rear of the strut usually occurs over the region where duct curvature already results in a large flow deceleration. The result is that if the combination of strut diffusion and duct diffusion is too high, a corner separation will occur in the flow between the strut and the hub wall.

The nondimensional design space of annular S-ducts (unstrutted) depends on four main parameters. The four parameters that are most commonly used are $\Delta R/L$, h_{in}/L, A_{out}/A_{in}, and R_{in}/h_{in}. Increasing the first three parameters by either increasing the change in radius, ΔR, or reducing the length, L, or increasing the exit area, has a similar effect on the duct's performance. The large deceleration on the hub wall increases in magnitude and the flow begins to separate. This is commonly referred to as increasing duct "loading." If a strut is added to the duct an extra nondimensional design parameter is added. This is the thickness-to-chord ratio, t/c. As this parameter is raised the local diffusion along the strut-hub corner rises moving it toward separation.

During the aeroengine design process, there is a requirement to fix the annulus line early. This encourages the designers to "play safe" so as to avoid any chance of strut-hub corner separation. This often limits the design space in which the duct designer operates. The consequence of such design decisions can lead to nonoptimal designs of the neighboring compressor stages. It can also result in an unnecessary rise in engine length and thus weight
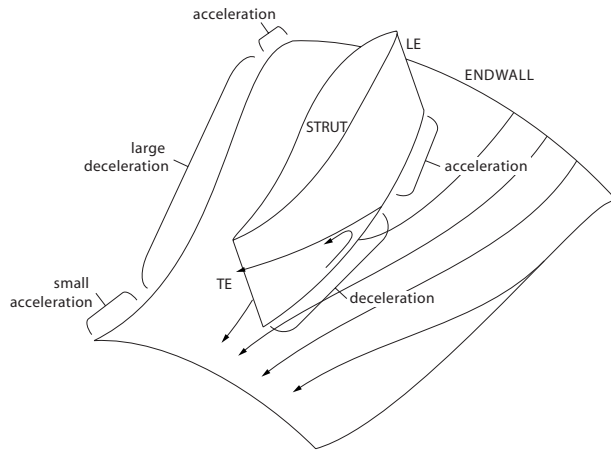
Fig. 1 Schematic of the duct pressure fields

or it can lead to restricted service access to the engine core. It is thus very important that, early in the engine design process, the designer has a good understanding of the true limits of the compressor S-shaped duct design space.

A number of researchers have investigated the flows in unstrutted annular S-ducts. Most of these investigations [1–5] have involved the experimental testing of a single geometry of duct. The geometries tested are typically of low "loading" (not close to separation). Ortiz Dueñas et al. [6] investigated the effect of varying the duct loading by keeping ΔR and h_{in} constant and reducing the duct length. The area ratio A_{out}/A_{in} was set to 1 and R_{in}/h_{in} was infinite because a two-dimensional duct was used for the study. Three lengths of duct were tested; the first was designed to be characteristic of the limits of current duct designs (100% duct), whereas the second and third had lengths equal to 74% and 64% of the length of the first duct. For each duct length, the duct turning angle at the geometrical center of the duct was optimized. It was found that reducing the length to 74% of its original length only caused a small rise in loss. But, reducing the length to 64% caused a much larger rise in loss. These results implied that the design space in which ducts operated was larger than had been previously thought.

Two researchers have experimentally investigated the flows in strutted annular S-ducts. Bailey et al. [5] investigated the effect on a compressor S-shaped duct of a single strut with a 0.12 thickness-to-chord ratio. The strut's blockage was found to have a significant effect on the duct's pressure field. The design of the duct and strut was such that geometry had a low loading and no hub corner separation occurred. Sonoda et al. [7] investigated the effect of varying the inlet boundary layer thickness on the flow development in a strutted compressor S-shaped duct. The strut had a thickness-to-chord ratio of 0.21 and the hub-strut corner had a small separation from 80% to 100% chord. Two thicknesses of the inlet boundary layers were tested, one 5% of span and one 30% of span. Changing the thickness of the inlet boundary layer was found to alter the size of the hub corner separation. Thickening the hub inlet boundary layer was found to raise the net duct loss by 33%.

The research to date has shown that as either duct loading or strut thickness-to-chord ratio is increased, the streamlines with the highest deceleration occur in the hub-strut corner. Classically the streamwise area distribution of the duct is adjusted to compensate for the extra blockage of the strut. This is often referred to as "area ruling." Wallin and Eriksson [8] performed an axisymmetric optimization with four design variables on an unstrutted turbine duct and a nonlifting strut in a compressor duct with swirling flow. The compressor nonlifting struts had a thickness-to-chord ratio of 0.21 and the duct was characterized by moderate loading ($\Delta R/L = 0.5$ and $h_{in}/L = 0.3$). They showed that net duct loss reductions

of up to 16% are achievable through what is essentially area ruling, but the design was compromised, due to a small increase in duct loss away from the strut, in order to reduce the extent of the corner separations. This raises the question of whether a nonaxisymmetric optimization, where the area is altered locally around the strut, would be more beneficial.

The aim of this paper is to take a duct that is of sufficiently high loading that when an engine representative strut with engine representative thickness-to-chord ratio is added, hub-strut corner separation occurs, and then to use nonaxisymmetric endwall profiling to remove the separation. The authors have not found any previous research on the use of nonaxisymmetric endwall profiling in compressor interstage ducts. However, the use of nonaxisymmetric profiling in other turbomachinery components has been reported by several authors [9–14]. Harvey et al. [9] described a design methodology for using nonaxisymmetric endwall profiling to control secondary flows in turbines. The proposed design was experimentally verified by Hartland et al. [10]. A significant reduction in the secondary flows was achieved along with a reduction in the net loss. Wallin and Eriksson [13] applied nonaxisymmetric profiling to an aggressive intermediate turbine duct with a lifting vane. The aim of the research was also to control secondary flows. They showed that by using optimized endwall profiling during the design process, both the improved performance and a reduced weight could be achieved.

The paper will start by describing the design of a highly loaded duct/strut combination that suffers from a strut-hub corner separation and is thus outside the normal design limits. An area-ruled design will be outlined. A numerical optimization will then be undertaken to design a nonaxisymmetric endwall profile. The endwall profiling methodology developed in this paper differs from that discussed above. In previous research publications it has been used to control endwall secondary flows whereas in this paper, it is used to reduce the peak deceleration experienced by the flow in the strut-hub corner region without adversely affecting the loss away from the strut. Finally the performance of the axisymmetric and nonaxisymmetric profiling will be compared with the baseline duct.

2 Experimental Methods

The geometry is described in Ref. [6] and is shown in Fig. 2. The duct inlet height was 137 mm. Inlet and exit flow conditioning were used to create engine representative boundary conditions. This included an inlet turbulence grid, of solidity 56%, that created a freestream turbulence of 5%. Inlet boundary layer trips were used to create hub and casing boundary layers with a thickness based on 95% of the freestream velocity, δ_{95}, of 20% of the inlet duct height, h_{in}. An exit gauze was used to simulate the presence of the downstream compressor with a loss coefficient, $\Delta P_0/q_{in}$, of 1.1. Several gauzes were tested to obtain the required loss coefficient that best represented the pressure rise created by a downstream rotor, using the method described by Place et al. [15]. The location of the gauze was chosen to be equivalent to the location of a rotor in a downstream compressor stage.
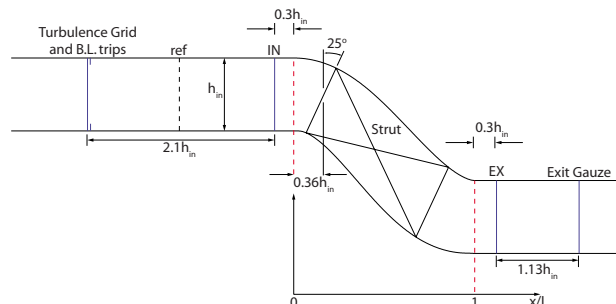

Fig. 2 Rig schematic

The nondimensional parameters of the duct are $\Delta R/L = 0.67$, $h_{in}/L = 0.40$, $A_{out}/A_{in} = 1$, and $R_{in}/h_{in} = \infty$. The thickness-to-chord of the strut is 0.271. The strut had uniform fillets with a radius of 2% of chord. The strut-hub and strut-casing corners were inclined at 25 deg relative to the radial direction. The chord based Reynolds number of the strut was 2.7×10^5. The profiled hub endwall was machined in a single piece from modeling board and replaced the original hub wall of Ortiz Dueñas et al. [6].

The strut has three rows of 27 tappings (10%, 50%, and 90% spans). The static pressure coefficients in the paper are defined as

$$C_p = \frac{P - P_{ref}}{P_{0ref} - P_{ref}} \tag{1}$$

Traversing of the flow was undertaken with a five-hole probe at $0.3h_{in}$ upstream of the start of the duct and at $0.3h_{in}$ downstream of the end of the duct (labeled "IN" and "EX" in Fig. 2). All net duct losses are calculated between these planes. The net duct loss was defined as the difference between the circumferentially mixed out and radially mass-averaged loss. The diameter of the probe was 2 mm (5–10% of the boundary inlet boundary layer height). The accuracy of the total pressure loss coefficient, Y_p, measurements is ± 0.005. The coefficient is defined as

$$Y_P = \frac{\widetilde{P}_{0_{IN}} - \widetilde{P}_{0_{EX}}}{P_{0_{ref}} - P_{ref}} \tag{2}$$

where $P_{0_{ref}}$ and q_{ref} are the freestream total pressure and dynamic head measured at the reference location (labeled in Fig. 2). For more details on measurement setup and results see Ortiz Dueñas [16].

3 Numerical Methods

The computational fluid dynamics (CFD) solver used in the present work is the 3D hybrid mesh flow solver HYDRA. The spatial discretization is based on an upwind edge-based finite volume scheme [17]. The upwind scheme chosen is the flux difference splitting approach of Roe [18]. A multigrid technique is used to accelerate the convergence to steady state. The coarser meshes are automatically generated by using an element-collapsing algorithm [19]. The performance of the multigrid technique takes advantage from a Jacobi preconditioning [20] and a five-stage Runge–Kutta scheme [21]. Turbulence is modeled using a high Reynolds number k-ε model. The high Reynolds number form of the k-ε model cannot be integrated to a viscous wall. Instead, standard equilibrium wall functions based on the "law of the wall" are used to set the wall shear stress, the production of turbulent kinetic energy, and the dissipation rate at the near wall grid nodes. Parallelization of the solver is handled through the OPLUS library [22,23] and message passing interface (MPI). The mesh generator used is the Rolls-Royce in-house code PADRAM [24]. PADRAM is based on both transfinite interpolation and elliptic grid generators to produce hybrid H–O meshes. An orthogonal body-fitted O mesh is used to capture the gradients close to the strut, while a H mesh is used in the passage. The mesh is independently generated for every stream section.

The inlet to the domain was located $3.35h_{in}$ upstream of the duct inlet to allow a boundary layer of the correct thickness to form. An actuator disk is located downstream of the duct to simulate the exit gauze. The computational mesh used had 725,000 nodes. The first grid point was located at a y^+ of approximately 20. Radial profiles of total pressure, flow angle, k, and ε were specified at the inlet. These were iteratively adjusted to match the measured values at the inlet plane of the S-shaped duct. The outlet boundary condition was a circumferentially uniform static pressure profile that was fixed to give the correct massflow through the domain. Convergence was achieved when the change in the
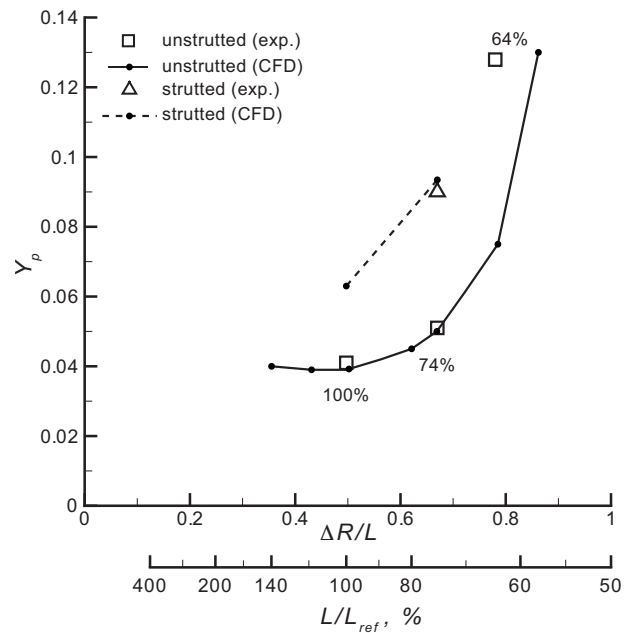

**Fig. 3   Net duct loss for unstrutted and strutted ducts**

computed total pressure loss calculated between the inlet and exit of the computational domain was less than $|1 \times 10^{-5}|$. This was typically achieved after 800 iterations.

4 Baseline Duct

The project requires a baseline duct to be designed, which is outside the limits of the current design space and is thus separated. This duct will then be used as a test case for applying the endwall profiling.

4.1 Geometry Choice. Initially, an unstrutted duct was selected that is highly loaded and was near the limit of attached flow. The measured variation of net duct loss with $\Delta R/L$ presented in Ref. [6] is reproduced in Fig. 3 (square symbols). The 100% duct was designed to be characteristic of the duct loadings used in modern aeroengines ($\Delta R/L = 0.5$ and $h_{in}/L = 0.3$). The area ratio, A_{out}/A_{in}, was set equal to 1. The results show that as the duct length is reduced to 74% there is a small rise in loss while a further reduction of 64% shows a large rise. Figure 3 also shows the numerical predictions for the 100%, 74%, and 64% unstrutted ducts. The same sharp rise in loss between 74% and 64% lengths is seen. It was therefore decided that the 74% duct geometry was sufficiently highly loaded and close to the edge of the design space that it could be used in the study. The strut chosen in this project has a thickness-to-chord ratio of 0.271. This is thicker than previous struts reported in literature and is meant to be characteristic of the struts used in modern aeroengines. To examine the effect of the strut on duct performance, the strut was added to both the 100% and 74% ducts and numerical simulations undertaken. The results of this are shown in Fig. 3. The predictions show that in the case of the 100% duct, the presence of the strut creates a 50% increase in duct loss while in the case of the 74% duct, the presence of the strut caused an 88% increase in duct loss. The strut in the 100% duct was found to have a small hub endwall separation while the strut in the 74% duct was found to have a large hub separation.

It is important that the baseline duct geometry that is chosen in this study is unseparated when no strut is present but has a large separation when the strut is added. This is because the endwall profiling local to the strut is aimed at removing the extra local diffusion caused by the strut but is not able to alter the duct shape
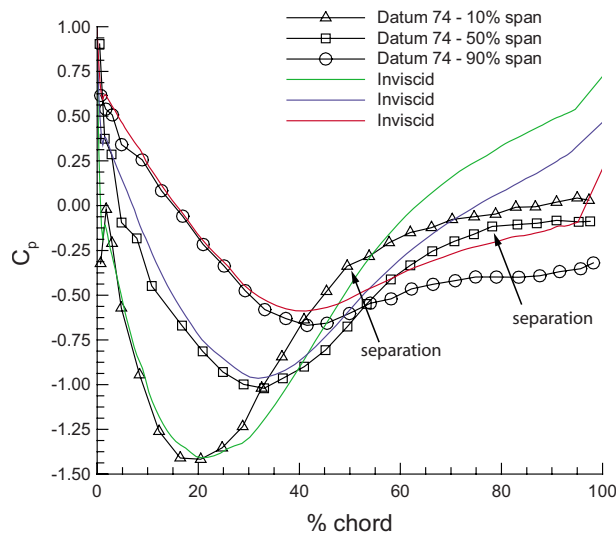
Fig. 4 Measured strut pressure distribution compared with the inviscid static pressure distribution for 74% length duct

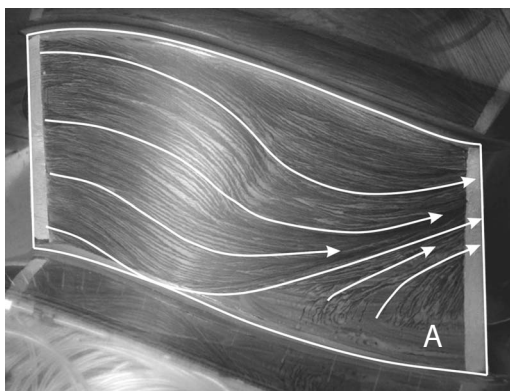Fig. 6 Measured exit contours of total pressure coefficient for 74% length duct

away from the strut. The baseline duct was therefore chosen to be the 74% duct with a strut with thickness-to-chord ratio of 0.271.

4.2 Experimental Duct Test. The experimentally measured pressure distribution around the strut in the baseline duct is shown in Fig. 4. To aid interpretation, the results of an inviscid numerical prediction have been included. The experimentally measured pressure distribution at 10% span shows a change in gradient at ~50% chord, while at 50% span it shows a change at ~80% chord. This indicates that the strut has a hub corner separation. Even though the flow on the strut surface is not two-dimensional, the magnitude of the diffusion on the strut surface at 10% span can be gauged using Lieblein's diffusion factor (D_{local}), which is defined as

$$D_{local} = \frac{V_{max} - V_{TE}}{V_{max}} \qquad (3)$$

Using compressor cascade data Lieblein showed that losses increased significantly when $D_{local} > 0.47$. At 10% span the numerically predicted inviscid pressure distribution gives a $D_{local} = 0.75$.

The exact size and location of the strut-hub corner separation were investigated using surface flow visualization, see Fig. 5. The strut-hub corner separation occupies a significant fraction of the strut surface. The separation occurs just aft of maximum strut thickness, at approximately 40% of chord. The radial pressure gradient generated by the second bend in the duct drives the low

Fig. 5 Flow visualization on the surface of the strut in the 74% length duct experimental test

momentum fluid in the separation bubble radially outwards. By the time this low momentum fluid reaches the trailing edge, it has migrated to approximately 80% of span. On the rear part of the strut surface close to the hub wall (labeled "A" in Fig. 5) a region of zero wall shear stress can be observed, where the flow visualization did not move. In addition to the strut-hub corner separation the flow visualization also shows evidence of boundary layer transition. As the boundary layer approaches 40% it starts to migrate toward the hub then exhibits a sharp deviation toward the casing. This behavior could be evidence of transition occurring on the strut. Calculations performed using ANSYS-CFX 10 (not shown) with the transition model of Menter et al. [25] showed a similar phenomenon to occur in the calculated surface streamlines to that present in the test. When the same calculation was run with fully turbulent boundary layers the "kink" in the streamlines disappeared. The tests were undertaken at a chord based Reynolds number of 2.7×10^5 with an inlet turbulence intensity of 5%. In an aeroengine, the Reynolds numbers are approximately five times greater while the turbulence intensities are likely to be similar. It is thus likely that in a real machine, the transition location will be further upstream.

The measured net duct loss coefficient Y_p was 0.09 (shown in Fig. 3). This agrees relatively closely with the computationally predicted value of 0.093. The flow field at the exit of the duct is presented in Fig. 6, in terms of total pressure coefficient. The effect of the strut corner separation on the exit traverse can be observed as the high loss region between 0% and 50% spans. Due to high levels of unsteadiness in this region, the contours of the total pressure coefficient do not appear smooth. Hotwire measurements were used to measure the unsteadiness in this region. No distinct frequency peaks were found and the spectra had a turbulent character.

5 Axisymmetric Profiling

In order to test the effect of axisymmetric profiling the streamwise area distribution of the baseline duct was adjusted in order to compensate for the blockage of the struts. Figure 7 shows the streamwise area distribution for the unstrutted duct (Duct74), the strutted duct (baseline), and the area-ruled duct (area rule).

The computed distributions of total pressure coefficient at the exit of the baseline and area-ruled ducts are shown in Figs. 8 and 9. The loss core associated with the large strut-hub corner separation in the baseline case now occurs closer to the hub endwall. This is a direct result of area ruling. The area-ruled duct reduces the maximum velocity on the strut surface and therefore reduces the maximum deceleration experienced along a streamline. Figures 10 and 11 show the predicted near wall surface flow lines. Figure 10 can be compared with the experimental flow visualization in Fig. 5. The kink in the streaklines seen in the experiment is not present in the numerical calculations due to the boundary layers being modeled as fully turbulent. This is more appropriate to the actual compressor where the Reynolds numbers are higher. The boundary layer separates from the strut in the baseline design at approximately 30% of chord. The separation extends to 60% of
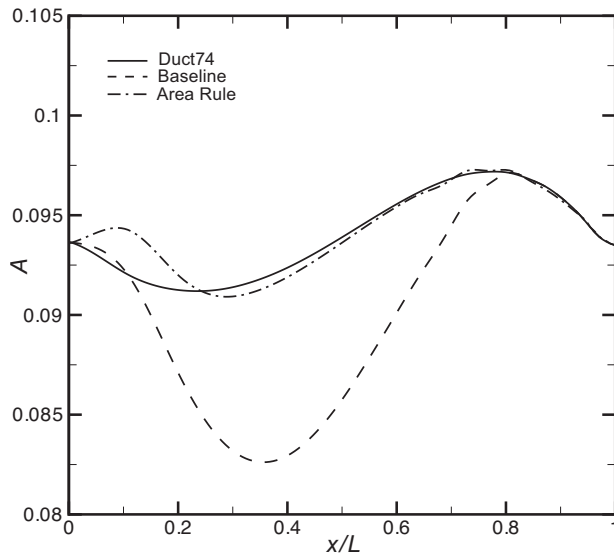
Fig. 7 Area distribution of Duct74, baseline duct, and area-ruled duct with blockage of strut removed
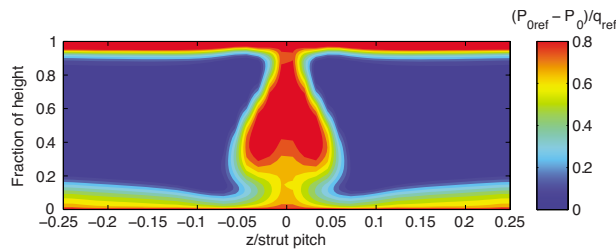

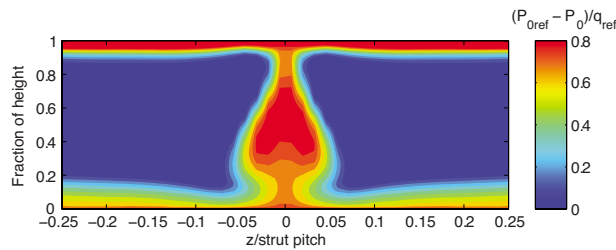Fig. 8 Computed exit total pressure coefficient for the baseline design

Fig. 9 Computed exit total pressure coefficient for the axisymmetric profiled design
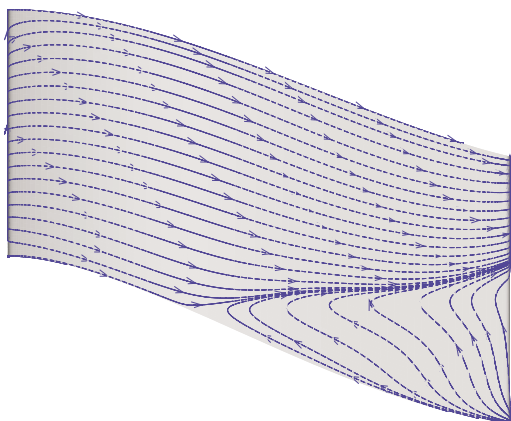

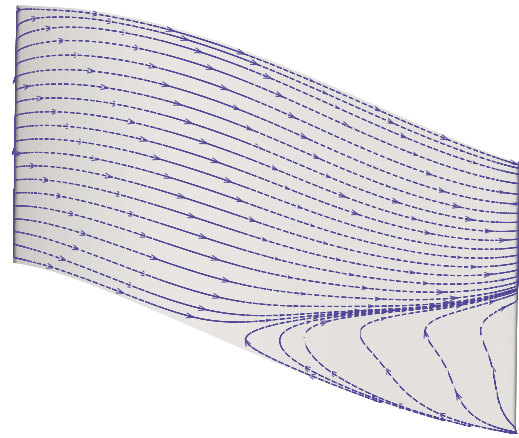Fig. 10 Computed near wall streamlines on the baseline strut

Fig. 11 Computed near wall streamlines on the axisymmetric profiled design

the duct height at the trailing edge. The area-ruled strut-hub corner separation starts at approximately 50% of chord and extends to 50% of duct height at the trailing edge.

Area ruling has clearly had a beneficial effect on the strut-hub corner separation; the predicted net duct loss has decreased by 10%. Although the overall net duct loss has decreased, the midpitch duct loss was predicted to increase by 6%. The increase in midpitch duct loss is generated by the diffusion (see Fig. 7) and increase in curvature around the first bend on the hub endwall.

6 Optimization of Nonaxisymmetric Profiling

The aim of the optimization is to move the portions of the hub and casing endwalls that are close to the vane in such a way that the extra deceleration on the hub wall caused by the presence of the strut is canceled. This is intended to reduce the local deceleration in the strut-hub corner to a safe level and thus prevent hub corner separation. The following sections describe the numerical optimization process and the final design chosen.

6.1 Response Surface Methodology. Shahpar [26] successfully demonstrated that design of experiments and response surface methods could be successfully used for optimization in a turbomachinery environment. This method was therefore chosen for this optimization. One particular advantage of response surface methods that Shahpar [26] highlighted was its ability to take full advantage of large parallel computers.

In the present work, the optimization is performed using the smart optimization for turbomachinery (SOFT) system [27] of Rolls-Royce. SOFT provides a library of different optimizers, design of experiment techniques, statistical analysis of variation, and advanced response surface methods.

The initial database was built using the quasirandom sequence generator LP-τ [28]. Unlike pseudorandom sequences, quasirandom sequences provide uniform distribution in spaces with dimensions greater than 3. The number of candidate designs used to build the database was $n=10k$, where k is the number of design variables. The response surface methodology (RSM) used to approximate the design space was the linear radial basis function. Radial basis functions were developed for scattered multivariate data interpolation [29]. The linear radial basis function is expressed as

$$\hat{y} = \sum_{i=1}^{N} \beta_i (r_i + c) \quad (4)$$

where $r_i = \|x - x_i\|$ is the Euclidean distance of the point x from the ith data point x_i in parameter space. Other radial basis functions
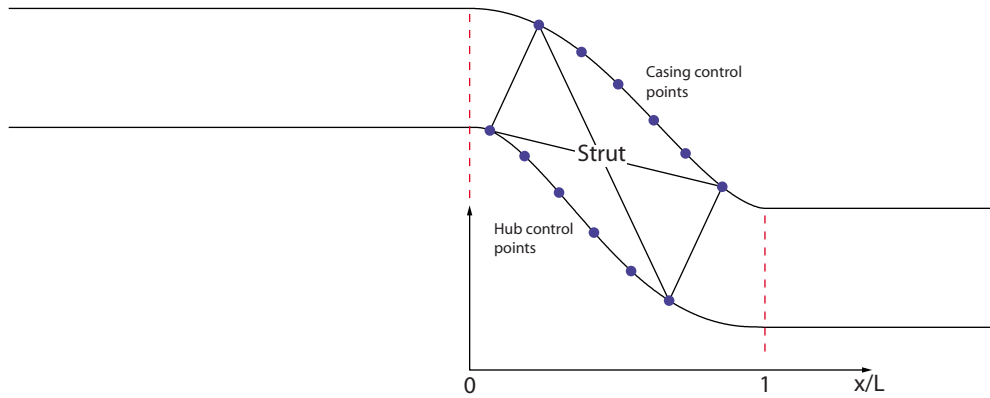
Fig. 12 Axial location of control points

are available in SOFT, e.g., cubic and Gaussian, but the linear combination was found to best fit the design space.

The adaptive range multi-objective genetic algorithm (AR-MOGA) was used to minimize the fitted response of the cost functions [30]. The adaptive range multi-objective genetic algorithm concentrates the search on the most promising area out of the initial design space. The search range is adapted according to the population statistics of the average and standard deviations, hence focusing on promising areas. The population size was based on 10 individuals that were evolved for 400 generations.

6.2 Parametrization and Constraints. The parametrization of the endwalls was performed using the method described by Harvey et al. [9]. In this approach, perturbations to the axisymmetric endwall surface are created by the product of two curves in the axial and circumferential directions. The axial profile of the perturbation is defined by a *B*-spline curve through six control points, giving six design variables per endwall, as shown in Fig. 12. The circumferential perturbations of the profiles were created using the first harmonic of a cosine function applied symmetrically about the strut center line. The perturbation is given by

$$\delta r(\theta) = AA + \frac{1}{\text{coe}} b \cos\left(\frac{2\pi\theta}{p}\right) \quad (5)$$

where p is the blade pitch, b is the amplitude of the cosine, and coe is a normalizing coefficient. The static pressure field created by the strut was found to stretch over approximately half the strut pitch. The pitch of the endwall profiling, p, was therefore set at half the strut pitch. The maximum radial amplitude applied to the 12 control points was limited to $0.07h_{\text{in}}$.

The optimization targets were to minimize the S-shaped duct total pressure loss, defined by Eq. (2), and the pitchwise static pressure distortion at inlet to the duct, defined by Eq. (6). A pressure variation equal to zero indicates a uniform static pressure field at the inlet to the duct and therefore reduced forcing on upstream components. Limits were applied to the mass-averaged radial flow angle (β) at the inlet and exit of the duct. The root mean square pressure variation (RMSPV) (inlet static pressure distortion) is given by

$$\text{RMSPV} = \left.\sqrt{\frac{\sum_i^N (P(\theta_i) - \widetilde{P})^2}{N}}\right|_{10} + \left.\sqrt{\frac{\sum_i^N (P(\theta_i) - \widetilde{P})}{N}}\right|_{90} \quad (6)$$

where $\widetilde{P}$ is the mean static pressure at the height.

6.3 Hub and Casing Profiling. The first design optimization study focused on the profiling of both the hub and the casing endwalls. The Pareto front for the fifth update to the response surface model is shown in Fig. 13. The *x*-axis represents the change in duct loss coefficient compared with the baseline duct, ΔY_p. The *y*-axis represents the inlet pressure variation expressed as a static pressure coefficient, C_p. Marked in Fig. 13 are two possible designs: the lowest duct loss design, which achieved reductions of approximately 23% of Y_p and 26% of C_p, and the lowest root mean square pressure variation design, which achieved reductions of approximately 15% of Y_p and 34% of C_p.

The minimum duct loss design was rerun, once with a plane hub surface and profiled casing surface (labeled casing only in Fig. 13) and then with a plane casing surface and profiled hub surface (labeled hub only in Fig. 13). Profiling the casing only achieved a reduction in inlet pressure distortion of 5% of C_p, while the net duct loss was increased by 8% of Y_p when compared with the baseline duct. When profiling was applied to the hub endwall only, the inlet pressure distortion was reduced by 19% of C_p, and duct loss was reduced by 22%. This shows that, as expected, the hub profiling controls the static pressure field on the hub wall and therefore plays a dominant role in controlling strut-hub corner separation.

The dominant source of loss in the strutted duct is the strut-hub corner separation. Therefore, the influence of hub profiling on this separation is investigated by comparing the static pressure distribution around the strut at the hub for the baseline duct, the duct with both endwalls profiled, and with only the hub endwall pro-
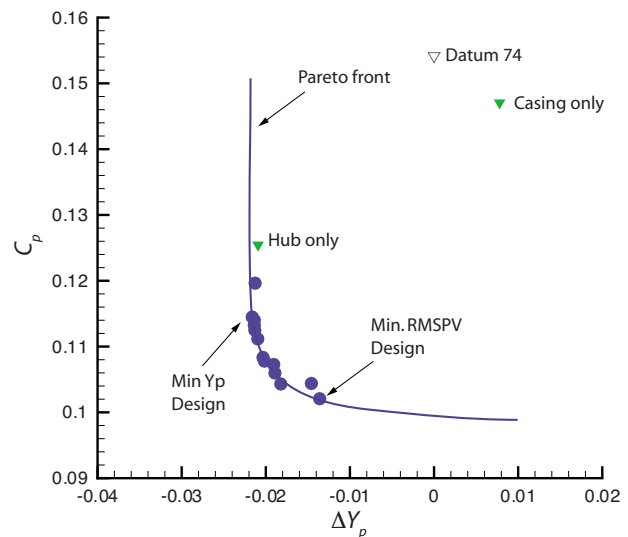

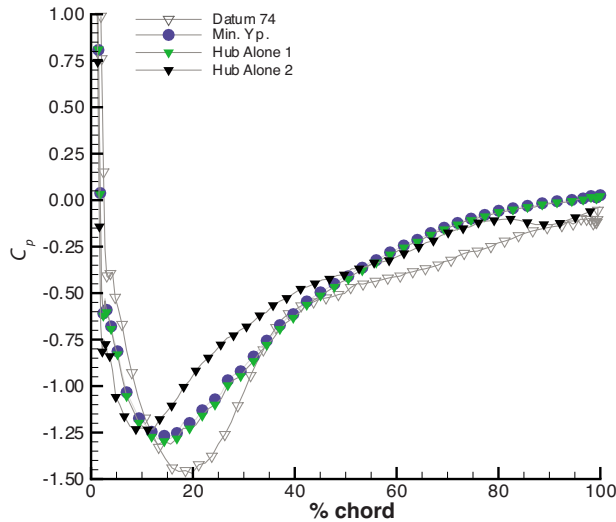**Fig. 13 Predicted Pareto solutions for the fifth update to response surface**

Fig. 14 Computed C_p distributions at the strut-hub interface

Fig. 16 Computed baseline C_p distribution on the hub endwall

filing, as shown in Fig. 14. The baseline case shows a change in gradient at 40% of chord that is caused by the strut-hub corner separation. The effect of the optimal endwall profiling ("minimum Y_p" case) is to reduce the peak velocity and move its location forward. This reduces the magnitude of the deceleration and raises the length over which it occurs, both of which help to suppress corner separation. The "hub alone 1" case is very similar to the minimum Y_p case.

Inspection of near wall streamlines (not shown) for the minimum duct loss design and the hub alone design showed the presence of a small separation close to the trailing edge. It was found that the control points close to the strut trailing edge had reached their perturbation limit of $0.07h_{in}$. The maximum allowable perturbation in the optimization was raised from $0.07h_{in}$ to $0.20h_{in}$ in the areas where the limits had been reached and the optimization was rerun, with only the hub control points active. The strut-hub corner pressure distribution for this design is shown in Fig. 14 (labeled "hub alone 2"). The new optimized hub endwall did not have a hub corner separation because it had a lower peak velocity, which had been moved further forward. The net duct loss was 26% of Y_p lower than the baseline case and 7% of Y_p lower than the initial hub alone 1 case. In addition the predicted midpitch duct loss was found to increase by 2% of Y_p compared with 6% of Y_p for the area-ruled duct design.

The hub endwall of the hub alone 2 duct geometry is shown in Fig. 15. The contours in Fig. 15 highlight the extent of profiling
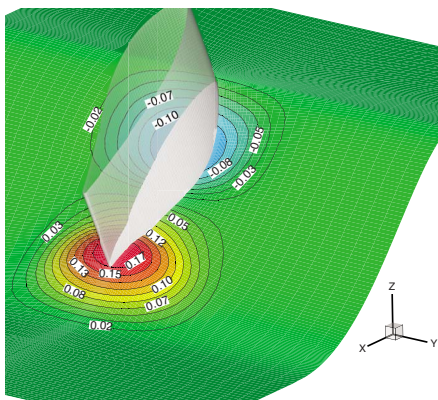
applied. Negative contours are regions of reduced endwall height and positive are regions of increased endwall height. The profile endwall can be seen to lower the wall in the front portion of the duct and to raise it in the rear portion. To see the effect this has on the static pressure distribution on the hub endwall, Figs. 16 and 17 show contours of C_p with and without endwall profiling. Figure 17 has the contours of profiled endwall's perturbation height superimposed and the labels indicate the additional concavity and convexness due to the profiling. The presence of the profiling can be seen to reduce the effect that the strut has on the hub surface static pressure. Close to the strut leading edge the profiling increases the convex curvature of the streamlines and so lowers the static pressure. This compensates for the raised static pressure caused by the front of the strut. Close to maximum strut thickness, the profiling increases the concave curvature of the streamlines, thereby raising the static pressure. This compensates for the re-

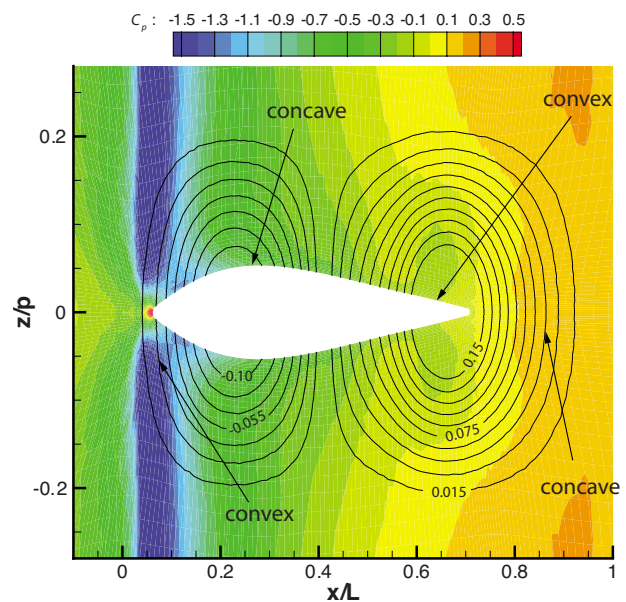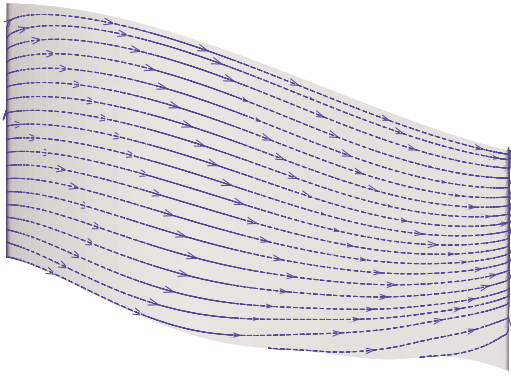**Fig. 15 Predicted optimal hub endwall design. Contours of perturbation height as a fraction of h_{in}.**

Fig. 17 Computed optimum hub C_p distribution on the hub endwall and lines of perturbation height

Fig. 18 Computed near wall streamlines for the predicted optimal design

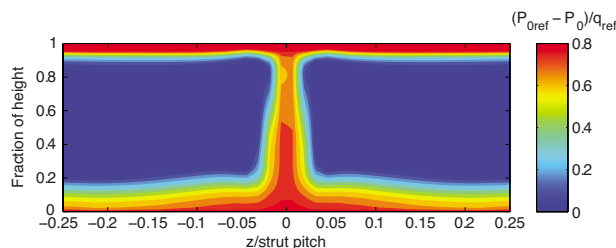Fig. 20 Measured C_p at 10% of span with and without endwall profiling

duced static pressure caused by the flow being accelerated by the strut. Along the rear part of the strut the profiling increases the convex curvature of the streamlines lowering the static pressure. This compensates for the raised static pressure caused by the deceleration of the flow by the strut. Downstream of the strut, profiling increases the concave curvature of the streamlines, thus raising the static pressure. This raises the diffusion of the flow immediately downstream of the strut. The net result is that the static pressure experienced by the hub endwall boundary layer close to the strut is now closer to that experienced by the hub boundary layer at the midpitch of the strut.

6.4 Final Design. The final design was chosen as the hub alone 2 case. Figure 18 shows the computationally predicted surface flow lines for the optimized case. Comparing Figs. 10 and 18, the effect that the nonaxisymmetric profiling has had is immediately clear. The near wall surface streamlines for the optimized design do not show any reverse flow regions on the strut surface. The corner separation present in the baseline design has been completely removed.
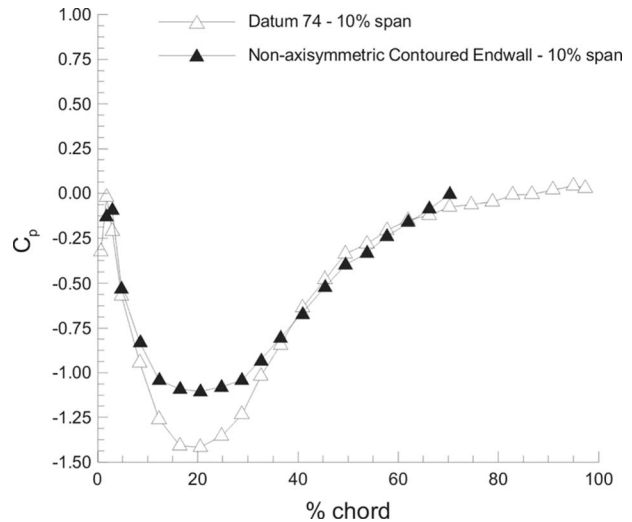
Figure 19 shows the computationally predicted duct exit total pressure coefficient. The predicted net duct loss coefficient Y_p was 0.069. In Fig. 8 the high loss core associated with the separated flow can be observed between 20% and 80% of the duct height. The wake width and depth of the optimized design are significantly reduced when compared with that of the baseline duct.

7 Profile Endwall Validation

The experimental setup for the profile endwall tests was identical to that used for the baseline tests except that the hub wall was replaced with the new profiled wall. It should be noted that the same instrumented strut was used. This meant that the pressure tappings on the strut are in an identical location to those in the baseline test. However, the presence of the endwall profiling means that they are no longer at, for example, 10% span. In fact, the rise in the hub wall at the rear of the strut meant that a number of the rear tappings were covered and are thus not used. A com-
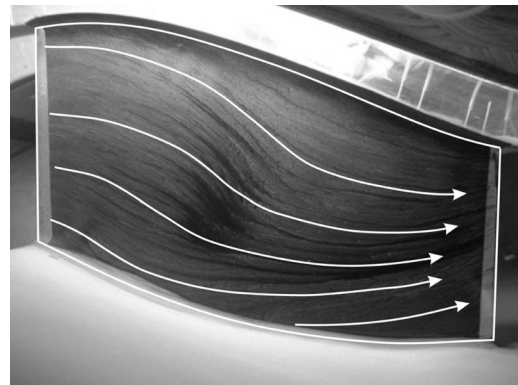
parison between the pressure distributions at 10% span of the strut with the baseline and profiled hub endwalls is shown in Fig. 20. The endwall profiling can be seen to reduce the peak velocity at 20% chord and thus reduce the peak deceleration experienced by the flow. This is consistent with the CFD predictions. The flow visualization shown in Fig. 21 shows that the presence of endwall profiling has removed the corner separation. It should also be noted that a similar boundary transition location is observed in Figs. 5 and 21.

The flow field at $0.3h_{in}$ downstream of the duct's exit is presented in Fig. 22 in terms of the total pressure coefficient. In the hub region, the presence of endwall profiling can be seen to have reduced the high loss region associated with the hub separation. It

Fig. 21 Flow visualization on the surface of the strut for the nonaxisymmetric experimental test

Fig. 19 Computed exit total pressure coefficient of the optimal design
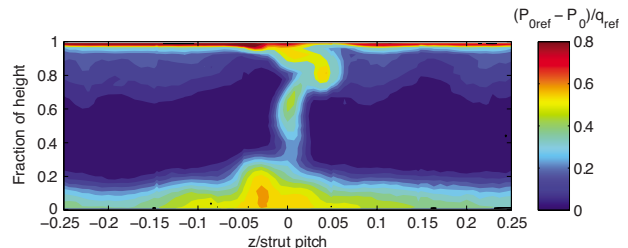
Fig. 22 Measured exit contours of total pressure coefficient for nonaxisymmetric test

can also be seen to have raised the loss over a region close to the hub wall between $-0.15z/p$ and $0.15z/p$. This is also observed in the results of the numerical predictions shown in Fig. 19. This is caused by the added deceleration caused by the endwall profiling downstream of the strut. The wake of the strut between 50% span and the casing is thinner and shallower than in the baseline case. This is due to the endwall profiling controlling the radial migration of the boundary layer fluid on the strut surface.

It is also interesting to note that the exit flow is asymmetric. In the baseline case, the strut was adjusted by fractions of 1 deg until the exit flow became symmetric. In the profiled endwall case the profiling locked the strut in one location with zero geometric incidence. This meant that it was impossible to adjust the strut. This sensitivity of the duct exit flow to small changes in incidence or small asymmetries in the flow is unusual in turbomachinery and is thought to be caused by the strut being symmetric.

8 Further Discussion

Figure 23 shows a compilation of all the measurements and predictions of net duct loss. The experimental results have shown that by removing the hub corner separation, the endwall profiling has reduced the net duct loss coefficient by 16%, without adversely affecting the loss away from the strut. This means that the range of $\Delta R/L$ over which a duct can be safely designed has been increased by 34%.

The 100% length duct was found to have a small hub separation and is thus unlikely to have achieved the minimum loss achievable for a duct of that $\Delta R/L$. This raises the question as to what the minimum achievable net loss is for a particular length of duct. In order to answer this question the two-dimensional duct loss for a particular duct length is added to the profile loss at midspan from the strut with hub profiling. This is a somewhat simplistic approach but points to the minimum loss achievable. The blue line in Fig. 23 shows this theoretical minimum loss for a range of $\Delta R/L$. This implies that a further reduction in net duct loss could be achieved.

Profiled endwalls in S-shaped ducts can be used in a number of ways to improve the performance of aeroengines. If used on existing strutted unseparated ducts it can reduce the upstream and downstream potential fields of the strut and secondary flows around the vane, thus improving efficiency. Profiling also allows the size of the design space in which aeroengine duct designers

can operate to be increased. This allows designers to increase the thickness of struts, decrease the length of the duct, or increase the radius change across the duct beyond current design limits.

9 Conclusions

Simple area ruling proved to be capable of reducing strut-hub corner separation, but the duct design was compromised. A new design methodology for the application of nonaxisymmetric endwall profiling for compressor S-shaped ducts has been described, which performs like area ruling close to the strut but crucially does not compromise the duct in regions not affected by the strut blockage. Numerical optimization of both hub and casing endwalls showed that profiling of the hub alone was critical to controlling the strut-hub corner separation and that similar levels of net duct loss could be achieved through profiling of the hub endwall alone. The nonaxisymmetric profiling of the hub endwall used curvature to minimize the pressure field imposed by the presence of the strut. This means that the static pressure experienced by the boundary layer near the strut is closer to that experienced by the hub boundary layer at midpitch. This reduces the deceleration experienced by the hub endwall boundary layer close to the strut thus avoiding strut-hub corner separation.

The use of endwall profiling has allowed a strutted duct to be designed, which has a $\Delta R/L$ that is 34% higher than current design limits with only a 11% increase in predicted net duct loss. Endwall profiling was shown to reduce the measured net duct loss by 16%. Analysis of the minimum achievable duct loss showed that by improved endwall profiling the loss could be reduced by a further 11%. In the future this may be achievable by allowing the pitch as well as the height of the profiled endwall to be optimized at each axial duct location. In practice designers may not wish to raise $\Delta R/L$ but wish to raise the thickness-to-chord ratio of the strut to increase service access to the inner annulus. The numerical predictions in Fig. 23 show that the presence of a strut of thickness-to-chord ratio of 0.271 causes the hub of both the 100% and 74% ducts to separate and thus for duct loss to rise. This shows that the thickness-to-chord ratio of the strut is likely in practice to determine whether the strut-hub corner separates. Endwall profiling is therefore likely to be of most use to designers as a method of allowing them to design thicker struts.

Fig. 23   Net duct loss

Nomenclature

A	=	area
C_p	=	static pressure coefficient
h	=	duct height
L	=	duct length
P_0	=	total pressure
P	=	static pressure
Q	=	dynamic pressure $(P_0 - P)$
R	=	radius
Re	=	Reynolds number, Uh_{in}/ν
U	=	velocity
y^+	=	$= u_\tau y/\nu$
Y_p	=	total pressure loss coefficient
ν	=	kinematic viscosity

Superscripts/Subscripts

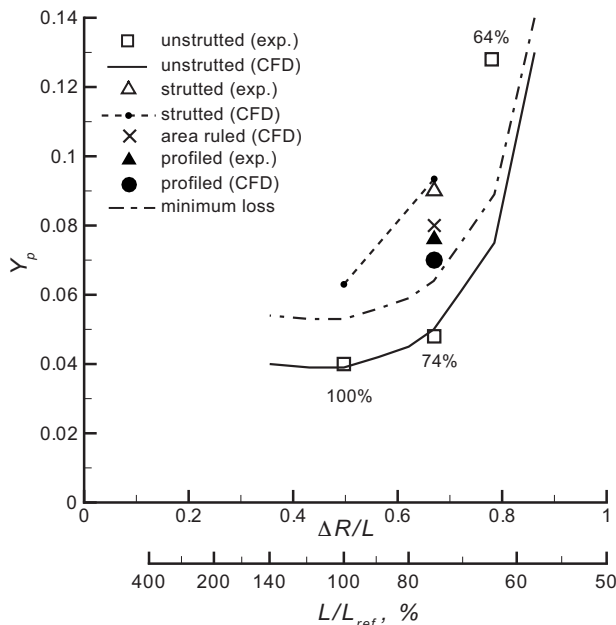|		
$\sim$	=	mixed out quantity
IN	=	duct inlet plane

EX = duct exit plane
ref = reference location
p = pitch

References

[1] Sucharov, L. J. P. H., 1971, "An Analysis of Flow in a Swan Necked Duct," MSc thesis, Cranfield University, Cranfield, Bedfordshire, UK.

[2] Abdalla, H. A., and Soundranayagam, S., 1989, "Flow in Compressor Inter-Stage Ducts," ISABE Paper No. 89-7020.

[3] Britchford, K. M., Manners, A. P., McGuirk, J. J., and Stevens, S. J., 1993, "Measurement and Prediction of Flow in Annular S-Shaped Ducts," *Engineering Turbulence Modelling and Experiments 2*, Elsevier Science Ltd., pp. 785–794.

[4] Britchford, K. M., Carrotte, J. F., Stevens, S. J., and McGuirk, J. J., 1994, "The Development of the Mean Flow and Turbulence Structure in an Annular S-Shaped Duct," ASME Paper No. 94-GT-457.

[5] Bailey, D. W., Britchford, K. M., Carrotte, J. F., and Stevens, S. J., 1997, "Performance Assessment of an Annular S-Shaped Duct," ASME J. Turbomach., **119**, pp. 149–156.

[6] Ortiz Dueñas, C., Miller, R. J., Hodson, H. P., and Longley, J. P., 2007, "Effect of Length on Compressor Inter-Stage Duct Performance," ASME Paper No. GT2007-27752.

[7] Sonoda, T., Arima, T., and Oana, M., 1998 "The Effect of Inlet Boundary Layer Thickness on the Flow With an Annular S-Shaped Duct," ASME Paper No. 98-GT-260.

[8] Wallin, F., and Eriksson, L-E., 2006, "Response Surface-Based Transition Duct Shape Optimisation," ASME Paper No. GT2006-90978.

[9] Harvey, N. W., Rose M. G., Taylor, M. D., Shahpar, S., Hartland, J., and Gregory-Smith, D. G., 2000, "Non-Axisymmetric Turbine End Wall Design: Part I—Three-Dimensional Linear Design System," ASME J. Turbomach., **122**, pp. 278–285.

[10] Hartland, J. C., Gregory-Smith, D. G., Harvey, N. W., and Rose, M. G., 2000, "Non-Axisymmetric Turbine End Wall Design: Part II—Experimental Validation," ASME J. Turbomach., **122**, pp. 286–293.

[11] Hoeger, M., Sievers, N., and Lawerenz, M., 2001, "On the Performance of Compressor Blades With Contoured Endwalls," MTU, Internal Report No. 21317.

[12] Corral, R., and Gisbert, F., 2006, "Profiled Endwall Design Using an Adjoint Navier-Stokes Solver," ASME Paper No. GT2006-90650.

[13] Wallin, F., and Eriksson, L.-E., 2007, "Non-Axisymmetric Endwall Shape Optimisation of an Intermediate Turbine Duct," ISABE Paper No. 2007-1300.

[14] Dorfner, C., Nicke, E., and Voss, C., 2007, "Axis-Asymmetric Profiled Endwall Design Using Multiobjective Optimisation Linked With 3D RANS-Flow-Simulations," ASME Paper No. GT2007-27268.

[15] Place, J. M. M., Howard, M. A., and Cumpsty, N. A., 1996, "Simulating the Multistage Environment for Single-Stage Compressor Experiments," ASME J. Turbomach., **118**, pp. 706–715.

[16] Ortiz Dueñas, C., 2007, "Investigation on the Effect of Length on Intermediate S-Shaped Compressore Duct Performance," PhD thesis, University of Cambridge, Cambridge.

[17] Moinier, P., and Giles, M. B., 1998 "Preconditioned Euler and Navier-Stokes Calculations on Unstructured Grids," Sixth ICFD Conference on Numerical Methods for Fluid Dynamics.

[18] Roe, P. L., 1981, "Approximate Riemann Solver, Parameter Vectors, and Differencing Schemes," J. Comput. Phys., **43**, pp. 357–372.

[19] Muller, J.-D., and Giles, M. B., 1991, "Edge-Based Multigrid Schemes for Hybrid," Sixth ICFD Conference on Numerical Methods for Fluid Dynamics, Oxford, UK.

[20] Moinier, P., Muller, J.-D., and Giles, M. B., 2002, "Edge-Based Multigrid and Preconditioning for Hybrid Grids," AIAA J., **40**, pp. 1954–1960.

[21] Martinell, L., 1987, "Calculations of Viscous Flows With a Multigrid Method," Ph.D. thesis, Princeton University, Princeton, NJ.

[22] Burgess, D. A., Crumpton, P. I., and Giles, M. B., 1994, "A Parallel Framework for Unstructured Grid Solvers," *Computational Fluid Dynamics'94: Proceedings of the Second European Computational Fluid Dynamics Conference*, Wiley, New York, pp. 391–396.

[23] Crumpton, P. I., and Giles, M. B., 1995, "Aircraft Computations Using Multigrid and an Unstructured Parallel Library," AIAA Paper No. 95-0210.

[24] Shahpar, S., and Lapworth, L., 2003, "PADRAM: Parametric Design and Rapid Meshing System for Turbomachinery Optimisation," ASME Paper No. GT2003-38698.

[25] Menter, F. R., Langtry, R. B., Likki, S. R., Suzen, Y. B., Huang, P. G., and Volker, S., 2004, "A Correlation-Based Transition Model Using Local Variables Part I—Model Formulation," ASME Paper No. GT2004-53452.

[26] Shahpar, S., 2004, "Design of Experiment, Screening and Response Surface Modelling to Minimise the Design Cycle Time," VKI Lecture Series on Optimisation Methods and Tools for Multicriteria/Multidisciplinary Design.

[27] Shahpar, S., 2002, "SOFT: A New Design and Optimisation Tool for Turbomachinery," *Evolutionary Methods for Design, Optimisation and Control*, CIMNE, Athens.

[28] Sobol, I. M., 1979 "On the Systematic Search in a Hypercube," SIAM (Soc. Ind. Appl. Math.) J. Numer. Anal., **16**, pp. 790–793.

[29] Buhmann, M. D., 2003, *Radial Basis Functions: Theory and Implementations*, Cambridge University Press, Cambridge.

[30] Sasaki, D., Keane, A. J., and Shahpar, S., 2006, "Multiobjective Evolutionary Optimisation of a Compressor Stage Using a Grid-Enabled Environment," AIAA Paper No. 2006-340.

Design and Experimental Verification of Mistuning of a Supersonic Turbine Blisk

Pieter Groth

Hans Mårtensson

Department of Aerothermodynamics,
Volvo Aero Corporation,
SE-461 81 Trollhättan, Sweden

Clas Andersson

Department of Turbines and Rotors,
Volvo Aero Corporation,
SE-461 81 Trollhättan, Sweden

A rotor blisk of a supersonic space turbine has previously been designed to allow for free flutter to occur in an air test rig (Groth Mårtensson, and Edin, 2010, "Experimental and Computational Fluid Dynamics Based Determination of Flutter Limits in Supersonic Space Turbines," 132(1), p. 011010). Flutter occurred at several operating conditions, and the flutter boundary for the test turbine was established. In this paper the rotor blisk is redesigned in order to inhibit flutter. The design strategy chosen is to introduce a mistuning concept. Based on aeroelastic analyses using a reduced order model a criterion for the required level of mistuning is established in order to stabilize the lower system modes. Proposals in literature suggest and analyze mistuning by varying blade mode frequencies in random patterns or by modifying blades in an odd-even pattern. Here a modification of sectors of the blisk is introduced in order to bring a sufficient split of the system mode frequencies. To verify that the redesigned blisk efficiently could inhibit flutter, an experiment similar to that in the work of Groth et al. is performed with the mistuned rotor blisk. By running the redesigned blisk at operating conditions deep into the unstable region of the tuned blisk, it is demonstrated that a relative low level of mistuning is sufficient to eliminate rotor flutter. [DOI: 10.1115/1.3072492]

1 Introduction

Turbomachinery for liquid rocket propulsion shares many of the design features and challenges found in gas turbines. The emphasis is on delivering very high power in a small machine, even to a greater extent than in jet engines.

The turbines used in gas generator cycle rocket engines are fed by bleeding off a percentage of the combustibles. A gas generator burns the combustibles to temperatures typically below 1000 K, allowing for blades without cooling. If the combustibles are hydrogen and oxygen this is done using a hydrogen rich mixture. In our context it is worth noting that the sonic speed is very high in this mixture due to the presence of hydrogen. The entry pressure is equal to the chamber pressure, 90–120 bars and an exit pressure that can be as low as atmospheric.

A rotor blisk of a turbine used in gas generator cycle rocket engines has previously been designed to allow for free system mode flutter [1] to occur in an air test rig [2]. The reason for this was to acquire product relevant test data for validation of design tools. The design allowed for operating the turbine at fully relevant similarity in aeroelastic properties of critical modes. It has been proposed based on computation in Ref. [3] that turbines in this application will be prone to flutter due to very low reduced frequencies. The blisk used in referenced test was tuned. Flutter occurred at several operating conditions, and the flutter boundary for the test turbine was established.

The objective of this work has been to introduce a design change on the same test hardware as in Ref. [2] in order to inhibit flutter and to demonstrate that the flutter boundary can be pushed away from the desired operating range. There are in principle two strategies to consider in order to eliminate flutter.

The first is to introduce structural damping. It can be done by coating the structure with another material or by introducing a damper device. Since the blisk in this application is very sturdy a thin coated layer is not likely to provide sufficient damping to inhibit flutter. Other possible damper devices for a shrouded blisk are, e.g., ring dampers. They provide damping by the energy dissipation due to friction between damper and the blisk. Common to the mentioned concepts of this strategy is the difficulty to accurately predict the damping provided by these devices. Development of such concepts has to rely on full scale testing at the true operating conditions for assessment and verification of damping capability.

The second strategy is to introduce mistuning of the rotor. Many researchers have studied mistuned systems. Most of these studies, however, have been focused on blade-to-blade variations in order to obtain an aeroelastically stable system. Proposals in literature suggest and analyze mistuning by varying blade mode frequencies in random patterns [4,5] or in an alternating high/low pattern [6].

In this work the design strategy chosen for inhibiting system mode flutter is to introduce a mistuning concept. A modification of sectors of the blisk is introduced in order to get a sufficient split of the system mode frequencies. The mistuned blisk is the same hardware as used in Ref. [2] turbine test, only modified by machining the sectors that give the mistuning. This approach guarantees that the only effects on the flutter limit are due to the mistuning.
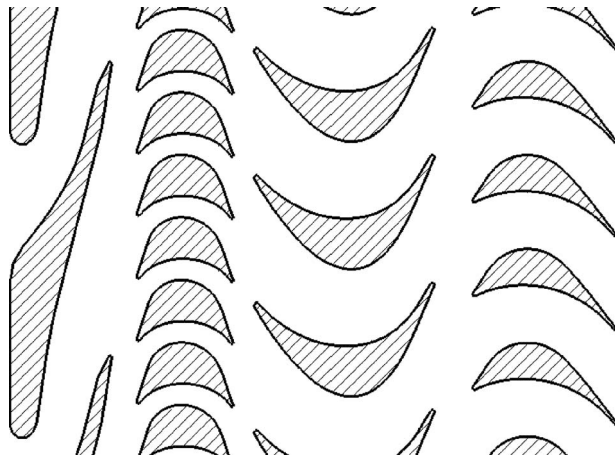
2 Background

The objective of this paper is to inhibit flutter of a supersonic rotor blisk by introducing a mistuning design and to experimentally verify that the modified rotor is flutter free. For this purpose a test turbine, which previously was made susceptible to flutter [2], has been used. In this section we will give a brief recapitulation of the test turbine and the major findings in Ref. [2] since it is the starting point of the present work.

The test turbine is based on a two-stage velocity-compounded impulse turbine, which is qualified for production. A two-dimensional layout of a similar turbine is shown in Fig. 1. The production turbine is part of a turbopump of a rocket engine. It is powered by a mixture of mainly hydrogen and some steam in the turbopump environment.

In the turbopump the turbine inlet total pressure is typically

Fig. 1 A two-dimensional layout of a two-stage impulse turbine

Fig. 2 Scaled critical damping versus nodal diameters for backward traveling disk modes

90–120 bars. The inlet total temperature is 900 K and the total-to-total pressure ratio is typically 15–20. Extensive testing in this environment is cumbersome and expensive. For more safe and controlled testing a turbine rig normally used for performance testing on site at Volvo Aero Corporation (VAC) was used. Air is used to power the turbine in the test rig, which means that no hot and explosive gases need to be handled. The maximum inlet total pressure in the test rig is 8 bars. The maximum inlet total temperature is 650 K and total-to-total pressure ratios up to 20 are possible to reach. With these differences, scaling laws have to be applied in order to restore both aerodynamic and aeroelastic properties to similarity by designing in suitable structural properties. Four scaling parameters were used in Ref. [2].

The first two parameters, which are purely aerodynamic, are easily obtained in the rig. They are the nondimensional speed, N_k, and pressure ratio defined as

$$N_k = \frac{\Omega \cdot r_m}{\sqrt{\gamma \cdot R \cdot T_{00}}} \qquad (1)$$

$$\pi = \frac{P_{00}}{P_3} \qquad (2)$$

The third and most difficult parameter to get equal in test rig and engine rig is the reduced frequency. In general it is almost impossible since the parameter depends on structural eigenfrequencies and the flow velocity according to

$$k = \frac{c\omega}{2v_{in}} \qquad (3)$$

where c is the blade chord, ω is the structural eigenfrequency, and v_{in} is the flow velocity entering the rotor.

The fourth parameter is the characteristic damping ζ^* defined as

$$\zeta^* = \frac{N \cdot P_{00} \cdot L}{2\pi M \omega^2} \qquad (4)$$

can be controlled by selecting the inlet manifold pressure carefully.

Two major modifications were introduced in the test turbine. First, the second rotor was removed. Thus, the test turbine was a 1.5 stage turbine. The second modification was aimed at making the first stage rotor susceptible to low nodal diameter (ND) system mode flutter. The first stage rotor of the production turbine, which is a bladed disk, was replaced by a rotor blisk. Moreover, to lower the frequency and to achieve similarity in reduced frequency for at least one mode, the disk part of the blisk was made as thin as the
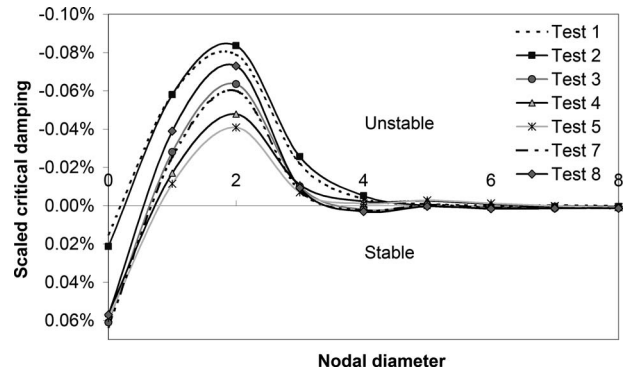
disk burst criterion permitted. In this way very good similarity between the test rig environment and the engine environment was obtained for the two ND mode.

Eight test sequences were performed during the test campaign. During seven test sequences flutter occurred. Based on these events it was possible to establish the flutter boundary. The flutter mode in all cases was identified as the backward traveling two ND system mode. The total damping at onset of flutter was estimated from the measured amplitude growth data. A very good agreement was found when comparing predicted values of the aerodynamic damping at flutter obtained using two-dimensional linear time-harmonic Euler analyzes [7] to those obtained in the tests. Figure 2 shows the predicted critical damping for backward traveling disk modes of zero to eight NDs and at the operation conditions of all flutter events. The figure shows that the most unstable mode at all flutter events is the two ND mode. Also, that all ND modes between 1 and 4 are critical.

A typical mean flow field at one of these flutter events is shown in Fig. 3. The figure shows that the flow is supersonic along the suction side through the blade passage until the exit region where series of shocks makes it subsonic. A normal shock near the leading edge makes the flow subsonic on the pressure side. It remains subsonic until the vicinity of the trailing edge where it locally is accelerated to supersonic speed. The driving mechanism for the type of flutter that occurred in all seven test sequences is the motion of the in-passage normal shock.

So far we have made a recapitulation of Ref. [2]. In the following we will focus on what is original for this work, i.e., to inhibit flutter through mistuning of the rotor.

3 Theory

This section outlines the derivation of the equations of motion for a mistuned blisk including both aerodynamic and structural couplings between orthogonal standing waves.

Designing a mistuned system to overcome flutter is an attempt to obtain an aeroelastically stable system. In order to facilitate the design of a mistuned blisk a suitable model must be constructed and appropriate criteria defined. Mistuning studies have mostly focused on blade-to-blade variation. Models like the fundamental mistuning model (FMM) used in Ref. [4] therefore describe the dynamics of blades with couplings to neighboring blades through aerodynamics and disk. Such representations are efficient in describing the effects of weight changes or blade-to-blade frequency variation on the dynamics of the system. In our case we have identified low nodal diameter modes 1–4 as the critical modes and will take a different route that leads to more compact reduced order models (ROMs) adapted for the lower modes. The model developed here resembles the model of Martel et al. [5]. For this application, the displacement is assumed to be axial and perfectly sinusoidal as a function of the tangential coordinate for a particular nodal diameter, which allows the direct use of a single mode as
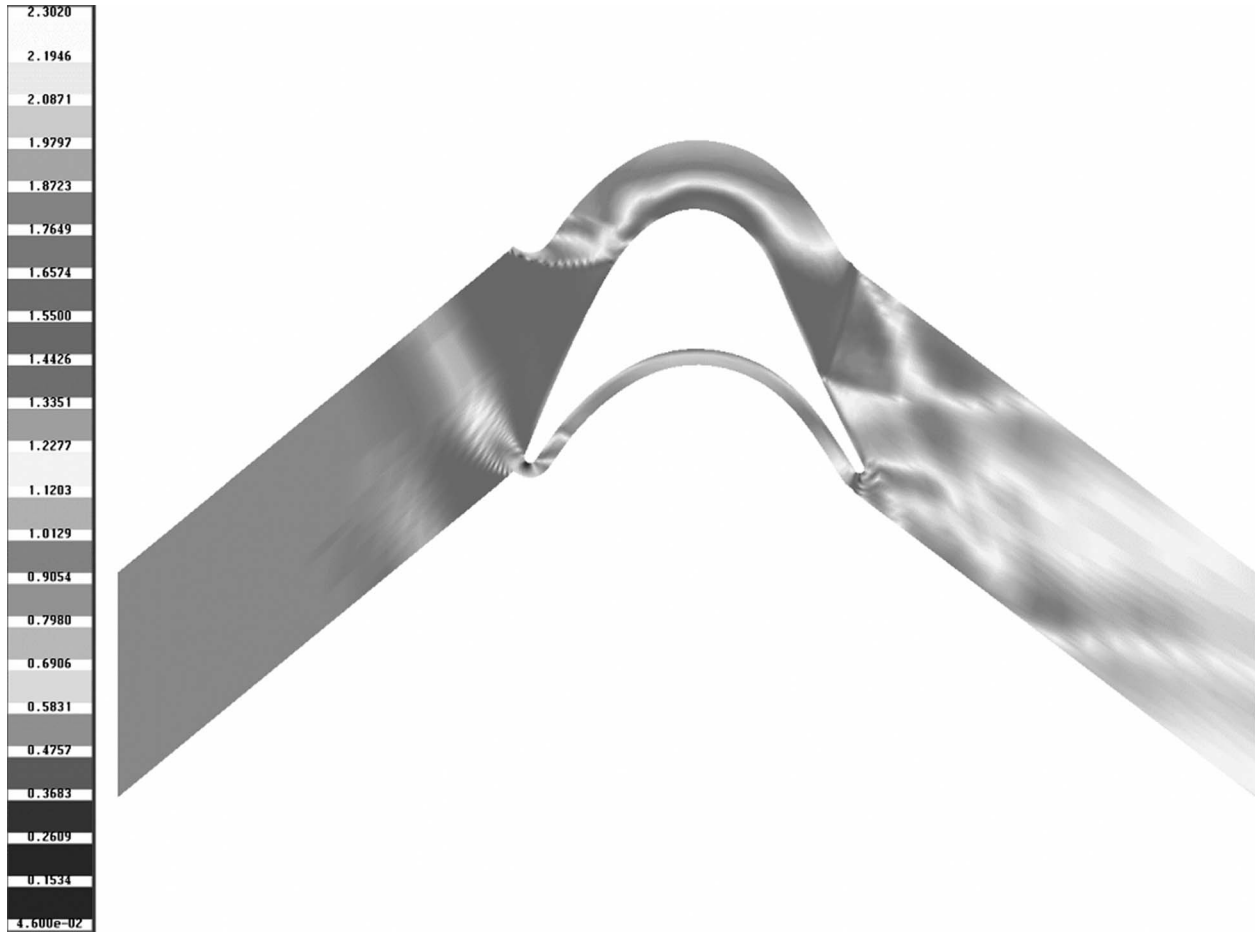
Fig. 3   Contours of relative Mach number (range from 0.0 to 2.3)

a projection basis for the ROM. The modes for small perturbations are assumed to conserve its modal shape. A very simple system consisting of only two spring-mass-damper systems describing the dynamics of each nodal diameter separately results from this. The mode shapes are the two orthogonal standing waves in the disk frame of reference. The modal mass, stiffness, and frequency of this tuned system are taken directly from the modal analysis using a standard finite element (FE) package. The structural equations are uncoupled forming a diagonal second order system. When including the modal mistuning by a small mass perturbation and a viscous damping term C, the equations of motion become

$$\begin{bmatrix} K & 0 \\ 0 & K \end{bmatrix}\begin{Bmatrix} x_1 \\ x_2 \end{Bmatrix} + \begin{bmatrix} C & 0 \\ 0 & C \end{bmatrix}\begin{Bmatrix} \dot{x}_1 \\ \dot{x}_2 \end{Bmatrix} + \begin{bmatrix} M+\Delta M & 0 \\ 0 & M \end{bmatrix}\begin{Bmatrix} \ddot{x}_1 \\ \ddot{x}_2 \end{Bmatrix}$$
$$= \begin{Bmatrix} F_1(t) \\ F_2(t) \end{Bmatrix} \tag{5}$$

The frequency of the basic modes is

$$\omega_0 = \sqrt{K/M} \tag{6}$$

In this context we will be working with small perturbations of the properties, $\Delta M/M$, in the order of a few percent.

Structural mistuning is introduced into the system simply by adding mass or stiffness to one of the modes. The simplest way of thinking of this is to place a point mass on the node line of one of the modes. This will have no effect at all on that mode but will lower the frequency of the other where the displacement is maximal at the position of the mass. In practice point masses do not exist, but form a reasonable model to work with in formulating the

equations. The FE analyses as used in Sec. 4 effectively solve the design problem using the derived design criterion.

In this model the aerodynamic terms are needed only for the positive and negative interblade phase angles given by the nodal diameter of the critical mode. Superimposing the backward and forward waves allows us to formulate the aerodynamic forces acting on the standing wave modes. The aerodynamic forces in this context are the forces onto the disk resulting from vibration in the modes themselves. With respect to flutter the important terms are the aerodynamic damping of a mode and the off-diagonal nonsymmetric coupling terms.

In order to derive the aerodynamic forces the motion of the blades is first described in the traveling wave domain. Rigid body motion in the axial direction describes the mode shape well. For the blade we have the motion described by

$$\hat{x}_k(t) = \hat{h} e^{i\omega t} e^{ik\sigma} \tag{7}$$

where $\hat{h}$ is the amplitude of the blade motion. The blade index k runs in the direction of rotation of the machine. The interblade phase angle, σ, is determined by the ND and the blade count, N, as

$$\sigma = \frac{2\pi \text{ND}}{N} \tag{8}$$

A positive interblade phase angle, σ, thus gives a backward traveling wave. Using the prescribed motion a linear Euler solver [7] calculates the force from the traveling wave on blade 0. The force for any blade can then be written as

$$\hat{F}_k(t) = \hat{F}e^{i\omega t}e^{ik\sigma} = \hat{A}(\sigma) \cdot \hat{h}e^{i\omega t}e^{ik\sigma} \qquad (9)$$

where

$$\hat{A}(\sigma) = \hat{F}/\hat{h} \qquad (10)$$

is the force as calculated in the CFD code. For linear systems we can freely superimpose any results. Summation of forward and backward traveling waves of the same nodal diameter gives a standing wave:

$$\hat{x}_{1,k}e^{i\omega t} = \hat{h}e^{i\omega t}(e^{ik\sigma} + e^{-ik\sigma}) = 2\hat{h}e^{i\omega t}\cos(k\sigma) \qquad (11)$$

For the second mode a phase shift is introduced on the traveling waves such that

$$\hat{x}_{2,k}e^{i\omega t} = 2\hat{h}e^{i\omega t}\sin(k\sigma) \qquad (12)$$

Performing the summation of forces we get for the force due to the standing wave motion in mode 1 as

$$\begin{aligned}\hat{F}_{1,k}(t) &= \hat{F}(\sigma)e^{i\omega t}e^{ik\sigma} + \hat{F}(-\sigma)e^{i\omega t}e^{-ik\sigma} \\ &= e^{i\omega t}[\cos(k\sigma)(\hat{F}(\sigma) + \hat{F}(-\sigma)) \\ &\quad + i\sin(k\sigma)(\hat{F}(\sigma) - \hat{F}(-\sigma))]\end{aligned} \qquad (13)$$

and for mode 2 the force becomes

$$\begin{aligned}\hat{F}_{2,k}(t) &= \hat{F}(\sigma)e^{i\omega t}e^{ik\sigma}e^{-i(\pi/2)} + \hat{F}(-\sigma)e^{i\omega t}e^{-ik\sigma}e^{i(\pi/2)} \\ &= e^{i\omega t}[-i\cos(k\sigma)(\hat{F}(\sigma) - \hat{F}(-\sigma)) \\ &\quad + \sin(k\sigma)(\hat{F}(\sigma) + \hat{F}(-\sigma))]\end{aligned} \qquad (14)$$

The modal force per blade onto the first standing wave due to itself is

$$\hat{F}_{11} = \frac{1}{N}\sum_N \hat{x}_{1,k} \cdot \hat{F}_{1,k} = \hat{h}(\hat{F}(\sigma) + \hat{F}(-\sigma)) \qquad (15)$$

The modal force per blade exerted on mode 2 due to mode 1 motion is

$$\hat{F}_{21} = \frac{1}{N}\sum_N \hat{x}_{2,k} \cdot \hat{F}_{1,k} = i\hat{h}(\hat{F}(\sigma) - \hat{F}(-\sigma)) \qquad (16)$$

The modal force per blade exerted on mode 1 due to mode 2 motion is

$$\hat{F}_{12} = \frac{1}{N}\sum_N \hat{x}_{1,k} \cdot \hat{F}_{2,k} = -i\hat{h}(\hat{F}(\sigma) - \hat{F}(-\sigma)) \qquad (17)$$

The modal force per blade onto the second standing wave due to itself is

$$\hat{F}_{22} = \frac{1}{N}\sum_N \hat{x}_{2,k} \cdot \hat{F}_{2,k} = \hat{h}(\hat{F}(\sigma) + \hat{F}(-\sigma)) \qquad (18)$$

The aerodynamic forces on the modes can thus be written on matrix form at a given frequency as

$$\begin{bmatrix} (\hat{A}(\sigma) + \hat{A}(-\sigma)) & -i(\hat{A}(\sigma) - \hat{A}(-\sigma)) \\ i(\hat{A}(\sigma) - \hat{A}(-\sigma)) & (\hat{A}(\sigma) + \hat{A}(-\sigma)) \end{bmatrix} \begin{Bmatrix} \hat{x}_1 \\ \hat{x}_2 \end{Bmatrix} = \begin{Bmatrix} \hat{F}_1 \\ \hat{F}_2 \end{Bmatrix} \qquad (19)$$

The frequency, ω_{a0}, at which the aerodynamic response is calculated is normally the tuned system frequency. This harmonic response is translated to an approximate temporal response in order to use the standard form of the dynamic equation to formulate the eigenvalue problem. The notation for the real coefficients is

$$A^+ = \tfrac{1}{2}\mathrm{Re}(\hat{A}(\sigma) + \hat{A}(-\sigma))$$

$$A^- = -\tfrac{1}{2}\mathrm{Im}(\hat{A}(\sigma) - \hat{A}(-\sigma))$$

$$B^+ = -\frac{1}{2\omega_{a0}}\mathrm{Im}(\hat{A}(\sigma) + \hat{A}(-\sigma))$$

$$B^- = \frac{1}{\omega_{a0}}\mathrm{Re}(\hat{A}(\sigma) - \hat{A}(-\sigma)) \qquad (20)$$

Introducing real coefficients in Eq. (19) and transforming it to the time domain we get the following expression for the aerodynamic forces in the vicinity of ω_{a0}:

$$\begin{bmatrix} A^+ & -A^- \\ A^- & A^+ \end{bmatrix} \begin{Bmatrix} x_1 \\ x_2 \end{Bmatrix} + \begin{bmatrix} B^+ & -B^- \\ B^- & B^+ \end{bmatrix} \begin{Bmatrix} \dot{x}_1 \\ \dot{x}_2 \end{Bmatrix} = \begin{Bmatrix} F_1 \\ F_2 \end{Bmatrix} \qquad (21)$$

The terms in this form are simple in structure and can be given some physical meaning. The A^+ term is the force from a standing wave onto itself, the equivalent of a spring to ground term. B^+ is in the same way equivalent to a viscous damper to the ground. These can, however, be negative in value. Normally, the A^- term would be the term to cause instability in the system. It is antisymmetric giving a nonreciprocal force acting between the modes. This either contributes to damping or amplification depending on whether the wave is forward or backward traveling.

$$\begin{bmatrix} K+A^+ & -A^- \\ A^- & K+A^+ \end{bmatrix} \begin{Bmatrix} x_1 \\ x_2 \end{Bmatrix} + \begin{bmatrix} C+B^+ & -B^- \\ B^- & C+B^+ \end{bmatrix} \begin{Bmatrix} \dot{x}_1 \\ \dot{x}_2 \end{Bmatrix} \\ + \begin{bmatrix} M+\Delta M & 0 \\ 0 & M \end{bmatrix} \begin{Bmatrix} \ddot{x}_1 \\ \ddot{x}_2 \end{Bmatrix} = \begin{Bmatrix} 0 \\ 0 \end{Bmatrix} \qquad (22)$$

The structural damping of blisks in the actual alloys is very small in itself. The viscous damping term, C, is therefore neglected, which is conservative with respect to flutter limits.

Using an increasing ΔM as a parameter the system damping can be plotted against the separation of the eigenfrequencies as found in the modal analysis. The frequency separation parameter, df^*, if defined as the frequency separation divided by the tuned system frequency and can be written as

$$df^* = \frac{\Delta\omega}{\omega_0} = 1 - \sqrt{\frac{M}{M+\Delta M}} \qquad (23)$$

This measure is very suitable for the purpose of finding a design criterion to evaluate using FE modal analysis due to its simplicity. The designer can use standard modal analysis and design tools with the goal to find a solution with the prescribed frequency split.

The system damping is calculated as the ratio of the real part of the eigenvalue to the imaginary or in other terms the growth rate divided by the frequency. This is equal to the critical damping ratio often used to express the damping characteristics. Solving the aeroelastic system on reduced form is quickly done in a standard numerical package. It amounts to solve the above nonsymmetric 4×4 eigenvalue problem for increasing mass perturbations.

Figure 4 shows the impact of the frequency separation, df^*, on the critical damping for the two ND mode at different operating conditions. The damping is shown as a function of the frequency separation for the most critical mode found in analysis and the turbine flutter test [2] using the same hardware, at different operating points. The selection comes from the turbine reference operating point and relevant extremes in the operating envelope. The behavior is similar in all cases, showing the identical result for zero separation when the damping is calculated directly for the tuned modes. The change in frequency is realized from either a stiffness or mass change over a sector of the disk or shroud, as described in Sec. 4 of this paper. Upon inspecting Fig. 4 different regions can be noted. For very small frequency separations the mistuning results in no effect. This is the separation over which the aerodynamics is sufficiently strong to bring the system into a coupled mode. For "large" separations the modes are effectively split and therefore become more or less equal. In this case the
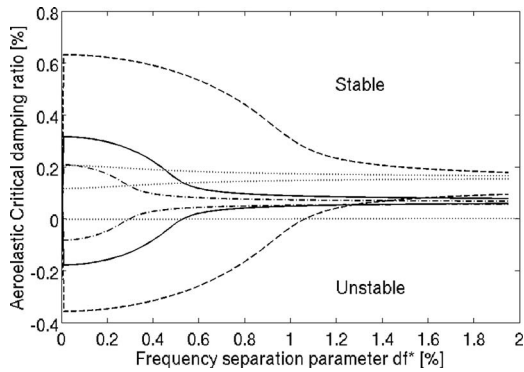
Fig. 4 The critical two ND mode damping as a function of the frequency separation parameter df^* under different operating conditions (— ref. point, -·- and ··· limit operating points, and - - - double pressure)

necessary symmetry is broken and the modes act as standing waves with no aeroelastic interaction. Both waves are stable.

The stability line is crossed for an intermediate separation where the slope of the damping is large. This would be the critical separation for structures with negligible structural damping. If viscous damping in the material is significant, this can be added to the system damping, thus changing the critical separation toward lower necessary values.

Figure 5 shows the behavior for different modes. The same pattern holds for all the lower modes, and for each of the modes shown, a separation should be provided.

Theoretically it is sufficient to bring the total system damping above zero in order to have a stable system. In practice, however, if the theoretical value is correct and just above 0, we expect that almost half of the hard wares would be unstable.

Hence, the following requirements on the design therefore have to be satisfied.

- Sufficient separation in order to be safely outside manufacturing variations; otherwise some could be accidentally in tune.
- Sufficient separation to act as pure split modes is preferred since the dynamic properties at this point would be rather insensitive to computational errors or variations in properties.

From Figs. 4 and 5 it is clear that 1% separation should be sufficient to render the system stable for any conceivable operating condition. Starting from a tuned blisk analysis the designer can now proceed to seek solutions by finding design that in a modal analysis provides the defined separation.
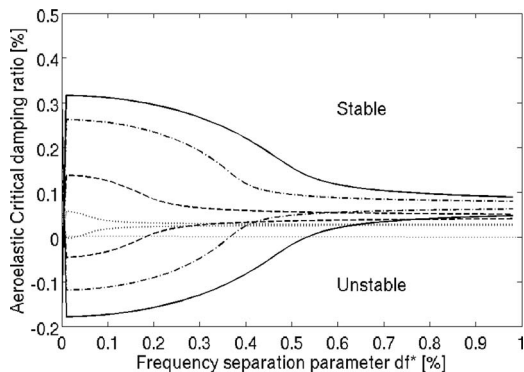
Fig. 5 Damping as a function of df^* for different nodal diameters (-·- one ND, — two NDs, - - - three NDs, and ··· four NDs)

Table 1 Eigenfrequencies of the tuned rotor at rest (hertz)

|	ND 1	ND 2	ND 3	ND 4
Eigenfrequencies	448	508	1034	1911

4 Design

The objective of the redesign is to introduce mistuning, i.e., to separate the nodal diameter eigenmodes prone to flutter in frequency. Predictions indicated a flutter risk for the eigenmodes corresponding one to four nodal diameters, see Fig. 2. The eigenfrequencies of these eigenmodes are presented in Table 1. These eigenfrequencies are valid for a nonrotating tuned blisk at room temperature. Moreover, as mentioned in Sec. 2 the most unstable motion has periodicity of two nodal diameters.

4.1 Introducing Mistuning. The level of mistuning needed to inhibit flutter is predicted in Sec. 3. The objective of the redesign is to obtain a rotor blisk having these properties. In reality, there are several sources that may contribute to mistuning. The redesign will introduce mistuning. In addition, there may be unintentional mistuning that most probably comes from manufacturing, instrumentation, balancing, and mounting of the turbine. Therefore, a margin is added to the predicted values so that the modified rotor blisk in reality renders values close to or above the frequency separation wanted. The margin should account for both the unintentional mistuning and errors in predictions of the frequency separation.

Figure 6 illustrates the modified rotor blisk. Two equally sized grooves are milled in the shroud. The tangential distance between the centers of these grooves is 180 deg. One groove can be seen while the other one is on the opposite side of the blisk. This pattern is the lowest order of cyclic symmetry and has the ability to introduce mistuning to the modes of interest. The level of mistuning of the design is therefore a matter of the size of the grooves.

A higher order cyclic symmetrical mistuning pattern does not have this feature of introducing mistuning to every nodal diameter. Four identical grooves in the shroud with the tangential distance of 90 deg, for instance, would have separated the eigenfrequencies corresponding to every second nodal diameter starting at No. 2.

Figure 7 shows predictions of the eigenmodes with two nodal diameters. In Ref. [2] it is demonstrated that these eigenmodes are the most critical ones concerning flutter. It can be seen that the modal displacement near the modified regions is small for mode (a) while it is large for mode (b). This difference renders a difference in eigenfrequency: The eigenfrequency of mode (a) is lower than the one of mode (b). A frequency separation may be obtained by changing the stiffness and/or the mass around the rotor blisk.
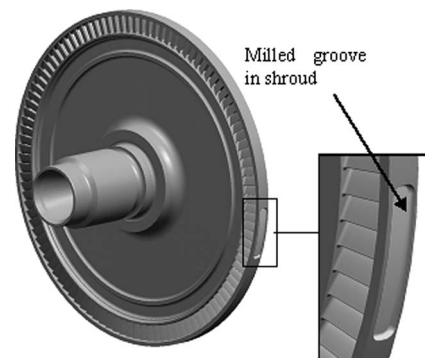
Fig. 6 The design of the rotor blisk with detuning
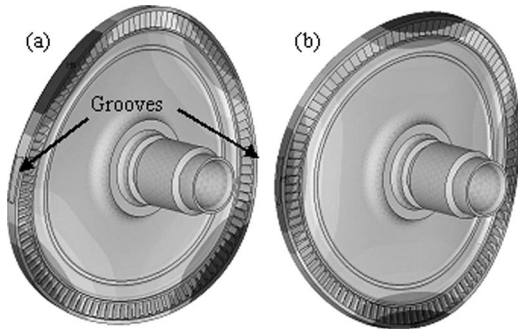
Fig. 7 Standing eigenmodes of nodal diameter 2 in the disk frame of reference

In this case, the mass effect is the dominating one. The mode with high modal displacement at the grooves, mode (b), has higher eigenfrequency than the other one.

4.2 Predictions and Experimental Verification. In the design process, the frequency split of nodal diameter two modes is critical and it governs therefore the size of the grooves in the shroud.

The objective value for these modes is set to 1.3% at reference operating conditions at the test: A margin of 0.2% is added to the predicted value of 1.1% from aeroelastic analyses, see Sec. 3.

The frequency split as a function of the size of the grooves is based on finite element analyses. In these analyses any impact from temperature, stress stiffening, and spin softening is included. Models of the whole rotor blisk including modifications are analyzed. The shaft and its boundary conditions are, however, modeled in a simplified manner.

The result from these analyses is that the removal of the material from the rotor blisk should be about 9 g in total for this specific rotor. Figure 7 shows predictions of the eigenmodes with two nodal diameters. The corresponding eigenfrequencies of this design are predicted to meet the objective 1.3% at reference operating conditions. The predicted values of the frequency split sufficient to suppress flutter together with the corresponding values after the redesign are presented in Table 2.

The values of the frequency separation were experimentally tested before and after milling the grooves in the shroud. The blisk was then at rest. The source of excitation was a loudspeaker, and the response was measured close to the shroud using an accelerometer. It should be mentioned that the mass of the accelerometer had little impact on the frequency separation. The frequency content of the excitation was chosen to excite the eigenmodes of interest. Results from the predictions and experimental frequency testing are gathered in Table 3. It should be noted that the redesign renders a level of mistuning higher than the unintentional mistuning of a tuned blisk. In addition, values from predictions and testing are in very good agreement except for modes with one nodal diameter. This is explained by the simplified modeling of the axle and the boundary conditions. The higher modes can be considered to be mainly disk modes while the axle is active for the modes with one nodal diameter. This renders that the modeling of the axle as well as the boundary conditions plays a role for the modes with one nodal diameter. Another observation that can be

Table 2 Frequency separation of eigenmodes with one to two NDs at reference operating conditions

	ND 1	ND 2	ND 3	ND 4
Results from aeroelastic analyses	0.7%	1.1%	0.4%	0.1%
Mistuned blisk, prediction	0.9%	1.3%	1.2%	1.0%

Table 3 Frequency separation of eigenmodes with one to four NDs for a nonrotating blisk

	ND 1	ND 2	ND 3	ND 4
Tuned blisk, test	0.2%	0.1%	0.1%	0.4%
Mistuned blisk, prediction	1.1%	1.5%	1.2%	1.0%
Mistuned blisk, test	0.5%	1.3%	1.2%	1.2%

made is that the frequency split predicted at rest is somewhat different as compared with reference operating conditions. This difference is a result of the phenomenon called stress stiffening.

The frequency separation during air testing is also found. These values are presented in Sec. 6.

5 Test Setup

As mentioned in Sec. 2, the test turbine of investigation [2] has also been used in the present work but with one modification only. The rotor blisk has been mistuned, as described in Sec. 4. Figure 8 shows the test hardware. The inlet manifold with the first stator is labeled 12. The rotor and second stator are labeled 13 and 14, respectively.

The blisk was instrumented with 16 strain gauges. Ten gauges were mounted at different angular positions on the disk rim to be able to assess the nodal diameter pattern of the eventual vibration. Two gauges were mounted on blades and four on the shroud. Figure 9 shows the instrumented blisk.

Two tape recorders were used to record strain gauge signals with a bandwidth of 40 kHz. The turbine was also instrumented with probes for measuring total temperature and total pressures at the inlet and at the outlet. Moreover, a Venturi probe for massflow measurement and pressure gauges between blade rows and accelerometers on bearing housings.

A water brake was used to load the turbine.
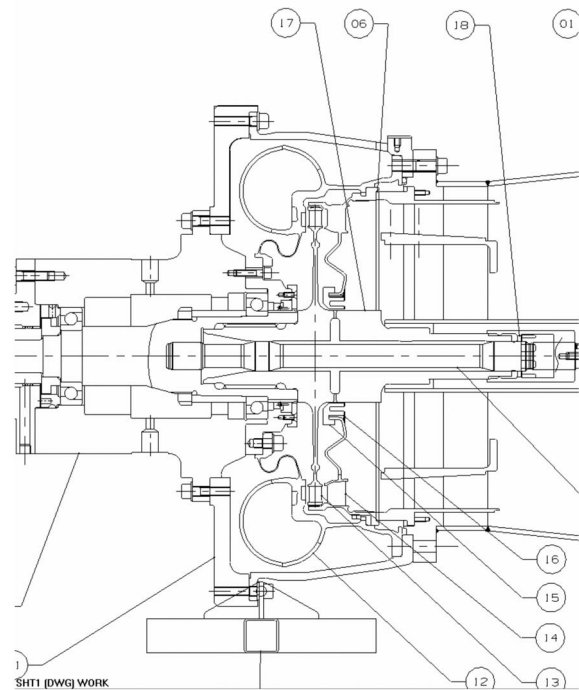
Fig. 8 Drawing of test turbine

Fig. 9   Instrumented blisk

Fig. 11   Time spectral map 20–750 Hz for test sequence with N_k 0.11

6   Results

The test campaign for verification of the mistuning concept was focused on exploring the region beyond the flutter boundary of the tuned rotor found in Ref. [2], see Fig. 10. For the test sequences shown in the figure the inlet total pressures varied between 150 kPa and 700 kPa and the inlet total temperature was 400 K.

Previously, in Sec. 3, it has been demonstrated that doubling the inlet pressure leads to higher requirements on the mistuning in order to obtain stable modes, see Fig. 4. A way of demonstrating the flutter margin in the test is therefore to operate at increased inlet pressures. The intention for the test campaign was to perform all test sequences at a maximum inlet total pressure of the rig, i.e., 800 kPa. The water break could, however, not provide sufficient moment to allow for testing at maximum inlet pressure and at very low nondimensional speeds, N_k, i.e., 0.13. Thus, the inlet total pressure varied between 450 kPa and 800 kPa, which in all sequences are substantially higher than in the reference test [2]. The inlet total temperature was kept at 400 K during the whole test campaign. Figure 10 shows the tested operating conditions defined by total-to-static pressure ratio, π_{ts}, and nondimensional speed, N_k. The pressure ratio is normalized by the pressure ratio at reference operating condition. The dashed line is the flutter boundary for the tuned blisk.

In order to understand the dynamics of the disk and to verify the absence of limit cycle type flutter, more detailed signal analysis of the responses was performed. Figures 11–14 show examples of the response at one of the rim gauges for 20–1500 Hz excitations during different test sequences.
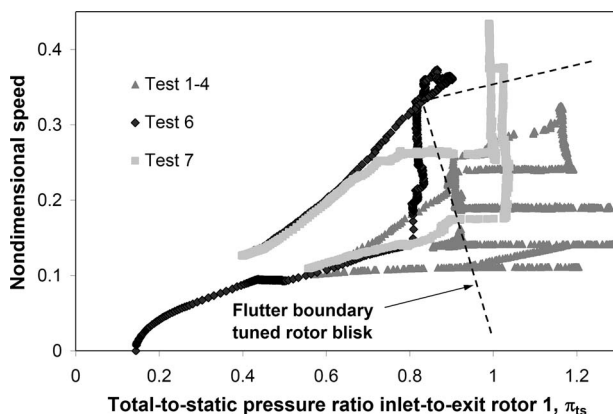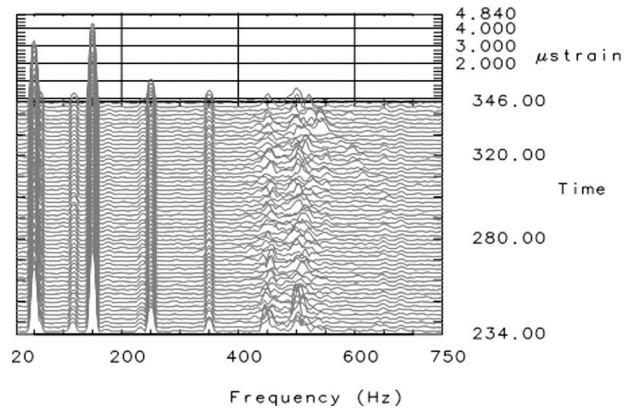
Figures 11 and 12 show the strain gauge responses versus frequency and time for the test sequences 1–4 with N_k equal to 0.11. The responses at 50 Hz, 150 Hz, 250 Hz, and 350 Hz in Fig. 11 are due to disturbances from electric field (ac). As can be seen in Figs. 11 and 12 the vibration amplitudes for one ND to three ND modes, i.e., responses at 450 Hz, 520 Hz, and 1020 Hz, are bounded and less than 5 μstrain. These types of low level responses are typically found in the application. They are due to the high level noise always present in the machine. For the rest of test sequences 1–4, figures similar to Figs. 11 and 12 were obtained from the signal analysis. They show the same behavior as Figs. 11 and 12. In other words only stable vibrations have been detected during this test sequence.

For the two other test sequences the entire sequences have been mapped out in logarithmic plots in order to identify any possible dynamic response. Figures 13 and 14 show the strain gauge response versus rotor speed and frequency. These sequences span over large ranges of speed, 1–250 rps, and normalized pressure ratio, 0.15–1.1. The maximum response is less than 10 μstrain.

Figures 13 and 14 show that there were only noise excited modes present in these test sequences. In other words only stable vibrations were detected during test sequences 6 and 7 of Fig. 10.

The entire test could be performed at increased pressure levels compared with those in Ref. [2] with no indications on high amplitude flutter at any mode. This is in itself an ultimate proof that the mistuning design has worked as intended. But, it is not sufficient to experimentally assess the flutter margin.

The design of the test hardware has been described in terms of taking the steps of deriving a necessary frequency separation and then the realization of a design that is analyzed in using modal
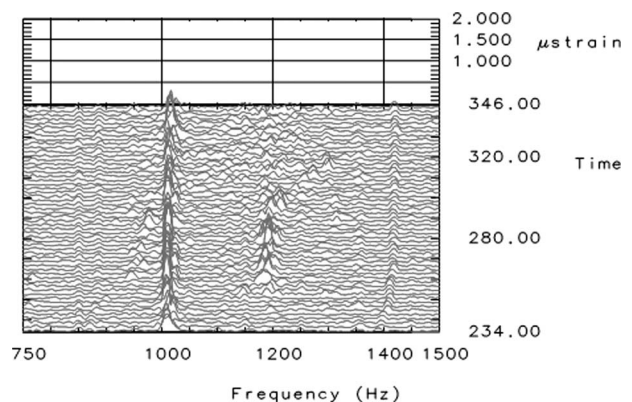

Fig. 10   Operating conditions in test

Fig. 12   Time spectral map 750–1500 Hz for test sequence with N_k 0.11
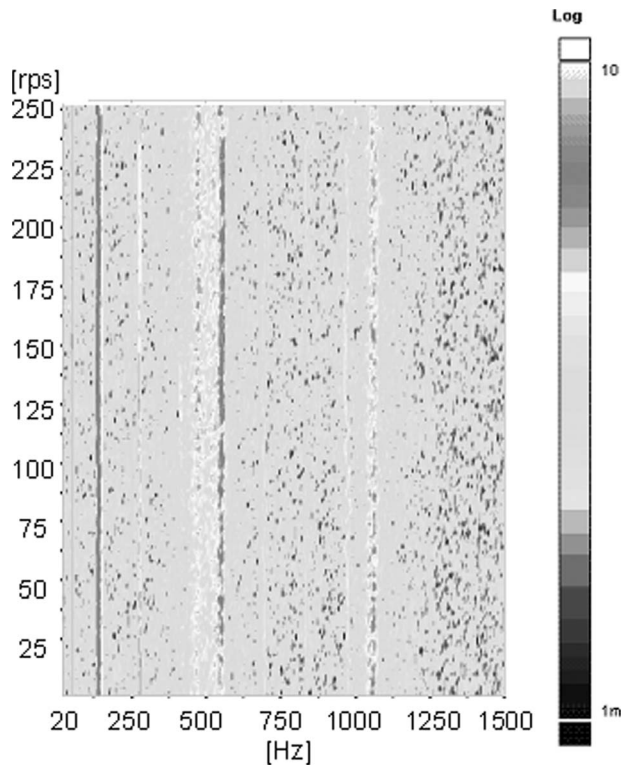
Fig. 13 Time spectral map 20–1500 Hz; test sequence 6 in Fig. 10

Fig. 15 Coherent output power spectrum for the one ND and two ND modes

analysis in FEM. The separation is small and therefore it was deemed necessary to verify that the design intent was met in terms of mode separation. In order to assess this during the test campaign the coherent out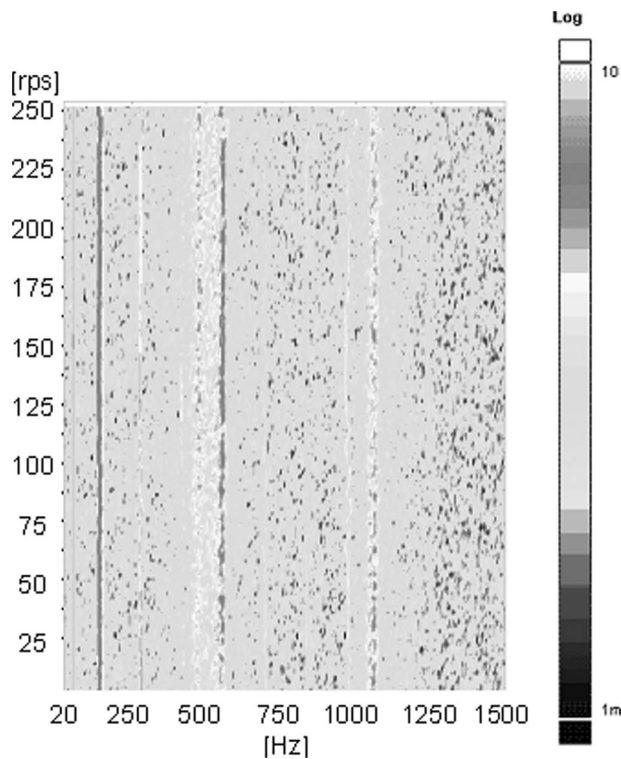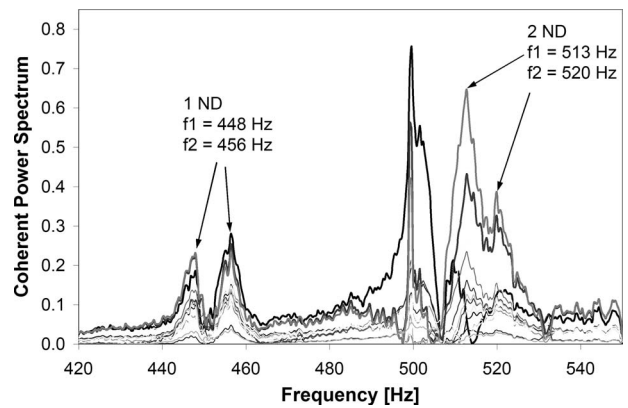put power spectrum has been extracted from the experimental data at specific test sequences. Figures 15 and 16 show the coherent output spectrum for test sequences 1–4 with N_k equal to 0.11 versus frequency. In the figures one can clearly see the frequency separation of eigenmodes of nodal diameters 1–3.

Table 4 summarizes the frequency separations for different modes measured and predicted at reference operating condition. Comparing the measured and predicted frequency separations for different modes we can see that they are in close agreement for the two ND to four ND modes.

In addition to the observations made on suppression of flutter, some high-frequency eigenmodes were excited by the stator harmonics. In general, mistuning can have a negative impact on forced responses. However, the responses obtained in the present test were low and indicated no amplitude amplification due to mistuning.
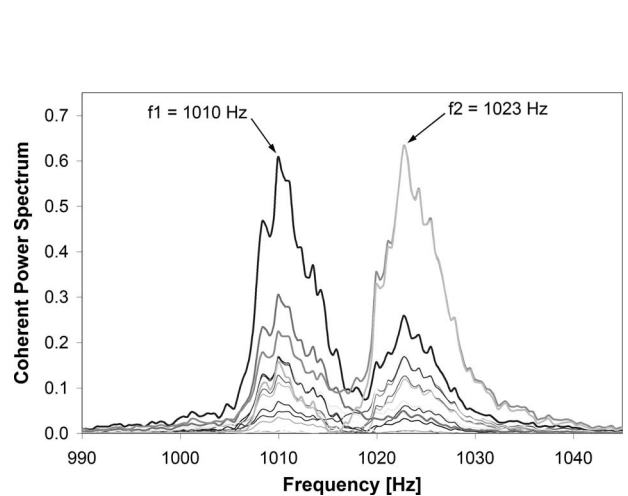

Fig. 14 Time spectral map 20–1500 Hz; test sequence 7 in Fig. 10

Fig. 16 Coherent output power spectrum for the three ND mode

Table 4 Measured and predicted frequency separation at reference operating conditions

	ND 1	ND 2	ND 3	ND 4
Measured in air test rig	1.7%	1.4%	1.0%	1.3%
Predictions using FEM	0.8%	1.2%	1.0%	0.9%

7 Concluding Remarks

A design method for removing flutter instability based on mistuning has been put forward. The methods allow analytical prediction of the system stability ahead of engine testing.

It has been applied to a rotor blisk. The blisk has intentionally been mistuned to stabilize it and to make it flutter free. A test campaign has been performed with the mistuned blisk. The tests were focused on exploration of the region beyond the flutter boundary of the tuned blisk. Flutter did not occur for any of the investigated operating conditions. Thus, it has been demonstrated that the chosen mistuning design was sufficient to push the flutter boundary far outside the turbine operating envelope.

Moreover, the test has shown that the method for prediction of frequencies and frequency separation of mistuned modes described in this paper is capable of doing so with good accuracy.

Acknowledgment

Nomenclature

A = vibration amplitude
c = chord
C = viscous damping
k = reduced frequency
K = modal stiffness
L = blade span
M = modal mass
N = number of blades of the blade row
ND = number of nodal diameters
N_k = nondimensional speed
P_{00} = manifold inlet total pressure
P_3 = exit static pressure
R = gas constant
r_m = mean radius
T_{00} = manifold inlet total temperature
v_{in} = relative inlet velocity
ζ = critical damping ratio
ξ^* = characteristic damping
γ = ratio of specific heats
π_{ts} = total-to-static pressure ratio
Ω = rotational speed
ω = circular frequency

References

[1] Sisto, F., 1987, "Introduction and Overview," *AGARD Manual on Aeroelasticity in Axial-Flow Turbomachines, Vol. 1, Unsteady Turbomachinery Aerodynamics*, M. F. Platzer and F. O. Carta, eds., AGARD-AG-298, Neuilly sur Seine, France.

[2] Groth, P., Mårtensson, H., and Edin, N., 2010, "Experimental and Computational Fluid Dynamics Based Determination of Flutter Limits in Supersonic Space Turbines," ASME J. Turbomach., **132**(1), p. 011010.

[3] Mårtensson, H., 2006, "Flutter Free Design of Aerodynamically Unstable Supersonic Turbines," 42nd AIAA/ASME/SAE/ASEE Joint Propulsion Conference and Exhibit, Sacramento, CA, July 9–12, Paper No. AIAA 2006-4381.

[4] Kielb, R., Feiner, D., Griffin, J., and Miyakozawa, T., 2004, "Flutter of Mistuned Bladed Disks and Blisks With Aerodynamic and FMM Structural Coupling," ASME Paper No. GT2004-54315.

[5] Martel, C., Corral, R., and Llorens, J.-M., 2008, "Stability Increase of Aerodynamically Unstable Rotors Using Intentional Mistuning," ASME J. Turbomach., **130**, p. 011006.

[6] Crawley, E. F., and Hall, K. C., 1985, "Optimization and Mechanisms of Mistuning in Cascades," ASME J. Eng. Gas Turbines Power, **108**, pp. 418–426.

[7] Lindström, D., and Mårtensson, H., 2001, "A Method for Flutter Calculations Based on the Linearized Compressible Euler Equations," *Proceedings of IFASD Conference*, Vol. II.

Measurements of Secondary Losses in a Turbine Cascade With the Implementation of Nonaxisymmetric Endwall Contouring

D. C. Knezevici
e-mail: dknezevi@connect.carleton.ca

S. A. Sjolander
Professor
Pratt & Whitney Canada Research Fellow
e-mail: ssjoland@mae.carleton.ca

Department of Mechanical and Aerospace
Engineering,
Carleton University,
Ottawa, ON, K1S 5B6, Canada

T. J. Praisner
e-mail: thomas.praisner@pw.utc.com

E. Allen-Bradley
e-mail: eunice.allen-bradley@pw.utc.com

E. A. Grover
e-mail: eric.grover@pw.utc.com

Turbine Aerodynamics,
United Technologies, Pratt & Whitney Aircraft,
400 Main Street, MS 169-29,
East Hartford, CT 06108

An approach to endwall contouring has been developed with the goal of reducing secondary losses in highly loaded axial flow turbines. The present paper describes an experimental assessment of the performance of the contouring approach implemented in a low-speed linear cascade test facility. The study examines the secondary flows of a cascade composed of Pratt & Whitney PAKB airfoils. This airfoil has been used extensively in low-pressure turbine research, and the present work adds intrapassage pressure and velocity measurements to the existing database. The cascade was tested at design incidence and at an inlet Reynolds number of 126,000 based on inlet midspan velocity and axial chord. Quantitative results include seven-hole pneumatic probe pressure measurements downstream of the cascade to assess blade row losses and detailed seven-hole probe measurements within the blade passage to track the progression of flow structures. Qualitative results take the form of oil surface flow visualization on the endwall and blade suction surface. The application of endwall contouring resulted in lower secondary losses and a reduction in secondary kinetic energy associated with pitchwise flow near the endwall and spanwise flow up the suction surface within the blade passage. The mechanism of loss reduction is discussed in regard to the reduction in secondary kinetic energy. [DOI: 10.1115/1.3072520]

1 Introduction

Implementation of high-lift airfoils in low-pressure turbine design is an attractive means to reduce engine weight and manufacturing costs. Several studies [1–3] have shown that increasing airfoil loading inherently leads to higher secondary losses. Thus it is desirable to manipulate the flow field in the endwall region to reduce secondary losses and potentially open the design envelope.

Geometric modifications to the endwall region have been shown to yield lower secondary losses. Both Chung and Simon [4] and Aunapu et al. [5] studied the effects of endwall fences on the secondary flow in a linear cascade representation of a single turbine blade passage. Their investigations showed that the size and strength of the passage vortex could be reduced with the application of endwall fences. The improvements were thought to be a result of altering the trajectory of the passage vortex within the blade passage.

The use of nonaxisymmetric endwall contouring within the blade passage for loss reduction has been studied by researchers in the past decade. Harvey et al. [6] and Yan et al. [7] presented methods for applying nonaxisymmetric full-passage endwall contouring. The authors relied on predictions of cross-passage pressure gradient and secondary kinetic energy for design optimization based on the notion that simulations using a mixing-length turbulence model were unable to accurately predict loss.

Experimental assessments of endwall contouring were conducted by Hartland et al. [8] and Rose et al. [9]. Both studies showed a marked improvement as a result of the application of a profiled endwall. The reduction in loss was attributed to a reduction in secondary kinetic energy and improved outlet flow quality based on reducing flow over-/underturning in the pitchwise direction. Ingram et al. [10] used the same design tool as Hartland et al. [8] to develop a contoured endwall that was supposed to achieve maximum loss reduction. However, the computations were unable to predict a separation of the intrapassage boundary layer that led to higher losses despite a reduction in blade row under-/overturning and lower outlet secondary kinetic energy.

The present study examines the flow field of a moderately loaded linear cascade of turbine airfoils with and without the implementation of endwall contouring. The focus is on the physics of the endwall flow in order to enhance the understanding of the relationship between losses and secondary kinetic energy. The nonaxisymmetric endwall contouring was designed by the method of Praisner et al. [11]. This work is part of an ongoing collaboration between Pratt & Whitney Aircraft and Carleton University aimed to exploit high-lift low-pressure turbine designs.

2 Experimental Apparatus and Procedures

Cascade test section. The study was conducted in Carleton University's low-speed linear cascade wind tunnel. The wind tunnel is an open circuit design, and the test section shown in Fig. 1 mounts downstream of a settling chamber and contraction. The same test section was used by McAuliffe and Sjolander [12] and Mahallati et al. [13] for measuring the midspan performance of PAKB. The apparatus has also been used for the study of secondary flows by Benner [14] and more recently by Zorić et al. [1,2]. Thus the experiment is at a mature state, and the operating procedures for establishing inlet uniformity and exit flow periodicity are well established. The cascade is comprised of nine PAKB airfoils. The geometric details of the cascade are given in Table 1. The probe measurements and flow visualizations were conducted on the fifth

Fig. 1 Linear cascade test section

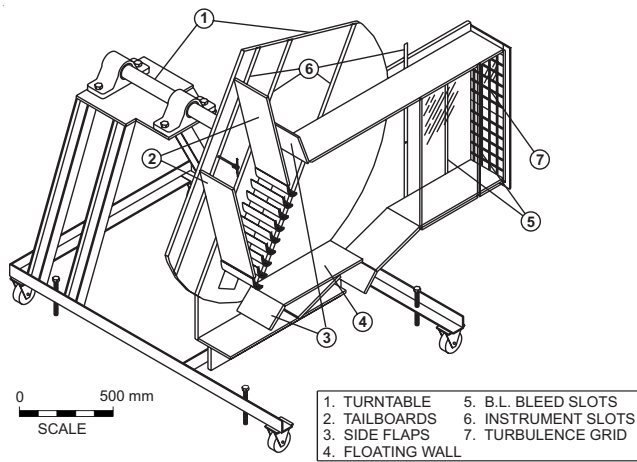|			
1.	TURNTABLE	5.	B.L. BLEED SLOTS
2.	TAILBOARDS	6.	INSTRUMENT SLOTS
3.	SIDE FLAPS	7.	TURBULENCE GRID
4.	FLOATING WALL		

blade passage from the top of the cascade. When the test section was switched over to the profiled endwall configuration, the planar endwall insert that mounts the blades to the turntable was replaced with a contoured endplate. The details of the contouring design and optimization are described by Praisner et al. [11]. The primary objective for the optimizations was mass-averaged total row loss reduction. Also, the local exit flow angle close to the endwall (5% span) was constrained to prevent significant overturning. All eight blade passages were profiled to ensure periodicity at the outlet. A rendering of the contoured endwall is presented in Fig. 2, showing the three predominant geometric features. The contouring is comprised of a hill (H) and two valleys (V_1) and (V_2) located within the blade passage. The maximum positive and negative amplitudes of the contoured endwall are 7.1% and 4.7% of axial chord, respectively. The effect of these

Table 1 Cascade geometry

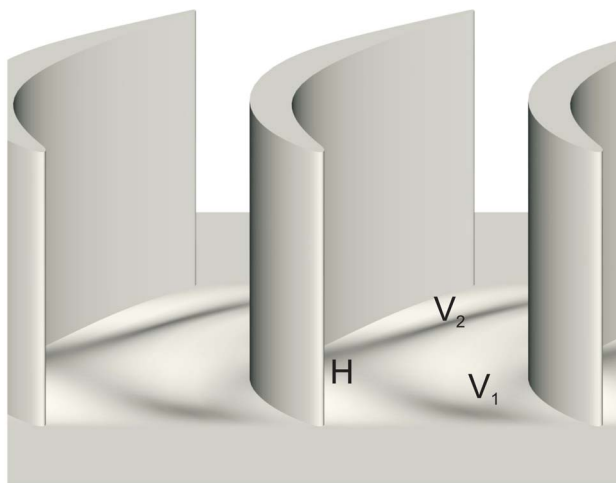|	
Chord, C (mm)	83.9
Axial Chord, B_x (mm)	75.4
Pitch, s (mm)	66.8
Span, h (mm)	203.2
Design inlet flow angle, α_1 (deg)	35
Design outlet flow angle, α_2 (deg)	−60
Stagger angle, γ (deg)	26

Fig. 2 Isometric view of profiled endwall

geometric features on the flow field relative to the planar endwall will be discussed in regard to the flow visualizations and pressure probe measurements.

Oil surface flow visualization technique. Oil surface flow visualizations were carried out by mixing titanium dioxide pigment with oil mixtures of various viscosities. Visualizations were conducted on the blade suction surface as well as on the turntable wall of the test section (the same wall where probe measurements were taken). The opposing wall of the test section is removable and made of Plexiglas to allow visual access.

Instrumentation and data acquisition. Pressures were measured with Data Instruments ASG DRAL505DN differential transducers having an operating range of ±1250 Pa. The estimated uncertainty in pressure measurement due to calibration, linearity, and hysteresis is ±0.2% of full scale range. Transducer voltage output was sampled using a United Electronics Industries PowerDAQ PD2-MFS-8-800/14 board. Measurements were sampled for 10 s at 1 kHz upstream of the cascade. Downstream and intrapassage measurements were sampled for 15 s at 1 kHz.

The inlet boundary layer was measured using a Pitot tube having inner and outer diameters of 0.33 mm and 0.64 mm, respectively. Pitot probe total pressure measurements have an estimated uncertainty of ±0.3% of inlet midspan dynamic pressure. The cascade inlet flow quality was documented using a three-hole pressure probe having a wedge angle of 45 deg. The probe tip has a width of 0.64 mm and a thickness of 2 mm. The three-hole probe was calibrated over a range of ±21 deg in 0.5 deg increments. Measured flow angles have an estimated uncertainty of ±0.4 deg; dynamic and total pressures have uncertainties of ±0.6% and ±0.3% of inlet midspan dynamic pressure, respectively.

To facilitate intrapassage measurements near the wall, a new gooseneck seven-hole probe and mounting system was designed. The new probe has the same head geometry used in the previous secondary flow studies conducted at Carleton (60 deg cone angle), but uses smaller hypodermic tubing resulting in a smaller head diameter (1.83 mm). The new probe mounting assembly allows the axial position of the probe to be modified independent of the pitchwise and spanwise alignment or position. Thus the angular misalignment errors between measurement planes are negligible, and the position of the traverse planes relative to one another is known. The probe was calibrated in 2 deg increments over a range of ±50 deg of misalignment in both pitch and yaw. The estimated uncertainty for measured flow angles is ±0.5 deg; measured dynamic and total pressure uncertainties are estimated to be ±1.1% and ±0.4% of inlet midspan dynamic pressure, respectively.

The seven-hole probe measurements were taken on axial planes consisting of 976 data points within the blade passage. The exit conditions of the cascade were documented using 1288 measurement points at 140% axial chord downstream of the leading edge. Spanwise resolution of the measurement grids was held constant at 1.33% of span. The pitchwise resolution varied from 2.78% of pitch at 63% axial chord to 4.05% of pitch at the downstream measurement plane.

Operating conditions. The investigation was conducted at a Reynolds number of $(1.26 \pm 0.02) \times 10^5$ based on inlet midspan velocity and axial chord. The inlet midspan velocity was approximately 25 m/s. The inlet and outlet Mach numbers were approximately 0.073 and 0.111, respectively; thus the flow in the test section was essentially incompressible.

A turbulence generating grid installed 18.4 axial chords upstream of the leading edge of the middle blade in the cascade is used to produce a freestream turbulence intensity of 4% with an integral length scale of $0.4B_x$. Mahallati et al. [13] showed that an elevated level of freestream turbulence tends to suppress PAKB's suction-surface separation bubble resulting in lower profile loss. Their investigation found that the PAKB did not stall with this level of turbulence intensity and length scale over the range of Reynolds numbers tested $(5.5 \times 10^4 - 1.5 \times 10^5)$. Gregory-Smith
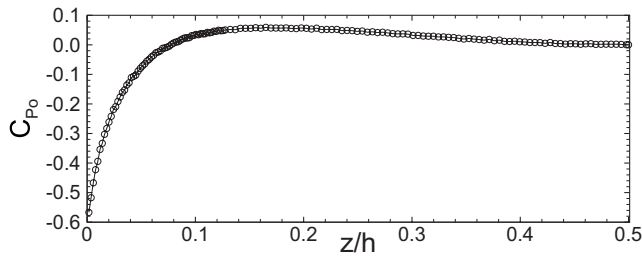
Fig. 3 Spanwise variation in total pressure coefficient as measured with a Pitot probe $1.2B_x$ upstream of the leading edge at $y/s=0.5$

and Cleak [15] studied the effects of freestream turbulence intensity on secondary flows and found little influence on secondary loss and secondary kinetic energy. Zorić [16] conducted a similar study investigating the effects of turbulence intensity on row loss for PAKB. Akin to Ref. [15], installing the turbulence generating grid resulted in a thinner inlet boundary layer and led to slightly lower secondary losses. Based on these studies it is suggested that the flow physics discussed herein are relatively insensitive to Reynolds number and level of freestream turbulence intensity.

3 Results and Discussion

Cascade inlet conditions. The turbulence generating grid used in the present study caused a total pressure surplus to develop over a significant spanwise distance between the endwall and midspan. The total pressure surplus is seen in Fig. 3 measured by a boundary layer traverse using a Pitot probe $1.2B_x$ upstream of the leading edge of the cascade at $y/s=0.5$. A similar inlet total pressure distribution was reported by Hartland et al. [8] for their upstream mounted grid. To account for the nonuniformities caused by the grid, the inlet was traversed with a three-hole pressure probe over one blade pitch from the wall to half span; the total pressure was mass averaged as the reference total pressure coefficient ($C''_{Po,1}$). The mass-averaged total pressure coefficient as well as the inlet boundary layer parameters are summarized in Table 2.

Blade loading distribution. Blade loading [1–3] and static pressure distribution [1,2,17] are known to have significant impacts on the size and strength of secondary flows. The midspan loading distribution for PAKB is shown in Fig. 4 as measured by Mahallati et al. [13] using the same test section and turbulence generating grid as the current study. The loading distribution is plotted as static pressure coefficient (C_P) versus fraction of surface length (S/S_{max}). Figure 4 shows that varying the Reynolds number from 1.0×10^5 to 1.5×10^5 has negligible effect on loading. The present study was conducted at a Reynolds number of 1.26×10^5, which falls nearly halfway between the conditions shown. The aerofoil exhibits a "short" suction-surface separation bubble (see Ref. [18]) that extends from roughly $0.61S/S_{max}$ to $0.78S/S_{max}$ or $0.74S/S_{max}$ at Reynolds numbers of 100,000 and 150,000, respectively. PAKB is considered to be an aft-loaded airfoil, with a suction peak at approximately $0.50S/S_{max}$. The suction-surface boundary layer sees a gradual and consistent acceleration up to the suction peak. The pressure surface boundary layer sees a deceleration up to $0.3S/S_{max}$ where it begins to accelerate toward the trailing edge. It is commonly accepted that the static pressure difference across the blade passage drives the migration of the pressure leg of the horseshoe vortex toward the suction surface of the adjacent blade [19–21]. The application of endwall contouring is known to modify the static pressure distribution in the endwall region [6,22] and to affect the formation of the secondary flow [8]. The subsequent discussion focuses on the changes to the flow field interpreted from the limiting streamlines of the oil surface flow visualizations.

Table 2 Summary of results

Location	Flow quantity	Endwall	
		Planar	Contoured
Inlet	δ/h	0.16	
	δ^* (mm)	1.9	
	θ (mm)	1.6	
	H	1.2	
	$C''_{Po,1}$	0.00025	
Outlet $B_x=1.40$	$C''_{Po_{total}}$	−0.098	−0.091
	$C'_{Po_{profile}}$	−0.057	−0.054
	$C''_{Po_{secondary}}$	−0.041	−0.037
	Y_{total}	0.043	0.039
	$Y_{profile}$	0.024	0.023
	$Y_{secondary}$	0.019	0.016
	C''_{SKE}	0.015	0.013
	α''_2 (deg)	−57.2	−57.1
	α'_{MS_2} (deg)	−57.7	−57.6
	q''_2/q'_{MS_1}	2.304	2.326
	q'_{MS_2}/q'_{MS_1}	2.312	2.332
	AVR	0.979	0.988
Mixed out	$C''_{Po_{total}}$	−0.117	−0.108
	$C'_{Po_{profile}}$	−0.058	−0.055
	$C''_{Po_{secondary}}$	−0.059	−0.053
	Y_{total}	0.052	0.047
	$Y_{profile}$	0.025	0.024
	$Y_{secondary}$	0.027	0.023
	α''_2 (deg)	−57.7	−57.6
	α'_{MS_2} (deg)	−57.7	−57.6
	q''_2/q'_{MS_1}	2.259	2.281
	q'_{MS_2}/q'_{MS_1}	2.309	2.329

Flow visualization results. Figure 5 shows oil surface flow visualizations overlaid with interpreted separation streamlines for the planar endwall. The nomenclature of Sieverding [19] is used wherever possible. On the endwall (Fig. 5(a)), the flow enters the figure from the right and exits nominally through the top. The incoming stagnation streamline meets the primary separation line S_1 at the separation saddle point A_1. S_1 marks the separation of the inlet boundary layer from the endwall. The incoming inlet boundary layer fluid is funneled to either side of the blade where S_1 meets the suction surface. The second major separation line on the
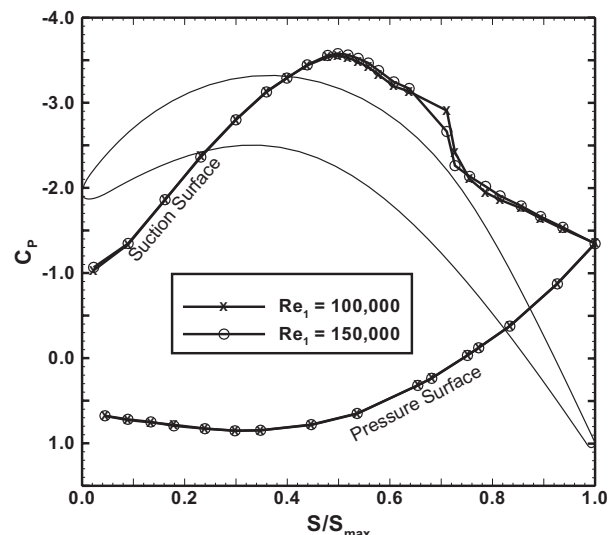

Fig. 4 Loading distribution measured by Mahallati et al. [13]

Journal of Turbomachinery
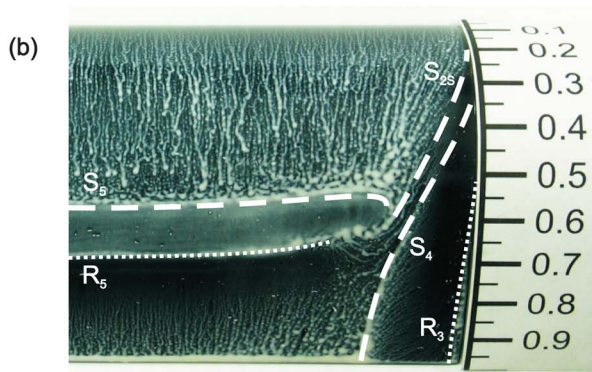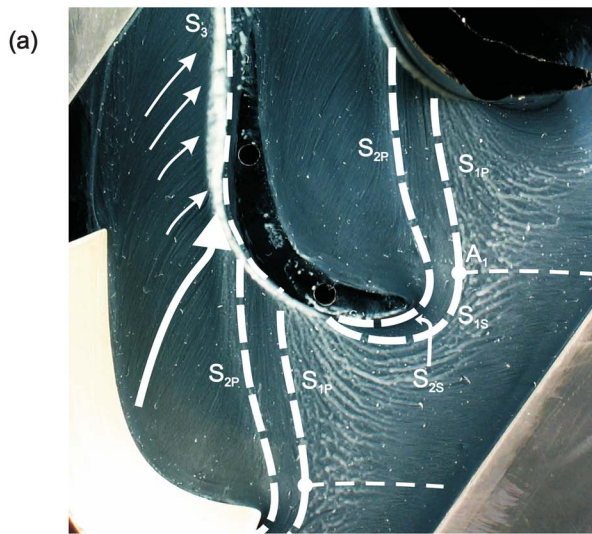
Fig. 5 (*a*) Endwall and (*b*) suction-surface oil surface flow visualization for the planar endwall

Fig. 6 (*a*) Endwall and (*b*) suction-surface oil surface flow visualization for the contoured endwall

endwall, S_2, corresponds to the liftoff line of the horseshoe vortex. The horseshoe vortex is wrapped around the leading edge of the aerofoil downstream of S_2. The area between the airfoil leading edge and S_2 has the least pigment in every endwall photograph taken during the flow visualization study. Observing the formation of the endwall oil flow pattern, it was found that the first shearing of oil occurred away from the leading-edge/endwall-junction toward S_2. This suggests that the surface shear stress is highest there and is congruent to the findings of Praisner and Smith [23].

The pressure legs of the separation lines (S_{1P} and S_{2P}) travel across the blade passage; in doing so, the pressure leg of the horseshoe vortex related to S_{2P} evolves into the passage vortex. S_{1P} and S_{2P} encounter the suction surface of the adjacent blade at high angle of attack; this results in what Sieverding [19] refers to as a "strong interaction." The consequence of a strong interaction is the formation of the corner vortex at the endwall/suction-surface junction marked by S_3. S_3 appears to have its origin just downstream of where the suction leg of the primary inlet boundary layer separation (S_{1S}) meets the suction surface. Hodson and Dominy [24] found that the growth of the corner vortex can be seen as the distance between S_3 and the suction surface increases. The size and strength of the corner vortex are driven by the cross-flow within the blade passage. The intensity with which the corner vortex is energized can be seen as surface streamlines are directed toward S_3 and the angle of incidence they make with it. The corner vortex would be energized most if the surface streamlines met the suction surface at a right angle. The new boundary layer that forms downstream of the pressure leg of the horseshoe vortex is
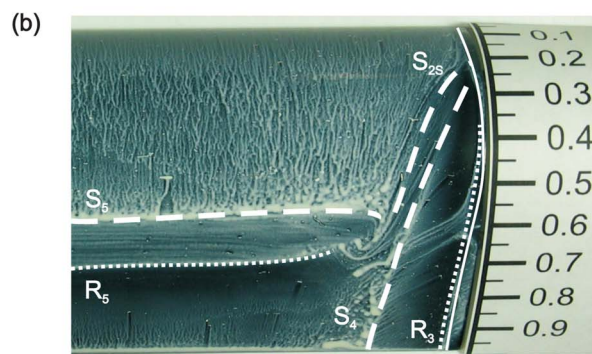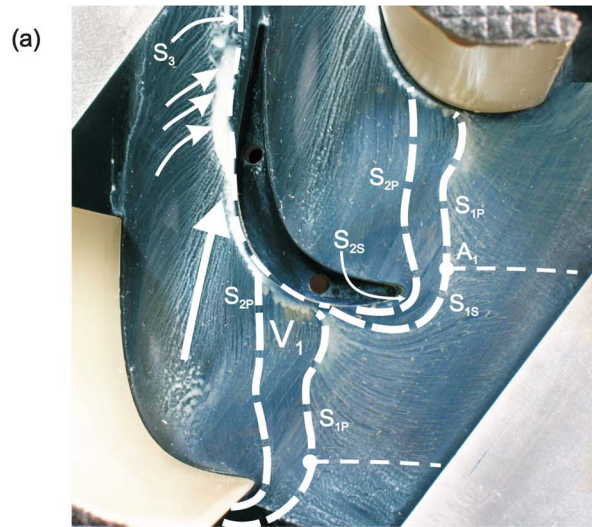
swept toward the suction surface by the pitchwise cross-passage flow (shown schematically by the large arrow). Near the exit of the cascade, at about midpitch, significant surface streamline curvature occurs as the new boundary layer falls under the influence of the lower static pressure near the suction-surface/endwall-junction (highlighted shown by the small arrows).

The suction-surface flow visualization is shown Fig. 5(*b*) with a ruler marking the approximate fraction of suction-surface length from the leading edge. Figure 5(*b*) shows three dominant separation lines and two reattachment lines. S_5 and R_5 mark the separation and reattachment of the suction-surface boundary layer. The reattachment of the corner vortex separation (S_3) is marked by R_3. S_4 is typically associated with the passage vortex, while S_{2S} is the extension of the suction leg of the horseshoe vortex that has been swept off the endwall. As the suction leg of the horseshoe vortex works its way toward the trailing edge, it migrates toward midspan until it encounters the suction-surface separation (S_5) where it appears to vanish. The smoke flow visualizations of Wang et al. [25] have shown that the suction leg is lifted from the endwall by the passage vortex and is wrapped around it. This notion has also been suggested by other researchers [26–28].

The suction-surface flow visualizations show an appreciable distance between the S_{2S} and S_4 separation lines. Several researchers [24,25,27,29] support the notion that this region is filled with inlet boundary layer fluid that has been directed there by the primary inlet boundary layer separation S_1. In the present study, when the endwall flow visualizations were conducted and no oil was applied to the suction surface of the blade, most of the oil

from the endwall pooled against S_3 and was slowly convected toward the trailing edge. This buildup of oil is clearly seen in Fig. 5(a). On occasion it was observed that a small amount of oil was swept off the endwall onto the suction surface of the airfoil and was convected toward the trailing edge between S_{2S} and S_4. It is believed that the wall induced vortex as shown in Fig. 7 is comprised of inlet boundary layer fluid.

The application of the contoured endwall did not change the underlying flow physics given that the separation and reattachment lines of Fig. 5 are also seen in the oil surface flow visualizations of Fig. 6. Consequently the same vortical structures are present in both flows. The contouring affects the local static pressure on the endwall by means of streamline curvature [22]. A convex curvature locally accelerates the flow, thus reducing the local static pressure. A concave wall curvature causes a relative diffusion of the flow, thereby raising the local static pressure. Valley V_1 (Figs. 2 and 6(a)) represents one such concave curvature, and the local diffusion of the flow can be seen by the increased distance between S_{1P} and S_{2P} relative to Fig. 5(a). The increased static pressure, compared with that of the nominal endwall height, caused the initial separation of the inlet boundary layer (marked by S_{1P}) to move upstream. When observing the formation of the pattern in that region, it was found that the oil approached stagnation at the upstream turning of S_{1P} and was slowly swept toward the suction surface along the separation line. This feature is similar in appearance to the endwall boundary layer separation of Ingram et al. [10] but does not seem to harm performance.

The contouring reduces the cross-passage flow and influences the formation of the corner vortex marked by S_3. As with the planar case, S_3 has its origin downstream of where S_{1S} meets the suction surface; however, the corner vortex remains small over a much larger fraction of the suction surface. The new intrapassage boundary layer that forms downstream of S_{2P} is relatively unswept compared with the planar case (shown by the large arrow). The endwall flow visualizations of Ingram et al. [30] also showed a reduction in cross-flow for both contoured endwalls tested. In Fig. 6(a) of the current work, the angle of incidence of the intrapassage boundary layer is almost tangent to the suction surface. This results in a weak convergence [19] that imparts little energy to the corner vortex. Just downstream of the large arrowhead, the contouring begins to blend back to the nominal endwall height in the direction of the outlet metal angle. In doing so the flow is accelerated, the static pressure drops, and the surface streamlines turn abruptly toward the suction surface of the blade. As a result the corner vortex is energized. A similar increase in cross-flow near the exit of the cascade was documented by the endwall surface flow visualizations of Hartland et al. [8] for their contoured endwall. The influence of the contouring on the cross-passage flow and its effect on the roll-up of the passage vortex will be discussed further with regard to the pneumatic probe measurements presented below.

The suction-surface oil flow visualization for the contoured endwall is presented in Fig. 6(b). The endwall height is shown by the solid white line as the blades are recessed into the contoured endwall. In comparison to the planar case, S_{2S} and S_4 are driven further toward midspan near their origins by the higher local static pressure at the suction-surface/endwall-junction resulting from the presence of valley V_1. The penetration height of S_4 at the trailing edge has been reduced; this is a sign of a reduction in passage vortex size.

Pressure probe results. Figure 7(a) shows line contours of total pressure loss coefficient overlaid with a flood of streamwise vorticity coefficient measured at the trailing edge plane for the planar endwall. The view is looking upstream with the passage suction surface on the left and pressure surface on the right. The streamwise vorticity is derived from the incompressible Euler equations as per Gregory-Smith et al. [31]. It is a property that is useful for
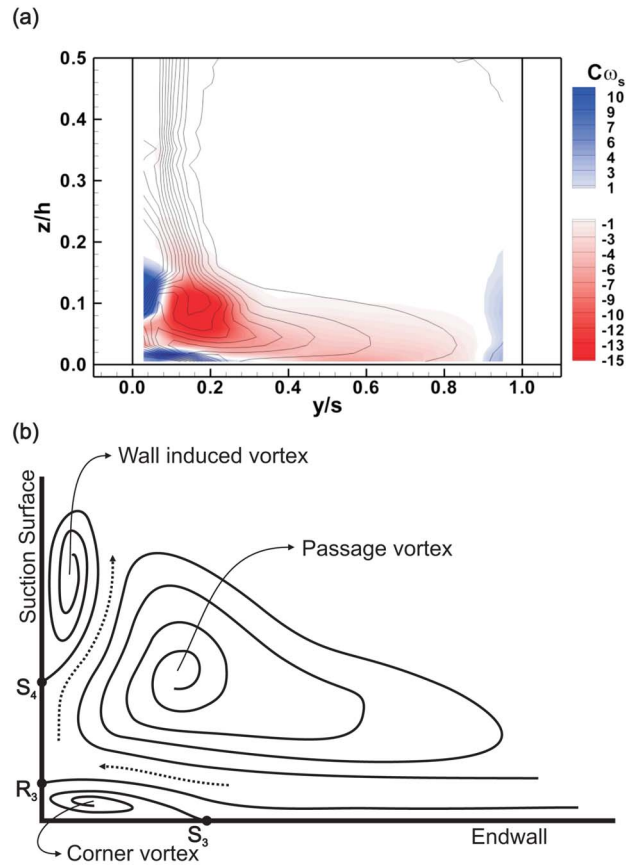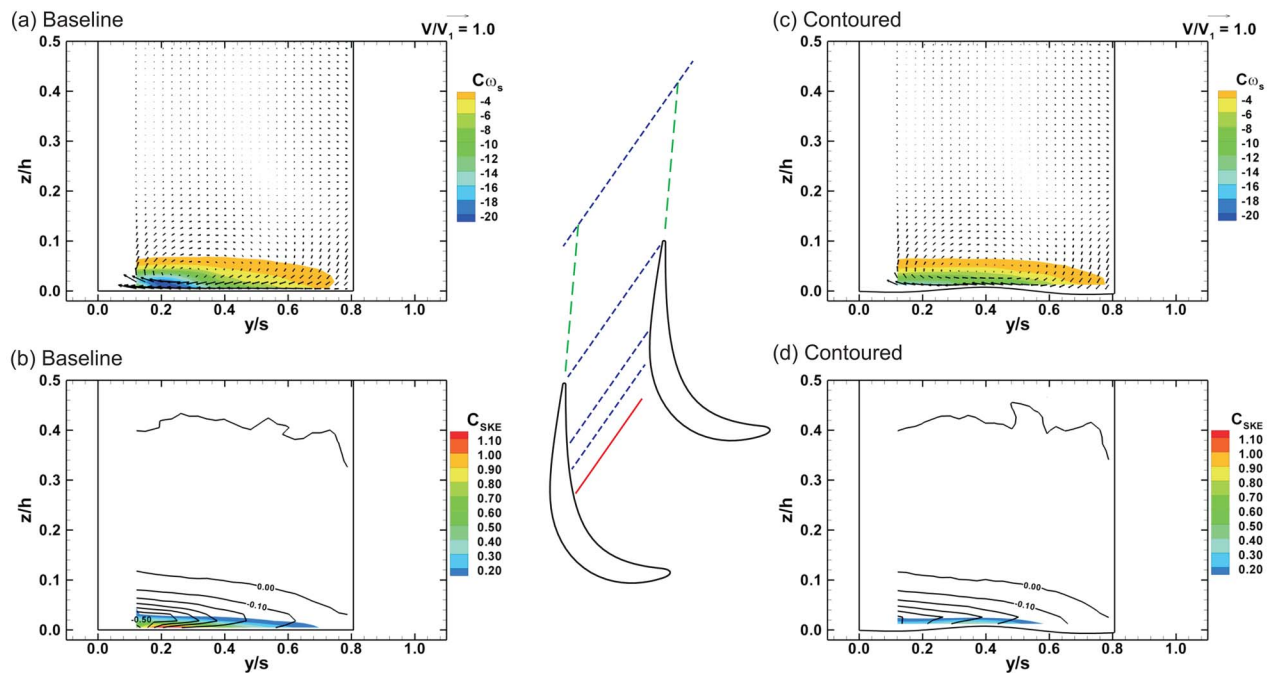

Fig. 7 (a) Line contours of total pressure loss coefficient superimposed with flood of streamwise vorticity and (b) interpreted vortex structure at the trailing edge plane (1.00B_x)

identifying vortical structures and quantifying their strength and sense of rotation. For the right-handed coordinate system selected, the passage vortex has negative vorticity (clockwise rotation) about the streamwise direction. Two counter-rotating vortical structures are evident; the corner vortex located where the suction surface meets the endwall, and the wall induced vortex located near the blade suction surface beginning at about 8% up the span.

Figure 7(b) depicts an interpretation of the vortical structures as they exist just upstream of the trailing edge plane of the cascade and their relationship to the separation and reattachment lines discussed above. The corner vortex is bound by S_3 and R_3 and has a sense of rotation opposite to that of the passage vortex. The wall induced vortex is rooted at S_4 and also has a counterclockwise sense of rotation. The dotted arrows show the direction in which it is believed that low momentum fluid is convected into the secondary flow structure. The application of endwall contouring is thought to reduce this convection process leading to lower losses. This will be discussed with relation to the pressure probe measurements presented next.

The seven-hole probe traverse data for the 0.63B_x plane are presented in Fig. 8. The thumbnail in the center of the figure highlights the location and pitchwise extent of the measurement plane. The figure contains two different types of plots, showing the modifications to the flow field caused by the application of endwall contouring. Secondary velocity vectors are superimposed with a flood of negative streamwise vorticity coefficient ($C_{\omega s}$) for the baseline and contoured endwall in Figs. 8(a) and 8(c), respectively. The secondary velocity vectors show the components of velocity on a plane normal to the mass-averaged flow velocity vector (primary flow direction). Streamwise vorticity is convected

Fig. 8 Secondary velocity vectors with flood of streamwise vorticity coefficient ($C_{\omega s}$) and ((*b*) and (*d*)) line contours of total pressure loss coefficient (C_{Po}) with flood of secondary kinetic energy coefficient (C_{SKE}) at 63% axial cord

with fluid particles, thus enabling these plots to track the passage vortex in subsequent figures. Note that the peak of negative vorticity (Fig. 8(*a*)) does not coincide with the point about which the secondary velocity vectors revolve. The profiled endwall in Fig. 8(*c*) exhibits a weaker passage vortex; no distinct peak of negative vorticity is obvious. The other plots in Fig. 8 (Figs. 8(*b*) and 8(*d*)) display line contours of total pressure loss coefficient (C_{Po}) overlaid with a flood of secondary kinetic energy coefficient (C_{SKE}). The secondary kinetic energy coefficient is the kinetic energy associated with the secondary velocity vectors normalized by the kinetic energy on the inlet centerline of the cascade. Thus C_{SKE} illustrates the strength of the cross-flow near the endwall, whose peak is approximately 2.7 times stronger for the planar endwall. The pitchwise cross-flow is believed to be responsible for rolling up the boundary layer near the endwall, and this process appears more advanced for the planar case judging from the C_{Po} contours of Figs. 8(*b*) and 8(*d*). Hartland et al. [8] also found weaker cross-flows and less convection into the suction-surface corner resulting from the application of their profiled endwall; they attribute this to an alleviation of the cross-passage static pressure gradient in the early part of the passage.

Figure 9 shows the secondary flow structures at 71% axial chord. The passage vortex has strengthened for the planar endwall in Fig. 9(*a*) relative to Fig. 8(*a*) (note the change in scale for the $C_{\omega s}$ flood contours). The contoured case (Fig. 9(*c*)) is beginning to show a peak of negative vorticity near the suction surface at z/h =0.06, yet its strength is weaker than that of the planar endwall. In Fig. 9(*b*), the planar endwall exhibits stronger pitchwise cross-flow as determined by C_{SKE}, and the roll-up of the secondary flow is more advanced because of the high secondary kinetic energy that existed upstream near the endwall in Fig. 8(*b*). The core of high total pressure loss is starting to rise away from the endwall, displaced by higher energy fluid convected from the pressure side of the passage. The bottom left corner of Fig. 9(*b*) shows a high loss region, marking the existence of the corner vortex. The presence of the corner vortex is expected at this axial location judging from the surface flow visualizations of Fig. 5(*a*). The loss con-

tours of Fig. 9(*d*) show no evidence of a corner vortex or an appreciable loss core associated with the roll-up of the boundary layer.

Figure 10 shows the traverse results from a plane located at 80% axial chord. In Fig. 10(*a*), the planar endwall has a large kidney shaped mass of fluid with high negative vorticity, while the contoured endwall generates two distinct accumulations of fluid with negative vorticity and milder magnitudes (Fig. 10(*b*)). The contours of C_{SKE} for the planar endwall show two discrete peaks, the first, located near the endwall at y/s=0.22, is linked to the pitchwise cross-flow as discussed above. The second peak, located near the suction surface at z/h=0.06, is related to spanwise flow away from R_3 toward midspan. Examining the loss contours of Fig. 10(*c*) reveals a lobe of lossy fluid marked by the C_{Po} =−0.50 line that is displaced off the suction surface of the blade by fluid that has been convected into the corner, across the limiting streamline connecting S_3 and R_3, and up the blade suction surface. To the authors' knowledge, this has not been documented previously.

The secondary kinetic energy coefficient in Fig. 10(*d*) has a peak value approximately 68% that of the planar endwall. This peak is associated with spanwise flow up the blade suction surface. Also noteworthy is the appearance of the corner vortex forming at the suction-surface/endwall-junction, but its evolution has been delayed relative to the planar case. The delayed evolution of the corner vortex was discussed above in relation to the flow visualization results of Figs. 5(*a*) and 6(*a*).

By the trailing edge plane the contoured endwall is blended back to the nominal endwall height. This has a significant effect on the pitchwise cross-flow, which is now stronger for the contoured endwall for the first time (Fig. 11(*d*)). The strong cross-flow energizes the corner vortex, which in a short streamwise distance has grown to a size and strength comparable to that of the baseline case. Nevertheless, the planar endwall has stronger spanwise flow associated with the peak of C_{SKE} located near the suction surface at z/h=0.08 (Fig. 11(*c*)), which will continue to convect fluid away from the endwall downstream of the blade
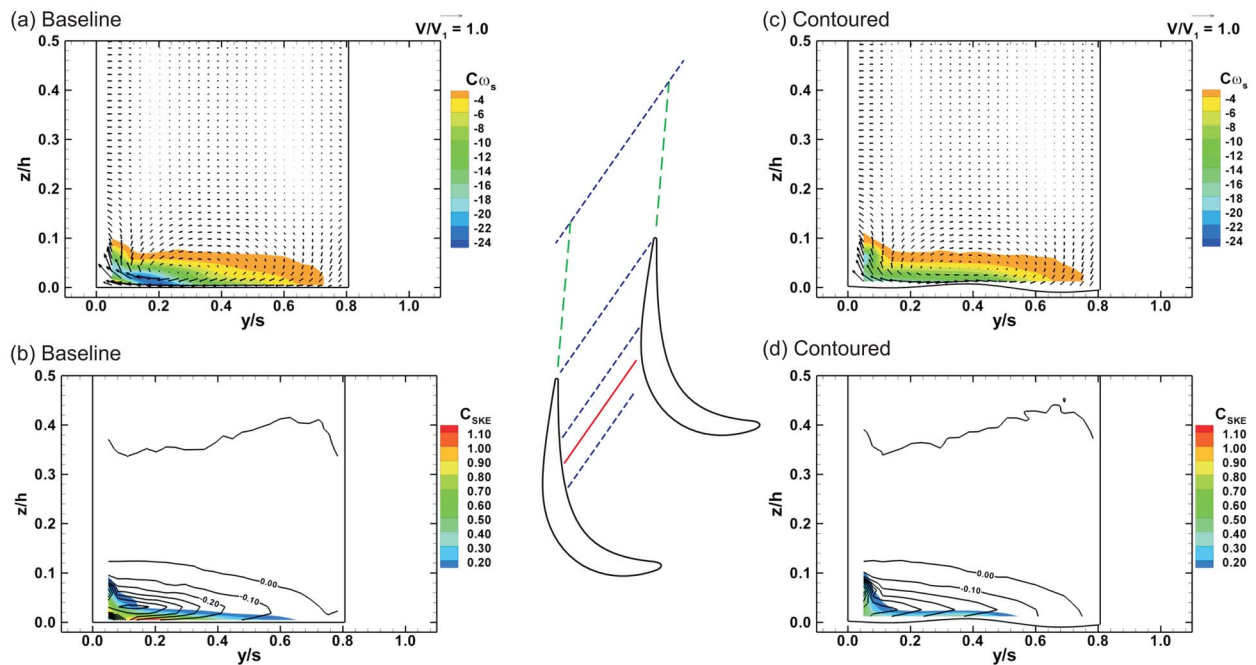
Fig. 9 Secondary velocity vectors with flood of streamwise vorticity coefficient ($C_{\omega s}$) and ((b) and (d)) line contours of total pressure loss coefficient (C_{Po}) with flood of secondary kinetic energy coefficient (C_{SKE}) at 71% axial cord

passage. The application of endwall contouring results in a 31% reduction in peak strength of the passage vortex at the exit plane of the cascade as determined by the streamwise vorticity.

The exit traverse plane was measured 140% B_x downstream of the leading edge of the cascade, and the results are presented in Fig. 12. The projection of the trailing edges is shown as dashed lines at $y/s=0$ and $y/s=1$. Overall the flow fields for the two test cases appear similar, but several features are worth discussing.

The peak negative vorticity that is associated with the passage vortex has been reduced by about 10% by the profiled endwall. The area of the traverse plane that contains fluid of negative vorticity is smaller; thus it can be said that the contouring reduces the overall size and strength of the passage vortex. To the left and slightly above the passage vortex is a core of fluid with positive vorticity. The origin of this fluid is unclear; however, it has been suggested that it is the shed vorticity from the trailing edge [24] or
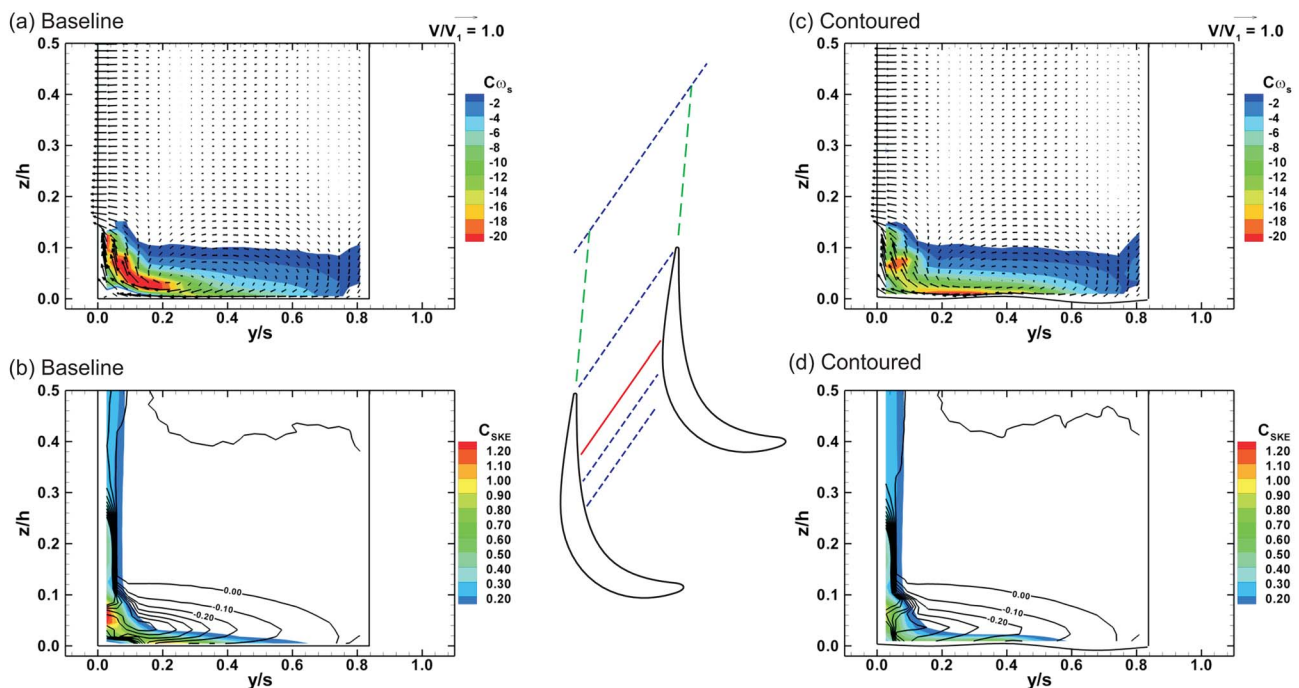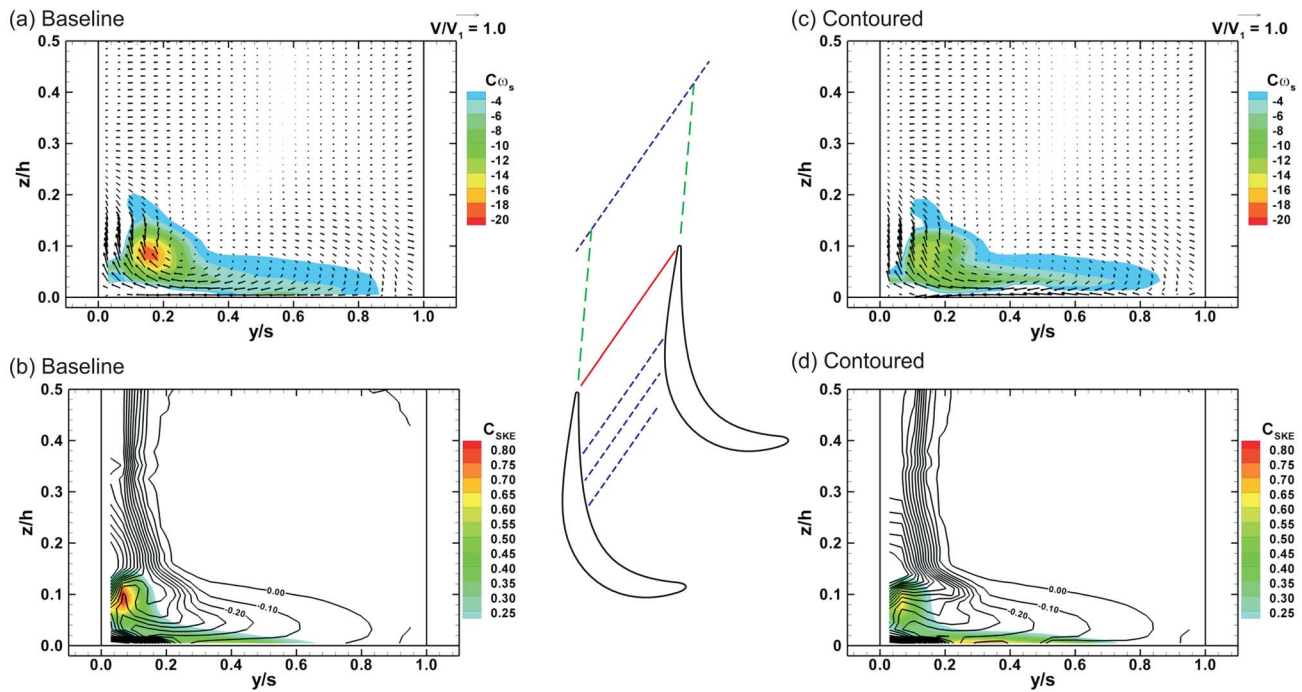

Fig. 10 Secondary velocity vectors with flood of streamwise vorticity coefficient ($C_{\omega s}$) and ((b) and (d)) line contours of total pressure loss coefficient (C_{Po}) with flood of secondary kinetic energy coefficient (C_{SKE}) at 80% axial cord
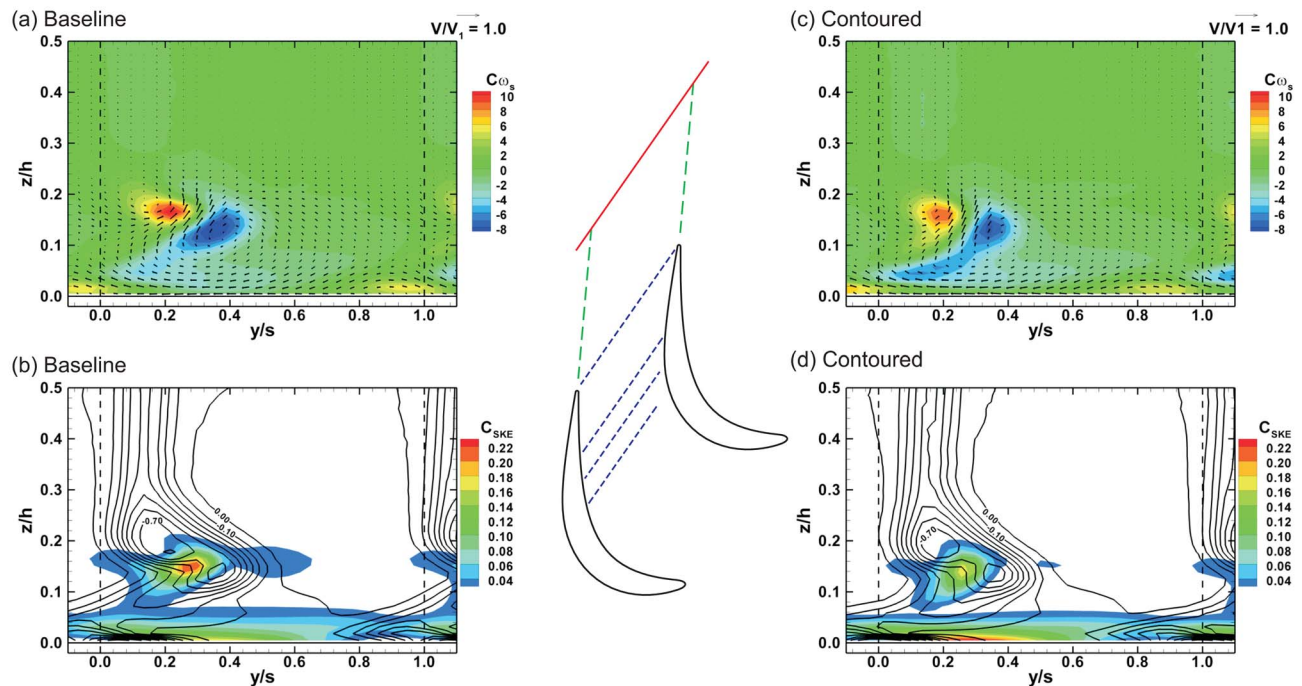
Fig. 11 Secondary velocity vectors with flood of streamwise vorticity coefficient ($C_{\omega s}$) and ((b) and (d)) line contours of total pressure loss coefficient (C_{Po}) with flood of secondary kinetic energy coefficient (C_{SKE}) at the trailing edge plane

that it is the wall induced vortex described above [27]. The peak strength of this counterclockwise rotating vortex has been reduced by about 20% relative to the planar endwall. The fact that the peak vorticity of these two structures is linked suggests a physical connection between them. It is plausible that this positive vorticity is generated in the blade suction-surface boundary layer between R_3 and S_4 (see Fig. 7(b)), induced by the passage vortex. Near the

endwall and to the left of the trailing edge projection lines, there are two cores of positive vorticity. These are the corner vortices of the passage measured (near $y/s=0$) and the adjacent passage in the cascade (near $y/s=1$). The strength of the corner vortex is comparable in Figs. 12(a) and 12(c).

The floods of secondary kinetic energy coefficient in Fig. 12 display the same trend that had developed by the trailing edge

Fig. 12 Secondary velocity vectors with flood of streamwise vorticity coefficient ($C_{\omega s}$) and ((b) and (d)) line contours of total pressure loss coefficient (C_{Po}) with flood of secondary kinetic energy coefficient (C_{SKE}) at 140% axial cord
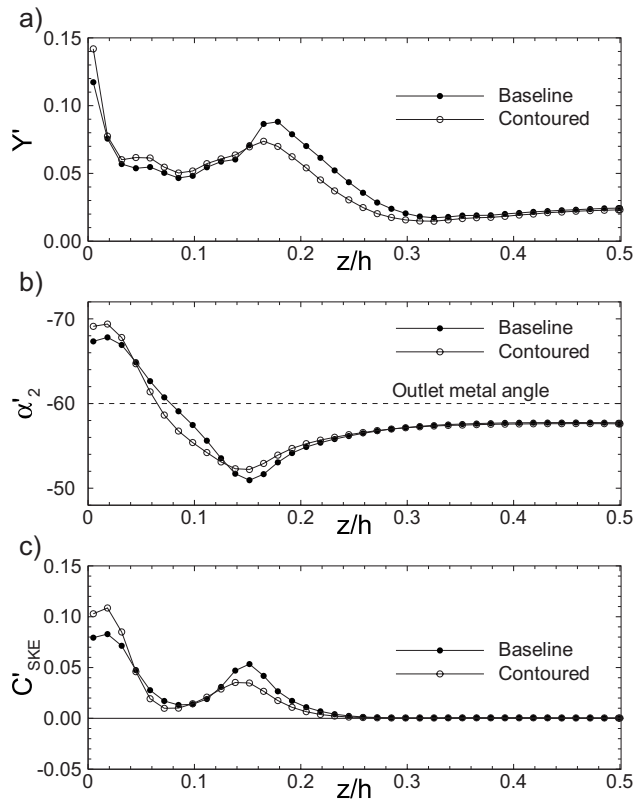
Fig. 13 Pitchwise mass-averaged results for the 140% B_x measurement plane: (a) total pressure loss coefficient, (b) outlet flow angle, and (c) secondary kinetic energy coefficient

plane. Near the endwall, the contouring generates higher secondary kinetic energy resulting from the overturning developed in the aft part of the passage. Away from the endwall, a distinct peak of secondary kinetic energy exists between the two vortical structures discussed above. This kinetic energy appears to belong to the spanwise flow up the blade suction surface that was evident at the trailing edge. Inspection of the secondary velocity vectors of Fig. 12 reveals that the spanwise flow has been turned clockwise and that the degree of turning seems proportional to the strength of the passage vortex.

The total pressure loss contours of Figs. 12(c) and 12(d) have peaks of similar magnitudes except along the endwall. The highest losses for both the flat and profiled cases occur near the endwall, marked by the liftoff of the corner vortex. The next loss core from the endwall, located further toward midspan, is linked to the passage vortex. The peak loss in these cores is almost identical for the two cases (within the error of the experiment). The most substantial difference in loss is seen in the third loss core located farthest from the endwall and roughly in line with the wake. This lossy fluid is comprised of suction-surface boundary layer fluid that has been displaced by the passage vortex, and fluid that has been convected into the suction corner and up the blade surface by the cross-flow and spanwise flow. It is unclear what happens to the wall induced vortex at the trailing edge of the blade; it may find itself in this loss structure or it might be wrapped around the passage vortex. In the latter case, its location could be lost due to the resolution of the measurement grid. The peak loss of this third structure is comparable between the planar and contoured configurations; however, the size of the structure has been reduced with the contouring. The reduction in size is believed to be a result of less convected fluid, as shown by the dashed arrows of Fig. 7(b).

The exit flow of the cascade is analyzed by pitchwise mass-averaging in Fig. 13. The total pressure loss coefficient is normal-ized by the outlet dynamic pressure at midspan. The contouring produces slightly higher losses from the wall out to 10% span, and the two configurations have almost equal loss over the next 6%. From 16% to 34% of span, an appreciable loss reduction is achieved by the profiled endwall as discussed above. Between 32% and midspan, a slight increase in loss is measured for both configurations as a result of the inlet total pressure surplus discussed in regard to Fig. 3. The mass-averaged and mixed-out mass-averaged exit flow results are summarized in Table 2. The endwall contouring reduces the mixed-out Y_{total} by 9.6% and mixed-out $Y_{secondary}$ was reduced by 14.8%.

Figure 13(b) shows that the blade row produces a classic over/underturning of the flow. The application of contouring increases the overturning at the endwall by 1.8 deg and reduces the maximum underturning by 1.3 deg. The mixed-out mass-averaged flow angle was unchanged within the error of the experiment.

The secondary kinetic energy distribution for the blade row is presented in Fig. 13(c). The high C_{SKE} near the endwall is a direct consequence of the flow overturning there. The peak between $z/h=0.1$ and $z/h=0.2$ results from the underturning as well as the spanwise flow as discussed above. At the downstream measurement plane, endwall profiling has the effect of increasing the secondary kinetic energy near the endwall and reducing it between 10% and 20% of span. Overall, the measured mass-averaged C_{SKE} has been reduced by 13%.

4 Conclusions

Experimental results have been presented documenting changes to the flow field as a result of the application of nonaxisymmetric endwall contouring. In broad terms, the results confirm what has been shown by a number of earlier researchers; endwall contouring is an effective means of reducing endwall losses.

Endwall contouring reduces the strength of pitchwise cross-passage flow near the endwall and spanwise flow up the suction surface of the blade, resulting in a weaker passage vortex. The weaker passage vortex delays the roll-up of the secondary flow and reduces the amount of fluid convected into it.

This paper has also put forth a detailed interpretation of the three dimensional flow field within the blade passage of a PAKB linear cascade, further expanding the database for this established research airfoil. The interpretation is based on oil surface flow visualizations and a series of intrapassage seven-hole pressure probe measurements.

Finally, the results presented herein lay the ground work of a research program investigating secondary loss reduction for high-lift turbine airfoils. Future publications will examine the effect of overall loading level and loading distribution on loss reduction mechanisms and build on the discussions put forth.

Nomenclature

AVR = axial velocity ratio $=u'_{MS_2}/u'_{MS_1}$

B_x = axial chord

C = true chord length

C_P = static pressure coefficient $=(P-P_{CL_1})/q_{CL_1}$

C_{Po} = total pressure coefficient $=(Po-Po_{CL_1})/q_{CL_1}$

$C_{Po_{profile}}$ = profile pressure loss coefficient $=(Po'_{MS_2}-Po'_{MS_1})/q'_{MS_1}$

$C_{Po_{secondary}}$ = secondary loss coefficient $=C_{Po_{total}}-C_{Po_{profile}}$

$C_{Po_{total}}$ = total pressure loss coefficient $=(Po''_2-Po''_1)/q_{CL_1}$

C_q = dynamic pressure coefficient = $(Po - P)/q_{CL_1}$

C_{SKE} = secondary kinetic energy coefficient = SKE/q_{CL_1}

C_{ω_s} = streamwise vorticity coefficient = $\omega_s \cdot C/V_{CL}$

H = boundary layer shape factor = δ^*/θ

h = blade span

q = dynamic pressure = $1/2\rho V^2$

Re = Reynolds number = $\rho V_{CL} C/\mu$

P = static pressure

P_o = total pressure

S = separation streamline

S/S_{max} = fraction of surface length

SKE = secondary kinetic energy = $1/2\rho(v_{sec}^2 + w_{sec}^2)$

s = blade pitch

$u, v,$ and w = axial, pitchwise, and spanwise components of velocity

V = velocity

v_{sec}, w_{sec} = normal components of the secondary velocity vector

$Y_{profile}$ = mass-averaged profile loss coefficient = $(C'_{Po_{MS_1}} - C'_{Po_{MS_2}})/q'_{MS_2}$

$Y_{secondary}$ = mass-averaged secondary loss coefficient = $Y_{total} - Y_{profile}$

Y_{total} = mass-averaged total pressure loss coefficient = $(C''_{Po_1} - C''_{Po_2})/q''_2$

α = pitchwise flow angle

γ = stagger angle

δ^* = displacement thickness

μ = dynamic viscosity

θ = momentum thickness

ρ = density

ω_s = streamwise vorticity = $\omega_x \cos \alpha'' + \omega_y \sin \alpha''$

ω_x = x-component of vorticity = $(\partial w/\partial y) + (\partial v/\partial z)$

ω_y = y-component of vorticity = $1/u(v \cdot \omega_x + (1/\rho) \times (\partial P_o/\partial z))$

Subscripts

1, 2 = cascade inlet and outlet

CL = midspan value mass averaged over one blade pitch

MS = midspan

S, P = suction or pressure leg of the separation streamlines

Superscripts

$'$ = pitchwise mass-averaged value

$''$ = mass-averaged value

Abbreviations

H = hill

R = reattachment

S = separation

V = valley

References

[1] Zorić, T., Popović, I., Sjolander, S. A., Praisner, T., and Grover, E., 2007, "Comparative Investigation of Three Highly Loaded LP Turbine Airfoils: Part I—Measured Profile and Secondary Losses at Design Incidence," ASME Paper No. GT-2007-27537.

[2] Zorić, T., Popović, I., Sjolander, S. A., Praisner, T., and Grover, E., 2007, "Comparative Investigation of Three Highly Loaded LP Turbine Airfoils: Part II—Measured Profile and Secondary Losses at Off-Design Incidence," ASME Paper No. GT-2007-27538.

[3] Hodson, H. P., and Dominy, R. G., 1987, "The Off-Design Performance of a Low-Pressure Turbine Cascade," ASME J. Turbomach., **109**, pp. 201–209.

[4] Chung, J. T., and Simon, T. W., 1991, "Three-Dimensional Flow Near the Blade/Endwall Junction of a Gas Turbine: Application of a Boundary Layer Fence," ASME Paper No. 91-GT-45.

[5] Aunapu, N. V., Volino, R. J., Flack, K. A., and Stoddard, R. M., 2000, "Secondary Flow Measurements in a Turbine Passage With Endwall Flow Modification," ASME J. Turbomach., **122**, pp. 651–658.

[6] Harvey, N. W., Rose, M. G., Shahpar, S., Taylor, M. D., Hartland, J., and Gregory-Smith, D. G., 2000, "Nonaxisymmetric Turbine End Wall Design—Part I: Three-Dimensional Linear Design System," ASME J. Turbomach., **122**, pp. 278–285.

[7] Yan, J., Gregory-Smith, D. G., and Walker, P. J., 1990, "Secondary Flow Reduction in a Nozzle Guide Vane by Non-Axisymmetric End-Wall Contouring," ASME Paper No. 99-GT-339.

[8] Hartland, J., Gregory-Smith, D. G., Harvey, N. W., and Rose, M. G., 2000, "Nonaxisymmetric Turbine End Wall Design—Part II: Experimental Validation," ASME J. Turbomach., **122**, pp. 286–293.

[9] Rose, M. G., Harvey, N. W., Seaman, P., Newman, D. A., and McManus, D., 2001, "Improving the Efficiency of the Trent 500 HP Turbine Using Non-Axisymmetric End Walls: Part II Experimental Validation," ASME Paper No. 2001-GT-0505.

[10] Ingram, G., Gregory-Smith, D., and Harvey, N., 2005, "Investigation of a Novel Secondary Flow Feature in a Turbine Cascade With End Wall Profiling," ASME J. Turbomach., **127**, pp. 209–214.

[11] Praisner, T. J., Allen-Bradely, E., Grover, E. A., Knezevici, D. C., and Sjolander, S. A., 2007, "Application of Non-Axisymmetric Endwall Contouring to Conventional and High-Lift Turbine Airfoils," ASME Paper No. GT-2007-27579.

[12] McAuliffe, B. R., and Sjolander, S. A., 2004, "Active Flow Control Using Steady Blowing for a Low-Pressure Turbine Cascade," ASME J. Turbomach., **126**, pp. 509–537.

[13] Mahallati, A., McAuliffe, B. R., Sjolander, S. A., and Praisner, T. J., 2007, "Aerodynamics of a Low-Pressure Turbine Airfoil at Low-Reynolds Numbers Part 1—Steady Flow Measurements," ASME Paper No. GT-2007-27347.

[14] Benner, M. W., 2003, "The Effects of Leading Edge Geometry on Profile and Secondary Losses in Turbine Cascades," Ph.D. thesis, Carleton University, Ottawa, ON, Canada.

[15] Gregory-Smith, D. G., and Cleak, J. G. E., 1992, "Secondary Flow Measurements in a Turbine Cascade With High Inlet Turbulence," ASME J. Turbomach., **114**, pp. 173–183.

[16] Zorić, T., 2006, "Comparative Study of Secondary Losses for 3 Highly-Loaded Low-Pressure Turbine Cascades," MS thesis, Carleton University, Ottawa, ON, Canada.

[17] Weiss, A. P., and Fottner, L., 1995, "The Influence of Load Distribution on Secondary Flow in Straight Turbine Cascades," ASME J. Turbomach., **117**, pp. 133–141.

[18] Mayle, R. E., 1991, "The Role of Laminar-Turbulent Transition in Gas Turbine Engines," ASME J. Turbomach., **113**, pp. 560–569.

[19] Sieverding, C. H., 1985, "Recent Progress in the Understanding of Basic Aspects of Secondary Flows in Turbine Blade Passages," ASME J. Eng. Gas Turbines Power, **107**, pp. 248–257.

[20] Langston, L. S., 2001, "Secondary Flows in Axial Turbines—A Review," Ann. N.Y. Acad. Sci., **934**, pp. 11–26.

[21] Gregory-Smith, D. G., 1997, "Physics of Secondary Flows," *Secondary and Tip-Clearance Flows in Axial Turbines* (VKI Lecture Series 1997-01), C. H. Sieverding, ed., Von Karman Institute for Fluid Dynamics, Sint-Genesius-Rode, Belgium.

[22] Rose, M. G., 1994, "Non-Axisymmetric Endwall Profiling in the HP NGV's of an Axial Flow Gas Turbine," ASME Paper No. 94-GT-249.

[23] Praisner, T. J., and Smith, C. R., 2006, "The Dynamics of the Horseshoe Vortex and Associated Endwall Heat Transfer Part II: Time-Mean Results," ASME J. Turbomach., **128**(4), pp. 755–762.

[24] Hodson, H. P., and Dominy, R. G., 1987, "Three-Dimensional Flow in a Low-Pressure Turbine Cascade at Its Design Condition," ASME J. Turbomach., **109**, pp. 177–185.

[25] Wang, H. P., Olson, S. J., Goldstein, R. J., and Eckert, E., 1997, "Flow Visualization in Linear Turbine Cascade of High Performance Turbine Blades," ASME J. Turbomach., **119**, pp. 1–8.

[26] Sharma, O. P., and Butler, T. L., 1987, "Predictions of Endwall Losses and Secondary Flows in Axial Turbine Cascades," ASME J. Turbomach., **109**, pp. 229–236.

[27] Benner, M. W., Sjolander, S. A., and Moustapha, S. H., 2004, "The Influence of Leading Edge Geometry on Secondary Losses in a Turbine Cascades at the Design Incidence," ASME J. Turbomach., **126**, pp. 277–287.

[28] Sieverding, C. H., and Van Den Bosche, P., 1983, "Use of Coloured Smoke to Visualize Secondary Flows in a Turbine Blade Cascade," J. Fluid Mech., **134**(1), pp. 85–89.

[29] Denton, J. D., 1993, "Loss Mechanisms in Turbomachines," ASME J. Turbomach., **115**, pp. 621–650.

[30] Ingram, G. L., Gregory-Smith, D. G., Rose, M. G., Harvey, N. W., and Brennan, G., 2002, "The Effect of End-Wall Profiling on Secondary Flows and Loss Development in a Turbine Cascade," ASME Paper No. GT-2002-30339.

[31] Gregory-Smith, D. G., Graves, C. P., and Walsh, J. A., 1988, "Growth of Secondary Losses and Vorticity in an Axial Turbine Cascade," ASME J. Turbomach., **110**, pp. 1–8.

Investigation of Loss Generation in an Embedded Transonic Fan Stage at Several Gaps Using High-Fidelity, Time-Accurate Computational Fluid Dynamics

Michael G. List
Compressor Aero Research Laboratory,
Air Force Research Laboratory,
Propulsion Directorate,
Wright-Patterson Air Force Base, OH 45433
e-mail: michael.list@wpafb.af.mil

Steven E. Gorrell
Department of Mechanical Engineering,
Brigham Young University,
Provo, UT 84602
e-mail: sgorrell@byu.edu

Mark G. Turner
Department of Aerospace Engineering and
Engineering Mechanics,
University of Cincinnati,
Cincinnati, OH 45221
e-mail: mark.turner@uc.edu

The blade-row interaction (BRI) rig at the Air Force Research Laboratory, Compressor Aero Research Laboratory, has been simulated at three axial gaps between the highly loaded upstream stator row and the downstream transonic rotor using TURBO. Previous work with the stage matching investigation (SMI) demonstrated a strong dependence of mass flow rate, efficiency, and pressure ratio on the axial spacing between an upstream wake generator and the downstream rotor through the variation of the axial gap. Several loss producing mechanisms were discovered and related to the spacings, referred to as close, mid, and far. In the SMI work, far spacing had the best performance. The BRI experiments were a continuation of the SMI work with the wake generator replaced with a swirler row to turn the flow and a deswirler row to create a wake by diffusion. Results of the BRI experiments showed a performance degradation between mid- and far spacings, which was not observed in SMI. This trend is seen in the numerical work as well, and the time-averaged data show that the majority of this performance change occurred in the rotor. An unsteady separation bubble periodically forms and collapses as shocks reflect through the stator passage, creating additional aerodynamic blockage. The shed vortices induced by the unsteady loading and unloading of the stator trailing edge are chopped, with a frequency related to the spacing, by the rotor leading edge and ingested by the rotor. Once ingested the vortices interact in varying degrees with the rotor boundary layer. A treatment of the loss production in the BRI rig is given based on the time-accurate and time-averaged, high-fidelity TURBO results. [DOI: 10.1115/1.3072522]

1 Introduction

As part of an ongoing effort to increase stage loading and efficiency, the Air Force Research Laboratory (AFRL), Compressor Aero Research Laboratory (CARL), has been conducting experimental and computational research on transonic compressor blade-row interactions. The stage matching investigation (SMI) was the first such effort and was intended to characterize the effect of blade-row spacing on the interaction between a downstream transonic rotor and an upstream wake generator in a simulated compressor stage. The results of the investigation demonstrated the reduction in pressure ratio, mass flow rate, and efficiency with axial spacing between the blade rows. As a continuation of this effort, the blade-row interaction (BRI) rig has been tested and several simulations have been completed to further quantify and analyze the interaction mechanisms that occur in highly loaded, embedded transonic fan stages. The SMI and BRI rigs were designed to permit the stator-to-rotor axial spacing to be set to three values—"close," "mid," and "far." The major differences between the BRI fan and SMI core rotors are fewer blades (28 versus 33), higher tip speed (414.53 m/s versus 341.37 m/s) resulting in an increased tip relative Mach number (1.389 versus 1.191), and the hub relative Mach number being supersonic (1.100 versus 0.963).

The SMI rig, described in detail by Gorrell et al. [1], was designed to have a variable number of upstream wake generator stators upstream of the transonic rotor. Because the rotor was designed for incoming axial flow, the wake generator was uncambered. In order to produce a wake through base drag, which was representative of the 2D total pressure loss of an upstream fan or compressor stage, the trailing edge was designed to be blunt. As a first attempt to understand the blade-row interactions, the wake generator geometries were designed with the goal of simplifying the flow field. As reported by Gorrell et al. [2] the SMI rig test documented that the axial spacing between an upstream stator and downstream transonic rotor had a significant effect on stage performance. Time-accurate simulations by Gorrell et al. [3] of the SMI experiment revealed some important aspects of the production of additional loss. At close spacing the rotor bow shock was chopped by the wake generator trailing edge and formed a pressure wave on the upper surface of the wake generator that propagated upstream until it weakened. The bow shock was oblique as it interacted with the wake generator trailing edge, but the resulting pressure wave that formed was turned more normal to the wake generator blade surface. The resulting moving shock produced an entropy rise. The magnitude of loss production was affected by the strength of the bow shock and how much it turned as it interacted with the trailing edge of the wake generator. At far spacing the rotor bow shock degenerated into a bow wave before it interacted with the stator trailing edge and no significant pressure wave formed on the stator upper surface. For this condition, no additional loss was produced.

Additional details of the unsteady flow environment were analyzed with measurements using digital particle image velocimetry (DPIV) and with refined time-accurate simulations using the 3D, unsteady, Navier–Stokes computational fluid dynamics (CFD) solver TURBO by Gorrell et al. [4], Turner et al. [5], and
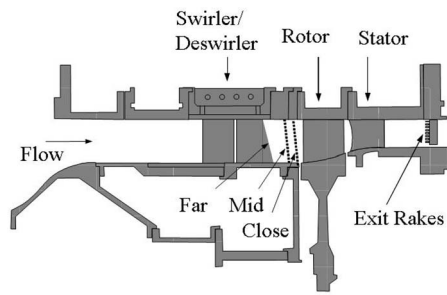

Fig. 1 Blade-row interaction rig

Estevadeordal et al. [6]. Generally there was excellent agreement between the measurements and simulations, instilling confidence in both. At close spacing vortices were shed from the trailing edge of the upstream stationary blade row in response to the unsteady, discontinuous pressure field generated by the downstream rotor bow shock. Shed vortices increased in size and strength and generated increased loss as spacing decreased, a consequence of the effective increase in rotor bow shock strength at the stationary blade-row trailing edge. A relationship for the change in shed vorticity as a function of rotor bow shock strength was presented that predicts the difference between close and far spacing TURBO simulations.

The BRI rig, shown in Fig. 1, was a variation of the AFRL SMI rig. The BRI rig used much of the same hardware with the main difference being the replacement of the blunt, uncambered wake generator of the SMI rig with two upstream stator rows, called the swirler and deswirler. These rows generated a wake by diffusion and the deswirler had realistic stator trailing edge geometry. As the axial inlet flow passed through the swirler row, a tangential velocity was introduced to the flow. By adjusting the stagger angle of the swirler, the incoming flow angle to the deswirler row was adjusted and gave control to the loading experienced by the second blade row. Additionally, the swirler row could be clocked relative to the deswirler to control the pitchwise position of the wake from the first blade row and to optimize the total pressure loss at the entrance of the rotor. The highly loaded deswirler stator row then created a wake and returned the flow to axial for entry into the rotor. A downstream stator row was also present. The BRI investigation focused on the effect of changing the swirler stagger angle, the stator-to-rotor axial spacing, and the operating condition.

With a more realistic upstream stator design, the BRI experiments were able to address the question of whether the interaction observed between the rotor bow shock and the SMI wake generator was a product of the blunt, thick trailing edge or if the behavior would occur with any stator geometry. Langford et al. [7] showed that large vortices can be produced from the passing of a shock over the thin trailing edge of an upstream stator in a cascade. van de Wall et al. [8] showed numerically using TURBO that this occurred in both the cascade and in a turbomachinery stage.

List et al. [9] and List [10] discussed the high-fidelity TURBO simulations in detail and showed many of the interaction effects that were found in BRI. As axial spacing was decreased from far to close the strength of the rotor bow shock as it impinged on the deswirler trailing edge increased. This caused an unsteady loading followed by an immediate unloading, which caused vortex shedding with the strength of the vortex related to the strength of the bow shock. During this interaction, the shock was turned normal to the flow on the pressure side of the deswirler within the region close to the blade. This effect was the same as in SMI and the forward propagating normal pressure wave, supersonic in the relative frame, created an additional entropy rise. The remainder of the bow shock set up a reflected train of high gradient pressure waves, which then interacted with the suction side of the deswirler. As discussed in Refs. [7,8] with respect to the upstream stator, the suction side of the deswirler row separated periodically and then collapsed, causing an additional thick wake to be shed. This wake, combined with the shed vortices from the trailing edge were ingested by the rotor with some of the wake being chopped by the rotor leading edge, dependent on spacing, and the remainder passing through the bow shock, causing the loss across the shock to be amplified. Varying amounts of interaction occurred between the wake from the deswirler and the rotor boundary layer.

2 Numerical Approach

The solver used during this work, TURBO, is a 3D, viscous, unsteady Reynolds averaged Navier-Stokes (RANS) solver and has been previously discussed by Chen and Whitfield [11] and Chen et al. [12–15]. It employs a finite volume Roe scheme to obtain up to third order spatial accuracy and an implicit time integration to obtain second order temporal accuracy. The two-equation turbulence model, the NASA/CMOTT k-ε model, has been specially developed for turbomachinery calculations by Zhu and Shih [16]. TURBO integrates to the wall in the case of $y+$ < 10.5 and otherwise uses wall functions. The turbulence model includes a near-wall damping term, which allows the use of the k-ε model at this resolution. TURBO has been shown to run on 8996 processors using message passing interface (MPI).

Phase-lag methodologies offer solutions restricted to the neighboring blade row's blade passing frequency and higher harmonics. This generally causes an aliasing of many of the unsteady frequencies experienced within turbomachinery flow. As noted by Van Zante et al. [17] phase-lag is inadequate for the resolution of circumferential variation and effects from other blade rows within the same frame of reference. Since the primary features of interest in the BRI simulations are the interactions occurring between the deswirler and rotor, it was important to capture all of the frequencies associated with those interactions and model correct blade counts. By removing the downstream stator blade row it was possible to model a quarter-annulus section of the rig including eight swirlers, eight deswirlers, and seven rotor passages. These are based on the correct blade counts for the three blade rows, 32, 32, and 28, respectively. In addition to allowing a periodic computation, the simulation of only the first three blade rows in BRI allowed additional refinement in the region between the deswirler trailing edge and rotor leading edge, the region of interest. The reduction in required computational resources when moving from four blade-row simulations to three row simulations was also crucial in allowing additional spanwise resolution to capture radial migration of the flow. The simulation of three blade rows instead of four was justified by the results of the SMI simulations by Gorrell et al. [2], which showed that the performance in two blade-row and three blade-row simulations in the SMI rig was very similar. Simulations presented in Refs. [3,4] showed excellent agreement between the measured efficiency difference and the two blade-row CFD. While the BRI rig is very different, the focus was on the loss production in the first three blade rows.

2.1 Computational Grid. The computational grids used in this study were single block H-grids. The turbomachinery gridding system (TGS) [18] was used to create elliptically smoothed meshes for each blade passage. In order to maintain a consistent cell size in the gap between the deswirler trailing edge and the rotor leading edge, a pure H-grid block with point counts proportional to gap size was appended to the deswirler row. This allowed the meshes for each blade passage to be identical between close, mid-, and far spacings. Figure 2 shows an axisymmetric view of the midspacing computational domain.

Table 1 gives the dimensions used for the baseline blade passages. For simplicity, the grids of the swirler and deswirler were identical in each spacing, with an appropriately sized block attached to the inlet or the outlet. The rotor grids were identical. The difference between the tangential spacing of the deswirler and the
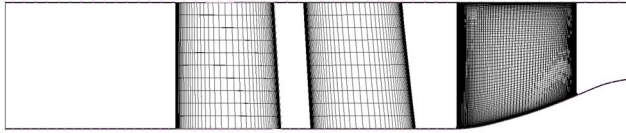
Fig. 2 Axisymmetric view of midspacing computational domain

rotor gave comparable cell sizes and allowed wake capture in the rotor. The final grid dimensions are given in Table 2. Gorrell et al. [3] suggested that the level of resolution of the interface between blade rows caused a loss of accuracy in the SMI simulations. The resolution of the BRI simulations was more than double in the tangential direction and almost 1.5 times the radial resolution. Note that the final grid for the SMI rotor (33 blades) was 189 $\times$ 71 $\times$ 81 nodes in the axial, radial, and tangential directions, respectively. The initial grids for the upstream wake generator (24 blades) used 61 nodes in the tangential direction. This grid had adequate resolution because the trailing edge thickness was so large. The improved resolution in later SMI simulations [4] and in BRI has had a particularly positive effect on the propagation of wakes and vortices through the sliding interfaces. The meshes used in the current BRI simulations are also finer than those used by van de Wall et al. [8], who used 385 $\times$ 80 $\times$ 160 nodes in each passage. The resolution, as noted in Ref. [4], was essential for the capture of wake shedding and transport.

In addition to these grids, for all spacings a pure H-grid block was merged upstream of the swirler, and for mid- and far spacings, a block was appended to the deswirler row. The blocks were sized appropriately to obtain 225 mm of grid upstream of the rotor leading edge to match the end of the bellmouth; the rotor passage extended axially 83 mm downstream of the rotor leading edge to move the exit boundary condition half a chord length downstream of the trailing edge. The axial spacing of the block appended to the deswirler was set to maintain the resolution from the exit of the primary deswirler grid all the way to the rotor interface plane. The resultant grid sizes were quite large. Table 2 shows the final grid point counts and the CPU resources needed to run each of the fine quarter-annulus cases. Close spacing, totaling over 140 $\times 10^6$ grid points required 784 processors, midspacing with over 156 $\times 10^6$ points required 848 processors, and far spacing with more than 166 $\times 10^6$ points required 912 processors.

Both the swirler and the deswirler blades had a hub and tip clearance. This clearance was not gridded but instead modeled as described by Kirtley et al. [19]. Van Zante et al. [20] employed this condition with success. A wall boundary condition was used across the appropriate expanse of the gap to simulate the presence of a button at the swirler hub and hardware connections at the swirler tip and the deswirler hub and tip. The rotor tip clearance

Table 1   Typical BRI grid sizes

	Axial	Radial	Tangential
Swirler	223	101	151
Deswirler	256	101	201
Rotor	391	101	226

Table 2   Total BRI grid nodes and number of CPUs

	Total (close)	Total (mid)	Total (far)
Swirler	4,926,073	4,468,543	4,011,013
Deswirler	5,197,056	7,328,661	9,358,761
Rotor	8,924,966	8,924,966	8,924,966
No. of CPU	784	848	912

Table 3   BRI experimental results

	Close	Mid	Far
Mass flow rate (kg/s)	14.846	14.892	14.840
Pressure ratio	2.057	2.061	2.078
Efficiency (%)	81.748	82.067	81.979

was also treated with this clearance model. Four cells were placed in the hub gap region and eight cells were placed in the tip gap region to capture the tip flows.

2.2 Initialization and Boundary Conditions. Freestream conditions were used as an initial condition for each of the simulations. Various techniques were used, including reduced accuracy and finer time steps, in order to pass the initial transients. The flow required roughly two full revolutions to set up and approximately ten revolutions to converge. The actual time to converge was shown to be related to the wave speeds in the axial direction by List [10].

An isentropic inlet was used with a total pressure and total temperature profile matching that of the rig just upstream of the swirler row. A freestream turbulence intensity was also specified at 2%. The proper numerical application of the inlet profile and turbulence intensity by TURBO has been confirmed in the analysis. Between blade rows an interface boundary condition is used to interpolate the flow solution in a time-accurate sense to the neighboring grids. At the exit, a mass flow rate imposition was used as a boundary condition. Periodicity is assumed tangentially at the extents of the quarter-annulus mesh.

2.3 Simulations. The TURBO simulations corresponded to the peak efficiency configuration for the hardware rig. Close, mid-, and far spacings were each run to their corresponding mass flow rates. The simulations were run second order accurate in time and third order in space. TURBO employed six Newton subiterations with three Gauss–Seidel passes at each subiteration. TURBO was executed on the Air Force Research Laboratory Major Shared Resource Center (AFRL MSRC) SGI Altix and HP Opteron systems, each with 2000 batch-processing CPUs.

Previous work by van de Wall et al. [8] used a coarser computational mesh and recommended 800 time steps per blade passing period to fully resolve the vortex propagation through the rotor passage. The BRI simulations have been obtained for 120, 160, and 320 time steps per blade passing. Although these temporal resolutions are lower than was required by van de Wall et al. [8], the additional grid resolution was able to compensate in the capture of the vortex propagation. Axial grid refinement at the exit of the deswirler and the inlet of the rotor was critical for the capture of the shed vortex physics.

3   Results

The quantities used to discuss loss are the change in entropy level, Δs, and the entropy flux, as defined in Eq. (1) and described by Gorrell et al. in Refs. [3,4]. This parameter includes an axial momentum term and more clearly defines flow features such as vortex shedding and fluid wakes.

$$s_{\text{flux}} = \frac{\rho u \Delta s}{Cp} \qquad (1)$$

In the SMI experiments and numerics, the dominant blade-row interaction effects, which caused a performance decrease, subsided as the axial spacing between blade rows was increased. The experimental effort for BRI, described by Estevadeordal et al. [21], showed that midspacing had the highest efficiency and mass flow rate. Far spacing had slightly lower efficiency and close spacing was the least efficient. The performance data for BRI are given in Table 3. This trend was mirrored in the computational effort and suggests that the loss mechanisms are augmented by the
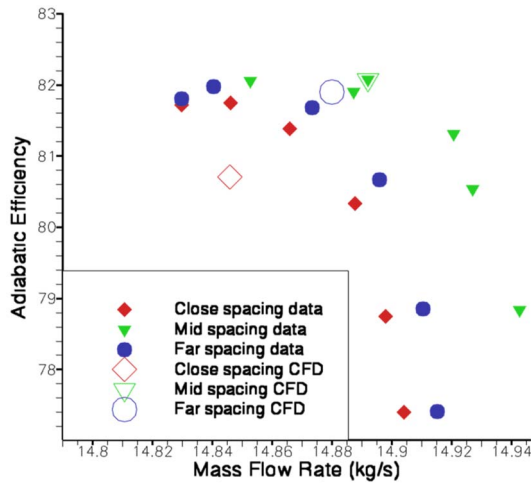
Fig. 3 Comparison of CFD efficiencies to experimental efficiencies

diffusion of the deswirler row. The results of the three blade-row CFD simulation were scaled by a constant factor of approximately 0.93 to fit with the overall four blade-row experimental efficiency, shown in Fig. 3 as previously presented by List [10].

3.1 Time-Accurate Solutions. Time-accurate analyses of data sets of this size require special postprocessing capabilities. A parallel visualization tool, as described by List et al. in Ref. [22], was used to extract planes and isosurfaces of data from the solutions of each of the three spacings. These surfaces were then animated using TECPLOT or ray-tracing software. Unsteady visualization of flow features, particularly the interactions between the rotor and the deswirler wake, has been crucial in the understanding of the loss generation in BRI. In addition to using unsteady visualization, viewing successive blade passages within a single time-step can also give information about the unsteady phenomena. Due to the enforcement of the periodic boundary conditions and the relative blade counts between the rotor and the upstream blade rows the passages exhibit a time-lag.

Figure 4 shows contours of entropy flux for a single time-step at midspan. This shows a time-accurate representation of the propagation of the swirler and deswirler wakes into the rotor passages. From left to right, close, mid-, and far spacings are presented. Each of the spacings exhibits the key loss producing mechanisms discussed by Gorrell et al. [2–4] with regard to the SMI simulations. These include the stronger vortices shed at close spacing, the propagation upstream along the pressure surface of the chopped rotor bow shock, a strengthening of vortices ingested into the rotor as they pass through the bow shock, and wake-

chopping by the rotor leading edge. These mechanisms were discussed for the numerical simulations by List et al. [9,10] and experimentally by Estevadeordal et al. [21].

The wake-chopping seen in Fig. 4 for close spacing results in larger vortex structures interacting with the blade surface boundary layer. The spacing between the deswirler and rotor is small enough that many of the vortices are chopped by the rotor leading edge, but many also pass only through the rotor bow shock. As this process occurs, the vortices are broken down and travel along both surfaces of the rotor. Based on observation in unsteady visualization that the vortices primarily travel along the pressure or suction side in close spacing, it is appropriate to state that this interaction is of principle importance in the detriment of efficiency. The snapshot of far spacing also indicates an interaction between some of the vortices and the rotor boundary layer. Because the wakes of the swirler and deswirler have additional time to mix with the core flow, the tangential extent of the wakes entering the rotor passage is greatly increased from either close or midspacing. This mixing, however, spreads the wake such that a portion of the vortices travel down the center of the passage. In the midspacing simulations, most of the vortices propagated downstream through the center of the passage.

An additional region of loss has been observed in each of the simulations. A separation bubble periodically forms and collapses on the suction side of the deswirler aft of 50% chord. The formation of this separation region is affected by shock and pressure wave reflections and the corresponding interactions with the suction-side boundary layer and amplified by the deswirler's diffusivity. A similar separation region was discussed by Langford et al. [7] and van de Wall et al. [8]. The spanwise extent of this region varies in time. As the region collapses, additional vortices are shed along with a thicker wake from the deswirler trailing edge. This wake has a higher loss and tends to interact with the rotor pressure and suction surfaces.

3.2 Time-Averaged Solutions. Analysis of the time-averaged flow field for the three BRI simulations revealed specific characteristics, which contribute to the resulting efficiency, pressure ratio, and mass flow rate behavior. The time-averaged behavior of the flow as expressed by Δs is given as a mass-averaged distribution in Fig. 5 and a circumferentially averaged rotor exit profile in Fig. 6, taken upstream of where the stator leading edge would be in a simulation including the stator. The distribution of entropy shows that at the trailing edge of the deswirler, for each respective spacing, far spacing has the lowest entropy level. At the rotor leading edge, however, the entropy levels for close and far spacings are consistent and midspacing is the lowest. Within the rotor passage the values of entropy in far spacing follow the same trend as midspacing but close spacing diverges indicating a greater performance detriment. This behavior indicates that the mechanisms of greatest importance in this investigation are the deswirler wake
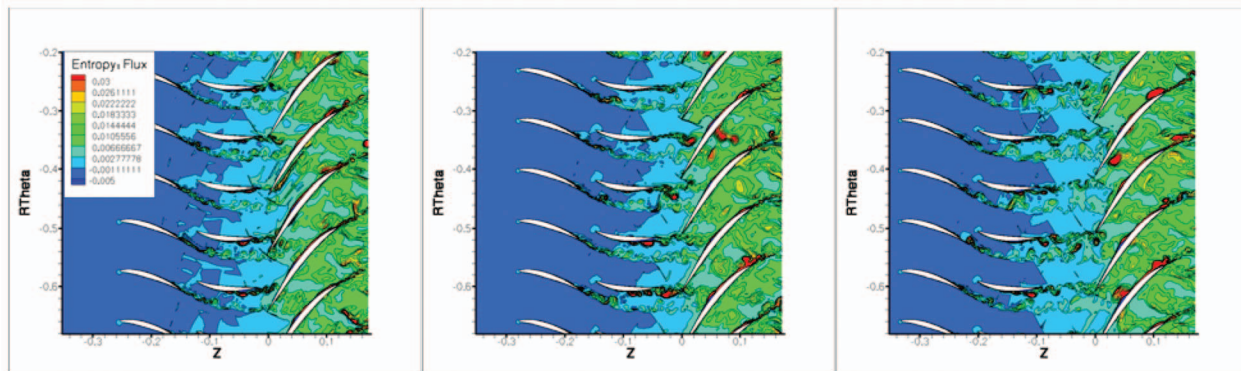

Fig. 4 Entropy flux contours at midspan for (a) close, (b) mid-, and (c) far spacings
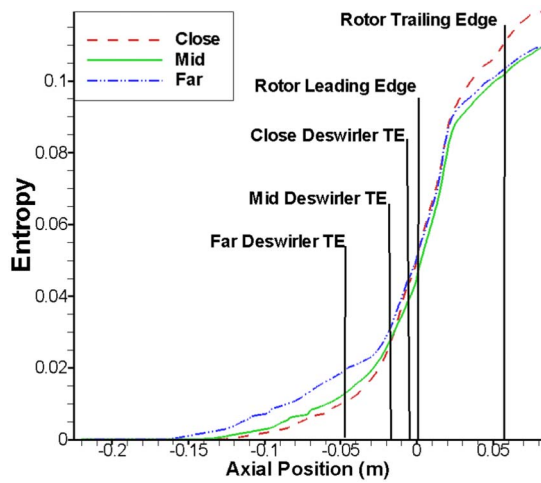
Fig. 5 Time-averaged entropy distribution through the computational domain

Fig. 7 Near linear relationship between efficiency and entropy

behavior and the resulting interaction with the rotor flow field. From the entropy exit profile the radial variation of the flow can be observed. The regions that differ are below 25% span, at midspan, and above 80% span. Comparison of the exit profile of entropy with the exit profile of efficiency showed that there was a nearly linear correlation between the entropy and the efficiency, thus making it appropriate to discuss performance in terms of entropy and entropy flux. Figure 7 demonstrates this point showing that the core flow matches this assumption and deviates only at the hub and tip for all three cases.

Contours of loss given in Fig. 8 shows the extent of a region of high loss associated with the suction-side boundary layer. The blade-to-blade extent of this region in midspacing is less significant than that of far or close spacing. It is known that the wake of the upstream deswirler does interact with the rotor suction and pressure surfaces. The extent of this region implies that the frequency of interaction, which occurs on the suction surface, is highest in close spacing and smallest in midspacing.

An analysis of the momentum in the deswirler passage showed that the momentum is greater in midspacing than the others throughout the majority of the deswirler passage. The region of momentum deficit near the suction side is minimum in midspacing indicating that the separation region in close and far spacings is larger in the time-averaged sense. This accounts for the difference in the entropy distribution given in Fig. 5 aft of the deswirler

trailing edge. There is also additional momentum deficit in the swirler wake in close spacing. The shedding of the swirler trailing edge is likely more heavily influenced by the rotor blade passing frequency in close spacing than in mid- and far spacings.

The extent of the wake exiting the deswirler and its effect on the rotor inlet is shown in Fig. 9. Two distinct regions of loss are apparent in the flow: first the swirler wake, which in close and midspacings is a separate region at roughly 35% pitch from the left (suction) side. The second is the deswirler wake visible at 0% pitch. Close spacing has the strongest and most distinct wakes for both upstream blade rows. This coherent wake results in smaller, stronger vortices being chopped by the rotor leading edge. At midspacing the wakes have mixed out to an extent and the swirler wake begins to interact more with the deswirler wake. Far spacing shows that the effects of the two wakes have merged into a wide region of loss. This region is being ingested by the rotor and results in a circumferentially larger loss region in the rotor passage. The majority of the differences between the spacings occur at the same radial location as the suction-side separation bubble. Additionally, the region between the swirler wake and 100% pitch exhibits stronger loss in close and far spacings but the core flow in midspacing maintains a lower loss level.

Figure 10 gives contours of Δs at midspan for close, mid-, and far spacings in the rotor. The time-average values confirm the discussion regarding where the ingested vortices travel through the rotor passage. The concentration of entropy in the center of the passage in midspacing indicates that this was the highest frequency path for the stronger wake components. Far spacing also
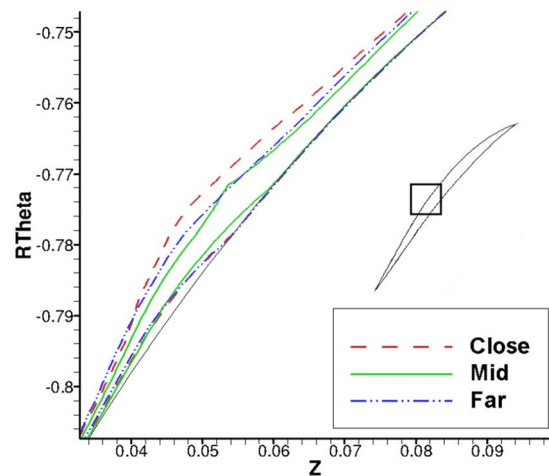

Fig. 6 Time-averaged entropy profile at the rotor exit

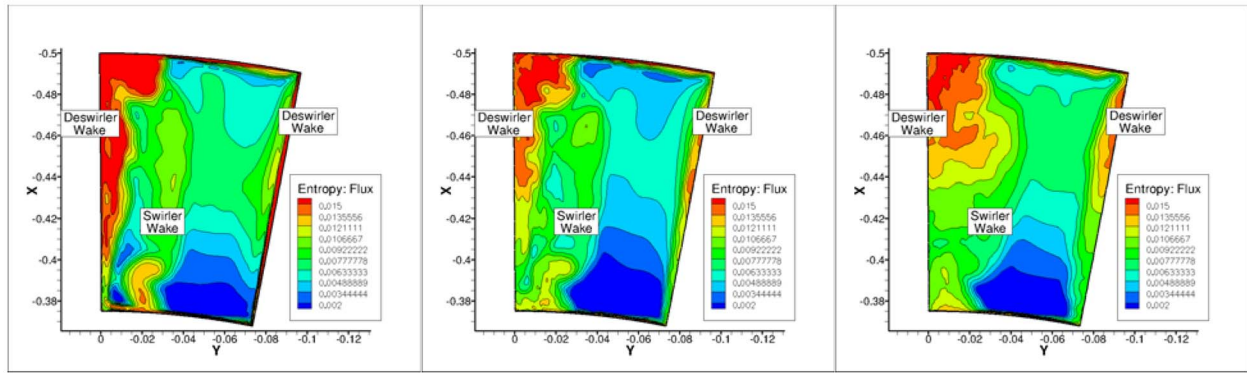Fig. 8 Time-averaged entropy flux contours at midspan of the rotor near 50% chord

Fig. 9 Time-averaged entropy flux contours at an axial cut upstream of the rotor leading edge for (*a*) close, (*b*) mid-, and (*c*) far spacings

shows a larger amount of entropy generation in the center of the passage than close spacing. This figure near the suction side of each passage also gives perspective to the extent of the region shown in Fig. 8. At higher spans the high entropy regions tend toward the suction side in all three spacings as seen in Fig. 11. A region of high entropy also exists aft of 50% chord on the pressure side.

Figure 12 is an aft to fore view of an isosurface of entropy flux in the rotor passage (i.e., looking through the exit of the rotor passage). The isosurface level is 0.0123 and corresponds to the higher entropy region seen at midpitch in midspacing in Fig. 10. This is colored by radial vorticity. As discussed regarding Fig. 9, the loss region entering the rotor is stronger in close spacing. As the wakes are chopped by the rotor leading edge and modulated by the bow shock it can be observed that the spanwise extent is greater than either mid- or far spacing. The region is also confined

to the pressure surface of the rotor. Midspacing has a wider isosurface of loss, but has the smallest spanwise extent and additionally is concentrated near the center of the passage. Recalling that the additional time to mix with the core flow for the far spacing wakes created a wider region of loss, the entropy flux surfaces show that the loss in the rotor passage is wider than in midspacing. This region is also slightly greater in spanwise extent just aft of the bow shock.

4 Conclusions

A numerical investigation of the BRI rig using the solver TURBO has been carried out for one configuration at three spacings. The results have been used to explain the experimental data taken. The resolution of the grids used in this study enabled the capture of shed vortices initiated by interaction between the tran-
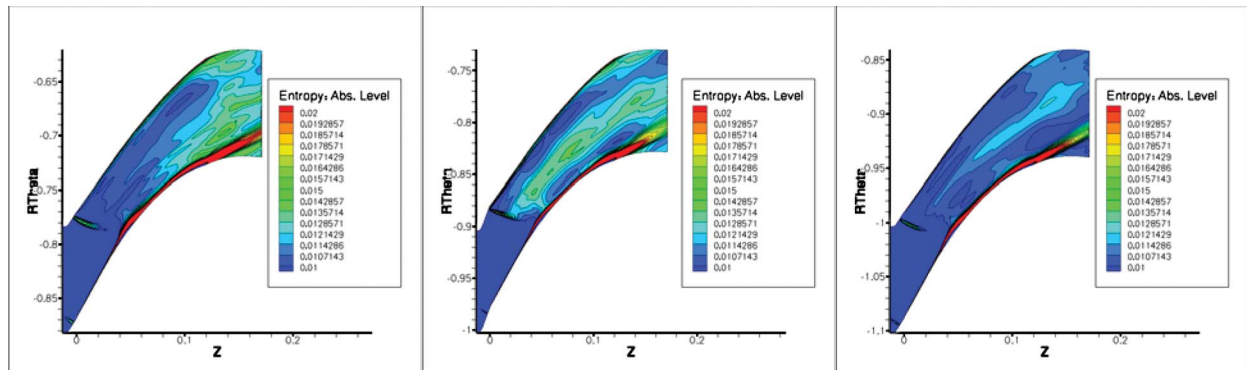

Fig. 10 Time-averaged absolute entropy contours at midspan for (*a*) close, (*b*) mid-, and (*c*) far spacings
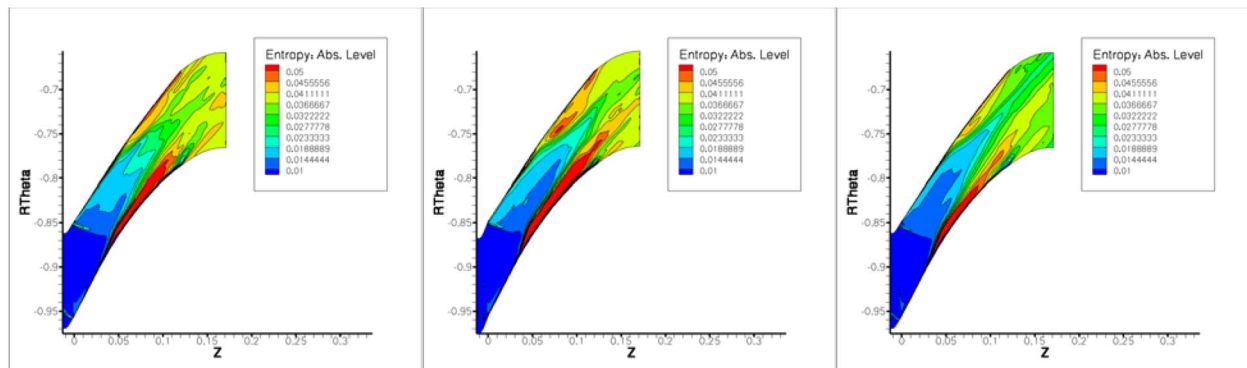

Fig. 11 Time-averaged absolute entropy contours at 85% span for (*a*) close, (*b*) mid-, and (*c*) far spacings
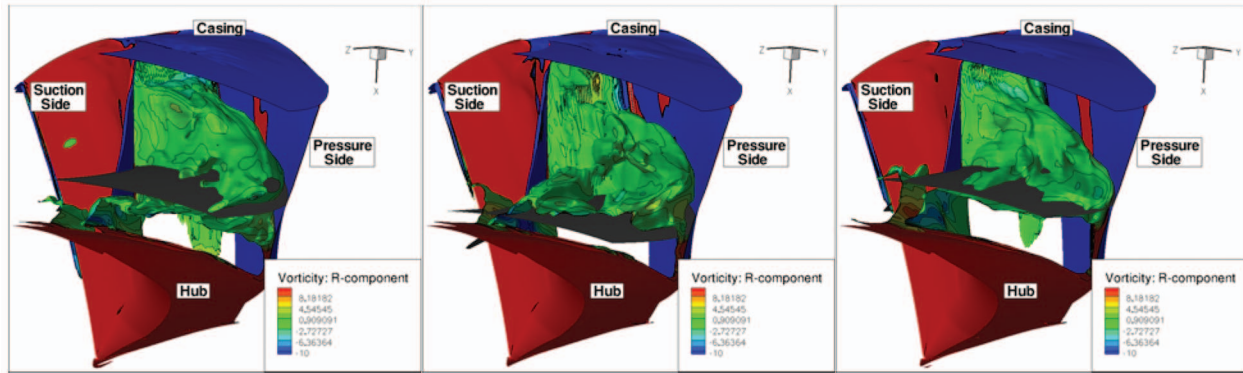
Fig. 12 Isosurface of entropy flux colored by radial vorticity for (*a*) close, (*b*) mid-, and (*c*) far spacings

sonic rotor and the upstream stationary deswirler row. The majority of the grid clustering focused on keeping consistent cell sizes in the region between the deswirler and the rotor which would provide good resolution of the vortex cores. The temporal resolution required was on the order of 9000 per rev due to the grid density. It was shown that midspacing exhibited the best performance due to the propagation of the wakes primarily through the center of the rotor passage. Far spacing behaves in much the same way but has a loss region entering the rotor with greater pitchwise extent, accounting for the performance deficit with respect to midspacing. The loss region associated with the closest axial spacing is greatest in spanwise extent and is concentrated closer to the pressure side of the rotor passage where it interacts with the boundary layer. Resultantly, close spacing has the lowest efficiency of the three spacings. The mechanisms seen in the BRI simulations were consistent with many of the mechanisms seen in SMI. The strength of the rotor bow shock, and thus axial spacing between blade rows, directly affected the strength of the shedding vortices and the wake behavior from the upstream blade rows. As a direct consequence, the path of the wake migration through the rotor passage impacts the rotor pressure ratio and efficiency. The understanding of these mechanisms will ultimately lead to design systems which account for the blade-row interactions of transonic turbomachinery.

Acknowledgment

Nomenclature

ρ = density
u = flow axial velocity
Cp = specific heat
Δs = change in absolute entropy
s_{flux} = entropy flux

References

[1] Gorrell, S. E., Copenhaver, W. W., and Chriss, R. M., 2001, "Upstream Wake Influences on the Measured Performance of a Transonic Compressor Stage," J. Propul. Power, **17**, pp. 43–48.
[2] Gorrell, S. E., Okiishi, T. H., and Copenhaver, W. W., 2003, "Stator-Rotor Interactions in a Transonic Compressor, Part 1: Effect of Blade-Row Spacing on Performance," ASME J. Turbomach., **125**, pp. 328–335.
[3] Gorrell, S. E., Okiishi, T. H., and Copenhaver, W. W., 2003, "Stator-Rotor Interactions in a Transonic Compressor, Part 2: Description of a Loss Producing Mechanism," ASME J. Turbomach., **125**, pp. 336–345.
[4] Gorrell, S. E., Car, D., Puterbaugh, S. L., Estevadeordal, J., and Okiishi, T. H., 2006, "An Investigation of Wake-Shock Interactions With Digital Particle Image Velocimetry and Time-Accurate Computational Fluid Dynamics," ASME J. Turbomach., **128**, pp. 616–626.
[5] Turner, M. G., Gorrell, S. E., and Car, D., 2005, "Radial Migration of Shed Vortices in a Transonic Rotor Following a Wake Generator: A Comparison Between Time Accurate and Average Passage Approach," ASME Paper No. GT2005-68776.
[6] Estevadeordal, J., Gorrell, S., and Copenhaver, W., 2007, "PIV Study of Wake-Rotor Phenomena in a Transonic Compressor Under Various Operating Conditions," J. Propul. Power, **23**(1), pp. 235–242.
[7] Langford, M. D., Breeze-Stringfellow, A., Guillot, S. A., Solomon, W., Ng, W. F., and Estevadeordal, J., 2007, "Experimental Investigation of the Effects of a Moving Shock Wave on Compressor Stator Flow," ASME J. Turbomach., **129**, pp. 127–135.
[8] van de Wall, A., Breeze-Stringfellow, A., and Dailey, L., 2006, "Computational Investigation of Unsteady Flowmechanisms in Compressors With Embedded Supersonic Rotors," ASME Paper No. GT-2006-90633.
[9] List, M. G., Gorrell, S. E., Turner, M. G., and Nimersheim, J. A., 2007, "High Fidelity Modeling of Blade Row Interaction in a Transonic Compressor," AIAA Paper No. 2007-5045.
[10] List, M. G., 2007, "Quarter Annulus Simulations of Blade Row Interaction at Several Gaps and Discussion of Flow Physics," MS thesis, University of Cincinnati, Cincinnati, OH.
[11] Chen, J. P., and Whitfield, D. L., 1993, "Navier-Stokes Calculations for the Unsteady Flowfield of Turbomachinery," AIAA Paper No. 1993-0676.
[12] Chen, J., Celestina, M. L., and Adamczyk, J. J., 1994, "A New Procedure for Simulating Unsteady Flows Through Turbomachinery Blade Passages," ASME Paper No. 94-GT-151.
[13] Chen, J. P., Ghosh, A. R., Sreenivas, K., and Whitfield, D. L., 1997, "Comparison of Computations Using Navier–Stokes Equations in Rotating and Fixed Coordinates for Flow Through Turbomachinery," AIAA Paper No. 97-0878.
[14] Chen, J. P., and Barter, J., 1998, "Comparison of Timeaccurate Calculations for the Unsteady Interaction in Turbomachinery Stage," AIAA Paper No. 98-3292.
[15] Chen, J. P., and Briley, W. R., 2001, "A Parallel Flow Solver for Unsteady Multiple Blade Row Turbomachinery Simulations," ASME Paper No. 2001-GT-0348.
[16] Zhu, J., and Shih, T. H., 2000, "CMOTT Turbulence Module for NPARC," NASA Glenn Research Center, NASA Contract Report No. CR 204143.
[17] Van Zante, D. E., Chen, J., Hathaway, M. D., and Chriss, R., 2008, "The Influence of Compressor Blade Row Interaction Modeling on Performance Estimates From Timeaccurate, Multi-Stage, Navier-Stokes Simulations," ASME J. Turbomach., **130**(1), p. 011009.
[18] Kamp, M. A., Nimersheim, J., Beach, T., and Turner, M. G., 2007, "A Turbomachinery Gridding System," AIAA Paper No. 2007-18.
[19] Kirtley, K. R., Beach, T. A., and Adamczyk, J. J., 1990, "Numerical Analysis of Secondary Flows in a Two-Stage Turbine," AIAA Paper No. 90-2356.
[20] Van Zante, D. E., Strazisar, A. J., Wood, J. R., Hathaway, M. D., and Okiishi, T. H., 2000, "Recommendations for Achieving Accurate Numerical Simulation of Tip Clearance Flows in Transonic Compressor Rotors," ASME J. Turbomach., **122**(4), pp. 733–742.
[21] Estevadeordal, J., Gorrell, S., Gebbie, D., and Puterbaugh, S., 2007, "Piv Study of Blade-Row Interactions in a Transonic Compressor," AIAA Paper No. 2007-5017.
[22] List, M. G., Turner, M. G., Galbraith, D. S., Nimersheim, J. A., and Galbraith, M. C., 2007, "High-Resolution, Parallel Visualization of Turbomachinery Flowfields," AIAA Paper No. 2007-5043.

Web-Based, Interactive Laboratory Experiment in Turbomachine Aerodynamics

Nalin Navarathna

Vitalij Fedulov

Andrew Martin

Torsten Fransson

Royal Institute of Technology (KTH),
Brinellvägen 68,
Stockholm 10044, Sweden

Remote laboratory exercises are gaining popularity due to advances in communication technologies along with the need to provide realistic yet flexible educational tools for tomorrow's engineers. Laboratory exercises in turbomachinery aerodynamics generally involve substantial equipment in both size and power, so the development of remotely controlled facilities has perhaps not occurred as quickly as in other fields. This paper presents an overview of a new interactive laboratory exercise involving aerodynamics in a linear cascade of stator blades. The laboratory facility consists of a high-speed fan that delivers a maximum of 2.5 kg/s of air to the cascade. Traversing pneumatic probes are used to determine pressure profiles at upstream and downstream locations, and loss coefficients are later computed. Newly added equipment includes cameras, stepper motors, and a data acquisition and control system for remote operation. This paper presents the laboratory facility in more detail and includes discussions related to user interface issues, the development of a virtual laboratory exercise as a complement to experiments, and comparative evaluation of virtual, remote, and local laboratory exercises.
[DOI: 10.1115/1.3106030]

1 Introduction

In engineering education, laboratory exercises provide critical training in a variety of topics. When students perform a laboratory exercise in the traditional sense (i.e., locally), they receive a complete impression of being in the laboratory hall as they use all their senses to identify the devices and their functions. This state of local attendance of a laboratory exercise allows students to gain a so-called "hands-on" experience. In the field of turbomachinery, laboratory exercises are often large and expensive, so it is not practical for each educational institution to have a full ensemble of equipment that covers all relevant fields. Many educational institutions are also revamping their curriculum to offer added flexibility in time and place to their students (e.g., distance education). Both of these facts point to the strong need for developing new and advanced laboratory exercises that can be run remotely. One may of course argue on the issue of the usefulness of remote laboratories. Some researchers doubt that remote laboratories can provide students with practical experience in the learning process [1]. Others believe that remote laboratories are not the best educational tools, but still in cases where there are not sufficient laboratory facilities, remote laboratories can be a good compromise [2]. In the end everyone agrees that remote laboratories cannot replace hands-on experience that would ideally be provided to students as practical training whenever possible, but they can be used in cases where laboratory facilities are not sufficient or not accessible. This point is primarily addressed to countries and institutions that lack laboratory facilities and to people that cannot have access to the laboratory, either because they have to travel long distances, have limited access due to physical disabilities, etc.

It should be mentioned that remote laboratories are not the only alternative to traditional laboratory exercises. Simulations are also a good way for the students to couple theory and practice.

Pedagogically sound simulations are sometimes more difficult to design than remotely controlled facilities, but they are easy distributed to many users at a low cost [2]. Another point of comparison between simulations and remote laboratories is that when developing a simulation, the developer often introduces artificial elements in order to make it more realistic [2]. This is due to the fact that reality always is more complicated and "uncertain" than theory. On the contrary, a remote laboratory developer tries to minimize complications by making the laboratory as easy to control as possible so that the remote user will be able to perform it without problems. Since remote laboratories are real, the developer has to deal with all the difficulties that one meets in a traditional laboratory exercise; there is no need to introduce the above-mentioned elements artificially.

Remote laboratory exercises have another important advantage as compared with simulations: The fact that the experiment is "real" provides a tremendous boost to the student's level of interest. The student is thus much more motivated and engaged, which in turn should enhance the pedagogical experience. That is why remote laboratories have been called "second best to being there" [1]. Indeed, this expression embodies a governing philosophy behind remote laboratories and their success as measured in pedagogical terms. In designing remote laboratories, it is also important to ensure that the user has the feeling of performing an experiment, which is real and not virtual [3].

This paper presents an overview of a newly developed interactive laboratory exercise in turbomachinery aerodynamics. The facility has been developed by the Division of Heat and Power Technology at KTH within the framework of the I-Labs Project, a collaborative effort between KTH, Stanford University, and the Learning Lab of Lower Saxony (L3S). KTH has been very active in the development of e-learning material in turbomachinery, e.g., CompEdu [4], and the new remote facility continues in this tradition.

2 Description of Remote Laboratory Facility and Laboratory Exercise

Currently, KTH students studying for degrees in Mechanical Engineering or Energy Technology have the opportunity to acquire some understanding about specific topics such as turbomachinery aerodynamics. This is accomplished by means of lectures
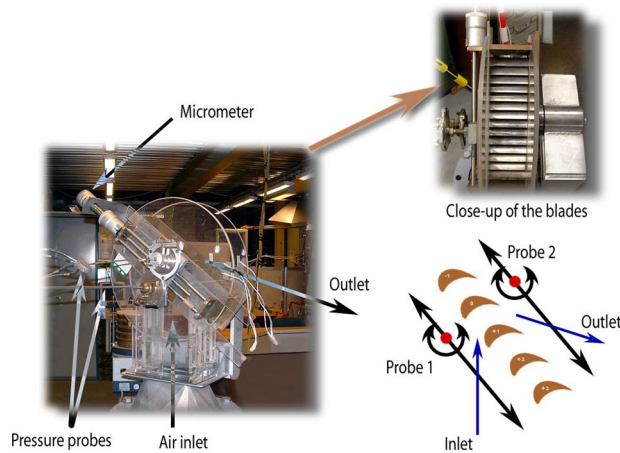
Fig. 1 Existing linear cascade laboratory facility

given as a part of the elective course "Thermal Turbomachines" and by related laboratory exercises. For example, in the laboratory exercise "Flow Losses in a Linear Cascade," students are given the opportunity to experience realistic experiments with high air mass flow rates and to use appropriate instrumentation to study the characteristics of airfoils. Students more clearly understand the influence of the turbine cascade on the flow and the resulting pressure losses due to this. In addition, the students performing this laboratory exercise can see the blades of the stator of the turbine cascade, their shape, and orientation first hand, and they thus form an understanding of the influence of these factors on the fluid dynamics in turbomachinery.

Figure 1 shows details of the linear cascade facility. As mentioned previously, it consists of a single row of blades attached on the grid holder. The grid holder is supported by movable sidewalls of the cascade that are situated below it. This arrangement allows for the inlet flow angle to be varied to provide different inlet conditions of the flow (i.e., angle of attack). Two aerodynamic probes are used to measure pressures upstream (four-hole probe) and downstream (five-hole probe) of the cascade. A stepper motor controlled micrometer moves the probes along the pitch direction (Fig. 1, top left). A compressor located in the basement of the laboratory hall supplies the airflow (2.5 kg/s maximum at a pressure just above ambient). When the compressor is in operation, air is driven through a horizontal pipe toward the test facility. After the stagnation chamber at the end of the horizontal pipe, the flow changes direction to vertical. Finally the flow passes through the test section and after it blows out to the laboratory room.

3 Outline of Laboratory Exercise Procedure

To initiate the experiment, the compressor is turned on and the airflow passes through the cascade. (At this point, it is important to say that for safety reasons there is always a qualified technician present to start up the compressor). After the desired airflow is attained the next step is to observe the manometers connected to the aerodynamic probes and turn these until the pressure readings become stabilized. Then the following measurements are taken:

(1) flow inlet angle
(2) angle of the downstream probe at the point where the pressure difference is zero
(3) the upstream stagnation pressure
(4) the downstream stagnation pressure

After the above measurements are taken the probes are moved to a different position along the pitch direction. When the readings in the manometers become stable again, the same measurements are recorded for the new position. Students use the experimental data with relations given for determination of pressure losses in a

linear turbine cascade. The pressure loss coefficient ξ [1] is calculated for the different positions and illustrated in a diagram with the measuring positions in the horizontal axis [5].

4 Remote Laboratory Features

Figure 2 shows a schematic of the interconnectivity of the remote laboratory. Currently remote users with reasonably good Internet connections (preferably at least 0.1 Mbyte/s) have the opportunity to run this laboratory exercise.

An online web service was created to support the remote users and contains the necessary information about the laboratory. To further enhance learning, this remote online laboratory exercise was integrated into CompEduHPT [4,6].

Some of the key features of this remote laboratory exercise include the following:

- live streaming video, which allows direct observation of experiment
- remote control and data acquisition
- instant feedback and suggestions during laboratory operation
- online communication (chatting) between students
- online scheduling, allowing multiple students to efficiently use laboratory facilities
- detailed explanation of laboratory for instructor (both printed and online)
- online instructor tools for evaluating students' performance
- online documentation: laboratory description, procedure, and background theory

5 Hardware Configuration

To access the laboratory remotely, the main hardware components introduced to the existed laboratory were stepper motors, stepper motor controllers, pressure transducers, hardware video server, and communication cameras.

6 Automation of Probe Motion

In this laboratory exercise the remote user can control the movement of the two pressure probes. The two probes are each placed upstream and downstream of the cascade blades. The remote user needs to rotate each probe to follow the angle of the flow, which is different for every position along the pitch direction, in order to correctly measure the stagnation pressure. When the probes are placed in the correct pitchwise angle it means that they are perfectly aligned with the direction of the flow and measurements for the stagnation pressure can take place.

Two stepper motors are connected with each one of the probes to take care of this rotation. Figure 1 shows the motion requirements of probes 1 and 2.

The remote user also needs to move the probes along the pitch direction in order to obtain measurements with different characteristics, i.e., different downstream flow angles, different loss coefficients, etc. In order to achieve this, a stepper motor was installed to enable this linear motion.

7 Pressure Measurements

The pressure measurements in the traditional laboratory exercise were obtained via liquid manometers. In the remote laboratory there are pressure transducers as well as liquid manometers. These pressure transducers provide the remote user with data in digital form, which is conveniently assimilated in the web-based program. The reason to keep the liquid manometers comes from the pedagogical considerations of the project.

---

[1]The pressure loss coefficient $\xi = 1 - \eta$, where the efficiency of flow through a stator of turbine, η, is the ratio between *actual kinetic energy* and *ideal kinetic energy* [5].
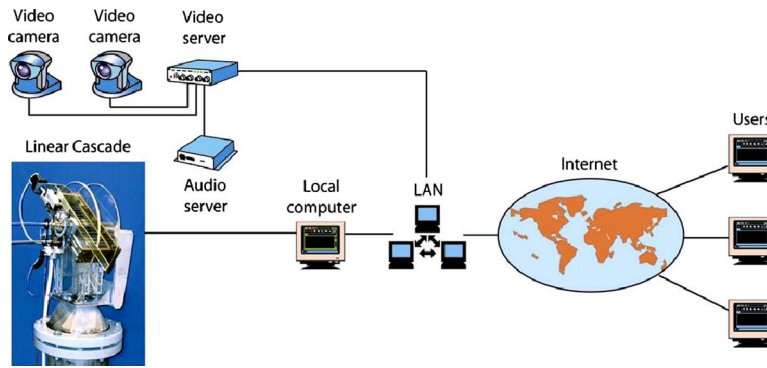
Fig. 2 Schematic of remotely control online laboratory exercise

8 Live Video Streaming

Two communication cameras were installed around the rig, in different arrangements, to capture and transfer image from different viewing angles. This system comprises of the following components:

(1) Canon communication camera (VC-C4)
(2) Canon communication camera (VC-C4R)
(3) video server (AXIS 2400)
(4) audio server (AXIS 2191)

These communication cameras have their own internet protocol (IP) addresses. They are connected to the network as network devices and they have a built-in software for a web server, file transfer protocol (FTP) server, FTP client, electronic mail client, etc. They also have the capability of running scripts, i.e., small programs. In order to transmit images captured from these cameras over the network, a network video server has been installed. The video server connects in parallel with the existing equipment and transmits original video over a computer network. Using built-in serial ports these servers can control pan/tilt/zoom (PTZ) cameras. Network video servers also have digital inputs and outputs. The inputs can be used to trigger the server to start transmitting images. Figure 3 shows the user interface that was developed to link the home page of the project with the two communication cameras and the interface by which the remote user can control the movement of the cameras.

9 Laboratory Control Interface

To control the equipment and data acquisition the laboratory user interface was designed with software "LABVIEW remote panel." (To access the remote panel for the first time the remote user must install the LABVIEW runtime engine on the remote user's computer.) Figure 3 shows the control panel (along with several subpanels), including the live video image of the test rig from the side of the rig and above from the rig. Figure 4 shows the live video image of the test rig from the side of the rig. The user has
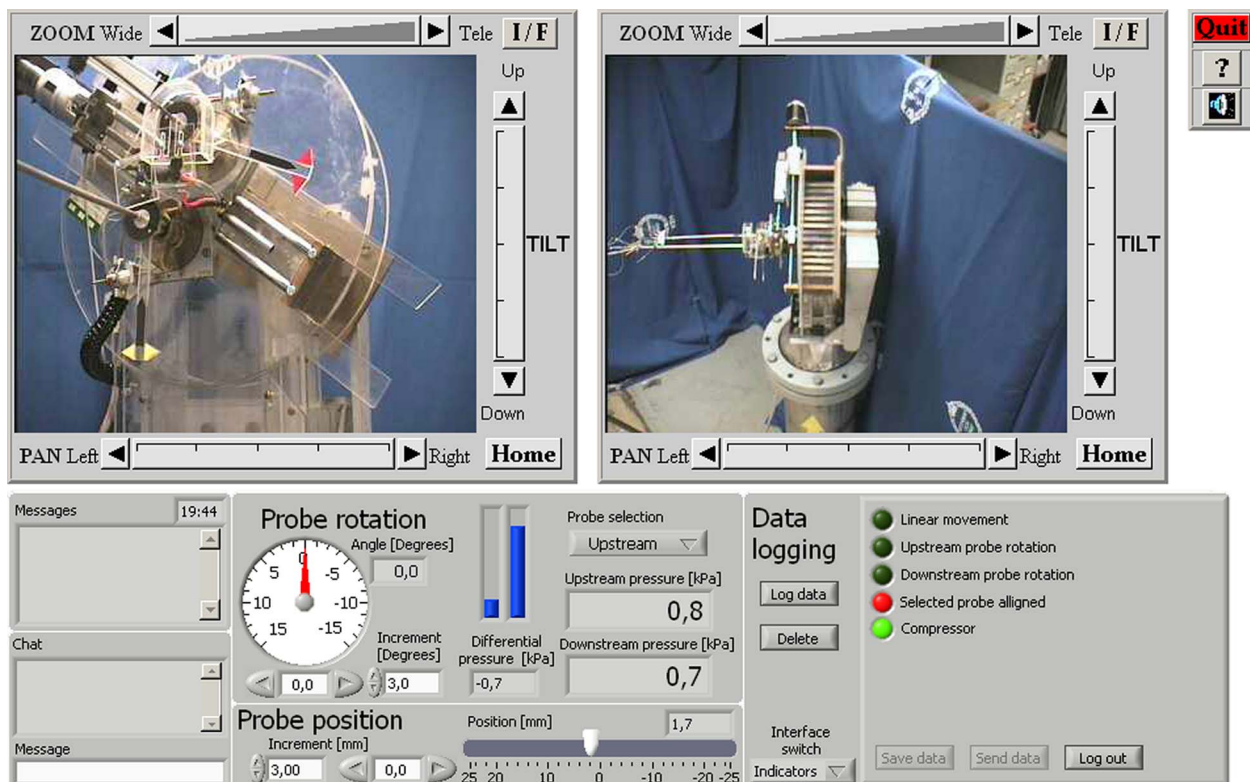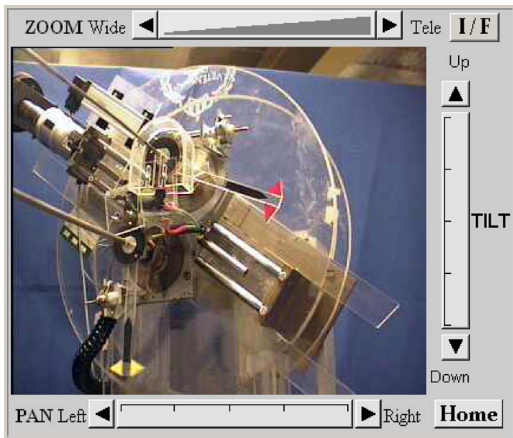

Fig. 3 Remote laboratory user interface

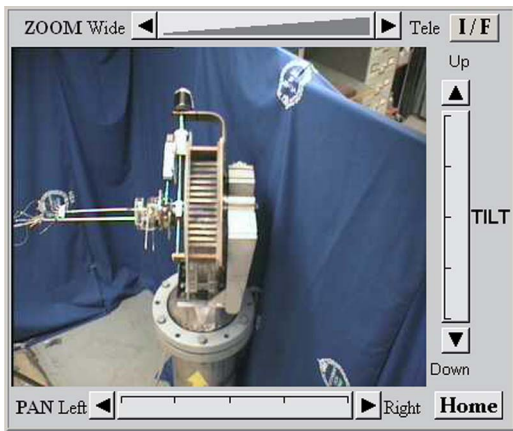**Fig. 4 Live video image of the side camera**

Fig. 5 Live video image of the top camera

PTZ control, and clicking on the image will render a centered image about that point.

Figure 5 shows the live video image of the test rig from the above. Again, the user has full PTZ control for this camera.

Three critical buttons—quit, help, and sound on/off—are located conveniently in the upper right hand corner of the screen (Fig. 3). The chat and message window can be see in the lower left.

10 Safety

Safety issues were taken in to consideration since the laboratory operates with a high-speed fan that delivers a maximum of 2.5 kg/s of air to the cascade. There is technician available to operate the high-speed fan while the remote user accesses the laboratory. This is arranged with the help of laboratory reservation system. Since remote users have full control over many physical processes, safety issues (equipment, system, and human) have to be considered very carefully [1].

Before starting this laboratory, students are provided ample background information and theory via CompEdu and the laboratory's homepage. Prior to the remote laboratory exercise it is obligatory to perform the virtual exercise. Afterwards they can request the permission to run the remote laboratory from the laboratory assistant at KTH. Students then log on the web service with the provided username and password (Fig. 6).

Once they are ready they can reserve convenient time for them at remote laboratory reservation system, which is in the remote laboratory web service (Fig. 7).

Quizzes test the knowledge of the students relative to the theory and virtual laboratory experience. After successful completion of this section students then have the possibility to go to remote laboratory exercise or the laboratory control panel (Fig. 3).

11 Evaluation of Virtual, Remote, and Local Laboratory Exercises

The goal of the evaluation effort is (a) to improve the laboratory technology, (b) to answer general questions in technology-

Fig. 6 Login page to the remote laboratory

Fig. 7 Laboratory reservation page at remote laboratory

enhanced learning, and (c) to identify success factors for cross-continental remote laboratory usage. To clearly explain the details of the evaluation process, it is suitable to first define the terms we use for our laboratories. Virtual laboratory is a computer simulation of a laboratory that helps to prepare to operation of the (expensive) real facility. Measurements are simulated by a prerecorded real set of data acquired from a previous session. Remote laboratory is a real laboratory operated distantly and measurements are taken distantly. Local laboratory is a real laboratory operated in traditional way with measurements taken locally. The laboratory procedures are nearly the same for virtual laboratory, remote laboratory, and local laboratory, so no further comments are needed on this aspect.

Virtual laboratories attempt to artificially emerge a learner into experimental environment without the synchronous use of the actual hardware [2]. Virtual laboratories can simulate several aspects of experimental work, such as visual settings/environment, the phenomena studied, measurement devices, and measurement processes. Learners have direct influence on parameters of the simulated experimental work, so that output depends on certain learner-defined values. Simulated experimental output, including data visualization and analysis, can be a part of the virtual laboratory as well.

The linear cascade virtual laboratory is based on collected real measurements. In many ways it resembles the remote laboratory although video images and audio are not included. Figure 8 shows a screen snapshot of the virtual laboratory. In this exercise, pressure readings are interactively simulated. Students can change probe positions and orientation toward airflow direction just as it is in the real laboratory exercise. Simulated measurements have real irregularities in data output, so that learners can see the difference between the theoretical pressure drop profile and the real one. The virtual laboratory interface consists of several panels controlling atmospheric condition measurement, probe positioning, manometers, probes/cascade positioning visualization, probe/flow angular setting, and profile loss graphical representation (Fig. 8).

Initially the virtual laboratory exercises in CompEduHPT, including the linear cascade virtual laboratory, were intended as a prelaboratory experience for the students to prepare themselves for a more effective real hands-on laboratory exercise, and serve also as an extremely useful tool for the students when they prepare themselves for the exam [6]. With introduction of CompEduHPT for distance learning the learning paradigm for the virtual laboratories is widening. Now it can be used as a substitute for real laboratory experience in cases when access to real facilities is not possible in any form (remote or local).
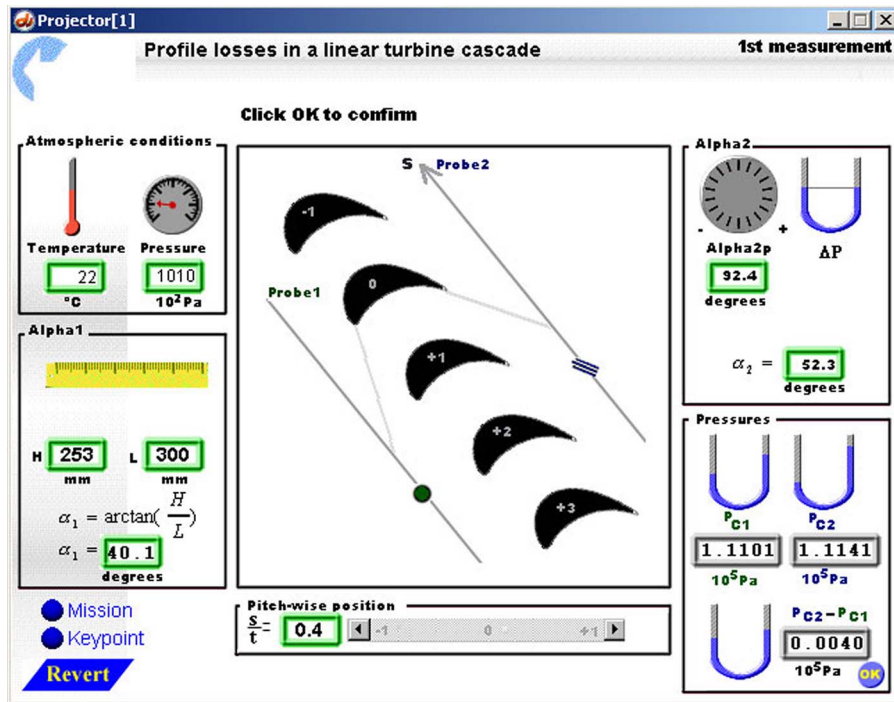
Fig. 8 Virtual laboratory user interface

12 Evaluation Conditions

The first part of the evaluation compares the remote laboratory against the virtual laboratory in order to clarify the role of these learning techniques and to compare their effectiveness in the educational process. The comparison also helps to understand how far one can be a substitute of the other.

The second part of the evaluation considers the remote laboratory versus the local laboratory. This study explores the educational impact (advantages/disadvantages) of offering a remote laboratory to students instead of the traditional exercise. The evaluation takes into consideration the fact that the remote laboratory is not a full-value substitute of the local laboratory. For this case, comparisons were broken down into two phases. In phase I, the virtual laboratory was evaluated separately by a group of 20 students. After performing the virtual laboratory, the students were given a questionnaire and were interviewed for the topics related to their experience in experimental work (motivation level, knowledge in measurement techniques, computer literacy, etc.). Their personal approach toward the use of computerized educational tools was measured. Finally the knowledge gain during the laboratory performed was evaluated. Aspects related to motivation changes were also considered. Phase II served for direct comparison between the remote laboratory and the virtual laboratory. The key issue to be answered here relates to whether or not the virtual laboratory fulfills an educational function close enough to a real object of learner's practical exercise.

The third part of the evaluation also included all the three laboratory types in a training sequence virtual laboratory, remote laboratory, and local laboratory. Here, an additional 20 students attending the Fluid Machinery course at KTH participated.

13 Evaluation Results

Comparison between students' usage of the remote laboratory and the virtual laboratory revealed that interfaces of both the laboratory should not necessarily be the same. This contradicted our first assumption that similarity of interfaces would increase motivation to study and learning efficiency. In fact, diversity of interfaces increases the interest/motivation for learning as well as learning efficiency. Learning efficiency is increased, because different interfaces might represent different approaches on solution of the same problem offering more information to learn.

Somewhat surprisingly, the remote laboratory was found to have several advantages compared with the local laboratory. The remote laboratory was generally found to be more comfortable to perform. Users reported that they had more control over the laboratory environment. It is possible to switch off the sound from the laboratory, which is mainly noise from the high mass flow airstream. The sound creates a tangible feeling of power, especially when the compressor starts, but it can be disturbing if students do not have possibility to switch it off or at least to reduce the volume. It is very difficult for the students to communicate with each other and with the instructor while working as a group. Students expressed this difference as more comfortable feeling when doing the remotely controlled laboratory. (Some of these aspects could be overcome with the use of headsets and microphones during the local laboratory exercise.) The evaluation revealed another important advantage of the remote laboratory. When the students conduct the real laboratory, they have no possibility to look into the linear cascade from the outlet of the airflow, because it might be dangerous, noisy, and physically impossible (strong dynamic force from the moving air). But it is important to see how the pressure probe changes its position along the cascade. This is possible in the remote laboratory—the camera is installed just from the front of the outlet so that it can zoom on the probe. Movements of the probe can be seen very clearly with the camera system.

Students reported the feeling of reality in the remote laboratory as "close," which is mainly because there is realistic sound and the possibility to view the laboratory from two video cameras installed in the laboratory. Prior to starting the measurements the learners can look around the laboratory using the cameras. Realistic sound gives the feeling of environment with real machines in work. There were some smaller calls for improvements, namely, a need for one more camera and coloring pressure measurement liquid in glass tubes.

What is missing in the remote laboratory is that "the students do not get their hands dirty." This includes touch-sensory percep-

tion, specific spatial/dimensional perception, and feeling of smells. The spatial/dimensional perception should be definitely improved, in order to assure even higher proximity to real physical conditions. One simple idea would be to manufacture several blade replicas in plastic and to send these by mail to the remote user.

An additional advantage of remotely controlled laboratory compared with the real laboratory is that the remote laboratory has certain gamelike elements that might induce a learner's interest. This includes exploration of spatial conditions in unusual ways (e.g., quests [7]) and uncertainty of action consequences. These elements are unavailable or are reduced in real environment. The presence of the elements in remote laboratory might increase motivation to learn and explore. Our evaluation showed that there were no clear preferences for "having fun" when doing the remote laboratory compared with the local laboratory. Some students definitely found the remote laboratory to be the most fun, but others preferred the local laboratory. Nevertheless this also means that some sensory disadvantages of the remote laboratory can be successfully compensated by additional motivational elements based on game principles.

One part of our evaluation concerned time spent to become familiar with interfaces and usage principles of the virtual laboratory, remote laboratory, and local laboratory. In our evaluation all the three laboratories were performed in the same general sequence. We noticed great reduction in time needed to become familiar with the remote laboratory compared with the local laboratory. This supports important principle of positive transfer of training [8], which is the basis for aircraft staff preparation, for example. But comparison of times spent to become familiar with the virtual laboratory versus remote laboratory did not indicate the positive transfer of training. The main reason for this is that the laboratory simulation (virtual laboratory) is easier to complete than the remote laboratory.

The conclusion from evaluation of the virtual laboratory was that a simulation might well serve as a preparation phase to operation of real laboratory (remotely or locally controlled). It is also a good means for learning, when real laboratory is not available. The evaluation showed that students definitely found it valuable to perform the virtual laboratory prior to remote laboratory [9,10].

14 Concluding Remarks

The virtual laboratory was reported to serve well as a preparatory phase to the real laboratories (remote or local). For the case where the real laboratories are not available in any form, the virtual laboratory still has a significant educational value for the learners. Differentiation between interfaces of the virtual laboratory and remote or local laboratories was a suggested area of improvement. Contact with reality in the remote laboratory is much different from predetermined sequential action in the virtual laboratory due to richer uncertainty factors and delayed responses of the real objects. Gamelike properties of remote laboratory and more comfortable conditions for performing the laboratory compensate the disadvantages of physical separation. Results from the student groups suggest that the remote laboratory is a positive alternative to the traditional laboratory exercise. More data are required to confirm this finding. Evaluation of these laboratories is currently ongoing. In the near future student groups located abroad (Finland and Sri Lanka, in particular) will be involved. These evaluations will help us to ascertain the true value of this remote laboratory and will hopefully assist others in establishing new facilities.

References

[1] Aktan, B., Bohus, C. A., Crowl, L. A., and Shor, M. H., 1996, "Distance Learning Applied to Control Engineering Laboratories," IEEE Trans. Educ., **39**(3), pp. 320–326.

[2] Tuttas, J., and Wagner, B., 2001, "Distributed Online Laboratories," International Conference on Engineering Education, Oslo, Norway.

[3] Böhne, A., Faltin, N., and Wagner, B., 2002, "Self-directed Learning and Tutorial Assistance in a Remote Laboratory," *Interactive Computer Aided Learning Conference*, Villach, Austria, Learning Lab Lower Saxony, Hanover, Germany.

[4] Salomón, M., Fridh, J., Kessar, A., and Fransson, T., 2003, "Gas Turbine Simulations in the Computerized Educational Program CompEduHPT: Educational Aspects," ASME Paper No. GT-2003-38164.

[5] Wei, N., 1996, "Determination of Losses in a Linear Cascade," Laboratory Notes, Division of Heat and Power Technology, Royal Institute of Technology, Stockholm, Sweden.

[6] Fransson, T. H., Hillion, F.-X., and Klein, E., 2000, "An International, Electronic and Interactive Teaching and Life Long Learning Platform for Gas Turbine Technology in the 21st Century," ASME Paper No. 2000-GT-0581.

[7] Yee, N., 2003, "Appeal of Game Elements," The Daedalus Project, http://www.nickyee.com/daedalus/archives/000628.php.

[8] 2009, "Positive Transfer of Training," Encyclopedia Britannica Online, http://www.britannica.com/EBchecked/topic/471863/positive-transfer-of-training.

[9] Fraenkel, J. R., and Wallen, N. E., 2003, *How to Design and Evaluate Research in Education*, McGraw-Hill Higher Education, Boston, MA.

[10] Krathwohl, D. R., 1998, *Methods of Educational and Social Science Research*, Addison-Wesley, Reading, MA.

Effects of Reynolds Number and Freestream Turbulence Intensity on the Unsteady Boundary Layer Development on an Ultra-High-Lift Low Pressure Turbine Airfoil

Xue Feng Zhang
Gas Turbine Laboratory,
Institute for Aerospace Research,
National Research Council Canada,
M-10, 1200 Montreal Road,
Ottawa, ON, K1A 0R6, Canada

Howard Hodson
Whittle Laboratory,
Department of Engineering,
Madingley Road,
Cambridge CB3 0DY, England

The effects of Reynolds numbers and the freestream turbulence intensities (FSTIs) on the unsteady boundary layer development on an ultra-high-lift low-pressure turbine airfoil, so-called T106C, are investigated. The measurements were carried out at both Tu =0.5% and 4.0% within a range of Reynolds numbers, based on the blade chord and the isentropic exit velocity, between 100,000 and 260,000. The interaction between the un- steady wake and the boundary layer depends on both the strength of the wake and the status of the boundary layer. At Tu =0.5%, both the wake's high turbulence and the negative jet behavior of the wake dominate the interaction between the unsteady wake and the separated boundary layer on the suction surface of the airfoil. Since the wake turbulence cannot induce transition before separation on this ultra-high-lift blade, the negative jet of the wake has the opportunity to induce a rollup vortex. At Tu =4.0%, the time-mean separation on the suction surface is much smaller. With elevated FSTI, the turbulence in the wake just above the boundary layer is no longer distinguishable from the background turbulence level. The unsteady boundary layer transition is dominated by the wake's negative jet induced boundary layer variation. [DOI: 10.1115/1.3106031]

1 Introduction

The increasing demands for higher efficiency and lower weight and cost of aircraft engine have led to the development of highly loaded low-pressure (LP) turbine airfoils. Increasing the airfoil loading results in a larger adverse pressure gradient on the rear portion of the airfoil suction surface. Given the low Reynolds numbers at the last stages of the LP turbine, the boundary layer might be expected to separate from the airfoil suction surface. However, the flow in turbomachines is essentially unsteady due to the relative motion of the rows of airfoils. Since the flow is sub-sonic, wakes from the upstream blade rows, which periodically pass through a downstream blade row, provide the dominant source of unsteadiness in the LP turbine. In this case, the wakes can reduce the size of separation.

Meyer [1] was one of the first to use the idea of the negative jet to explain the unsteady wake behavior in the blade passage. How- ever, the wake convection in a blade passage is more complex. Due to the nonuniform velocity/pressure field inside the blade passage, the wake segment is distorted [2,3]. Hodson [4] and Ko- rakianitis [5] showed that simple kinematics could be used to explain the wake convection through downstream blade rows. Since much of the boundary layer flow is laminar, one of the most important consequences of this unsteadiness is the interaction of the turbulent wakes with the suction side boundary layer of a downstream airfoil.

The interaction between the unsteady wakes and the boundary layer, especially the separated boundary layer, on the suction sur- face has received much interest recently, such as Refs. [6–8]. This interaction is important because the blade suction surface bound- ary layer is responsible for most of the loss of efficiency and because the combined effects of random (wake turbulence) and periodic disturbances (wake velocity defect and pressure fields) cause the otherwise laminar boundary layer to undergo transition and eventually become turbulent. This will reduce or even prevent the boundary layer separation caused by the large adverse pressure graduate on the rear part of the airfoil's suction surface [9].

The literature on wake-boundary layer interaction, such as Refs. [10,11], was mainly conducted at low freestream turbulence inten- sities (FSTI). Under these flow conditions (Tu < 1.0%), the effect of the unsteady wake on the boundary layer development is pos- sibly more easily studied. There are few detailed studies on wake- boundary layer interaction at more realistic engine conditions, i.e., Tu > 3.0%. However, the unsteady boundary layer development at high FSTI may be different than that at low FSTI. Some of the observations and conclusions drawn from the measurement with low SFTI may be no longer valid at realistic engine conditions. Opoka and Hodson [12] are one of the few who have studied the unsteady boundary layer developments at both low and high FS- TIs. They concluded that the inlet freestream turbulence and the Reynolds number were both important and related factors in that they affected the unsteady transition process. The higher FSTI prevented the formation of the suction surface separation bubble on the highly loaded LP turbine airfoil under unsteady flow con- ditions.

Further increase in the airfoil loading will increase the severity of the adverse pressure gradient on the suction surface and the distortion of the wake in the blade passage. Therefore, at elevated FSTI, the suction boundary layer may still separate underneath the passing wakes. In the current paper, the effects of both Reynolds
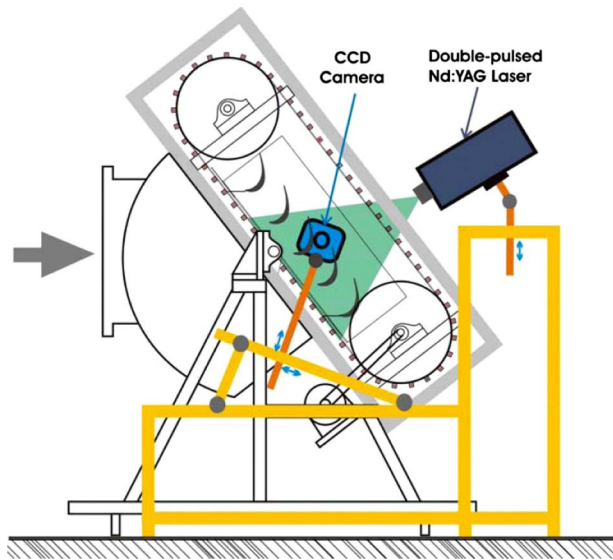
Fig. 1 Schematic of T106C moving-bar test rig with PIV measurement system

number and the FSTI on the unsteady boundary layer development on an ultra-high-lift LP turbine blade are investigated. The measurements were carried out at both Tu=0.5% and 4.0% within a range of Reynolds numbers between 100,000 and 260,000.

2 Experimental Facilities and Techniques

The reported work was conducted in a low-speed linear cascade with a moving-bar system at the Whittle Laboratory. A schematic of the T106C linear cascade test rig is shown in Fig. 1. The details of the bar-passing cascade facility are presented in Table 1. The cascade consists of five T106C profile blades with a chord of 198 mm, a span of 375 mm, and a pitch of 189.6 mm. The flow turning angle is about 93 deg and the Zweifel coefficient is 1.19. The Reynolds numbers based on the blade chord (C) and the isentropic exit velocity (V_{2is}) covered a range between 100,000 and 260,000.

To create more realistic LP turbine conditions, the FSTI can be increased by placing a biplanar, cylindrical rod, turbulence grid in the inlet to the test section. The turbulence grid, which was deigned based on Ref. [13] with 8.0 mm cylindrical rods, was placed at 520 mm upstream of the leading edge of the middle airfoil. The turbulence intensity (Tu) and integral length scale (Λ_x) measured at the cascade inlet plane were about 4.0% and 12.9 mm, respectively.

A glass window on the sidewall provides the access for optical measurements. The upstream unsteady wakes were generated by moving bars with a diameter of 2.05 mm. The axial distance between the bar moving plane and the blade leading edge is 70 mm. A flow coefficient ($\phi=V_{1x}/U_{bar}$) of 0.83 and a reduced frequency ($f_r=U_{bar}/s_{bar}C/V_{2is}$) of 0.57 were chosen. A detailed description of the T106C moving-bar linear cascade test rig can be found in Ref. [14].

The time-mean blade surface static pressure distributions were measured by using a Scanivalve system. The surface static pressure coefficient, C_p, is defined as the ratio of the local dynamic head to the isentropic exit dynamic head, i.e.,

$$C_p = \frac{P_{01} - P_s}{P_{01} - P_{s2}} = \left(\frac{V}{V_{2is}}\right)^2 \tag{1}$$

where P_{01} is the inlet total pressure, P_{s2} is the exit static pressure, and P_s is the measured surface static pressure. The velocities V and V_{2is} are the measured local isentropic surface velocity and isentropic exit velocity, respectively. Kulite SCX-062 fast response pressure transducers were used to measure the unsteady surface static pressure. Further details concerning the use of the Kulite sensors can be found in Ref. [15].

A constant temperature anemometry system was used for hot-wire measurements. The boundary layer was surveyed by a Dantec single-wire 55P15 boundary layer probe. The hot-wire was calibrated in accordance with a modified form of King's law. The effects of the ambient temperature drift were taken into account using the correction of Bearman [16]. Hot-wire traverses were performed normal to the blade surface. In order to account for the influence of the surface proximity on the cooling of the heated wire, the Cox correction [17] was applied to the measured data.

A Lavision two-dimensional particle image velocimetry (PIV) system was used for the PIV measurements. The schematic arrangement of a PIV measurement system with the moving-bar test rig is presented in Fig. 1. Two pulsed Nd:YAG (yttrium aluminum garnet) lasers were used to produce two successive pulses of light in order to illuminate the seeded flow field of interest in rapid succession. A double frame 12 bit digital camera with a 1280 ×1024 charge-coupled device (CCD) array was used to acquire the two successive images of the illuminated flow through a 105 mm lens. The maximum data rate of the current PIV system was 7 Hz so it was not possible to capture a sequence of images within one wake-passing period. An initial delay was applied to a trigger signal generated by the bar passing thereby allowing the PIV images to be acquired at selected phases relative to the bar-passing trigger. The flow was seeded by using a commercial vaporizing fog generator. The acquired image pairs (300 at each phase) were processed using LAVISION software. The initial interrogation window size was chosen as 32×32 pixel then 16×16 pixel final interrogation window size with 50% overlap was used. Therefore, a minimum spatial resolution of about 0.25 mm was achieved.

The profile loss coefficients (Y_P) of the linear cascade were determined from a series of Pitot tubes placed upstream of the bars and the pitchwise traverses of a Neptune probe that were conducted at $0.5C_x$ downstream of the blade trailing edge. The profile loss values given here include the measured loss and the calculated mixing loss. In the case of unsteady flow conditions, the change in stagnation pressure across the moving bars is subtracted from the total loss to give the profile losses [6].

3 Results and Discussions

The boundary layer development on the suction surface of the T106C airfoils under steady and unsteady flow conditions was investigated at Reynolds numbers covering a range between 100,000 and 260,000 with FSTIs of 0.5% and 4.0%. Figure 2 presents the measured total pressure loss coefficients at different flow conditions. At low FSTI (Tu=0.5%), under steady flow conditions, there are high total pressure losses at low Reynolds numbers due to the large separation bubble on the suction surface. At

Table 1   T106C bar-passing linear cascade details

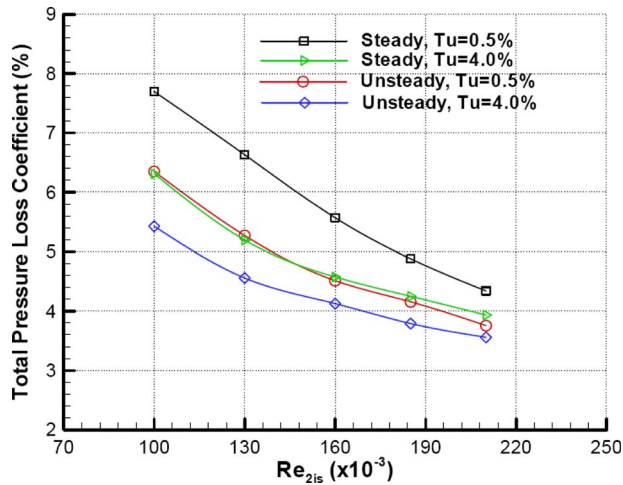|	
Chord, C (mm)	198.0
Axial chord, C_x (mm)	170.0
Pitch, s (mm)	189.6
Suction surface length, S_0 (mm)	264.7
Design inlet flow angle, α_1 (deg)	32.7
Design exit flow angle, α_2 (deg)	63.2
Incident angle, i (deg)	−5.0
Zweifel coefficient, Z_w	1.19
Bar diameter, d_{bar} (mm)	2.05
Axial distance: bars to LE, d (mm)	70.0
Flow coefficient ($\phi=V_{x1}/U_{bar}$)	0.83
Reduced frequency ($f_r=f_{bar}C/V_{2is}$)	0.57

Fig. 2   Total pressure loss coefficients

high Reynolds numbers, the separated boundary layer transition occurs earlier, which reduces the separation bubble size and results in smaller stagnation pressure losses.

The unsteady passing wakes periodically interact with the boundary layer and induce earlier transition, which reduces the total pressure losses. The elevated FSTI helps to reduce the blade profile losses under steady flow condition to a level similar to that under unsteady flow conditions with Tu=0.5%. Under unsteady flow conditions with Tu=4.0%, the total pressure losses are further reduced at all tested Reynolds numbers. The reduction at low Reynolds numbers is larger than that at high Reynolds numbers. The boundary layer development on the suction surface at Re_{2is} =130,000 and 210,000 with Tu=0.5% and 4.0% will be discussed next.

3.1   Baseline (Re_{2is}=130,000 and Tu=0.5%). As the baseline, the boundary layer development under the flow conditions of Re_{2is}=130,000 and Tu=0.5% will be discussed first. Figure 3 presents the surface pressure coefficient (C_p) distributions. Under steady flow condition, the boundary layer on the suction surface separates at $51\%S_0$, which is about $10\%S_0$ downstream of the suction peak, because of the large local diffusion that is required to produce the high loading on the ultra-high-lift airfoil. Due to the boundary layer transition in the separated shear layer, the flow reattaches at about $75\%S_0$, resulting in a separation bubble of a
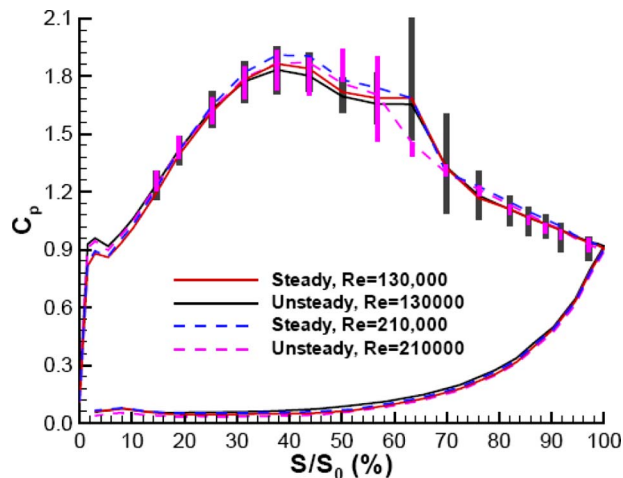

Fig. 3   Time-mean surface pressure coefficient distributions and unsteady pressure variations at Tu=0.5%

length of about 24% of the suction surface length.

Under unsteady flow condition, the incidence of the incoming flow was changed slightly due to the passing bars turning the inlet flow. However, there is no significant difference in the time-mean C_p downstream of $20\%S_0$ except around the separation region. The incoming wakes interact with the separation bubble and periodically change the separation bubble size, which can be identified from the difference between the time-mean C_p with and without the unsteady wakes in the separation region. Due to the large separation bubble existing at this low Re, the incoming wakes do not have a noticeable effect on the distribution of the time-mean C_p.

The unsteady pressure variations (normalized by the exit dynamic head) are also plotted in Fig. 3. There are large pressure fluctuations in the time-mean separation region, i.e., between $50\%S_0$ and $70\%S_0$. The maximum fluctuation occurs at about $12\%S_0$ downstream of the separation onset location and its magnitude is about 60% of the exit dynamic head. The fluctuation downstream the time-mean reattachment point (around $69\%S_0$) is still clearly visible. These fluctuations are caused by the rollup vortex generated by the interaction between the wake's negative jet and the inflectional shear layer through a forced Kelvin–Helmholtz mechanism [15].

Figure 4 presents the traces of the ensemble-averaged unsteady surface static pressure at different streamwise locations. The unsteady pressure was normalized such that the traces vary between 0 and 1 to show the variation more clearly. Lines L, C, and T indicate the leading, center, and trailing edges of the wake, respectively, which are defined based on the freestream velocity as shown in Fig. 7. The variation upstream of the time-mean separation point shows the effects of the wake's negative jet on the attached boundary layer. There is a low pressure associated with the front part of the wake and a high pressure underneath the wake center. As shown in Fig. 4(a), the rollup vortex (the wiggles appearing in the signals) first occur at $63\%S_0$. The vortex then convects downstream along the blade surface at about 70% of the local freestream velocity [14]. The signature of the rollup vortex does not appear immediately downstream of the separation onset location, which suggests that the vortex can form only when the separation bubble reaches a certain height or length. The signature of the vortices in the pressure traces becomes smaller after the reattachment point. However, it is still clearly visible close to the blade trailing edge.

The unsteady boundary layer on the suction surface was traversed with a hot-wire at different streamwise locations. The ensemble-averaged velocities, normalized by the exit freestream velocity, at selected phase (t^*) during one wake-passing period are presented in Fig. 5 as contoured s-y diagrams. The abscissa shows the normalized suction surface length (S/S_0) while the ordinate is the normal distance (Y_n) above the airfoil suction surface. The abscissa has been exaggerated by a factor of about 5.

At $t^*=1.00$, the leading edge of the wake moves to $58\%S_0$, i.e., approximately to the middle of the laminar part of the separation bubble. The unsteady surface pressure presented in Fig. 4 shows that the rollup vortex has been formed at this instant. Due to its small size, the existence of the rollup vortex only is shown by the raw velocity traces, which are presented in Fig. 7 and will be discussed later. At $t^*=1.05$, the wake's negative jet has induced a rollup vortex. This is visible in the ensemble-averaged velocity data. The rollup vortex reduces the size of the "dead air" region and forces the boundary layer away from the blade surface.

Since the rollup vortex convects downstream at about 70% of the freestream velocity, it lags behind the wake's leading edge as it moves downstream, as shown at $t^*=1.10$. At this phase, the front part of the separation is covered by the positive or higher unsteady pressure within the wake. The slope of the free shear layer of the laminar part of the separation bubble is reduced. The rollup vortex is located in the recovery region of the separation bubble. At $t^*=1.20$, the rollup vortex moves downstream of the
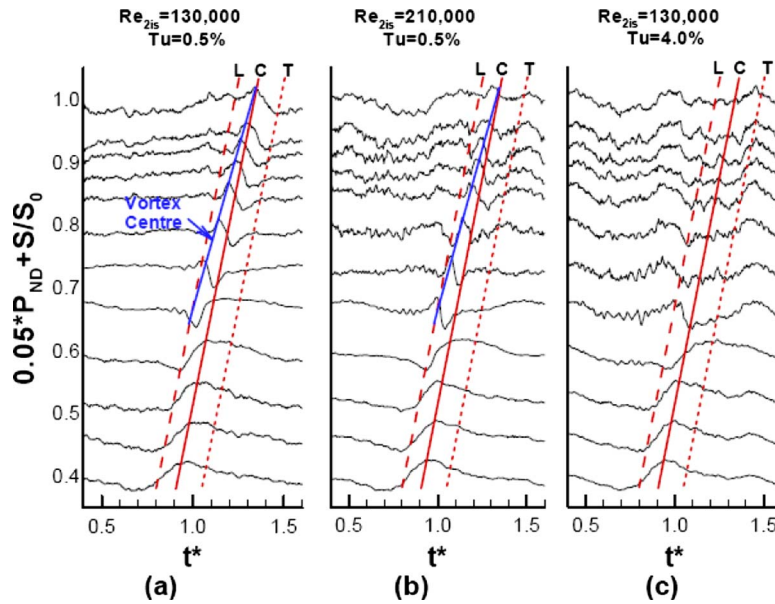
Journal of Turbomachinery

Fig. 4 Normalized unsteady surface static pressures on the suction surface

boundary layer separation region, which can be detected from the increased boundary layer thickness around $76\%S_0$. At this phase, the decelerating rear part of the wake covers the separation region. The severity of the local adverse pressure gradient is reduced. The slope of the free shear layer of the laminar part of the separation bubble is further reduced. The height of the separation bubble decreases but its length seems to be unchanged. As the wake moves further downstream such as at $t^*=1.30$, the turbulence in the wake's tail induces transition in the separated shear layer, which forces the separated boundary layer to reattach earlier. The separation bubble size continues to decrease due to the effects of

the wake-induced transitional region and the calmed region after it ($t^*=1.40$). On this ultra-high-lift blade, the separation on the suction surface is never completely suppressed by the unsteady passing wakes.

Two-dimensional (2D) PIV measurements on the blade suction surface have been conducted to further investigate the rollup vortex. The measurements were taken using four sets of overlapping images to cover the rear part of the suction surface. Figure 6 presents the normalized ensemble-averaged velocity contours in the region of interest at selected phases (t^*) during one wake-
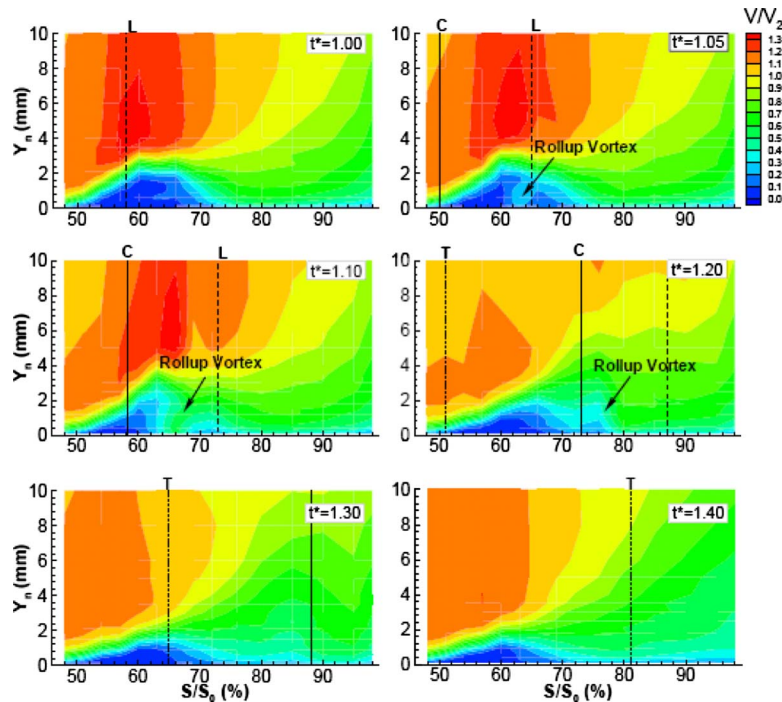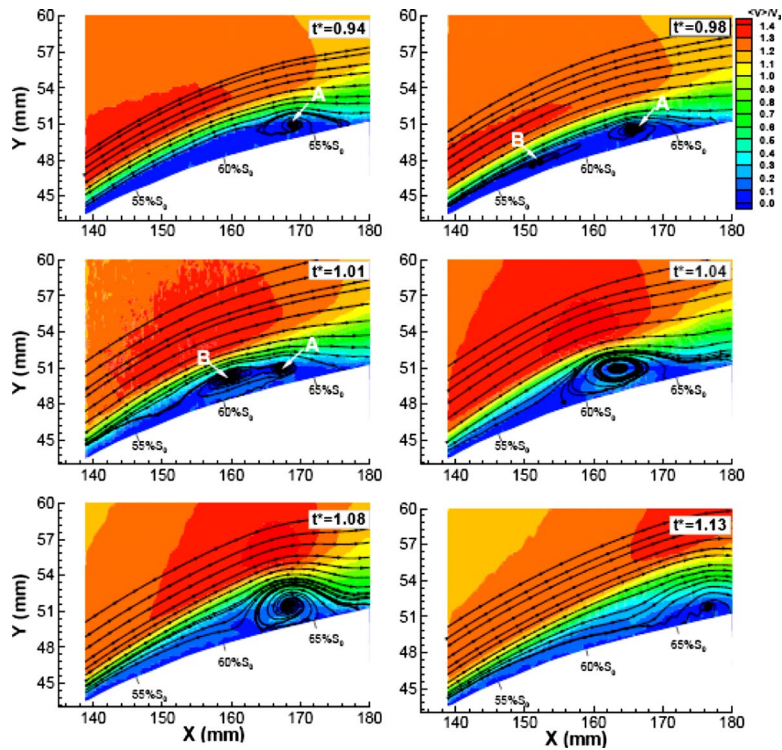

Fig. 5 Unsteady normalized velocity at selected instants on the suction surface at $Re_{2is}=130,000$ and $Tu=0.5\%$

Fig. 6 Unsteady normalized velocity at selected instants on the suction surface at $Re_{2is}=130{,}000$ and $Tu=0.5\%$ from PIV measurements

passing period. The abscissa and ordinate show the PIV measurement domain in real scale (i.e., in millimeters). The abscissa has been exaggerated by a factor of about 2. The normalized suction surface length S/S_0 is also indicated in the figures. The streamlines calculated from the measured 2D velocity vectors are shown in the figures as well.

At $t^*=0.94$, the front part of the wake just arrives into the measurement domain, which can be detected from the acceleration in the freestream. In the reversed flow region of the separation bubble, there is one vortex, labeled as A, with its center located at the maximum boundary layer displacement location (around $64\%S_0$). This vortex is associated with the reattachment of the separated boundary layer. At $t^*=0.98$, the wake's negative jet interacts with the inflectional or separated shear layer and one rollup vortex, labeled as B, is generated. At this instant, the center of the rollup vortex B is located at $58\%S_0$ and midway between the blade surface and the boundary layer edge. Once formed, the vortex convects downstream at about 70% of the local freestream velocity, as shown in Fig. 4. While traveling downstream, the rollup vortex becomes larger in size and locally increases the boundary layer thickness, as shown at $t^*=1.01$. At $t^*=1.04$, the rollup vortex merges with the existing vortex A in the separation reverse flow region and gets even stronger. The maximum peak-to-peak variation in the unsteady surface pressure shown in Fig. 3 occurs at this instant and at this streamwise location. As the rollup vortex convects further downstream, it forces the separated shear layer to move away from the surface and downstream as well, such as is shown at $t^*=1.08$. However, when the rollup vortex moves to the reattachment point, as shown at $t^*=1.13$, it is partially dissipated but it is still visible. The unsteady surface pressures indicate that the rollup vortex exists and convects as far as the blade trailing edge. After the rollup vortex moves out of the separation zone, the separation bubble size is reduced due to the separated boundary layer transition caused by the wake's turbulence.

The normalized rms of the unsteady velocity as well as the raw traces of the velocity measured from how-wire boundary layer traverses at selected streamwise locations are presented in Fig. 7. The rms was normalized by the local time-averaged freestream velocity and is shown as contoured t-y diagrams. The abscissa shows the normalized time (phase) relative to the wake-passing period while the ordinate is the normal distance (Y_n) above the airfoil suction surface. The raw velocity traces are taken from the hot-wire measurements at 0.2 mm above the surface. The ensemble-averaged freestream velocity traces are also shown in the figures to indicate the location of the wake's accelerating leading (L), center (C), and decelerating trailing edges (T). The ensemble-averaged unsteady surface static pressure variations are also plotted in the figures.

At $51\%S_0$, which is just downstream of the time-mean separation onset location, the smooth periodically varying raw velocity trace indicates the separated boundary layer is laminar. The velocity variation in the freestream agrees with the unsteady surface pressure, where the high pressure occurs at the wake's center. As shown in Fig. 7(a), in the freestream (away from the boundary layer edge, such as at $Y_n>8$ mm) the highest turbulence in the wake occurs at the center of the wake, i.e., along line C. However, just above the boundary layer edge, such as at $Y_n<6$ mm, the high turbulence lags behind the wake center and occurs after line T. The fact that the wake's high turbulence occurs behind the wake center close to the edge of the boundary layer can be explained by the distortion of the wake in the blade passage (discussed in detail later with reference to Fig. 8). Therefore, as the wake convects to the separation region on the suction surface of the airfoil, there is no high turbulence associated with the wake center. Thus, the wake's negative jet interacts with the inflectional boundary layer and is able to create the rollup vortices. The different times of arrival of the wake's high turbulence and the negative jet (velocity perturbation) over the separation region provide the necessary condition that allows the wake's negative jet inducing rollup vortex before the wake's turbulence can induce sepa-
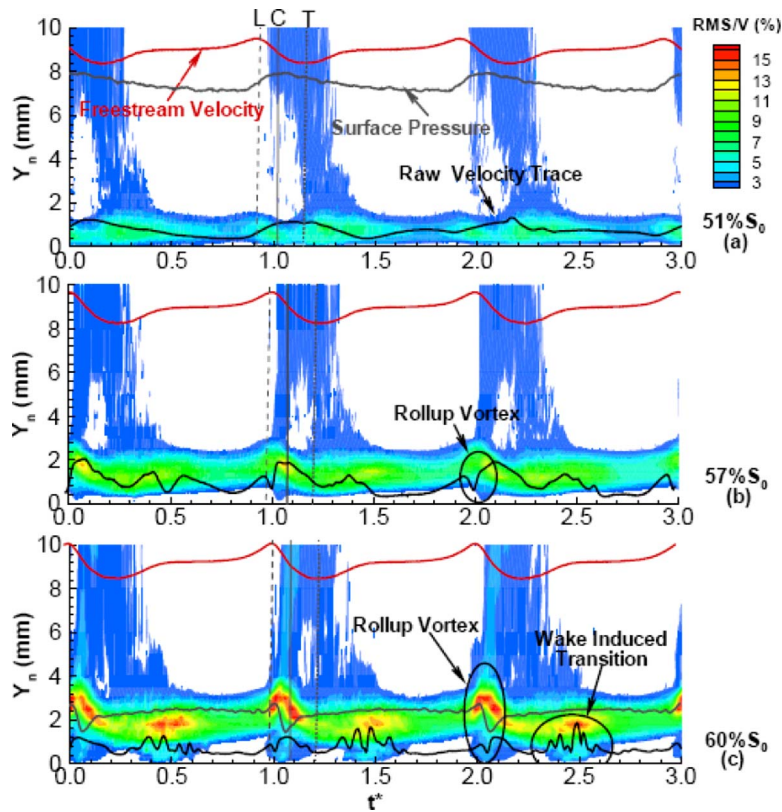
Fig. 7 Unsteady normalized rms of velocity at selected streamwise locations on the suction surface at $Re_{2is}=130{,}000$ and $Tu=0.5\%$

rated boundary layer transition.

Stieger and Hodson [18] conducted detailed flow field measurements in the blade passage of T106A linear cascade by using 2D laser doppler anemometry (LDA). Figure 8 shows the measured turbulent kinetic energy (solid contour) and velocity perturbation vectors at a certain phase. The wake segment is bowed, broad-
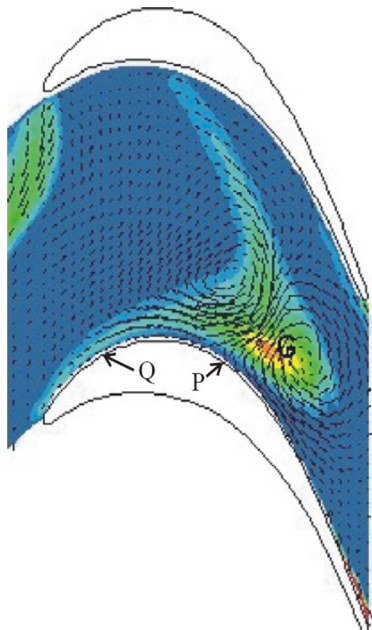
Fig. 8 Ensemble-averaged turbulent kinetic energy (TKE) and velocity perturbation vectors in the blade passage of T106 [18]

ened, and sheared by the nonuniform pressure/velocity field as it convects through the blade passage. In the blade passage, the highest turbulence occurs around the wake's center. Close to the blade suction surface, the wake has an accelerating leading edge and a decelerating trailing edge. At this instant, the velocity perturbation vectors show that the wake center is at point P. However, the high turbulence in the wake center does not impinge on the blade suction surface due to the distortion of the wake segment. Only the wake's lengthened tail impinges on the blade suction surface at point Q and the turbulence level is relatively lower in the tail. This is the same as what is shown in Fig. 7(a).

As shown in Fig. 7(b), at $57\%S_0$, just above the boundary layer, such as $Y_n > 3.0$ mm, there are two high-turbulence regions. The one lagging behind the wake center is caused by the tail of the wake, which is the same as that shown in Fig. 7(a). The other one, occurring between L and C, is caused by the rollup vortex. The existence of rollup vortex is also indicated by the wiggles in the raw velocity trace at this streamwise location. The raw velocity traces suggest that the wake turbulence still could not induce separated boundary layer transition due to the low Re_θ at this streamwise location [9].

At $60\%S_0$, as shown in Fig. 7(c), the existence of the rollup vortex is clearly shown in the rms contour plot, the velocity trace, and the surface static pressure trace. Except for the wiggles caused by the rollup vortices, there are spikes occurring after the wake's trailing edge in the raw velocity traces. They are caused by the wake turbulence-induced separated boundary layer transition [14], which lags behind the wake's centerline by about 40% of the wake-passing period.

The effects of the unsteady wake on the boundary layer development can also be seen from the s-t diagram of the momentum thickness θ in Fig. 9. The abscissa shows the normalized suction surface length (S/S_0) and the ordinate shows the time normalized by the wake-passing period (t^*). In addition to the lines L, C, and
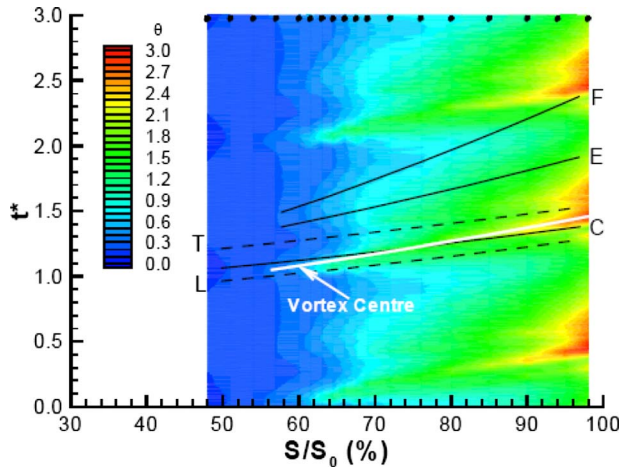
Fig. 9 *s-t* diagram of ensemble-averaged unsteady boundary layer (BL) momentum thickness θ on the suction surface at $Re_{2is}=130,000$ and $Tu=0.5\%$

Fig. 10 Normalized rms of velocity at selected streamwise locations on the suction surface at $Re_{2is}=210,000$ and $Tu=0.5\%$

T, there are line *E* corresponding to the trailing edge of the wake-induced transitional or turbulent region and line *F* corresponding to the trailing edge of the calmed region. They travel at 50% and 30% of the freestream velocity, respectively.

As shown in the figure, two ridges in θ develop along two different paths to form two wedges. One develops underneath the wake between lines *L* and *T* along the white line convecting downstream at about 70% of the freestream velocity. This ridge is caused by the strong rollup vortex due to the large separation at the low Reynolds number and results in the highest loss during one wake-passing period. The other ridge in θ occurs in the wake turbulence-induced turbulent region between lines *T* and *E*, which generates the second highest loss due to the late wake turbulence-induced *separated* flow transition. Although the calmed region only lasts for a short distance on this blade, the beneficial effect is still visible. There is a lower momentum thickness between lines *E* and *F*.

3.2 Effects of Reynolds Number ($Tu=0.5\%$). The boundary layer development on the suction surface at the higher Reynolds numbers was also studied under steady and unsteady flow conditions. The surface static pressure distributions, C_p, with $Re_{2is}=210,000$ and $Tu=0.5\%$ are presented in Fig. 3 as well. Under steady flow condition, the suction peak at the higher Re is higher than that at the lower Re, which increases the blade loading slightly. The boundary layer on the suction surface separates at slightly downstream of the location at lower Re. Due to the earlier boundary layer transition at the higher Re, the separation bubble is smaller. This is indicated by the shorter pressure plateau.

The large difference between the steady and unsteady distributions of time-mean C_p in the separation region shows that the unsteady passing wakes help to reduce the size of the separation bubble significantly. In comparison to the results at $Re_{2is}=130,000$, the magnitudes of the unsteady surface pressure fluctuations at $Re_{2is}=210,000$ are smaller and the extension of the large pressure variation region in the streamwise direction is shorter. However, the maximum peak-to-peak variation is still about 40% of the isentropic exit dynamic head. The normalized ensemble-averaged surface static pressure traces presented in Fig. 4(*b*) indicate the existence of a rollup vortex at this flow condition. Due to the smaller size of the separation bubble, the rollup vortex is smaller and weaker at this higher Reynolds number. However, the effects of the rollup vortex can be still detected close to the blade trailing edge.

Figure 10 presents the normalized rms of the unsteady velocity as well as the surface pressure and the raw velocity traces mea-
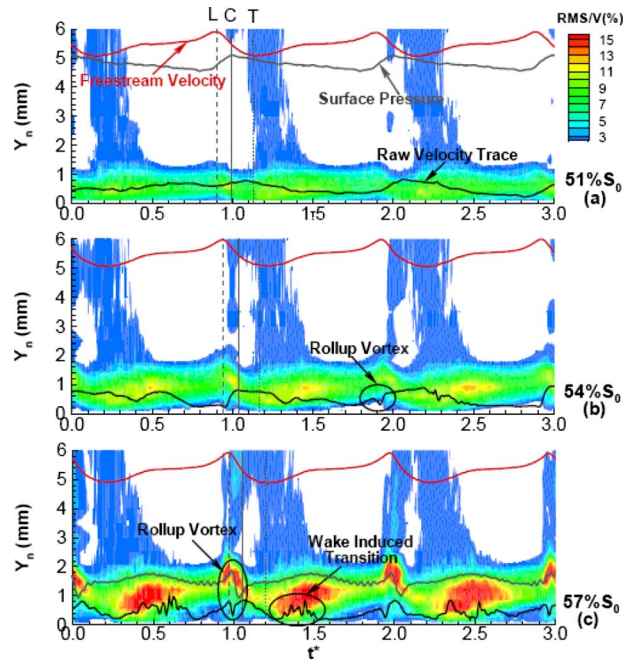
sured from how-wire boundary layer traverses at $Y_n=0.2$ mm at selected streamwise locations. Although at this higher Reynolds number, the onset of the wake's turbulence-induced transition moves upstream at $57\%S_0$, it still happens approximately $6\%S_0$ downstream of the separation point. Therefore, the negative jet of the wake can generate the rollup vortex. This is indicated by the oscillation between *L* and *C* in the raw signals at $54\%S_0$ and $57\%S_0$. The wake turbulence-induced transition still lags behind the wake center. Comparing Figs. 7 and 10 indicates that the distortion of the wake segment in the blade passage as well as the interaction between the wake and the separated boundary layer are similar at both high and low Reynolds numbers. The only difference is the strength and extent of the interaction due to the separation bubble size at different Reynolds numbers.

Figure 11 presents the *s-t* diagram of the unsteady boundary layer momentum thickness, θ. It clearly shows that the unsteady
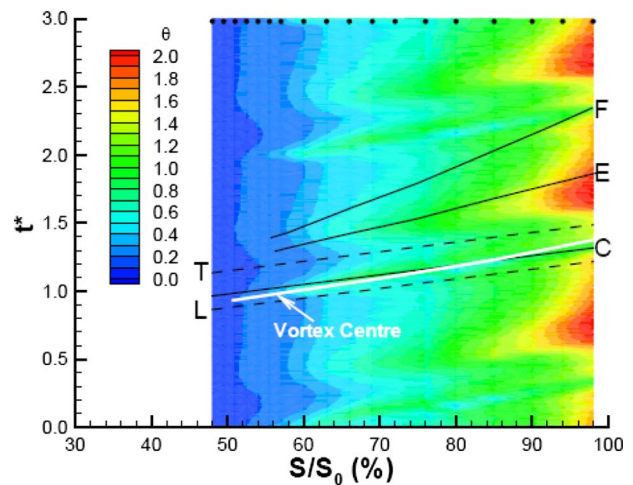

Fig. 11 *s-t* diagram of ensemble-averaged unsteady B.L. momentum thickness θ on the suction surface at $Re_{2is}=210,000$ and $Tu=0.5\%$
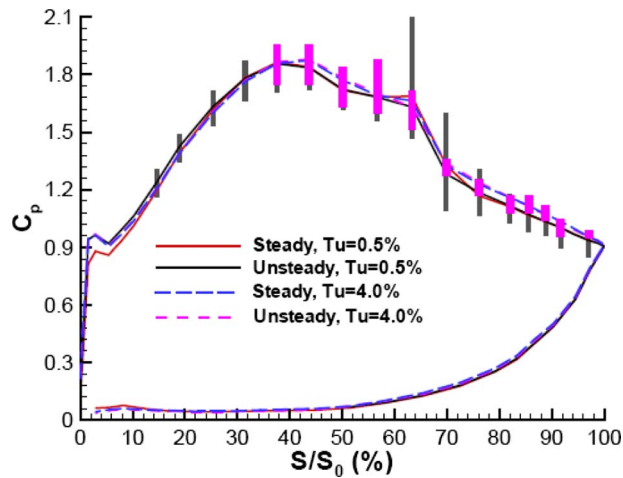
Fig. 12 Time-mean surface pressure coefficient distributions and unsteady pressure scatters at $Re_{2is}=130,000$

Fig. 13 Unsteady normalized rms of velocity at selected streamwise locations on the suction surface at $Re_{2is}=130,000$ and Tu=4.0%

boundary layer is dominated by the wake's turbulence-induced turbulent region between T and E. Even at the higher Reynolds number, the boundary layer is still separated before the turbulence in the wake's tail can induce transition. The rollup vortex is associated with a high momentum thickness once it forms and it extends toward the blade trailing edge along the trajectory line of 70% of the freestream velocity. Due to the smaller size of the rollup vortex at this high Reynolds number, the effect of the rollup vortex on the boundary layer, i.e., on the momentum thickness here, is weaker.

3.3 Effects of Inlet Turbulence Intensity ($Re_{2is}=130,000$). The boundary layer development was studied at more realistic engine conditions, i.e., at Tu=4.0%. The time-mean C_p distribution at $Re_{2is}=130,000$ in Fig. 12 shows that at the elevated FSTI the separation bubbles on the airfoil suction surface under both steady and unsteady flow conditions are smaller than those at Tu=0.5% due to the earlier separated boundary layer transition. The unsteady surface pressure fluctuations in the time-mean separation region as well as in the reattached region are much smaller than those at low FSTI. There is no clear evidence in the normalized ensemble-averaged unsteady pressure traces in Fig. 4(c) to show the existence of the rollup vortex. However, the raw pressure and velocity traces still indicate the occasional existence of the negative jet induced rollup vortex under this flow condition although it is much weaker and breaks down upstream of the blade trailing edge. A rollup vortex was also captured in some raw images of the PIV measurement but this does not show in the ensemble-averaged results.

The normalized rms of the unsteady velocity as well as the surface pressure and the raw velocity traces measured from how-wire boundary layer traverses at selected streamwise locations are presented in Fig. 13. Even with the elevated FSTI, the boundary layer still separates underneath the passing wake and the transition does not occur before $57\%S_0$, which is about $7\%S_0$ downstream of the separation point. Therefore, the wake's negative jet still can induce a rollup vortex. However, the raw velocity trace at $57\%S_0$ in Fig. 13(b) shows that the rollup vortex is not generated by every passing wake and it breaks up very quickly due to the earlier boundary layer transition. Sometimes, the bypass transition can even occur at upstream of the location where the rollup vortex can be generated. In this case, the wake's negative jet can no longer generate a rollup vortex. Another interesting phenomenon shown in Fig. 13(b) is that the transition of the separated boundary layer between the wakes occurs at almost the same streamwise location as that induced by the wake turbulence. Sometimes, the transition first occurs even more upstream and just before the
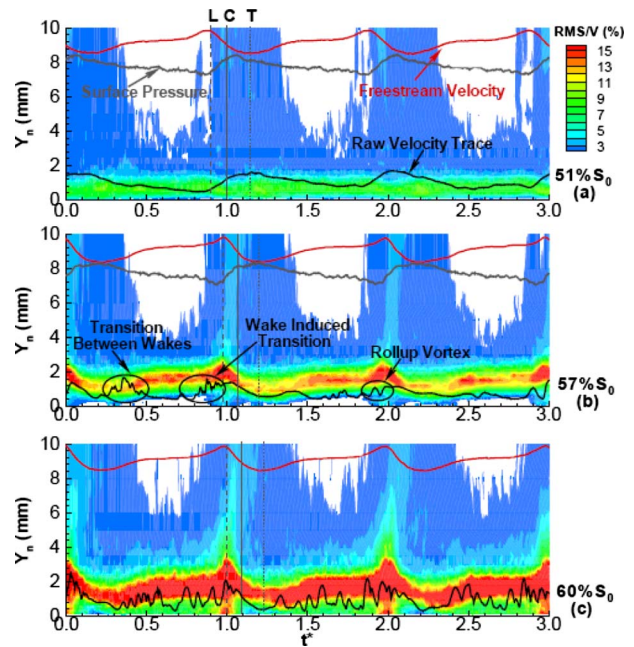
wake. The high turbulence in the wake does not seem to dominate the unsteady boundary layer transition. This is different to that under low FSTI condition.

The normalized rms contours in Fig. 13(a) shows that under the current high FSTI condition, the turbulence close to the edge of the boundary layer is almost uniform during one wake-passing period. The turbulence in the wake's tail shown under low FSTI conditions is no longer distinguished from the background turbulence between wakes. This is because the elevated background turbulence enhances the diffusion of the wake's high turbulence to the thinner boundary layer. Although the highest turbulence above the boundary layer occurs between L and C, the existence of rollup vortex, if it exists, may prevent the wake turbulence from inducing transition. Therefore, between the passing wakes, under the effect of the almost uniform turbulence, where the boundary layer transition will first occur depends on the status of the unsteady boundary layer.

The variation in the unsteady static pressure associated with the wake passing periodically changes the boundary layer development. The thickest laminar boundary layer occurs just before the wake's leading edge (L), where the effects from the previous passing wakes is least and the unsteady pressure is low as shown in Fig. 4. Therefore, the most receptive region, where the boundary layer transition would first occur, would be expected to occur before the line L. Actually this is the case, as shown in the raw velocity traces in Fig. 13(b). Due to the positive unsteady pressure in the wake, the boundary layer between L and T has a lower boundary layer thickness. Furthermore, in this region, the flow in the free shear layer accelerates in time. Therefore, the boundary layer in this region is more stable and the boundary layer transition may occur further downstream.

As shown in Fig. 14, the behavior of the unsteady momentum thickness associated with the passing wakes is different at the high and low FSTIs. At Tu=4.0%, there is no high momentum thickness resulting from the rollup vortex and from the wake turbulence-induced separated boundary layer transition. This is the main source of the loss reduction at high FSTI. Furthermore, there is no clear evidence to show the existence of the calmed region as well. As discussed above, at Tu=4.0%, the dominant
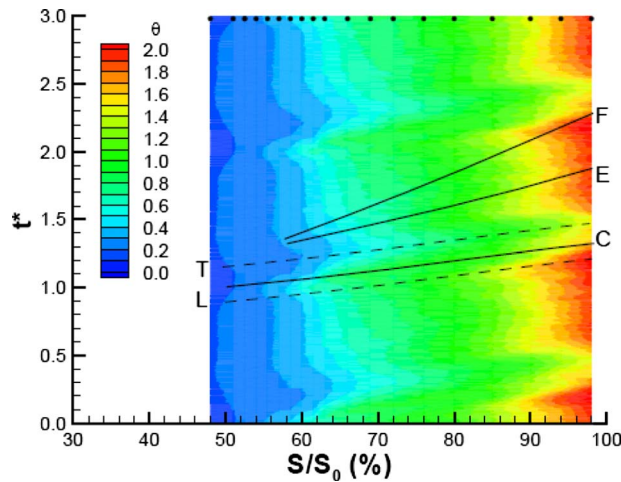
Fig. 14 *s-t* diagram of ensemble-averaged unsteady B.L. momentum thickness θ on the suction surface at $Re_{2is}=130,000$ and $Tu=4.0\%$

character is the effects of the wake's negative jet behavior on the boundary layer development underneath the passing wake. There is higher θ before the wake's leading edge, L, and low θ underneath the wake between L and T. These two events travel downstream with the freestream velocity.

The measurement results at $Re_{2is}=210,000$ with $Tu=4.0\%$ (not included in this paper) show that the unsteady boundary layer develops in a similar manner as that discussed above under the flow condition of $Re_{2is}=130,000$ and $Tu=4.0\%$ except that the boundary layer transition occurs further upstream. Consequently, the rollup vortex has even less chance of being generated due to the further reduced separation bubble size.

4 Conclusions

The transition of the unsteady boundary layer on the suction surface of the ultra-high-lift low pressure turbine blade can be initiated by both the wake turbulence and the kinematics of the wake convection. The predominance of one type of wake-induced transition or another depends on the local receptivity of the laminar boundary layer and the flow conditions at the edge of the boundary layer.

With low FSTI, i.e., $Tu=0.5\%$, at low Reynolds numbers (such as $Re_{2is}=130,000$), the interaction between the wake and the separated boundary layer is dominated by the wake's negative jet induced rollup vortex, which is caused by the nonsymmetry of the wake turbulence and the velocity/pressure perturbation due to the distortion of the wake in the blade passage. Since the wake turbulence-induced transition occurs downstream of the separation onset location, a high boundary layer loss is generated in the wake-induced turbulent region as well. At higher Reynolds numbers (such as $Re_{2is}=210,000$), the onset of the boundary layer transition moves upstream. This reduces the separation bubble size and, consequently, reduces the strength of the rollup vortex. Under this flow condition, the unsteady boundary layer development is dominated by the wake turbulence-induced transition.

With elevated FSTI, i.e., $Tu=4.0\%$, the separation bubble is largely reduced. The effect of the rollup vortex on the boundary layer gets much weaker. Sometimes, the rollup vortex may not even form. Furthermore, since the FSTI is elevated, at the edge of the boundary layer, the turbulence in the wake is no longer distinguishable from the background level. The unsteady boundary layer transition is dominated by the effects of the unsteady pressure/velocity perturbation associated with the wake in a bypass mode.

Nomenclature

C = blade chord
C_p = surface static pressure coefficient
C_x = blade axial chord
f_r = reduced frequency, $f_r=U_{bar}/s_{bar}C/V_{2is}$
$P_{01,2}$ = inlet and exit total pressures, respectively
P_{s2} = exit static pressure
P_{ND} = normalized unsteady pressure varying between 0 and 1
Re_{2is} = Reynolds number based on C and V_{2is}
rms = root mean square
S = distance along the suction surface
S_0 = suction surface length
s_{bar} = moving-bar pitch
t^* = time normalized by wake-passing period
Tu = turbulence intensity
U_{bar} = bar moving velocity
V_{1x} = axial inlet velocity
V_{2is} = isentropic exit velocity
Y_n = surface normal coordinate
Y_P = total pressure loss, $Y_P=(P_{01}-P_{02})/(P_{01}-P_{s2})$
Z_w = Zweifel lift coefficient
$\alpha_{1,2}$ = inlet and outlet flow angles, respectively
ϕ = flow coefficient, $\phi=V_{1x}/U_{bar}$
θ = boundary layer momentum thickness
Λ_x = integral length scale

References

[1] Meyer, R. X., 1958, "The Effect of Wakes on the Transient Pressure and Velocity Distributions in Turbomachines," Trans. ASME, **80**, pp. 1544–1552.
[2] Smith, L. H., Jr., 1966, "Wake Dispersion in Turbomachines," ASME J. Basic Eng., **88**, pp. 688–690.
[3] Hodson, H. P., 1985, "Measurements of Wake-Generated Unsteadiness in the Rotor Passages of Axial Flow Turbines," ASME J. Eng. Gas Turbines Power, **107**, pp. 467–476.
[4] Hodson, H. P., 1984, "Boundary Layer and Loss Measurements on the Rotor of an Axial Flow Turbine," ASME J. Eng. Gas Turbines Power, **106**, pp. 391–399.
[5] Korakianitis, T., 1993, "On the Propagation of Viscous Wakes and Potential Flow in Axial-Turbine Cascades," ASME J. Turbomach., **115**, pp. 118–127.
[6] Schulte, V., and Hodson, H. P., 1998, "Unsteady Wake-Induced Boundary Layer Transition in High Lift LP Turbines," ASME J. Turbomach., **120**, pp. 28–35.
[7] Funazaki, K., Sasaki, Y., and Tanuma, T., 1997, "Experimental Studies on Unsteady Aerodynamic Loss of a High-Pressure Turbine Cascade," ASME Paper No. 97-GT-52.
[8] Hodson, H. P., and Howell, R. J., 2005, "The Role of Transition in High-Lift Low Pressure Turbines for Aeroengines," Prog. Aerosp. Sci., **41**(6), pp. 419–454.
[9] Zhang, X. F., Vera, M., Hodson, H. P., and Harvey, N., 2006, "Separation Control on an Aft-Loaded Ultra-High-Lift LP Turbine Blade: Low-Speed Investigation," ASME J. Turbomach., **128**(3), pp. 517–527.
[10] Gostelow, J. P., and Thomas, R. L., 2003, "Response of a Laminar Separation Bubble to an Impinging Wake," ASME Paper No. GT2003-38972.
[11] Stieger, R. D., and Hodson, H. P., 2004, "The Transition Mechanism of Highly-Loaded LP Turbine Blades," ASME J. Turbomach., **126**(4), pp. 536–543.
[12] Opoka, M. M., and Hodson, H. P., 2005, "An Experimental Investigation of the Unsteady Transition Process on the High Lift T106A Turbine Blade," Proceedings of the 17th ISABE, Munich, Germany, Paper No. ISABE-2005-1277.
[13] Roach, P. E., 1987, "The Generation of Nearly Isotropic Turbulence by means of Grids," Int. J. Heat Fluid Flow, **8**(2), pp. 82–92.
[14] Zhang, X. F., and Hodson, H. P., 2005, "The Combined Effects of Surface Trips and Unsteady Wakes on the Boundary Layer Development of an Ultra-High-Lift LP Turbine Blade," ASME J. Turbomach., **127**(3), pp. 479–488.

[15] Stieger, R. D., Hollis, D., and Hodson, H. P., 2004, "Unsteady Surface Pressures Due to Wake Induced Transition in a Laminar Separation Bubble on a LP Turbine cascade," ASME J. Turbomach., **126**(4), pp. 544–550.

[16] Bearman, P. W., 1971, "Correction for the Effect of Ambient Temperature Drift on Hotwire Measurements in Incompressible Flow," DISA Inf., **11**, pp. 25–30.

[17] Cox, R. N., 1957, "Wall Neighborhood Measurements in Turbulent Boundary Layers Using Hot-Wire Anemometer," A.R.C., Report No. 19101.

[18] Stieger, R. D., and Hodson, H. P., 2005, "The Unsteady Development of a Turbulent Bar Wake Through a Downstream Low-Pressure Turbine Cascade," ASME J. Turbomach., **127**, pp. 388–394.

Letterbox Trailing Edge Heat Transfer: Effects of Blowing Rate, Reynolds Number, and External Turbulence on Heat Transfer and Film Cooling Effectiveness

N. J. Fiala

I. Jaswal

F. E. Ames

Department of Mechanical Engineering,
University of North Dakota,
Grand Forks, ND 58202

Heat transfer and film cooling distributions have been acquired for a vane trailing edge with letterbox partitions. Additionally, pressure drop data have been experimentally determined across a pin fin array and a trailing edge slot with letterbox partitions. The pressure drop across the array and letterbox trailing edge arrangement was measurably higher than for the gill slot geometry. Experimental data for the partitions and the inner suction surface region downstream from the slot have been acquired over a four-to-one range in vane exit condition Reynolds number (500,000, 1,000,000, and 2,000,000), with low (0.7%), grid (8.5%), and aerocombustor (13.5%) turbulence conditions. At these conditions, both heat transfer and adiabatic film cooling distributions have been documented over a range of blowing ratios (0.47 ≤ M ≤ 1.9). Heat transfer distributions on the inner suction surface downstream from the slot ejection were found to be dependent on both ejection flow rate and external conditions. Heat transfer on the partition side surfaces correlated with both exit Reynolds number and blowing ratio. Heat transfer on partition top surfaces largely correlated with exit Reynolds number but blowing ratio had a small effect at higher values. Generally, adiabatic film cooling levels on the inner suction surface are high but decrease near the trailing edge and provide some protection for the trailing edge. Adiabatic effectiveness levels on the partitions correlate with blowing ratio. On the partition sides adiabatic effectiveness is highest at low blowing ratios and decreases with increasing flow rate. On the partition tops adiabatic effectiveness increases with increasing blowing ratio but never exceeds the level on the sides. The present paper, together with a companion paper that documents letterbox trailing edge aerodynamics, is intended to provide engineers with the heat transfer and aerodynamic loss information needed to develop and compare competing trailing edge designs.
[DOI: 10.1115/1.3106703]

1 Introduction

The design of a trailing edge cooling scheme is typically a trade off between cooling effectiveness and aerodynamic losses. Aerodynamic loss and turbine flow considerations limit the maximum diameter of the trailing edge. Trailing edge durability issues limit the minimum wall thickness. These constraints often push trailing edge coolant discharge locations forward on the pressure surface. The resulting uncovered region of the trailing edge is challenging to cool. The objective of the present study has been to investigate heat transfer in a pressure surface discharge slot with partitions. The heat transfer rates and adiabatic effectiveness levels of this "letterbox" cooling configuration have been examined for three separate regions: the inner suction surface, the partition side, and the partition top. Experimental data have been acquired over a range of chord exit Reynolds numbers (500,000–2,000,000), turbulence levels (0.7%, 8.5%, and 13.5%), and local blowing ratios (0.47–1.9). In a companion paper [1], aerodynamic losses and surface pressure distributions have been documented for the same configuration across similar boundary conditions.

2 Background

The cooling analysis for a letterbox trailing edge configuration involves defining heat transfer coefficients and adiabatic wall temperatures for the surfaces exposed to both the coolant discharge and external gas flows. A letterbox configuration consists of partitions exposed to gas path temperatures and velocities on the top surface, and coolant discharge temperatures and velocities on the side surfaces. These same velocities and temperatures also drive heat transfer on the inner suction surface downstream from the discharge slot and between the partitions.

Ames et al. [2] investigated heat transfer and film cooling downstream from a gill slot (pressure side cutback). Their internal geometry was comprised of an eight-row converging pin fin array. In spite of using three external turbulence conditions they found that heat transfer on the inner suction surface, directly downstream from the gill slot ejection, correlated with the pin array heat transfer when the decay of turbulence downstream from the array was considered. They were able to correlate their converging array heat transfer with the short pin ($H/D=1$) staggered array correlation of Metzger and Haley [3] for streamwise and spanwise spacing of 2.5 diameters ($X/D=Z/D=2.5$).

$$\mathrm{Nu}_D = 0.069 \ \mathrm{Re}_D{}^{0.728} \qquad (1)$$

They applied the converging channel multiplying factor of Metzger et al. [4] to account for the influence of accelerating flow.

$$\phi = 2.28 \ \text{Re}_D^{-0.096} \qquad (2)$$

They developed a correlation for the influence of the decay of turbulence on heat transfer downstream from a staggered array based on the data of Nordquist [5]. They based their turbulence characteristics on the measurements of Ames and Dvorak [6] who found Lu/D was about 1.5 for their staggered pin fin array ($X/D = Z/D = 2.5$, $H/D = 2$, and $\text{Lu} = 1.5|u'|^3/\varepsilon$). Ames et al. [2] wrote their heat transfer decay estimate in terms of Nu/Nu_0.

$$\text{Nu}/\text{Nu}_0 = 1/\{1 + [X/(3D) - 0.08]^*\text{Tu}_0\}$$

$$\text{for} \ \ 0.5 \leq X/D \leq 4 \qquad (3)$$

Here, Tu_0, the turbulence just downstream from the last pin fin row, is taken as 0.30. Generally, after accounting for the unheated starting length issue in their data, inner suction surface heat transfer matched this correlation for about three to four slot heights before the heat transfer results began to become driven by the external Reynolds number.

Generally, Ames et al. [2] found high effectiveness levels (≈ 0.9) in the near slot region, but noticeably depressed values near the trailing edge suggesting an interaction with the shedding. However, at the lowest blowing ratio ($M = 0.33$), a substantial decay of effectiveness generally occurred after a few slot heights.

Martini et al. [7] investigated heat transfer and film cooling effectiveness downstream from their cutback trailing edge model for three internal cooling configurations. Two consisted of six staggered arrays of equilateral spaced pins with diameter to spacing ratios of 2, 2.5, and 3. One of these geometries had one row close to the discharge exit, and one had the row absent. A third geometry had an in-line rib row. They compared their heat transfer results to a turbulent correlation. Their heating typically started three slot heights upstream from the trailing edge discharge. They compared their heat transfer results to a correlation for a turbulent boundary layer starting at the exit. Generally, over the first few slot heights, their heat transfer levels were a monotonic function of exit blowing ratio ($0.2 \leq M \leq 1.25$). Downstream, heat transfer levels gathered toward the turbulent correlation. The pin fin array, which included a last row, had the highest heat transfer levels while the inline ribs produced the lowest. Laterally averaged film cooling effectiveness levels were also measured. In all cases, initial values were very high. However, effectiveness levels generally decayed rapidly for the pin fin array with the last row, while the in-line ribs produced the highest levels. At the lowest blowing ratios effectiveness levels decayed rapidly after a few slot heights. In a companion paper Martini et al. [8] performed a detached eddy simulation for the film cooling performance. They identified shedding from the blunt cutback lip as a clear mechanism that influenced the mixing process between the coolant and external flow, and ultimately affected the film cooling distribution. They suggested that steady Reynolds averaged Navier-Stokes (RANS) calculations failed to accurately predict film cooling levels because they could not model this unsteady interaction.

Martini and Schulz [9] investigated trailing edge cutback film cooling through circular wall jets. At the exit they typically found that two adjacent jets grouped together producing very good film coverage. However, in the region between jets that had grouped, coverage was relatively poor. They also observed that these jets could regroup into different patterns.

Cakan and Taslim [10] investigated heat transfer to an airfoil trailing edge slot separated with partitions they called lands in a trailing edge test section. They used naphthalene sublimation as a means to determine relative heat transfer levels. They investigated three geometries including a slot with no step, a slot with a step immediately downstream from discharge, and a slot placed in a downstream position. Generally, they found a 9–14% higher mass transfer on the slot sidewalls compared with the slot floor or inner suction surface.
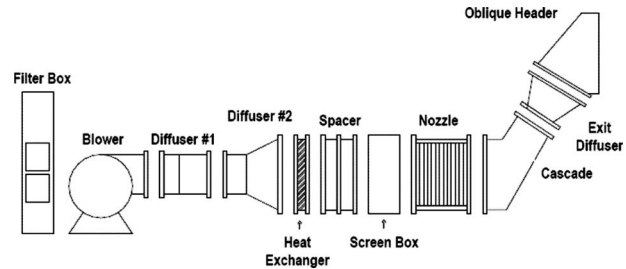
Fig. 1 Schematic of large-scale incompressible flow vane cascade wind tunnel

Chen et al. [11] investigated heat transfer on a pressure side cutback segmented by shaped pedestals in a trailing edge model using a transient liquid crystal technique. Upstream of their discharge they had four staggered rows of pin fins with spacing at two diameters ($X/D = Z/D = 2$). They generally found increasing adiabatic effectiveness levels with increasing blowing ratio ($0.7 \leq M \leq 2.0$).

Kim et al. [12] measured heat transfer and adiabatic effectiveness in a trailing edge model with a discharge slot separated by partitions. They measured heat transfer and adiabatic effectiveness in the slot bottom and partition sides and top. Inside the slot adiabatic effectiveness levels were found to be high. Partition top heat transfer levels for a blowing ratio of 0.5 were approximately double the value estimated by a turbulent correlation for the external flow, and adiabatic effectiveness levels were quite low. Effectiveness levels on the rib side for a blowing ratio of 0.5 were quite high.

Cunha et al. [13] conducted a general heat transfer analysis of airfoil trailing edge configurations. They developed a list of critical parameters such as size of cooling passage, internal cooling features, trailing edge thickness, pressure side lip thickness, roughness, and slot film coverage, which can be used to base a trailing edge design optimization.

Brundage et al. [14] conducted a study of trailing edge heat transfer and aerodynamic losses in a film cooling blow down facility. They fabricated shaped sidewalls to develop appropriate pressure distributions for the pressure and suction surfaces of their flat plate trailing edge model. They evaluated heat transfer in their trailing edge model in terms of an internal effectiveness parameter and a normalized wall temperature.

An extensive review of slot film cooling was previously reported by Hartnett [15].

The present study investigates a trailing edge geometry (letterbox) similar to other investigations. However, the present heat transfer and adiabatic effectiveness measurements have been conducted in a large scale cascade facility with complimentary aerodynamic loss measurements documented by Fiala et al. [1].

3 Experimental Approach

The objective of this heat transfer experiment has been to investigate heat transfer rates and adiabatic effectiveness levels for the inner suction surface and partition surfaces of a letterbox trailing edge configuration. The purpose of this study has been to provide designers with the detailed heat transfer boundary conditions necessary to develop durable cooling designs using a letterbox trailing edge geometry. The experimental setup integrated a converging pin fin array upstream of the letterbox discharge into 11-times scale turbine vane. This vane was tested in a four-vane linear cascade test section. In addition to heat transfer and adiabatic effectiveness levels, measurements have documented the pressure drop across the pin fin array and the letterbox partitions.

Low speed wind tunnel. The large-scale low speed cascade wind tunnel facility used in this research is shown schematically in Fig. 1. The facility is powered by a 45 kW blower that moves
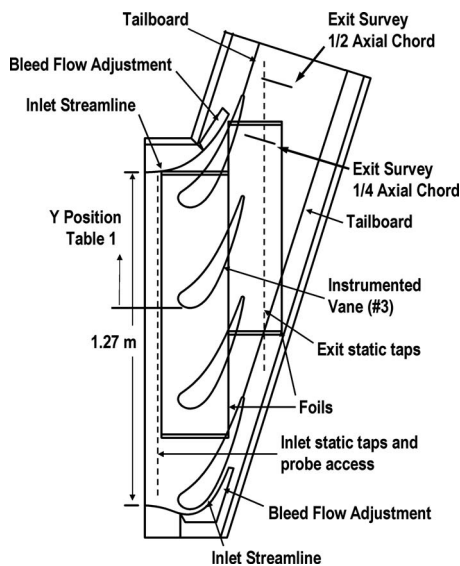
Table 1 Characteristics of inlet turbulence for low, grid, and aerocombustor conditions

	Reynolds	Tu	U (m/s)	Lx (cm)	Lu (cm)	ε (m^2/s^3)
Low turbulence (LT)	500,000	0.0069	4.96	8.12	127.0	0.00005
	1,000,000	0.0076	10.43	5.02	154.5	0.00035
	2,000,000	0.0060	18.71	3.58	15.5	0.0144
Aeroderivative combustor (AC)	500,000	0.1313	5.24	3.68	7.24	6.67
	1,000,000	0.1402	9.32	3.52	6.36	51.5
	2,000,000	0.1339	18.39	3.58	7.35	302.0
Grid	500,000	0.0821	4.77	2.00	3.27	2.70
	1,000,000	0.0861	10.19	2.04	3.35	29.8
	2,000,000	0.0884	19.27	2.35	3.53	206.8

6.6 m^3/s of air with a static pressure rise of 5000 Pa. Initially, the air is entrained into the blower through a large high efficiency filter. The air leaving the blower is directed through a two stage diffuser and into a heat exchanger, which keeps the test section air temperature constant. The air is ducted from the heat exchanger through a screen box used to dampen any velocity variations. The screen box is connected to a 3.6 to 1 area ratio nozzle used to accelerate the air into the cascade test section, further improving the inlet flow uniformity. The four-vane cascade test section turns the flow and directs the air through the exit traversing system into a multivane diffuser used to recover pressure and extend the Reynolds number range of the test section. An oblique header is attached to the diffuser to direct air away from lights in the ceiling.

Turbulence conditions. Three turbulence levels were generated for this experiment including a low (<1%), a grid (8.5%), and an aerocombustor (13.5%) turbulence condition. The setup for the low turbulence condition is shown in Fig. 1. The grid turbulence condition is generated by placing a square bar (1.27 cm), square mesh (6.35 cm) biplanar grid in a rectangular spool attached to the cascade, ten mesh lengths from the leading edge plane of the vane. The aerocombustor condition is generated by replacing the nozzle with a simulated aeroderivative combustor. The characteristics of the three turbulence conditions acquired using hot-wire anemometry are provided in Table 1.

Cascade test section. The four-vane, three-passage cascade test section is shown schematically in Fig. 2. The cascade uses an 11-times scale low Mach number vane designed to provide a fully loaded profile. The cascade produces a measured midspan turning angle ranging from 73.0 deg to 74.0 deg. The inlet bleed-flow adjustments and the row of inlet static pressures tap control and monitor inlet uniformity. The upper and lower tailboards together with the row of exit static pressure taps are used to establish exit periodicity. A comparison between the measured pressure and predicted distribution [16] for both incompressible and compressible flows is shown in Fig. 3. Experimental data are presented for both the current University Turbine System Research (UTSR) and a previous Advanced Gas Turbine System Research (AGTSR) study. This good agreement provides confidence in the experimental setup. The instrumented vane used to acquire heat transfer levels is located third from the bottom.

Heat transfer vane. A schematic of the letterbox heat transfer vane is shown in Fig. 4. The vane has a true chord of 47.8 cm, a leading edge diameter of 5.59 cm, and a trailing edge diameter of 0.98 cm. The vane is cast from epoxy with fine wire thermocouples set integrally around the surface in the positions shown in
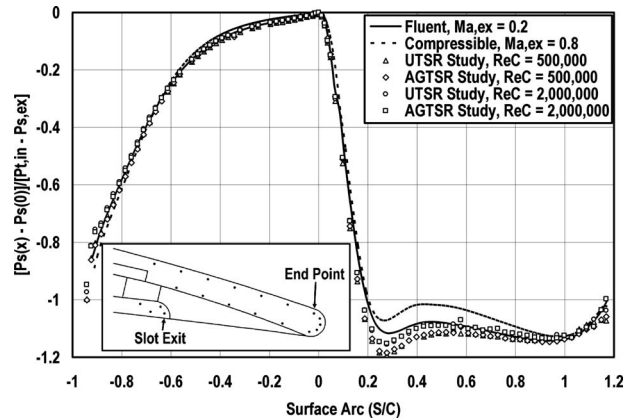
Fig. 3 Measured pressure distributions for 11-times scale vane compared with computational fluid dynamics (CFD) predictions for incompressible and compressible vanes

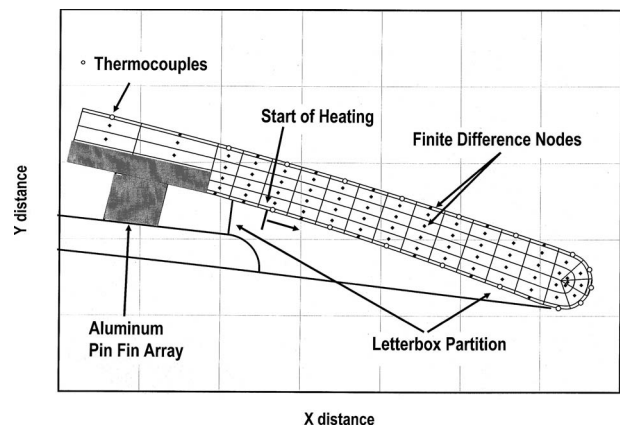**Fig. 2 Schematic of four-vane, 11-times scale cascade test section**
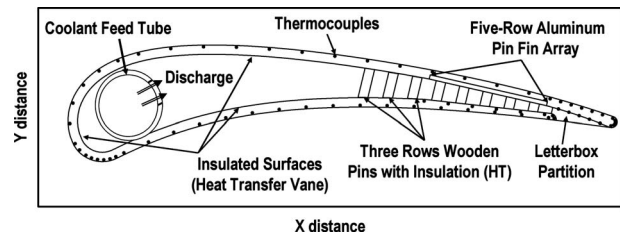
Fig. 4 Schematic of heat transfer vane cross-section showing coolant feed tube, location of thermocouples, pin fin arrays, and letterbox geometry
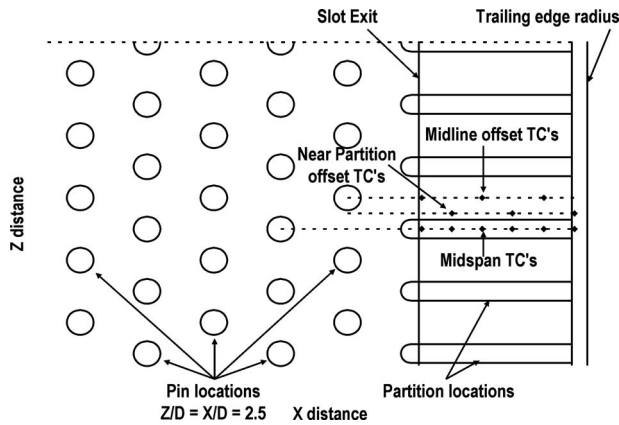
Fig. 5 Cross-sectional view of five-row aluminum pin fin array showing location of letterbox partitions and thermocouple (TC) instrumentation

Fig. 6 Schematic of conduction model in trailing edge region

Fig. 4. This letterbox vane was developed from the gill slot vane with the addition of the letterbox partitions. A complete description of the gill slot vane is provided in Ref. [2]. Cooling air conditioned with a heat exchanger and measured with an orifice tube is provided by a 2 kW high pressure blower. The cooling air enters the hollow epoxy vane through the coolant feed tube and is distributed across the tube by a spanwise flow contraction and out through ten discharge holes. The flow is directed into the letterbox discharge area through three rows of staggered wooden pins, and then into the staggered five-row converging pin fin array. The flow then discharges out of the pressure surface slot into the open regions between letterbox partitions. A cross-sectional view of the five-row aluminum pin fin array with the letterbox partitions and thermocouple locations is presented in Fig. 5. The leading edge of the letterbox partitions is located 1.5 pin diameters downstream from the trailing edge of the last row of pins. The inlet and exit heights of the five-row pin fin array are 1.872 cm and 0.653 cm, respectively. The internal cooling channel narrows to a minimum height of 0.559 cm at the leading edge of the letterbox partitions. The pressure side lip height is also 0.559 cm in thickness. The staggered array pin diameters are 0.838 cm, while the width of the letterbox partitions is 0.635 cm. The spanwise (Z) spacing of the pins and partitions is 2.5 pin diameters, and the partitions are staggered with respect to the positions of the last row of pins. Thermocouples located on the inner suction surface are midspan between the last row of pins, midspan between the partitions (midline offset), and between these two rows of thermocouples (near-partition offset). The inner suction surface heat transfer and adiabatic effectiveness levels reported in this paper are based on midline and near-partition offset thermocouples.

Conduction model. Heat transfer and adiabatic effectiveness levels on the inner suction surface and trailing edge were determined with the help of a finite difference conduction model. The trailing edge conduction model is presented schematically in Fig. 6. The schematic shows the placement of thermocouples and nodes, as well as the location of the aluminum pin fin array and letterbox partitions around the 2D finite difference model. The start of the constant heat flux boundary condition, generated using a 0.023 mm Inconel foil heater, begins just upstream from the first thermocouple on the inner suction surface. Fine wire type K thermocouples were placed across from each other on the external and internal sides of the suction surface to generate a wall boundary condition. A cubic spline was used to interpolate temperatures for intermediate surface nodes. Typically, a 1D conduction model produced results within 10% of the 2D model. However, the 2D model improved accuracy substantially in the trailing edge. Inner suction surface heat transfer measurements were corrected for heat conduction gain or loss from the external surface. Inner suc-

tion surface heat transfer data were also affected by the unheated starting length condition caused by the proximity of the start of heating to the initial fine wire thermocouple. Adiabatic effectiveness measurements were generated by heating the coolant flow entering the vane while recording the passive response of the trailing edge. Coolant outlet temperatures were based on measurements from two fine wire thermocouples, which monitored the slot exit gas temperature. Adiabatic effectiveness measurements were corrected for conduction based on the surface normal heat flux and the local heat transfer coefficient.

Letterbox partitions. The letterbox partition used to acquire average heat transfer and adiabatic effectiveness levels for the side surface is shown schematically in Fig. 7. The aluminum partition was heated using a resistor powered by a dc power supply. Voltage across and current through the resistor were monitored with the use of a calibrated shunt resistor and two additional lead wires to sense the resistor voltage. The aluminum partition was thermally insulated from the inner suction surface and exit slot lip using 1 mm thick balsa wood. The top of the partition was also insulated from convection with balsa wood. Finite difference conduction loss models were developed for the balsa wood strip on the partition bottom ($Q_{L,B}$), lip radius ($Q_{L,LP}$), and top surface ($Q_{L,TP}$) exposed to convection. Consequently, as shown in Eq. (4), the net heat flux for the side partition was the heat dissipated by the resistor (Q_D) less losses from the bottom, top, lip radius, and radiation. The heat transfer coefficient was consequently the net heat transfer divided by the convection surface area and the side partition (T_{SD}) to adiabatic wall ($T_{AW,SD}$) temperature difference.
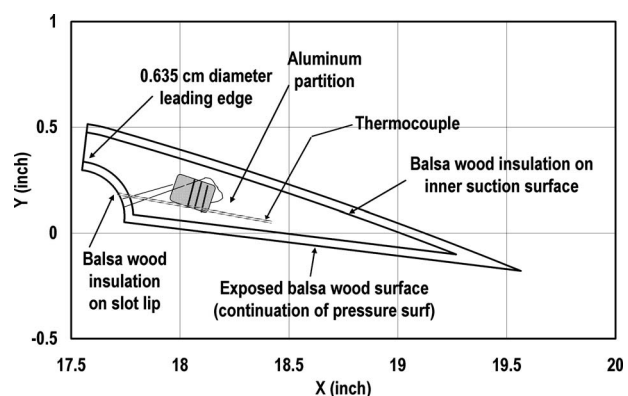
Fig. 7 Aluminum heat transfer partition used to acquire partition side heat transfer coefficients and adiabatic effectiveness
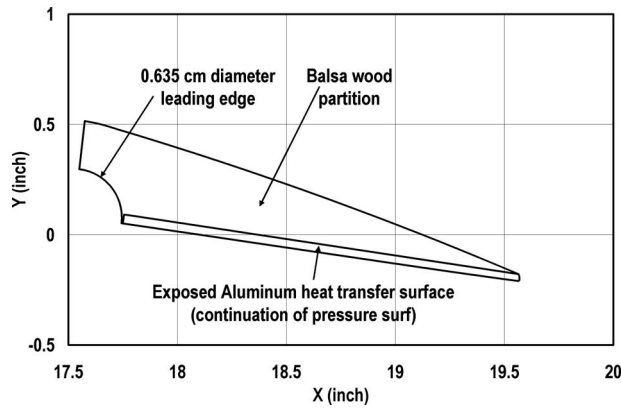
Fig. 8 Balsa wood partition with active aluminum heat transfer surface used to acquire partition top heat transfer coefficients and adiabatic effectiveness measurements

Fig. 9 Letterbox and gill slot vane surface pressure distributions compared with fluent prediction for base vane

$$h_{SD} = (Q_D - Q_{L,B} - Q_{L,LP} - Q_{L,TP} - Q_R)/(T_{SD} - T_{AW,SD})/A_{SD} \tag{4}$$

The adiabatic wall temperature was used rather than the coolant out (T_{CO}) temperature due to some small differences between the coolant out and gas (T_G) temperatures.

$$T_{AW,SD} = T_G + \eta_{SD}(T_{CO} - T_G) \tag{5}$$

A schematic of the partition used to measure the surface heat transfer and adiabatic effectiveness on top of the partition is shown in Fig. 8. This 0.8 mm thick aluminum heat transfer surface was heated using length of fine Chromel wire epoxied to its back side, while its temperature was sensed using a fine wire thermocouple epoxied into a shallow groove at the back of the thin plate. The heat transfer coefficient was based on the sum of the energy dissipated (Q_D) less the conduction out the bottom ($Q_{L,B}$), and the radiation from the surface (Q_R) divided by the plate to adiabatic wall temperature difference and the convective area (A_{TP}).

$$h_{TP} = (Q_D - Q_{L,B} - Q_R)/(T_{TP} - T_{AW,TP})/A_{TP} \tag{6}$$

Again, the adiabatic wall temperature was used rather than the coolant out temperature due to some small differences between the coolant out and gas temperatures.
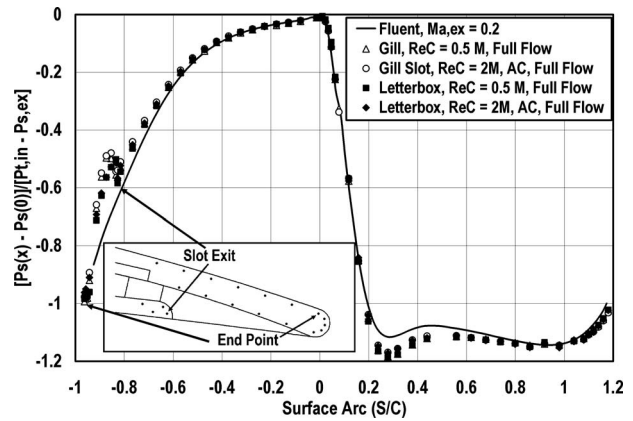
$$T_{AW,TP} = T_G + \eta_{TP}(T_{CO} - T_G) \tag{7}$$

In the analysis for adiabatic effectiveness of the side and top surfaces, the adiabatic wall temperature was determined to be the measured temperature adjusted for conduction losses. Since the heat transfer surface was passive for the adiabatic wall temperature measurement, the conduction rates were small but had significance. Generally, the adiabatic wall temperature was taken as the measured temperature plus the net losses divided by the product of the heat transfer coefficient and the convective area. The relationships used to estimate T_{AW} for the side and top surface areas are given by

$$T_{AW,SD} = T_{SD} + (Q_{L,B} + Q_{L,LP} + Q_{L,TP} + Q_R)/h_{SD}/A_{SD} \tag{8}$$

$$T_{AW,TP} = T_{TP} + (Q_{L,B} + Q_R)/h_{TP}/A_{TP} \tag{9}$$

Data acquisition system. The PC based data acquisition system used for heat transfer measurements on the letterbox vane relied on an HP3497A data acquisition unit to acquire pressure sensor, heater, and thermocouple voltages. The HP3497A features low noise relays and an integral multimeter with 1 μV sensitivity. The data acquisition unit interfaces to the computer through an IEEE interface. The system scans pressures using a custom made pressure scanner, which incorporates two Rosemount 3051 pressure

transmitters with full scale ranges of 250 Pa and 5000 Pa. The pressure transmitters are connected in parallel, and the most sensitive reading within scale is used to provide the pressure. Accuracy is reported by the manufacturer as 0.1% of full scale. Thermocouples are connected to the HP3497A scanner through a passive constant temperature junction, which is referenced to an ice bath. Heater voltages are sensed through connections close to the heater, and current is measured using calibrated constantan shunt resistors.

Experimental uncertainties. Error estimates were determined using the root sum square method described by Moffat [17]. Uncertainty in the side partition heat transfer coefficient was estimated at a maximum of 13% for the 500,000 Reynolds number and 7% for the 2,000,000 Reynolds number. Uncertainty in the top partition heat transfer rate ranged from a maximum of 6% for the 500,000 Reynolds number to 4% for the 2,000,000 Reynolds number. Uncertainty in the inner suction surface heat transfer rate ranged up to 10%. Estimates for the absolute or U.95 uncertainty in the adiabatic effectiveness for the inner suction surface and side and top partitions ranged to 0.05. Uncertainty values for the overall pressure drop were estimated at 5%.

4 Experimental Results

This present investigation focused on acquiring heat transfer and adiabatic effectiveness levels on the letterbox partitions, and on the inner suction surface between the partitions downstream from the slot exit. These data were studied over a range of Reynolds numbers (500,000, 1,000,000, and 2,000,000), across a range of turbulence conditions (low (0.7%), grid (8.5%), and aerocombustor (13%)), and over a range of flow rates. The letterbox slot coolant discharge flow rates were chosen to be consistent with an earlier study, which investigated gill slot heat transfer and aerodynamics. Full or design flow is nominally equal to mass flow rates of 0.0135 kg/s, 0.027 kg/s, and 0.054 kg/s at Reynolds numbers of 500,000, 1,000,000, and 2,000,000, respectively. These flow rates are nominally equal to the local slot exit blowing ratio of 0.94. This blowing ratio is larger than for the gill slot vane at the same flow due to the 30.3% blockage of the letterbox partitions. Also, these coolant flows amount to about 2.57% of passage flow.

Vane surface pressure distribution. Upstream of the pressure surface discharge, the vane surface pressure distribution is quite similar to the base vane pressure distribution. The measured surface static pressure distribution, referenced to the inlet total pressure and normalized on the inlet total to average exit static pressure, is plotted as a function of fraction of surface arc in Fig. 9. This figure compares letterbox distributions for full design flow at the 500,000 and 2,000,000 Reynolds numbers with the gill slot distributions. Additionally, the calculated base vane pressure dis-
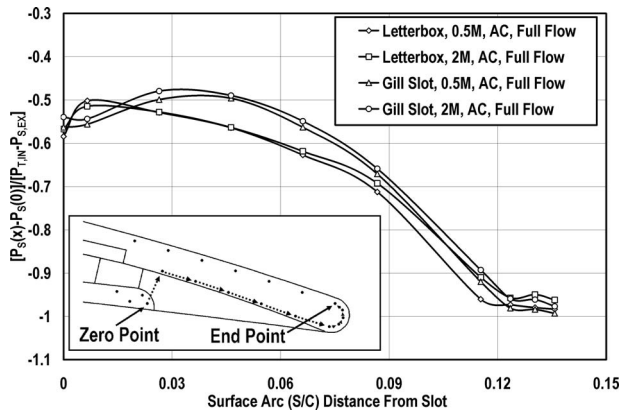
Fig. 10 Comparison between pressure distribution downstream from gill slot ejection with distribution downstream from letterbox ejection

Fig. 12 Comparison of normalized pressure drop across the pin fin array to the vane exit for the gill slot and letterbox vanes with V_{max} defined for the last row in the converging pin fin array

tribution is shown for reference. While the suction surface and most of the pressure surface distributions are very similar to the base vane, the pressure distribution changes substantially in the region of the letterbox discharge. Figure 10 presents pressure distributions in the slot discharge region comparing the letterbox vane and the gill slot vane at the full flow condition, normalizing pressure in the same manner as Fig. 9. However, in Fig. 10, fraction of surface arc is plotted from the last pressure tap on the pressure surface. The letterbox vane shows an immediate pressure rise between the last point on the pressure surface and the first point on the inner suction surface. Subsequently, flow along the inner suction surface accelerates rapidly toward the trailing edge. The gill slot pressure distribution differs from the letterbox vane showing an initial pressure on the inner suction surface consistent with the last pressure on the pressure surface. Subsequently, a mild pressure recovery is shown on the gill slot vane. As the flow approaches the trailing edge, pressure levels for the two vanes become similar.

Coolant flow rate has a substantial influence on the pressure distribution in the region of the letterbox discharge. Figure 11 shows the normalized pressure distributions for coolant flow rates of half, full, one and a half, and double design flow as a function of surface arc for a Reynolds number of 1,000,000. Similar to Fig. 10 fraction of surface arc is taken from the last point on the pressure surface. Increasing cooling discharge flow rate produces a substantially increased pressure just downstream from the slot exit. Subsequently, the flow shows a strong favorable pressure gradient to the trailing edge. At the trailing edge, pressure systematically decreases with increasing coolant discharge.
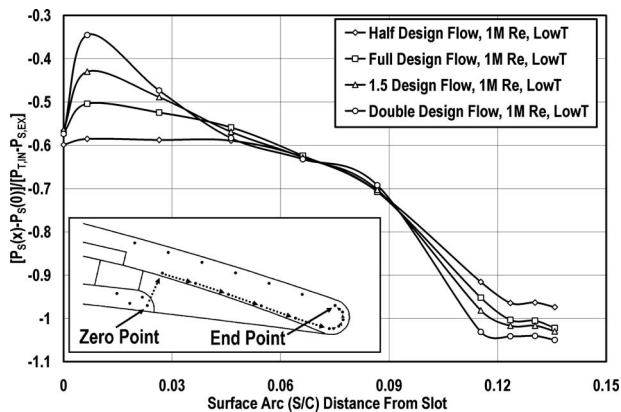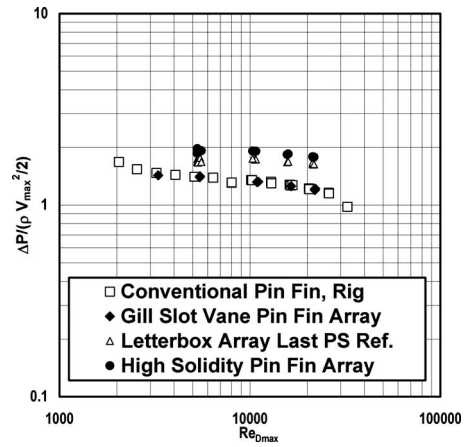

Fig. 11 Comparison of pressure distribution downstream from letterbox ejection for various flow rates, $Re_C = 1,000,000$

Trailing edge pressure drop. Assessing the pressure drop in the trailing edge region of a vane for a given coolant flow is critical to developing an efficient yet reliable heat transfer design. In the present letterbox vane flow enters the trailing edge through a converging pin fin array before exiting the pressure side trailing edge slot through letterbox partitions. However, assessing pressure drop through a given trailing edge configuration is complicated. Ames et al. [2] suggested that flow through a pin fin array had three regions, an entrance region, a streamwise periodic region, and an exit region. The pressure drop in the entrance region of a pin fin is primarily influenced by flow acceleration due to flow around pin fins, and the blockage due to wakes. The pressure drop in the streamwise periodic region that follows the entrance region is largely controlled by the extent of the separated region in the back side of the pin. Finally, the pressure drop in the exit region is characterized by a high loss due to the lack of a downstream row of pins, which helps to reduce the size of the separated region. This pressure loss is further complicated in the trailing edge region of a vane where the pin fin array converges. The letterbox trailing edge region has the additional pressure loss due to flow acceleration through the initial restriction at the start of the partition and then the flow expansion out the exit slot. As a result of the difficulty of assigning a pressure loss due to each feature in the trailing edge region, the overall pressure drop across the five-row converging pin fin array and the letterbox partitions was assessed collectively. Figure 12 presents the combined pressure loss across the pin fin array and exit slot comparing the letterbox pressure loss with the gill slot pressure loss. The loss is plotted as a function of converging pin array Reynolds number based on flow through the last pin row. The pressure loss based on the first pressure tap on the inner suction surface as shown in Figs. 10 and 11 is given by the round solid symbols. However, Fig. 11 shows that the pressure at this pressure tap location varies significantly with flow rate. Consequently, the last pressure tap on the pressure surface proves to be a much more stable region for the assessment of pressure drop and is presented in the open triangular symbols in Fig. 12. The incremental pressure loss for the letterbox with the pressure surface reference averages $0.39 \rho V_{max}^2 / 2$ above the gill slot loss and $0.57 \rho V_{max}^2 / 2$ above the gill slot loss based on the inner suction surface reference. Here, V_{max} is the average velocity through the last row of pins in the converging array.

Partition heat transfer. Heat transfer to the side and top of the partition was acquired using the partitions shown in Figs. 7 and 8. Heat transfer to the side partition is presented in terms of Nusselt number based on pin diameter versus diameter Reynolds number (Re_D) in log coordinates in Fig. 13. The diameter Reynolds number is based on the average velocity through the last row of pins.
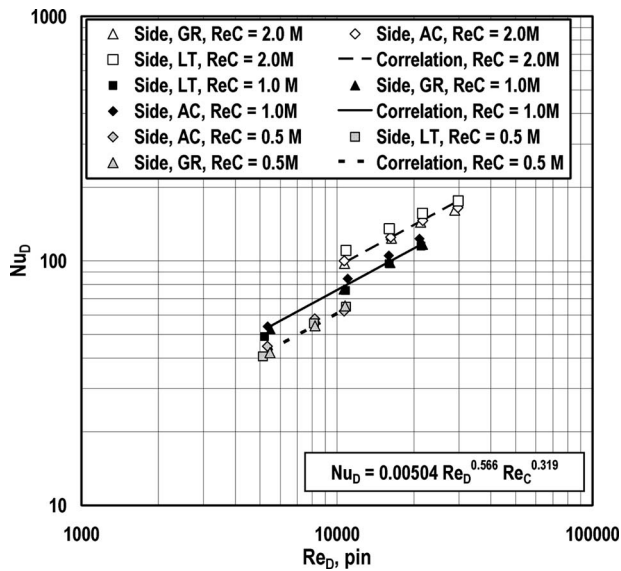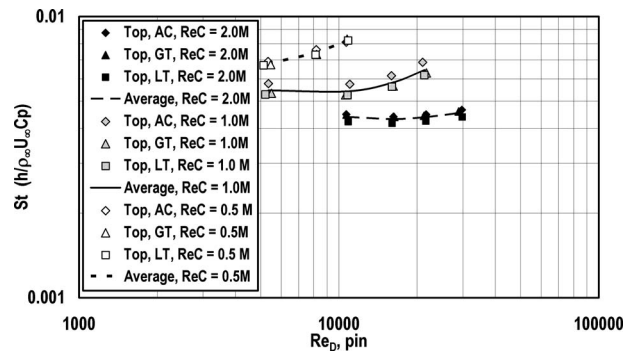
Fig. 13 Letterbox partition side heat transfer levels with Re$_{Dmax}$ based on the last row of pin fin array and Re$_C$ the exit chord Reynolds number

Fig. 14 Letterbox partition top Stanton number levels with Re$_{Dmax}$ based on the last row of pin fin array showing the effect of exit chord Reynolds number with no upstream heating

The side partition heat transfer data acquired over the three exit chord Reynolds numbers (Re$_C$), with the three turbulence conditions and across the range of flow rates, correlate well with the relationship for Nu$_D$ shown at the bottom of the figure. This relationship was based on a linear regression of the heat transfer data in terms of the external and internal flow Reynolds numbers. Based on the Reynolds number dependencies the heat transfer on the partition side is dependent on both external flow Reynolds number and internal flow Reynolds number. However, a regression analysis, which included the influence of the external turbulence condition, showed no dependency on the turbulence, length scale, and Reynolds number (TLR) parameter of Ames and Moffat [18]. (Note that the TLR parameter is used to correlate the influence of external turbulence with turbulent boundary layer heat transfer augmentation.) The internal flow shows a stronger dependence on Reynolds number with an exponent of 0.566. This internal flow Reynolds number effect on Nusselt number is similar to the converging pin fin array of Ames et al. [2] who found a dependence (Re$_D^{0.62}$) similar to Metzger et al. [4]. The diameter Reynolds number of the last pin row was chosen to represent the internal flow Reynolds number. Ames et al. [2] were able to show that heat transfer levels on the inner suction surface of the gill slot vane were consistent with heat transfer levels within the pin fin array when levels were adjusted for the decay of turbulence. However, no heat transfer data on the partition or inner suction surface between partitions have been taken with the absence of the converging pin array.

Heat transfer on the partition top surface is presented in Fig. 14 in log coordinates plotting Stanton number based on exit conditions versus pin diameter Reynolds number. These data were taken without heating on the vane upstream from the partition. The data are plotted for the three turbulence conditions over a range of coolant discharge ratios at the three exit condition Reynolds numbers. The average of the three turbulence conditions is plotted as a line. The data show that the turbulence condition has little significance and the flow rate is shown to have an effect only at discharge rates above full flow. At the design flow rate and below Stanton number has a simple dependence on chord Reynolds number. At higher design flows a mild dependence on discharge rate is also apparent.

Partition adiabatic effectiveness. The partition adiabatic effectiveness is a critical heat transfer boundary condition in the analysis of the trailing edge cooling design. In Fig. 15 adiabatic effectiveness for the side (open symbols) and the top (solid symbols) of the partition is presented as a function of local blowing ratio for the 500,000 chord Reynolds number cases. The data show no significant dependence on the external turbulence condition but a substantial dependence is shown on blowing ratio. The side surface shows decreasing adiabatic effectiveness with increasing blowing ratio while the top surface shows the opposite behavior. This dependence is a clear indication of the increasing interaction of the discharge flow with the external flow as blowing ratio increases. A similar behavior is seen at the 2,000,000 chord Reynolds number cases shown in Fig. 16. Again, the turbulence conditions appear to have no significant influence. At low blowing ratios effectiveness levels are high on the side of the partition and low on the top of the partition while at higher blowing ratios effectiveness decreases on the side while increasing on the top. In Fig. 17 the effectiveness levels for all three turbulence conditions are averaged at a given blowing ratio at each Reynolds number and are presented in one plot. At a blowing ratio of 0.48 the effectiveness level on the side partition is very high at 0.79 while on the top the value is only about 0.24 indicating a relatively weak interaction between the trailing edge discharge flow and the external flow. However, at a blowing ratio of 1.89, the interaction is much more significant as the side partition effectiveness has dropped to 0.50 while the effectiveness of the top partition has increased to around 0.44. The pressure distribution in the discharge area may be a significant driver of this interaction. Figure 11 shows this pressure distribution in the discharge area as a function of relative design flow rate. The data show an increasing rise in the pressure between the last point on the pressure surface and
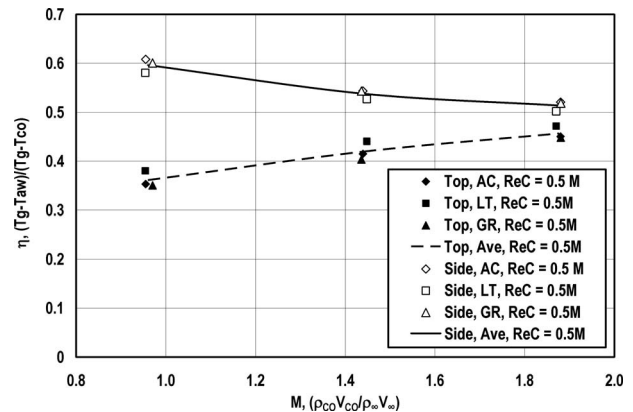
Fig. 15 Letterbox partition adiabatic effectiveness for side (open symbols) and top (solid symbols) surfaces as a function of local blowing ratio, Re$_C$=500,000
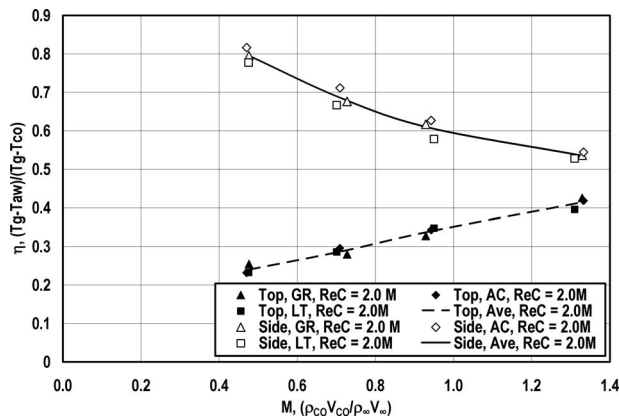
Fig. 16 Letterbox partition adiabatic effectiveness for side (open symbols) and top (solid symbols) surfaces as a function of local blowing ratio, Re$_C$=2,000,000.

Fig. 18 Comparison of gill slot and letterbox inner suction surface heat transfer levels for 500,000 and 2,000,000 Reynolds numbers at relative design flow with aerocombustor turbulence

the first in the discharge area with increasing design flow or blowing ratio. This strong adverse pressure gradient coupled with the deteriorating effectiveness levels suggests that increasing blowing ratio produces separation off the partition and increasing interaction with the freestream. This interaction between the coolant discharge and external flow enhances the adiabatic effectiveness on the partition top.

Inner suction surface heat transfer. The level of inner suction surface heat transfer for letterbox discharge is quite consistent with the heat transfer on the inner suction surface for gill slot discharge. Figure 18 displays the inner suction surface heat transfer coefficient as a function of distance from the end of the aluminum pin fin array. The location of the pin fin array, the leading edge of the letterbox partition, the start of heating, the lip of the exit slot, and the beginning of the trailing edge can be seen in Fig. 6. The locations of the start of heating and the beginning of the trailing edge radius are also indicated in Fig. 18. In this figure the heat transfer coefficient in the midline between partitions and adjacent to partitions is compared with distributions for the gill slot at the same flow rate and external condition. The location of the thermocouples is given in Fig. 5. The reported heat transfer coefficient has been adjusted for the unheated starting length. The data are shown for design flows at 500,000 and 2,000,000 chord Reynolds numbers for the aerocombustor turbulence condition. Clearly, the letterbox configuration data are consistent with the gill slot data. Generally, the midline heat transfer data appear to be a little bit higher than the gill slot data, and the data adjacent to
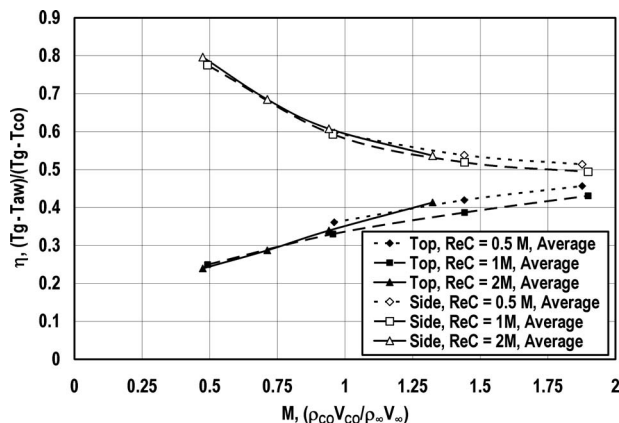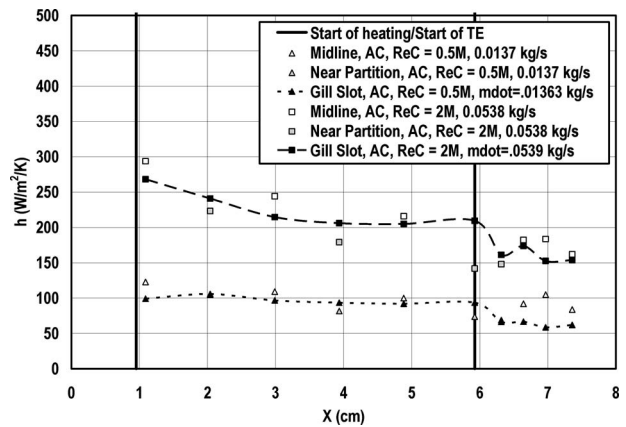
the partitions have values a little lower. Ames et al. [2] found heat transfer on the inner suction surface downstream from gill slot ejection to consistently scale on pin array heat transfer when a reduction due to decay of turbulence was accounted for.

Inner suction surface adiabatic effectiveness. Inner suction surface film cooling protection is clearly affected by introduction of the letterbox partitions. Figure 19 shows a comparison of adiabatic film cooling distributions as a function of distance from the pin fin array for both the letterbox configuration and the gill slot. The letterbox data are plotted for the aerocombustor turbulence condition at the design flow (M=0.94) for Reynolds numbers of 500,000, 1,000,000, and 2,000,000. The location of the start of heating for the corresponding heat transfer measurements and the beginning of the trailing edge radius is also indicated on the plot. Near the exit of the slot, the midline distributions are similar in level to the gill slot but fall off by roughly 0.1 near the trailing edge. This indicates a stronger interaction between the shedding at the trailing edge and the film cooling coverage than found for the gill slot vane. The distributions near the partition are much lower but are consistent with the values for the partition side. Generally, effectiveness levels are found to increase with increasing Reynolds number. Adiabatic effectiveness levels in the near-partition region are presented in Fig. 20. This figure shows the influence of both Reynolds number and blowing ratio. Similar to the partition side, adiabatic effectiveness levels decrease with increasing blowing ratio. This reduction in protection, compared with the gill slot,

Fig. 17 Letterbox partition adiabatic effectiveness for side (open symbols) and top (solid symbols) surfaces as a function of local blowing ratio; Re$_C$=500,000, 1,000,000, and 2,000,000
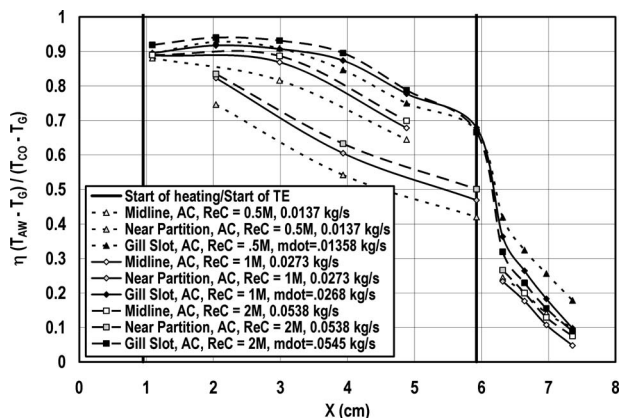

Fig. 19 Comparison of gill slot and letterbox inner suction surface adiabatic effectiveness as a function of distance from pin array exit over a four-to-one range in chord Reynolds number at relative design flow and aerocombustor turbulence
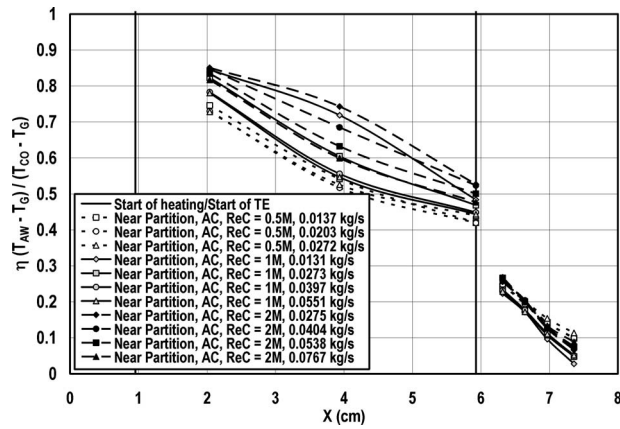
Fig. 20 Adiabatic effectiveness distributions at the near-partition location with varying coolant flow rates at each Reynolds number for the aerocombustor turbulence condition

suggests that the partitions increase the interaction between the film cooling flow and the gas path flow.

5 Conclusions

Heat transfer and adiabatic effectiveness results were acquired for the inner suction surface downstream of the slot and on the side and top surfaces of the partition. Heat transfer results on the partition side correlate with both internal and external flow Reynolds numbers but turbulence condition was found to have no influence. Heat transfer results on partition top are primarily a function of external Reynolds number, although flow rate has a small influence at high flows.

Partition side adiabatic effectiveness levels are high at low blowing rates but decrease with increasing blowing rate. Partition top adiabatic effectiveness values are low at low blowing rates but increase with increasing blowing rate. The external turbulence condition and exit chord Reynolds number are found to have a little influence on the partition adiabatic effectiveness levels.

Inner suction surface heat transfer levels are very similar to gill slot values. Midline values are slightly higher than gill slot values, and near-partition rates are slightly lower. Inner suction surface adiabatic effectiveness levels are similar to gill slot values midway between partitions, but near-partition effectiveness levels are much lower.

Acknowledgment

Nomenclature

A = surface area (m^2)

A_{min} = minimum array flow path area, m^2

C = true chord length of vane, m

Cp = specific heat at constant pressure, J/(kg K)

D = pin diameter, m

h = heat transfer coefficient, W/(m^2 K),

H = channel height, m

k = thermal conductivity, W/(m K)

Lu = energy scale, $Lu = 1.5|u'|^3/\varepsilon$, m

Lx = longitudinal integral scale, m

M = blowing ratio, $\rho_{CO} V_{CO}/(\rho_\infty V_\infty)$

Ma = Mach number

Nu_D = Nusselt number, $Nu = hD/k$

P = pressure, Pa

Q = heat transfer rate, where a loss from the surface is positive, W

Re_C = Reynolds number, based on exit conditions and true chord

Re_{Dmax} = diameter Reynolds number, based on V_{max}

S = vane surface distance, m

St = Stanton number, $h/(\rho U_\infty Cp)$

Tu = turbulence level, $Tu = u'/U_\infty$

T = temperature, K

U = streamwise velocity, m/s

u' = rms streamwise fluctuation velocity, m/s

V_{max} = the average velocity through A_{min}, m/s

X = axial distance, m

Y = endwall normal distance, m

Z = spanwise distance, m

Greek Letter Symbols

ε = turbulent dissipation rate, m^2/s^3

η = adiabatic effectiveness, $\eta = (T_G - T_{AW})/(T_G - T_{CO})$

ϕ = Nu_D-converging channel/Nu_D-constant H channel

ρ = fluid density, mass per unit of volume, kg/m^3

Subscripts

0 = reference condition

AW = adiabatic wall condition

B = conduction loss through partition bottom

CO = coolant outflow condition

D = energy dissipated in the heating element

ex = exit condition

G = gas or inlet total condition

in = inlet condition

L = energy lost (gained) by conduction

LP = conduction loss through lip radius

R = radiation loss

S = static property

SD = side partition

T = total property

TP = top heat transfer partition or balsa strip

UH = unheated starting length

∞ = freestream condition

References

[1] Fiala, N. J., Johnson, J. D., and Ames, F. E., 2008, "Aerodynamics of a Letterbox Trailing Edge—Effects of Blowing Rate, Reynolds Number and External Turbulence on Aerodynamics Losses and Pressure Distribution," ASME Paper No. GT2008-50475.

[2] Ames, F. E., Fiala, N. J., and Johnson, J. D., 2007, "Gill Slot Trailing Edge Heat Transfer—Effects of Blowing Rate, Reynolds Number, and External Turbulence on Heat Transfer and Film Cooling Effectiveness," ASME Paper No. GT2007-27397.

[3] Metzger, D. E., and Haley, S. W., 1982, "Heat Transfer Experiments and Flow Visualization for Arrays of Short Pin Fins," ASME Paper No. 82-GT-138.

[4] Metzger, D. E., Shepard, W. B., and Haley, S. W., 1986, "Row Resolved Heat Transfer Variations in Pin Fin Arrays Including Effects of Non-Uniform Arrays and Flow Convergence," ASME Paper No. 86-GT-132.

[5] Nordquist, C. A., 2006, "Pin Fin Endwall Heat Transfer Distributions With an Adiabatic Pin Acquired Using an Infrared Camera," Independent Study, University of North Dakota, Grand Forks, ND.

[6] Ames, F. E., and Dvorak, L. A., 2006, "Turbulent Transport in Pin Fin Arrays—Experimental Data and Predictions," ASME J. Turbomach., **128**, pp. 71–81.

[7] Martini, P., Schulz, A., and Bauer, H.-J., 2005, "Film Cooling Effectiveness and Heat Transfer on the Trailing Edge Cut-Back of Gas Turbine Airfoils With

Various Internal Cooling Designs," ASME Paper No. 68083.

[8] Martini, P., Schulz, A., Bauer, H.-J., and Whitney, C. F., 2005, "Detached Eddy Simulation of Film Cooling Performance on the Trailing Edge Cut-Back of Gas Turbine Airfoils," ASME Paper No. GT2005-68084.

[9] Martini, P., and Schulz, A., 2004, "Experimental and Numerical Investigation of Trailing Edge Film Cooling by Circular Coolant Wall Jets Ejected From a Slot With Internal Rib Arrays," ASME J. Turbomach., **126**, pp. 229–236.

[10] Cakan, M., and Taslim, M. E., 2006, "Experimental and Numerical Study of Mass/Heat Transfer on an Airfoil Trailing-Edge Slots and Lands," ASME Paper No. GT2006-91201.

[11] Chen, S. P., Peiwen, W. L., and Chyu, M. K., 2006, "Heat Transfer in an Airfoil Trailing Edge Configuration With Shaped Pedestals Mounted Internal Cooling Channel and Pressure Side Cutback," ASME Paper No. GT2006-91019.

[12] Kim, Y. W., Coon, C., and Moon, H. K., 2005, "Film-Cooling Characteristics of Pressure-Side Discharge Slots in an Accelerating Main Stream Flow," ASME Paper No. GT2005-69061.

[13] Cunha, F. J., Dahmer, M. T., and Chyu, M. K., 2005, "Analysis of Airfoil Trailing Edge Heat Transfer and Its Significance in Thermal-Mechanical Design and Durability," ASME Paper No. GT2005-68108.

[14] Brundage, A. L., Plesniak, M. W., Lawless, P. B., and Ramadhyani, S., 2007, "Experimental Investigation of Airfoil Trailing Edge Heat Transfer and Aerodynamic Losses," Exp. Therm. Fluid Sci., **31**(3), pp. 249–260.

[15] Hartnett, J. P., 1985, "Mass Transfer Cooling," *Handbook of Heat Transfer Application*, 2nd ed., McGraw-Hill, New York, Chap. 1.

[16] FLUENT 6.0, 2001, FLUENT 6.0 User's Guide, Fluent, Inc., Lebanon, N. H.

[17] Moffat, R. J., 1988, "Describing Uncertainties in Experimental Results," Exp. Therm. Fluid Sci., **1**, pp. 3–17.

[18] Ames, F. E., and Moffat, R. J., 1990, "Heat Transfer With High Intensity, Large Scale Turbulence: The Flat Plate Turbulent Boundary Layer and the Cylindrical Stagnation Point," Ph.D. thesis, Stanford University, Stanford, CA.

An Experimental Study of Vane Clocking Effects on Embedded Compressor Stage Performance

Nicole L. Key

Patrick B. Lawless

Sanford Fleeter

Purdue University,
West Lafayette, IN 47907

Previous research has shown that vane clocking, the circumferential indexing of adjacent vane rows with similar vane counts, can be an effective means to increase stage performance, reduce discrete frequency noise, and/or reduce the unsteady blade forces that can lead to high cycle fatigue. The objective of this research was to experimentally investigate the effects of vane clocking in an embedded compressor stage, focusing on stage performance. Experiments were performed in the intermediate-speed Purdue three-stage compressor, which consists of an IGV followed by three stages. The IGV, Stator 1, and Stator 2 vane rows have identical vane counts, and the effects of vane clocking were studied on Stage 2. Much effort went into refining performance measurements to enable the detection of small changes in stage efficiency associated with vane clocking. At design loading, the change in stage efficiency between the maximum and minimum efficiency clocking configurations was 0.27 points. The maximum efficiency clocking configuration positioned the Stator 1 wake at the Stator 2 leading edge. This condition produced a shallower and thinner Stator 2 wake compared with the clocking configuration that located the wake in the middle of the Stator 2 passage. At high loading, the change in Stage 2 efficiency associated with vane clocking effects increased to 1.07 points; however, the maximum efficiency clocking configuration was the case where the Stator 1 wake passed through the middle of the downstream vane passage. Thus, impingement of the upstream vane wake on the downstream vane leading edge resulted in the best performance at design point but provided the lowest efficiency at an off-design condition.
[DOI: 10.1115/1.3072714]

1 Introduction

Vane clocking is the circumferential indexing of adjacent vane rows with similar vane counts. The vane clocking configuration can be arranged so that either all downstream vanes are positioned in the wake shed from the upstream vane, or the upstream vane wakes pass through every passage of the downstream vane row without any interaction. The designer must determine the tradeoff between the number of vanes needed to achieve an optimal loading distribution and the number of vanes needed to match the adjacent stage vane count to be able to implement vane clocking. If the physics of vane clocking are understood, employment of the optimum circumferential position in compressors with similar vane counts is an efficiency improvement requiring no additional hardware.

One of the first vane clocking experiments was performed to study the effect of vane clocking on discrete frequency noise [1]. Researchers have shown that proper circumferential positioning of the vanes can result in a reduction by 10–15 dB in the sound pressure level of discrete frequency noise at the compressor inlet [2,3].

Vane clocking has also been experimentally shown to affect unsteady blade loading [4,5]. Vane clocking essentially changes the phase between the maximum vortical gust (when the rotor chops the upstream vane wake) and maximum potential gust (when the rotor passes in front of the downstream vane). The clocking configuration that minimizes unsteady blade forces is not necessarily the clocking configuration for maximum efficiency [6]. This paper will focus on compressor efficiency variations associated with vane clocking.
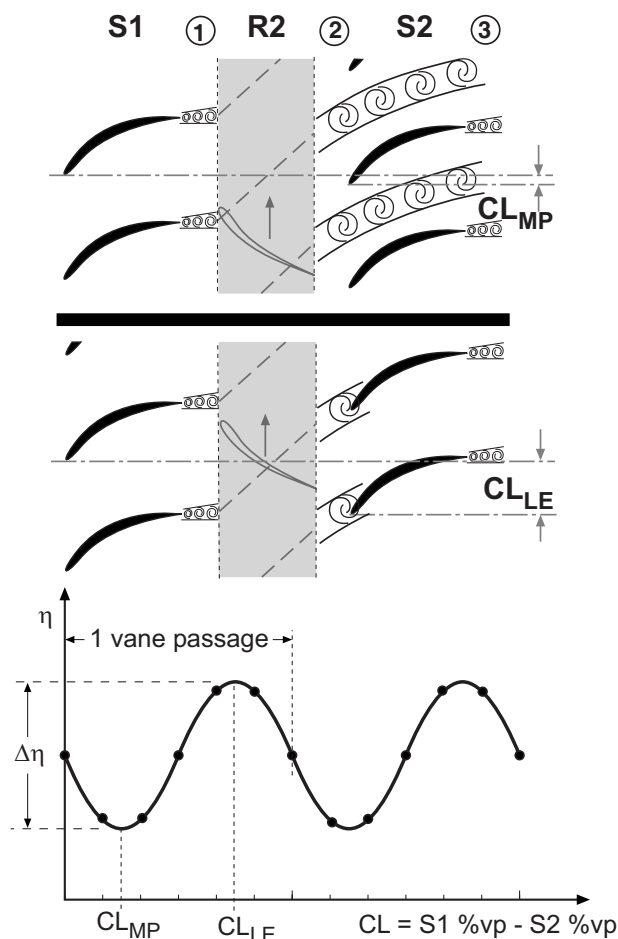
In every paper that reported a conclusive measured change in efficiency with vane clocking, the efficiency trend appears somewhat sinusoidal with clocking configuration, as shown in Fig. 1. The clocking configuration for maximum efficiency typically positions the wake shed from the upstream vane row at the leading edge of the downstream vane row, CL_{LE}. The configuration for minimum efficiency is half a vane passage out-of-phase with the maximum efficiency case and positions the upstream vane wake in the middle of the downstream vane passage, CL_{MP}.

The majority of vane clocking research has been performed in turbines. One of the first turbine vane clocking experiments showed an overall difference in efficiency associated with vane clocking to be 0.3 points. Local spanwise efficiency calculations indicated that local changes in efficiency were as high as 1.0 point, but since the hub and the tip cyclic variation in efficiency were out-of-phase with the middle portion of the span, some of the benefits canceled out [7]. Other experiments in low pressure turbines gave similar results, where efficiency variations associated with vane clocking ranged from 0.3 points to 2.0 points [8–10]. Computational efforts at predicting efficiency variations associated with turbine vane clocking support these experimental findings [11–15].

The wake-shock interactions present in modern high pressure turbines provide another possible environment for use of vane clocking as a means of improving performance and modifying unsteady blade row interactions. Optimum efficiency conditions occur when rotor shock strengths are reduced by interactions with passing wake segments [16,17].

Unfortunately, there are few articles in the open literature reporting experimental results of vane clocking effects on compressor efficiency. Conclusive measurements of the change in compressor efficiency with vane clocking are difficult to detect in

Fig. 1 Clocking configurations for maximum and minimum efficiencies, according to literature

have small potential field interactions, and the low pressure ratio renders detection of small changes in efficiency difficult. The 1.5 stage high-speed machines do not accurately model the multistage environment experienced by an embedded stage where both rotor-rotor and vane-vane wake interactions exist.

The objective of this research was to study vane clocking effects on embedded stage efficiency in a medium-speed three-stage compressor. A significant contribution of this work is the measured change in performance associated with vane clocking in an embedded compressor stage environment. These results were obtained by a detailed traverse of the steady flow field. In addition to the circumferentially averaged flow properties, the pitchwise variations associated with vane clocking are captured with a high-resolution traverse in the circumferential direction.

Steady total pressure and total temperature measurements acquired at the exit of Stator 1 and Stator 2 allow for calculation of the Stage 2 efficiency for six clocking configurations. Two operating conditions at design speed are investigated: design point and a high loading condition. The high loading condition provides larger wakes, larger potential fields, and a more unstable blade boundary layer. In a companion paper [22], the maximum and minimum Stage 2 efficiency clocking configurations are further studied by acquiring unsteady flow field measurements at the exit of each blade row to further understand the underlying flow physics associated with the change in performance. The scope of this paper is directed at the effect of clocking on steady compressor performance.

3 Test Facility and Instrumentation

The Purdue Three-Stage Compressor Facility provides a multi-stage environment with geometry representative of the back stages of a high pressure compressor. The compressor geometry is a scaled-up (24 in. tip diameter) derivative of the rear stages of a Rolls-Royce Indianapolis design [23]. The IGVs and all blades are double circular arc designs while the remaining vanes are NACA 65-series airfoils. The IGV and first two vane rows have 44 vanes providing a unique opportunity to study vane clocking. All vane rows are individually indexable allowing the vanes to be moved relative to the casing over an angular range of 10 deg. The repeatability of the vane position measurement system with precision string potentiometers is better than 0.1% of the vane passage.

To investigate the variation in stage performance due to vane clocking, six clocking configurations were studied. The clocking configuration (CL) is defined by the Stator-1 percent vane passage (vp) location minus the Stator-2 percent vp location. The six configurations investigated were 0%, 15%, 32%, 49%, 66%, and 83% vp and referred to as CL1, CL2, CL3, CL4, CL5, and CL6, respectively. A clocking offset of 100% vp provides the same relative vane position as 0% vp. The relative position of IGV and Stator 1 was unchanged, and the relative position of Stator 2 and Stator 3 was unchanged, thus, isolating the effect of vane clocking to Stage 2.

Data were acquired at design point and a high loading condition at design speed, shown as red symbols in Fig. 2. Also shown in Fig. 2 is the normalized compressor adiabatic efficiency based on torque meter measurements. The design point was characterized as the highest efficiency condition. The high loading case not only had a higher pressure rise but also a decreased efficiency. Thus, in addition to higher pressures, the high loading case had larger levels of loss.

Stage efficiency variations with vane clocking were calculated based on interstage total pressure and total temperature rakes. Station numbering is shown in Fig. 1 where Stator 1 exit is station 1, Stator 2 inlet is station 2, and Stator 2 exit is station 3. Since the changes in stage performance associated with vane clocking effects were expected to be small, it was critical to reduce any inaccuracies in the measurements where possible.

Space restrictions limited the temperature sensor type to thermocouples installed in specially manufactured rakes to provide a

low-speed compressor facilities characterized by a low pressure rise. One such experiment investigated vane clocking effects on overall and Stator 3 performance in NASA's Four-Stage Axial Compressor Facility. The overall change in compressor efficiency due to vane indexing was 0.2 points. The impact of vane clocking on efficiency variations was considered small and within the band of uncertainty associated with manufacturing variations and assembly tolerances in the test compressor [18]. The change in loss coefficient increased from 5% at peak efficiency to 10% at peak pressure rise. The clocking configuration for minimum loss coefficient was slightly different for the two operating conditions.

Computational efforts have shown that vane clocking efficiency variations in compressors are similar to those for turbines with differences in efficiency between 0.5 and 0.8 points [19,20]. Some simulations have suggested a difference in vane performance when the upstream vane wake convects along the pressure surface versus the suction surface of the downstream vane [19].

One of the few published experimental studies on vane clocking performance benefits in a high-speed stage-and-a-half compressor showed that clocking provided a change in efficiency of 1 point. However, the change in efficiency was as high as 7–8 points in the endwall regions. As in the turbine vane clocking studies, the configuration for optimum efficiency placed the upstream vane wake at the leading edge of the downstream vane [21].

2 Research Objective

There have been few experimental vane clocking studies performed in compressors. Low-speed multistage test compressors

Fig. 2 Overall compressor performance at a corrected speed of 5000 rpm

Fig. 3 Stator 2 inlet total pressure, $P_{o2}/P_{o\text{-inlet}}$, at design

measure of the radial total temperature distribution. Accurate thermocouple measurements depend on many factors including, but not limited to, the homogeneity of the thermocouple wire, the accuracy of the voltmeter, and the cold junction compensation. An integrating voltmeter, Hewlett-Packard 3852A data acquisition unit with a 44708 multiplexer, allowed accurate measurements with resolution to 1 μV. It also provided an isothermal block for cold junction compensation, the temperature of which was measured with a built-in thermistor.

The thermocouple sensor and thermocouple-grade extension wire were designated as "special limits of error." For Type T thermocouples, the manufacturer specified uncertainty was $\pm 0.5\,°$C. In an effort to reduce this value, the thermocouples were placed in a temperature bath and calibrated over the temperature range of $0-100\,°$C. The calibration process identified the smallest gauge thermocouple wire capable of providing the most accurate measurement as 30Ga Type T thermocouples. The uncertainty for this group of wires was $\pm 0.1\,°$C.

The pressures were measured with a Scanivalve DSA 3217 temperature-compensated digital sensing array with a range of 5 psi (gauge) and $\pm 0.05\%$ full scale accuracy. The pressure scanner contained pneumatic valves that allowed the sensors to be rezeroed during compressor operation, minimizing zero-drift effects that can become significant over an extended testing period.

To determine the effects of vane clocking on Stage 2 performance, measurements were acquired at the exit of Stator 1 and Stator 2 with seven-element rakes featuring ports at 12%, 20%, 30%, 50%, 70%, 80%, and 88% span. Two rakes at each axial location provided total temperature and total pressure measurements. The angular acceptance of the 0.08 in. diameter Kiel head rakes, as determined by the deviation in measured total pressure as less than 0.01%, was ± 42 deg for velocities similar to those encountered in the compressor test facility. Pneumatic five-hole probe measurements provided flow angle information for rake alignment. Further details on rake geometry can be found in Ref. [23].

The vanes were indexed past the rakes in a particular clocking configuration in 2% vp increments. It is of interest to note that the vanes were indexed in a pattern such that the vanes moved half a passage in successive measurements. For example, rather than measuring in ascending vane passage position, optimum control of vane position occurred when measured in a pattern such as 5%, 55%, 10%, 60% vp, etc. Thus, if measurement drift should occur, it would be noticed by an abnormal, "chopped" wake profile.

In fact, to avoid any drift in the pressure transducers, they were rezeroed prior to acquiring data at each circumferential position. By choosing a day of stable atmospheric pressure, the compressor
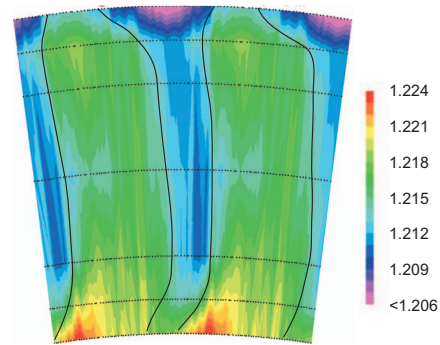
operating point was set after approximately one hour of run time, which was sufficient to reach steady state operation. Once the throttle position was set, it was not adjusted until all passage data for all six clocking configurations were acquired, resulting in a 10–12 h test per operating condition. As the inlet total temperature changed, the compressor mechanical speed was adjusted to keep the compressor operating within ± 5 rpm of a corrected speed of 5000 rpm.

4 Results at Design Loading

Figure 3 shows the total pressure field at the leading edge plane of Stator 2. These data were acquired by placing a Kiel head total pressure probe at the leading edge of Stator 2 and traversing the IGV and Stator 1 in unison past the probe. Notice that the Stator 1 wake is essentially radial, with slight skew in the endwall regions. One passage was measured, but two passages are shown assuming periodicity. The dots represent the measurement locations (12%, 20%, 30%, 50%, 70%, 80%, and 88% span in 2% vp increments). Data are not extrapolated to the endwalls. The rotors were designed to provide a hub-strong total pressure profile, as seen in Fig. 3.

Figure 4 shows the total pressure distribution as normalized by compressor inlet total pressure at the Stator 2 exit for all six clocking configurations. The Stator 2 Reynolds number based on chord was 4.6×10^5 at design point. The scales have been adjusted to highlight the Stator 1 wake, which is shown in green with an approximate outline sketched in black. The results are shown with respect to the Stator 2 coordinate system, and thus, as the clocking configuration is changed, the location of the Stator 2 wakes (purple) is unchanged, but the Stator 1 wakes are relocated to a different place within the Stator 2 passage. The clocking configuration for wake impingement along the majority of the span is CL3, where the Stator 1 wake fluid has coalesced with the Stator 2 wake fluid. At half a passage out-of-phase, clocking configuration CL6 results in the Stator 1 wake residing in the midpassage region of Stator 2 for the majority of the span. Because of secondary flow effects, the Stator 1 wake is more skewed in the endwall regions by the time it convects to the exit of Stator 2, compared with the Stator 2 inlet data shown in Fig. 3.

Figure 5 shows the circumferential average of the Stage 2 total pressure ratio for all six clocking configurations. The largest effect of vane clocking occurs at 70% and 80% spans. Figure 6 provides the radial distribution of circumferentially averaged total pressure at Stator 1 exit for all six clocking configurations at design loading. It appears that there is no obvious vane clocking trend associated with Stator 1 exit pressures. These Stator 1 exit profiles are shown as a baseline with which to compare the differences in Fig. 5. Thus, the vane clocking effects are most pronounced at 70% and 80% spans for design loading, and these radii will be the focus of the following discussion at this operating condition.

A further investigation of Stator 1 wake profiles at 70% and 80% spans, Fig. 7, indeed shows that there is no measurable effect
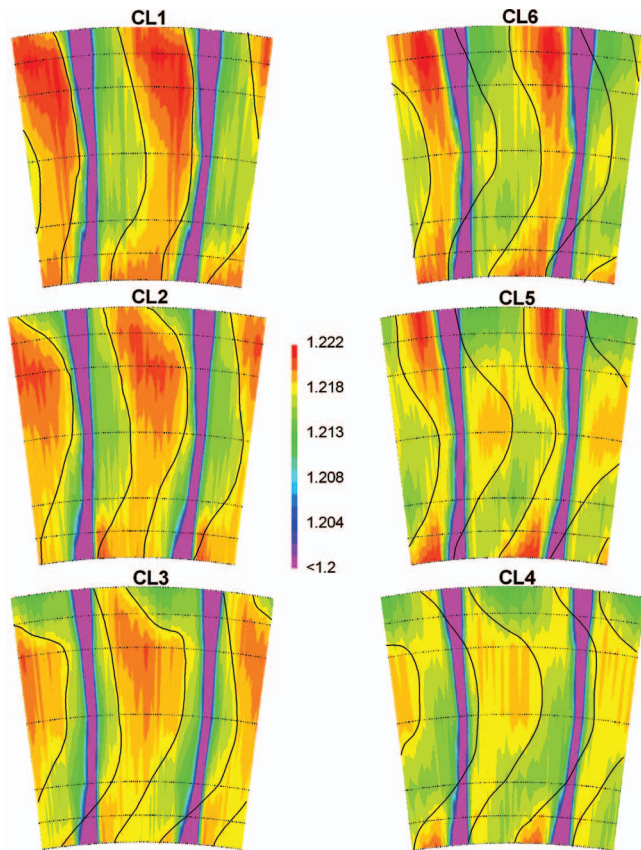
Fig. 4 Stator 2 exit total pressure, $P_{o3}/P_{o\text{-inlet}}$, for all six clocking configurations at design loading

Fig. 6 Circumferentially averaged Stator 1 exit total pressure at design loading

tions. The repeatability in the measurement of vane position allowed for this level of accuracy in the wake profiles.

The differences associated with vane clocking occur in the wake thickness, wake depth, and freestream total pressure. The minimum wake (as far as depth and width) occurs for clocking configurations CL3 and CL4. The maximum wake occurs for configurations CL1 and CL6. Thus, the case when the Stator 1 wake impinges on Stator 2 results in the thinnest Stator 2 wake. Even though the profiles are not shown here, it is worth mentioning that the differences in the wakes at 30% and 50% spans for the different clocking configurations are very small in comparison. In general, the wake depth and width are the smallest at these spanwise locations. As the size of the wake changes, the freestream velocity must adjust to be able to pass the mass flow. This, in addition to the location of the Stator 1 wake within the Stator 2 passage, accounts for variations in total pressure outside of the wake for the different clocking configurations.

The measured total temperature profiles are shown in Fig. 9 at 70% span for both the Stator 1 and Stator 2 exits. The measurements appear to be noisy with no clear trend associated with vane clocking. These measurements were performed with calibrated

of clocking the downstream vane at the Stator 1 exit. In fact, the repeatability in the Stator 1 wake profiles is excellent. This reinforces the fact that the compressor operating condition was held constant throughout the entire test.

Figure 8 shows the Stator 2 wake total pressure profiles for the six clocking configurations at design loading at 70% and 80% spans. The suction side and pressure side of the wake are denoted as SS and PS, respectively. The high-resolution in the circumferential direction is justified since the differences in the wakes are small. The pressure sides of the wake profiles line up nearly identically for all six clocking configurations at both spanwise loca-
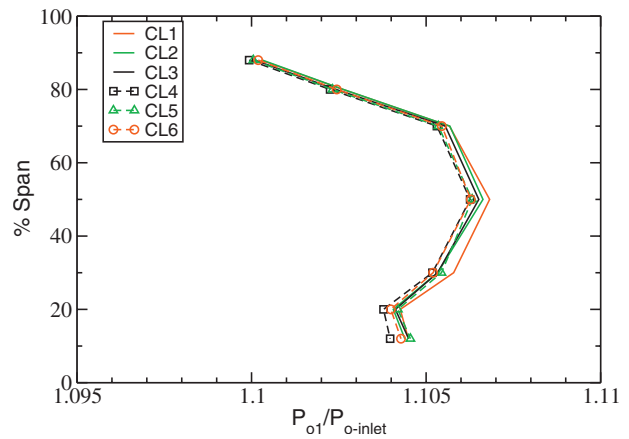

Fig. 5 Circumferentially averaged Stage 2 total pressure ratio at design loading

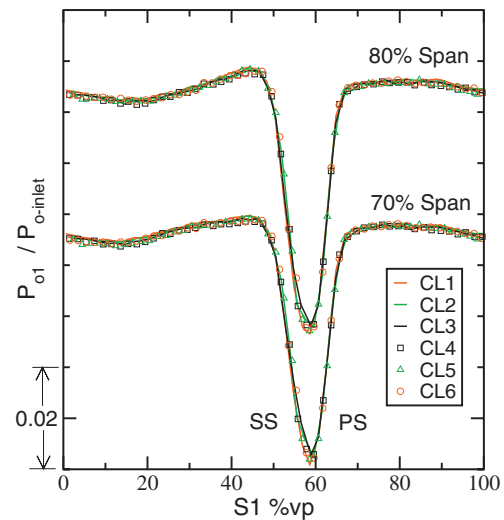**Fig. 7 Stator 1 wake profiles at 70% and 80% spans at design loading**

Fig. 8 Stator 2 wake profiles at 70% and 80% spans at design loading

Fig. 10 Total temperature profiles acquired with larger sample populations

Type T thermocouples. While the accuracy was expected to be $\pm 0.1\,^\circ$C, which corresponds to an uncertainty in $T_o/T_{o\text{-inlet}}$ of ± 0.0005, it was hoped that the repeatability would be much better. In later experiments the sample population was increased, resulting in improved characterization of the temperature profiles.

Follow-on experiments in Ref. [22] attempted to better resolve the total temperature profiles. The extensive run time associated with these measurements, although impractical to implement for all clocking configurations, allowed five times the number of temperature readings to be acquired from the integrating voltmeter with respect to the data shown in Fig. 9. Figure 10 shows the total temperature profiles at both stator exits at 70% span. The improvement in the total temperature measurements is associated with the larger sample population and reduced standard deviation when acquiring more measurements. A small peak in the total temperature profile occurs off the pressure side of the wake. This is the result of high enthalpy rotor wake fluid accumulating along the pressure side of the stator due to the rotor wake slip velocity, as introduced by Ref. [24]. It is in this region that effects of vane clocking on rotor wakes should be identifiable, but it appears that
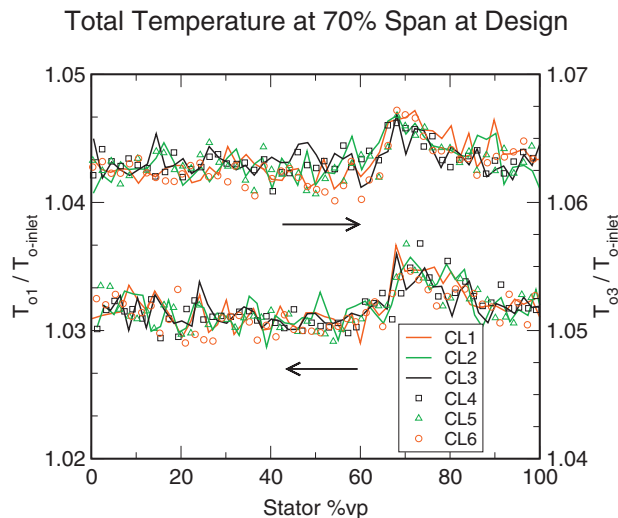
there is no measurable vane clocking effect on the total temperature of the rotor wakes measured at the Stator 2 exit. The results are nearly identical for the two clocking configurations.

Measurements were repeated on 5 days, and thus the area-averaged total temperature ratios for the five different runs are shown in Fig. 11. The difference in Stage 2 area-averaged total temperature ratio for the two clocking configurations is less than 0.0001 for each day. This is less than one-fifth of the uncertainty in temperature ratio indicating good repeatability of the temperature measurements. Since the focus of this investigation is to compare the results of different clocking configurations, repeatability is the most important characteristic of the measurement chain.

No trend exists as far as which clocking configuration provides the higher total temperature ratio, either. Therefore, based on these repeated results, it is concluded that vane clocking does not have a measurable effect on the work done by Rotor 2 at this loading condition in this compressor. Additionally, there were no changes in Rotor 2 turning with clocking configuration as measured by a cross-film sensor. This further supports the claim that vane clocking was not affecting the work done by Rotor 2.

Based on this conclusion, the Stage 2 efficiency is calculated based on the average of the area-averaged Stage 2 total temperature ratio for all six clocking configurations. Thus, the change in efficiency will be associated with the change in total pressure ratio between the different clocking configurations only.

Fig. 9 Stator 1 and Stator 2 total temperature profiles at design loading

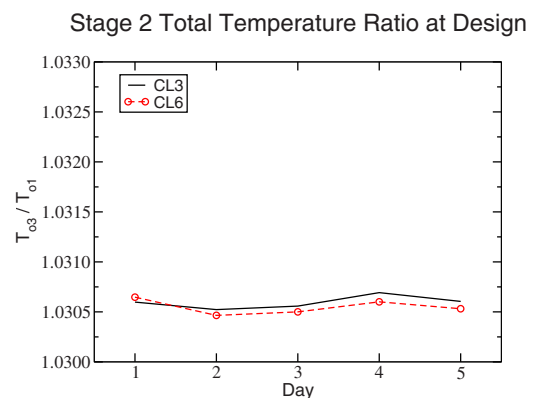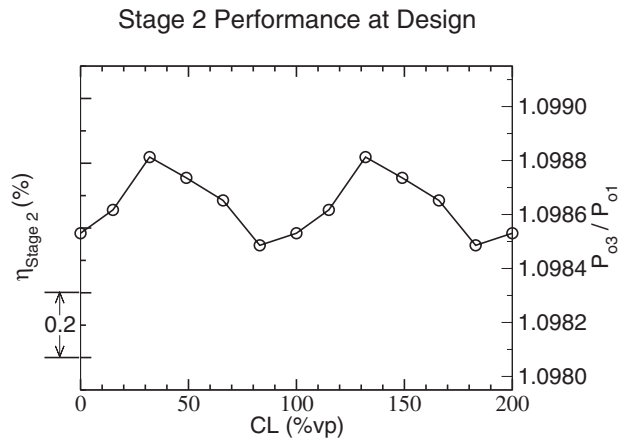Fig. 11 Average Stage 2 total temperature ratio as measured on five different days at design loading

Fig. 12 The effect of vane clocking on Stage 2 performance at design loading

Figure 12 shows that the resulting maximum change in area-averaged Stage 2 efficiency associated with vane clocking is 0.27 points. Results are shown for two cycles, assuming periodicity. The maximum efficiency condition occurs at CL3 while the minimum efficiency clocking configuration occurs at CL6. The area-averaged Stage 2 total pressure ratio differed by 0.000312 between the maximum and minimum clocking configurations. This is larger than the uncertainty based on the pressure scanner supplier data, and thus, is considered to be a measurable vane clocking effect. The accuracy of the pressure transducers as given by the manufacturer is ± 0.0025 psi (gauge) (uncertainty in $P_{o1}/P_{o\text{-inlet}} = \pm 0.00017$) and covers linearity, hysteresis, and repeatability.

The maximum Stage 2 performance occurs for clocking configuration CL3, which was shown to locate the Stator 1 wake at the Stator 2 leading edge for the majority of the span giving rise to a smaller Stator 2 wake (CL_{LE}). The clocking configuration with the worst performance was CL6, which located the Stator 1 wake in the middle of the Stator 2 passage (CL_{MP}). These results are in line with the reported results from previous vane clocking research in both turbines and compressors.

5 Results at High Loading

A high loading condition at design speed was investigated to look at vane clocking effects in an embedded stage environment characterized by larger wakes, larger potential fields, and less stable vane boundary layers. Figure 13 shows the Stator 2 inlet total pressure results for high loading. As at design point, a Kiel head total pressure probe traversed along the Stator 2 leading edge as the IGV and Stator 1 traversed in unison, in 2% vp increments.
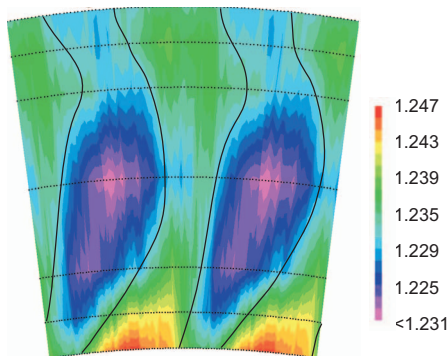
Fig. 13 Steady Stator 2 inlet total pressure, $P_{o2}/P_{o\text{-inlet}}$, at high loading
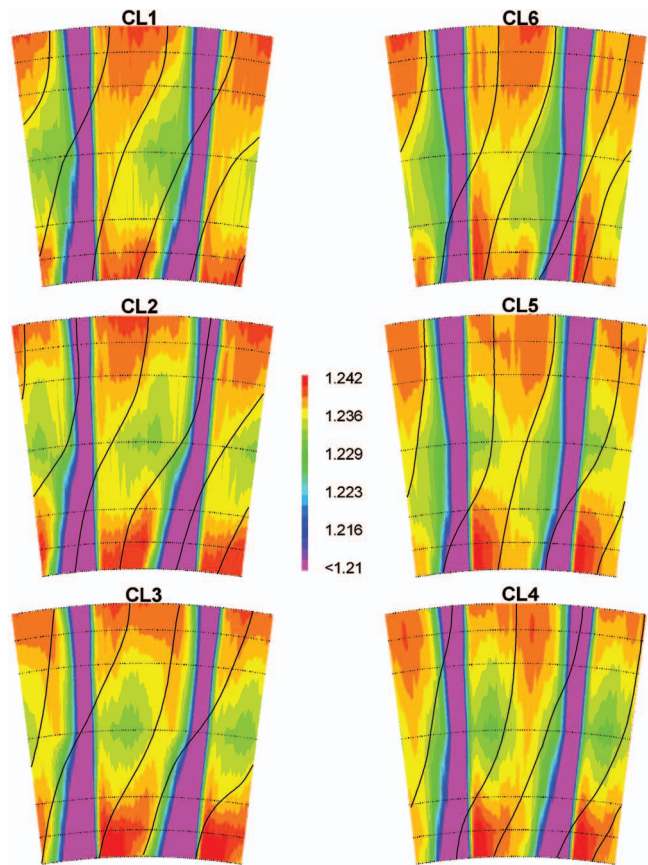
Fig. 14 Stator 2 exit total pressure field, $P_{o3}/P_{o\text{-inlet}}$, at high loading

The contour plot shows a much wider Stator 1 wake compared with that shown in Fig. 3 at design loading. Also, rather than the mostly radial Stator 1 wake at design, the Stator 1 wake at high loading shows an almost constant lean angle in the circumferential direction from 12% to 70% span. The larger total pressures measured near the hub in Fig. 13 are indicative of a rotor hub-strong profile.

Figure 14 shows the Stator 2 exit total pressure distribution for all clocking configurations at high loading. The scales have been adjusted to highlight the location of the Stator 1 wake fluid, shown in green at midspan. The Stator 2 Reynolds number based on chord was 4.0×10^5 at high loading. An approximate outline of the Stator 1 wake fluid is also shown by the black lines. There is significant tangential skew in the Stator 1 wake by the time it convects to the Stator 2 exit. The clocking configuration that locates the Stator 1 wake at the Stator 2 leading edge thus varies with spanwise location. Clocking configuration CL3 is the configuration for leading edge impingement (CL_{LE}) at the lower radii while CL6 is the configuration for leading edge impingement near the tip.

A significant difference with the results at design loading is present in Fig. 15 where the circumferentially averaged Stator 1 exit total pressure is shown. The effects of clocking the downstream vane have a strong effect on the hub total pressure at the exit of the upstream vane. The case for Stator 1 wake impingement on the downstream vane at 12% span, CL3, shows the highest Stator 1 exit total pressure at the hub.

To further investigate the results shown in Fig. 15, Fig. 16 shows the Stator 1 wake total pressure profiles at 12% span, where the largest variations in circumferentially averaged pressure occurred. Additionally, the Stator 1 wake profiles at 50% span, where the minimum variations associated with vane clocking oc-
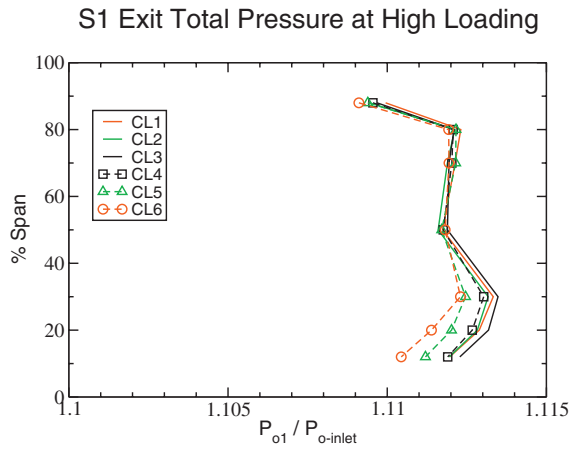
Fig. 15 Circumferentially averaged Stator 1 exit total pressure at high loading

Fig. 17 Circumferentially averaged Stator 2 exit total pressure at high loading

cur, are also shown in Fig. 16. The wake profiles show that there is indeed more variation in the Stator 1 wake between the clocking configurations as compared with the Stator 1 wake results at design point (Fig. 7). The lowest amount of variation occurs at 50% span where the wake is the smallest. The variations at 12% span occur in the portion of the wake shed from the suction side of the vane.

Stator 2 exit total pressures at high loading, Fig. 17, show a significant difference between the CL3 (leading edge impingement at the hub) case and the CL6 case (leading edge impingement near the tip). For the CL6 case, the profile is almost uniform, except for a deficit at the hub. The CL3 case, however, shows pressures linearly increasing from the hub to the tip. This large difference in the radial total pressure profile resulting from upstream vane-wake placement could have significant implications to a compressor designer and indicates the importance of having the capability to model these multistage effects with CFD tools, especially for machines with similar vane counts.

Figure 18 shows the Stator 2 wake total pressure profiles at all spanwise locations at high loading. The effect of vane clocking is clearly identifiable in the Stator 2 wake width and depth. As at design loading, the effects of vane clocking occur in the suction side of the wake. The pressure sides of the wakes for all clocking configurations align nearly perfectly at all spanwise locations. Near the hub, the minimum Stator 2 wake occurs for CL6 (CL_{MP} in the hub region) while the maximum wake occurs for the clocking configuration half a passage out-of-phase, CL3 (CL_{LE} in the

hub region). The maximum Stator 2 wake condition corresponds to Stator 1 wake impingement. This is true for the entire span, and the clocking configuration that corresponds to the Stator 1 wake impingement case changes with span just as the maximum wake clocking configuration changes with span. This is opposite of the trend seen at design loading where wake impingement created the thinnest Stator 2 wake.

Looking at the steady axial velocity results obtained at the Stator 2 inlet with a cross-film sensor for the two clocking configu-

S2 Exit Total Pressure at High Loading

Fig. 16 Stator 1 wake profiles at 12% and 50% spans at high loading

Fig. 18 Stator 2 wake profiles at high loading

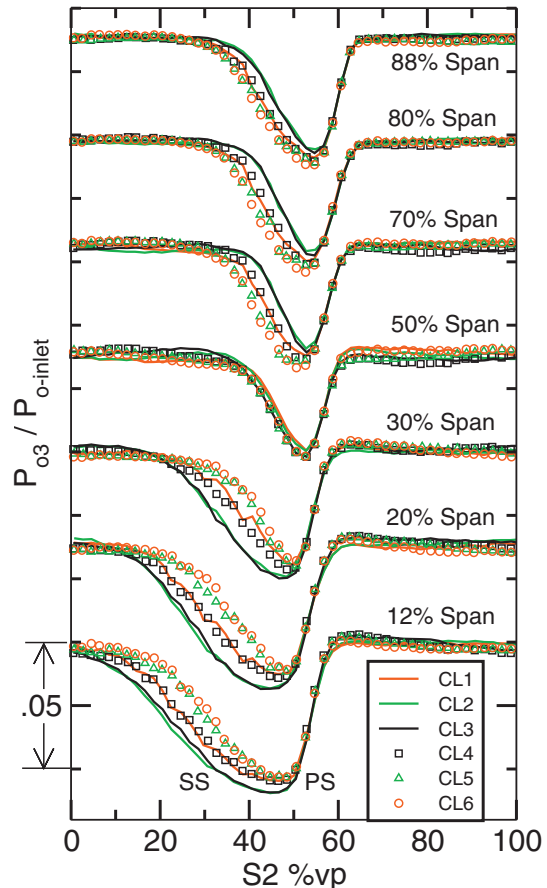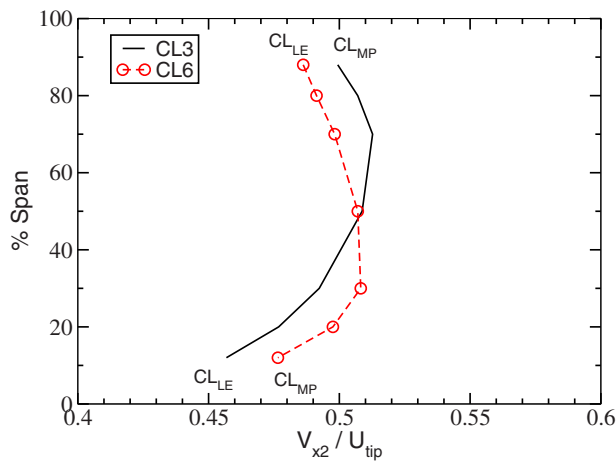## Axial Velocity at S2 Inlet at High Loading

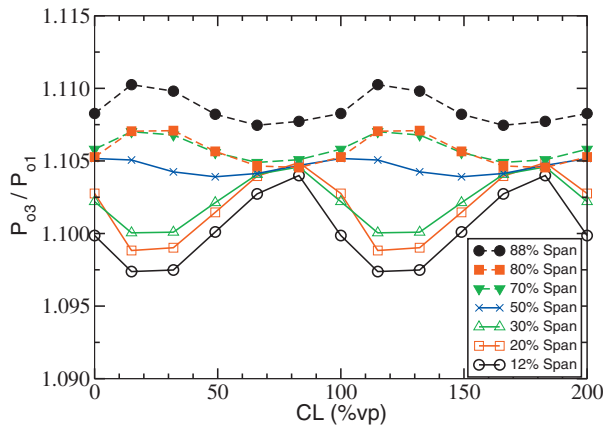**Fig. 19** Time-averaged axial velocity distribution at the Stator 2 inlet at high loading

Stage 2 Total Temperature Ratio at High Loading

Fig. 21 Average Stage 2 total temperature ratio at high loading as measured on five different days

rations, CL3 and CL6, it is observed that the large Stator 2 wake created by Stator 1 wake impingement near the hub creates a blockage significant enough that less flow will go through the hub streamtube for the CL3 configuration, as shown by the decrease in axial velocity near the hub in Fig. 19. Thus, for the CL3 configuration, Stator 2 is unloaded near the hub, as shown by the decreased pressure in Fig. 17. This could account for why Stator 1 shows an increased hub loading for configuration CL3.

The clocking configuration for Stator 1 wake impingement created the larger Stator 2 wake and resulted in locally lower average total pressure ratios. The maximum total pressure ratio clocking configuration near the tip was out-of-phase with the maximum total pressure ratio clocking configuration near the hub, Fig. 20. However, the near-hub variations in total pressure ratio were larger than the variations in the outer half of the span. Therefore, the clocking configuration for the maximum total pressure rise for the lower half of the vane was the clocking configuration that provided the highest area-averaged total pressure rise. The overall change in Stage 2 area-averaged total pressure ratio with vane clocking was 0.00134 at high loading.

The total temperature results at high loading were similar to the results at design loading. No vane clocking effects could be observed in the total temperature profiles. The data acquired on the

five other days when the long temperature acquisitions are available for CL3 and CL6 were area-averaged and compared. There was no trend in Stage 2 area-averaged total temperature ratio for the two clocking configurations, Fig. 21. Therefore, as was done for design loading, the total temperature was considered to be constant for all clocking configurations concluding that vane clocking effects are mainly affecting Stage 2 losses.

The Stage 2 efficiency variation due to vane clocking at high loading is shown in Fig. 22 along with the results from design loading. At high loading, the minimum efficiency condition occurs for CL3 (CL_{LE} near hub) while the maximum efficiency condition is CL6 (CL_{MP} near hub). This is exactly opposite to the results at design loading. However, at high loading, the change in efficiency is 1.07 points, more than three times the measured effect at design loading. The effect of vane clocking at high loading showed that when the upstream vane wake impinged on the downstream vane, the downstream vane wake became larger. This larger wake created a flow blockage and caused the flow to radially redistribute. These data show that the clocking configuration for leading edge impingement may not always be the optimum efficiency configuration, especially at off-design conditions. These results hint at the complicated vane-wake interactions that occur in a compressor.

The obvious question is the uncertainty associated with the efficiency measurements. Using the uncertainty in pressure and temperature measurements based on supplier data and calibration pro-

Stage 2 Total Pressure Ratio at High Loading

Fig. 20 Average Stage 2 total pressure ratio for all clocking configurations at high loading

Vane Clocking Effects on Stage 2 Efficiency
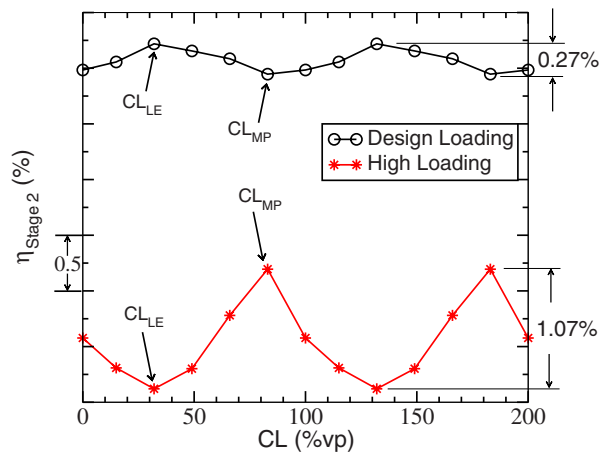
Fig. 22 Vane clocking effects on Stage 2 efficiency at design and high loading conditions

Table 1 Summary of Stage 2 performance results for five additional tests performed for CL3 and CL6

| | $\eta_{CL3} - \eta_{CL6}$ | | Stage 2 total pressure ratio (CL3–CL6) | |
	Average	Std. Dev.	Average	Std. Dev.
Design	0.28	0.16	0.000314	0.000202
High	−0.77	0.22	−0.000960	0.000282

vides large uncertainties in efficiency, as much as ±0.5 points. However, the wake profiles seemed to be following a trend with vane clocking, and thus, the authors felt that the repeatability of the measurements was much better than the uncertainty. As mentioned previously, two clocking configurations were studied in detail on five separate testing days. While the pressure rakes were relocated to a different vane passage to allow for insertion of the unsteady flow measurement probes, steady flow data were acquired during these runs.

Results are summarized in Table 1. At design loading, the CL3 configuration was, on average, 0.28 points more efficient than the CL6 configuration, with a standard deviation of 0.16 points for those five tests. This resulted from a Stage 2 total pressure ratio for CL3 that was larger than that of CL6 by 0.000314, with a standard deviation of 0.000202. At high loading, the CL6 configuration was, on average, 0.77 points more efficient than the CL3 configuration, with a standard deviation of 0.22 points. This resulted from a Stage 2 total pressure ratio for CL6 that was larger than that for CL3 by 0.000960, with a standard deviation of 0.000282. Thus, the trends are repeatable. The efficiency differences at high loading are almost three times that seen at design, while the best efficiency clocking configuration at design provided the worst efficiency at high loading.

6 Summary and Conclusions

The objective of this research was to measure the effects of vane clocking on embedded compressor stage performance. The results at two loading conditions at design speed were discussed. The design operating condition produced Stator 1 wakes that were mostly radial, with slight skew near the endwalls. Clocking the downstream vanes did not have a measurable impact on Stator 1 wakes. For the clocking configuration where the Stator 1 wakes impinged on the downstream Stator 2 vanes, the resulting Stator 2 wakes were thinner and shallower, as measured by Kiel head total pressure rakes. The most notable vane clocking effects occurred at 70% and 80% spans. Since vane clocking had no measurable effect on the work done, changes in stage efficiency resulted from variations in stage losses only. Thus, the case of upstream vane-wake impingement resulted in the best efficiency configuration, with an overall difference in Stage 2 efficiency of 0.27 points. Previous vane clocking research has shown that the clocking configuration providing leading edge impingement of the upstream vane wake is the optimal efficiency condition, and these results concur.

At high loading, the Stator 1 wake had an almost constant lean angle in the circumferential direction from 12% to 70% span. Thus, the clocking configuration that resulted in Stator 1 wake impingement near the hub was out-of-phase with that at the tip. The case for optimum efficiency at design loading (leading edge impingement) resulted in the worst efficiency condition at high loading. The resulting Stator 2 wakes for this clocking configuration were much wider and deeper, perhaps the result of the Stator 1 wake impingement triggering an earlier suction surface boundary layer separation. In fact, when the Stator 1 wake impinged on the leading edge of Stator 2 near the hub at high loading, the Stator 2 suction side boundary layer separation caused significant hub blockage such that the flow radially redistributed, passing more flow through the tip streamlines, as shown by axial velocity

results. The near-hub variations in total pressure ratio associated with vane clocking were larger than the variations in the outer half of the span. Therefore, the clocking configuration with the maximum total pressure rise in the lower half of the vane was the best overall efficiency clocking configuration. The difference in efficiency with vane clocking at high loading was 1.07 points, more than three times that seen at design loading.

These results show that there is not one single rule that can be applied to implementation of vane clocking in compressors for efficiency improvements. The designer must weigh the benefits at one operating condition with the possible penalty at another. It is, perhaps, unreasonable to expect that compressor blade boundary layers will react in a similar manner as turbine blade boundary layers, especially at off-design conditions. This work also shows the importance of resolving the interaction effects of the upstream vane wakes when using CFD to compute the flow field in a multistage environment. Vane clocking has been shown to not only affect stage efficiency, but it has also had a significant impact on the radial distribution of total pressure and mass flow. The flow physics associated with the performance changes discussed in this paper are further investigated in a companion paper using unsteady flow measurements acquired for the maximum and minimum efficiency clocking configurations [22].

Nomenclature

CFD = computational fluid dynamics
CL = clocking configuration: S1% vp–S2% vp
CL_{LE} = CL where S1 wake impinges on S2 LE
CL_{MP} = CL where S1 wake passes in the middle of S2 passage
IGV = inlet guide vane
m_c = corrected mass flow rate
P_o = stagnation pressure
$S1$ = Stator 1
$S2$ = Stator 2
T_o = stagnation temperature
U_{tip} = tip wheel speed
V_x = axial velocity
η = adiabatic efficiency

Subscripts

1 = Stator 1 exit
2 = Stator 2 inlet
3 = Stator 2 exit
inlet = compressor inlet

References

[1] Walker, G. J., and Oliver, A. R., 1972, "The Effect of Interaction Between Wakes From Blade Rows in an Axial Flow Compressor on the Noise Generated by Blade Interaction," ASME J. Eng. Power, **94**, pp. 241–248.

[2] Schmidt, D. P., and Okiishi, T. H., 1977, "Multistage Axial-Flow Turbomachine Wake Production, Transport, and Interaction," AIAA J., **15**, pp. 1138–1145.

[3] Kamiyoshi, S., and Kaji, S., 2001, "Application of Airfoil Clocking Technology to Reduction of Multi-Stage Fan Tone," presented at the AIAA/CEAS Aeroacoustics Conference and Exhibit, Maastricht, Netherlands, May 28–30, AIAA Paper No. 2001–2149.

[4] Hsu, S. T., and Wo, A. M., 1998, "Reduction of Unsteady Blade Loading by Beneficial Use of Vortical and Potential Disturbances in an Axial Compressor With Rotor Clocking," ASME J. Turbomach., **120**, pp. 705–713.

[5] Mailach, R., and Vogeler, K., 2004, "Rotor-Stator Interactions in a Four-Stage Low-Speed Axial Compressor—Part 1: Unsteady Profile Pressures and the Effect of Clocking," ASME J. Turbomach., **126**, pp. 507–518.

[6] Gadea, J., Dénos, R., Paniagua, G., Billard, N., and Sieverding, C. H., 2004,

"Effect of Clocking on the Second Stator Pressure Field of a One and a Half Stage Transonic Turbine," ASME Paper No. GT2003–53463.

[7] Huber, F. W., Johnson, P. D., Sharma, O. P., Staubach, J. B., and Gaddis, S. W., 1996, "Performance Improvement Through Indexing of Turbine Airfoils: Part 1—Experimental Investigation," ASME J. Turbomach., **118**, pp. 630–635.

[8] Jouini, D. B. M., Little, D., Bancalari, E., Dunn, M., Haldeman, C., and Johnson, P. D., 2003, "Experimental Investigation of Airfoil Wake Clocking Impacts on Aerodynamic Performance in a Two Stage Turbine Test Rig," ASME Paper No. GT2003–38872.

[9] Reinmöller, U., Stepha, B., Schmidt, S., and Niehuis, R., 2002, "Clocking Effects in a 1.5 Stage Axial Turbine—Steady and Unsteady Experimental Investigations Supported by Numerical Simulations," ASME J. Turbomach., **124**, pp. 52–60.

[10] Behr, T., Porreca, L., Mokulys, T., Kalfas, A. I., and Abhari, R. S., 2006, "Multistage Aspects and Unsteady Effects of Stator and Rotor Clocking in an Axial Turbine With Low Aspect Ratio Blading," ASME J. Turbomach., **128**, pp. 11–22.

[11] Dorney, D. J., and Sharma, O. P., 1996, "A Study of Turbine Performance Increases Through Airfoil Clocking," AIAA Paper No. 96–2816.

[12] Cizmas, P. G. A., and Dorney, D. J., 1999, "Parallel Computation of Turbine Blade Clocking," Int. J. Turbo Jet Engines, **16**, pp. 49–60.

[13] Griffin, L. W., Huber, F. W., and Sharma, O. P., 1996, "Performance Improvement Through Indexing of Turbine Airfoils: Part 2—Numerical Simulation," ASME J. Turbomach., **118**, pp. 636–642.

[14] Arnone, A., Marconcini, M., Pacciani, R., Schipani, C., and Spano, E., 2002, "Numerical Investigation of Airfoil Clocking in a Three-Stage Low-Pressure Turbine," ASME J. Turbomach., **124**, pp. 61–68.

[15] Bohn, D., Ren, J., and Sell, M., 2005, "Influence of Stator Clocking on the Unsteady Three-Dimensional flow in a Two-Stage Turbine," ASME J. Tur-bomach., **127**, pp. 156–163.

[16] Marconcini, M. and Pacciani, R., 2003, "Numerical Investigation of Wake-Shock Interactions and Clocking in a Transonic HP Turbine," ASME Paper No. GT2003–38401.

[17] Haldeman, C. W., Dunn, M., Barter, J. W., Green, B. R., and Bergholz, R. F., 2005, "Experimental Investigation of Vane Clocking in a One and One-Half Stage High Pressure Turbine," ASME J. Turbomach., **127**, pp. 512–521.

[18] Barankiewicz, W. S. and Hathaway, M. D., 1997, "Effects of Stator Indexing on Performance in a Low Speed Multistage Axial Compressor," ASME Paper No. 97-GT-496.

[19] Gundy-Burlet, K. L., and Dorney, D. J., 1997, "Physics of Airfoil Clocking in Axial Compressors," ASME Paper No. 97-GT-444.

[20] Dorney, D. J., Sharma, O. P., and Gundy-Burlet, K. L., 1998, "Physics of Airfoil Clocking in a High-Speed Axial Compressor," ASME Paper No. 98-GT-82.

[21] Saren, V. E., Savin, N. M., Dorney, D. J., and Zacharias, R. M., 1997, "Experimental and Numerical Investigation of Unsteady Rotor-Stator Interaction on Axial Compressor Stage (With IGV) Performance," *Unsteady Aerodynamics and Aeroelasticity of Turbomachines*, Proceedings of the Eighth International Symposium, Stockholm, Sweden, Sept. 14–18, pp. 407–424.

[22] Key, N. L., Lawless, P. B., and Fleeter, S., 2008, "An Investigation of the Flow Physics of Vane Clocking Using Unsteady Measurements," ASME Paper No. GT2008–51091.

[23] Fulayter, R. D., 2004, "An Experimental Investigation of Resonant Response of Mistuned Fan and Compressor Rotors Utilizing NSMS," Ph.D. thesis, Purdue University, West Lafayette, IN.

[24] Kerrebrock, J. L., and Mikolajczak, A. A., 1970, "Intra-Stator Transport of Rotor Wakes and Its Effect on Compressor Performance," ASME J. Eng. Power, **92**, pp. 359–368.

O. Schennach

J. Woisetschläger
e-mail: jakob.woisetschlaeger@tugraz.at

Institute for Thermal Turbomachinery and
Machine Dynamics,
Graz University of Technology,
8010 Graz, Austria

B. Paradiso

G. Persico

P. Gaetani
e-mail: paolo.gaetani@polimi.it

Laboratorio di Fluidodinamica delle Macchine,
Dipartimento di Energia,
Politecnico di Milano,
Milano 20156, Italy

Three Dimensional Clocking Effects in a One and a Half Stage Transonic Turbine

This paper presents an experimental investigation of the flow field in a high-pressure transonic turbine with a downstream vane row (1.5 stage machine) concerning the airfoil indexing. The objective is a detailed analysis of the three-dimensional aerodynamics of the second vane for different clocking positions. To give an overview of the time-averaged flow field, five-hole probe measurements were performed upstream and downstream of the second stator. Furthermore in these planes additional unsteady measurements were carried out with laser Doppler velocimetry in order to record rotor phase-resolved velocity, flow angle, and turbulence distributions at two different clocking positions. In the planes upstream of the second vane, the time-resolved pressure field has been measured by means of a fast response aerodynamic pressure probe. This paper shows that the secondary flows of the second vane are significantly modified by the different clocking positions, in connection with the first vane modulation of the rotor secondary flows. An analysis of the performance of the second vane is also carried out, and a 0.6% variation in the second vane loss coefficient has been recorded among the different clocking positions.
[DOI: 10.1115/1.3072715]

1 Introduction

The objective of reduced costs and the continuous increase in the maximum combustion chamber exit temperature lead to turbine stages with high-pressure (HP) ratios and transonic conditions. To increase the efficiency of the high-pressure turbine, a detailed analysis of the unsteady flow is required, taking into account both the vane-rotor interaction and vane-vane/rotor-rotor clocking effects.

The basic idea of clocking is to improve the overall efficiency by varying the circumferential and/or the axial position of adjacent vanes or blades. The most common method is to rotate the nozzle ring with respect to a downstream vane row; as widely known from the available literature, the largest efficiency variation is obtained with equal blade counts. Moreover, it is well known that the maximum of efficiency is achieved when the segments of the first vane wake, released by the rotor, impinge on the leading edge of the second vane [1].

In low-pressure (LP) turbines the clocking is directly linked to the wakes, while in transonic HP turbines the effect is mainly related to the interaction of the total pressure and total temperature fields downstream of the first stage with the second stator. The flow field downstream of the rotor is nonuniform in the circumferential direction due to the trailing edge shocks and the secondary flows of the first vane; wakes have little effects compared with others flow structures [2].

The influence of the first vane shock on the rotor aerodynamics has been investigated by a number of authors. Significant static pressure oscillations on the rotor suction side were observed as a consequence of the shock interaction with the rotor blade that causes rotor loading fluctuations. Dénos and Paniagua [3] isolated the effects of the potential field of the vane on the total pressure distribution downstream of the stage. Gadea et al. [4] investigated the influence of clocking on the time-resolved pressure field of a second vane tested in a 1.5 stage HP turbine. In this work, it was

shown how the optimum clocking position for aerodynamics did not minimize the unsteady force. However Haldeman et al. [5] observed in a HP turbine a decrease in the envelope size of the static pressure for the optimum aerodynamic clocking position.

In low aspect ratio turbine stages, the stator secondary flow–rotor blade interaction represents an important unsteady effect. The transport of the incoming vortices inside the rotor channel and their interaction with the rotor secondary flows were discussed in Chaluvadi et al. [6]. Sharma et al. [7] observed a dramatic influence of the very strong rotor vortices on the second stator aerodynamics, resulting in a completely altered second stator secondary field.

Recently the clocking effects driven by the first stator secondary vortices have been studied in detail in a multistage subsonic turbine [8]. The goal of the present paper is to study the three-dimensional character of clocking by means of a detailed analysis of the unsteady flow in a transonic turbine stage.

2 Experimental Setup

The measurement campaign was carried out in the continuously operating transonic test turbine facility at Graz University of Technology. Some aspects of the test rig are reported in Table 1 (see Schennach et al. [9] for more details). The meridional section of the turbine stage is given in Fig. 1, together with the measurement planes and the clocking positions. The second vane has a simple cylindrical contour and was designed as a low-pressure vane to prevent condensation. The relative pitchwise position of the first and second stator can be changed in order to investigate stator-stator clocking effects. The clearance between the rotor blade tip and the casing as well as the one of the second vane to the hub are 1 mm.

Time-resolved flow velocity measurements were performed by means of laser Doppler velocimetry (LDV) in planes C2 and D1 (see Fig. 1). A detailed description of the optical setup and the measurement uncertainty is given in Schennach et al. [10] where a maximum error in velocity is shown to vary between 0.5% in the freestream and 5% in the wakes. Phase-resolved aerodynamic measurements were performed by means of a fast response aerodynamic pressure probe (FRAPP) (see Persico et al. [11] for more details) in planes C1 and C2. The probe aerodynamic accuracy

Table 1 Stage geometrical data and operating conditions

First vane/rotor/second vane number of blades	24/36/24
First vane/rotor/second vane chord (midspan) (mm)	78.9/55.9/88.3
First vane/rotor/second vane axial chord (midspan) (mm)	56.1/46.8/80.1
First vane/rotor/second vane geometric turning angle (deg)	70/107/53
First vane/rotor/second vane exit aspect ratio	0.70/1.24/0.88
Rotor/second vane tip clearance/span (%)	1.4/1.3
First vane–blade spacing (% nozzle axial chord)	47
Blade–second vane spacing (% blade axial chord)	73
Stage and overall pressure ratio	3.30–4.27
Rotational speed (rpm)	10600
Inlet total temperature (K)	413
Reynolds number nozzle guide vane exit	2.57×10^6
Reynolds number rotor blade exit	1.69×10^6
Isentropic first vane exit Mach number at midspan	1.13
Relative blade outlet Mach number at midspan	0.87
Flow coefficient at rotor exit midspan (V_{axial}/u)	0.65
Loading factor ($\Delta h / u^2$)	1.51

Table 2 FHP measurement uncertainties

α (deg)	+0.25	−0.08
ψ (deg)	+0.6	−0.3
Pt (mbar)	+1	−1
P (mbar)	+1	−1
Cpt	+0.001	−0.001
Cps	+0.001	−0.001
Y	+0.003	−0.003

measurements (95% confidence interval) related to the probe calibration, to the systematic error of the PSI Modules, and to the random errors.

3 Second Stator Inlet Flow Field

As described in Paradiso et al. [12], in the vane-rotor interaction analysis the most relevant unsteady phenomena are induced by the first vane shock. The presence of such a strong shock leads to a sudden increase in the rotor expansion ratio and a reduction in the rotor incidence angle. As a consequence, strong fluctuations of the rotor trailing edge shocks and of the rotor secondary flows were observed at the rotor exit (plane C1), mainly in the hub region.

In this section the streamwise development of the above mentioned structures and their interaction with the potential field of the second vane are studied. Prior to develop the multistage analysis, the evolution of the main 3D flow structures in plane C1 in the absolute frame is briefly reported. Then the time-averaged flow field in planes C1 and C2 is described, putting in evidence the main difference related to the two clocking positions under analysis. Finally phase-resolved FRAPP and LDV measurements will be presented in plane C2.

It is interesting to note that the flow field in C1 can be considered as the far field upstream of the second vane since the second vane potential field is almost completely decayed. As a consequence, some considerations on the clocking effect can be done on the basis of the analysis of this plane.

3.1 Rotor Exit Unsteady Flow Field. When the vane-vane and rotor–second stator interactions are of concern, the evolution of the flow field in the absolute frame is required for a proficient discussion. In Fig. 2 two instants of the unsteady flow field in plane C1 in the absolute frame are reported. It should be noted that in this frame the reference time span is the rotor blade passing period.

At t/RBPP=0.00 three rotor wakes are recognized at $\theta/\Delta\theta$ =0.1, 0.8, and 1.5, as clearly indicated by the thin regions of low Cpt_R all along the span. Focusing on the evolution of the flow field around the wake placed at $\theta/\Delta\theta$=0.8 at t/RBPP=0.00 (dashed line in Fig. 2), the shock surface is mainly radial and is placed at $\theta/\Delta\theta$=1.1 (dotted line in Fig. 2). As already discussed in Paradiso et al. [12], the maximum shock strength and the minimum secondary flow magnitude are found on this blade at this instant. As time proceeds, the wake and the shock of the rotor are shifted in the positive pitchwise direction, experiencing a dynamic evolution as a consequence of the vane-rotor interaction. As a consequence, the shock moves and weakens to become evanescent at $\theta/\Delta\theta$=1.6 for t/RBPP=0.75.

On the contrary the wake, placed at $\theta/\Delta\theta$=0.8 for t/RBPP=0, tends to progressively enlarge in the hub region, resulting in a wide loss core placed around $\theta/\Delta\theta$=1.35 at 25% span for t/RBPP=0.75; this phenomenon is linked to the growing of the rotor hub passage vortex placed in the range $\theta/\Delta\theta$=1.2–1.6 for t/RBPP=0.75.

It is now evident that the vane-rotor interaction effects result in space as well as time periodicity in the absolute frame. As a consequence in a one and a half stage, the second stator leading edge will differently interact with the rotor shocks or vortical structures

was evaluated in a calibrated nozzle, resulting in an extended uncertainty equal to ±0.5% of the dynamic head for the pressure measurements and equal to ±0.3 deg for the flow angle. Additionally time-averaged pneumatic measurements were performed with a conventional five-hole probe (FHP) in planes C1, C1.5, C2, and D1. The different circumferential positions on the measurement traverses were achieved by rotating both the stators, while probes and the LDV head were kept in a fixed position.

LDV and FRAPP measurements were performed for two clocking positions (CP1 and CP6); each LDV measurement plane consists of 20 measurement positions in the circumferential direction and approximately nine positions in the radial direction. The FRAPP measurement grid consists of 20 points in the circumferential direction and 17 points in the radial direction.

Steady flow measurements were performed by a FHP, developed at IST. RWTH Aachen (probe head diameter of 2.5 mm with a thermocouple on the probe head). The pressure was measured by a multichannel pressure transducer PSI 9016 with an accuracy of 0.05% of the full scale, and the temperature was recorded with a National Instruments Field Point FP-TC-120 thermocouple input module. The FHP is calibrated for Mach numbers between 0.2 and 0.8, yaw angles of ±20 deg, and pitch angles of ±16 deg. The measurement grid in each plane consists of 20 points in the circumferential direction and 19 points in the radial direction. In each measurement point, the probe was turned along the mean flow direction to minimize the effects of the yaw angle unsteadiness. Table 2 reports the measurement uncertainties of the FHP

Fig. 1 Up: meridional section, LDV (ticks) and probe (circles) measurement positions in C2 and D1. Bottom: blade to blade overview with clocking positions.
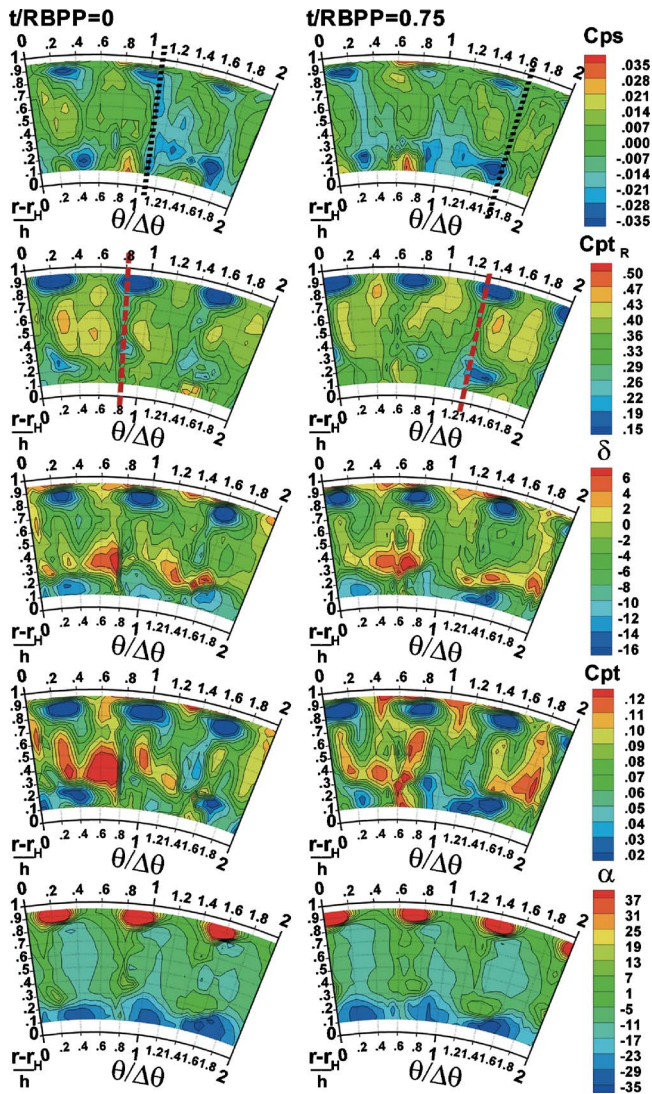
Fig. 2 FRAPP phase-resolved flow field downstream of the rotor in plane C1, absolute frame

depending on its tangential position.

On the basis of the discussion above, the evolution of the absolute quantities is now reported. The α distribution reflects, especially above a 40% span, the one of Cpt_R since low relative velocity regions result in zones of highly tangential absolute flow. In particular, where the relative velocity is extremely low, like in the core of the tip leakage vortex, the maximum α angle is found (up to 70 deg in C1). Similarly the rotor wake is characterized by values of α greater than that in the freestream. As a result the loss core at the tip and the wake periodically reduce the second stator incidence angle.

In the hub region the strong deviation angle gradients due to the hub passage vortex and the weakening of the wake make the former dominate in the composition of the absolute flow angle; the result is a clear trace of the rotor hub passage vortex also in the α angle map. Close to the hub endwall, the wide cross-flow due to the rotor hub passage vortex turns, in the negative direction, the mean absolute flow.

The total pressure map appears similar to that of the δ angle. Above 85% span a region of relatively high Cpt is observed, where the jet leaking through the tip clearance is encountered. In the remaining part of the map, the Cpt distribution is characterized by two loss regions, placed, at t/RBPP=0, for example, around $\theta/\Delta\theta=0.3$ at 80% span and around $\theta/\Delta\theta=0.3$ at 20% span. These

low Cpt regions are related to vortical structures released by the rotor where high shear layers induce relevant losses. Moreover low Cpt regions are found in zones of low axial Mach number; this feature is connected to the negative δ angle regions (i.e., the overturning legs of the rotor vortices) where a very low axial Mach number with respect to the freestream is detected. An opposite conclusion can be drawn for the high total pressure regions, related to the high absolute Mach number in the vortex underturning leg, as already found in Gaetani et al. [13].

Finally, the rotor shock leaves a trace also in the Cpt distribution due to the low absolute Mach number that makes the increase in the static pressure prevail on the reduction in Mach number; this feature is still visible in plane C1 (for example, at t/RBPP =0 at $\theta/\Delta\theta=1.1$), where the shocks have still a significant strength.

3.2 Time Averaged Flow Field. Figure 3 presents the distribution of α, Tt, Cpt, and Cps in planes C1 and C2 for different clocking positions measured by the FHP. Starting from plane C1, a region of high Cpt and Tt levels (marker A) can be observed at $\theta/\Delta\theta=0.6$ and at a blade span of 35%. At the bottom border of this region, low Cps and the highest gradients in the flow angle are visible.

If the rotor flow field were steady in the relative frame (case with no first vane–rotor interaction), a tangentially uniform flow angle distribution would arise from the time average of the rotor secondary flows. In the present case, the first vane–rotor interaction induces a periodic modulation of the rotor hub passage vortex that makes higher gradients appear in and below region A.

The underturning in the region A increases the flow angle and leads to a reduction in the work exchange and, hence, to high total pressure and total temperature. Due to the same mechanism, the increase in the overturning (bottom border of region A) causes low Cpt and Tt. Marker D labels a region of low Cpt, connected to the previous one, that contributes to the clocking effect discussed in plane D1.

These features clarify that the understanding of the rotor exit flow is possible only when unsteady measurements are available; otherwise a misleading vortical region might have been identified. In plane C1 no significant effects induced by the second stator are found in the steady and unsteady measurements.

Region A evolves following the mean flow direction being not significantly influenced by the different clocking position. The mean absolute flow angle distribution can be divided into two regions: the one at the tip characterized by high values related to the dominance of the rotor tip leakage vortex, the one in midspan-hub region where a high overturning is present (as a result of the mean cross-flow activated by the rotor hub passage vortex).

The presence of the second vane has a significant influence in the static pressure field: As the distance between the measuring plane and the second stator leading edge reduces, the effect of the potential field increases, being dominant at C2. The Cps distribution in plane C1 is found to modulate the second stator potential field in plane C2: For CP1 the minimum in plane C1 couples with the potential field, resulting in an increased pressure perturbation in plane C2, while for CP6 it smoothes the second stator effect, reducing the circumferential nonuniformity. It is interesting to note that the effects are appreciable only in the midspan-hub region, while flow at the tip is dominated by the rotor tip leakage flow, as also shown by all the flow quantities.

Moreover, identifying the position of the leading edge of the second vane by the potential field, it can be found that region A enters the second vane passage in the pressure side region for CP6 and in the suction side for CP1; for CP8.5 (not shown for the sake of brevity), region A impinges on the second vane leading edge, while for CP3.5 it enters at midpitch. Because of the dominance of the second stator potential field in C2, the α angle distribution accounts for the distortion of the flow direction around the vane leading edge. Since the static and the total pressure fields interfere in a different way depending on clocking, a slightly higher Mach

Journal of Turbomachinery
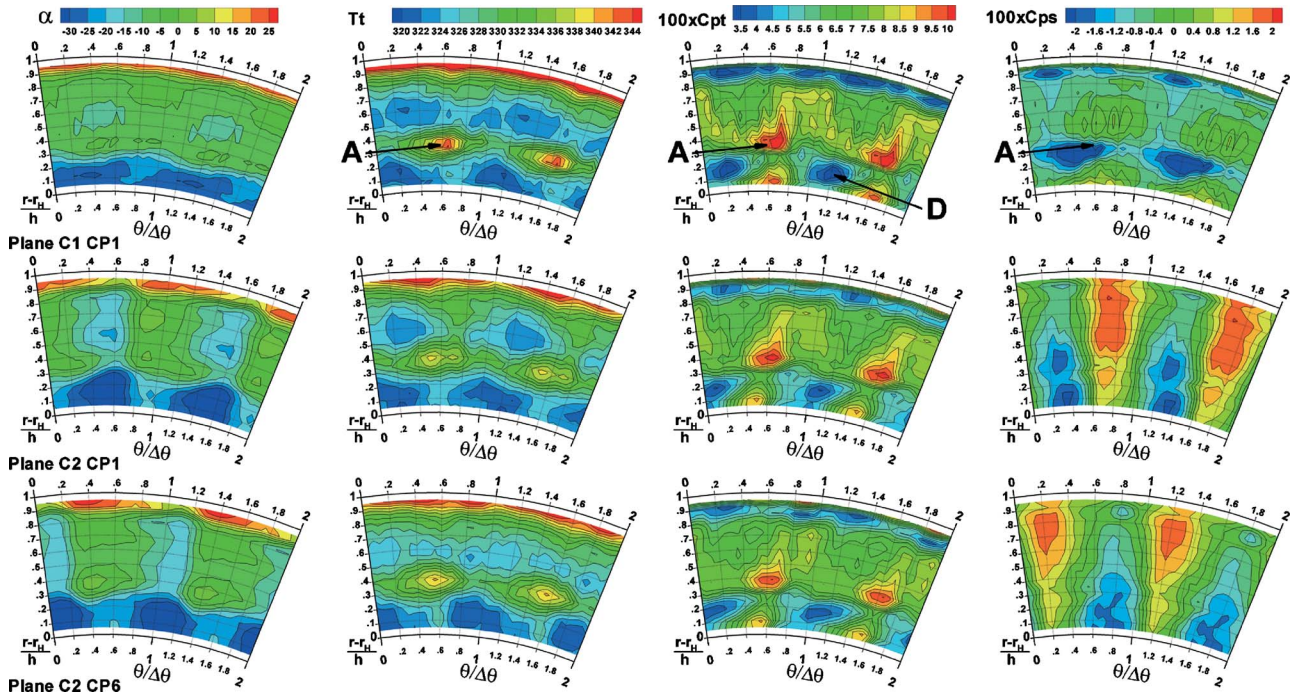
Fig. 3 FHP flow field in planes C1 (CP1) and C2 (CP1–CP6). From left: α, Tt, Cpt, and Cps.

number flow impinges on the blade for CP1 than for CP6. This effect is also highlighted by the intensity of the static pressure field in plane C2, which shows a higher circumferential gradient for CP1 probably due to the higher blade loading.

3.3 Periodic rms. The periodic rms is an estimation of the amplitude of the periodic fluctuations that affect the flow field; this quantity, reported in Fig. 4, is defined according to the following expression for a general phase-resolved variable f (with f_{TM} the time-mean value, N the number of instants, and φ the phase):

$$
\mathrm{rms}_f\left(\frac{\theta}{\Delta\theta}, \frac{r-r_h}{h}\right)
$$

$$
= \sqrt{\frac{\sum_{\varphi=1}^{N}\left(f\left(\varphi, \frac{\theta}{\Delta\theta}, \frac{r-r_h}{h}\right) - f_{TM}\left(\frac{\theta}{\Delta\theta}, \frac{r-r_h}{h}\right)\right)^2}{N}}
$$

At the exit of a single stage, in the absence of vane-rotor interaction effects, the distribution of rms would appear as a succession

Fig. 4 rms from FRAPP: Cpt, α, and Cps in plane C2 for CP1 (up) and CP6 (down)

Fig. 5   FRAPP phase-resolved flow field in plane C2 for clocking position CP1. From left: Cps, Cpt, α angle, and TKE.
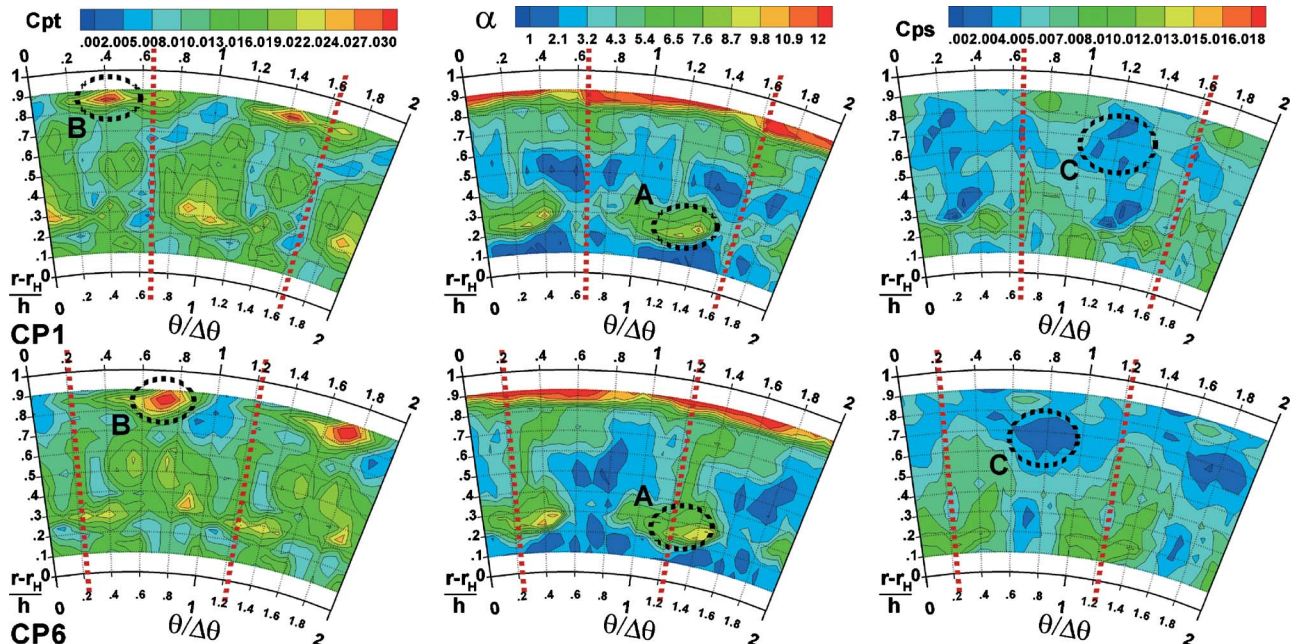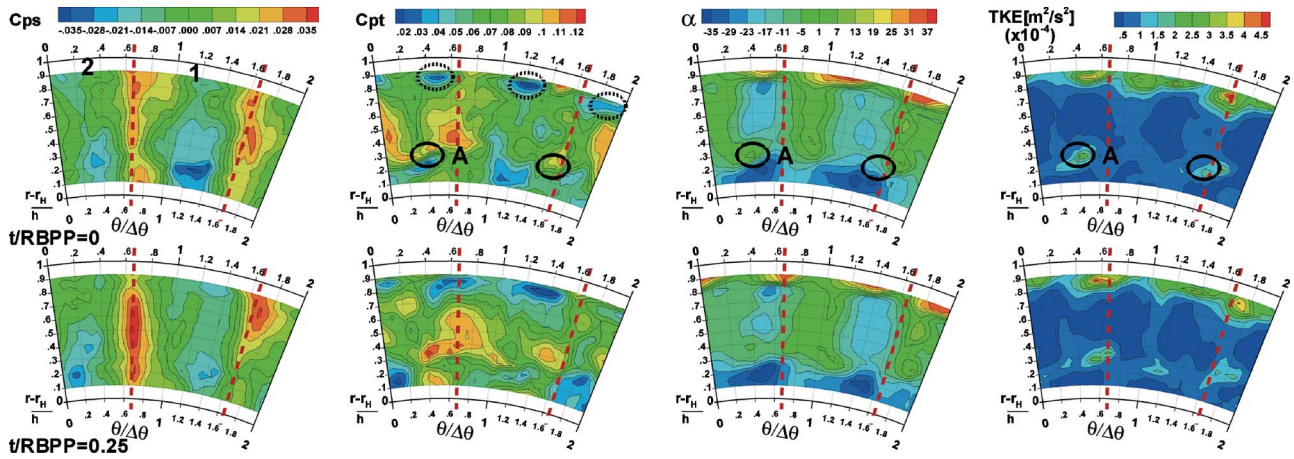
of circumferential strips with only radial gradients. Therefore any pitchwise-periodic feature in these maps marks the modulation of the rotor exit unsteadiness induced by the upstream stator. When a second stator is added downstream of the rotor, another source of unsteadiness (and hence periodic rms) may arise; in particular, the structures that keep the same position independently of the second stator are markers of the first vane-rotor interaction, while the structures that change according to the second stator position are linked to the rotor–second vane interaction.

In Fig. 4, the two clocking positions evidence some relevant differences and significant features characterized by the periodicity of the stator pitch. In particular, the two clocking positions show high rms of Cpt and α in the tip region (marked with B), but at a different circumferential position, displaced according to the second stator. In both cases the rms peak is shifted by 30% of the pitch with respect to the leading edge on the second vane suction side. Since the flow structures depending on the first stator are roughly at the same circumferential position, this feature is related to the interaction of the rotor tip leakage, characterized by a highly positive α angle, with the second vane potential field.

The rms of Cpt in the midspan-hub region does not show well defined structures; however the position of the high rms region changes with the airfoil indexing, suggesting a higher dependence on the second vane position rather than on the first vane flow field.

The rms of the flow angle in the midspan region shows a radial trace at $\theta/\Delta\theta=0.3$ characterized by high values not influenced by the second vane position. Also in the hub region the rms is independent of the second vane but evidences a region of high value at

30% of the blade span and at $0.8<\theta/\Delta\theta<1.5$. This region, roughly in the same position of region A (Fig. 3), is mainly related to the periodic fluctuation of the rotor passage vortex induced by the first vane shock.

The rms of Cps shows a first stator dependant structure at the margin of region A and generally medium levels on the whole plane. It is interesting to note that the tip region is characterized by minima whose position depends on the second vane position (marker C).

3.4   Phase-Resolved Flow Field. In this section the unsteady coupling between the rotor exit structures and the potential field of the second stator (CP1 and CP6) is discussed for two different clocking positions. Two different instants (t/RBPP=0 and t/RBPP=0.25) are reported in the following: Due to the time-space periodicity, the evolution in time of the flow field allows to have a complete representation of the rotor blade period only presenting these two instants. Channel 1 in Fig. 5 experiences, in the second half of the period, the same evolution of channel 2 in the first half of the period.

As the potential field of the vane propagates upstream, the increase in Cps over the span represents a marker of the downstream vane position, marked in Figs. 5 and 6 by a dashed line. In this plane the influence of the second stator pressure field strongly modulates the pitchwise variations in the static pressure. The rotor wakes, clearly visible in plane C1 (see α and Cpt in Fig. 2), are distorted and spread over the pitch; these structures are convected from the rotor exit to plane C2 following the mean absolute flow
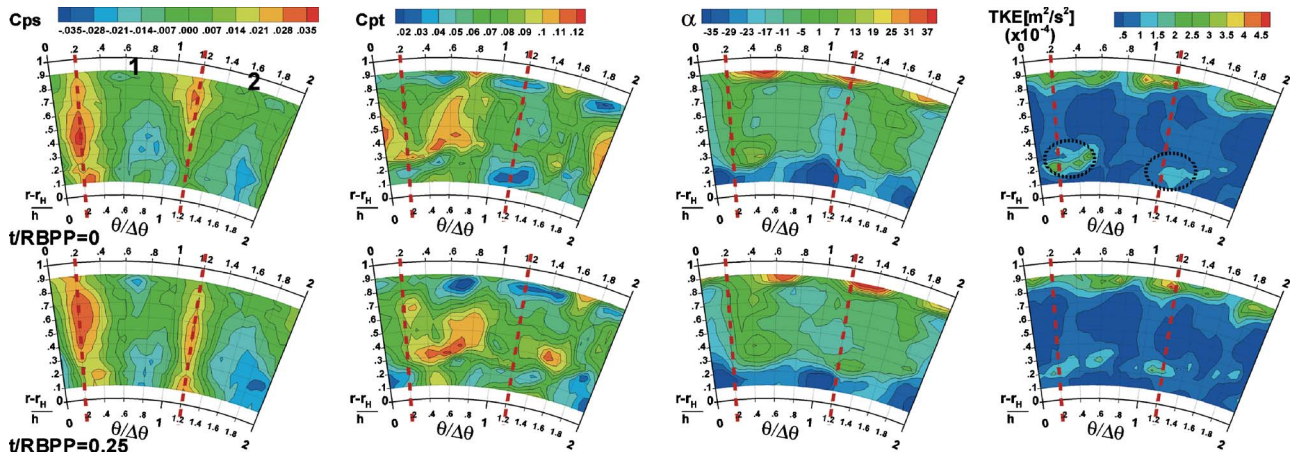

Fig. 6   FRAPP phase-resolved flow field in plane C2 for clocking position CP6. From left: Cps, Cpt, α angle, and TKE.

Journal of Turbomachinery

direction that is almost axial. The shock propagates downstream with an angle of about 20–30 deg interacting with the wake just upstream of the second vane.

In plane C1 at t/RBPP=0 a relatively strong shock is observed on the rotor SS; in plane C2 this shock is hard to identify. The potential field at the rotor exit interacts with the one of the second stator, modulating the static pressure field in plane C2.

Focusing on CP1 and looking first at Cpt, the tip region is dominated by the rotor periodicity (three peaks on two stator passages); related to the same peak regions, high α gradients are found, as already discussed in C1. Differently from C1 where the regions of low Cpt were very similar in terms of dimension and magnitude, in C2 the minima are different (see the dotted circles at t/RBPP=0) being correlated with different α gradients whose intensity has been modified by the second stator potential field.

Focusing on the midspan/hub region, α and Cpt show a change in the spatial periodicity and acquire the stator periodicity as the potential field has become dominant over the rotor structures. Moreover a detailed analysis of Cpt and α shows a strong modulation of the rotor hub passage vortex, identified in plane C1 on the basis of the deviation angle map, due to its periodic generation mechanism and to the interaction with the second vane. In particular, as evidenced at t/RBPP=0 by the regions of high α and Cpt gradients (marker of vortex cores as already discussed), the periodic evolution of the vortex makes it appear stronger in the channel on the left ($0<\theta/\Delta\theta<1$) than in that on the right ($1<\theta/\Delta\theta<2$). Despite the original periodicity is that of the rotor, the vortex magnitude is modulated by the first vane–rotor interaction, resulting in one almost negligible vortex out of three theoretically present. The turbulent kinetic energy (TKE) map supports this interpretation, reaching high values when the vortices are stronger. As time proceeds, the vortex core shifts tangentially: At t/RBPP=0.25 three vortices are present, while at t/RBPP=0 just two are visible. The dynamic of the rotor hub passage vortex makes the high TKE region interact mainly on the SS or leading edge of the second vane; when the vortex has a low magnitude, it enters the vane at midpitch (t/RBPP=0.25 at $\theta/\Delta\theta$=1.1).

Moreover, as reported in Fig. 5, the midspan/hub region centered at $\theta/\Delta\theta$=0.5 shows high total pressure weakly dependent on the different instants, confirming the time-averaged results obtained by means of the five-hole probe at the same measuring plane (region A in Fig. 3).

Changing the clocking position from CP1 to CP6 (see Fig. 6), the tip region presents the same pattern previously commented on, showing a very weak dependence on the second stator. Below midspan the vortex dynamics described for CP1 are present also for this clocking position with a different effect: The center of the strong vortices impinges mainly on the leading edge or on the PS of the blade, as also commented on in time-averaged maps. In agreement with the high frequency response measurements on the blade leading edge at midspan [14], it is observed that all along the blade span (except in the rotor tip leakage region) the static pressure fluctuation is higher for CP1 than for CP6.

In order to achieve a more schematic view of the second vane inlet flow field at different clocking positions, it is useful to divide the flow field and therefore the generalities of the blade row interaction in two distinct zones:

- *midspan-hub interaction region*, where the circumferential variation depends mainly on the first stator trailing edge shock instead of the wakes (see Fig. 2 of the paper of Paradiso et al. [12]). This feature is also visible in the time-averaged flow field, as reported in Fig. 3 at about 25% of the blade span.
- *tip interaction region* where the subsonic exit flow of the first stator and the negligible modulation of the rotor tip leakage lead only to a weak circumferential variation in the flow field downstream of the rotor. Therefore, only a weak potential for improving the performance of the second vane

through the airfoil indexing should be expected in the tip region.

4 Second Stator Outlet Flow Field

This section is devoted to the presentation and discussion of the data acquired by means of FHP and LDV in plane D1; due to geometrical constraints, it was not possible to apply the FRAPP downstream of the second stator. The discussion is introduced by a detailed analysis of the time-averaged flow field for four clocking positions; then, the phase-resolved LDV data are presented to investigate the unsteady features in two out of the four positions. It should be recalled that a clearance at the hub of 1 mm was necessary to allow the rotation of the vane.

4.1 Time Averaged Flow Field. Fig. 7 reports a summary of the time-averaged flow field downstream of the second stator. On the basis of the distribution of the flow angles and in correspondence with a very low Cpt zone, an extremely strong vortical structure was observed in the hub region for all the clocking positions. This highly dissipative vortex (marker E) results from the rolling up of the hub leakage flow.

Moreover, depending on the position of the second vane, a second vortical structure appears in the measuring plane at 25% of the blade span. The sense of rotation, the radial position, and its shift in the tangential direction suggest identifying it as the trace of the periodic vortex core entering the channel and related to region A in plane C2. As previously commented on, the position in plane C2 of this structure is almost independent of the position of the second vane: For CP1 it enters close to the suction side of the channel, for CP3.5 it enters at midpitch, for CP6 it is on the blade PS, while for CP8.5 it impinges on the leading edge. The distribution of TKE, calculated from LDV data acquired for CP1 and CP6 and reported in Fig. 8, supports the conclusion that the structure found in plane D1 at 25% span is dependent on the vorticity field entering the second vane channel. The TKE peak centered at 55% of the blade span on wake SS for CP1 and on wake PS for CP6 evidences the interaction of the incoming vortex with the second vane flow field.

The total pressure contours in the hub region are mainly determined by the hub leakage vortex and second stator wake, but they also reveal a difference in magnitude and extension depending on the clocking position. This feature is related to the upstream flow field, which is characterized by strong pitchwise gradients of the total pressure. In plane C2 an intense total pressure deficit has been found in the hub region, which is always placed at the same circumferential position and therefore enters the second stator channel in different positions with respect to the leading edge for the different clocking configurations. In particular it is placed on the PS of the second stator for CP1, where it is also found in plane D1 (marker D); as the second vane is rotated (toward the left), the total pressure defect displaces along the pitch, as shown by the marker in the figure. This correspondence between the position of the total pressure deficit upstream and downstream of the cascade is due to the low aerodynamic loading of the second stator. Moreover the total pressure loss of the hub leakage vortex is higher for CP1 than for CP6, as well as TKE (Fig. 8). It should be noted that in plane C2 the mean Mach number of the streamlines impinging on the blade is higher for CP1; this leads to a higher stator loading that drives the intensity of the leakage and thus its turbulence (as also shown by the higher potential field reported by Cps in Fig. 3).

The tip region is instead dominated by the tip passage vortex (see the gradients in the radial angle distribution), whose time-averaged intensity is modulated among the different clocking positions by the interaction with the vortex entering the channel and by the blade loading. At CP8.5 and CP1, the vortex seems to be stronger, and its interaction with the blade wake determines higher total pressure losses and TKE intensity. In particular, Fig. 8 shows for CP1 a higher peak in the wake and a second peak, not present in CP6, centered at 75% of the blade span on the wake SS; the
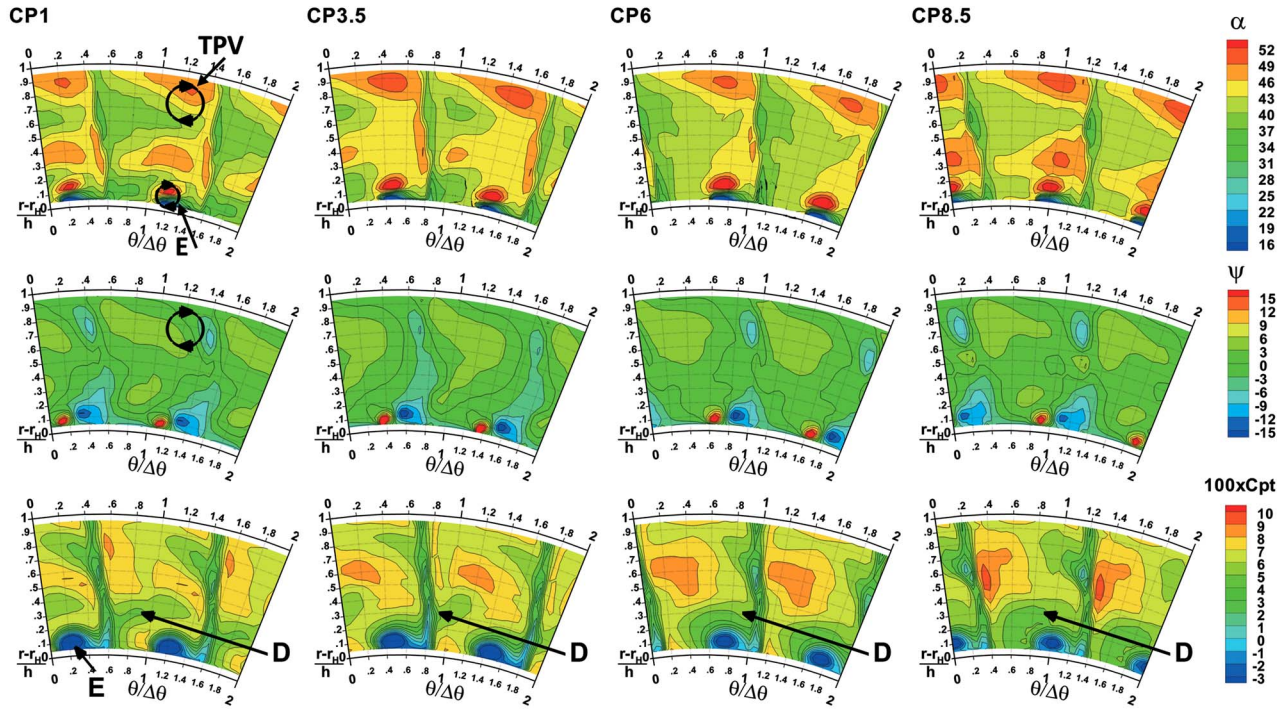
Fig. 7 FHP flow field in planes D1 for CP1, CP3.5, CP6, and CP8.5. From top: α, ψ, and Cpt.

latter structure could be related to the scraping of the high turbulent region, located at the tip and generated by the rotor tip leakage, operated by the stronger stator tip passage vortex. For CP6, the lower intensity of the passage vortex moves only slightly the turbulent region toward the suction side.

4.2 Phase-Resolved Flow Field. To analyze in detail the phase-resolved flow field, it is worthy to start from CP6. As Fig. 9 reports, in this configuration an almost steady flow field is found over the whole measuring plane; the velocity contours show negligible fluctuations in magnitude in the freestream region as well as in the wake. On the contrary the flow angle shows fluctuations in the midspan region on the PS of the wake. The TKE pattern is weakly modulated in the tip region, as a consequence of the blade loading unsteadiness and hence of the tip passage vortex, and in the wake PS where the trace of the interaction of the incoming vortex with the second vane flow field is found. It is interesting to note that for t/RBPP=0 the TKE peak at $\theta/\Delta\theta$=0.2 and 55% of the blade height corresponds to the maximum gradient of α; on the contrary for the adjacent channel, corresponding to the beginning of the second half of the period, a region of uniform flow direction is found in the same position. The modulation of the TKE in that region is related to the fluctuation of the rotor hub passage vortex, as described in planes C1 and C2 (region A).

Moreover the hub leakage vortex is also slightly modulated with an opposite phase with respect to the previous structure; focusing on the wake placed at $\theta/\Delta\theta$=1, a maximum of TKE and velocity defect are found when the α gradient on the PS is minimum. This feature is consistent with the modulation of the blade loading as visible from the Cps map in plane C2, as reported in Figs. 5 and 6.

CP1 shows a much higher unsteadiness on all the measured quantities: The velocity field is modulated in magnitude and direction, and periodic fluctuations of the flow angle occur in the vortex cores (Fig. 10). Also at t/RBPP=0 in the second channel ($0.6 < \theta/\Delta\theta < 1.6$), the high flow velocity in the freestream all along the span is coupled to three regions of intense α gradients: At the tip the region is centered at $\theta/\Delta\theta$=1.2–75% of the blade span and is acknowledged as the tip passage vortex; at midspan the region is placed around $\theta/\Delta\theta$=1.2 and seems to be related to the interaction of the flow field with the incoming vortex; at the hub it is placed at $\theta/\Delta\theta$=1.3 and depends on the very strong hub leakage vortex.

The TKE map shows high peaks in the passage vortex region (also where it interacts with the wake), in the region of the interaction with the incoming vortex, and at the hub leakage flow. As time proceeds, the tip passage vortex evolves in terms of flow angle gradients and TKE: This behavior is related to the periodic fluctuation of blade loading and to the interaction with the rotor tip leakage vortex (corotating with the stator tip passage vortex and periodically chopped by the stator leading edge). Moreover region A (in Fig. 3) seems to enhance the vorticity also in the tip region through a viscous mechanism, its evolution being in phase with the tip passage vortex one (a weaker vortex is found for the adjacent channel). The higher the magnitude of the tip passage vortex, the higher the TKE both in the wake and in the tip region due to the interaction of the vortex with the wake and the endwall turbulent regions. For CP1 the unsteadiness in the rotor hub passage vortex makes the latter reach its maximum strength in a position corresponding to the suction side of the second stator. Therefore, it is likely that the unsteadiness in the second stator secondary flows is amplified.
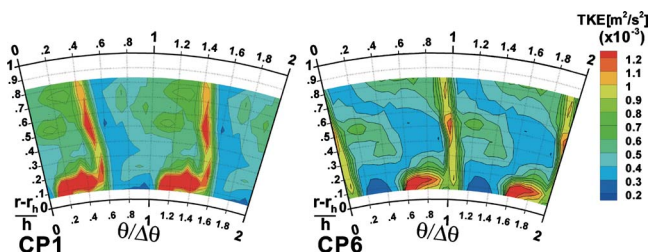

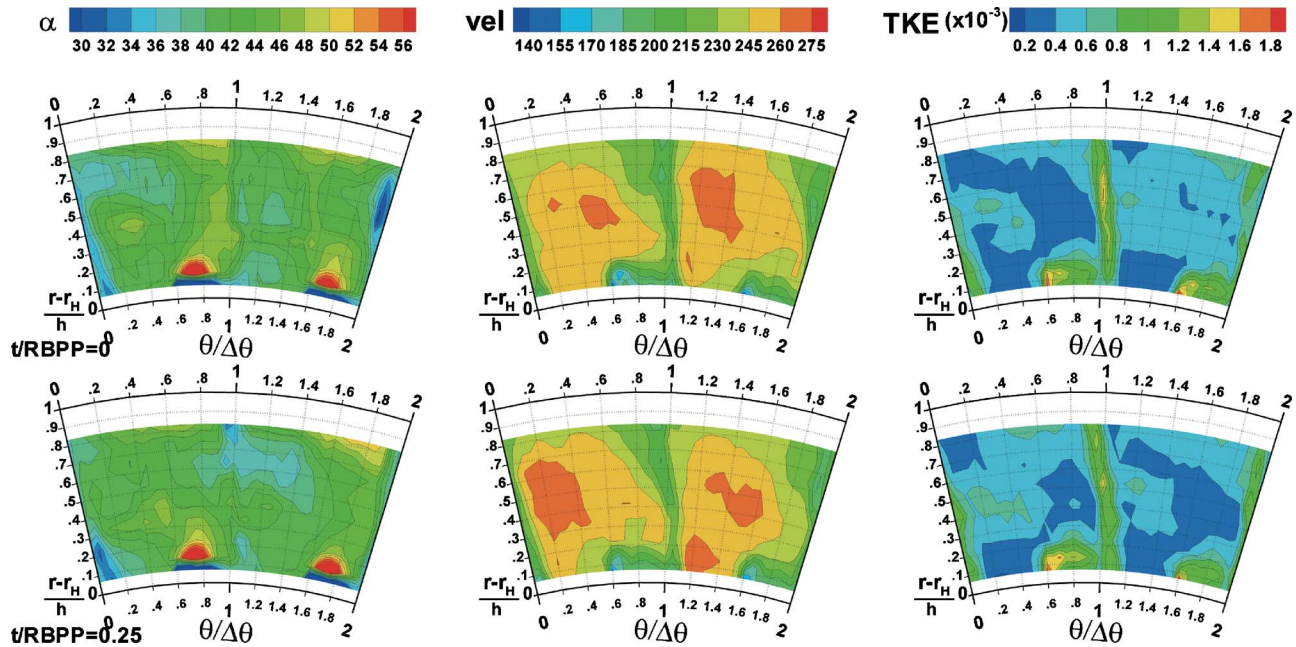**Fig. 8 TKE from LDV data in plane D1**

Fig. 9 LDV phase-resolved flow field in plane D1 for clocking position CP6. From left: α angle, velocity magnitude, and TKE.

The velocity magnitude shows a direct link with the inlet total pressure, being displaced in phase of about $\frac{3}{4}$ of the period; the lower second stator outlet velocity measured in $1 < \theta/\Delta\theta < 2$ at t/RBPP=0.5 seems to correspond to the inlet total pressure field of the instants at t/RBPP=0.75. The maximum TKE in the hub region at the outlet is found at t/RBPP=0.25, and the corresponding peak at the inlet suction side is at t/RBPP=0.5.

As also described in Gaetani et al. [15] for a subsonic turbine stage, the higher the blade loading fluctuation, the higher the fluctuations observed downstream of the blade row. These phenomena, together with the fact that the vortical region A enters the channel close to the blade SS, make the flow in the second vane more unsteady than for CP6.

5 Second Stator Performance

On the basis of the phenomenological discussion presented in Secs. 3 and 4, some general considerations can be drawn by analyzing the pitchwise-averaged second stator loss coefficient and exit flow angle at plane D1 (Fig. 11 together with error bars). The standard definition of the total pressure loss coefficient is used, with reference to an overall averaged value of Pt in plane C2.

Both the clocking positions show high losses at the hub (<20% of the blade span) as a consequence of the strong hub leakage; in particular, CP1 shows higher losses near the endwall, connected to the different incoming flow field.

Moreover CP6 shows a higher overturning on the upper bound-

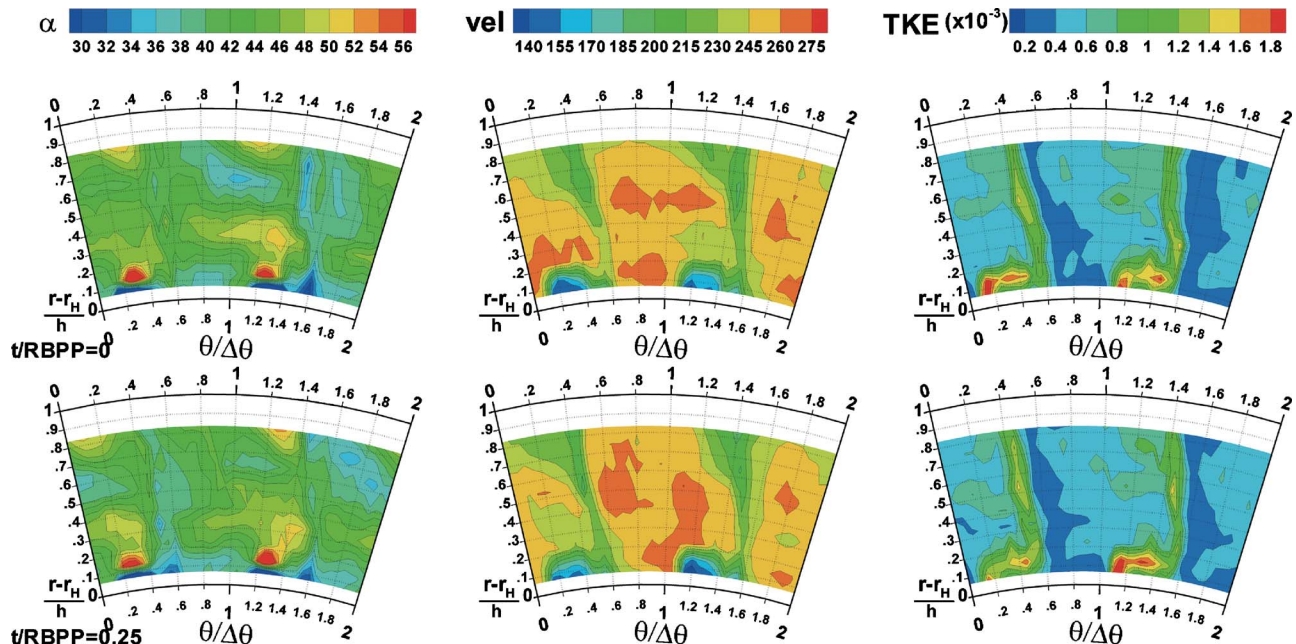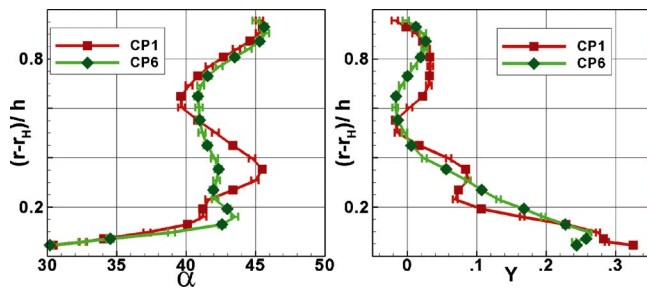**Fig. 10 LDV phase-resolved flow field in plane D1 for clocking position CP1. From left: α angle, velocity magnitude, and TKE.**

011019-8 / Vol. 132, JANUARY 2010 **Transactions of the ASME**

Downloaded 28 May 2010 to 128.113.26.88. Redistribution subject to ASME license or copyright; see http://www.asme.org/terms/Terms_Use.cfm

Fig. 11 Pitchwise-averaged quantities: α angle and pressure loss coefficient Y

ary of the hub leakage (h=15% of blade span) as a consequence of the weaker interaction of the hub leakage with the incoming vortical structure, entered close to the pressure side.

In the region between 20% and 50% of the span, CP1 shows alternatively lower and higher total pressure losses than CP6, which, in turns, shows a regular increasing trend; this behavior is related to the different positions of the incoming vortex (rotor hub passage vortex; see also the lower part of region A in Fig. 3) and of the total pressure deficit (region D in Fig. 3) that interacts in a different way with the hub leakage and with the stator freestream flow.

The third region is located from midspan to the tip, where higher performances are found with respect to the hub as a consequence of the absence of clearance and of the weakness of vane-vane interaction mechanisms. Comparing the two clocking positions in this region, CP6 shows higher performances with respect to CP1, as a consequence of the reduction in the tip passage vortex.

In quantitative terms, the configuration CP6 evidences a second stator total pressure loss (Y) reduction of about 0.6% with respect to CP1; smoother total pressure and flow angle profiles downstream of the second stator are also observed, which are going to minimize the mixing losses downstream of the measuring section. CP1 proves to be the worst configuration tested: Differences between CP6, CP3.5, and CP8.5 are inside of the uncertainty band.

The effect of clocking on the spanwise total to total efficiency is reported in Schennach et al. [9] and supports these observations. The largest efficiency variation due to the clocking was observed in the hub region, caused by the interaction of the modulated rotor hub passage vortex with the vortex system of the second vane.

6 Conclusions

In this paper the three-dimensional unsteady aerodynamics of a one and a half stage transonic turbine have been investigated. The modulation of the second vane aerodynamics operated by the first vane–rotor interaction effects has been studied. After a brief review of the unsteady rotor exit flow field (described in detail in Paradiso et al. [12]), the streamwise evolution of the flow field downstream of the first stage has been studied on a time-averaged basis. The mixing process of the rotor exit viscous structures as well as the growth of the second stator potential field have been discussed. On the measurement plane closest to the second stator leading edge, the time-averaged information has been coupled by a detailed analysis of the unsteady flow field. This approach has evidenced that the highly unsteady rotor hub passage vortex interacts with the second stator in different ways depending on the indexing; in particular, for CP1 this vortex reaches its maximum magnitude when entering the second vane channel close to the suction side of the airfoil, while for CP6 this occurs when entering close to the airfoil pressure side.

The effects of these different rotor–second vane interaction mechanisms on the aerodynamics of the second stator have been investigated, both in terms of time-averaged and phase-resolved quantities. Different steady and unsteady flow features have been observed downstream of the second vane in terms of secondary flows, wake, and hub leakage flow. The link between the incoming three-dimensional flow features and the second vane secondary vortices has been discussed, and the main clocking effects of these different rotor–second vane interaction mechanisms on the aero-dynamics of the second stator have been investigated both in terms of time-averaged and phase-resolved quantities. Different steady and unsteady flow features have been observed downstream of the second vane in terms of secondary flows, wake, and hub leakage flow. The main clocking effects were isolated in two distinct zones: the region below midspan, where the main vortex-vortex phenomena are found, although partially overshadowed by the hub leakage; and the tip region characterized only by a modulation of the tip passage vortex magnitude. As a general conclusion, the strong incoming vortex is observed to produce more relevant effects when entering close to the suction side of the second vane (CP1).

These mechanisms also produce detrimental effects on the second stator performance; an increase in total pressure loss of about 0.6% has been found for CP1 with respect to the other clocking positions. This is also going to modify the aerodynamics of a possible second rotor, which would work under more uniform inlet conditions for CP6. Moreover, on the basis of the analysis of the flow upstream of the second stator, the midspan-hub region was found to have the most potential for a performance improvement thanks to airfoil indexing, due to the stronger effect of the first stator shock.

Nomenclature

FRAPP	=	fast response aerodynamic pressure probe
FHP	=	five hole probe
LDV	=	laser Doppler velocimetry
HP	=	high pressure
LP	=	low pressure
Ps	=	static pressure (bar)
Pt	=	total pressure (bar)
Tt	=	total temperature (K)
Pref	=	downstream reference pressure (bar)
Ptm	=	stage upstream total pressure (bar)
$Cps=(Ps-Pref)/$ $(Ptm-Pref)$	=	static pressure coefficient
$Cpt=(Pt-Pref)/$ $(Ptm-Pref)$	=	total pressure coefficient
$y=(\overline{\overline{Pt_{C2}}}-\overline{\overline{Pt_{D1}}})/$ $(\overline{\overline{Pt_{C2}}}-\overline{Ps_{D1}})$	=	second stator loss coefficient
TPV	=	tip passage vortex
α	=	blade to blade absolute flow angle (positive in the peripheral direction) (deg)
δ	=	rotor deviation angle (deg)
Ψ	=	radial flow angle (positive in the radial outward direction) (deg)
RBPP	=	rotor blade passing period (s)
TKE	=	turbulent kinetic energy (m²/s²)
CP	=	clocking position
PS/SS	=	pressure/suction side of the blade
$\theta, \Delta\theta$	=	tangential coordinate, stator pitch
$(r-r_H)/h$	=	nondimensional blade height

Subscripts

R	=	rotor, relative

Superscripts

$-$ = pitchwise average

$=$ = pitchwise and spanwise average

References

[1] Huber, F. W., Johnson, P. D., Sharma, O. P., Staubach, J. B., and Gaddis, S. W., 1996, "Performance Improvement Through Indexing of Turbine Airfoils: Part 1—Experimental Investigation," ASME J. Turbomach., **118**, pp. 630–635.

[2] Miller, R. J., Moss, R. W., Ainsworth, R. W., and Harvey, N. W., 2003, "Wake, Shock, and Potential Field Interactions in a 1.5 Stage Turbine—Part I: Vane-Rotor and Rotor-Vane Interaction," ASME J. Turbomach., **125**(1), pp. 33–39.

[3] Dénos, R., and Paniagua, G., 2005, "Effect of Vane-Rotor Interaction on the Unsteady Flowfield Downstream of a Transonic HP Turbine," Proc. Inst. Mech. Eng., Part A: J. of Power and Energy, **219**, pp. 431–442.

[4] Gadea, J., Dénos, R., Paniagua, G., Billiard, N., and Sieverding, C. H., 2004, "Effect of Clocking on the Second Stator Pressure Field of a One and a Half Stage Transonic Turbine," ASME Paper No. 2004-GT-53463.

[5] Haldeman, C. W., Dunn, M., Barter, J. W., Green, B. R., and Bergholz, R. F., 2005, "Experimental Investigation of Vane Clocking in a One and One-Half Stage High Pressure Turbine," ASME J. Turbomach., **127**(3), pp. 512–521.

[6] Chaluvadi, V. S. P., Kalfas, A. I., Benieghbal, M. R., Hodson, H. P., and Denton, J. D., 2001, "Blade-Row Interaction in a High-Pressure Turbine," J. Propul. Power, **17**, pp. 892–901.

[7] Sharma, O. P., Pickett, G. F., and Ni, R. H., 1992, "Assessment of Unsteady Flows in Turbines," ASME J. Turbomach., **114**, pp. 79–90.

[8] Behr, T., Kalfas, A. I., and Abhari, R. S., 2007, "Stator-Clocking Effects on the Unsteady Interaction of Secondary Flows in a 1.5-Stage Unshrouded Turbine," Proc. Inst. Mech. Eng., Part A, **221**, pp. 779–792.

[9] Schennach, O., Woisetschläger, J., Fuchs, A., Göttlich, E., Marn, A., and Pecnik, R., 2007, "Experimental Investigations of Clocking in a One and a Half Stage Transonic Turbine Using Laser-Doppler-Velocimetry and a Fast Response Aerodynamics Pressure Probe," ASME J. Turbomach., **129**, pp. 372–381.

[10] Schennach, O., Woisetschläger, J., Marn, A., and Göttlich, E., 2007, "Laser-Doppler-Velocimetry Measurements in a One and a Half Stage Transonic Test Turbine With Different Angular Stator-Stator Positions," Exp. Fluids, **43**, pp. 385–393.

[11] Persico, G., Gaetani, P., and Guardone, A., 2005, "Design and Analysis of New Concept Fast-Response Pressure Probes," Meas. Sci. Technol., **16**, pp. 1741–1750.

[12] Paradiso, B., Schennach, O., Persico, G., Gaetani, P., Pecnik, R., and Woisetschläger, J., 2008, "Blade Row Interaction in a One and a Half Stage Transonic Turbine Focusing on Three Dimensional Effects: Part I—Stator-Rotor Interaction," ASME Paper No. GT2008-50291.

[13] Gaetani, P., Persico, G., Dossena, V., and Osnaghi, C., 2007, "Investigation of the Flow Field in a High-Pressure Turbine Stage for Two Stator-Rotor Axial Gaps—Part II: Unsteady Flow Field," ASME J. Turbomach., **129**, pp. 580–590.

[14] Schennach, O., Pecnik, R., Paradiso, B., Göttlich, E., Marn, A., and Woisetschläger, J., 2008, "The Effect of Vane Clocking on the Unsteady Flow Field in a One-and-a-Half Stage Transonic Turbine," ASME J. Turbomach., **130**(3), p. 031022.

[15] Gaetani, P., Persico, G., and Osnaghi, C., 2007, "Influence of Rotor Loading on the Unsteady Flowfield Downstream of a HP Turbine Stage," *Proceedings of the Seventh European Turbomachinery Conference*.

Transition Prediction on Turbine Blade Profile With Intermittency Transport Equation

Wladyslaw Piotrowski
GE Oil&Gas EDC,
Warsaw 02-256R, Poland

Witold Elsner

Stanisław Drobniak

Czestochowa University of Technology,
Czestochowa 42-200, Poland

*This paper presents the results of tests and validations of the γ-Re_θ model proposed by Menter et al. (2006, "A Correlation-Based Transition Model Using Local Variables—Part I: Model Formation," ASME J. Turbomach., **128**, pp. 413–422), which was extended by in-house correlations for onset location and transition length. The tests performed were based on experimental data from the flat plate test cases available at the ER-COFTAC database as well as on experimental data from the turbine blade profile investigated at Czestochowa University of Technology. Further on, the model was applied for unsteady calculations of the blade profile test case, where chosen inlet conditions (turbulent intensity and wake parameters) were applied. For the selected case, numerical results were compared not only with the experimental data but also with the results obtained with other transition models. It was shown that the applied model was able to reproduce some essential flow features related to the bypass and wake-induced transition, and the simulations revealed good agreement with the experimental results in terms of localization and extent of wake-induced transition.* [DOI: 10.1115/1.3072716]

Keywords: transition modeling, intermittency, boundary layer, bypass transition, wake-induced transition

1 Introduction

Proper prediction of transition is among the most challenging and important problems in the design of turbomachinery stages. The variety of possible transition mechanisms in turbomachinery flows makes it difficult to propose the general strategy for numerical simulation. Obviously, the best solution for modeling transitional boundary layer would be the application of either detached eddy simulation (DES) or large eddy simulation (LES). LES, unlike DNS, resolves only dynamically important (large) scales, and the effects of unresolved small scales are modeled. However, the application of LES for modeling transition is limited due to the required numerical mesh and resulting high computational time because when approaching the wall, the scales diminish their dimensions so that finer and finer grid is required.

Hence the Reynolds-averaged Navier-Stokes (RANS) methods and, for unsteady calculations, unsteady Reynolds-averaged Navier-Stokes (URANS) with an appropriately modeled transitional boundary layer remain the only available engineering tools to study the transitional flows. It means that it is worth making an effort to improve RANS or URANS modeling approaches especially because of the strong interest of the industry.

The application of existing low-Re turbulence models for laminar-turbulent transition in boundary layers, as reviewed by Savill [1], is a highly empirical procedure, which requires experimental data for proper calibration. It means that no model generates a reliable result for various combinations of Reynolds number, freestream turbulence, and pressure gradient. Additionally, the results are sensitive to initial conditions, boundary conditions, and grid resolution. In these methods usually various experimental correlations are used to determine the onset of transition.

The transition process may be described by the intermittency parameter γ, which gives information about the fraction of time when the flow is turbulent. This is why the coupling with intermittency seems to be the best way to take into account the physical mechanisms of transitional flow and to model transition in a proper way. One of the classical methods for modeling transition based on the intermittency parameter is a model formulated by Dhawan and Narasimha [2].

Recently, some new methods were developed, which rely on the intermittency parameter. The first one is the prescribed unsteady intermittency model (PUIM) developed at Cambridge University [3], which solely relies on empirical correlations. PUIM calculates a distance-time intermittency distribution as a function of space and time (constant in time in the case of steady flow simulation). To have this information PUIM employs a set of correlations for transition onset and for spot production rate. The high quality of this approach was confirmed among the others in T106A [3] and on N3-60 test cases [4]. The above model is used in connection with the linear low-Re Yang and Shih k-ε model. Another approach was proposed by Lardeau and Leschziner [5], where the intermittency based formulation was coupled with low-Re algebraic Reynolds-stress model. From this assumption, it results that this model should return properly all the Reynolds-stress components, which is especially important for the near-wall flows where strong turbulence anisotropy is present. The advantage of this modeling approach is its ability to model the pretransitional rise in turbulence intensity, which was experimentally confirmed, among others, by Elsner et al. [4]. This ability is achieved mainly due to the introduction of parameters modifying dumping functions, which control cross-flow and streamwise variations by taking into account Klebanoff mode properties observed in the pretransitional phase of boundary layer development. The experimental verification of this methodology based mainly on the ERCOFTAC database shows improvement in the prediction of onset transition and its length. Reasonably good results for the unsteady test case of the T106A aeroengine turbine profile with low background turbulence intensity as well as for the N3-60 turbine test case was also obtained for this model [5].

A more general description of intermittency is obtained from a dynamic intermittency convection-diffusion-source equation, which was for the first time applied by Lodefier and Dick [6] at Ghent University, and then a similar treatment of the problem was proposed in the work performed by Menter et al. [7]. According to the first approach, named Lodefier&Dick hereafter, two dynamic

equations for intermittency were proposed: one for near-wall intermittency γ and one for freestream intermittency ζ. The near-wall intermittency γ takes into account the fraction of time when the near-wall velocity fluctuations caused by transition have a turbulent character and tend to zero in the freestream region, while on the wall γ attains unity. The freestream intermittency factor ζ describes the intermittent behavior of turbulent eddies coming from the freestream and impacting into the underlying pseudolaminar boundary layer. This method proved to be an efficient tool for the prediction of wake interaction with the separation bubble and especially for wake interaction with the attached flow [8].

A different strategy was proposed by Menter et al. [7], with only local information being used to activate the production term in the intermittency equation and the link between the correlations and the intermittency equation achieved through the use of the vorticity Reynolds number. The proposed model is based on the shear stress transport (SST) turbulence model and two transport equations. The first one is the intermittency transport equation used to trigger the transition process. The second transport equation for momentum thickness Reynolds number $\mathrm{Re}_{\theta t}$ was implemented in order to avoid nonlocal operations introduced by experimental correlations. Outside the boundary layer, the transport variable was forced to follow the value of $\mathrm{Re}_{\theta t}$ given by correlations.

The paper contains the proposal of extension of the model of Menter et al., which is achieved by in-house correlations on onset location and transition length. The model proposed was named intermittency transport model (ITM), and its performance was tested against the flat plate test cases available at the ERCOFTAC database as well as on experimental data obtained for the turbine blade profile at Czestochowa University of Technology. The calculations have been done with the use of the commercial package FLUENT, where both the SST turbulence model and the transport equations for intermittency and momentum thickness Reynolds number were implemented via user defined functions (UDFs).

2 Model Description

The model proposed in this paper is based on the γ-Re_θ transition model by Menter et al. [7] and the SST turbulence model with a time scale bound according to Medic and Durbin [9]. For the purpose of transition modeling, some modifications were introduced into the turbulence model. The most important one was to express production P_k and destruction terms D_k of the turbulent kinetic energy equation in terms of effective intermittency γ_{eff} as follows:

$$\widetilde{P}_k = \gamma_{\mathrm{eff}} P_k \tag{1}$$

$$\widetilde{D}_k = \min(\max(\gamma_{\mathrm{eff}}, 0.1), 1.0) D_k \tag{2}$$

The effective intermittency was obtained from

$$\gamma_{\mathrm{eff}} = \max(\gamma, \gamma_{\mathrm{sep}}) \tag{3}$$

where γ_{sep} is separation intermittency, which is allowed to grow rapidly above 1 once the boundary layer separates. This should ensure high production rate of turbulent kinetic energy and more physical reattachment. The γ coefficient is calculated from the transport equation. The consecutive modification concerns the blending function F_1, which is responsible for switching between the k-ω and k-ε models. This modification was aimed to ensure that the F_1 function is always equal to 1 in a laminar boundary layer.

The γ-Re_θ model is based on two transport equations, i.e., the intermittency equation used to trigger the transition process and the transport equation of momentum thickness Reynolds number $\mathrm{Re}_{\theta t}$. The intermittency transport equation used to trigger the transition process is formulated as

$$\frac{\partial(\rho \cdot \gamma)}{\partial t} + \frac{\partial(\rho \cdot U_j \cdot \gamma)}{\partial x_j} = P_{\gamma 1} - E_{\gamma 1} + P_{\gamma 2} - E_{\gamma 2}$$
$$+ \frac{\partial}{\partial x_j}\left[\left(\mu + \frac{\mu_t}{\sigma_f}\right)\frac{\partial \gamma}{\partial x_j}\right] \tag{4}$$

where transition sources are defined as

$$P_{\gamma 1} = 2 F_{\mathrm{length}} \cdot \rho \cdot S \cdot [\gamma \cdot F_{\mathrm{onset}}]^{0.5} \tag{5}$$

$$E_{\gamma 1} = P_{\gamma 1} \cdot \gamma \tag{6}$$

and the destruction/relaminarization terms are described as

$$P_{\gamma 2} = 0.06 \rho \Omega \gamma F_{\mathrm{turb}} \tag{7}$$

$$E_{\gamma 2} = 50 P_{\gamma 2} \gamma \tag{8}$$

where S is the strain rate $(2 \cdot S_{ij} S_{ij})^{1/2}$ and Ω is the vorticity magnitude. F_{onset} triggers the intermittency production at the beginning of the transition, and the F_{length} controls the length of the transition zone. The onset function F_{onset} is formulated as a function of critical transition Reynolds number $\mathrm{Re}_{\theta c}$ and vorticity Reynolds number Re_V, i.e., $F_{\mathrm{onset}} = f(\mathrm{Re}_V, \mathrm{Re}_{\theta c})$. Vorticity Reynolds number is calculated locally and defined as

$$\mathrm{Re}_V = \frac{\rho y^2}{\mu}\frac{\partial u}{\partial y} = \frac{\rho y^2}{\mu} S \tag{9}$$

$\mathrm{Re}_{\theta c}$ determines the location where the intermittency starts to increase in the boundary layer, which occurs upstream of the transition Reynolds number $\mathrm{Re}_{\theta t}$. To determine $\mathrm{Re}_{\theta c}$, Menter et al. [7] proposed to tie its value with $\widetilde{\mathrm{Re}}_{\theta t}$, which comes from the transport equation for momentum thickness Reynolds number $\mathrm{Re}_{\theta t}$ according to the relation

$$\mathrm{Re}_{\theta c} = F_P \widetilde{\mathrm{Re}}_{\theta t} \tag{10}$$

where F_P is an unknown function, which was adjusted based on a number of numerical calculations of the flat plate and blade profile cases. The proposed procedure for the estimation of this function together with the correlation for the F_{length} parameter is presented in Sec. 3.

The main requirement for this transition model is that only local quantities can be used, and to resolve this problem the following transport equation for $\mathrm{Re}_{\theta t}$ is used:

$$\frac{\partial(\rho \cdot \widetilde{\mathrm{Re}}_{\theta t})}{\partial t} + \frac{\partial(\rho \cdot U_j \cdot \widetilde{\mathrm{Re}}_{\theta t})}{\partial x_j} = P_{\theta t} + \frac{\partial}{\partial x_j}\left[2(\mu + \mu_t) \cdot \frac{\partial \widetilde{\mathrm{Re}}_{\theta t}}{\partial x_j}\right] \tag{11}$$

where $P_{\theta t}$ is a source term defined as

$$P_{\theta t} = 0.03 \cdot \frac{\rho}{T_c} \cdot (\mathrm{Re}_{\theta t} - \widetilde{\mathrm{Re}}_{\theta t}) \cdot (1.0 - F_{\theta t}) \tag{12}$$

and T_c is a time scale defined as

$$T_c = \frac{500 \mu}{\rho U^2} \tag{13}$$

$F_{\theta t}$ is a blending function used to turn off the source term in the boundary layer and to allow the transported scalar to diffuse from the freestream, while $\mathrm{Re}_{\theta t}$ is a parameter calculated according to empirical correlation defined as

$$\mathrm{Re}_{\theta t} = 803.73 \cdot [\mathrm{Tu} + 0.6067]^{-1.027} \cdot F(\lambda_\theta, K) \tag{14}$$

In the above formula Tu is the local turbulence intensity, while $F(\lambda_\theta, K)$ is a function of the Thwaites pressure gradient λ_θ and the acceleration coefficient K.

The detailed description of the mathematical formulation of the γ-Re_θ model is given in the paper of Menter et al. [7]. All the transport equations for intermittency and momentum thickness Reynolds number as well as for the SST turbulence model were
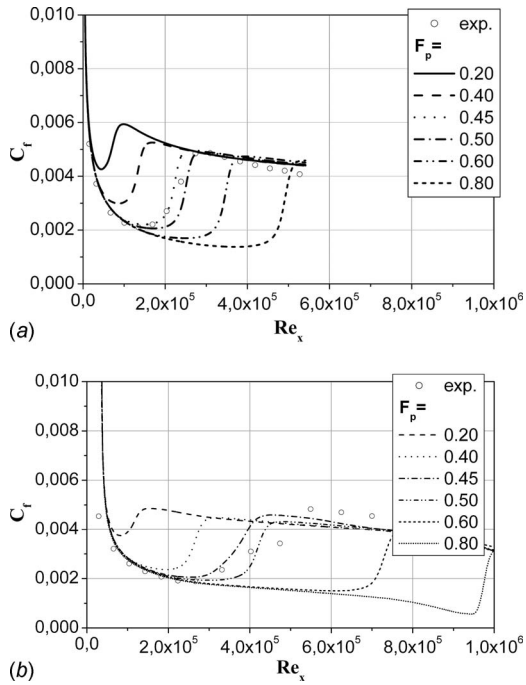
Fig. 1 Influence of F_P parameter on transition onset for (a) T3A and (b) T3C5 test cases

implemented in the commercial package FLUENT with the use of UDFs.

3 Model Refinement

It was stated above that the F_{onset} function plays a key role in the induction of laminar-turbulent transition because it triggers the intermittency production in the γ transport equation. The F_{onset} is determined in terms of the transition Reynolds number $\widetilde{Re}_{\theta t}$ given by Eq. (10), where the unknown function F_P exists. The determination of the F_P function was the first aim of the present investigations, and flat plate ERCOFTAC test cases were used for this study. These test cases, which are commonly used as benchmarks for verification of transitional models, are denoted as T3A, T3B, T3C1, T3C2, T3C3, T3C4, and T3C5. The first two test cases, i.e., T3A and T3B, are characterized by zero pressure gradient flow and the remaining ones by favorable/adverse pressure gradient.

The importance of F_P as the transition model parameter is proved by the results of computations performed for T3A and T3C5 test cases and presented in Fig. 1. The solid lines present the distributions of local friction coefficient C_f for selected values of F_P, while circles denote the experimental results. All these distributions in Fig. 1 were expressed in terms of Re_x, where x is the distance from the leading edge of the plate. One may notice that the increase in the F_P parameter shifts the beginning of l-t transition toward the trailing edge, while the length of the transition zone remains practically unchanged.

Results close to experiment were obtained for $F_P \approx 0.65$ in T3A and for $F_P \approx 0.45$ in T3C5 test cases, which means that F_P is case dependent. It results probably from the relation of F_P with global flow properties. To take into account this fact, it was decided to relate F_P to the value of $\widetilde{Re}_{\theta t}$, which would be treated as characteristic of particular flow cases.

One may expect that $\widetilde{Re}_{\theta t}$ changes along the distance from the leading edge and depends on the local pressure gradient, i.e., increases in the favorable pressure gradient and decreases in the zone of adverse pressure gradient. On the other hand, a much slower rate of increase in $\widetilde{Re}_{\theta t}$ close to the wall in comparison
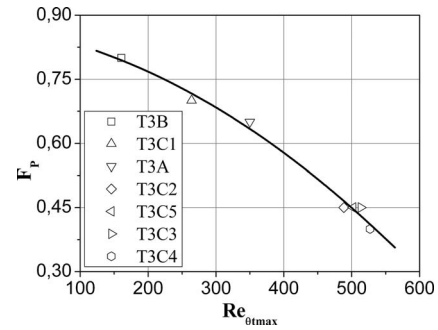
Fig. 2 Evolution of F_P parameter versus $\widetilde{Re}_{\theta t \, max}$

with freestream was reported by Menter et al. [7], which is due to the delay introduced by the $\widetilde{Re}_{\theta t}$ diffusion from the outer flow.

The initiation of l-t transition depends on inner boundary layer parameters, and this is why it was decided to use $\widetilde{Re}_{\theta t}$ values determined at the wall. It is known that l-t transition occurs usually in the zone of adverse pressure gradient, i.e., in the zone behind the maximum value of $\widetilde{Re}_{\theta t}$. Therefore, it seems reasonable to relate the F_P function to the maximum value of $\widetilde{Re}_{\theta t}$ determined in the wall vicinity, i.e., $\widetilde{Re}_{\theta t \, max}$. For all test cases analyzed, the values of $\widetilde{Re}_{\theta t \, max}$ and the corresponding values of F_P have been shown in Fig. 2, together with the approximating line given by the following function:

$$F_P = -1.115 \times 10^{-6} \widetilde{Re}_{\theta t \, max}^2 - 2.8 \times 10^{-4} \widetilde{Re}_{\theta t \, max} + 0.87$$

(15)

One may notice that the above relation approximates well the flow cases with all values of pressure gradient, which allows us to hope for its universal character.
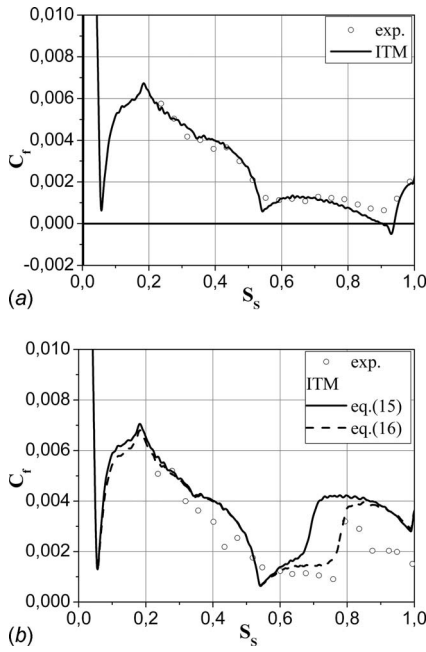
The transition model with the above formula was applied in computing the N3-60 turbine blade test cases with two different inlet turbulence intensities Tu=0.4% (N3-60-0.4) and Tu=4.0% (N3-60-4.0)—the detailed description of these test cases is included in Ref. [10].

Figure 3 presents the distributions of the local friction coefficient C_f obtained for both flow cases; computations (solid lines) are compared here with experimental results for N3-60 test cases (open circles). Considering the C_f distributions computed for the N3-60-4.0 test case (solid line in Fig. 3(b)), one may observe the shift in numerical results with respect to experimental data equal to 0.15 of normalized coordinate S_S toward the leading edge. For the lower Tu value (N3-60-0.4 test case), the origin of l-t transition is located at $S_S \approx 0.92$, which agrees fairly well with experimental data. It means that the correlation for F_P given by Eq. (15) is not adequate for higher values of Tu and $\widetilde{Re}_{\theta t \, max}$ and should further be modified.

In order to obtain a better fit in the wider data range, it was decided to split the analyzed range of $\widetilde{Re}_{\theta t \, max}$ into two subranges, i.e., $\widetilde{Re}_{\theta t \, max} > 525$ and $\widetilde{Re}_{\theta t \, max} \leq 525$. For the first subrange, only a minor modification of the proposed correlation was introduced (see also Eq. (15)). For the second subrange (i.e., $\widetilde{Re}_{\theta t \, max} \leq 525$), the new formula was proposed, and the final shape of the correlation is as follows:

$$\text{if } (\widetilde{Re}_{\theta t \, max} > 525)$$

$$F_P = -6.09 \times 10^{-10} \widetilde{Re}_{\theta t \, max}^3 + 2.05 \times 10^{-6} \widetilde{Re}_{\theta t \, max}^2$$
$$- 0.0023 \widetilde{Re}_{\theta t \, max} + 1.165$$

Fig. 3 Distribution of skin friction C_f on the suction side for (a) N3-60-0.4 (Tu=0.4%) and (b) N3-60-4.0 (Tu=4.0%)

else $F_P = 4.15 \times 10^{-9} \widetilde{\mathrm{Re}}_{\theta t \max}{}^3 - 4.85 \times 10^{-6} \widetilde{\mathrm{Re}}_{\theta t \max}{}^2 + 7.493$

$$\times 10^{-4} \widetilde{\mathrm{Re}}_{\theta t \max} + 0.773 \qquad (16)$$

The new function is presented in Fig. 4 for the entire range of $\widetilde{\mathrm{Re}}_{\theta t \max}$. One should keep in mind that the shape of F_P in the range of $\widetilde{\mathrm{Re}}_{\theta t \max} > 525$ was determined based on a rather small number of data, so it may not be as reliable as the one proposed for $\widetilde{\mathrm{Re}}_{\theta t \max} \le 525$. The C_f distribution for the N3-60-4.0 test case obtained with the new correlation is presented in Fig. 3(b) as the dashed line. The much better agreement with the experimental data may easily be noticed in the entire range of $\widetilde{\mathrm{Re}}_{\theta t \max}$.

The second aim which was realized during the present study was the development of correlation for the length of the transition, i.e., the F_{length} function. To have a more universal formulation, it was decided that the F_{length} function should be dependent on the inlet turbulence intensity and the pressure gradient.

Tests concerning the influence of the F_{length} parameter on the solution obtained for the boundary layer were performed for T3A ($dP/dx=0$) and T3C1 ($dP/dx \ne 0$) test cases. During these tests, the F_{length} parameter was varied within the range of 0.1–10, while the onset of l-t transition was determined according to the correlation given by Eq. (16).
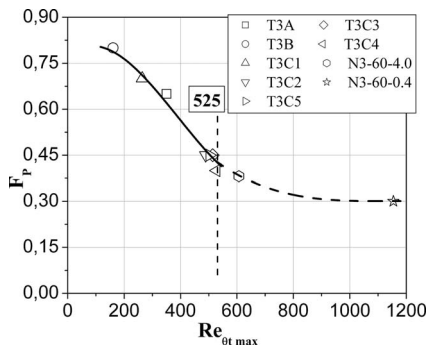

Fig. 4 Evolution of corrected F_P parameter versus $\widetilde{\mathrm{Re}}_{\theta t \max}$
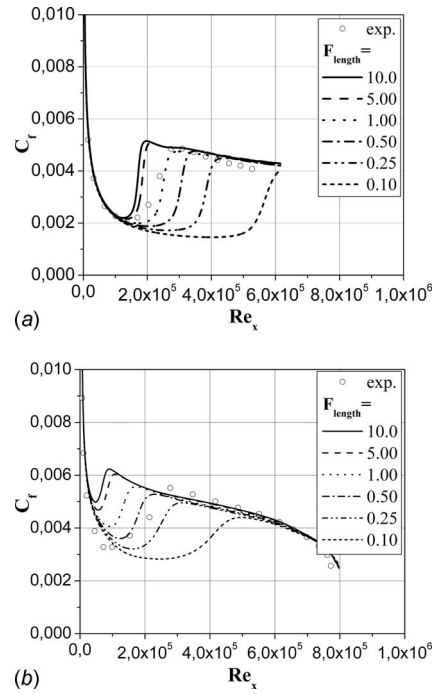
Fig. 5 Influence of F_{length} parameter on transition onset for (a) T3A and (b) T3C1 test cases

Figures 5(a) and 5(b) present the distributions of local friction coefficient C_f versus the consecutive values of F_{length} obtained for T3A and T3C1 test cases. One may notice that the change in the F_{length} parameter influences not only the length of the transition zone but also the onset location. The increase in the F_{length} parameter is accompanied by the shift of onset location toward the leading edge; however for larger values of F_{length}, this shift diminishes. It may be expected that for $F_{length} > 10$ one may hardly see any influence of F_{length} on the solution, as can be seen from a comparison of computations with experiment shown in Figs. 5(a) and 5(b), so large values of F_{length} are not applicable for a correct description of l-t transition. One may also notice that the increase in F_{length} shortens the transition zone, which is indicated by the increased inclination angle (with respect to the ordinate) of the line approximating the local friction coefficient C_f. On the other hand, too small values of this parameter (e.g., $F_{length}=0.1$) increase the length of the transition zone, but at the same time they introduce the nonphysical shift of the onset toward the trailing edge. That is why the selection of the F_{length} parameter should be accompanied by the analysis of correlation for the onset.
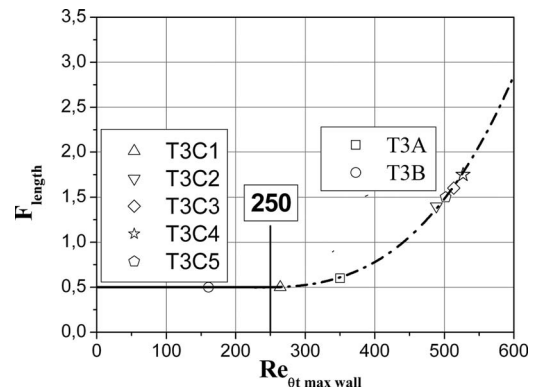
Fig. 6 Evolution of F_{length} parameter versus $\widetilde{\mathrm{Re}}_{\theta t \max}$

Table 1 Inlet conditions

Case	Pressure gradient	U_{in} (m/s)	Tu_{in} (%)	μ_t/μ	μ (kg/ms)	k (m²/s²)	ω (s⁻¹)
T3A	Zero	5.4	3	13.3	1.8×10^{-5}	0.042	232
T3B	Zero	9.4	6.12	100	1.8×10^{-5}	0.488	315
T3C4	Variable	1.37	3	8	1.8×10^{-5}	0.0025	21
N3-60	Variable	8.5	0.4	10.8	1.8×10^{-5}	0.15	924

The F_{length} parameter is also dependent on the global properties of the flow field, and in order to account for this observation it was decided to relate F_{length} to $\widetilde{Re}_{\theta t\,max}$, i.e., with the maximum value of $\widetilde{Re}_{\theta t}$ distribution at the wall. The $\widetilde{Re}_{\theta t\,max}$ values and the corresponding values of F_{length} have been shown in Fig. 6 for all test cases analyzed, and their distribution has been approximated with the following relation:

$$\text{if } ((\widetilde{Re}_{\theta t\,max} < 250))F_{length} = 0.5$$

$$\text{else } F_{length} = \max(0.274 + 0.0039Re_{\theta t\,max} - 2.13 \times 10^{-5}Re_{\theta t\,max}^2$$
$$+ 3.65 \times 10^{-8}Re_{\theta t\,max}^3, 1.75) \qquad (17)$$

The relation proposed above, together with correlations for the onset, supplements the transport equations for intermittency γ and Reynolds number $\widetilde{Re}_{\theta t}$ and forms the complete calculation procedure for l-t transition modeling, which is referred to as ITM in the following part of the paper.

4 Steady Flow Test Cases

For evaluation of the steady flow behavior of the model, several test cases with various inlet and boundary conditions were taken into account. It was decided to select two flat plate zero pressure gradient test cases (T3A and T3B), one test case with variable pressure distribution (T3C4) and the N3-60-0.4 turbine blade test case with inlet turbulence intensity Tu=0.4%.

Geometries T3A and T3B were computed with a structural numerical grid containing 150×150 nodes, while for case T3C4 a grid of 150×200 was used. These grids were selected as a result of grid-independence studies, with particular emphasis placed on the correct reproduction of the transition onset location. For the blade configuration, the computational domain consisted of 30,000 nodes, the structural grid was used in the vicinity of the wall, while a triangle based unstructured grid was used in the freestream. The higher mesh density was required due to the more complex geometry, and again grid-independence tests formed the basis for this choice.

Detailed information on the flow conditions for five test cases analyzed are given in Table 1 together with inlet parameters used in the calculations (i.e., inlet velocity and turbulent intensity). The value of inlet turbulence kinetic energy k was calculated according to

$$k = \frac{3}{2} \cdot U_{in}^2 \cdot Tu_{in}^2 \qquad (18)$$

The specific dissipation rate ω was formulated as follows:
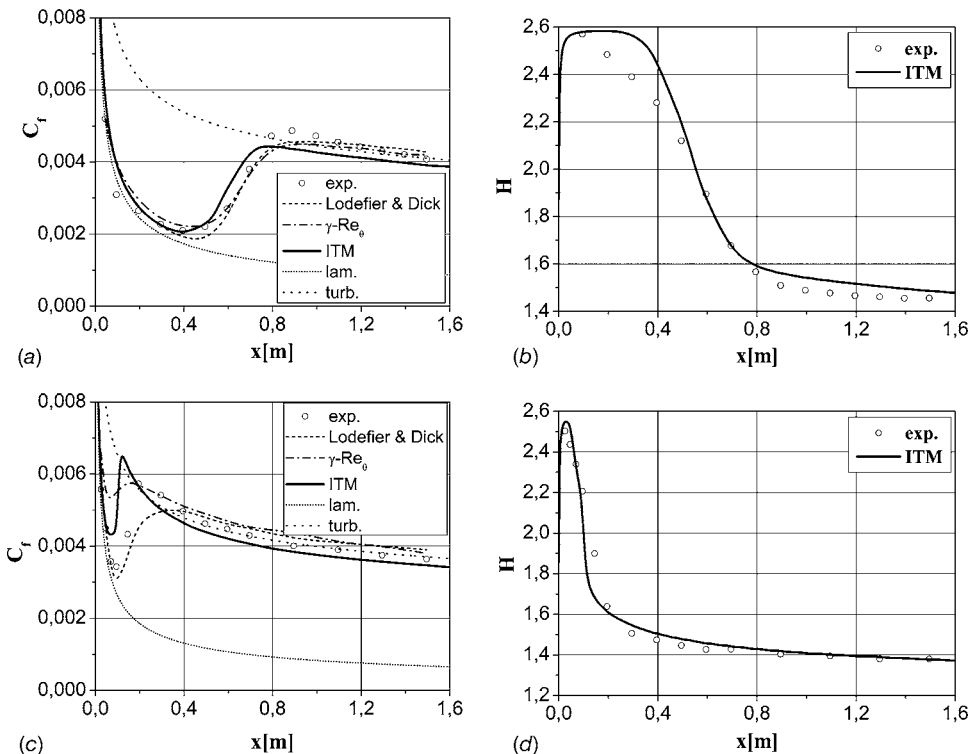
Fig. 7 Evolution of skin-friction and shape factor coefficients for the ((a) and (b)) T3A and ((c) and (d)) T3B test cases
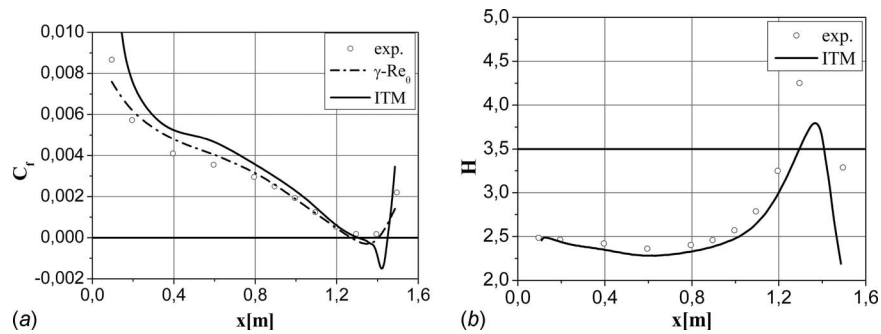
Fig. 8 Evolution of (a) skin-friction and (b) shape factor coefficients for the test case T3C4

$$\omega = \frac{\rho \cdot k}{\mu_t} \quad (19)$$

The boundary condition for γ at a wall was zero normal flux, while at the inlet γ was equal to 1. In order to capture the laminar and transitional boundary layers correctly, the grid had to have a closest to the wall $y+$ value smaller than 1. As it was proved during preliminary tests, if a minimum value of $y+$ was too large (i.e., >5), the transition onset location moved upstream. It is also important to note that the transition onset location proved very sensitive to the advection scheme used for solving the turbulence and transition model equations. For this reason all equations were solved with a bounded second order upwind scheme. Mass conservation was enforced via the SIMPLE pressure-correction algorithm.

Figure 7 shows distributions of local skin-friction coefficient C_f obtained with the use of the proposed model. These results were compared with the experimental data and numerical results obtained by Lodefier and Dick [6] as well as with the results obtained with the original (γ-$Re_{\theta t}$) model of Menter et al. [7]. In Fig. 7 the line marked as "lam" represents the exact Blasius solution, while the line "turb" represents the relation for the turbulent skin friction.

When analyzing the results for the T3A test case (Figs. 7(a) and 7(b)), one may notice a very good agreement between numerical and experimental results both for the transition onset location and for the extent of the transition region. It seems that transition onset location was slightly better reproduced with the new transitional model (ITM) than with other models. However, the slope of the C_f curve (Fig. 7(a)) in the transition area is a bit too steep, which results in a shorter transition region in comparison with Lodefier&Dick and γ-$Re_{\theta t}$ results. This conclusion is confirmed by the analysis of shape factor distribution H (Fig. 7(b)), which in

the range of ($x=0.1–0.45$) attains somewhat higher values in comparison to the experimental results, which indicates too small values of the laminar-turbulent transition length.

The T3B test case is characterized by a high value of inlet turbulence intensity (6.5%); therefore the transition onset must be located just after the leading edge of a flat plate. This statement is confirmed by experimental results, where a decrease in local skin-friction coefficient C_f (Fig. 7(c)) and a drop in shape factor H (Fig. 7(d)) after the leading edge of a flat plate are observed. It should be noted that it is a very demanding test case, characterized by high gradients of boundary layer parameters and short region of laminar-turbulent transition. The changes in local skin-friction parameter C_f in this region are best reflected by numerical results obtained with the use of the Lodefier&Dick model. In the case of the ITM method, the satisfactory transition onset location in comparison to the experiment is seen, while the length of the transition region calculated by the ITM model seems to be too small. Nevertheless, it may be concluded that the ITM model fits experimental data better than the original (γ-$Re_{\theta t}$) model. The quality of the results obtained with the ITM model is additionally confirmed by data from Fig. 7(d), where shape factor distribution is presented.

Figure 8 shows the results for the test case with variable pressure distribution (T3C4). An analysis of the C_f plot suggests the separation of the boundary layer at $x=1.3$ m. Experimental results do not indicate it clearly due to the fact that C_f is very close to zero, which makes it difficult to measure the backflow using a hot-wire technique. In this case the shape factor is a more precise indicator, which is obtained from the entire velocity profile and not only from the point located in the wall vicinity.

When comparing the computations obtained with γ-$Re_{\theta t}$ and ITM models, one may notice a substantial difference in the separation region. The γ-$Re_{\theta t}$ model indicates only a slight trace of
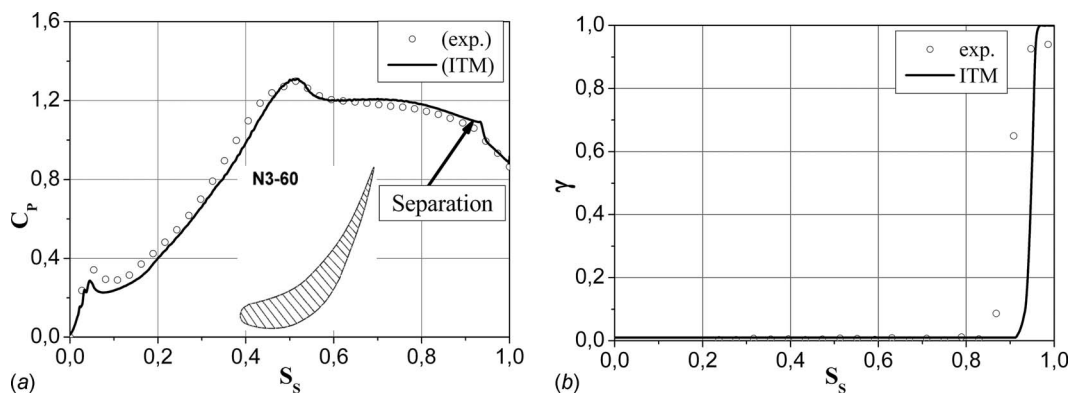
Fig. 9 Evolution of (a) pressure coefficient C_p and (b) intermittency γ for the N3-60-0.4 test case (Tu =0.4%)
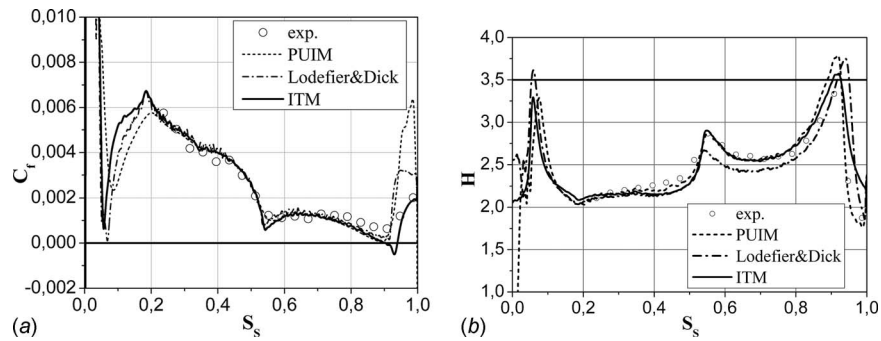
Fig. 10 Evolution of (*a*) skin-friction and (*b*) shape factor coefficients for the N3-60-0.4 test case (Tu=0.4%)

separation and, consequently, a too early onset of transition. In computations with the ITM model, C_f decreases to values as low as -0.0018, which is lower than the experimental value. However, the distribution of the shape parameter H indicates that both the extent and thickness of the separation bubble are still too small in comparison with experiment. One may conclude, therefore, that the ITM model gives in general the better reproduction of the test case considered.

Even more demanding is the turbine test case N3-60-0.4. Figure 9(*a*) presents the pressure coefficient C_p on the suction side of the profile, where one can see a small diffusion area close to the trailing edge. The key variable describing the boundary layer evolution during transition from laminar to turbulent state is the intermittency factor γ. In Fig. 9(*b*) one can notice that numerically obtained intermittency slightly lags the experimental data. The reason is that the intermittency factor determined from the hot-wire signal starts to increase prior to the change in general flow parameters such as skin friction or shape factor, while the numerical γ value has historically been derived from the evolution of global parameters.

When one looks at the shape factor distribution (Fig. 10(*b*)), it may be seen that numerical data follow the experiment almost all over the blade surface. The most important region is the rear part of the profile, where the boundary layer development decides about the magnitude of losses. One may see the qualitatively good agreement between ITM results and experiment, while for the Lodefier&Dick model (dash-dot line) [11], the onset is slightly shifted downstream. On the other hand the PUIM model (dotted

line) overpredicts the C_f (Fig. 10(*a*)) in the turbulent boundary layer. Again the best agreement is obtained with the ITM model.

It could be concluded, therefore, that the formulas for the transition onset and transition length proposed in the paper appear to be sufficiently precise and enable a satisfactory prediction of boundary layer development for various flow configurations.

5 Wake-Induced Cascade Test Case

Flow unsteadiness strongly affects the time dependent location of the laminar-turbulent transition region on the blade surface. The proper modeling of the unsteady flow is therefore a very demanding task for transition modeling.

For further tests of the ITM model, the same N3-60 test cases have been used, but at that time with the presence of upstream wakes interacting with downstream blades. For the simulation of upstream wakes, the moving cylindrical bars were applied in the experiment. The diameter of the bars ($d=4$ mm) was adjusted to produce wakes with characteristic parameters corresponding to those of the real blades.

The self-similar wake profiles, which were defined based on the experimental data, were used in numerical modeling. For the unsteady calculations, the profiles of velocity, turbulent kinetic energy (k), and specific rates of dissipation of turbulent kinetic energy (ω) were prescribed at the inlet to the computational domain.

The mean inlet stagnation pressure and temperature, the inflow angle, and the static pressure at the outlet were the same as for the steady flow. For the unsteady calculations, 800 time steps per
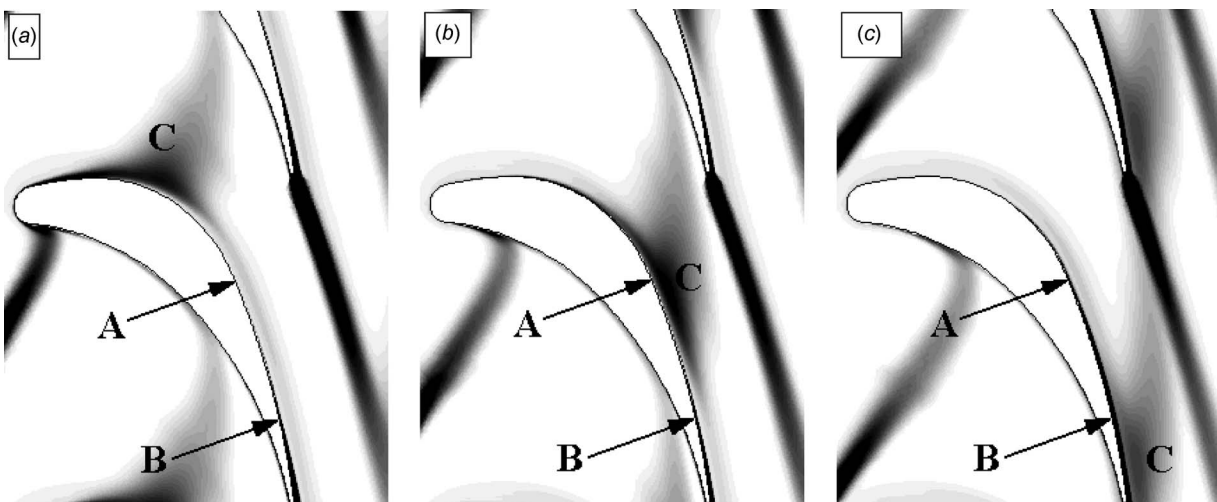
Fig. 11 Instantaneous solutions of turbulent kinetic energy *k* for the N3-60-4.0 test case (A, B, C – see explanation in the text)

wake period were used, which allowed for an accurate simulation of the motion of the wake and for proper modeling of the wake boundary layer interaction. Such a high time resolution was adopted after Lardeau and Leschziner [12], who showed that such a value was needed to obtain a time step independent solution for the bar wake. According to the results from Ref. [13], the number of cells across the wake at the inlet of the blade cascade should be at least 40, and this conclusion was followed in the present computations.

Figure 11 presents instantaneous solutions of turbulent kinetic energy for the N3-60-4.0 test case for three time instants ((a), (b), and (c)), which allow us to trace the development of the wake inside the blade channel. One may notice that the high energy core (C) of the wake is shifted toward the concave edge of the blade, which accelerates the transition on this side. Arrows (A) and (B) show the locations of unsteady and steady transition onsets, respectively.

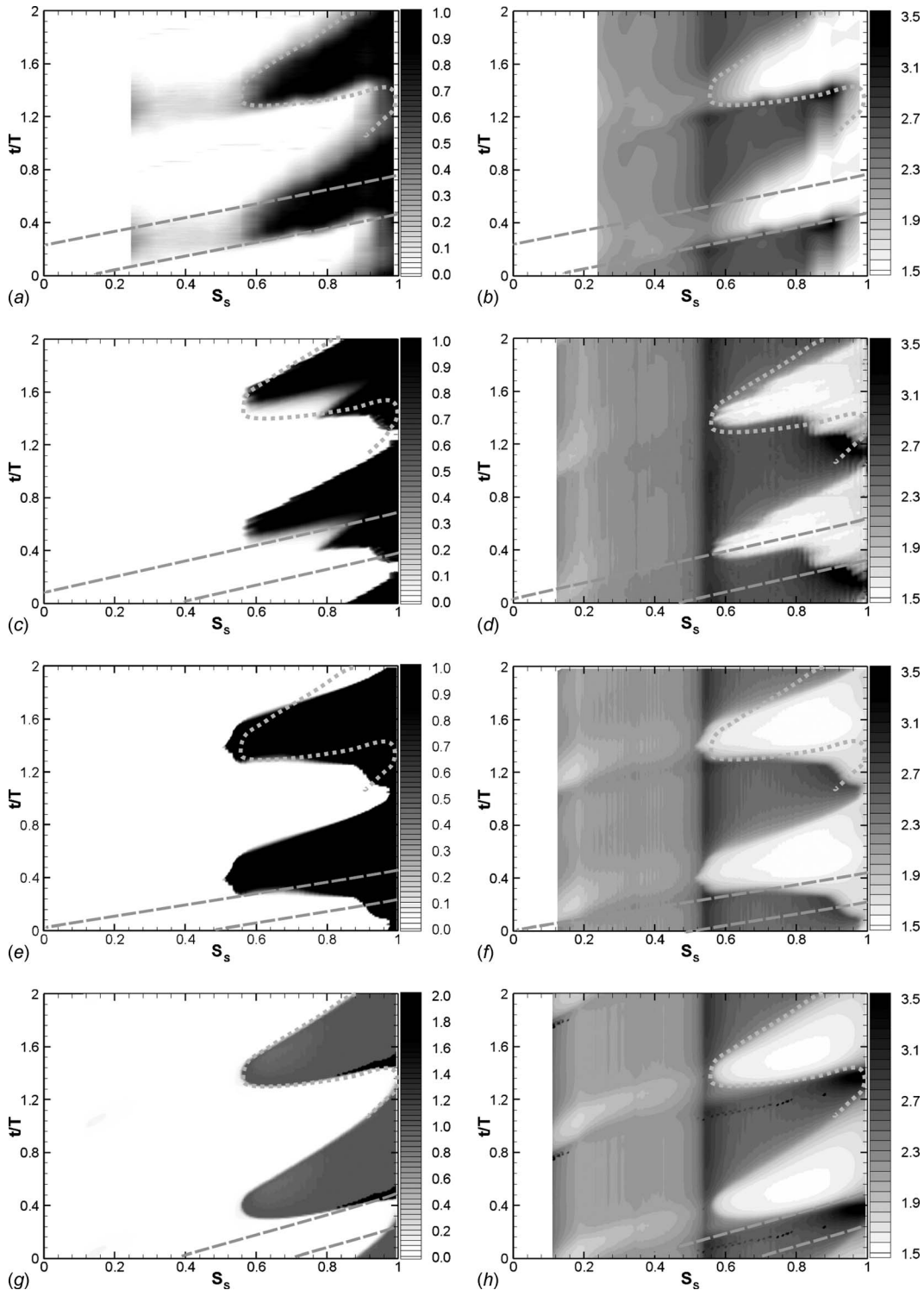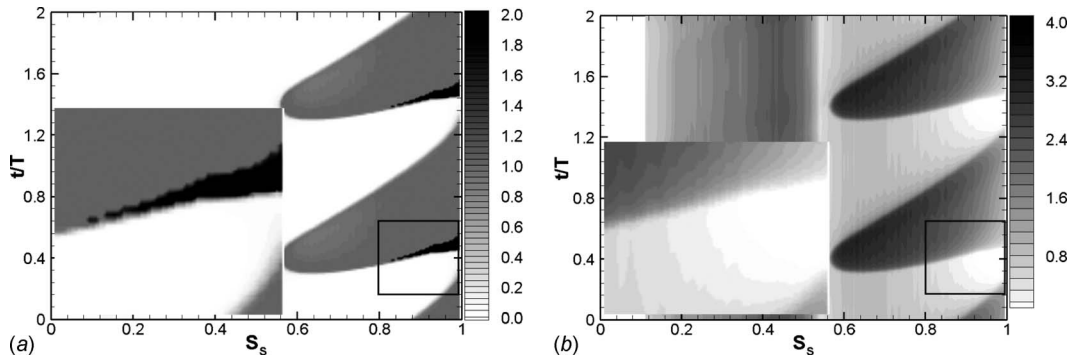The analysis of the response of the boundary layer to the pass-

Fig. 12 *s-t* diagrams over the suction side for N3-60-0.4 (Tu=0.4%) of intermittency (left column) and shape factor (right column)

Fig. 13 *s-t* diagrams over the suction side for N3-60-0.4 (Tu=0.4%) of intermittency (left column) and shear stresses τ_w (right column) obtained with ITM

ing wake is based on two key parameters, i.e., intermittency and shape factors. Intermittency controls the production of turbulent kinetic energy in the turbulence model, and the shape factor characterizes the state of the boundary layer, i.e., whether it is laminar, transitional, turbulent, or separated. Figure 12 presents the comparison of numerical results for intermittency obtained with ITM, PUIM, and Lodefier&Dick models with experiment. The experimentally obtained intermittency was calculated at a distance 0.2 mm from the wall based on hot-wire measurements. The two dashed lines show the location of the wake based on local boundary edge velocity, where the first one represents the path along which the periodic velocity perturbation reaches a maximum, while the second indicates the location of the minimum of the periodic velocity perturbation. The additional dotted line indicates the area of transitional and turbulent wedge induced by the wake. The area was defined based on the ITM model, and it was used for comparative analysis. It should be noticed that the intermittency γ_{eff} for the ITM model was presented using a different scaling than for the experiment and for other two models being compared. The scale from 0 to 2 was used in order to show the action of γ_{sep} on the boundary layer reattachment.

The start of the transition under the wake was found to be almost identical for all models, which show that the onset slightly shifted in time in comparison with the experimental results. There are some differences in the extent of the turbulent wedge and in the transition in between the wakes. One may notice that the wedge is a bit too narrow for PUIM and Lodefier&Dick models.

The experimental data reveal that after the wake passage the transition shifts downstream due to lower freestream turbulence intensity. Moreover, the shape factor in Fig. 12 reveals the trailing edge separation. It should be noticed that it is a very delicate and challenging region for transition models because it is the area

where the turbulent boundary layer state varies from laminar through separated, transitional, and turbulent as the new wake approaches the blade.

In Fig. 13 the *s-t* diagrams of intermittency γ_{eff} and shear stresses obtained with ITM are presented (the white area shows the negative values). On the enlarged picture of shear stresses, one may see that the separation starts for the value of relative coordinate larger than $S_S=0.9$ in between periods of $\tau/T=0.32-0.44$. Further on, in between periods of $\tau/T\approx0.4-0.52$, one may observe a narrow strip of γ_{eff} above 1. The ITM model shows the transition in a separated boundary layer. The separation is also captured by PUIM but not by the Lodefier&Dick model.

The quantitative comparison of the results analyzed above is given in Fig. 14, which presents the time evolution of the intermittency and the shape factor at the relative position $S_s=0.65$. One can notice that the shape factor distributions are similar, concerning not only their shapes but also their levels both under the wake and in between the wakes. Numerically obtained intermittency distributions agree fairly well, and only turbulent wake for PUIM is somewhat too narrow, which supports the conclusions based on field plots (Fig. 12). The only visible difference between experimental and numerical results is a time shift of the turbulent region. According to Ref. [13], it may be explained by the application to the unsteady case of empirical criteria for transition onset, which were derived from the steady case [14]. Physically, transition starts just under the high energy core of the impacting wake (region C in Fig. 11 phase (*b*)), while in numerical environment the transition is activated later as the turbulent wake approaches and elevates the freestream turbulence at the boundary layer edge (phase (*c*) in Fig. 11).

Results presented above confirm that the formulas for the tran-
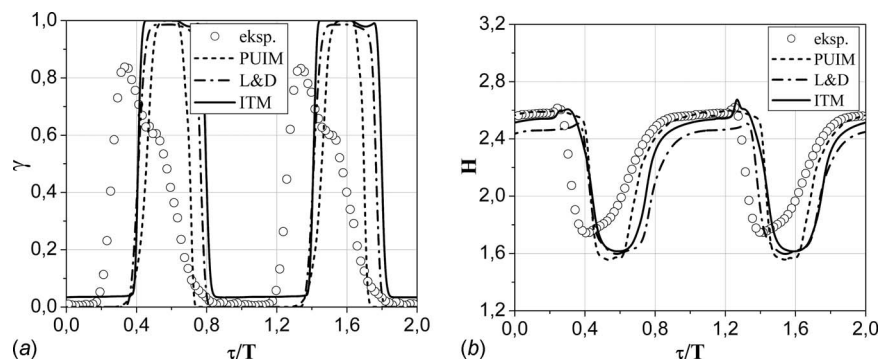
Fig. 14 Time traces of (*a*) intermittency and (*b*) shape factor at the location S_s =0.65 for N3-60-0.4 (Tu=0.4%)

sition onset and transition length proposed in the paper appear to be sufficiently precise and enable an accurate prediction of boundary layer development for various inflow conditions not only for uniform but also for unsteady inflow conditions. The quality of the prediction is at least comparable if not better than other intermittency based models. To confirm the universality of the model, however, further tests on different geometrical configurations are necessary.

6 Conclusion

The paper presents the results of tests and validations of the γ-Re_θ model, which was extended by in-house correlations on onset location and transition length. The correlations developed were based on the ERCOFTAC database and were further validated using experimental data for turbine blade profile N3-60 investigated at Czestochowa University of Technology. The proposed correlations for transition onset and transition length were formulated in terms of $\widetilde{Re}_{\theta t\,max}$, which is a local critical value of $\widetilde{Re}_{\theta t}$ calculated in the wall vicinity and obtained from the transport equation.

The tests proved that the formulas for the transition onset and transition length proposed in the paper appear to be sufficiently precise and enable an accurate prediction of boundary layer development for various flow configurations and inflow conditions. The quality of the prediction is at least comparable if not better than other intermittency based models.

In the last part of this paper, the comparison of the solutions obtained with the model proposed and two models previously given in literature was presented for the case of unsteady wake-induced transition. The start of the transition under the wake was found to be almost identical for all models, and only some minor differences in the extent of the turbulent wedge and in the transition in between the wakes were noticed. The obtained results reveal that for the case considered (i.e., N3-60 turbine blade), the best agreement with experiment was obtained for the ITM model. The universal character of correlations proposed in the paper needs further tests and evaluations; however authors believe that the method proposed may serve as a useful tool for modeling both steady and unsteady l-t transitions on turbomachinery blading.

Acknowledgment

Nomenclature

C_f = skin-friction coefficient
C_p = pressure coefficient, $Cp=(p_{01}-p)/(p_{01}-p_2)$
H = shape factor
k = turbulent kinetic energy
p = local static pressure
p_{01} = inlet total pressure
p_2 = static outlet pressure

Re_θ = momentum thickness Reynolds number
$Re_{\theta c}$ = critical Reynolds number
$Re_{\theta t}$ = transition Reynolds number
Re_V = vorticity Reynolds number
S = strain rate
S_s = streamwise coordinate
t = time
T = wake period
Tu = freestream turbulence intensity
U = velocity
x = distance from the leading edge

Greek Symbols

γ = near-wall intermittency factor
μ_t = turbulent viscosity
μ = molecular viscosity
ρ = density
λ_θ = Thwaites pressure gradient
ω = specific dissipation rate

References

[1] Savill, M., 2002, "New Strategies in Modelling By-Pass Transition," *Closure Strategies for Turbulent Transitional Flows*, B. E. Launder and N. Sandham, eds., Cambridge University Press, Cambridge, UK, pp. 493–521.
[2] Dhawan, S., and Narasimha, R., 1958, "Some Properties of Boundary Layer During the Transition From Laminar to Turbulent Flow Motion," J. Fluid Mech., **3**, pp. 418–436.
[3] Vilmin, S., Savill, M. A., Hodson, H. P., and Dawes, W. N., 2003, "Predicting Wake-Passing Transition in Turbomachinery Using an Intermittency-Conditioned Modelling Approach," 33rd AIAA Fluid Dynamics Conference and Exhibit, Orlando, June.
[4] Elsner, W., Vilmin, S., Drobniak, S., and Piotrowski, W., 2004, "Experimental Analysis and Prediction of Wake-Induced Transition in Turbomachinery," ASME Paper No. GT2004-T53757.
[5] Lardeau, S., and Leschziner, M., 2006, "Modeling of Wake-Induced Transition in Linear Low-Pressure Turbine Cascades," AIAA J., **44**(8), pp. 1854–1865.
[6] Lodefier, K., and Dick, E., 2006, "Modelling of Unsteady Transition in Low-Pressure Turbine Blade Flows With Two Dynamic Intermittency Equations," Flow, Turbul. Combust., **76**, pp. 103–132.
[7] Menter, F. R., Langtry, R. B., Likki, S. R., Suzen, Y. B., Huang, P. G., and Völker, S., 2006, "A Correlation-Based Transition Model Using Local Variables—Part I: Model Formation," ASME J. Turbomach., **128**, pp. 413–422.
[8] Lodefier, K., Dick, E., Piotrowski, W., and Elsner, W., 2007, "Validation of a Dynamic Intermittency Model for the Prediction of Wake-Induced Transition on Turbine Blades," *Proceedings of the Seventh European Turbomachinery Conference*, Athens, pp. 1379–1388.
[9] Medic, G., and Durbin, P. A., 2002, "Toward Improved Prediction of Heat Transfer on Turbine Blades," ASME J. Turbomach., **124**, pp. 187–192.
[10] Zarzycki, R., and Elsner, W., 2005, "The Effect of Wake Parameters on the Transitional Boundary Layer on Turbine Blade," Proc. Inst. Mech. Eng., Part A, **219**, pp. 471–480.
[11] Lodefier, K., Dick, E., Piotrowski, W., and Elsner, W., 2005, "Modelling of Wake Induced Transition With Dynamic Description of Intermittency," *Proceedings of the Sixth European Turbomachinery Conference*, Lille, pp. 730–739.
[12] Lardeau, S., and Leschziner, M., 2005, "Unsteady RANS Modelling of Wake-Blade Interaction: Computational Requirements and Limitations," Comput. Fluids, **34**, (1), pp. 3–21.
[13] Piotrowski, W., Lodefier, K., Kubacki, S., Elsner, W., and Dick, E., 2008, "Comparison of Two Unsteady Intermittency Models for Bypass Transition Prediction on a Turbine Blade Profile," Flow, Turbul. Combust., **81**, pp. 369–394.
[14] Mayle, R. E., 1991, "The Role of Laminar-Turbulent Transition in Gas Turbine Engines," ASME J. Turbomach., **113**, pp. 509–537.

Application of Artificial Neural Networks in Investigations of Steam Turbine Cascades[1]

Krzysztof Kosowski

Karol Tucki

Department of Ship Automatics and Turbine Propulsion,
Gdańsk University of Technology,
Narutowicza 11/12,
80952 Gdańsk, Poland

Adrian Kosowski

Department of Algorithms and System Modeling,
Gdańsk University of Technology,
Narutowicza 11/12,
80952 Gdańsk, Poland

We present the results of numerical tests of artificial neural networks (ANNs) applied in the investigations of flows in steam turbine cascades. Typical constant cross-sectional blades, as well as high-performance blades, were both considered. The obtained results indicate that ANNs may be used for estimating the spatial distribution of flow parameters, such as enthalpy, entropy, pressure, velocity, and energy losses, in the flow channel. Finally, we remark on the application of ANNs in the design process of turbine flow parts, as an extremely fast complementary method for many 3D computational fluid dynamics calculations. By using ANNs combined with evolutionary algorithms, it is possible to reduce by several orders of magnitude the time of design optimization for cascades, stages, and groups of stages.
[DOI: 10.1115/1.3103923]

1 Introduction

Nowadays, 3D calculations of compressible viscous flows through turbine stages are treated as state-of-the-art in turbine design practices. The design process of turbine blades or whole turbine stages, especially based on 3D Navier–Stokes solvers, takes a lot of time. For purposes of optimal turbine stage design, the set of geometrical stage parameters must be defined a priori, while computational fluid dynamics (CFD) analysis for a single variant (depending on the model simplification) may last up to several days on contemporary computers.

Artificial intelligence methods, including those based on artificial neural networks (ANNs), are often used for investigations of complex systems in which the relations between parameters and parts of the system are difficult to describe by explicit functions. For this reason, in recent years they have found application in turbomachinery and power plant technology. For example, in gas and steam turbine power plant diagnostics a number of successful ANN-based approaches have been put forward for the detection of faulty apparatus and estimation of the extent of malfunction [1–8]. ANN methods are also used in simulation models of gas turbine set operations and in the design of gas turbine engines [9]. ANN can also help accelerate the design process for turbine stages.

Some applications have already been proposed, e.g., for optimizing 3D blade profiles by maximizing efficiency with some mechanical constraints [10,11]. An ANN method for designing turbomachinery airfoils based on the underlying pressure distribution was proposed in Ref. [12] while examples of blade shape development and redesign of profiles are presented in Ref. [13]. The results of such calculations reduce computation time by several orders of magnitude in comparison to those obtained using 3D codes.

This paper describes the results of applying ANNs (see, e.g., Ref. [14] for a more detailed description) to determine the flow parameters in channels of turbine nozzles and rotor blades.

In turbomachinery practices most manufacturers apply their own blade profiles of fixed shape, varying only their size and arrangement in the cascade. For this reason, the shape of the blades is not an optimized parameter; however sets of considered reference data must correspond to the particular type of nozzle or rotor blade profiles. The geometry of a cascade of given shape (Fig. 1) is described by the set of parameters $(\beta, z, d, b, \alpha, l)$, where β denotes profile stagger angle, z denotes the number of blades, d is the cascade diameter, b is the profile chord, α represents the flow inlet angle, and l is the blade height.

2 Determining Flow Parameters in Turbine Cascades

The investigations were carried out for a data set of flow and geometrical characteristics of profiles used in HP and IP steam turbines.[2] Calculations using CFD code (FlowER) were then used to obtain distributions of flow parameters (such as pressure, enthalpy, entropy, and steam velocity) in cascade channels, at all sections of the grid. These calculations were performed for each profile in over 600 different geometrical arrangements (for different values of chord, stagger angle, inlet angle, blade height, cascade diameter, and cascade pitch). The results of the calculations were then applied for training an artificial neural network. After the training process was complete, the ANN was applied to predict flow parameters for different sets of geometrical cascade characteristics (about 20% of the data from the calculated knowledge base was not used in the training process but was used as reference test data).

2.1 Structure of the Network. All the tests were performed using three-layer backpropagation networks, implemented in a MATLAB software package [15]. The networks were designed with a linear perceptron structure in the output layer and tangent transformation in the hidden layer. Different network architectures were compared, including feedforward networks (newff), cascade-forward networks (newcf), and Elman networks (newelm). The following training methods were examined: Levenberg–Marquardt (trainlm), resilient backpropagation (trainrp), conjugate gradient methods (trainscg, traincgb, traincgf, traincgp), quasi-Newton methods (trainbfg, trainoss), and a variable learning rate method (traingdx). A detailed description of the network structures and implementation of particular algorithms can be found in Ref. [15]. An exemplary comparison of training and testing outcomes for different network structures and training methods is provided in Table 1 for a nozzle cascade. Similar results were obtained for rotor cascades.

Based on the results of these preliminary investigations, the feedforward network (Fig. 2) with backpropagation and a Levenberg–Marquardt training algorithm was selected as the most suitable solution. Such a network was chosen for further optimization, by setting the number of neurons in the hidden layer and the number of training epochs. For the analyzed data set, the best results were obtained when the number of neurons in the hidden layer was equal to 30. The supervised network training algorithm was applied for 50 epochs, iterated with a learning coefficient of
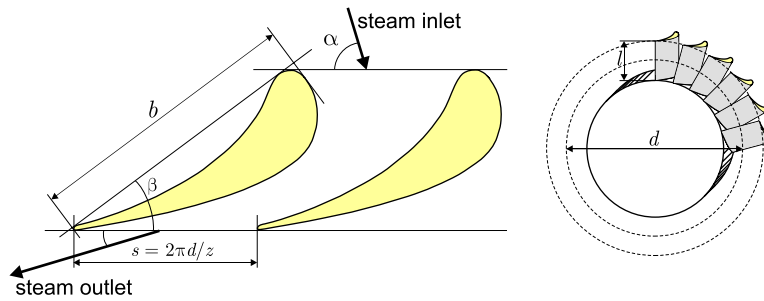
Fig. 1 Geometry of a turbine cascade

0.2 until the relative error was below a threshold of 10^{-3} or the gradient of change was below machine data type precision. This allowed us to reduce relative error values to a level of about 1%.

2.2 Results of Numerical Tests. The enthalpy distribution for an exemplary rotor cascade channel in different axial cross sections is shown in Fig. 3. The enthalpy and velocity component distributions in a nozzle channel in different sections along the nozzle height are presented in Figs. 4 and 5, respectively. In all the cases the results obtained using neural networks are compared with those from the FlowER solver, showing good correspondence. In most cases the prediction errors are under 1%; some examples are provided in Table 2. Analyses of pressure or entropy distribution show very similar results.

The examples presented so far concerned cascade channels formed by relatively short constant cross-sectional blades, but similar methods can be successfully applied for twisted blades and high-performance blades, such as blades with compound lean and compound sweep.

We present an example of such an approach for the ANN-aided design of the cascades of the last turbine stage of a great output steam turbine (see Refs [16,17] for a description). Different variants of nozzle and rotor cascades were calculated by means of the FlowER solver and then an ANN was applied to determine flow characteristics of the modified cascades. The considered modifications were as follows:

- blades with straight lean for different values of angle φ (Fig. 6(a))
- blades with compound lean for different parameters dy, dx of the parabolic part of the trailing edge (Fig. 6(b))
- blades with compound sweep for different values of parameters dy, dx, γ (Fig. 6(c))

All calculations were performed for nominal and off-design parameters (for different volume flow rate at the stage outlet). Exemplary relations of energy loss coefficient ζ as a function of volume flow rate V, obtained when testing the ANN and when using CFD code, are shown in Fig. 7. The loss coefficient ζ is

Table 1 Examples of relative learning errors δ_l, test errors δ_t, and learning time t for different types of neural networks and training algorithms. The given error value is the maximum relative error, taken over all tested parameters, for a nozzle cascade.

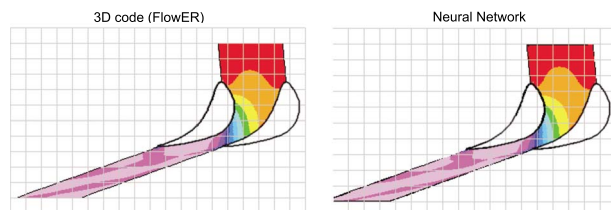|	neurons	newff			newcf			newelm		
		δ_l (%)	δ_t (%)	t (s)	δ_l (%)	δ_t (%)	t (s)	δ_l (%)	δ_t (%)	t (s)
trainlm	20	1.7	3.8	10.8	2.9	35	10.8	2.5	25	19.6
	40	1.2	2.8	11.8	1.5	29	11.7	1.6	28	173.6
	60	1.2	3.7	12.8	1.0	51	14.0	1.6	24	1052.3
trainrp	20	7.5	15.8	9.8	53	64	11.9	44	64	9.5
	40	8.1	17.8	10.1	49	162	10.1	25	62	8.9
	60	7.2	8.9	10.5	43	90	10.5	19	90	10.5
trainscg	20	7.9	12.1	9.9	37	57	9.9	24	61	9.7
	40	4.7	6.0	10.3	30	122	10.4	20	58	10.2
	60	4.4	8.6	11.0	27	62	11.1	18	54	11.0
traincgb	20	6.9	10.1	10.0	38	69	10.0	25	67	10.0
	40	7.8	16.1	10.8	28	45	10.6	19	60	10.7
	60	3.5	9.8	11.4	23	45	11.6	13	51	12.0
traincgf	20	6.7	13.8	10.1	38	37	10.0	25	60	9.9
	40	3.4	6.0	10.7	36	45	10.6	18	28	10.8
	60	3.2	8.8	11.4	28	64	11.5	14	51	12.0
traincgp	20	5.5	11.9	10.0	40	40	10.1	29	65	9.9
	40	4.5	15.1	10.6	34	54	10.6	18	50	10.8
	60	4.3	16.1	11.3	27	59	11.5	16	38	12.1
trainbfg	20	3.8	4.8	10.2	34.0	64	10.2	22.0	46	17.3
	40	2.6	6.1	13.1	17.6	47	16.1	11.1	45	212.3
	60	1.8	10.6	22.2	8.2	22	27.7	4.5	35	2163.2
trainoss	20	6.5	14.7	9.9	45	64	9.9	34	64	9.9
	40	5.6	8.9	10.3	39	76	10.6	24	63	10.5
	60	5.2	14.9	11.3	34	90	11.4	17	43	11.7
traingdx	20	27.0	24.1	9.7	148	118	9.8	135	121	9.4
	40	25.0	18.0	10.0	147	190	10.0	92	114	9.9
	60	18.5	30.6	10.4	147	186	10.5	65	61	10.5
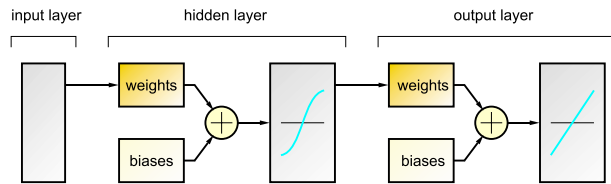
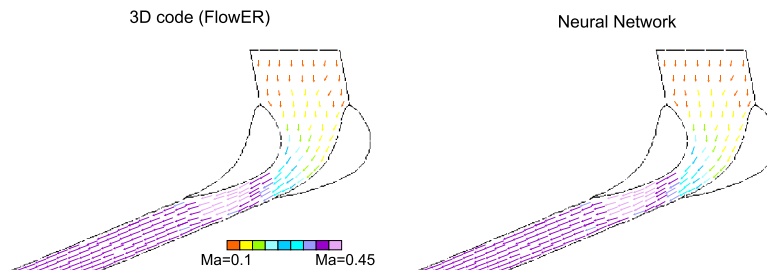**Fig. 2** **Schematic of a feedforward network** (**according to Ref.** [**15**])

understood here as the ratio of the enthalpy loss to the total enthalpy drops in the cascade. Discrepancies between the values obtained from the ANN and the reference values are within 0.5%.

Fig. 3 **A comparison of enthalpy distribution predicted using ANN and calculated by the FlowER solver at the axial section at 62% of the rotor blade channel**

Fig. 4 **A comparison of enthalpy distribution predicted using ANN and calculated by the FlowER solver at the section at 30% of nozzle channel height, counting from the hub**
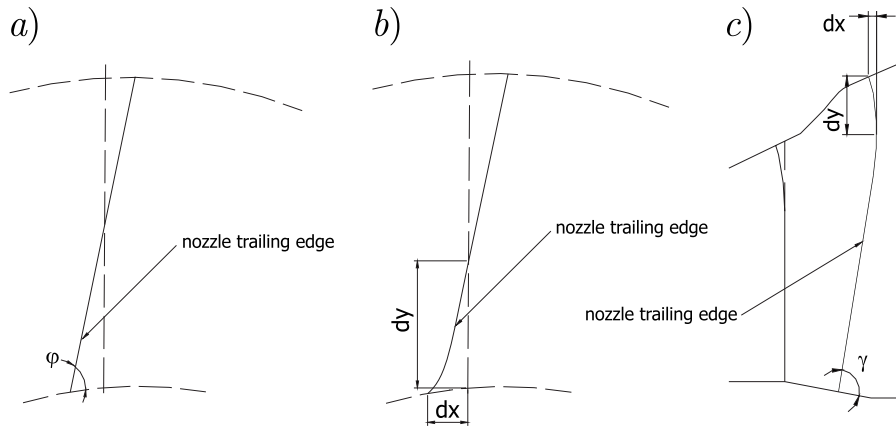
3 Conclusions and Applications

The performed calculations and simulations have proven that artificial neural networks can be applied to estimate the flow parameters of nozzle and rotor blade cascades of steam turbine stages. The main advantage of this approach is the time required for computation: whereas simulating a single case using 3D CFD code usually takes hours of CPU time, an ANN provides a nearly instantaneous response on the same machine. This allows for a substantial acceleration of the process of designing the flow part of a steam turbine. Of course, similar conclusions can be obtained when analyzing other types of flow machinery.

The correct functioning of the ANN requires a well-chosen initial database. The type of applied neural network has a major influence on the quality of the obtained results; all results presented herein correspond to the network configuration discussed in Sec. 2. For an exemplary set of data, application of teaching methods different from feedforward backpropagation, such as cascade-forward backpropagation or Elman backpropagation, leads to relative prediction errors of up to 30%, as compared with errors not exceeding 2.5% for feedforward backpropagation (Table 1).

3.1 ANN-Aided Turbine Cascade Design. It has to be emphasized that when performing calculations using CFD codes we assumed that all geometrical parameters are given at input, while the flow parameters, such as flow rate and efficiency, are sought. This is not the case, which can be directly applied to a design task. Usually we know the mass flow rate G and need to determine some of the missing geometrical parameters (for example, blade height l) and cascade loss coefficient ζ. Such a problem could be solved by an ANN of the form $(l, \zeta) = f(\beta, z, d, b, \text{Ma}, \alpha, G)$, where Ma denotes the Mach number at the cascade outlet.

In the performed simulations, the relative error of prediction of a trained ANN for test cases from outside the training set is presented in Fig. 8. In most cases the discrepancy between the results of ANN and CFD is equal to about 0.2–0.5%, a value negligible when taking into account the simplifications of the model and inaccuracy of numerical calculations.

3.2 ANN-Aided Turbine Stage Design. The proposed ANN-based method of investigation and design of nozzle and rotor

Fig. 5 **A comparison of velocity component distribution predicted using ANN and calculated by the FlowER solver at the section at 29% of nozzle channel height, counting from the hub**

Table 2 **Examples of maximum values of relative error of enthalpy and velocity values predicted using ANN for different cross sections**

Tested value	Relative error for different sections			
enthalpy, axial sections	0.35%	0.39%	0.44%	0.59%
(section location in % of channel width)	(23%)	(43%)	(62%)	(82%)
enthalpy, along blade height	0.48%	0.40%	0.56%	0.88%
(section location in % of blade height)	(30%)	(48%)	(66%)	(84%)
velocity, along blade height	0.93%	0.61%	0.91%	0.61%
(section location in % of blade height)	(29%)	(48%)	(66%)	(85%)

Fig. 6 Variants of nozzle modification: (*a*) straight lean, (*b*) compound lean, and (*c*) compound sweep
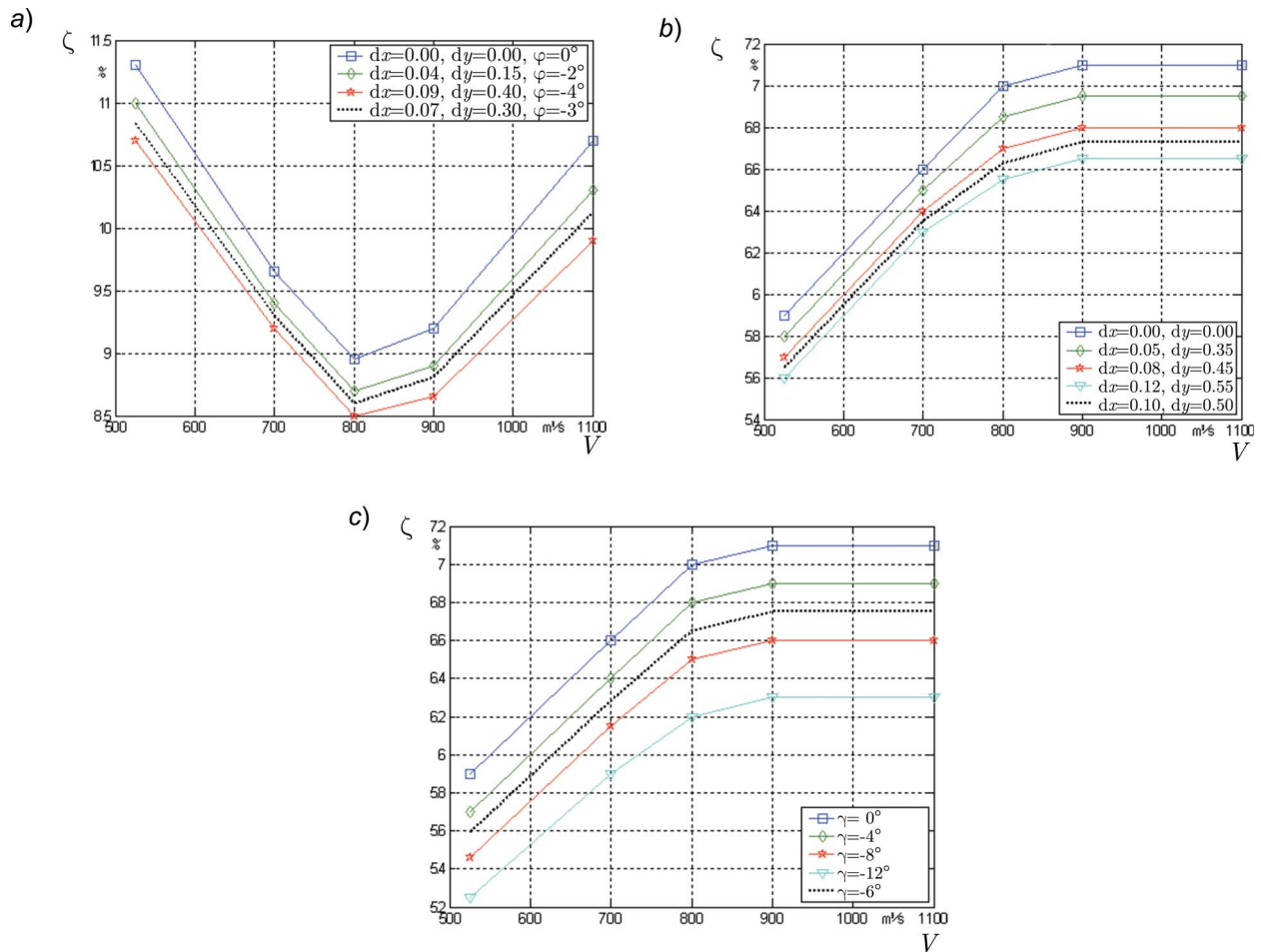

Fig. 7 Examples of relations between energy losses ζ and volume flow rate V at the stage outlet, used for training (solid lines; computed by CFD code) and testing (dotted lines) the ANN for different types of cascades: (*a*) rotor blades with straight lean, (*b*) nozzles with compound lean, and (*c*) nozzles with compound sweep. Test results obtained from ANN and CFD code for the same parameters are indistinguishable in the graph.
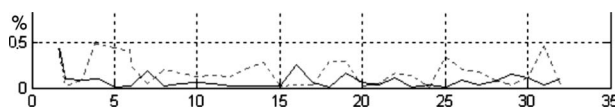
Fig. 8 Relative prediction errors of proposed neural networks for a test set of 32 real world cascade arrangements (solid line—prediction of cascade losses ζ; dashed line—prediction of blade height *l*)

blade cascades can be applied for designing a turbine stage or a group of turbine stages. An example of a group of 6 steam turbine stages designed using such a method (based on a genetical algorithm) is shown in Fig. 9. In this case, the design process was performed assuming known values of: total enthalpy drop in the group of stages, steam parameters at group inlet, constant value of hub diameter (rotor of disk type). For each cascade, we obtained
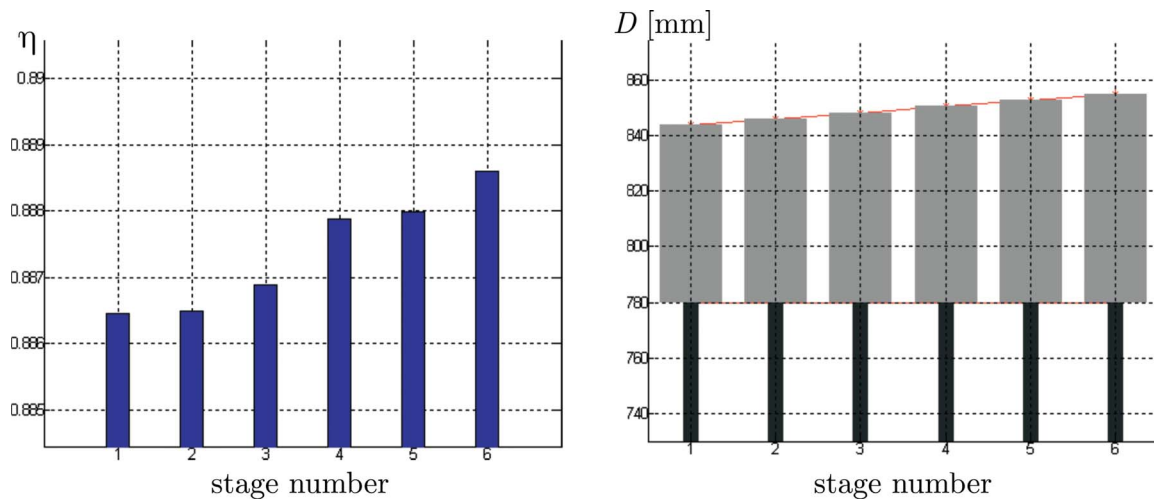
Fig. 9 Example of overall efficiency η of particular stages and schema of rotor blades of a group of six steam turbine stages designed using ANN and evolutionary algorithms

values of stagger angles, chords, blade heights, and the number of blades, leading to the highest overall efficiency of the designed group of stages.

It is important to point out that, whereas classical design using CFD computations sometimes takes several days to compute the optimal parameters of a single stage geometry, the implemented ANN-based heuristic algorithms produces a solution in a matter of seconds. By performing the calculations in a multiprocessor environment (parallel computing), it is possible to further reduce computational time, and enable real-time interaction with the designer. For the stage group shown in Fig. 9, the entire optimization process on an eight-processor machine lasted under a minute.

Acknowledgment

References

[1] DePold, H. R., and Gass, F. D., 1998, "The Application of Expert Systems and Neural Networks to Gas Turbine Prognostics and Diagnostics," ASME Paper No. 98-GT-101.
[2] Gluch, J., 1997, "Flow and Heat Diagnostic Analysis for a Group of Steam Turbine Stages," *Proceedings of the Second European Conference on Turbomachinery*, Antwerpen.
[3] Gluch, J., and Krzyzanowski, J., 2002, "Application of Preprocessed Classifier Type Neural Network for Searching of Faulty Components of Power Cycles in Case of Incomplete Measurement Data," ASME Paper No. GT-2002-30028.
[4] Joly, R. B., Ogaji, S. O. T., Singh, R., and Probert, S. D., 2004, "Gas-Turbine Diagnostics Using Artificial Neural-Networks for a High Bypass Ratio Military Turbofan Engine," Appl. Energy, **78**(4), pp. 397–418.
[5] Niebur, D., 1995, "Artificial Neural Networks for Power Systems," CIGRE Task Force 38–06–06 Report, Electra, **159**, pp. 76–101.
[6] Pong-Je Lu, P. J., Zhang, M. C., Hsu, T. C., and Jin Zhang, J., 2000, "An Evaluation of Engine Faults Diagnostics Using Artificial Neural Networks," ASME Paper No. 2000-GT-0029.
[7] Volponi, A. J., DePold, H., Ganguli, R., and Chen, D., 2000, "The Use of Kalman Filter and Neural Network Methodologies in Gas Turbine Performance Diagnostics: A Comparative Study," ASME Paper No. 2000-GT-0547.
[8] Willis, M. J., 1992, "Artificial Neural Networks in Process Estimation and Control," Automatica, **28**(6), pp. 1181–1187.
[9] Lazzaretto, A., and Toffolo, A., 2001, "Analytical and Neural Network Models for Gas Turbine Design and Off-Design Simulation," International Journal of Applied Thermodynamics, **4**(4), pp. 173–182.
[10] Pierret, S., 1999, "Designing Turbomachinery Blades by Means of the Function Approximation Concept Based on Artificial Neural Network, Genetic Algorithms, and Navier–Stokes Equations," Ph.D. thesis, Von Karman Institute for Fluid Dynamics, Belgium.
[11] Pierret, S., and Van Den Braembussche, R., 1998, "Turbomachinery Blade Design Using a Navier–Stokes Solver and Artificial Neural Network," ASME Paper No. 98-GT-4.
[12] Rai, M. M., and Madavan, N. K., 1998, "Application of Artificial Neural Networks to the Design of Turbomachinery Airfoils," AIAA Paper No. AIAA-1998-1003.
[13] Rai, M. M., and Madavan, N. K., 2000, "Aerodynamic Design Using Neural Networks," AIAA J., **38**(1), pp. 173–182.
[14] Fausett, L. V., 1994, *Fundamentals of Neural Networks: Architectures Algorithms and Applications*, Prentice-Hall, Englewood Cliffs, NJ.
[15] Demuth, H., Beale, M., and Hagan, M., 2008, *Neural Network Toolbox User's Guide*, The MathWorks Inc., Natick, MA.
[16] Lampart P., 2002, "Numerical Optimisation of Stator Blade Sweep and Lean in an LP Turbine Stage," ASME Paper No. IJPGC-2002–26161.
[17] Lampart, P., and Yershov, S., 2003, "Direct Constrained CFD-Based Optimization of Three-Dimensional Blading for the Exit Stage of a Large Power Steam Turbine," ASME J. Eng. Gas Turbines Power, **125**(1), pp. 385–390.